UNIVERSITY OF TRENTO

Doctoral School in Civil, Environmental and Mechanical Engineering

Curriculum 3. Modelling and Simulation

Patrick Covi

Multi-hazard analysis of steel structures subjected to fire following earthquake

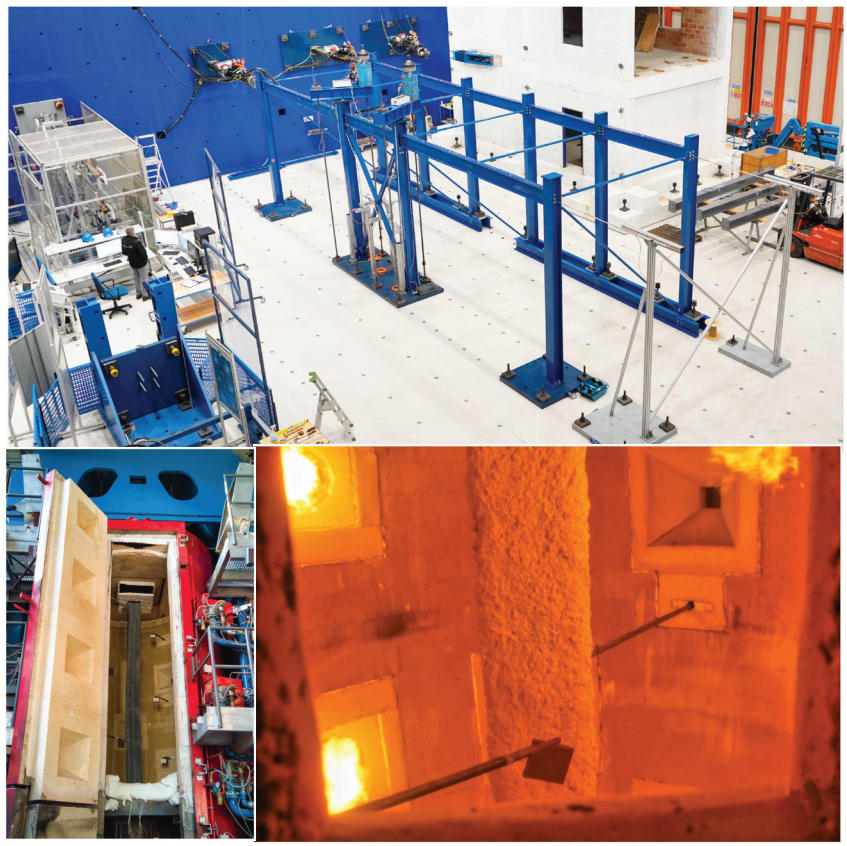

July 2021 - Doctoral thesis

UNIVERSITY OF TRENTO - Italy
Department of Civil, Environmental and Mechanical Engineering

Doctoral School in Civil Enviromental and Mechanical Engineering
Topic 3. Modelling and simulation - XXXIII cycle 2017/2020

Doctoral Thesis - July 2021

Patrick Covi

Multi-hazard analysis of steel structures subjected to fire following earthquake

Supervisor
Dr. Nicola Tondini, University of Trento, Italy

Credits of the cover image EQUFIRE project.

University of Trento
Doctoral School in Civil, Environmental and Mechanical Engineering
http://web.unitn.it/en/dricam
Via Mesiano 77, I-38123 Trento
Tel. +39 0461 282670 / 2611 - dicamphd@unitn.it

"It is difficult to say what is impossible, for the dream of yesterday is the hope of today and the reality of tomorrow."

Robert H. Goddard

Acknowledgements

My deepest gratitude goes first and foremost to my supervisor Prof. Nicola Tondini for his constant encouragement and guidance during my PhD study. Besides my supervisor, I would like to thank Prof. Oreste Salvatore Bursi and Prof. Giuseppe Abbiati for their expertise and precious advice during my PhD years.

I should like to extend my warmest thanks to my Family, who always supported my decisions.

I am also thankful to the European Laboratory for Structural Assessment (ELSA) of the Joint Research Centre as well as to Georgios Tsionis, Pierre Pegon, Marco Lamperti Tornaghi, Francisco Javier Molina, Artur Pinto, Martin Poljansek and Patrick Petit for their invaluable contribution to the experimental campaign and expertise.

I would like thank Dr. Ing. Manfred Korzen, who gave me the opportunity to spend valuable time at the Fire Engineering Laboratory of the Federal Institute for Materials Research and Testing (BAM) (Bundesanstalt für Materialforschung und -prüfung) as well to Sven Riemer, KaiUwe Ziener, F. Klemmstein, B. Klaffke, I.Uzelac, F Kiesel and Sascha Hothan for their invaluable contribution to the experimental campaign.

Finally a special thanks to all my colleagues along the way (Valentina Piccolo, Luca Possidente, Chiara Nardin, Roberto Andreotti, Giulia Giuliani, Lei Xiao, Rocco Di Filippo, Angela Beltempo, Jerome Randaxhe, Francesco Basone, Lorenzo Monaco) and to all my friends.

Publications

Journal Papers

- Abbiati G., Covi P., Tondini N., Bursi O.S, Stojadinović B. “A Real-Time Hybrid Fire Simulation Method Based on Partitioned Time Integration", Journal of Engineering Mechanics, 2020

Conference Papers

- P. Covi , G. Abbiati , N. Tondini , O.S. Bursi , B. Stojadinovic “A STATIC SOLVER FOR HYBRID FIRE SIMULATION BASED ON MODEL REDUCTION AND DYNAMIC RELAXATION”, SiF 2020– The 11th International Conference on Structures in Fire The University of Queensland, Brisbane, Australia, (original: June 24-26, 2020, postponed online to November 30 and December 1-2, 2020) Award: 2nd place “Best Student Paper Award at Structure in Fire 2020 conference”.

- Patrick Covi, Nicola Tondini, Manfred Korzen, Georgios Tsionis. “Hybrid fire following earthquake tests on fire protected steel columns” - EMI2020 Engineering Mechanics Institute Conference and Probabilistic Mechanics & Reliability Conference New York, New York (original: May 26-29, 2020, postponed May 25–28, 2021)

- Patrick Covi, Nicola Tondini, Manfred Korzen, Georgios Tsionis. “Numerical-experimental analysis of a braced steel frame subjected to fire following earthquake” Eurosteel 2020, (original: September, 2020, postponed 1-3 September 2021)

- M. Lamperti Tornaghi, G. Tsionis, P. Pegon, J. Molina, M. Peroni, M. Korzen, N. Tondini, P. Covi , G. Abbiati , M. Antonelli, B. Gilardi “Experimental study of braced steel frames subjected to

fire after earthquake", 17th World Conference on Earthquake Engineering, 17WCEE, Sendai, Japan - September 13th to 18th 2020 (submitted, publication delayed on on September 2021)

Other

- M. Lamperti Tornaghi, G. Tsionis, P. Pegon, J. Molina, M. Peroni, M. Korzen, N., Riemer S., Ziener, K.U., Tondini, P. Covi , G. Abbiati , M. Antonelli "EQUFIRE: Multi-hazard performance assessment of structural and non-structural components subjected to seismic action and fire following earthquake using hybrid simulation", SERA proceedings, 2020
- Covi P., Tondini N. "What is Hybrid testing and geographically distributed hybrid testing?", SERA Project, Project. No: 730900, H2020-EU – Seismology and Earthquake Engineering Research Infrastructure Alliance for Europe, Fact sheet 2, Spring 2019. Published on SERA website.

Additional Relevant Publications

In addition to the published works that formed the research chapters of this thesis, a number of other co-authored publications were relevant, but did not form part of the thesis itself. The bibliographic details for these papers are:

Conference Papers

- H. Crowley, D. Rodrigues, V. Silva, V. Despotaki, L. Martins, X. Romão, J.M. Castro, N. Pereira, A. Pomonis, A. Lemoine, A. Roullé, B. Tourlière, G. Weatherill, K. Pitilakis, L. Danciu, A.A. Correia, S. Akkar, U. Hancilar, P. Covi "The European Seismic Risk Model 2020 (ESRM 2020)", ICONHIC2019, 2nd International Conference on Natural Hazards & Infrastructure - 23-26 June, 2019, Chania, Greece

- R. Di Filippo, G. Abbiati, O. Saynginer, P. Covi, O.S. Bursi, F. Paolacci, "Numerical surrogate model of a coupled tank-piping system for seismic fragility analysis with synthetic ground motions " - ASME PVP 2019, 14-19 July 2019, San Antonio, Texas

DELIVERABLE/MILESTONE/OTHER

- Crowley H., Rodrigues D., Despotaki V., Silva V., Covi P., Pitilakis K., Pitilakis D., Riga E., Karatzetzou A., Romão X., Castro J.M, Pereira N., Hancilar U., “Methods for Developing European Residential Exposure Models”, Deliverable D26.2 published on SERA website and already submitted to SERA intranet platform on April 30, 2018

- Tsionis G., Santos J.P, Safak E., Atakan K., Bursi O.S, Covi P., Taylor C., “The potential for city-laboratory based multi-hazard research and proposals for development and evaluation studies”, Milestone M27.1 to be published on SERA website and already submitted to SERA intranet platform on August 2, 2018.

- Bursi, O. S., Covi P. et al., "Enhanced HDS due to order reduction, reduced epistemic uncertainties and complementary use of offline dynamic substructuring methods”, Deliverable D27.1, SERA Project, Project. No: 730900, H2020-EU – Seismology and Earthquake Engineering Research Infrastructure Alliance for Europe, January 2019. Published on SERA website.

- João Pedro Santos, Erdal Safak, Kuvvet Atakan, Oreste S. Bursi, Patrick Covi, Rocco di Filippo. “Assessment of the potential for city-laboratory based multihazards research and a long-term development route map” Deliverable D27.3, SERA Project, Project. No: 730900, H2020-EU – Seismology and Earthquake Engineering Research Infrastructure Alliance for Europe, April 2020. Published on SERA website.

List of abbreviations

- BAM - Federal Institute for Materials Research and Testing (Bundesanstalt für Materialforschung und -prüfung).
- ELSA - European Laboratory for Structural Assessment.
- EQUFIRE - Multi-hazard performance assessment of structural and non-structural components subjected to seismic action and fire following earthquake using hybrid simulation.
- FFE - Fire Following Earthquake.
- HES Hybrid earthquake simulation.
- HFS Hybrid fire simulation.
- JRC - Joint Research Centre.
- NIST - National Institute of Standards and Technology.
- NS - Numerical substructure.
- PS - Physical substructure
- RT-HFS Real time Hybrid fire simulation.
- SERA - Seismology and Earthquake Engineering Research InfrastructureAlliance for Europe.
- UNITN - University of Trento.

Contents

1 Introduction **1**
1.1 Purpose and scope of this research 2
1.2 Organization of the thesis 2
1.3 SERA 5
1.3.1 EQUFIRE project 7
Description of the original tests plan 9
Description of the modified tests plan 11
1.4 Historical events of FFE 12

2 State of the art **19**

3 EQUFIRE: design and numerical simulations **27**
3.1 Overview and Design of the prototype Buildings 27
3.1.1 Introduction 27
3.1.2 Structural Design Loads 29
3.1.3 Structural Design Loads 30
3.1.4 Snow load 31
3.1.5 Wind load 31
Peak velocity pressure 31
Distribution of external wind pressure on the walls 32
Distribution of external wind pressure on the roof 34
3.2 Seismic Hazard 35
3.3 Masses 38
3.4 Structural Analyses 39
3.4.1 Linear static 3D analysis 39
3.4.2 Linear dynamic 3D analysis 42
3.4.3 The period of the structure (Model A) 43
3.4.4 Bracing members 46
3.5 Columns (Model B) 47
3.5.1 Internal columns (Model B) 47
3.5.2 External columns (Model B) 49

3.6 Beams . . . 49
3.7 Internal beams . . . 50
Shear . . . 51
Bending and shear . . . 51
3.7.1 External beams . . . 51
Combined bending and axial strength checks . . . 51
Shear . . . 52
Bending and shear . . . 52
3.7.2 External and Internal beams for JRC setup . . . 52
3.10.3.1 Combined bending and axial strength checks . . . 52
Shear . . . 53
Bending and shear . . . 53
3.8 LAB Connections . . . 53
3.9 Ground Motions . . . 55
3.9.1 Ground Motion Record Set . . . 55
3.10 Numerical simulations . . . 59
3.10.1 Modal analyses . . . 62
3.10.2 Non-linear static analysis (Pushover) . . . 63
3.10.3 Non-linear dynamic analysis . . . 63
3.11 FFE analysis . . . 69
3.12 Conclusions . . . 70

4 Hybrid fire simulation dynamic relaxation component-mode synthesis partitioned time integration steel frame 73
4.1 Introduction . . . 73
4.1.1 Background and motivation . . . 74
4.1.2 Scope and organization . . . 76
4.2 Description of the RT-HFS method . . . 78
4.2.1 Dynamic relaxation and component-mode synthesis . . . 79
4.2.2 The Gravouil-Combescure algorithm with Localized-Lagrange multipliers . . . 81
4.2.3 Numerical validation . . . 89
4.3 Case study: Hybrid fire simulation of a virtual steel frame 92
4.3.1 Description of the case study . . . 92
4.3.2 Implementation of the virtual RT-HFS . . . 93
4.3.3 Results . . . 96
4.4 Conclusions . . . 100
4.5 Acknowledgements . . . 101

5 A static solver for Hybrid Fire Simulation based on model reduction and dynamic relaxation 105
5.1 Introduction . . . 105
5.2 HYBRID FIRE SIMULATION ALGORITHM . . . 106
5.3 VIRTUAL REAL-TIME HYBRID FIRE TEST . . . 112
5.3.1 EQUFIRE case study description . . . 112
5.3.2 FE models and Substructuring . . . 113
5.4 RESULTS AND COMPARISON . . . 115
5.5 Conclusion . . . 119

6 Fire following earthquake tests at BAM 123
6.1 Introduction . . . 123
6.2 Experimental Set-up . . . 123
6.2.1 Equivalent stiffness of the numerical substructure during the fire events . . . 128
6.3 Procedure . . . 133
6.4 Experimental tests and results . . . 134
6.4.1 Test #0 Column E . . . 134
6.4.2 Test #1 Column A . . . 143
6.4.3 Test #2 Column B . . . 152
6.4.4 Test #4 Column C . . . 165
6.4.5 Test #5 Column D . . . 176
6.5 Photogrammetry 3D model . . . 187
6.6 Main outcomes and discussion . . . 189

7 Numerical-experimental analysis of a braced steel frame subjected to fire following earthquake 191
7.1 Introduction . . . 191
7.2 SERA EQUFIRE project . . . 192
7.3 Case study . . . 193
7.3.1 Design of the prototype building . . . 193
7.3.2 Set of accelerograms . . . 194
7.4 Numerical models . . . 196
7.4.1 Model #2D_OPENSEES . . . 196
7.4.2 Model #3D_OPENSEES . . . 197
7.4.3 Model #3D_SAFIR . . . 198
Beam element . . . 199
Shell element . . . 200
7.4.4 Fire following earthquake simulation . . . 201
7.5 FFE tests at BAM . . . 202
7.5.1 Experimental setup . . . 202

7.5.2 Equivalent stiffness of the numerical substructure during the fire events . . . 204
7.6 Model calibration . . . 212
7.7 Opensees calibrated model . . . 217
7.7.1 Calibration . . . 217
7.7.2 Results . . . 218
7.8 Safir calibrated model . . . 219
7.8.1 Thermal Model (SAFIR) . . . 219
7.8.2 Calibration checks . . . 220
7.8.3 Results . . . 222
BAM Test #A . . . 222
BAM Test #E . . . 224
BAM Test #B . . . 225
BAM Test #C . . . 226
BAM Test #D . . . 227
7.9 Conclusion . . . 228

8 Seismic pseudo-dynamic tests at JRC 231
8.1 Introduction . . . 231
8.1.1 ELSA laboratory JRC . . . 231
8.2 Experimental programme and setup at JRC . . . 232
8.3 Dynamic substructuring of the EQUFIRE frame . . . 235
8.3.1 OpenSees model . . . 235
Modal analysis . . . 236
Pushover . . . 237
Non-linear dynamic analysis: ACC6_NS . . . 237
8.3.2 MATLAB model . . . 239
8.4 Simulation algorithm for the hybrid tests . . . 242
8.4.1 Time integration scheme for hybrid simulation . 242
8.4.2 Virtual hybrid earthquake simulation . . . 244
8.5 Experimental tests . . . 248
8.5.1 Frame #A . . . 248
8.5.2 Frame #B . . . 256
8.5.3 Frame #C . . . 266
8.5.4 Frame #D . . . 276
8.6 Comparison Virtual HES simulation versus experimental tests . . . 288
8.6.1 Frame #A . . . 288
8.6.2 Frame #B . . . 290
8.6.3 Frame #C . . . 292
8.7 Photogrammetry 3D models . . . 294
8.8 Main outcomes and discussion . . . 298

9 Calibration of the finite element numerical model with experimental data of the JRC tests. 301
9.1 Introduction . . . 301
9.2 Advanced 3D frame model . . . 301
9.2.1 SCBF connections . . . 301
9.2.2 Finite element model . . . 306
9.3 Numerical finite element models comparison . . . 307
9.4 3D advanced frame model calibration . . . 311
9.4.1 Damping parameters (Rayleigh) . . . 312
9.4.2 Loads . . . 313
9.4.3 Effective yield strength of steel grades . . . 314
9.4.4 Bolt hole clearance . . . 315
9.5 Comparison between the advanced FE model and the experimental results . . . 317
9.6 FFE comparison . . . 323
9.7 Main outcomes and discussion . . . 325

10 Fire following earthquake framework for multi-hazard probabilistic analyses 327
10.1 Introduction . . . 327
10.2 OpenSees Software . . . 327
10.2.1 New Material: SteelFFEThermal . . . 328
Earthquake/cyclic module . . . 329
Fire module . . . 331
Coordinator module . . . 333
10.3 FFE framework: basic idea . . . 333
10.4 FFE decision tree algorithm . . . 334
10.4.1 "First stage" . . . 335
10.4.2 "Second stage" . . . 336
10.4.3 "Third stage" . . . 339
10.4.4 OpenSees: bug fix and other improvements . . . 341
10.5 Validation . . . 342
10.5.1 SteelFFEThermal . . . 342
Earthquake/cyclic simulation (cold module) . . . 342
Fire simulation (Fire module) . . . 343
FFE simulation (cold and Fire module) . . . 347
10.5.2 Thermal section (Third stage) . . . 353
10.6 Multi-hazard Fire Following analysis . . . 357
10.6.1 Ground Motions . . . 360
10.6.2 FE model . . . 362
10.6.3 Results . . . 363
10.7 Main outcomes and discussion . . . 373

11 Conclusions and future developments **377**
11.1 Summary and Conclusions 377
11.2 Future developments 379

List of Figures

1.1 SERA website: http://www.sera-eu.org/ [1] 5
1.2 Second SERA Annual Science Meeting (May 2019 - Edinburgh, United Kingdom) [1]. 6
1.3 (a) Case study. Dimensions in m.; (b) Geographically distributed framework; c) TEST #1 - left setup @ JRC – right furnace @ BAM; d) TEST #4 - left setup @ JRC – right furnace @ BAM; e) Box-shape fire protection. . . . 10
1.4 EQUFIRE project 12

3.1 EQUFIRE case study: a) 3D render of the building; b) Isometric view of the structure. 28
3.2 Typical Floor Framing Plan. Dimensions are in meters. . 28
3.3 Configuration of the frame (dimensions are in meters). . 29
3.4 Section of cold formed profiled steel sheeting element. . 30
3.5 Pressure zones for side walls of building (EN1991-1-4). . 32
3.6 Pressure zones for flat roofs, reproduced from EN1991-1-4 Figure 7.6. 34
3.7 Building's location on the map. 35
3.8 Mainland Portugal seismic zonation for Portuguese National Annex of NP EN 1998-1 [7]. 36
3.9 Mean seismic hazard map in peak ground acceleration (g) for rock (return period of 475years) [8]. 37
3.10 Elastic spectral $S_e(T)$ and design spectral $S_d(T)$. . . . 38
3.11 3D model of the buildings in ETABS. 39
3.12 Design response spectra and fundamental period of the structure. 41
3.13 Linear dynamic 3D analysis: a) Model A: Both the bracing diagonal in tension and compression; b) Model B: Only the diagonal in tension. 43
3.14 Mode. 45
3.15 Axial force in the beam. 50

3.16 Connection: a) beam-column-brace connection; b) Column base connection; c) beam-column connection. . . . 54
3.17 Acceleration Response Spectra: a) Original; b) Scaled; c) Scaled Average Spectrum. 57
3.18 Earthquake acceleration time-history (ACC6_NS). . . . 58
3.19 a) 3D model of the full structure; b) 2D model of the frame. 60
3.20 Base constraint of the models. 60
3.21 Beam-column connection. 60
3.22 Beam-column-brace connection. 61
3.23 Brace-column connection. 61
3.24 Braces connection. 61
3.25 Capacity curve (Pushover) comparison. 63
3.26 Horizontal displacement: a) 1st floor; b) 2nd floor; c) 3r floor; d) 4th floor. 64
3.27 ACC6 NS - dissipation 1st floor. 65
3.28 ACC6 NS - dissipation 2nd floor. 66
3.29 ACC6 NS - dissipation 3rd floor. 67
3.30 ACC6 NS - dissipation 4th floor. 68
3.31 Test frame and fire load location. 69
3.32 Numerical fire following earthquake simulation using OpenSees 70

4.1 Example of a component-mode basis: a) 5-DoFs chain-like system, b) *constraint* mode, c) *rigid-body* mode. . . 81
4.2 Three-substructure coupling example based on the LLM method: a) reference system; b) partitioned system. . . . 83
4.3 Architecture of the implementation of RT-HFS method based on the LLM-GC algorithm. 88
4.4 5-DoF nonlinear chain-like system. 89
4.5 Time history response of the PS of the 5-DoF chain-like system without experimental errors: a) displacement and b) restoring force. REF curves refer to the exact reference solution computed with a nonlinear static analysis whereas LLM-GC-FUL and LLM-GC-RED curves refer to the solutions computed with the LLM-GC algorithm without and with CMS of the NS, respectively. 90

4.6 Time history response of the PS of the 5-DoF chain-like system with experimental errors: a) displacement and b) restoring force. REF curves refer to the exact noiseless reference solution computed with nonlinear static analysis, LLM-GC-RED curves refer to the noisy solutions computed with the LLM-GC algorithm with CMS of the NS, and MOD-NEWTON curves refer to the noisy solution computed with the modified Newton-Raphson algorithm. 91
4.7 Case-study steel frame structure: a) emulated steel frame; b) time-temperature heating curves. 93
4.8 Substructuring of the case study steel frame: a) NS; b) PS. 94
4.9 Bending moment diagram in the SAFIR model of the case study steel frame at: a) t = 0 s; b) t = 740 s. 97
4.10 Deformed configuration of the case study steel frame at: a) 735 s; b) 745 s (end of the simulation). 97
4.11 Comparison of horizontal displacement histories measured at Node # 103: a) full time history; b) zoomed plot. 98
4.12 Comparison of horizontal displacement histories measured at Node # 503: a) full time history; b) zoomed plot. 98
4.13 Comparison of vertical displacement histories measured at Node #2303: a) full time history; b) zoomed plot. . . . 99
4.14 Comparison of vertical displacement histories measured at Node #2403: a) full time history; b) zoomed plot. . . . 99
4.15 Comparison of displacement histories measured at Node #2103: a) horizontal displacement; b) vertical displacement. 99
4.16 Comparison of displacement histories measured at Node #4: a) horizontal displacement; b) vertical displacement. 100

5.1 Architecture of the implementation of RT-HFS method based on the LLM-GC algorithm reproduced from Abbiati et al. (2020) [7]. 111
5.2 EQUFIRE case study. 113
5.3 (a) Emulated steel frame; (b) plan view of the building (c) time-temperature heating curves. (dimensions in m). . 114
5.4 Substructuring scheme adopted for HFS. 115
5.5 Bending moment diagram in the SAFIR model of the case study steel frame at: a) t = 0 s; b) t = 740 s. 117

5.6 Bending moment diagram in the SAFIR model of the case-study steel frame at (a) t = 0 s; (b) t = 700 s; (c) t = 1001 s 118

5.7 (a) Comparison of the horizontal displacement at Node 103; (b) comparison of the horizontal displacement at Node 103 zoomed plot; (c) comparison of the horizontal displacement at beam midspan Node 1303; (d) comparison of the vertical displacement beam midspan Node 1303; (e) comparison of the horizontal displacement measured at Node 8; (f) comparison of the vertical displacement measured at Node 8. 119

6.1 General view of the laboratory: a) from the control room; b) from the lab; c) View of the vertical furnace for testing columns; d) View of the furnace for testing slabs and beams; e) View of the furnace for testing walls and other compartmentation materials. 123

6.2 Simplified vertical and horizontal drawings of furnace: a) column specimen; b) thermocouples; c) hydraulic jack; d) oil burners; e) mineral fiber seal; f) furnace door; g) smoke vents [1], ... 124

6.3 Vertical furnace: analog servo-hydraulic control loops. . 124

6.4 Substructuring method (basic idea) [2] 125

6.5 a) Vertical furnace for testing columns; b) furnace's burners; c) Hydraulic system. 126

6.6 a) equipment to control the hydraulic system; b) equipment to control the furnace; c) equipment to control the temperature sensors, the vent system and the video cameras; d) Master PC (Left) and target PC (Right). 127

6.7 (a) Emulated steel frame; (b) Substructuring scheme adopted for the FFE tests. 128

6.8 Static non-linear analysis to determine the axial stiffness value of the surrounding structure. 129

6.9 Axial stiffness of the surrounding structure vs axial displacement curve. 130

6.10 Equivalent stiffness - Option A: a) The gravity load and the earthquake load (F=290.77 kN) is applied to the column; b) An axial spring with a constant equivalent stiffness (K) is modelled; c) A time-temperature curves is used. 131

6.11 Equivalent stiffness - Option A: a) The gravity load and the earthquake load (F=290.77 kN) is applied to the column; b) An axial spring with a constant equivalent stiffness (K) is modelled; c) A time-temperature curves is used. 131
6.12 Comparison between the reference numerical solution and the single column with constant axial stiffness: a) axial displacements vs temperature curve; b) axial forces vs temperature curve. 132
6.13 Test procedure: a) specimen inside e vertical furnace; b) top plate during the earthquake; c) earthquake event; d) top plate during the fire; e) constant numerical axial stiffness; f) fire event. 133
6.14 Column test E: cross section with position of the thermocouples. 135
6.15 Views of column of test E: a) before test; b) time = 30 minutes; c) time = 43 minutes; d) time = 54 minutes; e) time = 60 minutes; d) after test. 136
6.16 Column test E: evolution of the temperatures during the test. 137
6.17 Column test E: evolution of the axial displacement. . . . 138
6.18 Column test E: evolution of the axial force. 139
6.19 Column test E: evolution of the horizontal displacement. 140
6.20 Column test E: evolution of the horizontal force. 141
6.21 Column test E: displacement vs force. 142
6.22 Column test A: cross section with position of the thermocouples. 143
6.23 Views of column of test E: a) before test; b) time = 35 minutes; c) time = 41 minutes; d) time = 54 minutes; e) time = 60 minutes; d) after test. 144
6.24 Column test A: evolution of the temperatures during the test. 145
6.25 Column test A: evolution of the axial displacement. . . . 146
6.26 Column test A: evolution of the axial force. 147
6.27 Column test A: evolution of the horizontal displacement. 148
6.28 Column test A: evolution of the horizontal force. 149
6.29 Column test A: displacement vs force. 150
6.30 Comparison before and after the test a) south side (before); b) east side (before); c) north side (before); d) west side (before); e) south side (after); f) east side (after); g) north side (after); h) west side (after). 151

6.31 Steel column with PROMATECT®-200 and reinforced joints. 152
6.32 Column test B: cross section with position of the thermocouples. 153
6.33 Test interruption: a) axial force and axial displacement; b) component subjected to the malfunction (overheat); c) axial force and axial displacement. 154
6.34 a) axial force; b) axial displacement. 155
6.35 Views of column of test B: a) before test; b) time = 26 minutes; c) time = 79 minutes; d) time = 116 minutes; e) time = 130 minutes; d) after test. 156
6.36 Column test B: evolution of the temperatures during the test. 157
6.37 Column test B: evolution of the axial displacement. . . . 158
6.38 Column test B: evolution of the axial force. 159
6.39 Column test B: evolution of the horizontal displacement. 160
6.40 Column test B: evolution of the horizontal force. 161
6.41 Column test B: displacement vs force. 162
6.42 Comparison before and after the test a) south side (before); b) east side (before); c) north side (before); d) west side (before); e) south side (after); f) east side (after); g) north side (after); h) west side (after). 163
6.43 Damage on the fire protection elements due to the combination of seismic and fire actions: test #2 column B . . 164
6.44 Steel column with PROMATECT®-H and normal joints. 165
6.45 Column test C: cross section with position of the thermocouples. 166
6.46 Views of column of test C: a) before test; b) time = 38 minutes; c) time = 48 minutes; d) time = 69 minutes; e) time = 85 minutes; d) time = 110 minutes. 167
6.47 Column test C: evolution of the temperatures during the test. 168
6.48 Column test C: evolution of the axial displacement. . . . 169
6.49 Column test C: evolution of the axial force. 170
6.50 Column test C: evolution of the horizontal displacement. 171
6.51 Column test C: evolution of the horizontal force. 172
6.52 Column test C: displacement vs force. 173
6.53 Comparison before and after the test a) south side (before); b) east side (before); c) north side (before); d) west side (before); e) south side (after); f) east side (after); g) north side (after); h) west side (after). 174

6.54 Damage on the fire protection elements due to the combination of seismic and fire actions: test #2 column B . . 175
6.55 a) and b) layer of mechanical reinforcing mesh; c) PROMOSPRAY®-P300 series (CAFCO 300) application. 176
6.56 Column test D: cross section with position of the thermocouples. 177
6.57 Views of column of test D: a) before test; b) time = 5 minutes; c) time = 49 minutes; d) time = 113 minutes; e) time = 170 minutes; d) after test. 178
6.58 Column test D: evolution of the temperatures during the test. 179
6.59 Column test D: evolution of the axial displacement. . . . 180
6.60 Column test D: evolution of the axial force. 181
6.61 Column test D: evolution of the horizontal displacement. 182
6.62 Column test D: evolution of the horizontal force. 183
6.63 Column test D: displacement vs force. 184
6.64 Comparison before and after the test a) south side (before); b) east side (before); c) north side (before); d) west side (before); e) south side (after); f) east side (after); g) north side (after); h) west side (after). 185
6.65 Damage on the fire protection elements due to the combination of seismic and fire actions: test #2 column B . . 186
6.66 a) example matches between photos; b) Point Clouds. . . 187
6.67 3D model of the column #D obtained using the photogrammetry methodology: a) wired model; b) Textured model. 188
6.68 EQUFIRE tests at Fire Engineering laboratory (BAM) (From Left: P. Covi, M. Korzen, S. Riemer, K. Ziener, F. Klemmstein, B. Klaffke, I.Uzelac, F Kiesel), November 2019. 190

7.1 Test frame. Dimensions are in meters. 194
7.2 Comparison of the response spectra for original and modified vs the target spectrum. 195
7.3 Selected accelerogram for simulations and tests. 196
7.4 2D non-linear finite element model of the full frame in OpenSees 197
7.5 3D non-linear finite element model of the column in OpenSees 198
7.6 Mesh column using beam elements 199
7.7 Sections: a) Columns #A and #E; b) Columns #B and #C; c) Column #D. 200
7.8 Mesh column using beam elements 200

7.9 Sections: a) Columns #B and #C; b) Column #D. 201
7.10 Numerical fire following earthquake simulation using OpenSees 202
7.11 Sub-structuring method [17] 203
7.12 Static non-linear analysis to determine the axial stiffness value of the surrounding structure. 204
7.13 Axial stiffness of the surrounding structure vs axial displacement curve. 205
7.14 Comparison between the reference numerical solution and the single column with constant axial stiffness: a) axial displacements vs temperature curve; b) axial forces vs temperature curve. 206
7.15 Seismic test: Comparison between the numerical solution and the tests: a) axial displacement and b) axial force. 207
7.16 Comparison between the results of the numerical model and the FFE tests on the unprotected columns. 208
7.17 COLUMN #B: Comparison between numerical models and the tests on columns with fire protection. 209
7.18 Results of the FFE tests on columns with fire protection. 210
7.19 COLUMN #B: Comparison between numerical models and the tests on columns with fire protection. 210
7.20 COLUMN #C: Comparison between numerical models and the tests on columns with fire protection. 211
7.21 COLUMN #D: Comparison between numerical models and the tests on columns with fire protection. 212
7.22 Axial stiffness of the surrounding structure vs axial displacement curve. 213
7.23 3D finite element model of the joint. 214
7.24 Column test A: a) cross section with position of the thermocouples; b) evolution of the temperatures during the test. 215
7.25 Axial force during FFE test of column A 216
7.26 Comparison of the top plate connection: a) during earthquake event (presence of bolts); b) during fire event (absence of bolts). 216
7.27 Axial stiffness of the surrounding structure vs axial displacement curve. 217
7.28 Comparison between the results of the numerical model, the calibrated 3D column and the FFE tests on the unprotected columns. 218
7.29 ix zones subdivision 219
7.30 Axial spring results: a) beam elements; b) shell elements. 221
7.31 Axial spring results: a) beam elements; b) shell elements. 222

7.32 Column #A - calibration results. 222
7.33 Column #E - calibration results. 224
7.34 Column #B - calibration results. 225
7.35 Column #C - calibration results. 226
7.36 Column #D - calibration results. 227

8.1 Dimensions and capacity of the ELSA Reaction Wall [1] 232
8.2 a) Render of the experimental setup. b) General view of the specimen and experimental setup at the ELSA Reaction Wall; c) detail of the brace. 233
8.3 Sensors setup. 234
8.4 Earthquake acceleration time-history (ACC6_NS). . . . 235
8.5 Frame EQUFIRE a) Real frame; b) Substructure. 236
8.6 Capacity curve (Pushover) comparison. 237
8.7 Pushover deformation a) Real frame; b) Substructure. . . 237
8.8 Comparison of the horizontal displacements at first floor (ACC6_NS). 238
8.9 Comparison of the horizontal displacements at second floor (ACC6_NS). 238
8.10 Comparison of the horizontal displacements at third floor (ACC6_NS). 239
8.11 Comparison of the horizontal displacements at fourth floor (ACC6_NS). 239
8.12 – First eigenmode of the: a) reference and the b) simplified FE models of the EQUFIRE frame case study. . . . 240
8.13 Displacement response histories of coupled DOFs of both reference and simplified FE models: a) horizontal displacement of the left inner column, b) vertical displacement of the left inner column, c) vertical displacement of the right inner column. 240
8.14 Ground-level diagonal bracing #1: a) displacement-force response, b) restoring force history. 241
8.15 FE models of the: a) NS and the b) PS with coupled DOFs highlighted in blue. 241
8.16 a) Emulated steel frame (dimensions in m); b) substructuring scheme adopted for HES. 245
8.17 Deformed shape at the end of the simulation and acceleration time-history. 246
8.18 Virtual Hybrid Earthquake simulation results. 247
8.19 a) General view of the specimen and experimental setup at the ELSA Reaction Wall; b) detail of the brace. 248

8.20 Test #A-32: evolution of the displacements of the three coupled DOFs between NS and PS. 249
8.21 Test #A-33: evolution of the displacements of the three coupled DOFs between NS and PS. 250
8.22 Test #A-32: evolution of the forces of the three coupled DOFs between NS and PS. 251
8.23 Test #A-33: evolution of the forces of the three coupled DOFs between NS and PS. 252
8.24 Test #A-32: evolution of the stiffness of the three coupled DOFs between NS and PS. 253
8.25 Test #A-33: evolution of the stiffness of the three coupled DOFs between NS and PS. 253
8.26 Axial force of the internal columns: a) test #A-32; b) test #A-33. 254
8.27 Columns' rotation: a) test #A-32; b) test #A-33. 254
8.28 Beams' axial force: a) test #A-32; b) test #A-33. 254
8.29 Displacement of the center node of the braces: a) test #A-32; b) test #A-33. 255
8.30 Axial displacement of the braces: a) test #A-32; b) test #A-33. 255
8.31 a) General view of the specimen and experimental setup at the ELSA Reaction Wall; b) detail of the brace. 256
8.32 Test #B-06: evolution of the displacements of the three coupled DOFs between NS and PS. 258
8.33 Test #B-07: evolution of the displacements of the three coupled DOFs between NS and PS. 259
8.34 Test #B-06: evolution of the forces of the three coupled DOFs between NS and PS. 260
8.35 Test #B-07: evolution of the forces of the three coupled DOFs between NS and PS. 261
8.36 Test #B-06: evolution of the stiffness of the three coupled DOFs between NS and PS. 262
8.37 Test #B-07: evolution of the stiffness of the three coupled DOFs between NS and PS. 262
8.38 Axial force of the internal columns: a) test #B-06; b) test #B-07. 263
8.39 Columns' rotation: a) test #B-06; b) test #B-07. 263
8.40 Beams' axial force: a) test #B-06; b) test #B-07. 263
8.41 Displacement of the center node of the braces: a) test #B-06; b) test #B-07. 264
8.42 Axial displacement of the braces: a) test #B-06; b) test #B-07. 264

8.43 Damages after two seismic tests at 1.0g: a) damage of the casing of the column; b) detachment of the boards at the bracing crossing; c) damage of the casing of the bottom connection. 265
8.44 a) General view of the specimen and experimental setup at the ELSA Reaction Wall; b) detail of the brace. 266
8.45 Test #C-04: evolution of the displacements of the three coupled DOFs between NS and PS. 268
8.46 Test #C-05: evolution of the displacements of the three coupled DOFs between NS and PS. 269
8.47 Test #C-04: evolution of the forces of the three coupled DOFs between NS and PS. 270
8.48 Test #C-05: evolution of the forces of the three coupled DOFs between NS and PS. 271
8.49 Test #C-04: evolution of the stiffness of the three coupled DOFs between NS and PS. 272
8.50 Test #C-05: evolution of the stiffness of the three coupled DOFs between NS and PS. 272
8.51 Axial force of the internal columns: a) test #C-04; b) test #C-05. 273
8.52 Columns' rotation: a) test #C-04; b) test #C-05. 273
8.53 Beams' axial force: a) test #C-04; b) test #C-05. 273
8.54 Displacement of the center node of the braces: a) test #C-04; b) test #C-05. 274
8.55 Axial displacement of the braces: a) test #C-04; b) test #C-05. 274
8.56 Damages after two seismic tests at 1.0g 275
8.57 Damages after the cyclic test tests. 275
8.58 a) General view of the specimen and experimental setup at the ELSA Reaction Wall; b) detail of the brace. 276
8.59 Xella®Murfor system. 277
8.60 Construction of the Xella®fire barrier walls. 277
8.61 Fire protection system PROMASPRAY®-P300 series (CAFCO 300) 278
8.62 Test #D-03: evolution of the displacements of the three coupled DOFs between NS and PS. 279
8.63 Test #D-04: evolution of the displacements of the three coupled DOFs between NS and PS. 280
8.64 Test #D-03: evolution of the forces of the three coupled DOFs between NS and PS. 281
8.65 Test #D-04: evolution of the forces of the three coupled DOFs between NS and PS. 282

8.66 Test #D-03: evolution of the stiffness of the three coupled DOFs between NS and PS. 283
8.67 Test #D-04: evolution of the stiffness of the three coupled DOFs between NS and PS. 283
8.68 Axial force of the internal columns: a) test #D-03; b) test #D-04. 284
8.69 Columns' rotation: a) test #D-03; b) test #D-04. 284
8.70 Beams' axial force: a) test #D-03; b) test #D-04. 284
8.71 Displacement of the center node of the braces: a) test #D-04; b) test #D-05. 285
8.72 Axial displacement of the braces: a) test #D-03; b) test #D-04. 285
8.73 Damages after two seismic tests at 1.0g. 286
8.74 Damages after the cyclic test tests. 287
8.75 comparison of the displacements (Test #A-32 and #A-33) 288
8.76 comparison of the forces (Test #A-32 and #A-33) 289
8.77 comparison of the displacements (Test #B-06 and #B-07) 290
8.78 comparison of the forces (Test #B-06 and #A-07) 291
8.79 comparison of the displacements (Test #C-04 and #C-05) 292
8.80 comparison of the forces (Test #C-04 and #C-05) 293
8.81 3D model of the Frame #B obtained using the photogrammetry methodology: a) wired model b) Textured model . 294
8.82 3D textured model of the Frame #B obtained using the photogrammetry methodology. 295
8.83 3D model of the Frame #D obtained using the photogrammetry methodology: a) wired model; b) Textured model before the tests; c) Textured model after the final tests. . 296
8.84 Comparison: a) 3D model of the Frame #D obtained using the photogrammetry methodology; b) Real pictures. . 297
8.85 EQUFIRE tests at European Laboratory for Structural Assessment (ELSA) of the Joint Research Centre (JRC) (From Left: P. Covi, N. Tondini, A. Pinto, P. Pegon, G. Tsionis), May 2021. 299

9.1 3D render of the EQUFIRE connection 302
9.2 a) Force-based fiber elements (Uriz and Mahin, 2008 [4]); b) Rotational hinge (Hsiao et al., 2012 [1]) 303
9.3 Nonlinear rotational spring model. 304
9.4 Bracing connection at base (Whitmore's section). 305
9.5 a) advanced 3D frame modelled in OpenSees: nonlinear elements in red, elastic elements in blue; b) Fiber Section. 307
9.6 geometric imperfections (scaled): a) 3D view, b) XZ plan. 307

9.7 Modal shapes: a) 1st mode; b) 2nd mode. 308
9.8 Pushover comparison 309
9.9 Horizontal displacement (ACC6_NS): a) 1st floor; b) 2nd floor; c) 3rd floor; d) 4thh floor. 310
9.10 Disipation braces at 1st floor: a) top-left; b) top-right; c) bottom-left; d) bottom-right 311
9.11 Horizontal displacement comparison of the first floor. . . 313
9.12 Loads a) real gravity load configuration b) equivalent experimental gravity load configuration 314
9.13 Horizontal displacement comparison of the first floor. . . 314
9.14 Outcomes of the S275 steel grade sensitivity analysis compared to the horizontal displacement of the experimental test. 315
9.15 Connection model 316
9.16 Horizontal displacement comparison of the first floor. . . 317
9.17 Comparison of the displacements: a) DOF 1 (Horizontal actuator); b) DOF 2 (Vertical left actuator); b) DOF 3 (Vertical right actuator). 318
9.18 Comparison of the forces: a) DOF 1 (Horizontal actuator); b) DOF 2 (Vertical left actuator); b) DOF 3 (Vertical right actuator). 319
9.19 Comparison of the force inside the columns: a) Internal left column (column B); b) Internal right column (column C). 320
9.20 Comparison of the rotation of the columns: a) external left column (column A); b) internal left column (column B); c) internal right column (column C); d) external right column (Column D). 321
9.21 Comparison of the displacements of the middle point of the bracing system: a) horizontal in-plane displacement; b) horizontal out of plane displacement; c) vertical displacement). 322
9.22 Comparison of the axial displacement of the braces: a) brace 1; b) brace 2. 323
9.23 a) gas temperature of ground floor and first floor; b) fire scenario after the ACC6_NS earthquake; c) deformed shape of the frame at the end of the simulation. 324
9.24 Results of the FFE numerical analysis. 325

10.1 SteelFFEThermal basic idea 329
10.2 Giuffrè-Menegotto-Pinto Steel model [4]. 330

10.3 Uniaxial constitutive law at high temperature (Elhami-Khorasani 2015)[2]: a) unloading/reloading procedure. b) plastic strain and strain reversals. 332
10.4 Strength retention factors versus temperature based on a continuous logistic fit for steel $k_{y,2\%,T}$ [5][7]. 332
10.5 FFE framework basic idea. 333
10.6 First stage scheme. 335
10.7 Gas pipe fragility curve [9]. 336
10.8 Second stage scheme. 336
10.9 Partition fragility curve (Walls BD-3.9.2 - table 13 for DS3, Full connections) [14]. 338
10.10 Glazing fragility curve (FEMA P-58/BD-3.9.1) [15] . . . 338
10.11 Third stage scheme. 339
10.12 Case study: a) geometry and data; b) reverse Cyclic Loading applied at the right end node. 342
10.13 Axial load versus axial displacement response. 343
10.14 Case study: a) geometry and data; b) evolution in time of the temperature in the cross section. 344
10.15 a) Vertical displacement at the mid-span; b) Computational time comparison. 346
10.16 Test frame. Dimensions are in meters. 347
10.17 Deformed shape of the numerical model at the end of the FFE simulation, earthquake acceleration time-history and thermal load of the braces 348
10.18 Axial force versus axial displacement response: a) brace top right; b) brace top left; c) brace bottom left; d) brace bottom right; e) internal column left; f) internal column right. 349
10.19 Axial force: a) brace top right; b) brace top left; c) brace bottom left; d) brace bottom right; e) internal column left; f) internal column right. 349
10.20 Axial displacement: a) brace top right; b) brace top left; c) brace bottom left; d) brace bottom right; e) internal column left; f) internal column right. 350
10.21 Hysteretic Behavior of Model w/o Isotropic Hardening at ambient temperature: a) Giuffrè-Menegotto-Pinto Material (Steel02, SteelFFEThermal cold module); b) uniaxial bilinear steel material (Steel01, Steel01Thermal) . . 351
10.22 Axial force: a) brace top right; b) brace top left; c) brace bottom left; d) brace bottom right; e) internal column left; f) internal column right. 352

10.23 Axial displacement: a) brace top right; b) brace top left; c) brace bottom left; d) brace bottom right; e) internal column left; f) internal column right. 352
10.24 Axial force versus axial displacement response: a) brace top right; b) brace top left; c) brace bottom left; d) brace bottom right; e) internal column left; f) internal column right. 353
10.25 Computational time comparison: a) earthquake simulation; b) fire following earthquake. 353
10.26 a) 15 temperature zones defined using Beam3dThermalAction (OpenSees); b) extraction of 15 temperature zones (MATLAB); 355
10.27 Temperature distribution in the W14x283 section at 33 minutes of heat exposure: a) MATLAB thermal model; b) Equivalent OpenSees. 355
10.28 Temperature distribution of the W14x283 cross section in the points on the steel profile. 356
10.29 Temperature distribution in the HSS7x7x1/2 section at 33 minutes of heat exposure: a) MATLAB thermal model; b) Equivalent OpenSees. 356
10.30 Temperature distribution of the HSS7x7x1/2 cross section in the points on the steel profile. 357
10.31 Building [19]: a) Isometric view b) plan view. 358
10.32 Configuration of the frame (Dimensions are in meters). . 359
10.33 Acceleration Response Spectra: a) Original; b) Scaled; c) Scaled Average Spectrum. 361
10.34 Boundary conditions for thermal analysis: a) external column; b) column between two compartments (internal column); c) brace; d) beam. 363
10.35 Earthquake acceleration time-history. 364
10.36 Horizontal displacements of each floor. 365
10.37 Energy dissipations of the braces: a) 8th and 7th floors; b) 6th and 5th floors. 366
10.38 Energy dissipations of the braces: a) 4th and 3rd floors; b) 2nd and 1st floors. 367
10.39 First stage results of FFE decision tree algorithm: a) interstory drift ratio (IDR); b) maximum acceleration. . . . 368
10.40 Evolution of the temperature in each compartments: a) 5 min; b) 10 min; c) 15 min; d) 20 min; e) 25 min; f) 30 min; g) 35 min; h) 40 min; i) 45 min after the ignition. . 369
10.41 Evolution of the temperature inside the compartments. . 370
10.42 Evolution of the temperature inside the compartments. . 371

10.43a) Beam deflection; b) Horizontal displacement of end columns at each floor. 372
10.44Deformed shape of the numerical model at the end of the FFE simulation. 373

Patrick Covi

Multi-hazard analysis of steel structures subjected to fire following earthquake

1.0 Introduction

Earthquakes are destructive and unpredictable events with catastrophic consequences for both people and built environment. Moreover, secondary triggered effects can strike further an already weakened community, i.e. ground shaking, surface faults, landslides and tsunamis. In this respect, also fires following earthquake (FFE) have historically produced large post-earthquake damage and losses in terms of lives, buildings and economic costs, like the San Francisco earthquake (1906), the Kobe earthquake (1995), the Turkey earthquake (2011), the Tohoku earthquake (2011) and the Christchurch earthquakes (2011). In detail, FFEs are a considerable threat as they can be widespread both at the building level and at the regional level within the seismic affected area owing to the rupture of gas lines, failure of electrical systems etc. and at the same time failure of the compartmentation measures. Moreover, they are more difficult to tackle by the fire brigades because of their possible large number and extent as well as of possible disruptions within the infrastructural network that hinder their timely intervention and within the water supply system.

In this context, the structural fire performance can worsen significantly because the fire acts on an already damaged structure. Furthermore, passive and active fire protections may have also been damaged by the seismic action and the fire can spread more rapidly if compartmentation measures have failed. Thus, the seismic performance of the non-structural components may directly affect the fire performance of the structural members. As consequence, the minimization of the non-structural damage is paramount in mitigating the possible drop in structural fire performance. The loss of fire protection is particularly dangerous for steel structures because the high thermal conductivity associated with small profile thicknesses entails quick temperature rise in the profiles with consequent fast loss of strength and stiffness. Large-scale tests of an entire structure are generally prohibitively expensive, both in terms of finances and time, because of the need for expensive specialized facilities. As a result, most of the research regarding the behaviour of structures subjected to fire has been carried out on partial subassemblies or single components subjected to standard heating curves. Standard fire tests use simplified mechanical boundary conditions for the tested structural element. However, for some elements, these conditions can lead to results that are overly conservative. Hybrid fire and seismic simula-

tion emerged as a viable solution for performing component level experiments that account for the interaction between the tested specimen and a realistic yet virtual subassembly instantiated in a finite-element software.

1.1 Purpose and scope of this research

On these premises, the purpose of this work is the investigation of the experimental and numerical response of structural and non-structural components of steel structures subjected to fire following earthquake (FFE) to increase the knowledge and provide a robust framework for hybrid fire testing and hybrid Fire Following earthquake testing. A partitioned algorithm to test a real case study with substructuring techniques was developed. The framework is developed in MATLAB and it is also based on the implementation of nonlinear finite elements to model the effects of earthquake forces and post-earthquake effects such as fire and thermal loads on structures. These elements should be able to capture geometrical and mechanical non-linearities to deal with large displacements. Two numerical validation procedures of the partitioned algorithm simulating two virtual hybrid fire testing and one virtual hybrid seismic testing were carried out. Two sets of experimental tests in two different laboratories were performed with the purpose of providing valuable data for the calibration and comparison of numerical finite element case studies reproducing the conditions used in the tests. Another goal of this thesis is the development of a FFE numerical framework in order to perform probabilistic analysis of structures subjected to FFE.

1.2 Organization of the thesis

This thesis is divided into 11 chapters. The structure of the thesis is a collection of published/unpublished papers and other detailed Chapters related to the actual results of ongoing experimental tests and research. In detail, the thesis contains two published papers (Chapters 4, 5), one unpublished paper (Chapter 7) and four detailed Chapters on specific topics related on published/unpublished papers or ongoing experimental test results (Chapters 3, 6, 8, 8, 9) or preliminary results of ongoing research (Chapter 10). Some information and descriptions (e.g. the description of the EQUFIRE experimental campaign and case study) are repeated in different chapters due to the structure of the thesis that contains papers.

Chapter 1 - Introduction

In the chapter of introduction, the Fire Following Earthquake (FFE) problem has been introduced. The SERA and EQUFIRE projects were presented and a historical review of the most important Fire following earthquake events was made.

Chapter 2 - State of the art

A brief review of the State of the art is presented, concerning the hybrid testing and simulation of steel frames subjected to earthquake and/or fire event.

Chapter 3 - EQUFIRE: design and numerical simulations

The third chapter describes the design of a four-storey steel concentrically braced frame according to Eurocodes that will serve as a case study of EQUFIRE project and some preliminary numerical analyses using OpenSees are presented.

Chapter 4 - Hybrid fire simulation dynamic relaxation component-mode synthesis partitioned time integration steel frame

The fourth chapter contains the following published paper: **"A Real-Time Hybrid Fire Simulation Method Based on Dynamic Relaxation and Partitioned Time Integration."** In the first part of the paper, the development of a real-time hybrid fire simulation method is presented. Then, the effectiveness of the method is demonstrated on a virtual experimental campaign. In detail, Hybrid Fire simulation of a realistic moment-resisting frame subjected to fire is simulated numerically and validated against reference finite element (FE) solution.

Chapter 5 - A static solver for Hybrid Fire Simulation based on model reduction and dynamic relaxation

The fifth chapter contains the following published paper: **"A static solver for hybrid fire simulation based on model reduction and dynamic relaxation."** The paper contains a virtual application of the real-time hybrid fire simulation method, already explained in the third chapter, but applied to the EQUFIRE case study.

Chapter 6 - Fire following earthquake tests at BAM

The sixth chapter describes in detail the experimental programme of the Hybrid Fire Following earthquake tests performed at the Fire Engineering laboratory of the Federal Institute for Materials Research and Testing (BAM), in Berlin (Germany). Five preliminary FFE substructure tests were carried out at the BAM laboratory, two steel columns without fire protection and three columns with different fire protection solutions: conventional and earthquake-proof boards system and gypsum-based wet mix spray-applied fire-resistive material.

Chapter 7 - Numerical-experimental analysis of a braced steel frame subjected to fire following earthquake

The seventh chapter contains the following unpublished paper under preparation **"Numerical-experimental analysis of a braced steel frame subjected to fire following earthquake"**. The paper contains the test results of the Hybrid FFE tests on unprotected and protected columns performed at BAM and the numerical model calibration using OpenSees and SAFIR software.

Chapter 8 - Seismic pseudo-dynamic tests at JRC

The eighth chapter describes in detail the experimental programme of the seismic pseudo-dynamic tests performed at the European Laboratory for Structural Assessment laboratory (ELSA) of the Joint Research Centre (JRC) in Ispra (Italy). The development of a real-time hybrid seismic simulation method is presented in this chapter. Then, the effectiveness of the method is demonstrated on a virtual experimental campaign

and also used during the experimental tests. Several seismic pseudo-dynamic tests were carried out on one steel frame without fire protection and three frames with different fire protection solutions: conventional and earthquake-proof boards system and gypsum-based wet mix spray-applied fire-resistive material with fire barrier walls.

Chapter 9 - Calibration of the finite element numerical model with experimental data of the JRC tests

The ninth chapter describes the numerical model calibration of the first experimental test of Frame #A at JRC using an advanced finite element model to better model the real connections of the frame using OpenSees.

Chapter 10 - Fire following earthquake framework for multi-hazard probabilistic analyses

The tenth chapter presents a framework for structures subjected to fire following earthquake based on a modified version of the OpenSees software and several scripts developed in MATLAB in order to perform probabilistic analysis of structures subjected to FFE. As an example, this framework is used to evaluate the performance of an 8-story steel bracing office building under fire following earthquake events.

Chapter 11 - Conclusions and future developments

Conclusions and future works are presented in Chapter 11.

1.3 SERA

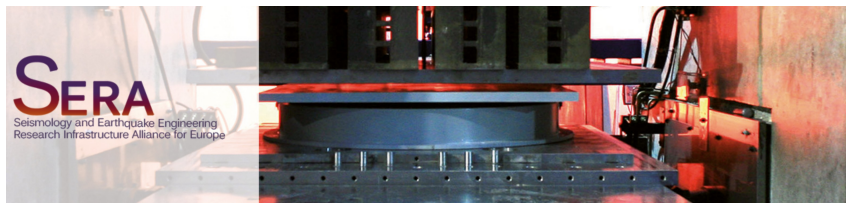

Figure 1.1: SERA website: http://www.sera-eu.org/ [1]

The Seismology and Earthquake Engineering Research Infrastructure Alliance for Europe (SERA) [1] is a Horizon 2020-supported programme

(grant agreement No. 730900) responding to the priorities identified in the topic INFRAIA-01-2016-2017 'Integrating Activities for Advanced Communities'. SERA involves 31 partners and 8 linked third parties in Europe. It started in May 2017 and lasted ended in April 2020.

SERA aims to reduce the risk posed by natural and anthropogenic earthquakes based on innovative research and development projects. SERA will significantly improve the access to data, services and research infrastructures for scientists and other professionals.

These efforts will lead to a revised European seismic hazard reference model. Also, the outcomes of the project will help to develop a first, comprehensive framework for seismic risk modelling at European scale. Furthermore, SERA will contribute to new standards for future experimental observations in earthquake engineering, for the design of instruments and networks for observational seismology, and reliable methodologies for real-time assessment of shaking and damage.

Figure 1.2: Second SERA Annual Science Meeting (May 2019 - Edinburgh, United Kingdom) [1].

In the SERA project I was involved in three different work packeges:

- WP 8: Access to ELSA reaction wall at JRC (TA1): EQUFIRE project [2] [3], explained in the Section 1.3.1.
- WP 26: Risk Modelling framework for Europe (JRA 4):
  Understanding the magnitude of human and economic losses from damaging natural hazard events is fundamental for the development and implementation of disaster risk reduction measures. The aim of this work package is to develop a European risk modelling

framework that brings together the strengths of previous projects and fills in the research gaps. It also integrates knowledge and data from many of the SERA WPs including the updated European hazard model of JRA3. Finally, it will build on the risk assessment framework and software established by the Global Earthquake Model.

- WP 27: Innovative testing methodologies for component/system resilience (JRA 5):
  Along with the drive to follow and exploit the developments both in the area of numerical modelling of non-linear systems and the area of advanced testing of components/systems using hybrid (numerical/physical) dynamic sub-structuring simulations (HDS), this work package pursues the following objectives:
  - Reduce the computational burden of complex hybrid nonlinear systems and provide additional significance to HDS both in civil engineering and mechanical engineering systems
  - Compare the performances of online and offline experimental sub-structuring methods
  - Study testing equipment able to properly impose complex loading on innovative isolation/dissipation devices made of fiber-reinforced rubber, shape-memory alloys, etc.
  - Conceptualize the smart city research, with the design and development for seismic and other natural hazard actions, like tsunamis, etc.

Only the research conducted in WP8 formed the research chapters of this thesis. The other two work packages were relevant, but did not form part of the thesis itself.

1.3.1 EQUFIRE project

In the framework of the H2020 SERA Transnational Access (TA) activities, the EQUFIRE [2] [3] proposal foresees an experimental campaign aimed at investigating the multi-hazard performance assessment of structural and non-structural components subjected to seismic and fire following earthquake In detail, the EQUFIRE project aims to investigate the experimental response of structural and non-structural components of a steel building to fire following earthquake in view of improving existing design guidelines and future standards. Most of the research has

focussed on steel moment-resisting frames. However, in Europe, they represent the minority because of the complexity of the moment connections and the relative associated costs. Therefore, a concentrically braced frame (CBF) with pinned connections was selected as a case study. The seismic damage was mainly concentrated in the bracing elements. In this regard, two damage scenarios was considered in the elements to be tested in the furnace as follows. For the column, the seismic damage was considered as "low", assuming that it still maintains its overall stability after the earthquake. For the bracing element, the seismic damage was considered as "high", with the assumption that it has already reached its plastic strength due to the earthquake loading. Non-structural components were tested, including box passive fire protections and fire barrier walls. The fire barrier wall was made of concrete bricks with assigned fire ratings, e.g. EI60 designated for an office building. Since full-scale tests foresee a significant budget, an hybrid testing for seismic and fire was employed. In this respect, it is important to stress that, when non-structural components are involved, e.g. fire protection elements, the structural response might be very sensitive to both loading and boundary conditions. However, large-scale structural fire tests are expensive and need specialized facilities. As a result, most of the research regarding the behaviour of structures in fire has been carried out on single components subjected to standard heating curves or partial subassemblies. Although they offer significant information for the understanding of fire performance of specific structural elements, they do not provide insight on the interaction between the fire development and the whole structure. In order to overcome such limitations, Hybrid Simulation (HS), extensively investigated in the seismic domain, represents a tempting approach. The hybrid model of the prototype structural system combines numerical and physical substructures (NSs and PSs). The dynamic response of the hybrid model is predicted using a time-stepping response history analysis with reduced costs and effort. The PSs of the hybrid model are tested in the laboratory because of their strongly nonlinear response and/or lack of a reliable mathematical model, while the NSs are instantiated in structural analysis software. In a typical hybrid simulation, a computer-controlled system applies displacements to the PSs using hydraulic actuators and feedback the corresponding restoring forces to the hybrid model integrator where the next solution step is computed. HS can significantly enhance the quality of benchmark experiments for validation and calibration of computational models, because it provides the response of a PS subjected to a realistic excitation, taking into account the interaction with the remaining part of the structural system.

Description of the original tests plan

This section contains the original description of the test plan, which was not applied due to the reason explained in the next section. Four geographically distributed FFE hybrid tests will be carried out. The ground floor of the concentrically braced frame illustrated in Fig. 1a will be substructured at the JRC and at the BAM facilities, as shown in Figures 1.3c and 1.3d. The remainder of the structure will be simulated numerically according to the finite element method and it will be kept at ambient temperature through the test. In particular, at the JRC the designated element will be tested against lateral cyclic loading at ambient temperature, whilst it will be subjected to the fire at BAM, simulating the fire after earthquake loading. A partitioned time integration algorithm will solve the hybrid model response online. Inertia forces will be accounted for during the seismic response simulation, whilst a static balance equation will be considered for the fire response simulation up to collapse. All tests will be performed according to the distributed geographically framework shown in Figure 1.3b. The test setup (TEST #1 and TEST #3), which is intended to test the post-earthquake fire effects on a protected/unprotected column, is depicted in Figure 1.3c. A set of horizontal actuators will serve to impose the cyclic lateral loading, simulating the earthquake load. The vertical actuators at the position of columns C1, C3 and C4 will impose the axial loading in terms of displacement at the interface between the physical substructure and the numerical substructure. During the hybrid seismic test, also C2 will be seismically loaded in the furnace at BAM by means of geographically distributed technique. Then, once the seismic test is finished, the furnace will be turned on to start the fire test. Similarly, the setup for TEST #2 and TEST #4 is shown in Fig. 1d with the bracing element substructured at BAM. Particular attention will be given to the box fire protection systems (Figure 1.3e) because they are likely to be damaged due to an earthquake.

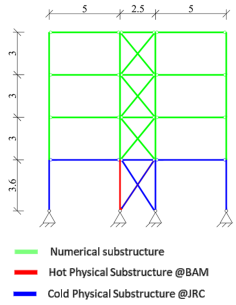

(a)

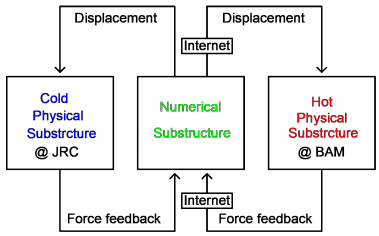

(b)

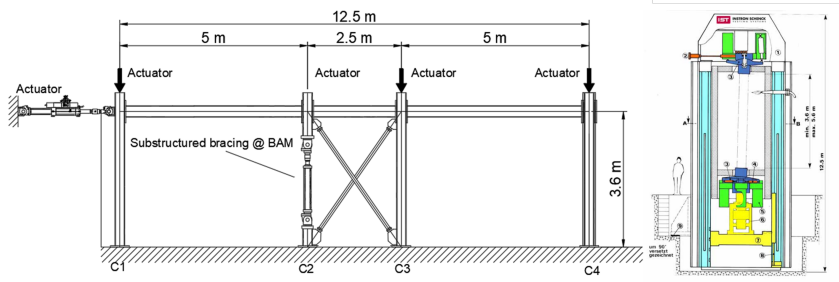

(c)

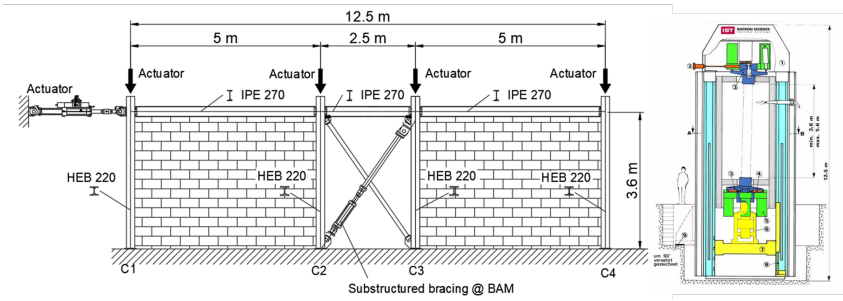

(d)

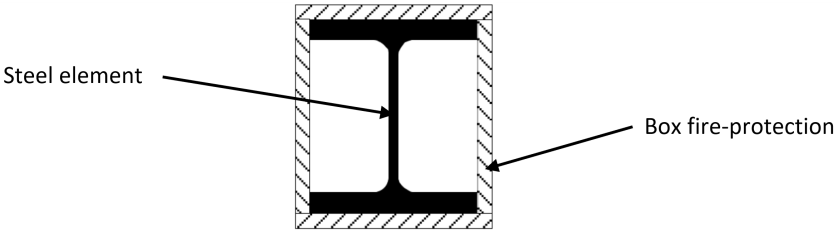

(e)

Figure 1.3: (a) Case study. Dimensions in m.; (b) Geographically distributed framework; c) TEST #1 - left setup @ JRC – right furnace @ BAM; d) TEST #4 - left setup @ JRC – right furnace @ BAM; e) Box-shape fire protection.

Description of the modified tests plan

A modification of the EQUFIRE project was needed in order to conduct the test at BAM before the retirement of the principal investigator (PI) (at end of 2019). Due to this reason was not possible to respect the original four geographically distributed FFE hybrid tests planned to be conducted in 2020. A new sequence of tests was agreed in order to split the hybrid tests according the different laboratories (BAM, JRC) and different time execution without using the geographically distributed hybrid test concept:

- BAM: Five fire following earthquake hybrid tests were performed, before December 2019, on a single element column of the building at the vertical furnace of the BAM : i) two columns without fire protection elements; ii) a column with standard fire protection boards, iii) a column with "seismic-resistant" fire protection boards, and iv) a column with sprayed vermiculite-type fire protection. The experimental tests were performed using a substructuring technique, in which the physical column was firstly subjected to the horizontal and vertical displacement time-histories computed through numerical modelling. Then, the column was heated by the ISO 834 standard heating curve and a constant numerical axial stiffness representative of the surrounding structure was applied as a boundary condition at the top of the physical column.

- JRC: Several seismic pseudo-dynamic tests were performed on the test frame with five different fire protections at the European laboratory Joint Research Centre (JRC), in Ispra (Italy): i) frame without fire protection elements; ii) frame with standard fire protection boards, iii)frame with "seismic-resistant" fire protection boards, and iv) frame with sprayed vermiculite-type fire protection and fire barrier walls. These tests were originally planned to begin in April 2020. However, the execution of the tests has been delayed due to the lockdown period that happened in Italy in spring 2020 and the subsequent restrictions. Therefore the test campaign officially started in December 2020.

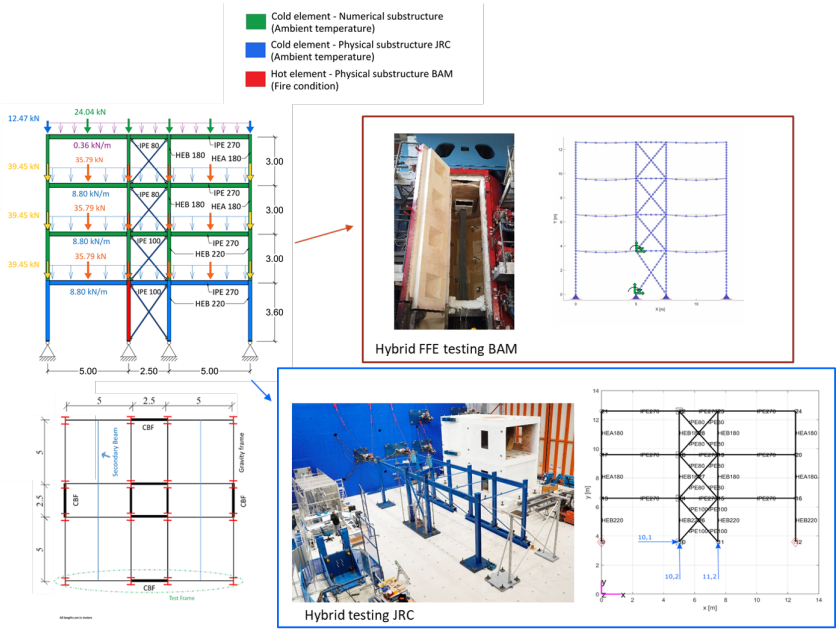

Figure 1.4: EQUFIRE project

1.4 Historical events of FFE

This section provides a list of historical earthquakes and the extent of fire damage in each event, focusing primarily on the earthquake characteristic, the nature of fire ignitions and fire spread, major reasons for conflagrations and measures taken by city officials and firefighters

Many aspects of Fire following earthquakes and the damage they cause have been investigated in recent years. Scawthon et al. (1988) [4] acknowledged that little research had been reported in the US on fires following earthquakes in urban areas.

Botting (1998) [5] presented a fire Engineering research report with an analysis of literature from international sources concerning fourteen recent earthquake events having fire impacts on major population centres. Elhami-Khorasani et al. (2017) [6] presented a literature review on the problem of fire following earthquake (FFE) as a potential hazard to communities in seismically active regions.

1755 Lisbon earthquake

The earthquake broke out on November 1, 1755 with an estimated magnitude between 8.5 and 9.0 on the Richter Scale. 85% of the buildings

in Lisbon had either collapsed by the earthquake, been flooded by the tsunami or burnt by the fires. Several buildings that had suffered little earthquake damage were destroyed by the subsequent fire.

1906 San Francisco earthquake

The earthquake broke out on April 18, 1906 with a magnitude of 7.8 and a main shock of 8.3 on the Richter Scale. According to Scawthom et al. (1988), EERI (1985) and Steinbrugge (1982) fire razed more than 10 sq. km of the city, destroying at least 28,000 buildings. Fifty outbreaks of fire were reported within the hour following the earthquake. The conflagration lasted three days due to the lack of water and caused substantially more damage than the earthquake.

1908 Messina earthquake

The 1908 Messina earthquake occurred on December 28 in Sicily and Calabria with a magnitude of 7.1 on the Richter Scale. The cities of Messina and Reggio Calabria were almost completely destroyed. Fires were also observed in some parts of Messina following the earthquake, which added to the devastation. Unfortunately, the impact of fire loss, separate from ground shaking loss, was not well-documented immediately following the event.

1923 Tokyo earthquake

The 1923 Tokyo earthquake occurred on September 1 in Japan with a magnitude of 8.3 on the Richter Scale. There were 277 reported outbreaks of fire in Tokyo, and 133 of these fires spread. About 40% of the area of Tokyo City was destroyed by fire, which burned for nearly 40 hours, and 90% of Yokohama was destroyed by earthquake and fire.

1931 Napier earthquake

The 1931 Napier earthquake occurred on February 3 in New Zealand with a magnitude of 7.75 on the Richter Scale. According to Botting (1998) and Kenna (1975), there were more than 10 reported outbreaks and ten acres of buildings were burnt out.

1933 Long beach earthquake

The 1933 Long beach earthquake occurred on March 10 in California (US) with a magnitude of 6.3 on the Richter Scale. At least 15 outbreaks

of fire without conflagration were reported.

1952 Kern country earthquake

The 1952 Kern country earthquake occurred on July 21 in Central California (US) with a magnitude of 7.7 on the Richter Scale. At the Paloma Cycling Plant, a major oil refinery, fire caused by a broken gas line did several million dollars' damages. A number of fires were initiated by the July 29 aftershock and other severe damage was caused by it, especially to buildings that had already been damaged.

1963 Skopje earthquake

The 1963 Skopje earthquake occurred on July 26 in Yugoslavia with a magnitude of 6.0 on the Richter Scale. Two fires without conflagration were reported.

1964 Niigata earthquake

The 1963 Niigata earthquake occurred on June 16 in Japan with a magnitude of 7.5 on the Richter Scale. According to Kenna (1975) and Botting (1998) extensive damage to oil refinery facilities and factories occurred due to fire that broke out in oil tanks. The conflagration destroyed about 300 houses.

1971 San Fernando earthquake

The 1971 San Fernando earthquake occurred on February 9 in Japan with a magnitude of 6.6 on the Richter Scale. There were 109 reported fires, especially in the gas pipeline, burning for several hours.

1972 Managau earthquake

The 1972 Managau earthquake occurred on December 23 in Nicaragua with a magnitude of 5.5-6.5 on the Richter Scale. Fire conflagration raged through the downtown for several days.

1983 Coalinga earthquake

The 1983 Coalinga earthquake occurred on May 2 in San Joaquin Valley in California (US) with a magnitude of 6.7 on the Richter Scale. Four structures on fires were reported.

1984 Morgan Hill earthquake

The 1984 Morgan Hill earthquake occurred on April 24 in northern California (US) with a magnitude of 6.2 on the Richter Scale. Three major structure fires occurred due to heating appliance gas pipe fractures.

1985 Mexico city earthquake

The 1985 Mexico city earthquake occurred on September 19 in Mexico with a magnitude of 8.1 on the Richter Scale. About 200 fires were reported caused by the earthquake and aftershocks. In most of the cases, fires were mainly confined to the building of origin.

1987 Whittier Narrows earthquake

The 1987 Whittier Narrows earthquake occurred on October 1 in Los Angeles in California (US) with a magnitude of 5.9 on the Richter Scale. According to Botting (1998), 57 structural fires, 76 gas fire ignitions and no conflagrations were reported

1989 Loma Prieta earthquake

The 1989 Loma Prieta earthquake occurred on October 17 in northern California (US) with a magnitude of 7.1 on the Richter Scale. A severe fire in a four-story building occurred.

1993 Hokkaido Nansei-oki earthquake

The 1993 Hokkaido Nansei-oki earthquake occurred on July 12 in northern Japan with a magnitude of 7.8 on the Richter Scale. The town of Aonae was destroyed by conflagration following earthquake and tsunami. The fire least for 11 hours.

1994 Northridge earthquake

The 1994 Northridge earthquake occurred on January 17 in San Fernando Valley in southern California (US) with a magnitude of 6.7 on the Richter Scale. A total of 110 fires and no conflagration were reported. The principal cause was gas leaks from natural gas pipelines and appliances. The restoration of gas and power in the days following caused a significant number of fires.

1995 Kobe earthquake

The 1995 Kobe earthquake occurred on January 17 in Japan with a magnitude of 6.9 on the Richter Scale. 108 fire ignitions were reported. Several conflagrations within 1 to 2 hours of the earthquake 97% of fires were reported and 5000 buildings were destroyed.

1999 Marmara earthquake

The 1995 Marmara earthquake occurred on August 17 in Turkey with a magnitude of 7.6 on the Richter Scale. A total of 17 naphtha tanks were lost during the fire.

2000 Napa earthquake

The 2000 Napa earthquake occurred on September 3 in California (US) with a magnitude of 7.4 on the Richter Scale. One fire in a hotel was reported.

2010 Maule earthquake

The 2010 Maule earthquake occurred on February 27 in Chile with a magnitude of 7.4 on the Richter Scale. A few major fires in factories and buildings were reported.

2010-2011 Christchurch earthquake

The 2010 Christchurch earthquake occurred on September 27 in New Zealand with a magnitude of 7.1 on the Richter Scale. Another big earthquake occurred on February 22, 2011 with a magnitude of 6.3. No major fires were reported, but extensive damages to passive and active fire protection systems were observed.

2011 Great-East earthquake

The 2011 Great-East earthquake occurred on March 11 in Japan with a magnitude of 7.4 on the Richter Scale. A total of 293 fire ignitions were reported due to earthquake or tsunami that followed the earthquake. 106 fires in the inland area that were not affected by the tsunami.

2014 South Napa earthquake

The 2014 South Napa earthquake occurred on August 24 in the North San Francisco Bay Area (US) with a magnitude of 6.0 on the Richter

Scale. Six fire ignitions were reported.

2019 Ridgecrest earthquake sequence

The 2019 Ridgecrest earthquake sequence occurred on July 4 and 5 in California (US) with three initial main shocks of magnitudes 6.4, 5.4 and 7.1 on the Richter Scale. Two building fires, one of which destroyed half of a home, occurred in Ridgecrest after the July 4 foreshock. Several fires broke out were reported after the July 5 mainshock hit, most of them in Ridgecrest and Trona.

2019 Cotabato earthquake

The 2014 Cotabato earthquake occurred on October 16 on the island of Mindanao in the Philippines with a magnitude of 6.4 on the Richter Scale. One mall was mostly damaged following a fire triggered by the earthquake.

2021 Fukushima earthquake

The 2021 Fukushima earthquake occurred on February 13, offshore east of Tohoku, in Japan, with a magnitude of 7.1 on the Richter Scale. Small fires broke out in Sendai and Shiogama in Miyagi as a result of the earthquake.

Bibliography

[1] SERA, "Sera website (http://www.sera-eu.org)," 2017.

[2] M. L. Tornaghi, G. Tsionis, P. Pegon, J. Molina, M. Peroni, M. Korzen, S. Riemer, K. Ziener, N. Tondini, P. Covi, G. Abbiati, and Antonelli, "EQUFIRE: Multi-hazard performance assessment of structural and non-structural components subjected to seismic action and fire following earthquake using hybrid simulation," sera proceedings, SERA, 2020.

[3] M. L. Tornaghi, G. Tsionis, P. Pegon, J. Molina, M. Peroni, M. Korzen, N. Tondini, P. Covi, G. Abbiati, M. Antonelli, *et al.*, "Experimental study of braced steel frames subjected to fire after earthquake," 2020.

[4] C. Scawthorn, F. Blackburn, and D. Seagraves, "Earthquakes, fires and urban areas. all the ingredients for a disaster," *Fire journal (Boston, MA)*, vol. 82, no. 4, pp. 20–30, 1988.

[5] R. Botting, "The impact of post-earthquake fire on the urban environment," 1998.

[6] N. E. Khorasani and M. E. Garlock, "Overview of fire following earthquake: Historical events and community responses," *International Journal of Disaster Resilience in the Built Environment*, 2017.

2.0 State of the art

The vulnerability to FFE of the structural system, which has been already weakened by the seismic event, can greatly increase. In a performance-based approach, it would be sensible to evaluate the effect of an earthquake on the fire safety level for buildings located in seismic-prone zones. However, no standards currently address this issue and the two actions are accounted for separately. In this context, it is legitimate to foresee that if FFE continues to be inadequately addressed, this can lead to major disasters again. As already highlighted, most of the works found in the literature involve numerical simulations on the steel moment resisting systems and only a few of them are dedicated to the steel braced frames. In this respect, Talebi et al., [1] studied numerically the fire resistance of a steel braced frame, which was damaged due to a severe earthquake. They investigated the influence of two types of bracing systems, namely buckling restrained brace systems (BRBs) and the conventional braces, on the overall stability of seismically damaged steel buildings in case of fire. Della Corte et al., [2] simulated the effect of fires following earthquake on an unprotected steel moment-resisting frame. Memari et al., [3] analysed the post-earthquake performance of moment-resisting frames with reduced beam section connections. They assumed a protected steel moment-resisting frame whose seismic damage was concentrated at the beam ends that were then considered unprotected in the fire scenarios. Behnam and Ronagh [4] studied the response of unprotected steel moment-resisting frames under FFE. A pushover static nonlinear analysis was performed in SAP2000 and successively, the fire analysis on an equivalent-damaged frame was carried out in SAFIR. Elhami-Khorasani et al., [5] developed a framework for evaluating the post-earthquake performance of steel structures in a multi-hazard context that incorporates tools that are capable of probabilistic structural analyses under fire and seismic loads. They used the finite element software OpenSees to simulate the seismic behaviour of a steel moment-resisting frame subject to fire following earthquake. At the material level, Sinaie et al., [6] proposed functions based on Bézier curves for structural mild steel. Depending on the temperature and the amplitude of previously applied strain cycles, the corresponding curves were used for deriving the stress-strain relationships. The proposed functions were validated against experimental tests on material coupons. At the element or component level, a series of tests on the seismic performance of

sprayed fire-resistive material applied to the steel elements were carried out by Braxtan et al., [7]. The seismic damage of the fireproofing was observed after quasi-static cycling loading. The post-earthquake performance was then analysed numerically because of the inability of the lab facility to perform fire tests on the seismically damaged specimens. The same research group [8] investigated the post-earthquake fire response of a steel moment-resisting frame protected with the fire protection material studied by them in [7]. Few attempts have been carried out to investigate experimentally the effect of earthquake on the fire performance of structural and non-structural components. In particular, Pucinotti et al., [9][10] analysed the post-earthquake fire behaviour of beam-to-concrete filled steel tube column joints. The low-cycle fatigue tests were performed at the lab facility of the University of Trento, whereas the fire tests followed at the Building Research Establishment (BRE) in the UK. Since it was not practical to deliver the seismically damaged specimens to the UK, at the BRE some specimens were pre-damaged before being subjected to fire loadings by imposing monotonic loads equivalent to damage levels induced by seismic loadings. A full-scale test on a reinforced concrete frame of dimensions 3 m x 3 m x 3 m has been recently performed by Kamath et al., [11] to investigate its fire performance after a seismic event. Actuators imposed the seismic loading according to a predefined cyclic loading history. The fire was then applied using kerosene oil as fuel in a pool fire. A large-scale test was carried at the University of San Diego [12][13] to study the post-earthquake performance of a 5-storey reinforced concrete building. The specimen was mounted on the shaking table and tests with seismic isolation and fixed-base were performed. Peak accelerations up to 0.8 g and peak inter-storey drift ratios of up to 6% were reached during the strongest fixed-base motion. The subsequent fire tests were mainly conceived to check how the non-structural components performed after an earthquake. Fires ranged from 500 kW to 2000 kW. The literature study reveals that several numerical studies on the post-earthquake fire behaviour of structural components have been carried out without being supported by comprehensive experimental research. Moreover, works on non-structural components are also very limited. Therefore, this research aims to provide more experimental data, which will be useful for improving the existing design guidelines and building codes. In addition, in the scope of the Performance-Based Earthquake Engineering (PBEE) framework, conditional probability relationships for Damage Measures (DMs) conditioned to Engineering Demand Parameters (EDPs) need to be established in the form of damage models. These models are useful not only for estimating the DM given a set of EDPs, e.g. failure of fire protection or loss of com-

partmentation (DM) given inter-story drift (EDP), but also for informing a computational model so that it can account for the change in thermal loading and compute the appropriate response [14][15]. In fact, these EDP-DM relationships in the form of seismic fragility functions of non-structural components may also be exploited for the future development of a probabilistic framework that includes FFE scenarios.

Compared to earthquake loading, which entails a dynamic structural response, fire development mainly induces a static structural response. Furthermore, the time-dependent behaviour of materials at high temperatures caused by creep and combustion limits the use of extended testing time scales, thus making the use of RT HS compelling for hybrid fire simulation (HFS). A static equation of equilibrium of the hybrid model was considered since the early stages of HFS development. In this regard, it is worth mentioning the seminal paper of Korzen and co-authors [16], where the *substructuring method* was presented in the scope of HFS. The verification of this method was presented in [17]. A realistic case study based on a restrained column was tested a few years later using the same methodology in collaboration with the University of Coimbra (Portugal) [18]. The testing of the PS was performed in displacement-control mode. Following the same idea, HFS of a concrete slab was performed at CERIB, Paris (France), but using actuators in force-control mode. This experimental campaign was documented in [19]. An elegant generalization of the *substructuring method* of Korzen and co-authors was recently published by Mergny and co-authors [20]. In this case, the NS is replaced by a proportional-integral controller designed upon a linear finite-element (FE) model.

The first attempt to extend the HFS paradigm to nonlinear NSs was done by Mostafaei and reported in two companion papers [21, 22]. In this case, at every simulation step, a human operator manually adjusted both the interface displacement of the NS, which was implemented in the SAFIR FE software [23], and the force applied to the PS by means of a servo-controlled actuator. However, Sauca and co-authors [24] demonstrated that the stability of the procedure proposed by Mostafaei is conditioned to the ratio of PS and NS stiffnesses. Moreover, the same procedure does not satisfy both displacement compatibility and force balance between substructures. Later, Sauca and co-authors [25] proposed the modified Newton-Raphson algorithm to solve the static equilibrium equation of the hybrid model relying on an estimate of the initial tangent stiffness matrix of the PS. The method satisfies both displacement compatibility and force balance at the interface between substructures. A purely numerical verification was reported in the same paper. As the main conclusion, the authors claimed that several iterations are neces-

sary to achieve convergence. As an improvement, Wang and co-authors [26] proposed a single-iteration variant to the modified Newton-Raphson method whose static balance equation accounts for residual forces from the previous time step. The same paper reports an experimental verification where the NS is linear.

Schulthess [27] performed the first experimental verification of a fully nonlinear HFS based on the Newton-Raphson algorithm. This work provides a thorough discussion of all numerical and experimental issues related to the coupling of substructures and reports a comprehensive verification of the testing procedure based on linear and nonlinear NSs implemented in the ABAQUS FE software [28].

Regarding the development of a framework to study steel structures subjected to Fire Following Earthquake, Carlton et al. [29] presented a generalized Performance-Based Engineering framework for earthquake and subsequent Fire Following Earthquake. Elhami-Khorasani et al. 1 [5] [15] presented a framework to evaluate the performance of a structure under fire and fire following earthquake by studying the response of the structure for several limit states and incorporating uncertainties in demand and capacity parameters, including fire load, yield strength and modulus of elasticity of steel at elevated temperatures. Mahmoud and Memari [30] developed a new framework for performance-based fire following earthquake engineering. The framework is established by combining stability analysis of isolated columns with system-level finite element analysis of a steel building while accounting for randomness in parameters associated with post-flashover fire, passive fire protection, and mechanical loads and it was used to study the performance of a column in a 3-story moment-resisting frame.

Bibliography

[1] E. Talebi, M. M. Tahir, F. Zahmatkesh, A. B. Kueh, and A. M. Said, "Fire resistance of a damaged building employing buckling restrained braced system," *Advanced Steel Construction*, vol. 14, no. 1, pp. 1–21, 2018.

[2] G. Della Corte, R. Landolfo, and F. Mazzolani, "Post-earthquake fire resistance of moment resisting steel frames," *Fire Safety Journal*, vol. 38, no. 7, pp. 593–612, 2003.

[3] M. Memari, H. Mahmoud, and B. Ellingwood, "Post-earthquake fire performance of moment resisting frames with reduced beam

section connections," *Journal of Constructional Steel Research*, vol. 103, pp. 215–229, 2014.

[4] B. Behnam and H. R. Ronagh, "Post-earthquake fire performance-based behavior of unprotected moment resisting 2d steel frames," *KSCE Journal of Civil Engineering*, vol. 19, no. 1, pp. 274–284, 2015.

[5] N. E. Khorasani, M. E. Garlock, and S. E. Quiel, "Modeling steel structures in opensees: Enhancements for fire and multi-hazard probabilistic analyses," *Computers & Structures*, vol. 157, pp. 218–231, 2015.

[6] S. Sinaie, A. Heidarpour, and X.-L. Zhao, "Stress–strain–temperature relation for cyclically-damaged structural mild steel," *Engineering structures*, vol. 77, pp. 84–94, 2014.

[7] N. L. Braxtan and S. P. Pessiki, "Postearthquake fire performance of sprayed fire-resistive material on steel moment frames," *Journal of Structural Engineering*, vol. 137, no. 9, pp. 946–953, 2011.

[8] W. J. Keller and S. Pessiki, "Effect of earthquake-induced damage to spray-applied fire-resistive insulation on the response of steel moment-frame beam-column connections during fire exposure," *Journal of Fire Protection Engineering*, vol. 22, no. 4, pp. 271–299, 2012.

[9] R. Pucinotti, O. Bursi, and J.-F. Demonceau, "Post-earthquake fire and seismic performance of welded steel–concrete composite beam-to-column joints," *Journal of constructional steel research*, vol. 67, no. 9, pp. 1358–1375, 2011.

[10] R. Pucinotti, O. Bursi, J.-M. Franssen, and T. Lennon, "Seismic-induced fire resistance of composite welded beam-to-column joints with concrete-filled tubes," *Fire safety journal*, vol. 46, no. 6, pp. 335–347, 2011.

[11] P. Kamath, U. K. Sharma, V. Kumar, P. Bhargava, A. Usmani, B. Singh, Y. Singh, J. Torero, M. Gillie, and P. Pankaj, "Full-scale fire test on an earthquake-damaged reinforced concrete frame," *Fire Safety Journal*, vol. 73, pp. 1–19, 2015.

[12] B. J. Meacham, "Post-earthquake fire performance of buildings: Summary of a large-scale experiment and conceptual framework for integrated performance-based seismic and fire design," *Fire Technology*, vol. 52, no. 4, pp. 1133–1157, 2016.

[13] E. Pantoli, M. C. Chen, X. Wang, R. Astroza, H. Ebrahimian, T. C. Hutchinson, J. P. Conte, J. I. Restrepo, C. Marin, K. D. Walsh, *et al.*, "Full-scale structural and nonstructural building system performance during earthquakes: Part ii–ncs damage states," *Earthquake Spectra*, vol. 32, no. 2, pp. 771–794, 2016.

[14] J. Moehle and G. G. Deierlein, "A framework methodology for performance-based earthquake engineering," in *13th world conference on earthquake engineering*, vol. 679, 2004.

[15] N. E. Khorasani, M. Garlock, and P. Gardoni, "Probabilistic performance-based evaluation of a tall steel moment resisting frame under post-earthquake fires," *Journal of Structural Fire Engineering*, 2016.

[16] M. Korzen, G. Magonette, and P. Buchet, "Mechanical Loading of Columns in Fire Tests by Means of the Substructuring Method," *Proceedings of the 8th Interflam Conference, Edinburgh 1999*, vol. 2, no. i, pp. 911–914, 1999.

[17] M. Korzen, K.-U. Ziener, S. Riemer, G. Magonette, and P. Buchet, "Some Remarks on the Substructuring Method Applied to Fire Resistance Tests of Columns," *World Congress on Housing*, 2002.

[18] M. Korzen, J. P. C. Rodrigues, and A. M. Correia, "Thermal restraint effects on the fire resistance of steel and composite steel and concrete columns," *Application of Structural Fire Engineering*, no. February, pp. 512–517, 2009.

[19] F. Robert, S. Rimlinger, and C. Collignon, "Structure Fire Resistance: A Joint Approach between Moedlling and Full Scale Testing (Substructuring System)," in *3rd fib International Congress*, 2010.

[20] E. Mergny, T. Gernay, G. Drion, and J. M. Franssen, "Hybrid fire testing in a non-linear environment using a proportional integral controller," *Journal of Structural Fire Engineering*, vol. 10, no. 2, pp. 245–258, 2019.

[21] H. Mostafaei, "Hybrid fire testing for assessing performance of structures in fire—Methodology," *Fire Safety Journal*, vol. 58, pp. 170–179, 2013.

[22] H. Mostafaei, "Hybrid fire testing for assessing performance of structures in fire—Application," *Fire safety journal*, vol. 56, pp. 30–38, 2013.

[23] J.-M. Franssen and T. Gernay, "Modeling structures in fire with SAFIR®: Theoretical background and capabilities," *Journal of Structural Fire Engineering*, vol. 8, no. 3, pp. 300–323, 2017.

[24] A. Sauca, T. Gernay, F. Robert, N. Tondini, and J.-M. Franssen, "Hybrid fire testing: Discussion on stability and implementation of a new method in a virtual environment," *Journal of Structural Fire Engineering*, vol. 9, no. 4, pp. 319–341, 2018.

[25] A. Sauca, E. Mergny, T. Gernay, and J. M. Franssen, "A method for hybrid fire testing: Development, implementation and numerical application," *Applications of Fire Engineering - Proceedings of the International Conference of Applications of Structural Fire Engineering, ASFE 2017*, pp. 225–234, 2018.

[26] X. Wang, R. E. Kim, O.-s. Kwon, I.-h. Yeo, and J.-k. Ahn, "Continuous Real-Time Hybrid Simulation Method for Structures Subject to Fire," *Journal of Structural Engineering*, vol. 145, p. 04019152, dec 2019.

[27] P. Schulthess, *Consolidated Fire Analysis - Coupled Numerical Simulation and Physical Testing for Global Structural Fire Analysis*. PhD thesis, ETH Zurich, 2019.

[28] ABAQUS Inc., "Abaqus."

[29] A. Carlton and Y. Li, "Performance-based engineering framework for fire following earthquake," in *Structures Congress 2015*, pp. 1608–1618, 2015.

[30] M. Memari and H. Mahmoud, "Framework for a performance-based analysis of fires following earthquakes," *Engineering Structures*, vol. 171, pp. 794–805, 2018.

3.0 EQUFIRE: design and numerical simulations

In the framework of the H2020 SERA Transnational Access (TA) activities, the EQUFIRE proposal foresees an experimental campaign aimed at investigating the multi-hazard performance assessment of structural and non-structural components subjected to seismic and fire following earthquake. In particular, a case study representative of steel concentrically braced frame is envisaged. This first part of the chapter describes the design of a four-storey steel concentrically braced frame according to Eurocodes that will serve as a case study. In the second part of the chapter, some preliminary numerical analyses using OpenSees are presented.

3.1 Overview and Design of the prototype Buildings

3.1.1 Introduction

The building is an office building with a square plan (12.5 m x 12.5 m), as reported in Figure 3.1 and Figure 3.2. It is located in Lisbon (Portugal) in an area of medium-high seismic activity. The storey height is 3 m with the exception of the first floor, which is 3.6 m high so that it can be possibly experimentally tested on a real scale. The lateral force resisting system is placed at the perimeter and in the middle of the building and the remainder of the frames are assumed to carry only gravity loads. Two different steel grades were used, namely S275 and S355 (EN 10025-2, 2005). S275 was adopted for the dissipative elements (bracing system), while S355 was selected for the non-dissipative members.

(a) *(b)*

Figure 3.1: EQUFIRE case study: a) 3D render of the building; b) Isometric view of the structure.

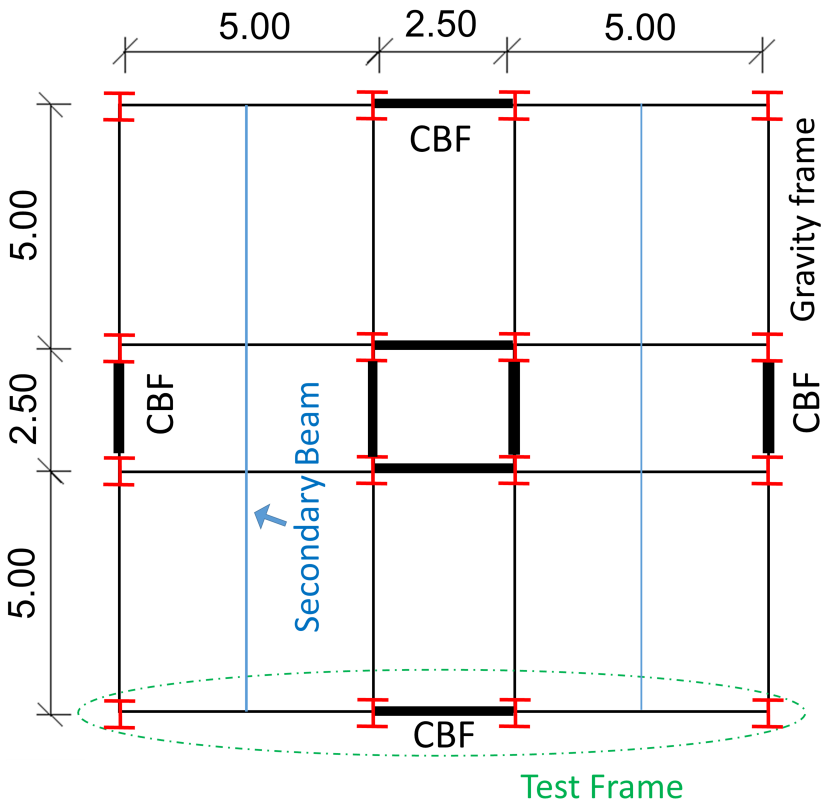

Figure 3.2: Typical Floor Framing Plan. Dimensions are in meters.

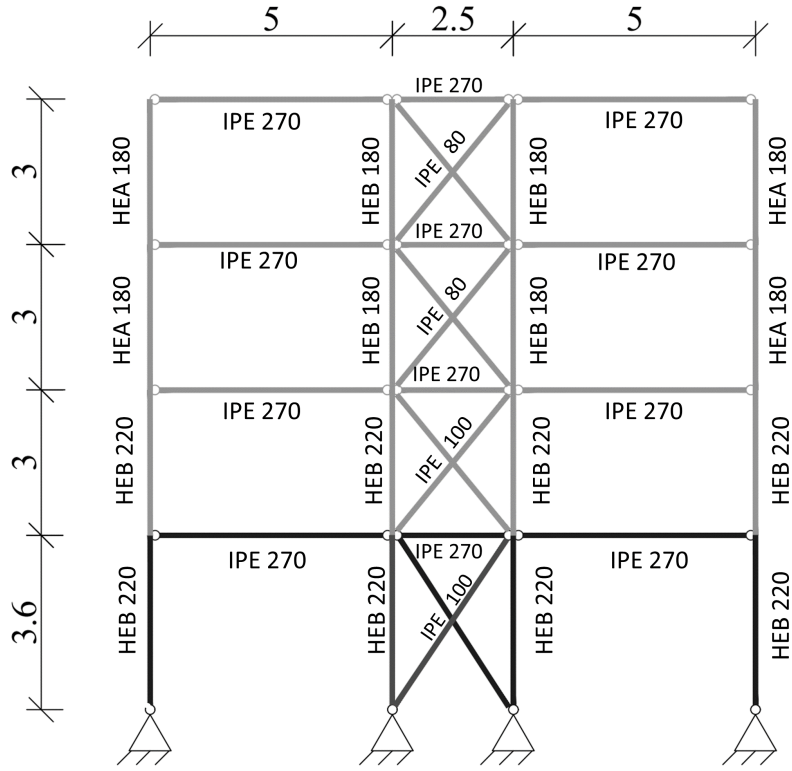

Figure 3.3: Configuration of the frame (dimensions are in meters).

The building is analyzed and designed for all load effects in accordance with the following:

- EN 1991-1-1 (2004) [1], EN 1991-1-3 (2004) [2] and EN 1991-1-3 (2004) [3] - for general actions.
- EN 1993-1-1 (2005) [4] – Design of steel structures.
- EN 1992-1-1 (2005) [5] and EN 1994-1-1 (2005) [6] for steel-concrete composite slab.
- EN 1998-1 (2005) [7] - General rules, seismic actions and rules for buildings.

3.1.2 Structural Design Loads

A summary of the design gravity loads is presented in Table 3.1.

Table 3.1: Design Gravity Loads

Load	Load type	Magnitude
Dead	Dead	2.4 kN/m²
Floor Superimposed Dead	Dead	2.7 kN/m²
Roof Superimposed Dead	Dead	1.3 kN/m²
Facade Dead (Curtain wall)	Dead	8.44 kN/m
Floor Live	Floor Live	2.0 kN/m²
Roof Live	Roof Live	0.5 kN/m²

3.1.3 Structural Design Loads

The composite floor is formed by a steel component (I section beam) which is attached to a concrete slab with a 1 mm thick cold-formed profiled steel sheeting element (type: HI-BOND A 55/P 770-G6). The floor presents a cross-section in which the profile ribs span is perpendicular to the beam.

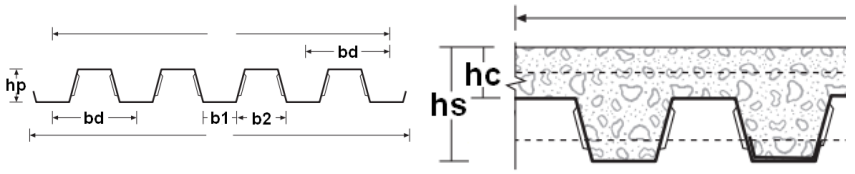

(a) *(b)*

Figure 3.4: Section of cold formed profiled steel sheeting element.

Table 3.2: HI-BOND A 55/P 770-G6

Parameter of composite floor	Value
h_s	120 mm
h_c	65 mm
b_d	154.2 mm
b_1	63.4 mm
b_2	90.8 mm
gk	2.4 kN/m²
Concrete class type	C30/37
Steel sheet grade	S 280 GD

The floor presents A 610 AD mesh reinforcement with 6-mm bars at 100 -mm spacing, both ways as supplementary reinforcement. The short-term elastic modulus and modular ratios is: $C30/37\ E_cm = 33GP_a$

$n_0 = E_a/E_c = 6.36$ For buildings, according EN 1994 permits the simplification that all strains may be assumed to be twice their short-term value: $n = 2\, n_0 = 12.7$

3.1.4 Snow load

For this section, EN 1991-1-3 (2004) is used. The building is located in Lisbon (Portugal) at 2 m above sea level. It is assumed that in the building area, there is no significant removal of snow by wind. So the normal topography ($C_E = 1$) value coefficient is adopted according to the requirements of EN 1991-1-3 (2004).

Table 3.3: Snow load.

Snow load	Value
Characteristic value of snow load on the ground S_k	0.1 kN/m²
Snow load shape coefficient μ_i	0.8
Exposure coefficient C_E	1
thermal coefficient C_T	1
Snow loads on roofs S	0.08 kN/m²

3.1.5 Wind load

For this section, EN 1991-1-4 (2004) is used. The building is located near the coast, the value of basic wind velocity is $v_b = 30.0$ m/s

Peak velocity pressure

Table 3.4: Wind load data.

WIND LOAD	VALUE
Basic wind velocity v_b	30.0 m/s
Basic velocity pressure q_b	0.563 kN/m²
Reference height for the wind action z_e	12.6 m
Terrain category	0 (Coast)
Orography factor $C_0(z_e)$	1
Minimum value of internal pressure coefficient $C_{pi,min}$	-0.3
Maximum value of internal pressure coefficient $C_{pi,max}$	0.2

For terrain category 0 the corresponding values roughness length are $z0 = 0.003m$ and $zmin = 1.0m$. The terrain factor k_r depending on the roughness length $z0 = 0.003m$ is calculated:

$$k_r = 0.19 * \ln\left(\frac{z_0}{z_{0,II}}\right)^{0.07} = 0.156\ m \tag{3.1}$$

The roughness factor $c_r(z_e)$ at the reference height ze For the case where $z_e \geq z_{min}$ is:

$$C_r\left(z_0\right) = k_r * \ln\left(z_e/z_0\right) = 1.302 \tag{3.2}$$

The mean wind velocity $v_m(z_e)$ at reference height z_e:

$$v_m\left(z_e\right) = C_r\left(z_e\right) * \ C_0\left(z_e\right) * \ v_b = 39.1\ m/s \tag{3.3}$$

For the case where $z_e \geq z_{min}$, the turbulence intensity $I_v(z_e)$ at reference height z_e is defined by the following equation:

$$I_v\left(z_e\right) = k_I * \ C_0\left(z_e\right) * \ln\left(z_e/z_0\ \right) = 0.12\ m/s \tag{3.4}$$

The peak velocity pressure $q_p(z_e)$ at reference height z_e is determined:

$$q_p\left(z_e\right) = \left(1 + 7 * \ I_v\left(z_e\right)\right) * \frac{1}{2} * \rho * v_m\left(z_e\right)^2 = 1.75\ kN/m^2 \tag{3.5}$$

Distribution of external wind pressure on the walls

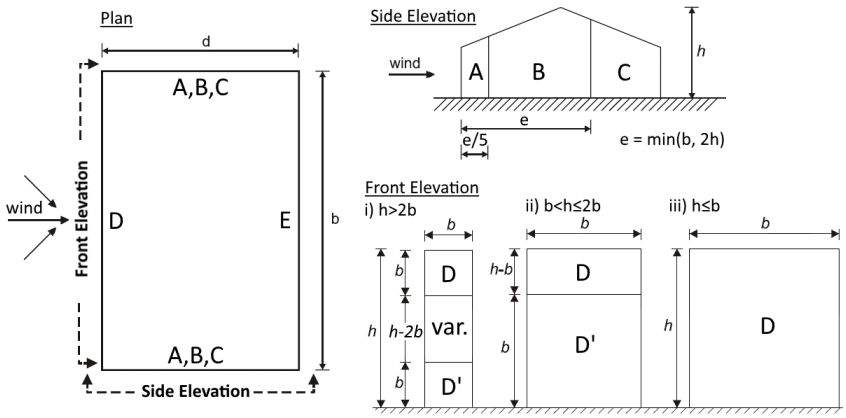

Figure 3.5: Pressure zones for side walls of building (EN1991-1-4).

Internal pressure coefficients c_{pi} are specified in EN1991-1-4 §7.2.9

Table 3.5: Internal pressure coefficients.

WIND LOAD	VALUE
Minimum value of internal pressure coefficient $C_{pi,min}$	-0.3
Maximum value of internal pressure coefficient $C_{pi,max}$	0.2

The external pressure coefficient c_{pe} for each of zones A, B, C, D, E is defined in EN1991-1-4 Table 7.1.

Table 3.6: Values of external pressure coefficients for vertical walls of rectangular plan buildings.

WIND LOAD	VALUE
For zone A: $C_{pe,A}$	-1.2
For zone B: $C_{pe,B}$	-0.8
For zone C: $C_{pe,C}$	-0.5
For zone D: $C_{pe,D}$	0.8
For zone E: $C_{pe,E}$	-0.5

The extend of the zones is defined according to the length e that is defined as:

$$e = \min(b,\ 2h) = 12.5\ m \tag{3.6}$$

The net wind pressure on the surfaces of the structure w_{net} corresponds to the combined effect of external wind pressure and internal wind pressure.

$$w_{net} = w_e - \ w_i = q_p(z_e) * \ C_{pe} - q_p(z_i) * \ C_{pi} \tag{3.7}$$

Table 3.7: Net wind pressure.

NET WIND PRESSURE	VALUE
For zone A: $w_{net,A}$	-2.454 kN/m²
For zone B: $w_{net,B}$	-1.753 kN/m²
For zone C: $w_{net,C}$	–
For zone D: $w_{net,D}$	-1.928 kN/m²
For zone E: $w_{net,E}$	-1.228 kN/m²

Distribution of external wind pressure on the roof

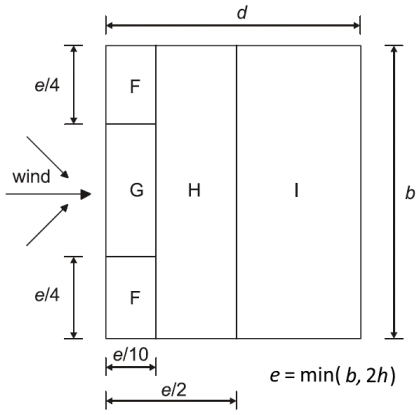

Figure 3.6: Pressure zones for flat roofs, reproduced from EN1991-1-4 Figure 7.6.

The external pressure coefficient cpe for each of F, G, H, I is defined in EN1991-1-4 Table 7.2

Table 3.8: External pressure coefficient.

WIND LOAD	VALUE
For zone F: $C_{pe,A}$	-1.8
For zone G: $C_{pe,B}$	-0.8
For zone H: $C_{pe,C}$	-0.5
For zone I: $C_{pe,D}$	0.8

The net wind pressure on the surfaces of the structure w_{net} corresponds to the combined effect of external wind pressure and internal wind pressure.

$$w_{net} = w_e - \ w_i = q_p\left(z_e\right) * \ C_{pe} - q_p\left(z_i\right) * \ C_{pi} \tag{3.8}$$

Table 3.9: Net wind pressure.

WIND LOAD	VALUE
For zone F: $w_{net,A}$	-3.506 kN/m2
For zone G: $w_{net,B}$	-2.454 kN/m2
For zone H: $w_{net,C}$	-1.578 kN/m2
For zone I: $w_{net,D}$	-0.701 kN/m2 or +0.877 kN/m2

3.2 Seismic Hazard

In accordance with EN1998-1 (2005), the frame was seismically designed according to the capacity design criterion and a linear dynamic 3D analysis was employed. In particular, a concept of "Ductility Class High (DCH)" is used. The dissipation is expected in the bracing members. The general modelling assumptions are the following:

- Only the bracing diagonal in tension was modelled at the ultimate (life safety) limit state.
- The columns were considered continuous along the height of the structure.
- All connections of the beams and diagonals were assumed pinned.
- Masses were considered lumped at the floors, following the assumption of rigid diaphragms.
- The building is regular in plan and in elevation.
- The building is located in Lisbon with a type B of the soil.
- An importance factor equal to 1 was assumed.

For the seismic part, a general design described by the EN 1998-1 [7] is adopted without using national annexes. The only exception is for the determination of the reference peak ground acceleration.

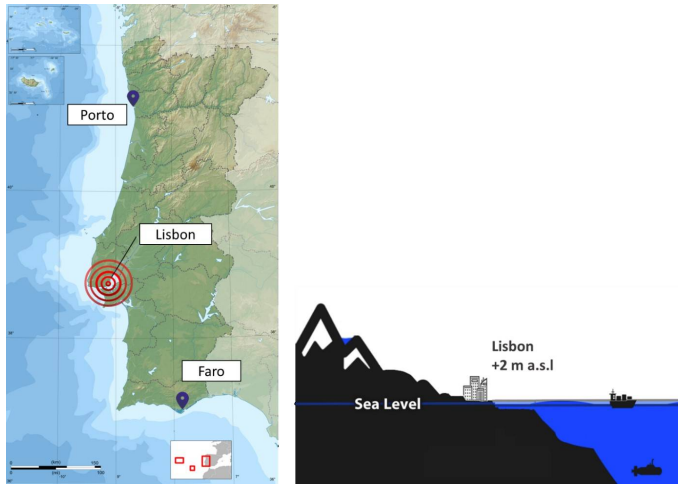

Figure 3.7: Building's location on the map.

The Portugal annexe of EC8 consider two scenarios:

- A hazard scenario labelled seismic action type 1, characterizing long distance severe magnitude earthquakes for the 475 years return period.

- A hazard scenario labeled seismic action type 2, characterizing short distance moderate magnitude earthquakes for the 475 years return period.

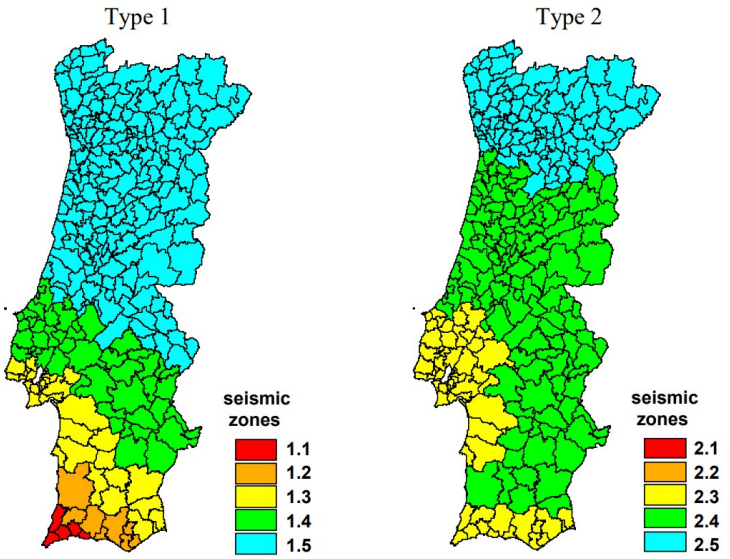

Figure 3.8: Mainland Portugal seismic zonation for Portuguese National Annex of NP EN 1998-1 [7].

The reference ground acceleration for Lisbon is equal to $a_g = 0.15g$ for seismic action type 1 and to $a_g = 0.17g$ for the seismic action type 2.

Some researches and reports [8] about seismic hazard and risk present peak ground acceleration for Portugal and in particular for MAL at the surface, propose more specific PGA values obtained considering the influence of soil conditions for seismic action Type 1 and Type 2. Using the study of Silva et al. [8], the building is located in an area where a reference acceleration is equal to $a_g = 0.186g$ with seismic action type 1. Therefore, a reference PGA of a $a_g = 0.186g$, type B soil and a type 1 elastic spectrum were assumed for a general preliminary design of the structure and then all the checks described by the EN 1998-1 were done.

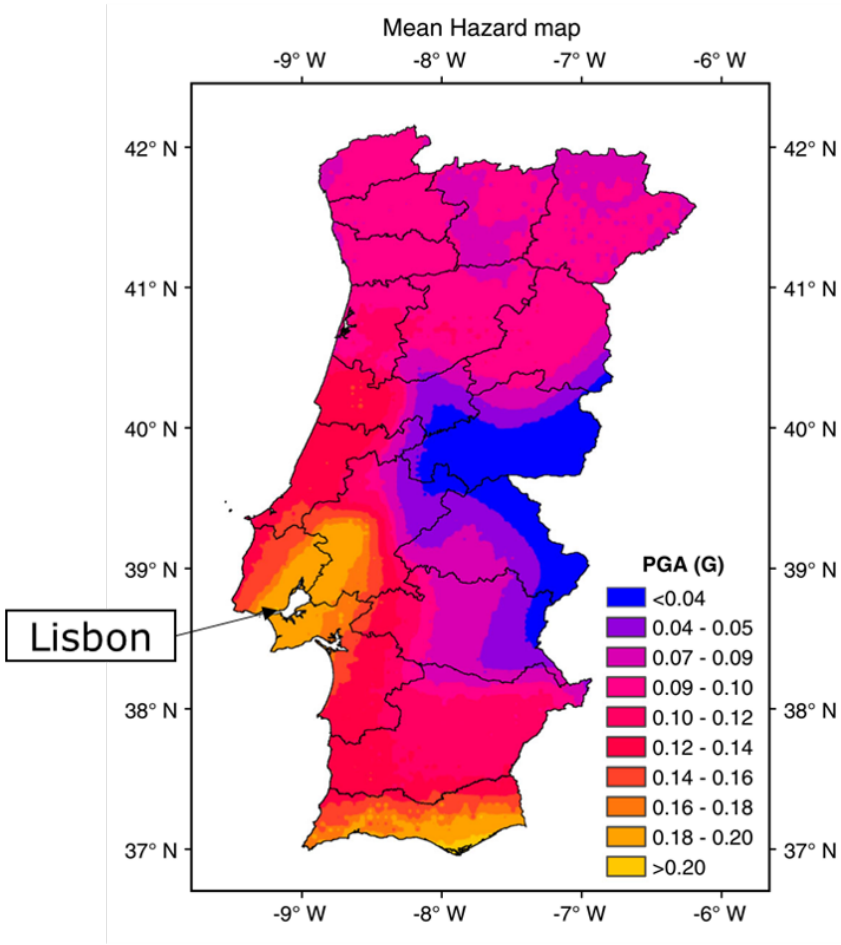

Figure 3.9: Mean seismic hazard map in peak ground acceleration (g) for rock (return period of 475years) [8].

The behaviour factor q is equal to 4, consistently with DCH concept (table 6.2 EN 1998-1, 2005). The lower bound factor β for the design response spectrum was assumed equal to 0.2 (EC8-1 3.2.2.5).

Table 3.10: Spectral parameters type 1 (EC8) of ground type B.

Ground type	S	T_B **[s]**	T_C **[s]**	T_D **[s]**
B	1.2	0.15	0.25	1.2

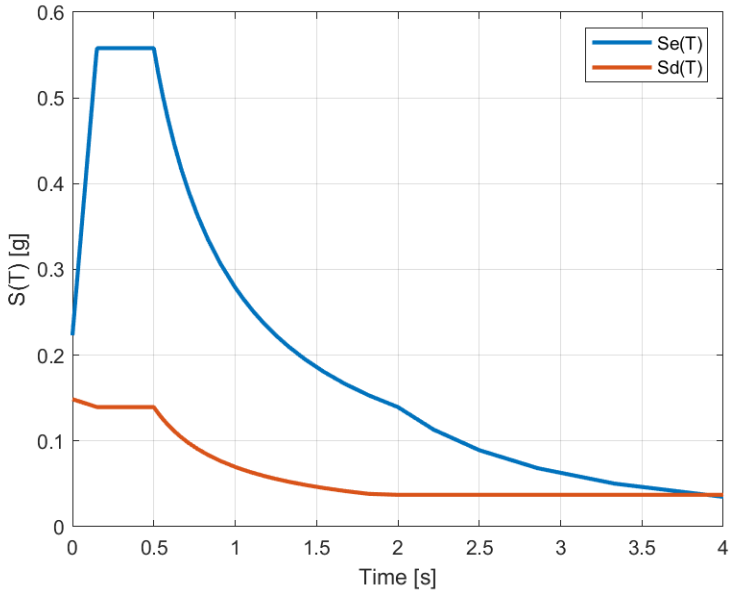

Figure 3.10: Elastic spectral $S_e(T)$ and design spectral $S_d(T)$.

3.3 Masses

The inertial effects in the seismic design situation have to be evaluated by taking into account the presence of the masses corresponding to the combination of permanent and variable gravity loads:

$$\sum (j \geq 1)\, G_{(k,j)} + \sum (i \geq 1)\, \psi_{(E,i)} Q_{(k,i)} \tag{3.9}$$

The value of $\Psi\_(E,i)$ and the corresponding combination coefficients ρ are:

Table 3.11: value of $\psi_{E,i}$.

TYPE OF VARIABLE ACTIONS	$\psi_{2,i}$	ρ	$\psi_{E,i}$
Storey – category B – Office (storey with correlated occupancies)	0.3	0.8	0.24
Roof	0	1	0
Snow (the site is located at altitude H<1000 m a.s.l)	0	1	0

Table 3.12

STOREY	MASS UX	MASS UY	X_{CM} [m]	Y_{CM} [m]	X_{CR} [m]	Y_{CR} [m]
IV	847.6	847.6	6.25	6.25	6.25	6.25
III	1361.4	1361.4	6.25	6.25	6.25	6.25
II	1375.1	1375.1	6.25	6.25	6.25	6.25
I	1394.3	1394.3	6.25	6.25	6.25	6.25

3.4 Structural Analyses

The structural design and analyses of the buildings were analyzed in SAP2000 and ETABS.

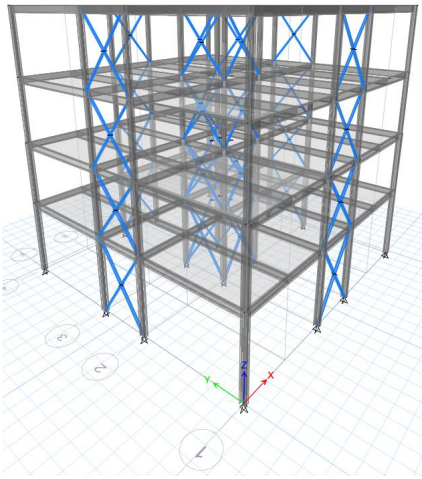

(a)

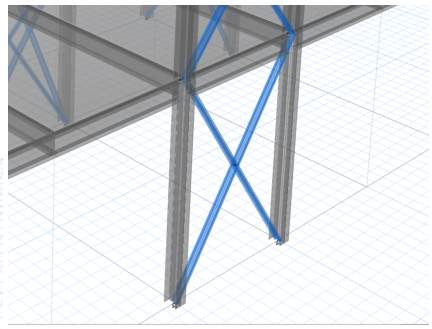

(b)

Figure 3.11: 3D model of the buildings in ETABS.

3.4.1 Linear static 3D analysis

The building examined in this report satisfies the criteria for regularity both in plan and in elevation. Regularity in plan (EC8-1 4.2.3.2):

- The building structure is symmetrical in plan with respect to two orthogonal axes in terms of both lateral stiffness and mass distribution.
- The plan configuration is compact; in fact, each floor may be delimited by a polygonal convex line. Moreover, in plan setbacks or

re-entrant corners or edge recesses do not exist.

- The structure has rigid in plan diaphragm behaviour (a slab thickness greater than 50 mm and total depth greater than 90 mm, as shown in sections 2.4 and 2.5).
- The in-plan slenderness ratio $\lambda = \frac{L_{max}}{L_{min}} = \frac{12.5}{12.5} = 1$ is lower than 4.
- At each level and for both the X and Y directions, the structural eccentricity e_0.

Regularity in elevation (EC8-1 4.2.3.3):

- All seismic resisting systems are distributed along the building height without interruption from the base to the top of the building
- Both lateral stiffness and mass at every storey practically remain constant and/or reduce gradually, without abrupt changes, from the base to the top of the building.
- The ratio of the actual storey resistance to the resistance required by the analysis does not vary disproportionately between adjacent storeys.
- There are no setbacks.

The following expression may approximate the determination of the fundamental period of the structure:

$$T_1 = C_t * H^{\frac{3}{4}} = 0.334\ s \tag{3.10}$$

where:

$$C_t = 0.05H = 12.6\ m \tag{3.11}$$

Alternatively, the estimation of T1 may be made by using the following expression:

$$T_1 = 2 * \sqrt{d} = 0.762\ s \tag{3.12}$$

where:

- d=0.145 m. It is the lateral elastic displacement of the top of the building due to the gravity loads applied in the horizontal direction.

To determine the fundamental period of vibration period T1 of the building, expression based on methods of structural dynamics may be used. In detail a modal analysis was done (see Chapter 3.4.3)

$$T_1 = 0.659\ s \tag{3.13}$$

Since a linear static analysis is used, the effects of actions have been determined by means of the lateral force method (EN 1998-1 4.3.3.2, 2005) and the design base shear force can be calculated according to EN 1998-1 4.3.3.2.2:

$$F_b = \ S_d\left(T_1\right)\ m\ \lambda = 429.5\ kN \tag{3.14}$$

where:

- $S_d\left(T_1\right)$ is the ordinate of the design spectrum at period ($S_d\left(T_1\right) = 0.1058$)
- T_1 is the fundamental period of vibration of the building ($T_1 = 0.659\ s$)
- m is the total mass of the building above the foundation.
- λ is the correction factor, which is equal 0.85 if $T_1 < 2\ T_C$

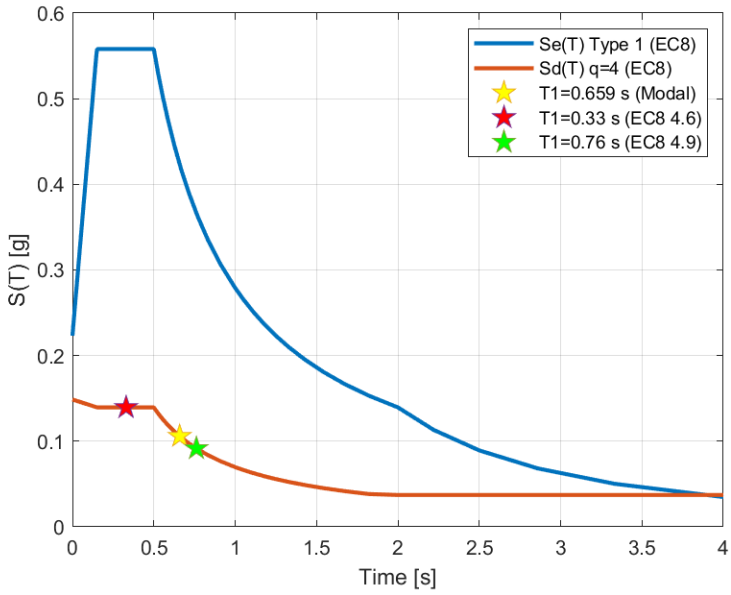

Figure 3.12: Design response spectra and fundamental period of the structure.

According to EN 1998-1 (2005), the relevant δ factor is calculated to consider the effects of the accidental eccentricity. This value has been estimated by the following relation:

$$\delta = 1 + 0.6 * \frac{x}{L_e} \tag{3.15}$$

This factor is equal to $\delta = 1.3$ for the external braces and $\delta = 1.06$ for the internal braces. Therefore, a mean value of the two factors was assumed ($\delta = 1.18$). All the horizontal forces are multiplied by the relevant δ factor.

Table 3.13: Horizontal seismic forces.

Storey	z_i **[m]**	m_i**[ton]**	$\sum(z_i * m_i)$ **[ton*m]**	F_{Hi} **[kN]**	$F_{Hi} * \delta$ **[kN]**
4	12.6	86.4	1088.6	121.2	143
3	9.6	138.8	1332.3	148.3	175
2	6.6	140.2	925.1	103	121.5
1	3.6	142.1	511.7	57	67.2
Total		507.5	3857.6	429.5	506.8

3.4.2 Linear dynamic 3D analysis

The 3D structure was modelled and a modal analysis with response spectrum was done. In particular, two models are considered.
Model A: Both the bracing diagonal in tension and compression were modelled to determine:

- The period of the structure
- Buckling check of the bracing in compression.

Model B: Only the diagonal in tension was modelled to determine:

- Tension check of the bracing.
- Check of beams, columns and connections according to the capacity design.

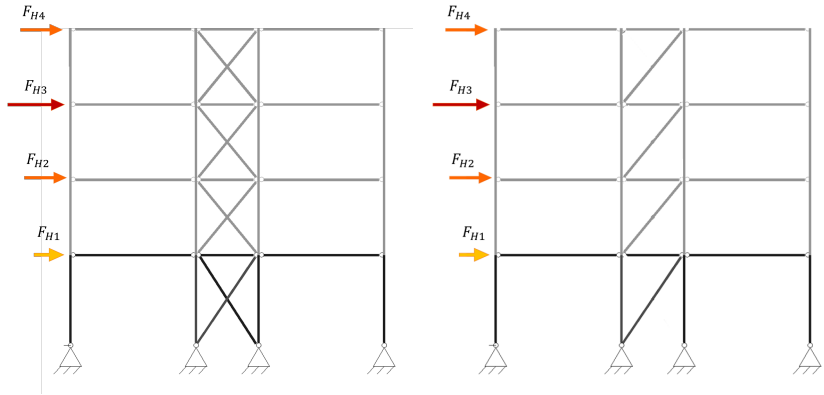

(a) *(b)*

Figure 3.13: Linear dynamic 3D analysis: a) Model A: Both the bracing diagonal in tension and compression; b) Model B: Only the diagonal in tension.

3.4.3 The period of the structure (Model A)

According to Eurocode, it is required to take into account a number of vibration modes that satisfy the following conditions:

- The sum of effective modal masses for the modes taken into account amounts to at least 90% of the total mass of the structure.

- All modes with effective modal masses greater than 5% of the total mass are taken into account.

Based on the considerations mentioned above, the first six modes were considered. The first nine modes with the largest modal masses, which in this case refer to the two translational directions (UX, UY) and the rotational DOF, are shown in Table 3.14.

Table 3.14: Fundamental periods of structures 3D model of the full structure.

Mode	**Dir.**	**T [s]**	m_x **[%]**	m_y **[%]**	m_z **[%]**	$\sum(m_x)$ **[%]**	$\sum(m_y)$ **[%]**	$\sum(m_z)$ **[%]**
Mode 1	UX	0.674	83.9	0	0	83.9	0	0
Mode 2	UY	0.674	0	83.3	0	83.9	83.3	0
Mode 3	RZ	0.682	0	0	84.4	83.9	83.3	84.4
Mode 4	UX	0.223	14.3	0	0	98.2	83.3	84.4
Mode 5	UY	0.223	0	14.1	0	98.2	97.4	84.4
Mode 6	RZ	0.208	0	0	13.8	98.2	97.4	98.2
Mode 7	UX	0.123	1.3	0	0	99.5	97.4	98.2
Mode 8	UY	0.119	0	1.4	0	99.5	98.8	98.2
Mode 9	RZ	0.116	0	0	1.3	99.5	98.8	99.5

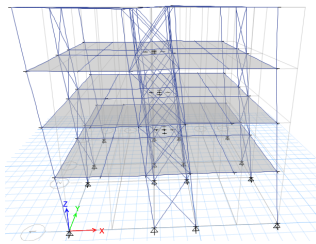

(a) Mode 1 (UX) T =0.659 s.

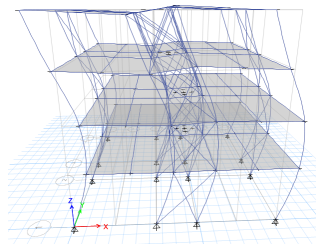

(b) Mode 4 (UX) T =0.218 s.

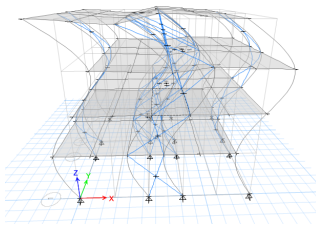

(c) Mode 7 (UX) T =0.123 s

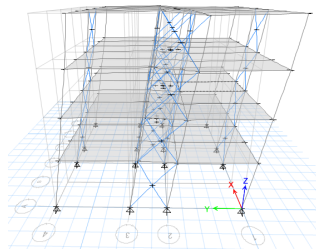

(d) Mode 1 (UY) T =0.659 s

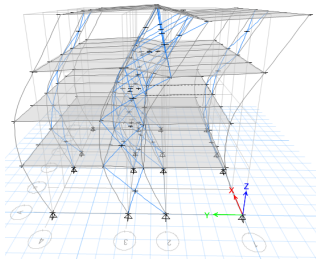

(e) Mode 1 (UY) T =0.215 s

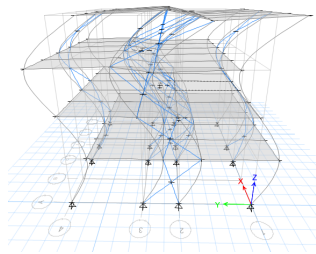

(f) Mode 1 (UY) T =0.119 s

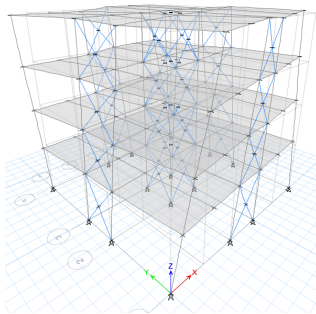

(g) Mode 3 (RZ) T =0.682 s

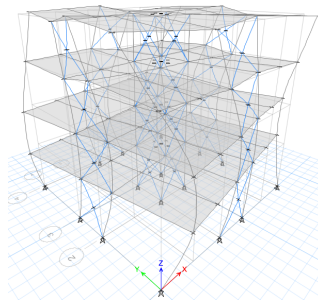

(h) Mode 6 (RZ) T =0.208 s

Figure 3.14: Mode.

Every translational direction of the seismic load is combined with 30% of other directions and these combinations are combined with other permanent and variable load cases.

3.4.4 Bracing members

The bracing cross sections are of Class 1, as defined by EN 1993:1-1 5.6 (2005).

Table 3.15: Proprieties of the braces

STOREY	BRACING CROSS SECTION	h [mm]	b [mm]	t_w [mm]	t_f [mm]	SECTION CLASSIFICATION
4	IPE 80	80	46	3.8	5.2	Class 1
3	IPE 80	80	46	3.8	5.2	Class 1
2	IPE 100	100	55	4.1	5.7	Class 1
1	IPE 100	100	55	4.1	5.7	Class 1

In this section, to respect lab constraints, not all the checks of Eurocode are satisfied, in particular:

- EC8 6.7.3 (1) In frames with X diagonal bracings, the non-dimensional slenderness O as defined in EN 1993-1-1:2004 should be limited to: $1.3 \leq \lambda \leq 2.0$. NOTE The 1,3 limit is defined to avoid overloading columns in the pre-buckling stage (when both compression and tension diagonals are active) beyond the action effects obtained from an analysis at the ultimate stage where only the tension diagonal is taken as active.

- EC8 6.7.3 (8) In order to satisfy a homogeneous dissipative behaviour of the diagonals, it should be checked that the maximum overstrength: Ω_i defined in 6.7.4(1) does not differ from the minimum value: by more than 25%.

Table 3.16

Storey	**1st floor**	**2nd floor**	**3rd floor**	**4th floor**
$\bar{\lambda}^*$ (out of plane)	1.24	1.10	1.39	1.39
$\bar{\lambda}^{**}$ (in plane)	1.42	1.27	1.49	1.49

Table 3.17: X-bracings design tension checks.

Storey	Bracing cross section	$\mathbf{N_{Ed,G+E}}$ [kN]	$\mathbf{N_{pl,Rd}}$ [kN]	$\frac{N_{Ed}}{N_{pl.Rd}}$	$\mathbf{\Omega_i = \frac{N_{pl,Rd}}{N_{Ed}}}$	$\mathbf{\frac{\Omega_i - \Omega}{\Omega}}$
4	IPE 80	68.1	210.1	0.32	3.08	1.66
3	IPE 80	134.3	210.1	0.64	1.56	0.35
2	IPE 100	189.3	283.3	0.67	1.50	0.29
1	IPE 100	244.0	283.3	0.86	1.16	0.00

$$\frac{max\Omega}{min\Omega} < 1.25 \rightarrow \frac{max\Omega}{min\Omega} = 2.66 \tag{3.16}$$

The minimum overstrength ratio Ω is equal to 1.07 and the maximum overstrength ratio is equal to 3.45. Hence, according to capacity design criteria, the seismic induced forces acting in the non-dissipative members should be amplified by:

$$1.1 \cdot \gamma_{0v} \cdot \Omega = 1.1 \cdot 1.25 \cdot 1.16 = 1.596 \tag{3.17}$$

Table 3.18: X-bracings design compression checks.

Storey	Bracing cross section	L [m]	$\mathbf{N_{Ed,G+E}}$ [kN]	$\mathbf{N_{b,Rd,y-y}}$ [kN]	$\mathbf{N_{b,Rd,z-z}}$ [kN]	$\mathbf{\frac{N_{Ed}}{N_{b,Rd,y-y}}}$	$\mathbf{\frac{N_{Ed}}{N_{b,Rd,z-z}}}$
4	IPE 80	1.953	-37.3	88.9	72.4	0.43	0.49
3	IPE 80	1.953	-81.3	89.0	72.4	0.84	1.04
2	IPE 100	1.953	-110.5	168.2	125.6	0.62	0.84
1	IPE 100	2.150	-146.8	143.4	105.6	1.00	1.36

3.5 Columns (Model B)

3.5.1 Internal columns (Model B)

Table 3.19: Axial checks for internal columns

Storey	Section	$\mathbf{N_{Ed,G}}$ [kN]	$\mathbf{N_{Ed,E}}$ [kN]	$N_{Ed} = N_{Ed,G} + \alpha \cdot N_{Ed,E}$ [kN]	$\mathbf{N_{pl,Rd}}$ [kN]	$\mathbf{N_{b,Rd}}$ [kN]	$\mathbf{\frac{N_{Ed}}{N_{b,Rd}}}$
4	HEB 180	-39.6	-52.3	-123.1	2318.2	1448.8	0.08
3	HEB 180	-127.7	-155.5	-375.9	2318.2	1448.8	0.26
2	HEB 220	-218.4	-301.0	-698.7	3230.5	2336.2	0.30
1	HEB 220	-308.9	-501.4	-1109.2	3230.5	2052.1	0.54

Table 3.20: Tension or minimum resistance for internal columns.

Storey	**Section**	$\mathbf{N_{Ed,G}}$ **[kN]**	$\mathbf{N_{Ed,E}}$ **[kN]**	$N_{Ed} = N_{Ed,G} + \alpha \cdot N_{Ed,E}$ **[kN]**	$\mathbf{N_{pl,Rd}}$ **[kN]**	$\frac{\mathbf{N_{Ed}}}{\mathbf{N_{p,Rd}}}$
4	HEB 180	-39.6	25.1	0.4	2318.2	0.01
3	HEB 180	-127.7	101.5	34.4	2318.2	0.01
2	HEB 220	-218.4	223.5	138.3	3230.5	0.04
1	HEB 220	-308.9	396.6	324.4	3230.5	0.10

Table 3.21: Shear checks for internal columns.

Storey	**Section**	$\mathbf{V_{Ed,G}}$ **[kN]**	$\mathbf{V_{Ed,E}}$ **[kN]**	$V_{Ed} = V_{Ed,G} + \alpha \cdot V_{Ed,E}$ **[kN]**	$\mathbf{V_{c,Rd}}$ **[kN]**	$\frac{\mathbf{V_{Ed}}}{\mathbf{V_{c,Rd}}}$
4	HEB 180	0	<1	<1.5	297.6	<0.01
3	HEB 180	0	<1	<1.5	297.6	<0.01
2	HEB 220	0	<1	<1.5	571.4	<0.01
1	HEB 220	0	<1	<1.5	571.4	<0.01

According to EN 1993-1-1 6.3.3 (2005), members who are subjected to combined bending and axial compression satisfy:

$$\frac{N_{Ed}}{\frac{\chi_y \cdot N_{Rk}}{\gamma_{M1}}} + k_{yy}\frac{M_{y,Ed} + \Delta M_{y,Ed}}{\chi_{LT}\frac{M_{y,Rk}}{\gamma_{M1}}} + k_{yz}\frac{M_{z,Ed} + \Delta M_{z,Ed}}{\frac{M_{z,Rk}}{\gamma_{M1}}} \leq 1$$

$$\frac{N_{Ed}}{\frac{\chi_z \cdot N_{Rk}}{\gamma_{M1}}} + k_{zy}\frac{M_{y,Ed} + \Delta M_{y,Ed}}{\chi_{LT}\frac{M_{y,Rk}}{\gamma_{M1}}} + k_{zz}\frac{M_{z,Ed} + \Delta M_{z,Ed}}{\frac{M_{z,Rk}}{\gamma_{M1}}} \leq 1 \tag{3.18}$$

Method 2 of Eurocode 3 is used to determine the factors.

Table 3.22: Combined bending-axial stability checks of internal columns.

Storey	**Section**	$\mathbf{N_{Ed,G+E}}$ **[kN]**	$\mathbf{M_{Ed,G}}$ **[kNm]**	$\mathbf{M_{Ed,E}}$ **[kNm]**	$\mathbf{M_{Ed}} = \mathbf{M_{Ed,G}} + \alpha \cdot \mathbf{M_{Ed,E}}$ **[kNm]**	**EC3 Equation 6.61** (≤ 1)	**EC3 Equation 6.62** (≤ 1)
4	HEB 180	-123.1	0.0	2.5	3.7	0.086	0.110
3	HEB 180	-375.9	0.0	2.5	3.7	0.211	0.284
2	HEB 220	-698.7	0.0	2.5	3.7	0.250	0.313
1	HEB 220	-1109.2	0.0	2.5	3.7	0.397	0.552

3.5.2 External columns (Model B)

Table 3.23: Axial checks for external columns.

Storey	Section	$N_{Ed,G}$ [kN]	$N_{Ed,E}$ [kN]	$N_{Ed} = N_{Ed,G} + \alpha \cdot N_{Ed,E}$ [kN]	$N_{pl,Rd}$ [kN]	$N_{b,Rd}$ [kN]	$\frac{N_{Ed}}{N_{b,Rd}}$
4	HEA 180	-26.4	0.0	-26.4	1608.2	995.4	0.03
3	HEA 180	-106.7	0.0	-106.7	1608.2	995.4	0.11
2	HEB 220	-187.9	0.0	-187.9	3230.5	2336.2	0.08
1	HEB 220	-270.0	0.0	-270.0	3230.5	2052.1	0.13

Table 3.24: Shear checks for external columns.

Storey	Section	$V_{Ed,G}$ [kN]	$V_{Ed,E}$ [kN]	$V_{Ed} = V_{Ed,G} + \alpha \cdot V_{Ed,E}$ [kN]	$V_{c,Rd}$ [kN]	$\frac{V_{Ed}}{V_{c,Rd}}$
4	HEA 180	0	<1	<1.5	297.6	<0.01
3	HEA 180	0	<1	<1.5	297.6	<0.01
2	HEB 220	0	<1	<1.5	571.4	<0.01
1	HEB 220	0	<1	<1.5	571.4	<0.01

Table 3.25: Combined bending-axial stability checks of external columns.

Storey	Section	$N_{Ed,G+E}$ [kN]	$M_{Ed,G}$ [kNm]	$M_{Ed,E}$ [kNm]	$M_{Ed} = M_{Ed,G} + \alpha \cdot M_{Ed,E}$ [kNm]	EC3 Equation 6.61 (≤ 1)	EC3 Equation 6.62 (≤ 1)
4	HEA 180	-26.4	0.0	2.5	3.7	0.040	0.062
3	HEA 180	-106.7	0.0	2.5	3.7	0.098	0.142
2	HEB 220	-187.9	0.0	2.5	3.7	0.072	0.094
1	HEB 220	-270.0	0.0	2.5	3.7	0.103	0.145

3.6 Beams

The assumption of the floor rigid diaphragms in their planes implies that the numerical model gives axial forces in the beams equal to zero. Nevertheless, it is possible to calculate the beam axial forces by simple hand calculations. In detail, it can be easily obtained by imposing static equilibrium of the forces acting on the beams.

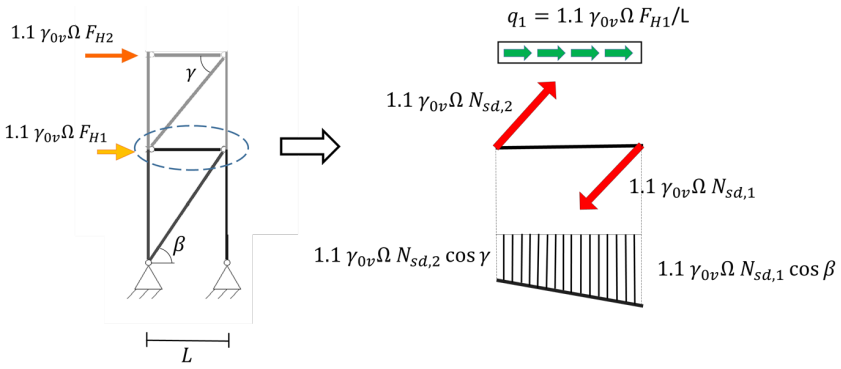

Figure 3.15: Axial force in the beam.

3.7 Internal beams

Table 3.26: Combined bending-axial strength checks at mid-length of internal beams.

Storey	**Section**	$\mathbf{N_{Ed,G}}$ **[kN]**	$\mathbf{M_{Ed,E}}$ **[kN]**	$\mathbf{N_{Ed} = N_{Ed,G} + \alpha \cdot N_{Ed,E}}$ **[kN]**	$\mathbf{N_{pl,Rd}}$ **[kN]**	$\mathbf{N_{b,Rd}}$ **[kN]**	$\frac{\mathbf{N_{Ed}}}{\mathbf{N_{b,Rd}}}$
4	IPE 270	0	-43.6	-69.6	1629.5	890.3	0.08
3	IPE 270	0	-86.0	-137.3	1629.5	890.3	0.15
2	IPE 270	0	-121.2	-193.4	1629.5	890.3	0.22
1	IPE 270	0	-139.2	-222.6	1629.5	890.3	0.25

Table 3.27

Storey	**Section**	$\mathbf{N_{Ed} = N_{Ed,G} + \alpha \cdot N_{Ed,E}}$ **[kN]**	$\mathbf{M_{Ed,G}}$ **[kNm]**	$\mathbf{M_{Ed,E}}$ **[kNm]**	$\mathbf{M_{Ed} = M_{Ed,G} + \alpha \cdot M_{Ed,E}}$ **[kNm]**	$\mathbf{M_{N,Rd}}$ **[kNm]**	$\frac{\mathbf{M_{Ed}}}{\mathbf{M_{N,Rd}}}$
4	IPE 270	-69.6	6.6	0.0	6.6	133.2	0.05
3	IPE 270	-137.3	6.6	0.0	6.6	133.2	0.05
2	IPE 270	-193.4	6.6	0.0	6.6	133.2	0.05
1	IPE 270	-222.6	6.6	0.0	6.6	133.2	0.05

Table 3.28

Storey	**Section**	$\mathbf{N_{Ed,G+E}}$ **[kN]**	$\mathbf{M_{Ed,G+E}}$ **[kNm]**	**EC3 Equation 6.61** (≤ 1)	**EC3 Equation 6.62** (≤ 1)
4	IPE 270	-69.6	6.6	0.090	0.126
3	IPE 270	-137.3	6.6	0.135	0.205
2	IPE 270	-193.4	6.6	0.172	0.271
1	IPE 270	-222.6	6.6	0.191	0.305

Shear

Table 3.29: Shear checks for internal beams.

Storey	**Section**	$\mathbf{V_{Ed,G}}$ **[kN]**	$\mathbf{V_{Ed,E}}$ **[kN]**	$\mathbf{V_{Ed} = V_{Ed,G} + \alpha \cdot V_{Ed,E}}$ **[kN]**	$\mathbf{V_{c,Rd}}$ **[kN]**	$\frac{\mathbf{V_{Ed}}}{\mathbf{V_{c,Rd}}}$
4	IPE 270	11.0	0.0	11.0	452.8	0.02
3	IPE 270	11.0	0.0	11.0	452.8	0.02
2	IPE 270	11.0	0.0	11.0	452.8	0.02
1	IPE 270	11.0	0.0	11.0	452.8	0.02

Bending and shear

Not significant for the element under study.

3.7.1 External beams

Combined bending and axial strength checks

Table 3.30: Combined bending-axial strength checks at mid-length of external beams.

Storey	**Section**	$\mathbf{N_{Ed,G}}$ **[kN]**	$\mathbf{N_{Ed,E}}$ **[kN]**	$\mathbf{N_{Ed} = N_{Ed,G} + \alpha \cdot N_{Ed,E}}$ **[kN]**	$\mathbf{M_{Ed,G}}$ **[kNm]**	$\mathbf{M_{Ed,E}}$ **[kNm]**	$\mathbf{M_{Ed} = M_{Ed,G} + \alpha \cdot M_{Ed,E}}$ **[kNm]**	$\mathbf{M_{N,Rd}}$ **[kNm]**	$\frac{\mathbf{M_{Ed}}}{\mathbf{M_{N,Rd}}}$
4	IPE 270	0.0	-43.6	-69.6	30.2	0.0	30.2	133.2	0.23
3	IPE 270	0.0	-42.4	-67.7	73.1	0.0	73.1	133.2	0.44
2	IPE 270	0.0	-35.2	-56.2	73.1	0.0	73.1	133.2	0.41
1	IPE 270	0.0	-18.0	-28.7	73.1	0.0	73.1	133.2	0.40

Table 3.31

Storey	**Section**	$\mathbf{N_{Ed,G+E}}$ **[kN]**	$\mathbf{M_{Ed,E+G}}$ **[kNm]**	**EC3 Equation 6.61** (≤ 1)	**EC3 Equation 6.62** (≤ 1)
4	IPE 270	-69.6	30.2	0.293	0.318
3	IPE 270	-67.7	73.1	0.636	0.650
2	IPE 270	-56.2	73.1	0.625	0.637
1	IPE 270	-28.7	73.1	0.607	0.601

Shear

Table 3.32: Shear checks for external beams

Storey	**Section**	$\mathbf{V_{Ed,G}}$ **[kN]**	$\mathbf{V_{Ed,E}}$ **[kN]**	$\mathbf{V_{Ed} = V_{Ed,G} + \alpha \cdot V_{Ed,E}}$ **[kN]**	$\mathbf{V_{c,Rd}}$ **[kN]**	$\frac{\mathbf{V_{Ed}}}{\mathbf{V_{c,Rd}}}$ **[kN]**
4	IPE 270	13.0	0.0	13.0	452.8	0.03
3	IPE 270	40.2	0.0	40.2	452.8	0.09
2	IPE 270	40.2	0.0	40.2	452.8	0.09
1	IPE 270	40.2	0.0	40.2	452.8	0.09

Bending and shear

Not significant for the element under study.

3.7.2 External and Internal beams for JRC setup

3.10.3.1 Combined bending and axial strength checks

Table 3.33: Combined bending-axial strength checks at mid-length of internal beams.

Storey	**Section**	$\mathbf{N_{Ed,G}}$ **[kN]**	$\mathbf{M_{Ed,E}}$ **[kN]**	$\mathbf{N_{Ed} = N_{Ed,G} + \alpha \cdot N_{Ed,E}}$ **[kN]**	$\mathbf{N_{pl,Rd}}$ **[kN]**	$\mathbf{N_{b,Rd}}$ **[kN]**	$\frac{\mathbf{N_{Ed}}}{\mathbf{N_{b,Rd}}}$
1	IPE 270 (internal)	0	-139.2	-222.6	1629.5	890.3	0.25
1	IPE 270 (external)	0	-139.2	-222.6	1629.5	890.3	0.25

Table 3.34

Storey	**Section**	$\mathbf{N_{Ed} = N_{Ed,G} + \alpha \cdot N_{Ed,E}}$ **[kN]**	$\mathbf{M_{Ed,G}}$ **[kNm]**	$\mathbf{M_{Ed,E}}$ **[kNm]**	$\mathbf{M_{Ed} = M_{Ed,G} + \alpha \cdot M_{Ed,E}}$ **[kNm]**	$\mathbf{M_{N,Rd}}$ **[kNm]**	$\frac{\mathbf{M_{Ed}}}{\mathbf{M_{N,Rd}}}$
1	IPE 270 (Internal)	-222.6	0.3	0.0	0.3	133.2	0.01
1	IPE 270 (External)	-222.6	1.15	0.0	1.15	133.2	0.01

Table 3.35

Storey	**Section**	$\mathbf{N_{Ed,G+E}}$ **[kN]**	$\mathbf{M_{Ed,G+E}}$ **[kNm]**	**EC3 Equation 6.61** (≤ 1)	**EC3 Equation 6.62** (≤ 1)
1	IPE 270 (Internal)	-222.6	0.3	0.148	0.264
1	IPE 270 (External)	-222.6	1.15	0.169	0.271

Shear

Table 3.36: Shear checks for internal beams.

Storey	**Section**	$\mathbf{V_{Ed,G}}$ **[kN]**	$\mathbf{V_{Ed,E}}$ **[kN]**	$\mathbf{V_{Ed} = V_{Ed,G} + \alpha \cdot V_{Ed,E}}$ **[kN]**	$\mathbf{V_{c,Rd}}$ **[kN]**	$\frac{\mathbf{V_{Ed}}}{\mathbf{V_{c,Rd}}}$
1	IPE 270 (Internal)	0.4	0.0	0.4	452.8	0.01
1	IPE 270 (External)	1.0	0.0	1.0	452.8	0.01

Bending and shear

Not significant for the element under study.

3.8 LAB Connections

Two types of approaches were adopted to verify connections:

- Every single part of the joint are checked using the Eurocode 3 provisions.
- The whole joint is modelled by a 3D finite element model.

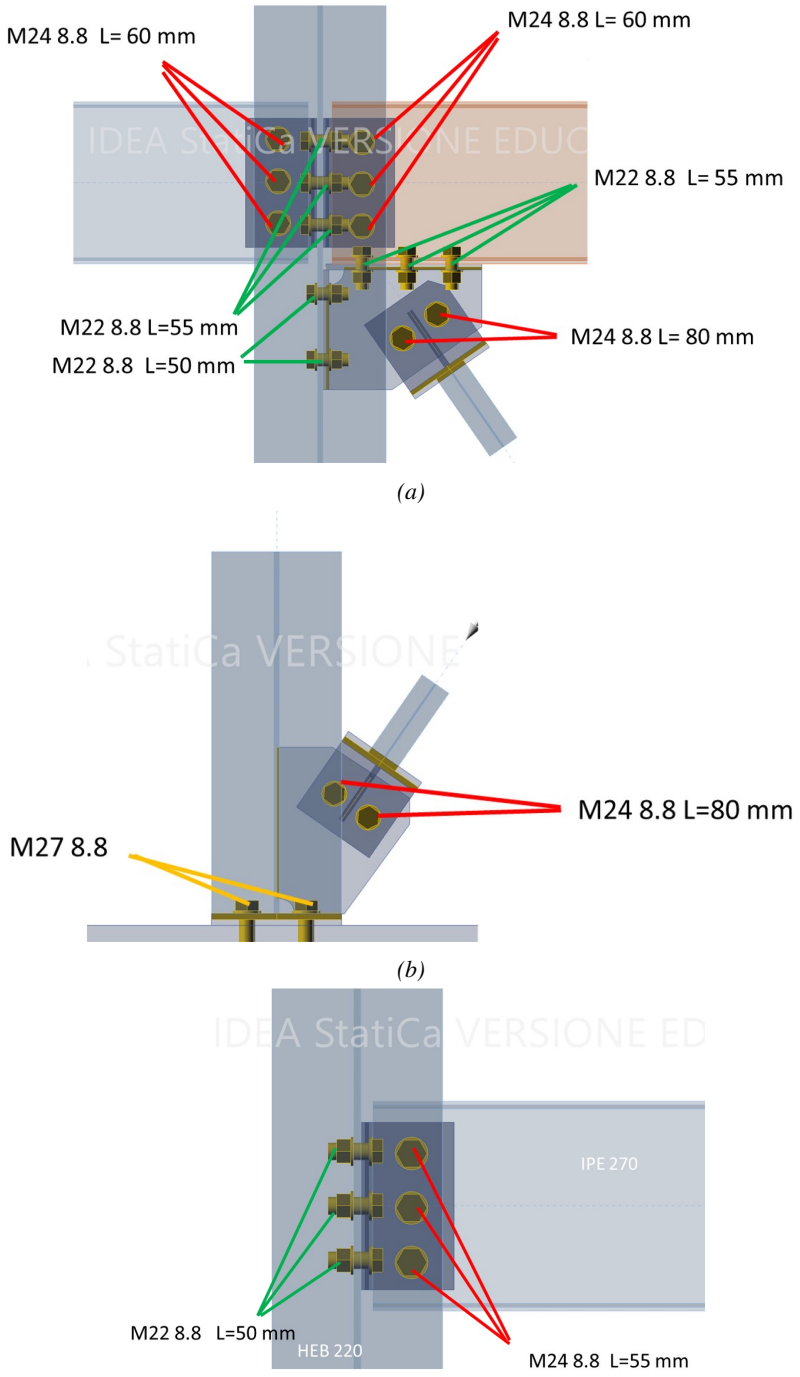

Figure 3.16: Connection: a) beam-column-brace connection; b) Column base connection; c) beam-column connection.

3.9 Ground Motions

3.9.1 Ground Motion Record Set

A set of fifteen accelerograms was selected considering the type of spectrum, earthquake scenario (magnitude range, distance range, style-of-faulting), local site conditions, period range, and ground motion components using the INGV/EPOS/ORFEUS European strong motion database [9]. In detail, the records were selected with the following criteria:

- Target spectrum
  - Peak Ground Acceleration [g]: 0.18
  - Site classification: B
- Preliminary record search
  - Station site classification: A*,B
  - Magnitude min: 6.0
  - Magnitude max: 6.5
  - Types of magnitude considered: null
  - Epicentral distance min [km]: 0.0
  - Epicentral distance max [km]: 50.0
  - Include late trigger events: no
  - Include analog recordings: yes
- Spectrum matching parameters and analysis options
  - Period range min [s]: 0.15
  - Period range max [s]: 0.6
  - Tolerance below average [%]: 1.0
  - Tolerance above average [%]: 10.0
  - Scaled records: no

Table 3.37: Accelerograms.

Label	Dir	Evento ID	Station	Date	Pga-raw [m/s2]	Pga-mod [m/s2]	Time [s]
ACC1	EW	EMSC-20161026_0000095	Amatrice giardino	20161026-191806	-1,69669	-2,3782	82,675
ACC1	NS	EMSC-20161026_0000095	Amatrice giardino	20161026-191806	-0,99808	-1,3978	82,675
ACC2	EW	EMSC-20161026_0000095	Poggio Vitellino	20161026-191806	1,791239	2,1904	73,065
ACC2	NS	EMSC-20161026_0000095	Poggio Vitellino	20161026-191806	-1,24202	-2,1041	73,065
ACC3	EW	EMSC-20161026_0000095	Amatrice agriturismo	20161026-191806	1,790094	1,91	73,285
ACC3	NS	EMSC-20161026_0000095	Amatrice agriturismo	20161026-191806	-1,10487	-2,6769	73,285
ACC4	EW	IT-1976-0030	S. rocco	19760915-092118	-2,44807	1,9337	16,875
ACC4	NS	IT-1976-0030	S. rocco	19760915-092118	-1,28428	-3,1061	16,875
ACC5	EW	GR-1993-0027	Patras	19930714-123148	1,466075	2,287	43,84
ACC5	NS	GR-1993-0027	Patras	19930714-123148	1,95304	2,5839	43,84
ACC6	EW	GR-1993-0027	Patras	19930714-123148	1,470768	-2,1626	43,84
ACC6	NS	GR-1993-0027	Patras	19930714-123148	1,984963	3,4241	43,84
ACC7	EW	EMSC-20161026_0000095	Castelluccio di norcia	20161026-191806	-1,79955	-2,5626	39,26
ACC7	NS	EMSC-20161026_0000095	Castelluccio di norcia	20161026-191806	-1,89388	-2,9773	39,26
ACC8	EW	EMSC-20160824_0000006	Mascioni (campotosto)	20160824-013632	1,079881	3,4377	49,84
ACC8	NS	EMSC-20160824_0000006	Mascioni (campotosto)	20160824-013632	0,775241	-2,434	49,84
ACC9	EW	EMSC-20161026_0000095	Matelica	20161026-191806	-1,22182	-2,0971	57,805
ACC9	NS	EMSC-20161026_0000095	Matelica	20161026-191806	-2,40469	-2,8802	57,805
ACC10	EW	EMSC-20160824_0000006	norcia la castellina	20160824-013632	1,979058	3,0447	39,95
ACC10	NS	EMSC-20160824_0000006	Norcia la castellina	20160824-013632	-1,7667	2,992	39,95
ACC11	EW	EMSC-20161026_0000095	Norcia la castellina	20161026-191806	2,107975	1,8352	73,86
ACC11	NS	EMSC-20161026_0000095	Norcia la castellina	20161026-191806	1,183564	1,9234	73,86
ACC12	EW	EMSC-20160824_0000006	Mmascioni (campotosto)	20160824-013632	0,775241	-3,6119	49,84
ACC12	NS	EMSC-20160824_0000006	Mascioni (campotosto)	20160824-013632	0,775241	4,9759	49,84
ACC13	EW	IT-1976-0030	Gemona	19760915-092118	2,501217	2,629	9,285
ACC13	NS	IT-1976-0030	Gemona	19760915-092118	2,474678	3,5561	9,285
ACC14	EW	EMSC-20161026_0000095	Gualdo macerata	20161026-191806	-1,18997	-2,5815	180,4
ACC14	NS	EMSC-20161026_0000095	Gualdo macerata	20161026-191806	1,281548	2,0741	180,4
ACC14	EW	EMSC-20161026_0000095	Domo	20161026-191806	-0,95317	-2,8145	103,06
ACC14	NS	EMSC-20161026_0000095	Domo	20161026-191806	-1,35427	-3,2617	103,06

The accelerograms were modified to match the target spectrum in the period range of 0.4 s - 0.9 s that includes the fundamental period of the structure.

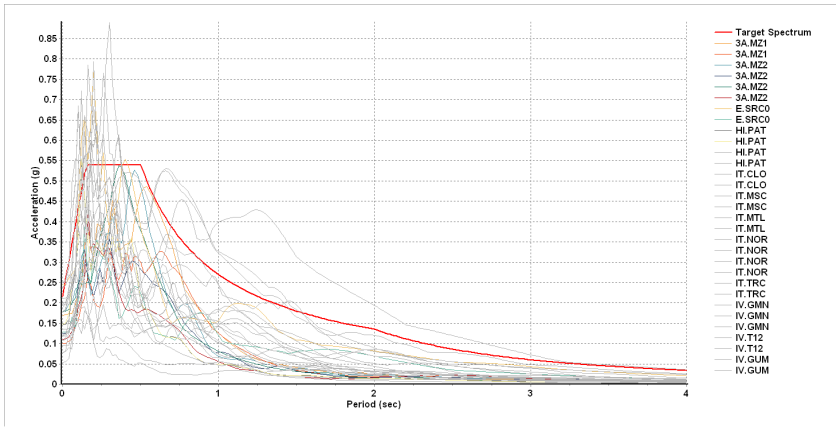

(a)

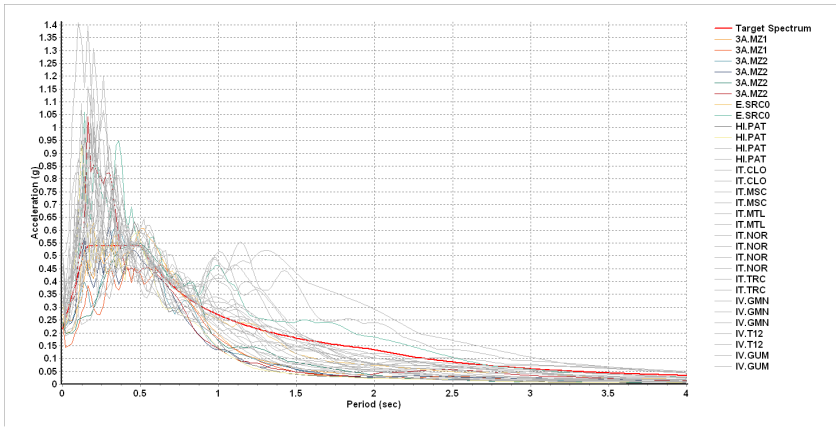

(b)

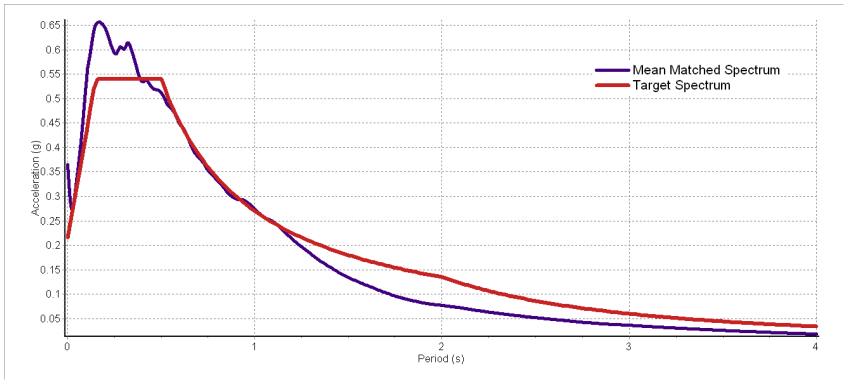

(c)

Figure 3.17: Acceleration Response Spectra: a) Original; b) Scaled; c) Scaled Average Spectrum.

Among the fifteen accelerograms, the one shown in Figure 3.18 was selected for the experimental hybrid tests and the numerical analyses, based on three main requirements:

- The selected accelerogram had to cause significant damage to the bracing elements.
- The horizontal displacement of the first floor had to be equal to or lower than ± 30 mm to be compatible with the stroke of the horizontal actuator inside the BAM furnace.
- The axial force of the interior columns at the base of the second floor had to be below 1000 kN to be compatible with the actuators used to impose the vertical loads on the specimen at the ELSA Reaction Wall.

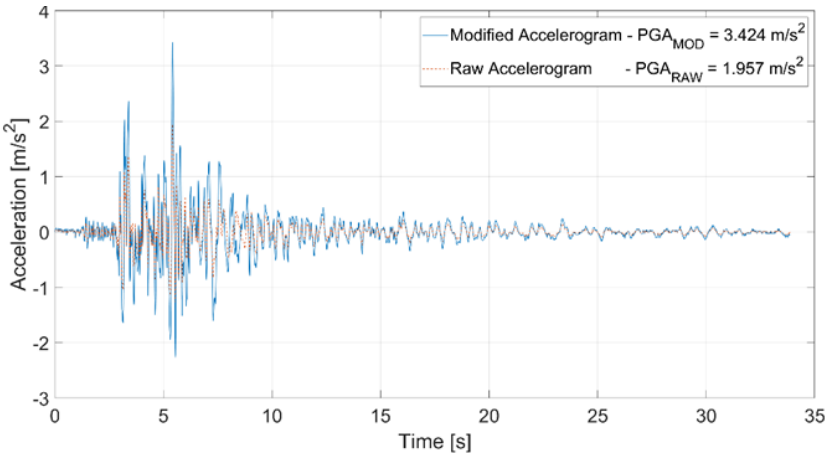

Figure 3.18: Earthquake acceleration time-history (ACC6_NS).

Table 3.38: OpenSees 2D

Partecipating mass ratio (X direction)	**Period [s]**	**Frequency Cyc/sec**	**Circular frequency**
83.7 %	0.6678	1.4975	9.4088
13.0 %	0.2168	4.6127	28.9817
1.2 %	0.1231	8.1234	51.0413
0.5 %	0.0971	10.2986	64.7084

3.10 Numerical simulations

OpenSees is a software framework for developing applications to simulate the performance of structural and geotechnical systems subjected to earthquakes. It is an object-oriented software that was developed at the University of California, Berkeley. In recent years, Professor Asif Usmani and his research team at the University of Edinburgh have been working on adding structures in fire modeling capacity to OpenSees. OpenSees supplies a wide assortment of materials, that are useful to define the cross-section of the elements. Each material is represented in the software by its stress-strain relationship, that describes its behaviour for different situation (cyclic, linear, seismic, fire). There are two types of element's formulations, displacement-based element (DBE) and force-based element (FBE). The displacement-based approach follows standard finite element procedures where the solver interpolates section deformations from an approximate displacement field then use the Principle of Virtual Displacement (PVD) to form the element equilibrium relationship. To approximate nonlinear element response, constant axial deformation and linear curvature distribution are enforced along the element length. Mesh refinement of the element is needed to represent higher-order distributions of deformations.

A 3d model of the building, illustrated in Figure 3.19a, and a 2D model of the frame, illustrated in Figure 3.19b, were created in OpenSees in order to perform non-linear numerical analyses. Geometric imperfections were included to allow for buckling EN 1993-1-1 [4]. Masses were considered lumped the floors, following the assumption of rigid diaphragms. Non-linear beam elements were used for all elements to check that non-dissipative elements remain in the elastic field owing to the seismic action. The columns were considered continuous along the height of the structure and all connections of the beams and diagonals were assumed pinned, as shown in Figures 3.20, 3.21, 3.22, 3.23 and 3.24.

For the 3D model, seven non-linear beam elements based on corotational formulation and the uniaxial Giuffre-Menegotto-Pinto steel material, with isotropic strain hardening (Steel02Material) [10] and geometric nonlinearities was used for the bracing diagonals. The constitutive law provided by EN 1993-1-2 [11] was adopted to model the mechanical properties of steel at elevated temperature when for the column that was heated after the earthquake.

For the 2D model of the frame fifteen nonlinear thermomechanical beam elements, endowed with material and geometric nonlinearities, were used for the column subjected to fire action. The elastic-plastic

constitutive law provided by Eurocode 3 was adopted to model the mechanical properties of steel at elevated temperatures. Temperature dependency of elastic modulus, yield strength and strain proportional limit was accounted for according to Eurocode 3. Seven nonlinear beam elements based on corotational formulation and the uniaxial Giuffre-Menegotto-Pinto steel material, with isotropic strain hardening (Steel02Material) and geometric nonlinearities, was used for the bracing diagonals.

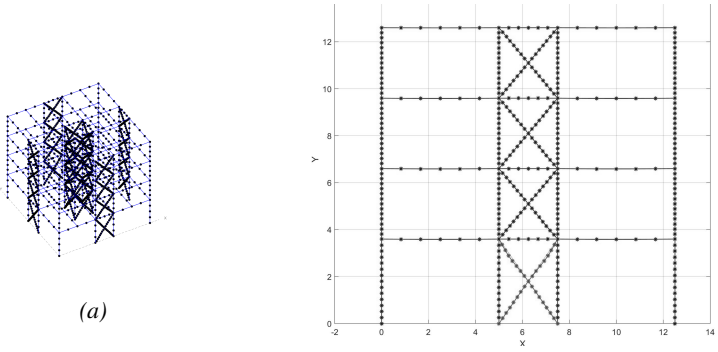

(a) *(b)*

Figure 3.19: a) 3D model of the full structure; b) 2D model of the frame.

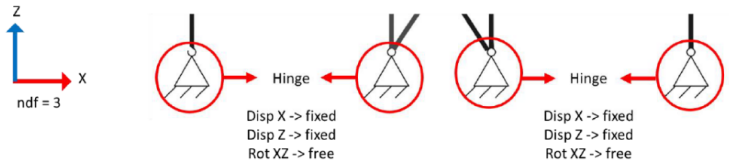

Figure 3.20: Base constraint of the models.

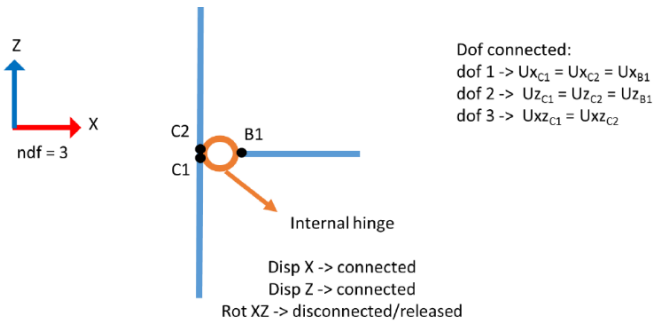

Figure 3.21: Beam-column connection.

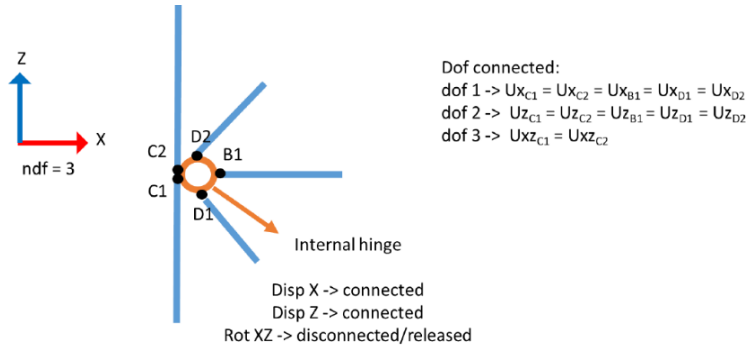

Figure 3.22: Beam-column-brace connection.

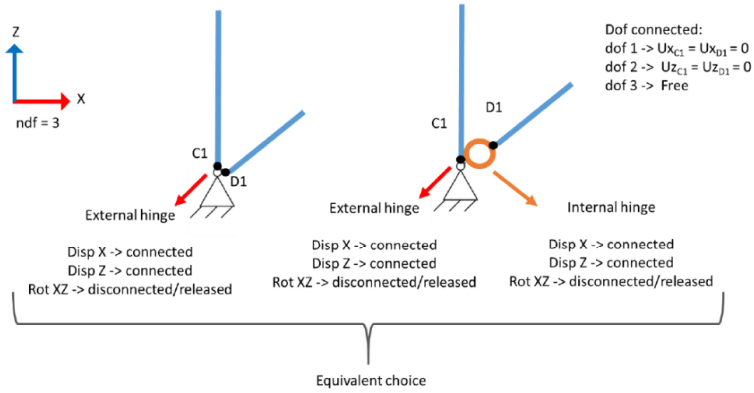

Figure 3.23: Brace-column connection.

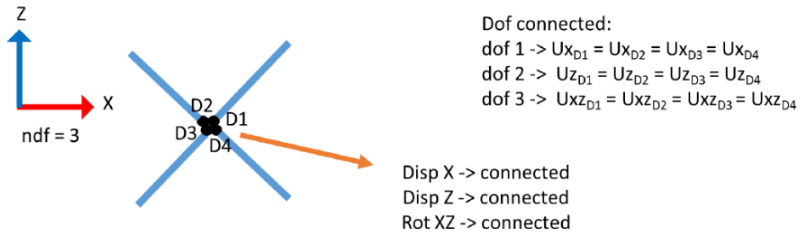

Figure 3.24: Braces connection.

Three different statistical indicators were used to compare the results of the analyses:

- Root-mean-square error (RMSE)

$$RMSE = \frac{||x_i - x_j||_2}{\sqrt{N}} \tag{3.19}$$

This indicator provides information on the root of the variance of a data item with respect to a comparison parameter.

- normalized root-mean error (NRMSE)

$$NRMSE = \frac{||x_i - x_j||_2/\sqrt{N}}{x_{j,MAX} - x_{j,MIN}} \tag{3.20}$$

This indicator gives information on the variance between two sets of data: A smaller NRMSE value corresponds a smaller value of the variance, i.e. the distance of the value of a variable from the expected value.

- Relative error (NENERR)

$$NENERR = \frac{||x_i||_2 - ||x_j||_2}{||x_j||_2} \tag{3.21}$$

3.10.1 Modal analyses

Table 3.39: SAP2000/ETABS

Partecipating mass ratio (X direction)	**Period [s]**	**Frequency Cyc/sec**	**Circular frequency**
83.9%	0.659	1.51745	9.53442
14.3%	0.218	4.5872	28.82195
1.26 %	0.123	8.1300	51.08281
0.5 %	0.096	10.4167	65.44985

Table 3.40: OpenSees 3D

Partecipating mass ratio (X direction)	**Period [s]**	**Frequency Cyc/sec**	**Circular frequency**
83.5 %	0.6739	1.4839	9.3236
12.3 %	0.2228	4.4883	28.201
1.22 %	0.123	8.1300	51.08281
0.1 %	0.2660	3.7593	23.621

3.10.2 Non-linear static analysis (Pushover)

In according with Eurocode 8 -1 [7] at least two lateral force distributions must be applied:

- a “uniform” pattern, based on lateral forces that are proportional to mass regardless of elevation (uniform response acceleration);
- a “modal” pattern, proportional to lateral forces consistent with the lateral force distribution in the direction under consideration determined in elastic analysis.

The results and the comparison of the non-linear static analysis are showed in Figure 3.25. The Figure displays step by step the displacement of a node located at the roof level of the building versus the total base shear of the frame. The comparison shows a good agreement between the 3D model of the entire structure and the 2D model of the frame.

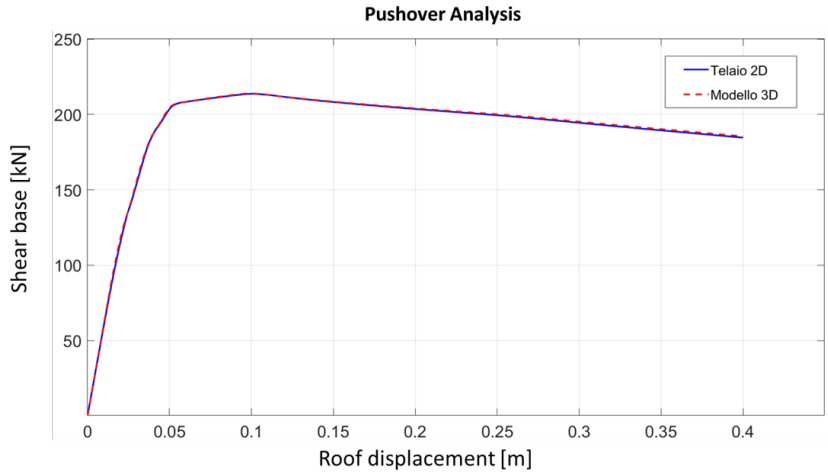

Figure 3.25: Capacity curve (Pushover) comparison.

3.10.3 Non-linear dynamic analysis

Figure 3.26 shows that the 2D and 3D analyses give very similar results with low margins of error.

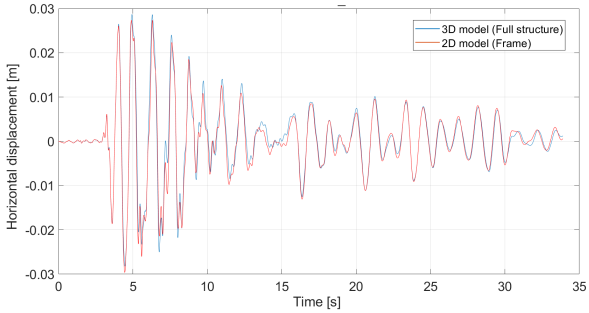

(a)

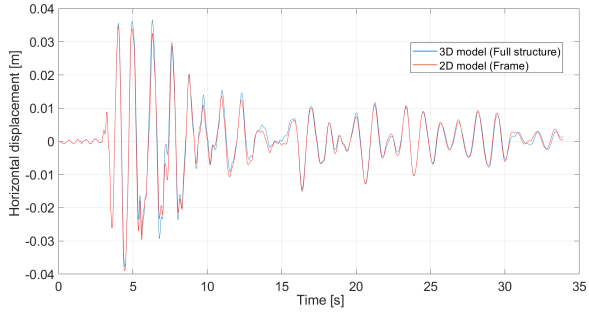

(b)

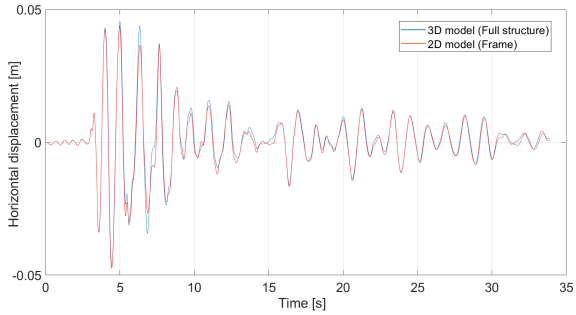

(c)

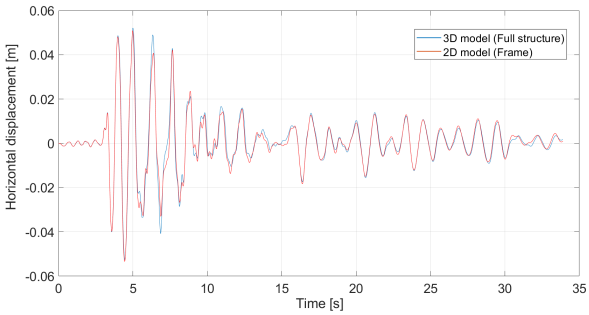

(d)

Figure 3.26: Horizontal displacement: a) 1st floor; b) 2nd floor; c) 3r floor; d) 4th floor.

For the accelerogram selected to perform the laboratory tests, it is significant to show the errors on the displacements at each floor in the Table 3.41.

Table 3.41

ACC6 NS: 3D Model - 2D Frame	NRMSE	RMSE [m]	NENERR
1st Floor	0.0015	0.026	3%
2nd Floor	0.0016	0.021	4%
3rd Floor	0.0018	0.019	5%
4th Floor	0.0020	0.020	5%

Figures 3.27 3.28 3.29 and 3.30 show the energy dissipation of the bracing system and the internal columns of the tested frame. As is possible to observe, the energy dissipation is concentrated in the braces and in particular at the ground floor. The internal columns and all the other elements remained in the elastic field during the seismic event.

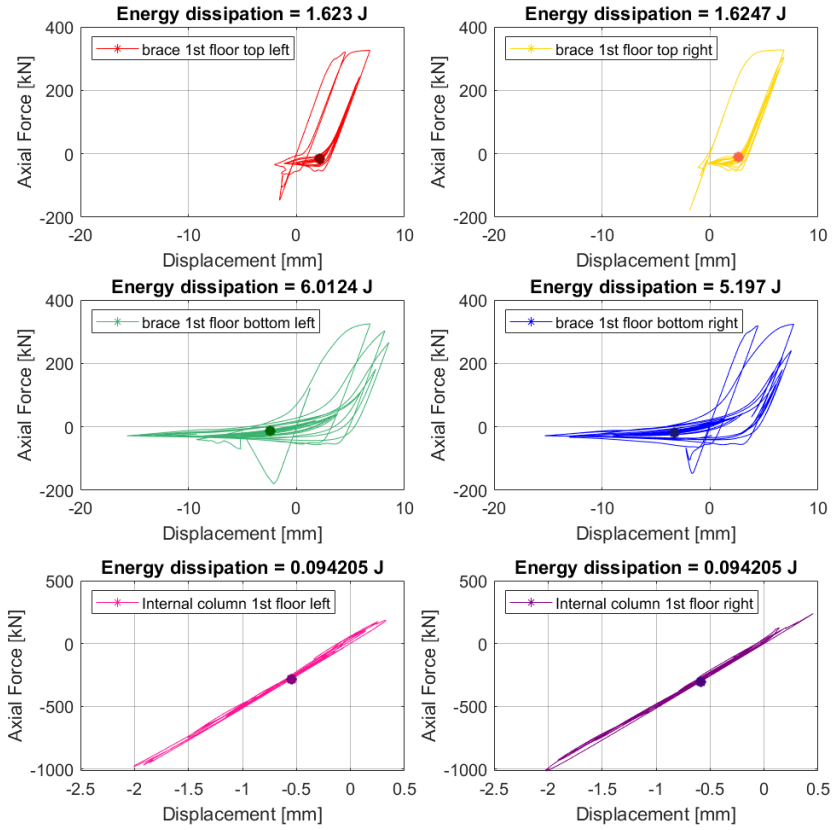

Figure 3.27: ACC6 NS - dissipation 1st floor.

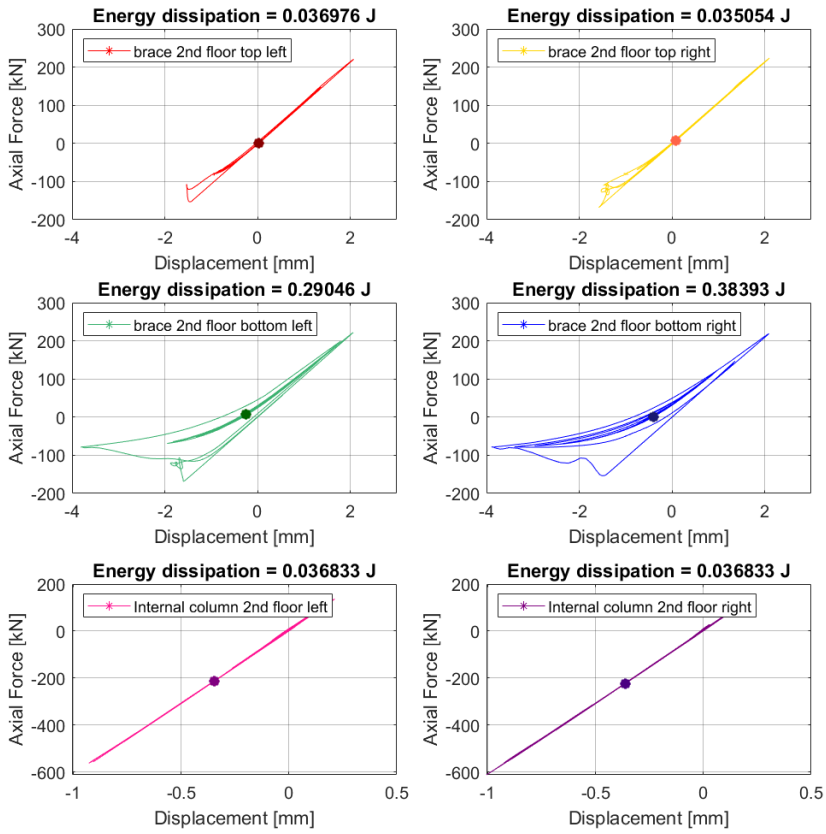

Figure 3.28: ACC6 NS - dissipation 2nd floor.

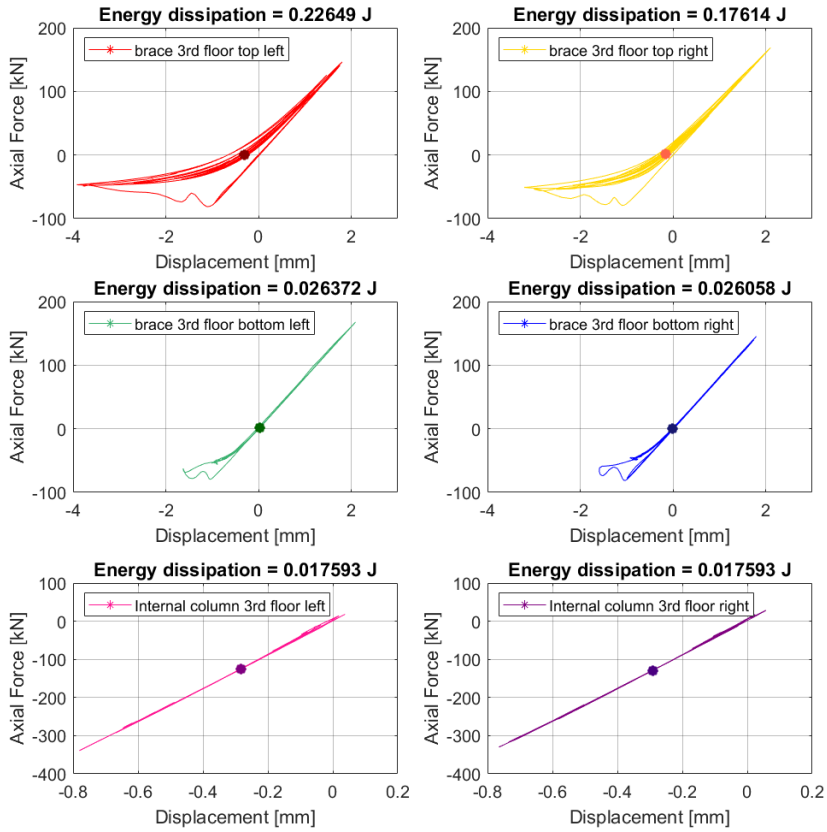

Figure 3.29: ACC6 NS - dissipation 3rd floor.

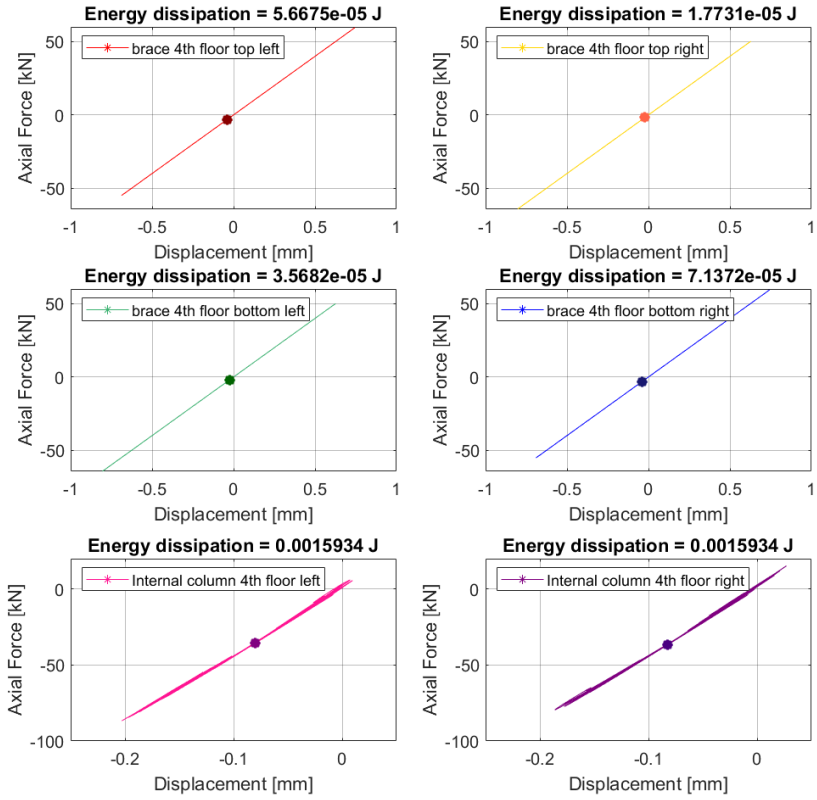

Figure 3.30: ACC6 NS - dissipation 4th floor.

The results obtained show how it is possible, for particular symmetry conditions, to analyse only the 2D frames of such a structure. This makes it possible to considerably reduce computational times, since in the three-dimensional field, the degrees of freedom increase exponentially, leading to analyses that last eleven days compared with similar results that can be obtained in few hours with a 3D frame or less than 1 hour for a 2D model of the frame and using PC with CPU's frequency of 3.5GHz.

Table 3.42: Computational time.

ACC	3D full structure	3D frame	2D frame
6 NS	11 days	4-5 hours	<1 hour
6 EW	11 days	4-5 hours	<1 hour

3.11 FFE analysis

Several FFE analyses were performed using the accelerogram set presented in this chapter and using different fire scenarios. In this section, the results of the FFE scenario chosen for the EQUFIRE tests are presented. Figure 23.31 shows the fire load considered at one column adjacent to the diagonals of the bracing.

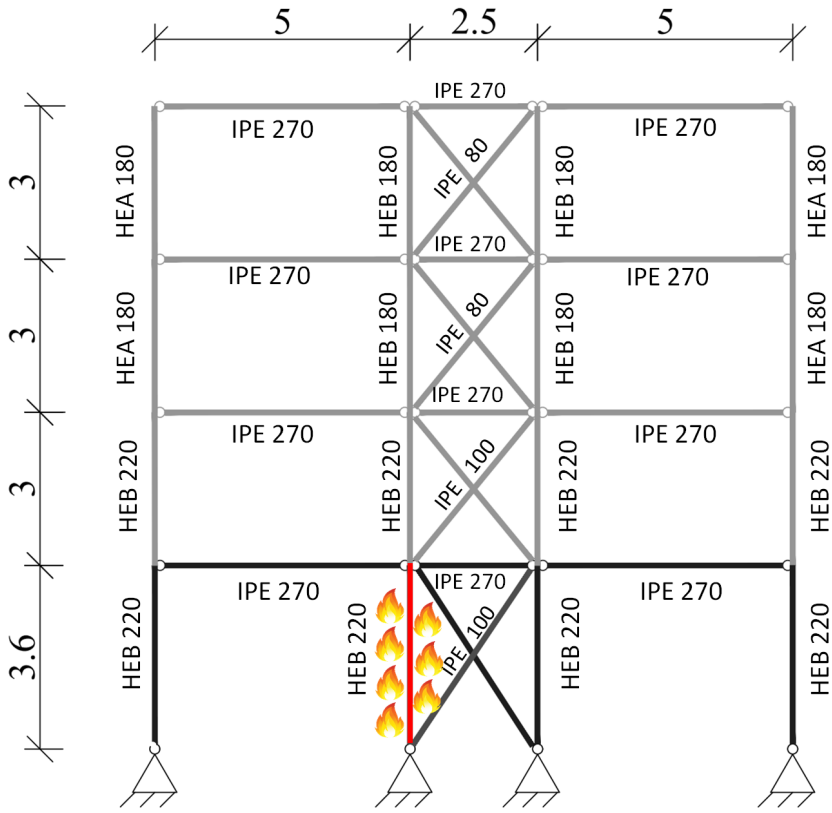

Figure 3.31: Test frame and fire load location.

The 2D nonlinear finite element model in OpenSees was used to evaluate the FFE response of the structure, which is expected to experience large displacements and plastic deformations of the bracing elements during the seismic action and nonlinear behaviour of the column under fire condition. This choice was made because it is easy to reproduce in a furnace.

Figure 3.32 illustrates the results of the numerical simulation of the FFE test on the bare structure (without fire protection) for the selected

acceleration time-history followed by the ISO 834 heating curve. After the earthquake, the fire was initiated and collapse occurred 24 minutes after the start of the fire. Figure 3.32 also shows the final deformed configuration of the steel frame at the end of the simulation.

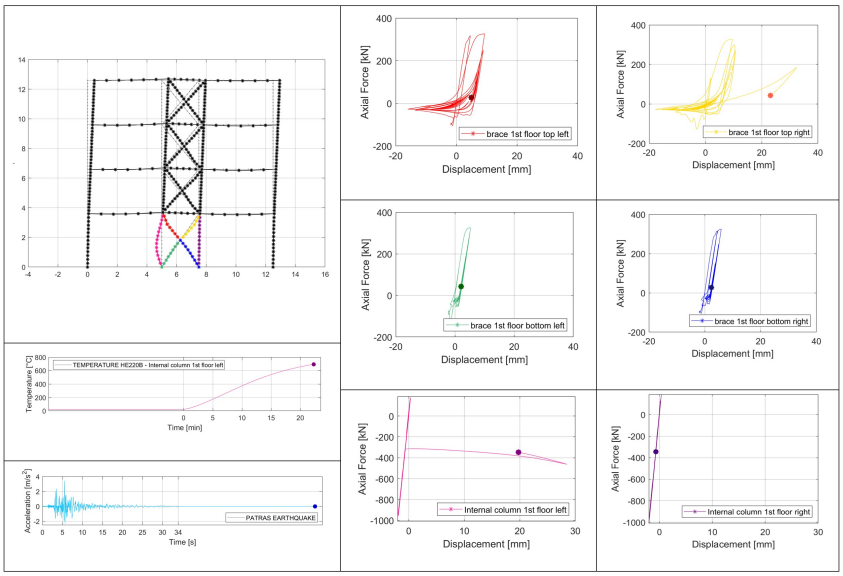

Figure 3.32: Numerical fire following earthquake simulation using OpenSees

3.12 Conclusions

This chapter presented the design and preliminary numerical simulations of a four-storey steel concentrically building and, in particular, the braced frame, designed according to Eurocode standards. The frame was used in the EQUFIRE project, that it studied the steel braced frame by seismic pseudo-dynamic tests of a real-scale one-storey frame at the ELSA Reaction Wall and tests of single elements subjected to fire following earthquake at the furnace of the Federal Institute for Materials Research and Testing (BAM).

Bibliography

[1] CEN, “Eurocode 1: Actions on structures - Part 1-1: General actions - Densities, self-weight, imposed loads for buildings,” european standard, European Union, 2004.

[2] CEN, “Eurocode 1 - Actions on structures - Part 1-3: General actions - Snow loads,” european standard, European Union, 2004.

[3] “Eurocode 1: Actions on structures - Part 1-4: General actions - Wind actions, author = CEN,” european standard, 2005.

[4] CEN, “Eurocode 3: Design of steel structures - Part 1-1: General rules and rules for buildings,” european standard, European Union, May 2005.

[5] CEN, “Eurocode 2: Design of concrete structures - Part 1-1: General rules and rules for buildings,” european standard, European Union, 2003.

[6] CEN, “Eurocode 4: Design of composite steel and concrete structures - Part 1-1: General rules and rules for buildings,” european standard, European Union, 2004.

[7] CEN, “Eurocode 8: Design of structures for earthquake resistance - Part 1: General rules, seismic actions and rules for buildings,” european standard, European Union, May 2004.

[8] V. Silva, H. Crowley, H. Varum, and R. Pinho, “Seismic risk assessment for mainland portugal,” *Bulletin of Earthquake Engineering*, vol. 13, no. 2, pp. 429–457, 2015.

[9] L. Luzi, R. Puglia, E. Russo, and W. Orfeus, “Engineering strong motion database, version 1.0,” *Istituto Nazionale di Geofisica e Vulcanologia, Observatories & Research Facilities for European Seismology. doi*, vol. 10, 2016.

[10] F. C. Filippou, E. P. Popov, and V. V. Bertero, “Effects of bond deterioration on hysteretic behavior of reinforced concrete joints,” 1983.

[11] CEN, “Eurocode 3: Design of steel structures - Part 1-2: General rules - Structural fire design,” european standard, European Union, May 2005.

4.0 Hybrid fire simulation dynamic relaxation component-mode synthesis partitioned time integration steel frame

This chapter contains the following published paper:

"A Real-Time Hybrid Fire Simulation Method Based on Dynamic Relaxation and Partitioned Time Integration." *Giuseppe Abbiati, Patrick Covi, Nicola Tondini, Oreste S. Bursi, Božidar Stojadinović - Journal of Engineering Mechanics, 2020 https://doi.org/10.1061/(ASCE)EM.1943-7889.0001826*

abstract

The use of simplified numerical substructures in hybrid fire simulation is clearly advantageous, as long as the resulting simulation accuracy is sufficient. However, excluding geometrical and material nonlinearities from the numerical substructure might make a significant difference in internal force redistribution and reduce the simulation accuracy beyond acceptable levels. Also, materials at a high temperature very often exhibit time-dependent behavior, including strain-rate dependency, high-temperature creep, and stress relaxation, which prohibit the use of extended testing time scale. This standpoint motivated the development of the real-time hybrid fire simulation method presented in this paper. Dynamic relaxation is proposed to solve the static response of the hybrid numerical-experimental fire simulation. As an equivalent dynamic solution method, dynamic relaxation allows for coupling substructure equations of motion by using a partitioned time integration approach. Minimal data exchange between substructures, negligible computational overhead plus ease of reusability of verified finite-element software makes the proposed algorithm suitable for coordinating real-time hybrid fire simulations. The hybrid fire simulation of a virtual steel frame case study is reported as a validation example.

4.1 Introduction

4.1.1 Background and motivation

Large-scale structural fire tests are rare because of the need for expensive specialized facilities. As a result, most of the research regarding the behavior of structures subjected to fire has been carried out on single structural components subjected to standard heating curves (i.e., standard temperature histories). Although such tests offer significant information about the fire performance of specific structural elements, they do not account for the force redistribution owing to the interaction of the tested structural component with the remaining part of the structure. In order to overcome such limitations, hybrid simulation (HS) emerged as a viable alternative to both large-scale and component fire testing in the last two decades.

HS is an *online* dynamic response simulation paradigm that computes the time history response of the hybrid numerical-physical model of a prototype structure to an excitation by solving the related equation of equilibrium using a compatible time-stepping analysis algorithm. The report of Schellenberg and co-authors [1] provides a comprehensive review of the state of the art on HS algorithms and methods used for earthquake engineering applications. In detail, the hybrid model of the prototype structure combines physical and numerical substructures (PS and NS, respectively). The former is tested in the laboratory by means of servo-controlled actuators equipped with force transducers, while a numerical model instantiated using a computer-based structural analysis simulation platform simulates the latter. At each time step of the time integration loop, servo-controlled actuators impose interface displacements and velocities to the PS and measure corresponding restoring forces, while the NS restoring force is evaluated numerically. Both restoring force vectors enter the coupled system of equations of equilibrium of the hybrid model, which are solved, possibly avoiding iterations, before moving to the next time step. The term *online* indicates that simulation of NS and testing of PS are parallel tasks that exchange interface forces and displacements at each solution step of the equation of equilibrium. In order to reduce actuator control errors and oil flow demands if the PS behavior is rate-independent, HS is performed in a pseudodynamic regime, that is, with an extended testing time scale typically $50-200$ times slower than real time, requiring inertia and damping forces to be modeled numerically also on the PS side. Real-time (RT) HS indicates the limit case of a unit simulation time scale, employed when the behavior of PS is rate-dependent.

Compared with earthquake loading, which entails a dynamic structural response, fire development mainly induces a static structural re-

sponse. Furthermore, the time-dependent behavior of materials at high temperatures caused by creep and combustion limits the use of extended testing time scales, thus making the use of RT HS compelling for hybrid fire simulation (HFS). A static equation of equilibrium of the hybrid model was considered since the early stages of HFS development. In this regard, it is worth mentioning the seminal paper of Korzen and co-authors [2], where the *substructuring method* was presented in the scope of HFS. The verification of this method was presented in [3]. A realistic case study based on a restrained column was tested a few years later using the same methodology in collaboration with the University of Coimbra (Portugal) [4]. The testing of the PS was performed in displacement-control mode. Following the same idea, HFS of a concrete slab was performed at CERIB, Paris (France), but using actuators in force-control mode. This experimental campaign was documented in [5]. An elegant generalization of the *substructuring method* of Korzen and co-authors was recently published by Mergny and co-authors [6]. In this case, the NS is replaced by a proportional-integral controller designed upon a linear finite-element (FE) model.

The first attempt to extend the HFS paradigm to nonlinear NSs was done by Mostafaei and reported in two companion papers [7, 8]. In this case, at every simulation step, a human operator manually adjusted both the interface displacement of the NS, which was implemented in the SAFIR FE software [9], and the force applied to the PS by means of a servo-controlled actuator. However, Sauca and co-authors [10] demonstrated that the stability of the procedure proposed by Mostafaei is conditioned to the ratio of PS and NS stiffnesses. Moreover, the same procedure does not satisfy both displacement compatibility and force balance between substructures. Later, Sauca and co-authors [11] proposed the modified Newton-Raphson algorithm to solve the static equilibrium equation of the hybrid model relying on an estimate of the initial tangent stiffness matrix of the PS. The method satisfies both displacement compatibility and force balance at the interface between substructures. A purely numerical verification was reported in the same paper. As the main conclusion, the authors claimed that several iterations are necessary to achieve convergence. As an improvement, Wang and co-authors [12] proposed a single-iteration variant to the modified Newton-Raphson method whose static balance equation accounts for residual forces from the previous time step. The same paper reports an experimental verification where the NS is linear.

Schulthess [13] performed the first experimental verification of a fully nonlinear HFS based on the Newton-Raphson algorithm. This work provides a thorough discussion of all numerical and experimen-

tal issues related to the coupling of substructures and reports a comprehensive verification of the testing procedure based on linear and nonlinear NSs implemented in the ABAQUS FE software [14]. The author proved that updating the tangent stiffness matrix of the PS strongly reduces the number of iterations required by the Newton-Raphson solver to achieve convergence. However, the author pointed out that the tangent stiffness matrix estimate of the PS is already noisy for a single-degree-of-freedom (single-DoF) system, suggesting that multiple-DoF implementations should rely on a constant stiffness matrix.

It is worth noting that this is a well-known issue in the earthquake engineering community: significant attempts to cope with this issue are summarized herein. Thewalt and co-workers proposed the BFGS algorithm to compute a rank-2 stiffness matrix update based on restoring force measurements for the purpose of calculating the spurious energy dissipation during HS [15]. Carrion and Spencer proposed a rank-1 stiffness matrix update based on the Broyden algorithm for the purpose of predicting actuator restoring forces as a delay mitigation strategy [16]. A recursive least-square regression algorithm was proposed by Hung and El-Tawil to update the tangent stiffness online in combination with an operator-splitting time integration scheme [17]. Instead of estimating each of the $n \times (n+1)/2$ entries of the symmetric $n \times n$ stiffness matrix, Ahmadizadeh and Mosqueda proposed to calibrate the parameters of a simplified numerical model of the PS and to evaluate the tangent stiffness matrix analytically [18]. In the HFS case, the issue of noisy tangent stiffness matrix estimates is further exacerbated by temperature fluctuations, which cause restoring force fluctuations.

4.1.2 Scope and organization

The use of simplified NSs in HS is clearly advantageous, as long as the resulting simulation accuracy is sufficient. In HFS, excluding geometrical and material nonlinearities from the NSs might make a significant difference in internal force redistribution in the hybrid model and reduce the accuracy of the simulation beyond acceptable levels. This situation is only exacerbated when the PS behavior is rate-dependent. Therefore, a RT-HFS method should support nonlinear NSs and, possibly, facilitate reusing of existing FE software.

The proposed RT-HFS method was formulated in response to both these needs. Instead of the modified Newton-Raphson approach proposed by Sauca and co-authors [11] and Schulthess [13], the RT-HFS method proposed in this paper adopts dynamic relaxation (DR) as a static solution algorithm. DR approximates the solution of a static problem by

means of an equivalent dynamic system with both mass and damping matrices derived from the initial tangent stiffness matrix [19]. An explicit Newmark scheme integrates the time history response of the equivalent dynamic system avoiding the factorization of the tangent stiffness matrix.

The first advantage of DR is that, as an equivalent dynamic solution method, it allows for coupling PS and NS equations of motion by using a two-stage solution approach based on partitioned time integration [20]. In detail, the first stage is referred to as *free* solution and entails the calculation of PS and NS responses by neglecting the coupling conditions. This means that PS and NS equations of motions are solved independently in parallel. The second stage of the solution is referred to as *link* solution and entails the calculation of a set of Lagrange multipliers that restore interface velocity compatibility between substructures. The *link* problem involves the solution of a system of linear equations with interface velocities as unknowns, which adds a small computational overhead to a simulation time step. Furthermore, the limited data exchange between substructures makes the proposed algorithm suitable for implementation as a RT-HFS coordinator in existing HS middleware (e.g., OpenFresco [21]).

The second advantage of DR is the possibility to overcome issues related to singular stiffness matrices caused by material or geometric nonlinearities. Namely, simulation using a conventional static solution scheme may stop when buckling of a member in statically indeterminate structures occurs. This, however, does not mean that a global instability of the entire model occurred. For example, the SAFIR FE software [9] implements a dynamic analysis based on the Newmark time integration scheme to solve the issue mentioned above.

This paper is organized as follows. First, the proposed RT-HFS method is presented, accompanied by an analysis of the propagation of experimental errors. The latter is not meant to be exhaustive but only to provide a preliminary insight into the algorithmic performance in the presence of experimental errors. This error investigation includes a comparison to the modified Newton-Raphson method, which seems to be the only alternative for simulating nonlinear NSs available in the state of the art [11, 13]. Subsequently, the effectiveness of the proposed method is demonstrated in a virtual experimental campaign, where the response of a realistic steel moment-resisting frame subject to fire is simulated using a purely numerical version of the proposed RT-HFS method. The obtained response is validated against reference nonlinear static response analyses of the same frame and fire performed using the SAFIR FE software [9].

4.2 Description of the RT-HFS method

When coupling multiple substructures using a primal formulation, common DoFs are merged, compatibility between substructures is assumed *a priori*, while equilibrium is imposed *a posteriori*. Classically, FE models are assembled in this primal manner. In a dual assembly formulation, conversely, interface DoFs of each substructure are retained, and a set of self-balanced Lagrange multipliers enforces compatibility among substructures [22]. Accordingly, equilibrium is assumed *a priori* while compatibility is imposed *a posteriori*. The class of finite element tearing and interconnecting (FETI) algorithms originally conceived for solving static problems [23], then extended to dynamics [24] adopts this coupling strategy, which is also used by partitioned time integration algorithms in HS. The Pegon-Magonette (PM) algorithm [25] is the first example of a partitioned time integration algorithm applied to HS. The PM algorithm coordinates two Newmark time integration schemes [26]. The compatibility of velocities at the interfaces, instead of displacements, guarantees a stable coupled simulation as long as each time integration scheme is stable when uncoupled. Along this line, we propose a RT-HFS method that relies on the Gravouil and Combescure (GC) algorithm [20] and the Localized Lagrange Multipliers (LLM) method [27] to couple multiple PS and NS.

The dynamic relaxation (DR) algorithm [19] is adopted in the proposed RT-HFS method to build fictitious mass, and damping matrices of substructures whose coupled dynamic response mimics the static response of the prototype structure. The DR algorithm does not require the evaluation and inversion of the stiffness matrix, and it is particularly appealing for solving highly nonlinear problems characterized by plastic deformations and/or instabilities. For instance, buckling of a compression member in a statically indeterminate truss may halt the analysis, but it does not necessarily imply the global collapse of the structure, or inability of the structure to redistribute its loads. This is common in structural fire engineering problems, where the loss of strength and stiffness of a structural member subjected to high temperature may lead to significant load redistribution. It is well-known that a faster convergence of the DR solution to the actual static structural response is achieved when the lower eigenfrequency of the equivalent dynamic system is closer to the stability limit of the central difference (CD) algorithm, which solves the equation of motion [19]. To this end, component-mode synthesis (CMS) [28] is used in the proposed RT-HFS method to derive reduced-order mass, damping and stiffness matrices for both NS and PS, thus maximizing the ratio between the minimum and the maximum eigenfre-

quencies of the hybrid model. As for all *a posteriori* model-order reduction methods, the adequacy of the retained component-mode vectors must be verified for the range of displacement trajectories likely to occur during the HFS. For example, if a traveling fire is expected, the retained component-mode vectors must be able to represent the corresponding displacement response with a reasonable degree of approximation.

4.2.1 Dynamic relaxation and component-mode synthesis

The basic idea behind DR is to obtain the displacement solution of a static structural problem,

$$\mathbf{r}\left(\mathbf{u}\right) = \mathbf{f}(t) \tag{4.1}$$

by computing the transient response of an equivalent dynamic system, whose equation of motion reads,

$$\mathbf{M}\ddot{\mathbf{u}} + \mathbf{C}\dot{\mathbf{u}} + \mathbf{r}\left(\mathbf{u}\right) = \mathbf{f}(t) \tag{4.2}$$

where $\mathbf{r}$ is the internal restoring force vector, which depends on the displacement vector $(\mathbf{u})$ (and, possibly, to its past time history) while $\mathbf{f}(t)$ represents a time varying external loading; $\mathbf{M}$ and $\mathbf{C}$ are fictitious mass and damping diagonal matrices, respectively. The CD algorithm, which is equivalent to the Newmark algorithm [26] with $\gamma = \frac{1}{2}$ and $\beta = 0$, is used to integrate (4.2). Expressions for diagonal entries of both fictitious mass and damping matrices read,

$$M_{ii} = \frac{(1.1\Delta t)^2}{4} \sum_j |K_{ij}| \tag{4.3}$$

$$C_{ii} = 2\omega_0 M_{ii} \tag{4.4}$$

which are derived to maximize the convergence rate of the DR algorithm, where K_{ij} is a generic element of the initial tangent stiffness matrix $\mathbf{K} = \partial\mathbf{r}/\partial\mathbf{u}$; ω_0 is the lowest undamped frequency of (4.2) after linearization of $\mathbf{r}\left(\mathbf{u}\right)$ at zero displacement and velocity; Δt is the time step size of the equivalent transient analysis. The expression of M_{ii} forces the upper bound ω_{max} of the eigenfrequencies of (4.2) to lay within the stability domain of the CD method close to the limit frequency $\omega_{lim} = 2/\Delta t$, and it is a direct consequence of the Gershgorin's circle theorem. It is well known that the rate of convergence of DR deteriorates

when $\omega_0/\omega_{max} \ll 1$. In order to achieve spatial convergence of lower eigenmodes and to remove higher frequency eigenmodes that do not participate in the static response of the emulated structure, CMS is adopted to derive a reduced-order counterpart of $\mathbf{K}$ and, thus, of $\mathbf{M}$ and $\mathbf{C}$. The term *component-mode* signifies Ritz vectors, or assumed modes, that are used in describing the displacement of points within a substructure or a component [28]. The primary use of CMS is to reduce the computational cost of dynamic simulations by replacing a large FE model with the assembly of reduced-order substructures. Here, CMS is used to maximize the ω_0/ω_{max} ratio of the hybrid model. CMS relies on the definition of a *component mode* matrix $\hat{\mathbf{\Psi}}$ that relates the displacement field $\hat{\mathbf{u}}$ of the reduced-order component to a generalized coordinate vector $\hat{\mathbf{p}}$ as,

$$\hat{\mathbf{u}} = \hat{\mathbf{\Psi}}\hat{\mathbf{p}} \tag{4.5}$$

where $\hat{\mathbf{u}}$ approximates the displacement field $\mathbf{u}$ of the full component model. Accordingly, component matrices and vectors are condensed as,

$$\hat{\mathbf{K}} = \hat{\mathbf{\Psi}}^T\mathbf{K}\hat{\mathbf{\Psi}}, \hat{\mathbf{C}} = \hat{\mathbf{\Psi}}^T\mathbf{C}\hat{\mathbf{\Psi}}, \hat{\mathbf{M}} = \hat{\mathbf{\Psi}}^T\mathbf{M}\hat{\mathbf{\Psi}}, \hat{\mathbf{f}}(t) = \hat{\mathbf{\Psi}}^T\mathbf{f}(t) \tag{4.6}$$

If a static condensation is pursued, the component-mode matrix reads,

$$\hat{\mathbf{\Psi}} = \begin{bmatrix}\hat{\mathbf{\Psi}}_e & \hat{\mathbf{\Psi}}_r\end{bmatrix} \tag{4.7}$$

where $\hat{\mathbf{\Psi}}_e$ and $\hat{\mathbf{\Psi}}_r$ indicate retained *constraint* and *rigid-body* modes. For the sake of clarity, the following matrix partitioning is used as reference for the derivation of the component-modes for an unconstrained component of the hybrid model,

$$\mathbf{K} = \begin{bmatrix}\mathbf{K}_{ii} & \mathbf{K}_{ie} & \mathbf{K}_{ir}\\ \mathbf{K}_{ei} & \mathbf{K}_{ee} & \mathbf{K}_{er}\\ \mathbf{K}_{ri} & \mathbf{K}_{re} & \mathbf{K}_{rr}\end{bmatrix}, \mathbf{M} = \begin{bmatrix}\mathbf{M}_{ii} & \mathbf{M}_{ie} & \mathbf{M}_{ir}\\ \mathbf{M}_{ei} & \mathbf{M}_{ee} & \mathbf{M}_{er}\\ \mathbf{M}_{ri} & \mathbf{M}_{re} & \mathbf{M}_{rr}\end{bmatrix}, \mathbf{f} = \begin{bmatrix}\mathbf{f}_i\\ \mathbf{f}_e\\ \mathbf{f}_r\end{bmatrix}, \mathbf{u} = \begin{bmatrix}\mathbf{u}_i\\ \mathbf{u}_e\\ \mathbf{u}_r\end{bmatrix} \tag{4.8}$$

where subscripts i, e and r denote *interior*, *excess* (or redundant) and *rigid-body* DoFs, respectively. If the component of the hybrid model is constrained, r-DoFs must provide a statically determined configuration. Accordingly, the matrix of *rigid-body* modes $\mathbf{\Psi_r}$ is computed as,

$$\mathbf{\Psi}_r = \begin{bmatrix}\mathbf{\Psi}_{ir}\\ \mathbf{\Psi}_{er}\\ \mathbf{I}_{rr}\end{bmatrix} = \begin{bmatrix}-\begin{bmatrix}\mathbf{K}_{ii} & \mathbf{K}_{ie}\\ \mathbf{K}_{ei} & \mathbf{K}_{ee}\end{bmatrix}^{-1}\begin{bmatrix}\mathbf{K}_{ir}\\ \mathbf{K}_{er}\end{bmatrix}\\ \mathbf{I}_{rr}\end{bmatrix} \tag{4.9}$$

A careful reader may have noticed that $\boldsymbol{\Psi}_r$ is reported without a hat in (4.9). This is done to distinguish between the full set of *rigid-body* modes $\boldsymbol{\Psi}_r$ and the corresponding retained subset $\hat{\boldsymbol{\Psi}}_r$ referred to in (4.6). The same notation is adopted also for *constraint* modes.

Constraint modes are computed by imposing a unit displacement on a single e-DoF while keeping other e-DoFs zero after constraining the set of r-DoFs. The matrix of *constraint* modes $\boldsymbol{\Psi_e}$ is defined as,

$$\boldsymbol{\Psi}_e = \begin{bmatrix} \boldsymbol{\Psi}_{ie} \\ \mathbf{I}_{ee} \\ \mathbf{0}_{re} \end{bmatrix} = \begin{bmatrix} -\mathbf{K}_{ii}^{-1}\mathbf{K}_{ie} \\ \mathbf{I}_{ee} \\ \mathbf{0}_{re} \end{bmatrix} \tag{4.10}$$

Figure 4.1 depicts *rigid-body* and *constraint* modes for a 5-DoFs chain-like system with homogeneous masses and springs.

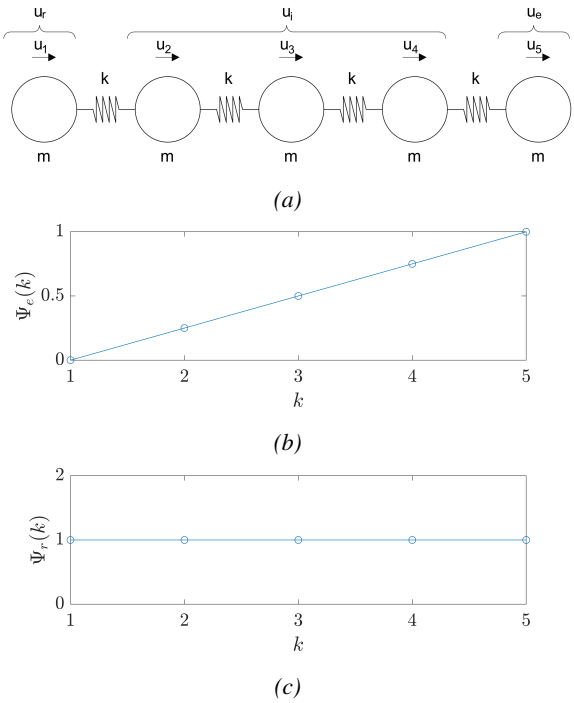

Figure 4.1: Example of a component-mode basis: a) 5-DoFs chain-like system, b) constraint *mode, c)* rigid-body *mode.*

4.2.2 The Gravouil-Combescure algorithm with Localized-Lagrange multipliers

It is well known that the classical method of Lagrange multipliers (CLM) allows for alternative sets of interface compatibility equations for model-

ing the same multi-point constraint, that is, a DoF connecting more than two substructures. Park and co-authors [27] proposed a localized version of the CLM method that admits a single set of compatibility equations, making computer implementation straightforward. In order to illustrate the use of the LLM, let us consider the following coupled system, in which n substructures are subjected to mechanical loads and temperature histories,

$$\begin{cases} \begin{cases} \mathbf{M}^{(i)}\ddot{\mathbf{u}}^{(i)} + \mathbf{C}^{(i)}\dot{\mathbf{u}}^{(i)} + \mathbf{r}^{(i)}\left(\mathbf{u}^{(i)}, \boldsymbol{\theta}^{(i)}\right) = \mathbf{f}^{(i)}(t) + \mathbf{L}^{(i)^T}\boldsymbol{\Lambda}^{(i)} \\ \mathbf{L}^{(i)}\dot{\mathbf{u}}^{(i)} + \bar{\mathbf{L}}^{(i)}\dot{\mathbf{u}}_g = \mathbf{0} \end{cases} & \forall i \in \{1, \ldots, n\} \\ \sum_{i=1}^{n} \bar{\mathbf{L}}^{(i)^T}\boldsymbol{\Lambda}^{(i)} = \mathbf{0} \end{cases} \tag{4.11}$$

with regard to a generic substructure i, either physical or numerical, $\mathbf{u}$, $\dot{\mathbf{u}}$ and $\ddot{\mathbf{u}}$ denote displacement, velocity and acceleration vectors while $\boldsymbol{\theta}$ is the vector of nodal temperatures. $\mathbf{M}$, $\mathbf{C}$, $\mathbf{r}$ and $\mathbf{f}(t)$ denote mass matrix, damping matrix, restoring force and external load vectors, respectively. For the sake of brevity, time dependence is omitted and, therefore, the independent variable t is dropped hereinafter. In order to cast compatibility and equilibrium equations among substructures, $\mathbf{L}$ and $\bar{\mathbf{L}}$, which are Boolean signed matrices, localize interface DoFs on every single substructure and on vector $\mathbf{u}_g$, respectively. The latter gathers all DoFs that are shared between at least two substructures, namely the interface DoFs. According to (4.11), a Lagrange multiplier vector $\boldsymbol{\Lambda}$ is defined for each substructure i-th to enforce velocity compatibility with $\dot{\mathbf{u}}_g$. It is important to stress that all Lagrange multiplier vectors form a set of self-balanced forces to ensure interface equilibrium a *a priori*. The solution of (4.11) enforces kinematic compatibility *a posteriori*. As highlighted by Gravouil and Combescure [20], velocity coupling guarantees the stability of the coupled simulation as long as the simulation of each uncoupled substructure is stable. In this respect, Figure 4.2 illustrates a three-substructure coupling example whose Boolean matrices and displacement vectors read,

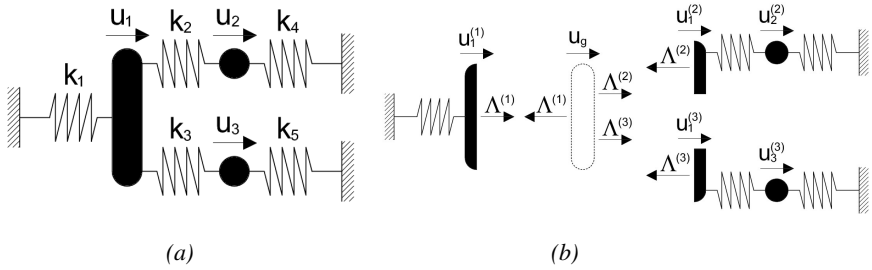

(a) *(b)*

Figure 4.2: Three-substructure coupling example based on the LLM method: a) reference system; b) partitioned system.

$$\mathbf{u}^{(1)^T} = \left[u_1^{(1)}\right], \mathbf{u}^{(2)^T} = \left[u_1^{(2)}, u_2^{(2)}\right], \mathbf{u}^{(3)^T} = \left[u_1^{(3)}, u_3^{(3)}\right]$$
$$\mathbf{L}^{(1)} = \left[1\right], \mathbf{L}^{(2)} = \left[1, 0\right], \mathbf{L}^{(3)} = \left[1, 0\right]$$
$$\bar{\mathbf{L}}^{(1)} = \left[-1\right], \bar{\mathbf{L}}^{(2)} = \left[-1\right], \bar{\mathbf{L}}^{(3)} = \left[-1\right]$$

In the worst case, when all n substructures share one and the same DoF, the CLM method leads to $n(n-1)/2$ linearly dependent systems of constraint equations, that is, one per substructure pair. The task of retaining a subset of n linearly independent constraint equations, which is not unique, has been a major issue in the CLM method. In the same situation, the LLM method casts all constraint equations with respect to a single generalized interface DoF $\mathbf{u}_g$, see (4.11), which leads to a unique set of n linearly independent systems of constraint equations. As a result, Boolean coupling matrices $\mathbf{L}$ and $\bar{\mathbf{L}}$ are uniquely derived and guarantee a non-singular Steklov-Poincaré coupling operator, as explained in the following sections.

The LLM-GC algorithm proposed in this paper relies on the coupling scheme of the GC method [20] adapted to the LLM method [27]. For the sake of simplicity, the LLM-GC algorithm is described for a hybird model comprising a single PS and a single NS. Accordingly, superscripts P and N replace (i) of (4.11). In this case, after time discretization, the system of coupled equations of motion reads,

$$\begin{cases} \begin{cases} \mathbf{M}^N \ddot{\mathbf{u}}_{k+1}^N + \mathbf{C}^N \dot{\mathbf{u}}_{k+1}^N + \mathbf{r}^N \left(\mathbf{u}_{k+1}^N, \boldsymbol{\theta}_{k+1}^N\right) = \mathbf{f}_{k+1}^N + \mathbf{L}^{N^T} \boldsymbol{\Lambda}_{k+1}^N \\ \mathbf{L}^N \dot{\mathbf{u}}_{k+1}^N + \bar{\mathbf{L}}^N \dot{\mathbf{u}}_{k+1}^g = \mathbf{0} \end{cases} \\ \begin{cases} \mathbf{M}^P \ddot{\mathbf{u}}_{k+1}^P + \mathbf{C}^P \dot{\mathbf{u}}_{k+1}^P + \mathbf{r}^P \left(\mathbf{u}_{k+1}^P, \boldsymbol{\theta}_{k+1}^P\right) = \mathbf{f}_{k+1}^P + \mathbf{L}^{P^T} \boldsymbol{\Lambda}_{k+1}^P \\ \mathbf{L}^P \dot{\mathbf{u}}_{k+1}^P + \bar{\mathbf{L}}^P \dot{\mathbf{u}}_{k+1}^g = \mathbf{0} \end{cases} \\ \bar{\mathbf{L}}^{N^T} \boldsymbol{\Lambda}_{k+1}^N + \bar{\mathbf{L}}^{P^T} \boldsymbol{\Lambda}_{k+1}^P = \mathbf{0} \end{cases} \tag{4.12}$$

It is important to remark that both fictitious damping matrices $\mathbf{C}^N$ and $\mathbf{C}^P$ are computed based on the lower eigenvalue of the coupled equations of equilibrium, as defined in (4.4), which is estimated with a linearized monolithic version of the partitioned hybrid model. For the sake of clarity, the LLM-GC algorithm is presented in algorithmic form to integrate (4.12) from time t_k to t_{k+1} with a time step Δt.

1. Solve the NS *free* problem at t_{k+1},

$$\begin{cases} \tilde{\mathbf{u}}_{k+1}^{N,free} = \mathbf{u}_k^N + \dot{\mathbf{u}}_k^N \Delta t + \left(\frac{1}{2} - \beta\right) \Delta t^2 \ddot{\mathbf{u}}_k^N \\ \tilde{\dot{\mathbf{u}}}_{k+1}^{N,free} = \dot{\mathbf{u}}_k^N + (1-\gamma)\, \Delta t \ddot{\mathbf{u}}_k^N \end{cases} \tag{4.13}$$

$$\ddot{\mathbf{u}}_{k+1}^{N,free} = \mathbf{D}^{N^{-1}} \left(\mathbf{f}_{k+1}^N - \mathbf{C}^N \tilde{\dot{\mathbf{u}}}_{k+1}^{N,free} - \mathbf{r}_{k+1}^N \left(\tilde{\mathbf{u}}_{k+1}^{N,free} \right) \right) \tag{4.14}$$

$$\begin{cases} \mathbf{u}_{k+1}^{N,free} = \tilde{\mathbf{u}}_{k+1}^{N,free} + \ddot{\mathbf{u}}_{k+1}^{N,free} \beta \Delta t^2 \\ \dot{\mathbf{u}}_{k+1}^{N,free} = \tilde{\dot{\mathbf{u}}}_{k+1}^{N,free} + \ddot{\mathbf{u}}_{k+1}^{N,free} \gamma \Delta t \end{cases} \tag{4.15}$$

where,

$$\mathbf{D}^N = \mathbf{M}^N + \mathbf{C}^N \gamma \Delta t + \mathbf{K}^N \beta \Delta t^2 \tag{4.16}$$

In detail, the displacement predictor $\tilde{\mathbf{u}}_{k+1}^{N,free}$ is sent to the FE software that computes the corresponding restoring force $\mathbf{r}_{k+1}^N$. First, the reduced-order displacement vector $\tilde{\mathbf{u}}_{k+1}^{N,free}$ is expanded to the full set of DoFs by using the NS component-mode basis. Then, a full-order restoring force vector is computed by summing up the *nonlinear* restoring force contributions of every single element following a Newton-Raphson procedure, which entails update and inversion of the full-order NS stiffness matrix, possibly reusing a verified FE software. After convergence or a predefined number of iterations is achieved, the NS restoring force vector is condensed to the set of retained DoFs using the same component-mode basis to obtain $\mathbf{r}_{k+1}^N \left(\tilde{\mathbf{u}}_{k+1}^{N,free} \right)$. A full-order finite-element model is used indeed to compute the restoring force of the NS. In contrast, the response of the hybrid model refers to a reduced-order dynamic system. It is noteworthy that the evaluation of NS restoring force vector does not require information about the tangent stiffness of the PS. According to (4.4), mass $\mathbf{M}^N$ and damping $\mathbf{C}^N$ matrices are computed based on the initial tangent stiffness matrix $\mathbf{K}^N = \frac{\partial \mathbf{r}^N}{\partial \mathbf{u}^N}|_{u_0, \dot{u}_0}$ once at the beginning of the simulation. Since the DR algorithm of [19] is used, $\gamma = \frac{1}{2}$ and $\beta = 0$.

2. Solve the PS *free* problem at t_{k+1},

$$\begin{cases} \tilde{\mathbf{u}}_{k+1}^{P,free} = \mathbf{u}_k^P + \dot{\mathbf{u}}_k^P \Delta t + \left(\frac{1}{2} - \beta\right) \Delta t^2 \ddot{\mathbf{u}}_k^{P,free} \\ \tilde{\dot{\mathbf{u}}}_{k+1}^{P,free} = \dot{\mathbf{u}}_k^P + (1-\gamma)\,\Delta t \ddot{\mathbf{u}}_k^{P,free} \end{cases} \tag{4.17}$$

$$\ddot{\mathbf{u}}_{k+1}^{P,free} = \mathbf{D}^{P^{-1}} \left(\mathbf{f}_{k+1}^P - \mathbf{C}^P \tilde{\dot{\mathbf{u}}}_{k+1}^{P,free} - \mathbf{r}_{k+1}^P \left(\tilde{\mathbf{u}}_{k+1}^{P,free} \right) \right) \tag{4.18}$$

$$\begin{cases} \mathbf{u}_{k+1}^{P,free} = \tilde{\mathbf{u}}_{k+1}^{P,free} + \ddot{\mathbf{u}}_{k+1}^{P,free} \beta \Delta t^2 \\ \dot{\mathbf{u}}_{k+1}^{P,free} = \tilde{\dot{\mathbf{u}}}_{k+1}^{P,free} + \ddot{\mathbf{u}}_{k+1}^{P,free} \gamma \Delta t \end{cases} \tag{4.19}$$

where,

$$\mathbf{D}^P = \mathbf{M}^P + \mathbf{C}^P \gamma \Delta t + \mathbf{K}^P \beta \Delta t^2 \tag{4.20}$$

Similarly to the NS, at each step k, the displacement predictor $\tilde{\mathbf{u}}_{k+1}^{P,free}$ is imposed to the PS by means of servo-controlled actuators and the corresponding restoring force vector $\mathbf{r}_{k+1}^P$ is measured with load cells. Mass $\mathbf{M}^P$ and damping $\mathbf{C}^P$ matrices are computed based on the initial tangent stiffness matrix $\mathbf{K}^P = \frac{\partial \mathbf{r}^P}{\partial \mathbf{u}^P}|_{u_0, \dot{u}_0}$, which is measured from the PS with small displacement perturbations once before the experiment. Since the DR algorithm of [19] is used, $\gamma = \frac{1}{2}$ and $\beta = 0$. It is noteworthy that displacement control errors affects the measured restoring force $\mathbf{r}_{k+1,mes}^{P,free}$ and may bias the emulated system response [29]. Accordingly, the method proposed by [30] is suggested to compensate for control errors,

$$\mathbf{r}_{k+1}^{P,free} = \mathbf{r}_{k+1,mes}^{P,free} + \mathbf{K}^P (\mathbf{u}_{k+1}^{P,free} - \mathbf{u}_{k+1,mes}^{P,free}) \tag{4.21}$$

where $\mathbf{u}_{k+1,mes}^{P,free}$ and $\mathbf{r}_{k+1,mes}^{P,free}$ are measured displacement and restoring force vectors.

Before introducing Step 3, the global Steklov-Poincaré matrix operator used to compute the interface Lagrange multipliers based on NS and PS *free* solutions, is derived. Let us start by splitting substructure velocities into *free* and *link* components,

$$\begin{cases} \dot{\mathbf{u}}_{k+1}^N = \dot{\mathbf{u}}_{k+1}^{N,free} + \dot{\mathbf{u}}_{k+1}^{N,link} \\ \dot{\mathbf{u}}_{k+1}^P = \dot{\mathbf{u}}_{k+1}^{P,free} + \dot{\mathbf{u}}_{k+1}^{P,link} \end{cases} \tag{4.22}$$

and recall that $\dot{\mathbf{u}}_{k+1}^{N,free}$ and $\dot{\mathbf{u}}_{k+1}^{P,free}$ are known after solving (4.15) and (4.19), respectively. Let us assume that *link* solutions are linear functions of related interface Lagrange multiplier vectors,

$$\begin{cases} \dot{\mathbf{u}}_{k+1}^{N,link} = \gamma \Delta t \mathbf{D}^{N^{-1}} \mathbf{L}^{N^T} \mathbf{\Lambda}_{k+1}^{N} \\ \dot{\mathbf{u}}_{k+1}^{P,link} = \gamma \Delta t \mathbf{D}^{P^{-1}} \mathbf{L}^{P^T} \mathbf{\Lambda}_{k+1}^{P} \end{cases} \tag{4.23}$$

where $\mathbf{D}^N$ and $\mathbf{D}^P$ are defined in (4.16) and (4.20), respectively. If one substitutes (4.23) into (4.22) to recast the compatibility equations of (4.12) in matrix form, the Steklov-Poincaré operator $\mathbf{G}$ of the LLM-GC algorithm can be easily derived,

$$\begin{bmatrix} \mathbf{L}^N \dot{\mathbf{u}}_{k+1}^{N^{free}} \\ \mathbf{L}^P \dot{\mathbf{u}}_{k+1}^{P^{free}} \\ \mathbf{0} \end{bmatrix} + \underbrace{\begin{bmatrix} \mathbf{L}^N \mathbf{D}^{N^{-1}} \mathbf{L}^{N^T} \gamma \Delta t & \mathbf{0} & \bar{\mathbf{L}}^N \\ \mathbf{0} & \mathbf{L}^P \mathbf{D}^{P^{-1}} \mathbf{L}^{P^T} \gamma \Delta t & \bar{\mathbf{L}}^P \\ \bar{\mathbf{L}}^{N^T} & \bar{\mathbf{L}}^{P^T} & \mathbf{0} \end{bmatrix}}_{\mathbf{G}} \begin{bmatrix} \mathbf{\Lambda}_{k+1}^{N} \\ \mathbf{\Lambda}_{k+1}^{P} \\ \dot{\mathbf{u}}_{k+1}^{g} \end{bmatrix} = \mathbf{0} \tag{4.24}$$

The mass matrix formulation following the Gershgorin's circle theorem ensures that the upper bound of the maximum eigenfrequency of the hybrid model falls within the stability limit of the CD algorithm [19], which is further increased by a multiplicative factor 1.1 in (4.4). Thus, it is not necessary to magnify the initial tangent stiffness matrix estimate of the PS to ensure the stability of the LLM-GC algorithm. At this point, one can resume the solution procedure of the LLM-GC algorithm.

4. Calculate the interface Lagrange multiplier vectors as,

$$\begin{bmatrix} \mathbf{\Lambda}_{k+1}^{N} \\ \mathbf{\Lambda}_{k+1}^{P} \\ \dot{\mathbf{u}}_{k+1}^{g} \end{bmatrix} = -\mathbf{G}^{-1} \begin{bmatrix} \mathbf{L}^N \dot{\mathbf{u}}_{k+1}^{N^{free}} \\ \mathbf{L}^P \dot{\mathbf{u}}_{k+1}^{P^{free}} \\ \mathbf{0} \end{bmatrix} \tag{4.25}$$

   It is important to point out that the Steklov-Poincaré operator $\mathbf{G}$ is computed only once based on the initial tangent stiffness of both PS and NS and inverted before the simulation starts. As a result, the calculation of *link* solutions consists of a few matrix multiplications.

5. Calculate the *link* accelerations,

$$\begin{cases} \ddot{\mathbf{u}}_{k+1}^{N,link} = \mathbf{D}^{N^{-1}} \mathbf{L}^{N^T} \mathbf{\Lambda}_{k+1}^{N} \\ \ddot{\mathbf{u}}_{k+1}^{P,link} = \mathbf{D}^{P^{-1}} \mathbf{L}^{P^T} \mathbf{\Lambda}_{k+1}^{P} \end{cases} \tag{4.26}$$

   and *link* velocities according to (4.23). Since DR is based on the CD algorithm ($\gamma = \frac{1}{2}$ and $\beta = 0$), *link* displacements are null.

6. Calculate the *coupled* accelerations,

$$\begin{cases} \ddot{\mathbf{u}}_{k+1}^{N} = \ddot{\mathbf{u}}_{k+1}^{N,free} + \ddot{\mathbf{u}}_{k+1}^{N,link} \\ \ddot{\mathbf{u}}_{k+1}^{P} = \ddot{\mathbf{u}}_{k+1}^{P,free} + \ddot{\mathbf{u}}_{k+1}^{P,link} \end{cases} \tag{4.27}$$

and *coupled* velocities according to (4.22). Since DR is based on the CD algorithm with $\gamma = \frac{1}{2}$ and $\beta = 0$, *link* displacements are null and *coupled* displacements are equal to *free* displacements.

The LLM-GC algorithm inherits second-order accuracy from the GC method [20]. Figure 4.3 provides a detailed representation of the procedure for integrating the coupled equation of motion of the hybrid model between times t_k and t_{k+1}. The quantities exchanged between the PS and the NS and the coordinator during the RT-HFS are also indicated. The one-step *free* solutions of the PS and the NS are clearly parallel processes. In fact, the PS approaches the target boundary conditions while a FE software evaluates the restoring force of the NS, possibly with a Newton-Raphson algorithm. The computation of interface forces $\mathbf{\Lambda}_k^N$ and $\mathbf{\Lambda}_k^P$, which determine the *link* solution, requires only interface velocities $\mathbf{L}^N \dot{\mathbf{u}}_k^{N,free}$ and $\mathbf{L}^P \dot{\mathbf{u}}_k^{P,free}$ and relies solely on the matrix-vector product defined in (4.25). The computational cost (and the related time overhead) of the latter is negligible compared to the computation of the one-step *free* solution of the NS and the PS responses. As long as the number of interface DoFs is determined by the number of actuation points of the PS and not on the total number of DoFs of the hybrid model, the LLM-GC algorithm enables RT-HFS with realistic nonlinear FE models used as NSs. Limited data exchange, as well as minimal computational overhead, make the proposed LLM-GC algorithm suitable for being implemented as a coordinator in existing HFS middleware thus facilitating reusing of existing verified FE software (e.g., OpenFresco [21]).

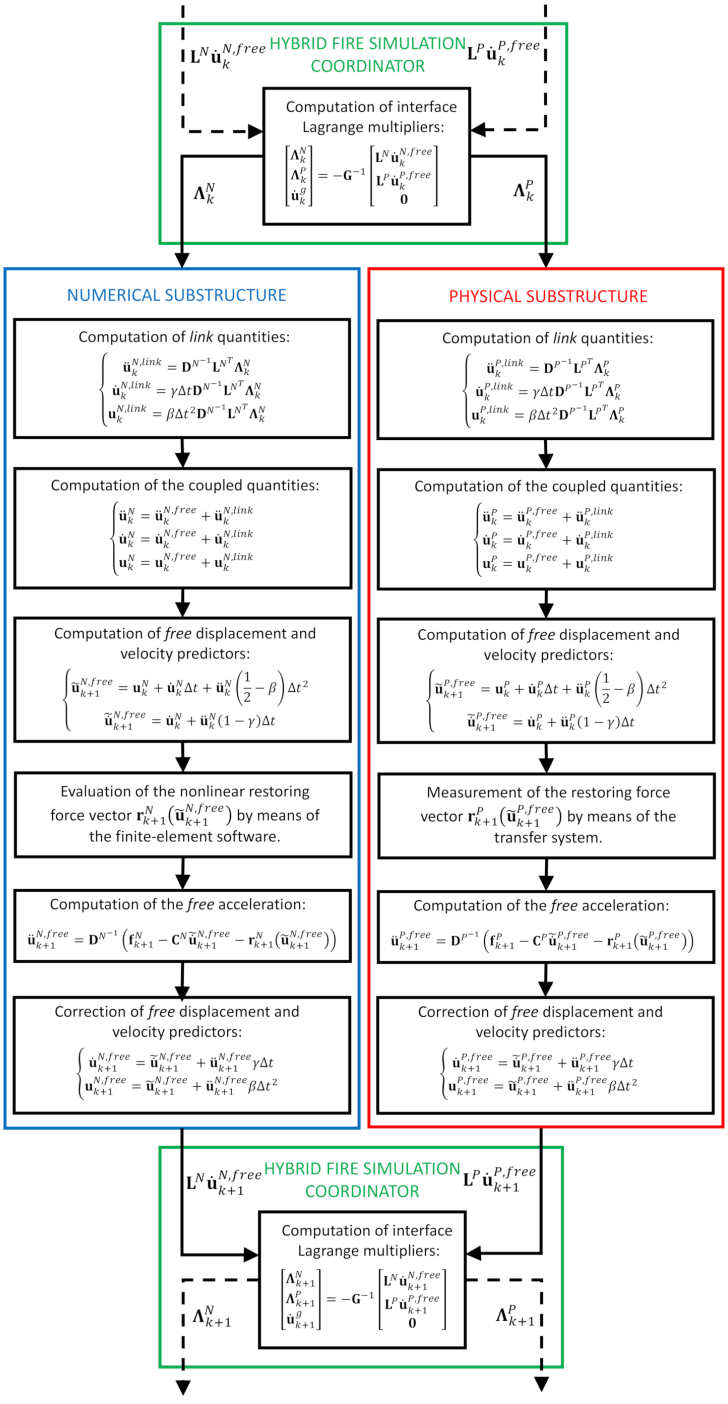

Figure 4.3: Architecture of the implementation of RT-HFS method based on the LLM-GC algorithm.

4.2.3 Numerical validation

The 5-DoFs chain-like system depicted in Figure 4.4 was formulated to investigate the algorithmic properties of the proposed RT-HFS method.

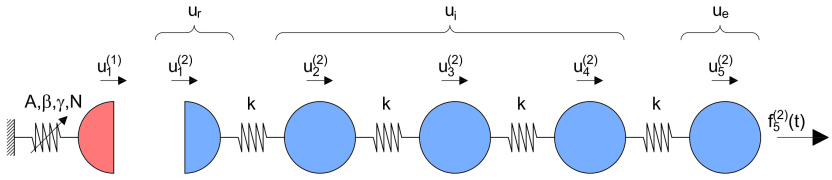

Figure 4.4: 5-DoF nonlinear chain-like system.

In detail, the 5-DoF chain-like (series) system comprises a nonlinear PS and a linear NS. A nonlinear Bouc-Wen hysteretic spring represents the PS rather than a physical spring in a laboratory, making this a virtual HS. A series of linear springs of stiffness $k = 2 \times 10^5$ forms the NS. A smooth force ramp $f_5^N(t) = 5000sin(\frac{\pi t}{400})$ is applied at Node #5 of the NS between zero and $t_{max} = 200$. Such a loading was selected to ensure a quasi-static structural response, which corresponds to the expected situation in RT-HFS. For completeness, the evolutionary equation of the PS Bouc-Wen spring restoring force is reported,

$$\dot{r} = (\alpha - (\beta sign(r\dot{u}) + \gamma)\,|r|^n)\,\dot{u} \tag{4.28}$$

where $\alpha = 1 \times 10^5$, $\beta = 5$, $\gamma = 0$, $n = 1$. The time history response of the system is evaluated using the proposed LLM-GC algorithm considering a time step size of 1 sec. It is important to stress that the selected time step size allows for averaging force measurements over an interval that is much larger than the typical actuation delay of about $10 \div 20$ msec. As anticipated in Section 4.2.1, the convergence rate of DR deteriorates for small values of ω_0/ω_{max}. Accordingly, static condensation, as reported in Section 4.2.1, is used to derive a 2-DoFs reduced-order model of the NS by retaining u_1^N and u_5^N as r-DoF and e-DoF, respectively.

Figure 4.5 compares the time history response of the PS of the 5-DoF chain-like system with both full- and reduced-order NS computed with the LLM-GC algorithm to a reference nonlinear static analysis computed with the Newton-Raphson algorithm.

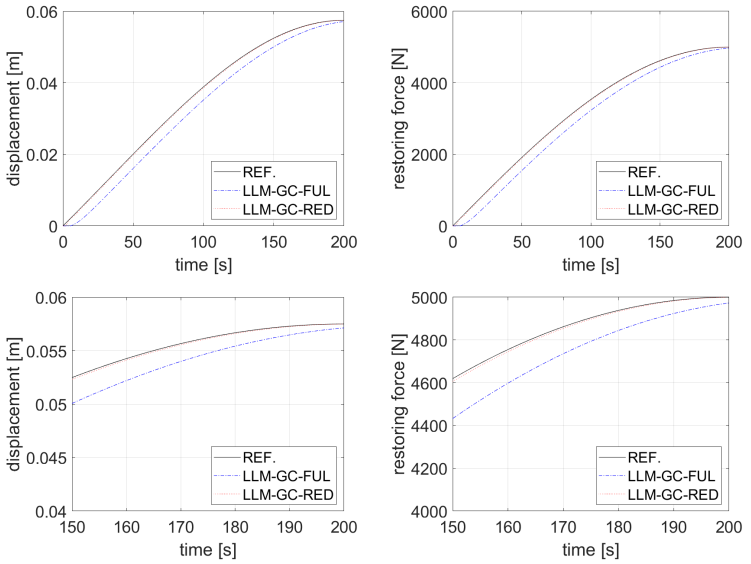

Figure 4.5: Time history response of the PS of the 5-DoF chain-like system without experimental errors: a) displacement and b) restoring force. REF curves refer to the exact reference solution computed with a nonlinear static analysis whereas LLM-GC-FUL and LLM-GC-RED curves refer to the solutions computed with the LLM-GC algorithm without and with CMS of the NS, respectively.

As can be appreciated from Figure 4.5, the time history response of the 5-DoF chain-like system computed with the LLM-GC algorithm without CMS of the NS (i.e., LLM-GC-FUL) lags with respect to the reference solution. On the other hand, if a reduced-order NS is used (i.e., LLM-GC-RED), the LLM-GC algorithm solution converges to the reference one. Additional simulations were performed to benchmark the error propagation performance of the proposed RT-HFS method. Both PS restoring force noise as well as perturbations of PS tangent stiffness matrix estimate, which inevitably propagate to fictitious mass and damping matrices according to (4.4), were simulated. The following expression describes the noise contamination of the PS restoring force,

$$r^{P,mes} = r^P + \Delta r^P, \Delta r^P \sim \mathcal{N}(0, 10) \tag{4.29}$$

where r^P is PS restoring force computed by the Bouc-Wen model while Δr^P is the force measurement error modeled using a Gaussian noise with standard deviation equal to 10 N. With regard to the procedure

outlined in Section 4.2.2, $r^{P,mes}$ enters (4.18). Similarly, the expression of the noisy estimate of the initial tangent stiffness matrix of the PS reads,

$$K^{P,mes} = K^P + \Delta K^P, \Delta K^P \sim \mathcal{U}\left(0.8K^P, 1.2K^P\right) \tag{4.30}$$

where K^P is the theoretical PS initial stiffness —equal to α —, while ΔK^P is the tangent stiffness estimation error, which is modeled using a uniform random variable to avoid negative terms. This range is assumed based on experience in estimating the initial tangent stiffness of the PS before experiments.

In this regard, Figure 4.6 compares the noisy response of the 5-DoF chain-like system with a reduced order NS computed with the LLM-GC algorithm to a reference noiseless solution computed with nonlinear static analysis. For the sake of completeness, such a comparison is extended to a simulation of the noisy response of the 5-DoF chain-like system computed with the modified Newton-Raphson algorithm suggested by both Sauca and co-authors [11] and Schulthess [13]. In this latter case, two iterations per time step were performed.

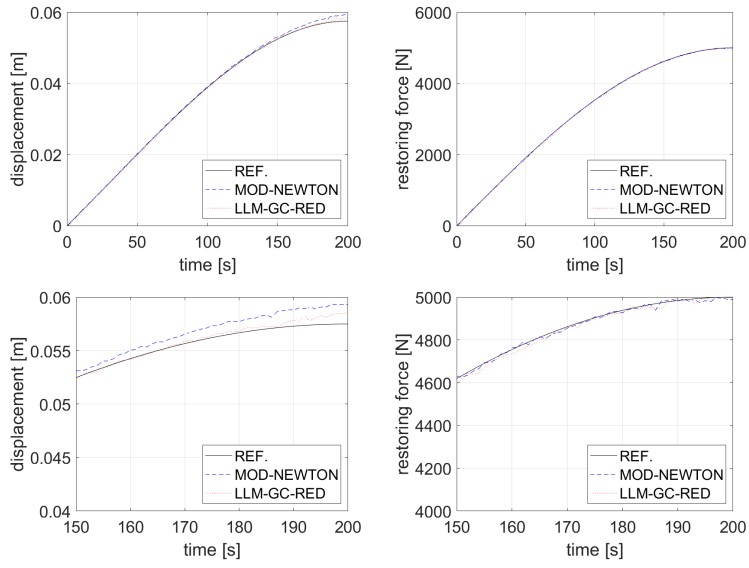

Figure 4.6: Time history response of the PS of the 5-DoF chain-like system with experimental errors: a) displacement and b) restoring force. REF curves refer to the exact noiseless reference solution computed with nonlinear static analysis, LLM-GC-RED curves refer to the noisy solutions computed with the LLM-GC algorithm with CMS of the NS, and MOD-NEWTON curves refer to the noisy solution computed with the modified Newton-Raphson algorithm.

As can be appreciated from Figure 4.6, the error propagation performance of the LLM-GC algorithm and the modified Newton-Raphson algorithm are similar. In both cases, deviations from exact solutions are not negligible even for a relatively small level of PS restoring force noise. This is because, for a static balance equation, restoring force errors propagate directly to displacements. In the dynamic case, restoring force noise affects accelerations directly, that is, second-order derivatives of displacements. The double integration from accelerations to displacements operated by the dynamic equation of motion acts as a low-pass filter that reduces the impact of noise. For this reason, particular care must be devoted to the conditioning of PS response signals in static RT-HFS. Such a simplified error propagation analysis is not meant to be exhaustive but only to provide a preliminary assessment of the algorithmic performance in the presence of experimental errors compared to the state-of-art algorithms.

4.3 Case study: Hybrid fire simulation of a virtual steel frame

In order to demonstrate the effectiveness of the proposed method and to illustrate the implementation of a real RT-HFS, a virtual RT-HFS case study investigation was conceived using a hybrid model where both NS and PS were numerically simulated in MATLAB. The thermomechanical beam element developed by Morbioli and co-authors [31], based on both a corotational formulation and local linear Bernoulli assumptions, was implemented. However, the branch-switching properties were deactivated in order to keep the analysis simpler. In the article, the ability of this beam element to capture the nonlinear behavior of steel members subjected to fire was shown by comparing experimental data and FE software, e.g., SAFIR [9].

4.3.1 Description of the case study

The three-storey three-bay unprotected steel frame reported in [32], which is designed according to the EN 1993-1- [33] using S235 steel, was selected for this virtual RT-HFS case study. The first two floors were subjected to fire. For simplicity, local geometric imperfections and fire protection were not included in the model, while global geometric imperfections were included according to the EN 1993-1-1 [33]. Figure 4.7a shows the layout of the steel frame indicating the steel member section sizes and the magnitude of the gravity loads acting simultane-

ously with the fire action. Figure 4.7b shows the evolution in time of the steel temperature in the heated frame members during the virtual simulation according to a lumped mass approach. In particular, the ISO 834 time-temperature heating curve was applied to the first two floors, and columns and beams were exposed on four sides.

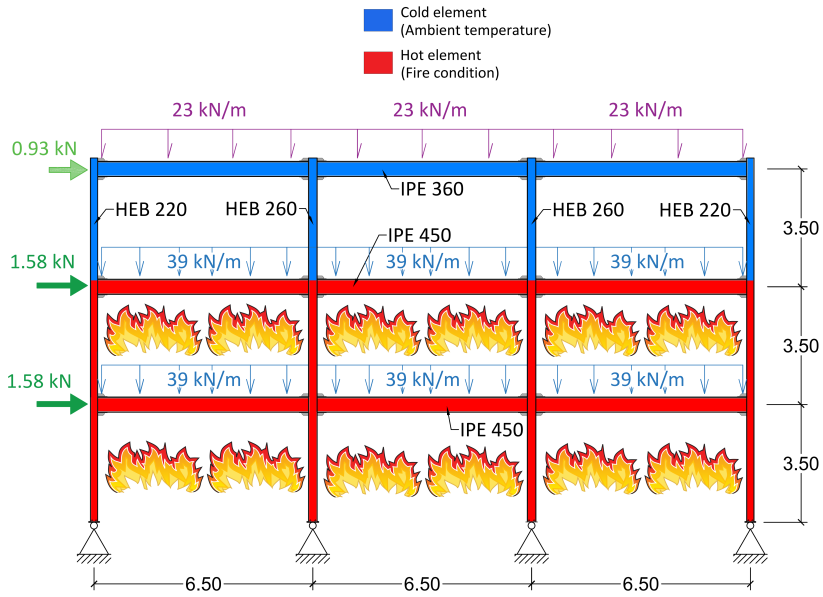

(a)

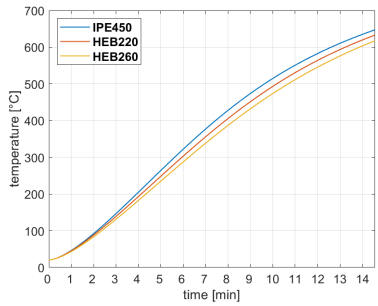

(b)

Figure 4.7: Case-study steel frame structure: a) emulated steel frame; b) time-temperature heating curves.

4.3.2 Implementation of the virtual RT-HFS

According to the procedure outlined in Subsection 4.2.2, the steel frame of Figure 4.7 was partitioned into a NS and a PS, respectively, as depicted

in Figure 4.8.

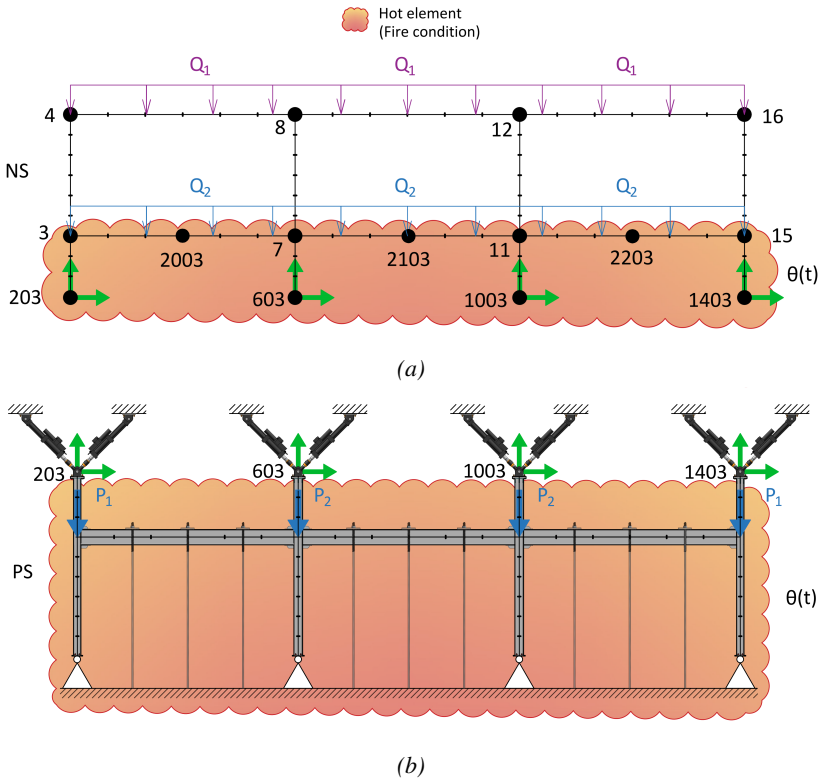

Figure 4.8: Substructuring of the case study steel frame: a) NS; b) PS.

As shown in Figure 4.8, in line with the substructuring strategy proposed by [34], the PS and NS were coupled at the translation DoFs, while continuity of rotational DoFs was neglected. The columns were subjected to bending with an inflection point close to mid-height, as well as to axial load due to gravity and axial elongation due to the fire action. Thus, a pair of actuators were pin-connected at mid-height of the columns to enable the simultaneous application of bending and axial loads and horizontal and vertical displacements on the column. In a real simulation, a loading system based on post-tension bars and hydraulic jacks would impose the gravity loads on the PS steel beams, while heat pads would be used to impose temperature histories to the PS beams and columns. Since the RT-HFS campaign is virtual, both NS and PS were numerically simulated.

Every member of the NS was subdivided into six beam elements endowed with material and geometric nonlinearity. Fire loading was also

applied to the NS to show that the proposed method still works when high nonlinearities are exhibited by the NS. In order to increase the convergence rate of DR, NS stiffness, damping and mass matrices were condensed to nodal translation DoFs, which are numbered in Figure 4.10. In detail, $u_{203,x}$, $u_{203,y}$ and $u_{1403,y}$ were retained as r-DoFs while the remaining ones were retained as e-DoFs.

It is important to remark, that, at every evaluation of the NS *free* solution, the reduced-order displacement vector is expanded to the full set of NS DoFs, and the restoring force vector is computed by summing up the *nonlinear* restoring force contributions of every single element. Then, such a vector is condensed to the set of retained DoFs using the same component-mode basis. Accordingly, a full-order FE model is used to compute the restoring force of the NS, whereas the response of the hybrid model refers to a reduced-order dynamic system. As for all *a posteriori* model-order reduction methods, the adequacy of the retained component-mode basis must be verified for the range of displacement trajectories likely to occur during the HFS. As an example, if traveling fire is expected, the component-mode basis must be able to represent the corresponding displacement response with a reasonable degree of approximation.

Similarly, six nonlinear thermomechanical beam elements endowed with material and geometric nonlinearities discretized every member of the PS. For both substructures, the elastoplastic constitutive law provided by the EN1993-1-2 [35] was adopted to model the mechanical properties of steel at elevated temperatures. Temperature dependence of elastic modulus, yield strength, and strain proportional limit was accounted for according to EN1993-1-2 [35]. It is important to underline that the full-order FE model of the PS provides the restoring forces of each single DoF, but that only the interface DoFs enter the time integration loop of RT-HFS. Thus, reduced-order fictitious mass and damping matrices were calculated according to (4.4) by condensing at the interface DoFs the linearized FE model of the PS.

At each time step of the LLM-GC algorithm outlined in Subsection 4.2.2, the PS restoring force was evaluated by imposing the interface displacements as computed in (4.17) to the FE model via displacement-controlled static nonlinear analysis. In particular, $\mathbf{f}^N$ of (4.12) included gravity loads, which ramped from zero to the design value within the first 500s of the RT-HFT. At the same time and with the same rate, vertical load ramped on the internal DoFs of the PS. As a result, RT-HFT emulated the static structural response to gravity loads. Then, fire, which was represented by the temperature-time heating curves imposed on the PS elements, was initiated, as shown in Figure 4.12. As a result, the virtual

RT-HFS accurately reproduced the response of the PS.

In order to probe the effect of experimental errors, an uncertainty propagation analysis was performed, which accounted for restoring force measurement noise and bias of the PS tangent stiffness matrix estimate. The uncertainty propagation analysis is not meant to be exhaustive but only to provide an overview of how experimental errors affect the hybrid model response. As analogously done for the simplified case study presented in Section 4.2.3, the PS restoring force was contaminated with Gaussian noise of zero mean and $100\,\mathrm{N}$ standard deviation, which is plausible for an actuator force capacity range of $1 \div 2\,\mathrm{MN}$. At the same time, all terms of the PS tangent stiffness matrix were perturbed by a multiplicative factor uniformly distributed between 0.8 and 1.2. The symmetry of the perturbed PS tangent stiffness matrix was enforced via averaging with its transpose matrix. Such a protocol reflects the practice of estimating the tangent stiffness matrix of the PS before experiments.

4.3.3 Results

The response history of the steel frame investigated in the RT-HFS case study described above is compared to the response of a reference FE model of the same frame implemented in SAFIR [9]. The latter was characterized by the same mesh discretization and nonlinearities as the RT-HFS case study hybrid model of Section 4.3.2. However, in order to represent a real frame, continuity of rotation was enforced at the interface between PS and NS in the reference frame analysis. For this reason, some discrepancies in the results were noticed. As expected, the location of the hinge at the column mid-height of the second floor was a good approximation at the beginning of the fire and during its first phases, as illustrated in Figure 4.9a. Nonetheless, as the fire progressed and the loss of strength and stiffness of the heated elements became significant, the loads redistributed, and the column moment diagram changed, moving the inflection point away from the column mid-height as shown in Figure 4.9b. Collapse times between the two models were the same,i.e. $745\,\mathrm{s}$ after the start of the fire. In this respect, Figure 4.10 compares the final deformed configuration of the steel frame at $735\,\mathrm{s}$ and at the end of the simulation ($745\,\mathrm{s}$). Indeed, the absence of the rotational continuity at boundaries between the PS and the NS in the hybrid model was responsible for a slightly different deformed shape at collapse. One can see that even though the presence of the differences mentioned above, the static response of the frame under gravity and fire loads obtained via RT-HFS agrees reasonably well with the reference solution obtained with the SAFIR FE code.

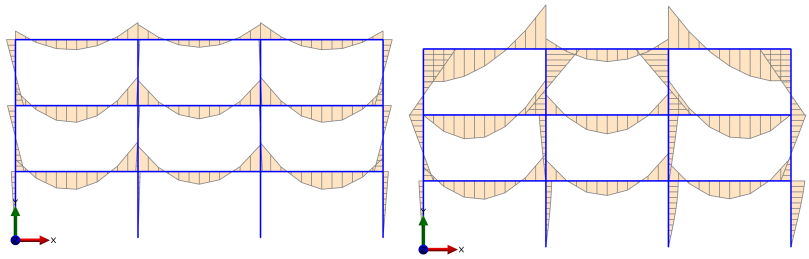

(a) *(b)*

Figure 4.9: Bending moment diagram in the SAFIR model of the case study steel frame at: a) t = 0 s; b) t = 740 s.

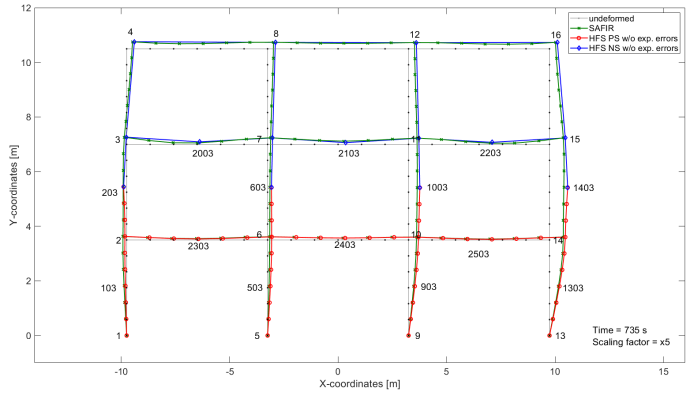

(a)

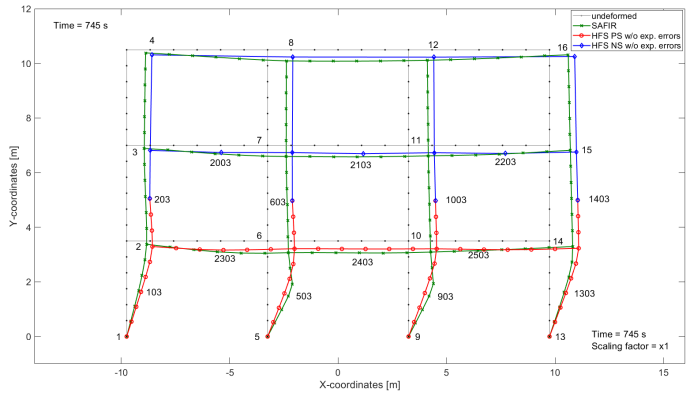

(b)

Figure 4.10: Deformed configuration of the case study steel frame at: a) 735 s; b) 745 s (end of the simulation).

Figures 4.11 and 4.12 compare the horizontal displacement responses measured at nodes #103 and #503, which correspond to the lateral responses of the first and the second columns of the PS measured at mid-height. Similarly, Figures 4.13 and 4.14 compare the vertical displacement responses of nodes #2303 and #2403, which correspond to the mid-span deflections of the first and the second beam of the PS. Time-history responses obtained via RT-HFS agree with the reference nonlinear FE analysis performed in SAFIR. The error propagation analysis provides satisfactory results, too. The variability of the system response is small for the given realistic range of measurement errors. Therefore, the proposed RT-HFS method can be considered as suitable to perform hybrid fire simulations involving real physical substructures tested under mechanical and thermal loads in laboratory conditions.

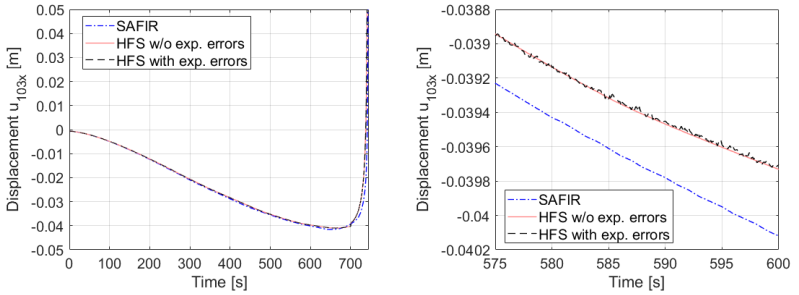

Figure 4.11: Comparison of horizontal displacement histories measured at Node # 103: a) full time history; b) zoomed plot.

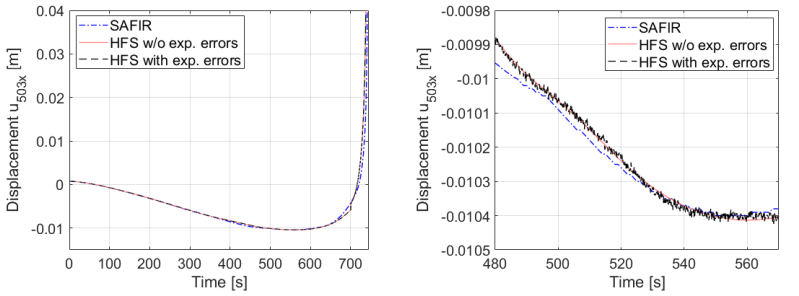

Figure 4.12: Comparison of horizontal displacement histories measured at Node # 503: a) full time history; b) zoomed plot.

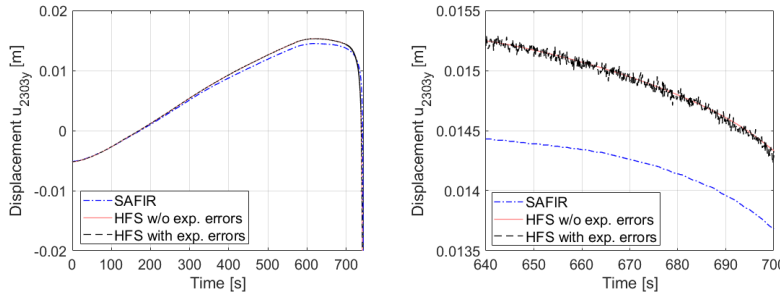

(a) *(b)*

Figure 4.13: Comparison of vertical displacement histories measured at Node #2303: a) full time history; b) zoomed plot.

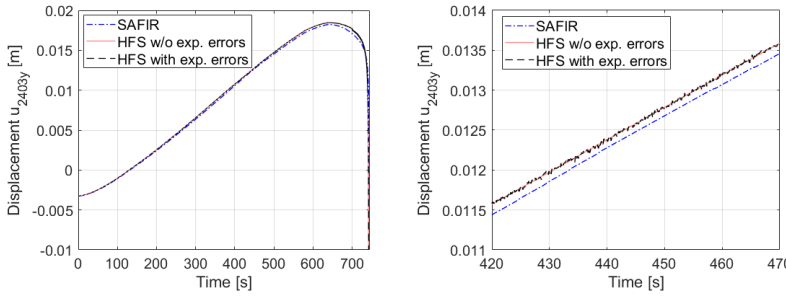

(a) *(b)*

Figure 4.14: Comparison of vertical displacement histories measured at Node #2403: a) full time history; b) zoomed plot.

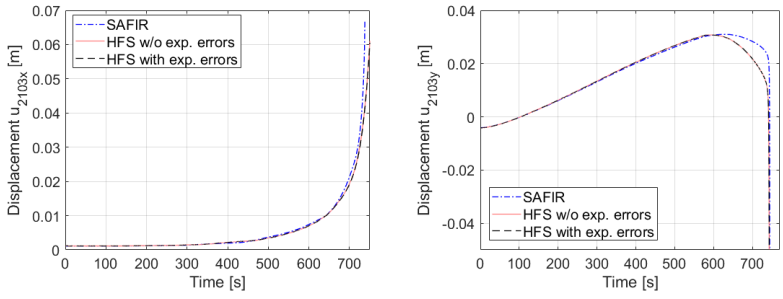

(a) *(b)*

Figure 4.15: Comparison of displacement histories measured at Node #2103: a) horizontal displacement; b) vertical displacement.

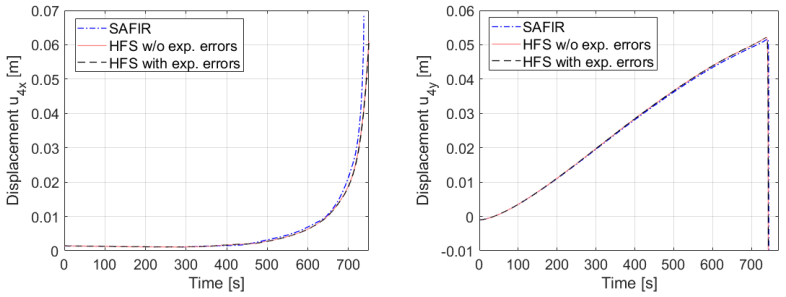

(a) *(b)*

Figure 4.16: Comparison of displacement histories measured at Node #4: a) horizontal displacement; b) vertical displacement.

4.4 Conclusions

The paper presented a real-time hybrid fire simulation (RT-HFS) method that combines dynamic relaxation and partitioned time integration to compute the static response of a hybrid numerical-experimental model subjected to fire loading. In the case of a 5-DoF series nonlinear system, the presented RT-HFS methods showed promising results when component-mode synthesis of the numerical substructure and experimental errors were applied. Moreover, the presented RT-HFS method was also verified in a case study of a virtual 3-story steel frame structure subjected to fire loading. Results in agreement with a reference model developed using thermomechanical finite element software SAFIR were observed under modeled experimental errors. The proposed RT-HFS highlighted error propagation performance similar to the modified Newton-Raphson method, which is the only alternative algorithm for nonlinear RT-HFS available from the state of the art. However, the proposed method minimizes the computational overhead for the coordination of a real-time hybrid fire simulation, and limits exchanged data to interface velocities. This is of paramount importance to enable RT-HFSs where physical and numerical substructures have material and geometric nonlinearities, with the numerical substructures possibly implemented in verified finite element software. Future work is focused on the implementation of the presented RT-HFS method in hybrid fire simulations involving a real physical substructure.

4.5 Acknowledgements

The first author wishes to acknowledge the Swiss Government for funding this research through the Swiss Government Excellence Scholarship REF. 2014.0588 devoted to the "Development of advanced temperature control strategies for hybrid fire simulation". This work has received funding from the European Union's Horizon 2020 research and innovation program under the SERA grant agreement No. 730900 and the related TA project EQUFIRE. Finally, the authors also acknowledge funding from the Swiss Federal Institute of Technology (ETH) Zurich, and the Italian Ministry of Education, University and Research (MIUR) in the frame of the Departments of Excellence Initiative 2018–2022 attributed to DICAM of the University of Trento.

Bibliography

[1] A. H. Schellenberg, S. A. Mahin, and G. L. Fenves, "Advanced implementation of hybrid simulation," PEER Report 2009/104, Pacific Earthquake Engineering Research Center, University of California, Berkeley, California, 2009.

[2] M. Korzen, G. Magonette, and P. Buchet, "Mechanical Loading of Columns in Fire Tests by Means of the Substructuring Method," *Proceedings of the 8th Interflam Conference, Edinburgh 1999*, vol. 2, no. i, pp. 911–914, 1999.

[3] M. Korzen, K.-U. Ziener, S. Riemer, G. Magonette, and P. Buchet, "Some Remarks on the Substructuring Method Applied to Fire Resistance Tests of Columns," *World Congress on Housing*, 2002.

[4] M. Korzen, J. P. C. Rodrigues, and A. M. Correia, "Thermal restraint effects on the fire resistance of steel and composite steel and concrete columns," *Application of Structural Fire Engineering*, no. February, pp. 512–517, 2009.

[5] F. Robert, S. Rimlinger, and C. Collignon, "Structure Fire Resistance: A Joint Approach between Moedlling and Full Scale Testing (Substructuring System)," in *3rd fib International Congress*, 2010.

[6] E. Mergny, T. Gernay, G. Drion, and J. M. Franssen, "Hybrid fire testing in a non-linear environment using a proportional integral controller," *Journal of Structural Fire Engineering*, vol. 10, no. 2, pp. 245–258, 2019.

[7] H. Mostafaei, "Hybrid fire testing for assessing performance of structures in fire—Methodology," *Fire Safety Journal*, vol. 58, pp. 170–179, 2013.

[8] H. Mostafaei, "Hybrid fire testing for assessing performance of structures in fire—Application," *Fire safety journal*, vol. 56, pp. 30–38, 2013.

[9] J.-M. Franssen and T. Gernay, "Modeling structures in fire with SAFIR®: Theoretical background and capabilities," *Journal of Structural Fire Engineering*, vol. 8, no. 3, pp. 300–323, 2017.

[10] A. Sauca, T. Gernay, F. Robert, N. Tondini, and J.-M. Franssen, "Hybrid fire testing: Discussion on stability and implementation of a new method in a virtual environment," *Journal of Structural Fire Engineering*, vol. 9, no. 4, pp. 319–341, 2018.

[11] A. Sauca, E. Mergny, T. Gernay, and J. M. Franssen, "A method for hybrid fire testing: Development, implementation and numerical application," *Applications of Fire Engineering - Proceedings of the International Conference of Applications of Structural Fire Engineering, ASFE 2017*, pp. 225–234, 2018.

[12] X. Wang, R. E. Kim, O.-s. Kwon, I.-h. Yeo, and J.-k. Ahn, "Continuous Real-Time Hybrid Simulation Method for Structures Subject to Fire," *Journal of Structural Engineering*, vol. 145, p. 04019152, dec 2019.

[13] P. Schulthess, *Consolidated Fire Analysis - Coupled Numerical Simulation and Physical Testing for Global Structural Fire Analysis*. PhD thesis, ETH Zurich, 2019.

[14] ABAQUS Inc., "Abaqus."

[15] C. Thewalt and M. Roman, "Performance Parameters for Pseudodynamic Tests," *Journal of Structural Engineering*, vol. 120, pp. 2768–2781, sep 1994.

[16] E. Carrion and B. Spencer, "Real-time hybrid testing using model-based delay compensation," in *4th International Conference on Earthquake Engineering*, no. 299, 2006.

[17] C.-C. Hung and S. El-Tawil, "A method for estimating specimen tangent stiffness for hybrid simulation," *Earthquake Engineering & Structural Dynamics*, vol. 38, pp. 115–134, jan 2009.

[18] M. Ahmadizadeh and G. Mosqueda, "Hybrid Simulation with Improved Operator-Splitting Integration Using Experimental Tangent Stiffness Matrix Estimation," *Journal of Structural Engineering*, vol. 134, pp. 1829–1838, dec 2008.

[19] P. G. Underwood, *Computational Methods for Transient Analysis*, ch. Dynamic relaxation techniques: a review. Amsterdam: North-Holland, 1983.

[20] A. Gravouil and A. Combescure, "Multi-time-step explicit–implicit method for non-linear structural dynamics," *International Journal for Numerical Methods in Engineering*, vol. 50, no. 1, pp. 199–225, 2001.

[21] C. A. Whyte, K. R. Mackie, and B. Stojadinovic, "Hybrid simulation of thermomechanical structural response," *Journal of Structural Engineering*, vol. 142, no. 2, p. 04015107, 2015.

[22] D. de Klerk, D. J. Rixen, and S. Voormeeren, "General Framework for Dynamic Dubstructuring: History, Review and Classification of Techniques," *AIAA journal*, vol. 46, no. 5, pp. 1169–1181, 2008.

[23] C. Farhat and F. X. Roux, "A method of finite element tearing and interconnecting and its parallel solution algorithm," *International Journal for Numerical Methods in Engineering*, vol. 32, no. 6, pp. 1205–1227, 1991.

[24] C. Farhat, P. S. Chen, and J. Mandel, "A scalable Lagrange multiplier based domain decomposition method for time-dependent problems," *International Journal for Numerical Methods in Engineering*, vol. 38, no. 22, pp. 3831–3853, 1995.

[25] A. Bonelli, O. S. Bursi, L. He, G. Magonette, and P. Pegon, "Convergence analysis of a parallel interfield method for heterogeneous simulations with dynamic substructuring," *International journal for numerical methods in engineering*, vol. 75, no. 7, pp. 800–825, 2008.

[26] N. Newmark, "A Method of Computation for Structural Dynamics," *Journal of the Engineering Mechanics Division*, no. 3, pp. 67–94, 1959.

[27] K. C. Park, C. A. Felippa, and U. A. Gumaste, "A localized version of the method of Lagrange multipliers and its applications," *Computational Mechanics*, vol. 24, pp. 476–490, Jan. 2000.

[28] R. R. Craig and A. J. Kurdila, *Fundamentals of structural dynamics*. John Wiley & Sons, 2006.

[29] P.-S. B. Shing and S. A. Mahin, "Cumulative experimental errors in pseudodynamic tests," *Earthquake engineering & structural dynamics*, vol. 15, no. 4, pp. 409–424, 1987.

[30] O. S. Bursi and P.-S. Shing, "Evaluation of some implicit time-stepping algorithms for pseudodynamic tests," *Earthquake Engineering & Structural Dynamics*, vol. 25, no. 4, pp. 333–355, 1996.

[31] A. Morbioli, N. Tondini, and J.-M. Battini, "A branch-switching procedure for analysing instability of steel structures subjected to fire," *Structural Engineering and Mechanics*, vol. 67, no. 6, pp. 629–641, 2018.

[32] N. Boissonnade, R. Greiner, J.-P. Jaspart, and L. J., *Rules for Member Stability in EN 1993-1-1: Background documentation and design guidelines*. Brussels, ECCS, 2006.

[33] CEN, "Eurocode 3: Design of steel structures - Part 1-1: General rules and rules for buildings," european standard, European Union, May 2005.

[34] M. J. Hashemi and G. Mosqueda, "Innovative substructuring technique for hybrid simulation of multistory buildings through collapse," *Earthquake Engineering & Structural Dynamics*, vol. 143, no. 14, pp. 2059–2074, 2014.

[35] CEN, "Eurocode 3: Design of steel structures - Part 1-2: General rules - Structural fire design," european standard, European Union, May 2005.

5.0 A static solver for Hybrid Fire Simulation based on model reduction and dynamic relaxation

This chapter contains the following published paper:

"A static solver for hybrid fire simulation based on model reduction and dynamic relaxation." *Patrick Covi, Giuseppe Abbiati, Nicola Tondini, Oreste S. Bursi, Božidar Stojadinović, 11th International Conference on Structures in Fire (SiF2020), The University of Queensland, 2020*
https://doi.org/10.14264/2ed186c

abstract

Large-scale tests of an entire structure are generally prohibitively expensive, both in terms of finances and time, because of the need for expensive specialized facilities. As a result, most of the research regarding the behavior of structures subjected to fire has been carried out on partial subassemblies or single components subjected to standard heating curves. Standard fire tests use simplified mechanical boundary conditions for the tested structural element. However, for some elements, these conditions can lead to results that are overly conservative. Hybrid fire simulation emerged as a viable solution for performing component level experiments that account for the interaction between the tested specimen and a realistic yet virtual subassembly instantiated in a finite-element software. On these premises, this work presents a virtual hybrid fire simulation campaign conceived for a steel braced frame. Numerical experiments demonstrate the effectiveness of a newly conceived hybrid fire simulation algorithm. Finite-element simulations performed with the software SAFIR are used as a reference for verification.

5.1 Introduction

Hybrid Simulation (HS) is an online dynamic simulation paradigm that combines classical experimental techniques with online computer simulation for cost-effective large-scale testing of the structure under simulated loads, as comprehensively reviewed in [1]. Hybrid simulation of

the response of a structure to a fire load was also investigated [2][3][4][5][6][7]. In this context, Hybrid Fire Simulation (HFS) utilizes sub-structuring: the part of the structure, whose behavior is difficult to simulate, is modeled physically, i.e., the physical substructure (PS); all other parts are simulated numerically, i.e., the numerical substructure (NS). Many tools for hybrid testing are coming from earthquake engineering, and in most the fire scenarios, there is exactly a complementary situation. For instance, the axial force in columns is variable during the fire development caused by the axial force redistribution due to the restrained thermal expansion, and the structural response is static because the temperature variation is slow compared to the mechanical frequency of the system. Conversely, in the seismic case, the inertia plays a substantial role, and the response is governed by the dynamic amplification. Axial degrees of freedom of the columns are typically activated by high modes associated with low participating masses. Therefore, in the seismic scenario, those degrees of freedom (DOFs) are usually removed from the hybrid simulation loop, but the same DOFs cannot be removed in the fire case. Another difference is that in most of the seismic engineering cases, the structural response can be assumed as rate-independent, which means that experiments can be performed with an extended time scale. Materials at a high temperature usually exhibit creep and stress relaxation, which entail a time-dependent structural response. These effects prohibit the adoption of an extended time scale, thus enforcing the use of real-time hybrid simulation.

5.2 HYBRID FIRE SIMULATION ALGORITHM

The Real-Time Hybrid Fire Simulation (RT-HFS) algorithm presented in this paper [7] relies on the Finite Element Tearing and Interconnecting (FETI) approach to couple PS and NS [8]. In particular, the Gravouil and Combescure (GC) algorithm [9] and the Localized Lagrange Multipliers (LLM) method [10] are used in combination to solve the coupled equation of motion of the hybrid model. Since the structural response to fire is quasi-static, the Dynamic Relaxation (DR) algorithm [11] is adopted to build an equivalent dynamic system that mimics the static response of substructures. The basic idea behind DR is to obtain the displacement solution of a static structural problem,

$$\mathbf{r}(\mathbf{u}) = \mathbf{f}(t) \tag{5.1}$$

by computing the transient response of an equivalent dynamic system, whose equation of motion reads,

$$\mathbf{M}\ddot{\mathbf{u}} + \mathbf{C}\dot{\mathbf{u}} + \mathbf{r}\left(\mathbf{u}\right) = \mathbf{f}(t) \tag{5.2}$$

where $\mathbf{r}$ is the internal restoring force vector, which depends on the displacement vector $(\mathbf{u})$ (and, possibly, to its past time history) while $\mathbf{f}(t)$ represents a time varying external loading; $\mathbf{M}$ and $\mathbf{C}$ are fictitious mass and damping diagonal matrices, respectively. Expressions for diagonal entries of both fictitious mass and damping matrices read,

$$\begin{array}{c} M_{ii} = \frac{(1.1\Delta t)^2}{4} \sum_j |K_{ij}| \\ C_{ii} = 2\omega_0 M_{ii} \end{array} \tag{5.3}$$

which are derived to maximize the convergence rate of the DR algorithm, where K_{ij} is a generic element of the initial tangent stiffness matrix $\mathbf{K} = \partial\mathbf{r}/\partial\mathbf{u}$; ω_0 is the lowest undamped frequency of (5.2) after linearization of $\mathbf{r}\left(\mathbf{u}\right)$ at zero displacement and velocity; Δt is the time step size of the equivalent transient analysis solved using the Central Difference (CD) algorithm, which is equivalent to the Newmark scheme with $\gamma = \frac{1}{2}$ and $\beta = 0$.

The LLM-GC algorithm proposed in this paper relies on the coupling scheme of the GC method [9] adapted to the LLM method [10] to couple the equations of motion of PS and NS, both represented by equivalent dynamic systems computed with DR. For the sake of simplicity, the LLM-GC algorithm is described for a hybrid model comprising a single PS and a single NS,

$$\begin{cases} \begin{cases} \mathbf{M}^N \ddot{\mathbf{u}}^N_{k+1} + \mathbf{C}^N \dot{\mathbf{u}}^N_{k+1} + \mathbf{r}^N\left(\mathbf{u}^N_{k+1}, \boldsymbol{\theta}^N_{k+1}\right) = \mathbf{f}^N_{k+1} + \mathbf{L}^{N^T} \boldsymbol{\Lambda}^N_{k+1} \\ \mathbf{L}^N \dot{\mathbf{u}}^N_{k+1} + \bar{\mathbf{L}}^N \dot{\mathbf{u}}^g_{k+1} = \mathbf{0} \end{cases} \\ \begin{cases} \mathbf{M}^P \ddot{\mathbf{u}}^P_{k+1} + \mathbf{C}^P \dot{\mathbf{u}}^P_{k+1} + \mathbf{r}^P\left(\mathbf{u}^P_{k+1}, \boldsymbol{\theta}^P_{k+1}\right) = \mathbf{f}^P_{k+1} + \mathbf{L}^{P^T} \boldsymbol{\Lambda}^P_{k+1} \\ \mathbf{L}^P \dot{\mathbf{u}}^P_{k+1} + \bar{\mathbf{L}}^P \dot{\mathbf{u}}^g_{k+1} = \mathbf{0} \end{cases} \\ \bar{\mathbf{L}}^{N^T} \boldsymbol{\Lambda}^N_{k+1} + \bar{\mathbf{L}}^{P^T} \boldsymbol{\Lambda}^P_{k+1} = \mathbf{0} \end{cases} \tag{5.4}$$

where superscripts N and P indicates NS and PS, respectively. In detail, vectors represent interface forces used to enforce velocity compatibility between NS and PS. and are Boolean matrices used to collocate these interface forces on both substructures' degrees-of-freedom. For a detailed description of how those matrices are defined, the reader is addressed to the paper of Abbiati and co-workers [7]. It is important to remark that both fictitious damping matrices and are computed based on

the lower eigenvalue of the coupled equations of equilibrium, as defined in equation (5.2), which is estimated with a linearized monolithic version of the partitioned hybrid model. The LLM-GC algorithm is presented in algorithmic form to integrate equation (5.4) from time t_k to t_{k+1} with a time step Δt:

1. Solve the NS *free* problem at t_{k+1},

$$\begin{cases} \tilde{\mathbf{u}}_{k+1}^{N,free} = \mathbf{u}_k^N + \dot{\mathbf{u}}_k^N \Delta t + \left(\frac{1}{2} - \beta\right) \Delta t^2 \ddot{\mathbf{u}}_k^N \\ \tilde{\dot{\mathbf{u}}}_{k+1}^{N,free} = \dot{\mathbf{u}}_k^N + (1-\gamma)\, \Delta t \ddot{\mathbf{u}}_k^N \end{cases} \tag{5.5}$$

$$\ddot{\mathbf{u}}_{k+1}^{N,free} = \mathbf{D}^{N^{-1}} \left(\mathbf{f}_{k+1}^N - \mathbf{C}^N \tilde{\dot{\mathbf{u}}}_{k+1}^{N,free} - \mathbf{r}_{k+1}^N \left(\tilde{\mathbf{u}}_{k+1}^{N,free} \right) \right) \tag{5.6}$$

$$\begin{cases} \mathbf{u}_{k+1}^{N,free} = \tilde{\mathbf{u}}_{k+1}^{N,free} + \ddot{\mathbf{u}}_{k+1}^{N,free} \beta \Delta t^2 \\ \dot{\mathbf{u}}_{k+1}^{N,free} = \tilde{\dot{\mathbf{u}}}_{k+1}^{N,free} + \ddot{\mathbf{u}}_{k+1}^{N,free} \gamma \Delta t \end{cases} \tag{5.7}$$

where,

$$\mathbf{D}^N = \mathbf{M}^N + \mathbf{C}^N \gamma \Delta t + \mathbf{K}^N \beta \Delta t^2 \tag{5.8}$$

In detail, the displacement predictor $\tilde{\mathbf{u}}_{k+1}^{N,free}$ is sent to the FE software that computes the corresponding restoring force $\mathbf{r}_{k+1}^N$. According to equation (5.3), mass $\mathbf{M}^N$ and damping $\mathbf{C}^N$ matrices are computed based on the initial tangent stiffness matrix $\mathbf{K}^N = \frac{\partial \mathbf{r}^N}{\partial \mathbf{u}^N}|_{u_0, \dot{u}_0}$ once at the beginning of the simulation.

2. Solve the PS *free* problem at t_{k+1},

$$\begin{cases} \tilde{\mathbf{u}}_{k+1}^{P,free} = \mathbf{u}_k^P + \dot{\mathbf{u}}_k^P \Delta t + \left(\frac{1}{2} - \beta\right) \Delta t^2 \ddot{\mathbf{u}}_k^{P,free} \\ \tilde{\dot{\mathbf{u}}}_{k+1}^{P,free} = \dot{\mathbf{u}}_k^P + (1-\gamma)\, \Delta t \ddot{\mathbf{u}}_k^{P,free} \end{cases} \tag{5.9}$$

$$\ddot{\mathbf{u}}_{k+1}^{P,free} = \mathbf{D}^{P^{-1}} \left(\mathbf{f}_{k+1}^P - \mathbf{C}^P \tilde{\dot{\mathbf{u}}}_{k+1}^{P,free} - \mathbf{r}_{k+1}^P \left(\tilde{\mathbf{u}}_{k+1}^{P,free} \right) \right) \tag{5.10}$$

$$\begin{cases} \mathbf{u}_{k+1}^{P,free} = \tilde{\mathbf{u}}_{k+1}^{P,free} + \ddot{\mathbf{u}}_{k+1}^{P,free} \beta \Delta t^2 \\ \dot{\mathbf{u}}_{k+1}^{P,free} = \tilde{\dot{\mathbf{u}}}_{k+1}^{P,free} + \ddot{\mathbf{u}}_{k+1}^{P,free} \gamma \Delta t \end{cases} \tag{5.11}$$

where,

$$\mathbf{D}^P = \mathbf{M}^P + \mathbf{C}^P\gamma\Delta t + \mathbf{K}^P\beta\Delta t^2 \tag{5.12}$$

Similarly to the NS, at each step t_{k+1}, the displacement predictor $\tilde{\mathbf{u}}_{k+1}^{P,free}$ is imposed to the PS by means of servo-controlled actuators and the corresponding restoring force vector $\mathbf{r}_{k+1}^P$ is measured with load cells. Mass $\mathbf{M}^P$ and damping $\mathbf{C}^P$ matrices are computed based on the initial tangent stiffness matrix $\mathbf{K}^P = \frac{\partial \mathbf{r}^P}{\partial \mathbf{u}^P}|_{u_0,\dot{u}_0}$, which is measured from the PS with small displacement perturbations once before the experiment. It is noteworthy that displacement control errors affect the measured restoring force $\mathbf{r}_{k+1,mes}^{P,free}$ and may bias the emulated system response. Accordingly, the method proposed by Bursi and Shing (1996)[12] is suggested to compensate for control errors,

$$\mathbf{r}_{k+1}^{P,free} = \mathbf{r}_{k+1,mes}^{P,free} + \mathbf{K}^P(\mathbf{u}_{k+1}^{P,free} - \mathbf{u}_{k+1,mes}^{P,free}) \tag{5.13}$$

where $\mathbf{u}_{k+1,mes}^{P,free}$ and $\mathbf{r}_{k+1,mes}^{P,free}$ are measured displacement and restoring force vectors.

3. Calculate the interface Lagrange multiplier vectors as,

$$\begin{bmatrix} \mathbf{\Lambda}_{k+1}^N \\ \mathbf{\Lambda}_{k+1}^P \\ \dot{\mathbf{u}}_{k+1}^g \end{bmatrix} = -\mathbf{G}^{-1} \begin{bmatrix} \mathbf{L}^N \dot{\mathbf{u}}_{k+1}^{N^{free}} \\ \mathbf{L}^P \dot{\mathbf{u}}_{k+1}^{P^{free}} \\ \mathbf{0} \end{bmatrix} \tag{5.14}$$

It is important to point out that the Steklov-Poincare' operator is computed only once based on the initial tangent stiffness of both PS and NS and inverted before the simulation starts. A full derivation of is reported in Abbiati et al. (2020) [7]. As a result, the calculation of link solutions requires only a few matrix multiplications.

$$\begin{cases} \ddot{\mathbf{u}}_{k+1}^{N,link} = \mathbf{D}^{N^{-1}}\mathbf{L}^{N^T}\mathbf{\Lambda}_{k+1}^N \\ \ddot{\mathbf{u}}_{k+1}^{P,link} = \mathbf{D}^{P^{-1}}\mathbf{L}^{P^T}\mathbf{\Lambda}_{k+1}^P \end{cases} \tag{5.15}$$

4. Calculate the coupled velocities and accelerations,

$$\begin{cases} \ddot{\mathbf{u}}_{k+1}^N = \ddot{\mathbf{u}}_{k+1}^{N,free} + \ddot{\mathbf{u}}_{k+1}^{N,link} \\ \ddot{\mathbf{u}}_{k+1}^P = \ddot{\mathbf{u}}_{k+1}^{P,free} + \ddot{\mathbf{u}}_{k+1}^{P,link} \end{cases} \tag{5.16}$$

$$\begin{cases} \dot{\mathbf{u}}_{k+1}^{N} = \dot{\mathbf{u}}_{k+1}^{N,free} + \ddot{\mathbf{u}}_{k+1}^{N,link}\gamma\Delta t \\ \dot{\mathbf{u}}_{k+1}^{P} = \dot{\mathbf{u}}_{k+1}^{P,free} + \ddot{\mathbf{u}}_{k+1}^{P,link}\gamma\Delta t \end{cases} \tag{5.17}$$

Consistently with DR, $\gamma = \frac{1}{2}$ and $\beta = 0$ for both PS and NS. Accordingly, link displacements are null and coupled displacements are equal to free displacements.

The LLM-GC algorithm inherits second-order accuracy from the GC method [9]. Figure 5.1 provides a detailed representation of the procedure for integrating the coupled equation of motion of the hybrid model between times t_k and t_{k+1}.

As can be appreciated from Figure 5.1, one-step free solutions of PS and NS are parallel processes. In fact, the PS approaches the target boundary conditions while a FE software evaluates the restoring force of the NS, possibly with a Newton-Raphson algorithm. The computation of interface forces and , which determine the link solution, requires only interface velocities and and relies solely on the matrix-vector product defined in equation (5.14). The computational cost (and the related time overhead) of the latter is negligible compared to the computation of the one-step free solution of the NS and the PS responses. As long as the number of interface DoFs is determined by the number of actuation points of the PS and not on the total number of DoFs of the hybrid model, the LLM-GC algorithm enables RT-HFS with realistic nonlinear FE models used as NSs. Limited data exchange, as well as minimal computational overhead, make the proposed LLM-GC algorithm suitable for being implemented as a coordinator in existing HFS middleware thus facilitating reusing of existing verified FE software (e.g., OpenFresco [13][14]).

In order to maximize the convergence rate of DR, Component-mode synthesis (CMS) [15] can be used to derive reduced-order matrices for both PS and NS.

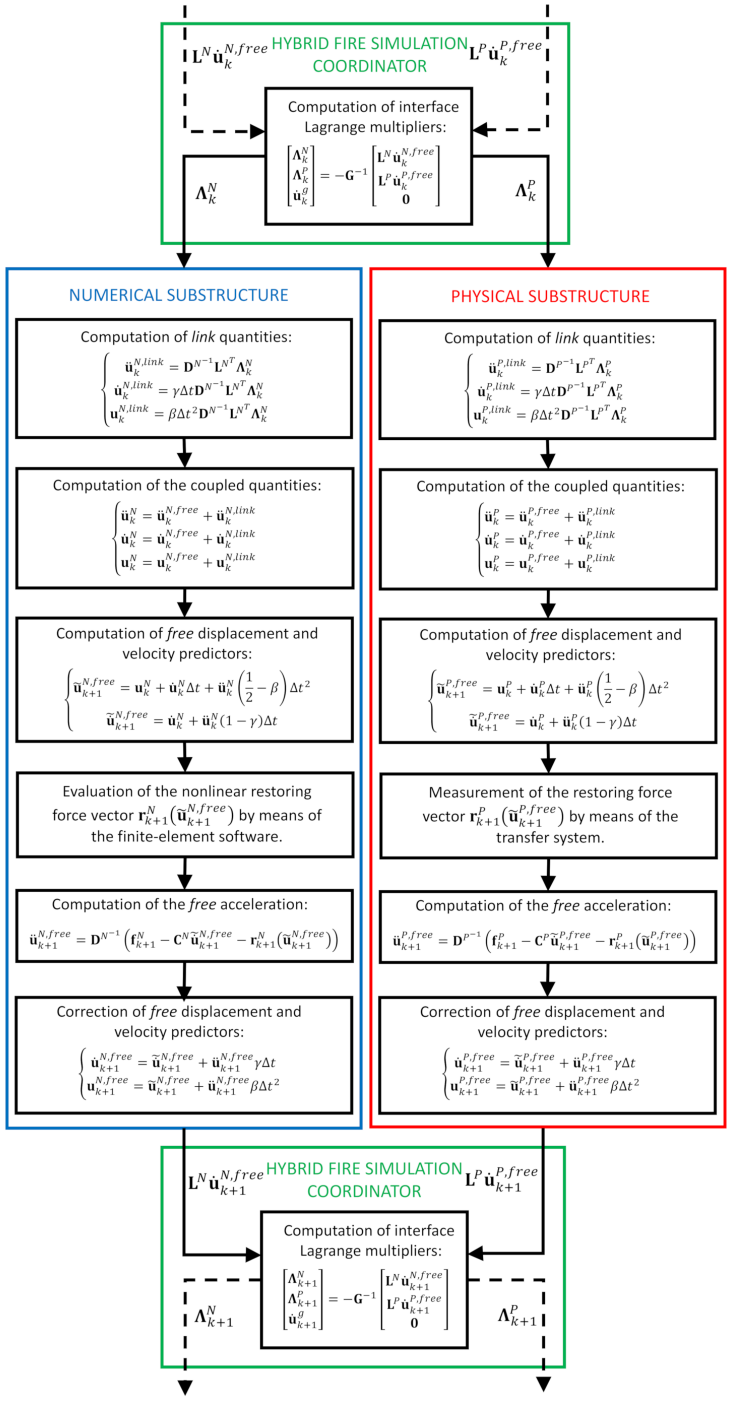

Figure 5.1: Architecture of the implementation of RT-HFS method based on the LLM-GC algorithm reproduced from Abbiati et al. (2020) [7].

5.3 VIRTUAL REAL-TIME HYBRID FIRE TEST

In order to demonstrate the effectiveness of the framework with the RT-HFS method [7] and to illustrate the implementation of a real test, a virtual HFS campaign was conceived for the case study selected in the EQUFIRE project [16], which is part of the Transnational Access activities of the SERA project (www.sera-eu.org). The case study is represented by a steel braced frame, and both NS and PS are simulated numerically. Results of the virtual real-time hybrid test were then verified against the monolithic solution developed in the thermo-mechanical software SAFIR [17].

5.3.1 EQUFIRE case study description

The EQUFIRE project [16] aims at investigating the post-earthquake fire performance of steel braced frames endowed with passive fire protection. In particular, a four-story three-bay steel frame with concentric bracing in the central bay was selected as a case study, as illustrated in Figure 5.2. The building is an office with a square plan of 12.5 m x 12.5 m. It is located in Lisbon, Portugal, in an area of medium-high seismicity. The story height is 3 m with the exception of the first floor, which is 3.6 m high. Each frame is endowed with a lateral force-resisting system. The columns are continuous, and all connections are regarded as pinned. Two different steel grades were used, namely S275 and S355. The S275 was adopted for the bracing system, which acts as a structural fuse during the seismic event according to the capacity design philosophy. Steel grade S355 was selected for columns and beams that are intended to remain elastic during a seismic event. The frame was designed according to the relevant parts of EN 1993 and according to EN 1998-1 [18] relative to the seismic action.

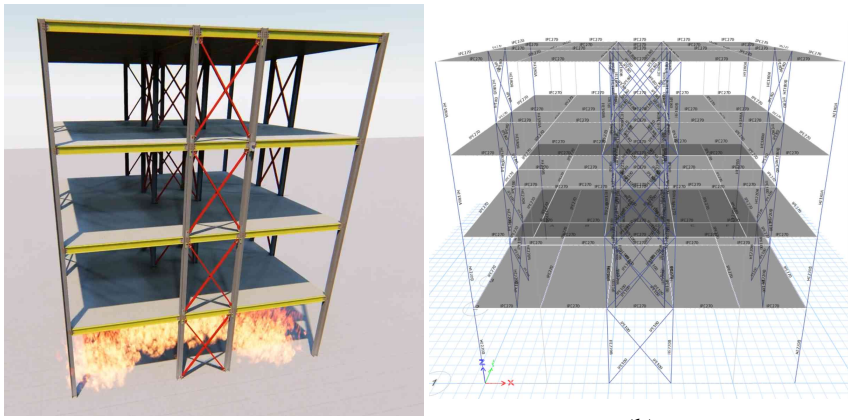

(a) *(b)*

Figure 5.2: EQUFIRE case study.

5.3.2 FE models and Substructuring

Figure 5.3a shows the member sizes and the magnitude of the gravity loads acting simultaneously with the fire action that for this case study was located at the base floor, whereas the remainder of the structure was kept cold. Figure 5.3b shows the location of the test frame. For the fire action, a prescriptive approach was chosen, and, in particular, the standard ISO 834 [19] heating curve was employed. This choice was made because it is easy to reproduce in a furnace. In this respect, Figure 5.3c illustrates the temperature evolution in time of the compartment and of the steel temperature in the unprotected members subjected to fire, i.e., IPE 100, IPE 270, and HEB 220, calculated according to a lumped mass approach and 4-side exposure. The IPE 100 profiles composing the bracing system were oriented according to the weak axis in the plane of the frame in order to force in-plane buckling so that a 2D modeling was representative. As shown in Figure 5.4, it was decided to couple the PS and NS at translational DoFs, whilst continuity of the rotational DoFs was neglected. Figure 5.4 also illustrates the possible subdivision between the NS and PS by highlighting the controlled DoFs with an actuator. It is possible to observe that, since it is difficult to directly control rotations, only translational DoFs are controlled. Moreover, it was decided to consider as a PS both the base and the first floor in order to accurately simulate the base floor behavior under fire by guaranteeing the continuity of the column at the top of the base floor. Nonetheless, if the budget does not allow only the base floor could be physically modeled in the laboratory by accepting a lower degree of accuracy. Each column and

beam element were discretized using six elements, while each brace element was discretized using eight elements. The partitioned simulation was then verified against nonlinear a thermomechanical FE analysis of the whole frame performed in SAFIR [17], which employs fiber-based thermomechanical Bernoulli beam elements. In order to reduce the frequency bandwidth of the NS, which deteriorates the convergence rate of the RT-HFT-FETI method, CMS was applied to condense NS matrices to the translational DoFs of the nodes numbered in Figure 5.3.

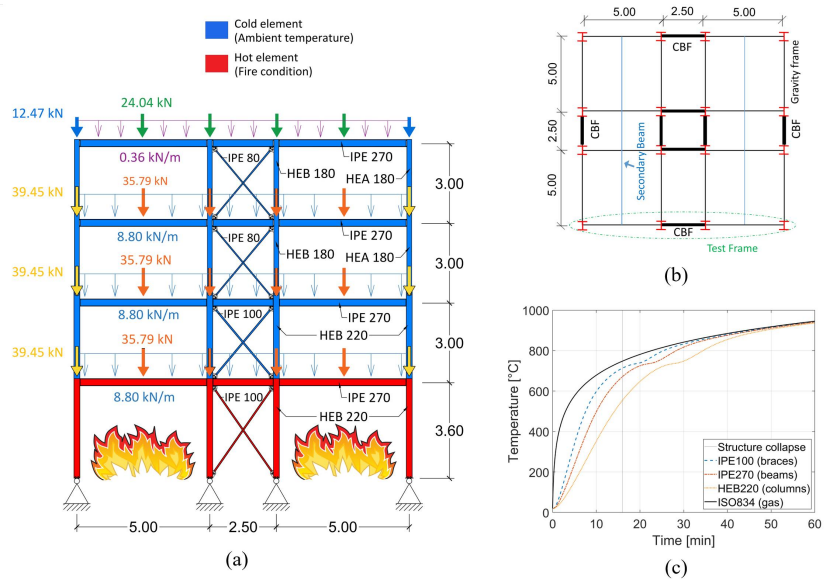

Figure 5.3: (a) Emulated steel frame; (b) plan view of the building (c) time-temperature heating curves. (dimensions in m).

As anticipated, the RT-HFS of the steel braced frame is numerically simulated. The proposed LLG-GC algorithm is implemented into a MATLAB thermomechanical FE environment developed in house by some of the authors. Such a simulation environment comes with a nonlinear beam element, which accounts for geometric nonlinearity and temperature-dependent nonlinear material behavior. The beam element is based on large deformation theory (corotational formulation) under the assumption of small strains [20][21]. The beam cross-section is treated such that a non-uniform temperature distribution can be simulated. Degradation in material strength and stiffness at increasing temperature is represented by steel retention factors for effective yield strength, elastic modulus, and proportional limit, and the material constitutive law is defined according to EN 1993-1-2 stress-strain curve [22]. Structures subjected to increas-

ing loads or temperatures are analyzed using an incremental Newton-Raphson iterative procedure. The analysis provides a complete load-deformation and temperature-deformation history for two-dimensional steel frames.

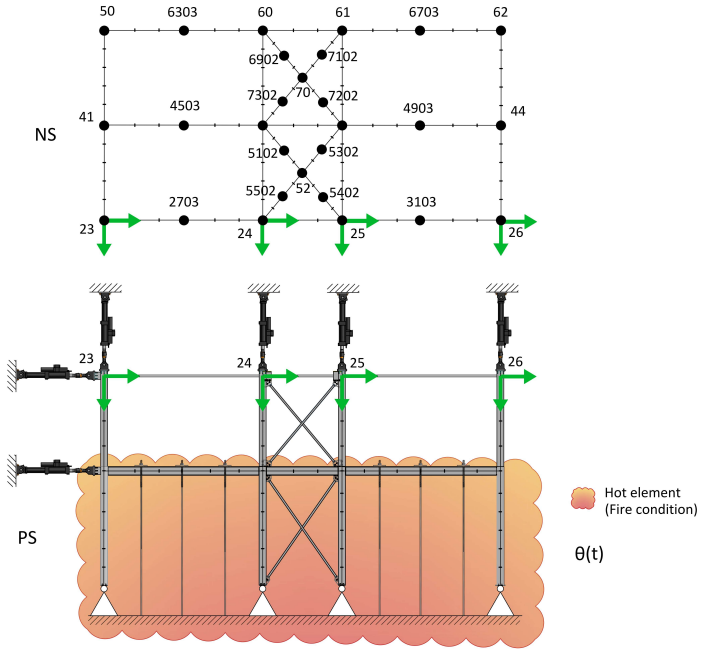

Figure 5.4: Substructuring scheme adopted for HFS.

5.4 RESULTS AND COMPARISON

The results of the virtual RT-HFS campaign are summarized herein. In order to assess the effect of experimental errors, the same simulation was performed by including noise on the restoring force of the PS and bias of the PS tangent stiffness matrix estimate. In particular, in the PS restoring force, a Gaussian noise of zero mean and 100 N standard deviation was superimposed, while all terms of the PS tangent stiffness matrix were perturbed by a random multiplicative factor that followed a uniform distribution bounded between 0.8 and 1.2. Figure 5.5a and Figure 5.5b compare the deformed configuration of the steel braced frame after 700 s and at the end of the simulation when the failure of beams occurred at time=1001 s. As can be appreciated in Figure 5.5a, the static response of the frame obtained via HFS well matches the reference SAFIR solution after 700 s, which represents the onset of the beam runaway. Conversely, since in the HFS continuity of rotation was not enforced at the interface

between PS and NS, some discrepancies are visible at failure, as depicted in Figure 5.5b. In fact, the location of the hinge at the top of the column of the first floor was a good approximation at the beginning of the fire and during its first phases. However, as the fire progressed and the loss of strength and stiffness of the heated elements became significant, the load redistribution determined a variation of the bending moment diagram that was not compatible with the choice of the DoFs to control during the HFS, as highlighted in Figure 5.6. A comparison with and without the effect of experimental errors can be appreciated in Figure 5.7a and b. The error propagation analysis provides satisfactory results, in fact, the variability of the system response is small, and the RT-HFS method results robust to measurement errors. Figure 5.7c-f compares the horizontal and vertical displacement responses measured at Node 1303 of the beam midspan and at Node 8 of the external right column of the PS measured at the top end of the base floor. Again, it is possible to observe a very good degree of accuracy between the partitioned and the monolithic solution, with some discrepancies occurred after the onset of the beam runaway owing to the lack of continuity of the rotational DoFs between the PS and the NS.

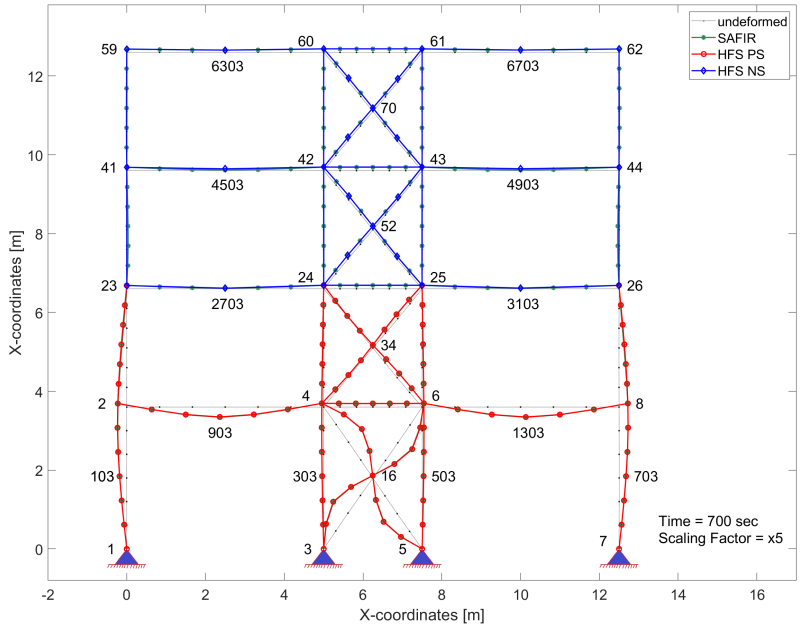

(a)

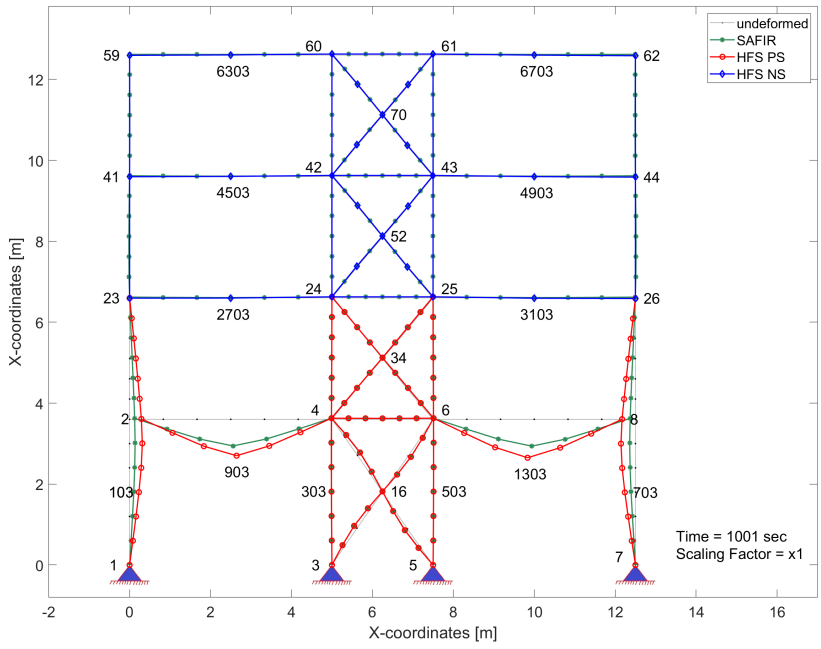

(b)

Figure 5.5: Bending moment diagram in the SAFIR model of the case study steel frame at: a) t = 0 s; b) t = 740 s.

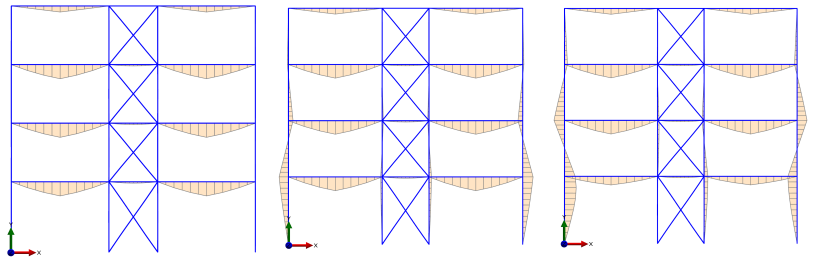

(a) *(b)* *(c)*

Figure 5.6: Bending moment diagram in the SAFIR model of the case-study steel frame at (a) t = 0 s; (b) t = 700 s; (c) t = 1001 s

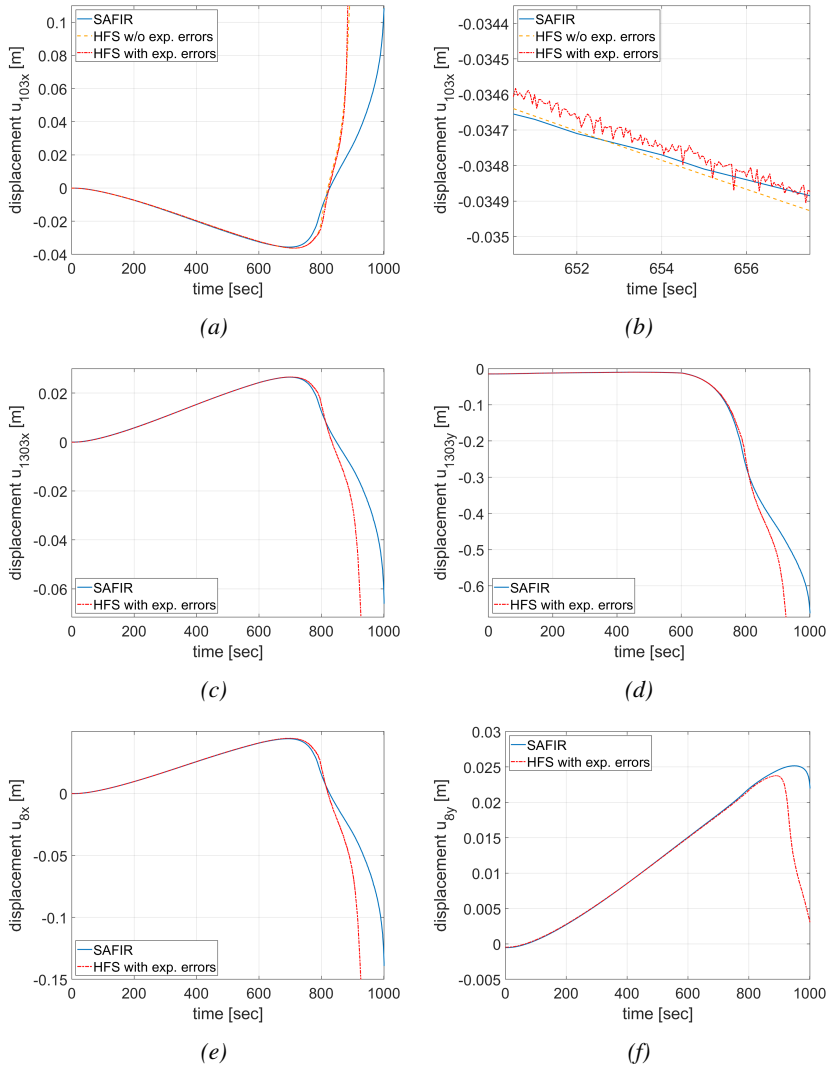

Figure 5.7: (a) Comparison of the horizontal displacement at Node 103; (b) comparison of the horizontal displacement at Node 103 zoomed plot; (c) comparison of the horizontal displacement at beam midspan Node 1303; (d) comparison of the vertical displacement beam midspan Node 1303; (e) comparison of the horizontal displacement measured at Node 8; (f) comparison of the vertical displacement measured at Node 8.

5.5 Conclusion

The results presented in this paper showed the effectiveness of the proposed RT-HFS method, which combines dynamic relaxation and parti-

tioned time integration to compute the static response of a virtual hybrid fire test. In fact, it was found that to obtain compatibility and equilibrium at the interface DoFs, the partitioned algorithm LLM-GC based on the FETI algorithm class is suitable to couple the PS with the NS. Indeed, the proposed method is robust to error propagation. With regard to the specific application case study, the substructuring scheme was conceived, accounting for experimental limitations associated with control or rotational degrees-of-freedom. The time-history response produced by virtual hybrid fire simulations showed good agreement with the monolithic references obtained from SAFIR. The validation carried out in a fully numerical framework is promising for forthcoming experimental implementations.

ACKNOWLEDGMENT

This work has received funding from the European Union's Horizon 2020 research and innovation program under the SERA Grant Agreement No. 730900 and the related TA project EQUFIRE. This work was also supported by the Italian Ministry of Education, University and Research (MIUR) in the frame of the 'Departments of Excellence' (grant L 232/2016).

Bibliography

[1] A. H. Schellenberg, S. A. Mahin, and G. L. Fenves, "Advanced implementation of hybrid simulation," PEER Report 2009/104, Pacific Earthquake Engineering Research Center, University of California, Berkeley, California, 2009.

[2] M. Korzen, G. Magonette, and P. Buchet, "Mechanical Loading of Columns in Fire Tests by Means of the Substructuring Method," *Zeitschrift für Angewandte Mathematik und Mechanik*, vol. 79, pp. 617–S618, 1999.

[3] A. Sauca, T. Gernay, F. Robert, N. Tondini, and J.-M. Franssen, "Hybrid fire testing: Discussion on stability and implementation of a new method in a virtual environment," *Journal of Structural Fire Engineering*, vol. 9, no. 4, pp. 319–341, 2018.

[4] X. Wang, R. E. Kim, O.-s. Kwon, I.-h. Yeo, and J.-k. Ahn, "Continuous Real-Time Hybrid Simulation Method for Structures Subject

to Fire," *Journal of Structural Engineering*, vol. 145, p. 04019152, dec 2019.

[5] M. Memari, X. Wang, H. Mahmoud, and O.-S. Kwon, "Hybrid simulation of small-scale steel braced frame subjected to fire and fire following earthquake," *Journal of Structural Engineering*, vol. 146, no. 1, p. 04019182, 2020.

[6] P. Schulthess, M. Neuenschwander, K. M. Mosalam, and M. Knobloch, "A computationally rigorous approach to hybrid fire testing," *Computers & Structures*, vol. 238, p. 106301, 2020.

[7] G. Abbiati, P. Covi, N. Tondini, O. S. Bursi, and B. Stojadinović, "A real-time hybrid fire simulation method based on dynamic relaxation and partitioned time integration," *Journal of Engineering Mechanics*, vol. 146, no. 9, p. 04020104, 2020.

[8] C. Farhat and F. X. Roux, "A method of finite element tearing and interconnecting and its parallel solution algorithm," *International Journal for Numerical Methods in Engineering*, vol. 32, no. 6, pp. 1205–1227, 1991.

[9] A. Gravouil and A. Combescure, "Multi-time-step explicit–implicit method for non-linear structural dynamics," *International Journal for Numerical Methods in Engineering*, vol. 50, no. 1, pp. 199–225, 2001.

[10] K. C. Park, C. A. Felippa, and U. A. Gumaste, "A localized version of the method of Lagrange multipliers and its applications," *Computational Mechanics*, vol. 24, pp. 476–490, Jan. 2000.

[11] P. G. Underwood, *Computational Methods for Transient Analysis*, ch. Dynamic relaxation techniques: a review. Amsterdam: North-Holland, 1983.

[12] O. S. Bursi and P.-S. Shing, "Evaluation of some implicit time-stepping algorithms for pseudodynamic tests," *Earthquake Engineering & Structural Dynamics*, vol. 25, no. 4, pp. 333–355, 1996.

[13] C. A. Whyte, K. R. Mackie, and B. Stojadinovic, "Hybrid simulation of thermomechanical structural response," *Journal of Structural Engineering*, vol. 142, no. 2, p. 04015107, 2016.

[14] M. A. Khan, L. Jiang, K. A. Cashell, and A. Usmani, "Analysis of restrained composite beams exposed to fire using a hybrid sim-

ulation approach," *Engineering Structures*, vol. 172, pp. 956–966, 2018.

[15] R. R. Craig and A. J. Kurdila, *Fundamentals of structural dynamics*. John Wiley & Sons, 2006.

[16] M. L. Tornaghi, G. Tsionis, P. Pegon, J. Molina, M. Peroni, M. Korzen, N. Tondini, P. Covi, G. Abbiati, M. Antonelli, *et al.*, "Experimental study of braced steel frames subjected to fire after earthquake," 2020.

[17] J.-M. Franssen and T. Gernay, "Modeling structures in fire with safir®: Theoretical background and capabilities," *Journal of Structural Fire Engineering*, 2017.

[18] CEN, "Eurocode 8: Design of structures for earthquake resistance - Part 1: General rules, seismic actions and rules for buildings," european standard, European Union, May 2004.

[19] ISO834, "Fire-resistance tests -Elements of building construction- Part 1: General requirements," international standard, International Standard ISO 834, 1999.

[20] A. Morbioli, N. Tondini, and J.-M. Battini, "A branch-switching procedure for analysing instability of steel structures subjected to fire," *Structural engineering and mechanics: An international journal*, vol. 67, no. 6, pp. 629–641, 2018.

[21] J.-M. Battini, *Co-rotational beam elements in instability problems*. PhD thesis, KTH, 2002.

[22] CEN, "Eurocode 3: Design of steel structures - Part 1-2: General rules - Structural fire design," european standard, European Union, May 2005.

6.0 Fire following earthquake tests at BAM

6.1 Introduction

Five fire following earthquake hybrid tests were performed at the Federal Institute for Materials Research and Testing (BAM), in Berlin (Germany), between October and November 2019. This chapter presents in detail the experimental set-up of the Fire Engineering laboratory (Division 7.3), the experimental tests and results.

6.2 Experimental Set-up

The Fire Engineering laboratory at BAM is provided with three furnaces as illustrated in Figure 6.1: one for testing loaded columns, another for testing slabs and beams and the third furnace used mainly for testing walls but also other compartmentation materials.

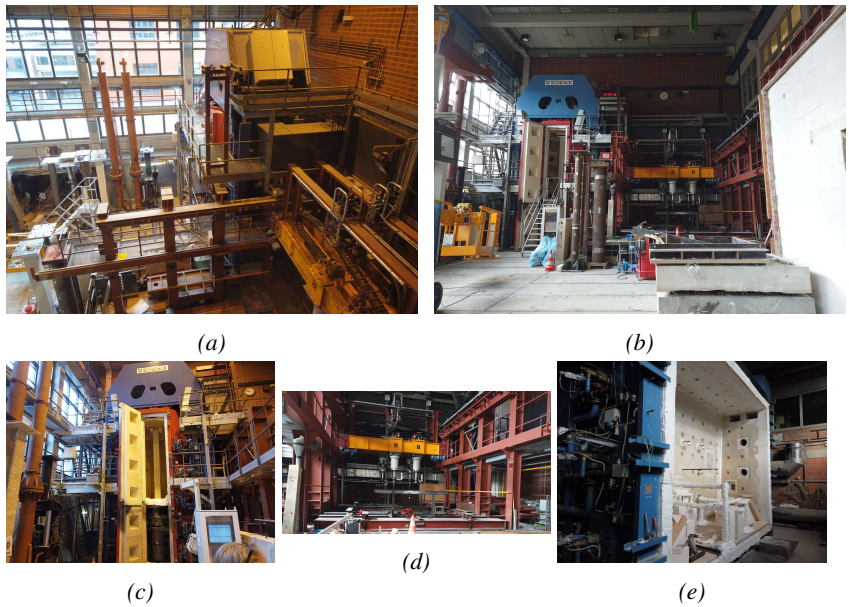

Figure 6.1: General view of the laboratory: a) from the control room; b) from the lab; c) View of the vertical furnace for testing columns; d) View of the furnace for testing slabs and beams; e) View of the furnace for testing walls and other compartmentation materials.

For the EQUFIRE tests, the vertical furnace for testing columns was used. It has a cylindrical shape with a diameter of 2.3 m. The movable bottom allows an adjustment of the combustion chamber height from 3.6 to 5.6 m. During the EQUFIRE tests, it was set to 3.6 m. Six oil burners arranged in two groups of three burners, orientated horizontally, are distributed almost regularly up the furnace's side. Two smoke vents lie above the highest pair of burners, and two lie above the lowest pair. From this furnace design, a strong vorticity of combustion gases, resulting in a rather constant gas temperature distribution in the axial direction, can be expected.

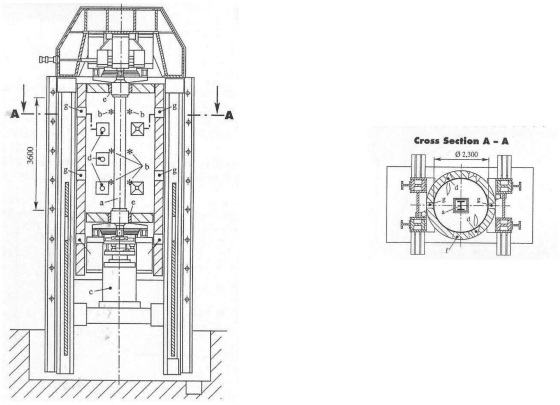

Figure 6.2: Simplified vertical and horizontal drawings of furnace: a) column specimen; b) thermocouples; c) hydraulic jack; d) oil burners; e) mineral fiber seal; f) furnace door; g) smoke vents [1],

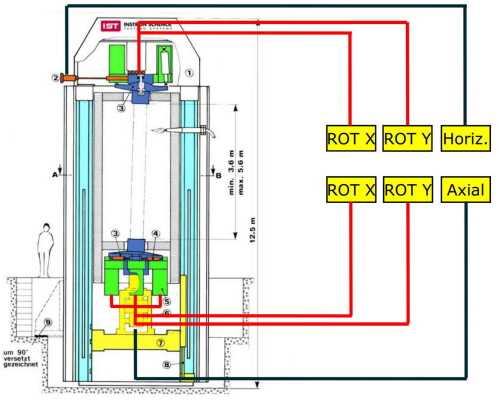

Figure 6.3: Vertical furnace: analog servo-hydraulic control loops.

The mechanical loading of the columns can be achieved by six ana-

log servo-hydraulic control loops representing two rotation degrees of freedom perpendicular to each other for bending at the upper and lower bearing, as well as one channel for the bottom axial and one for top horizontal loading. The furnace has a restraint frame placed on top of the set-up in order to provide the axial force to the specimen together with the vertical actuator placed under the column, as shown in Figure 6.3.

Figure 7.11 shows the basic idea of the substructuring method [2]. During the hybrid test, forces and moments at the lower and upper bearing of the column element (PS), are measured and sent to the real-time PC for the computation of the corresponding angles and displacements, which are sent back to the physical substructure in order to keep the entire structure in mechanical equilibrium.

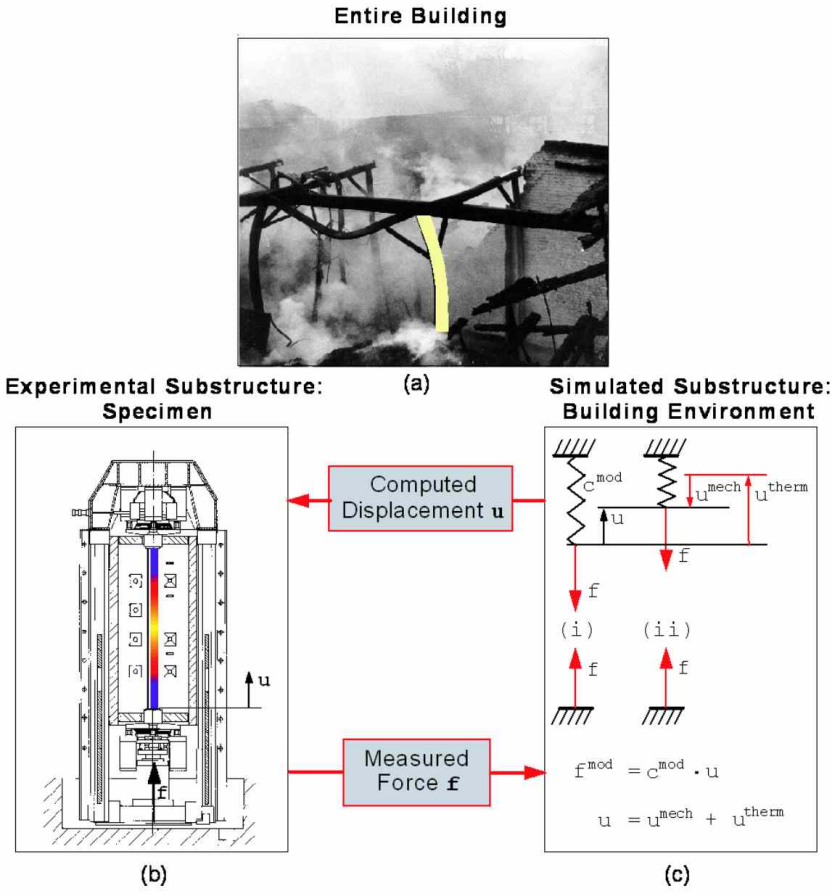

Figure 6.4: Substructuring method (basic idea) [2]

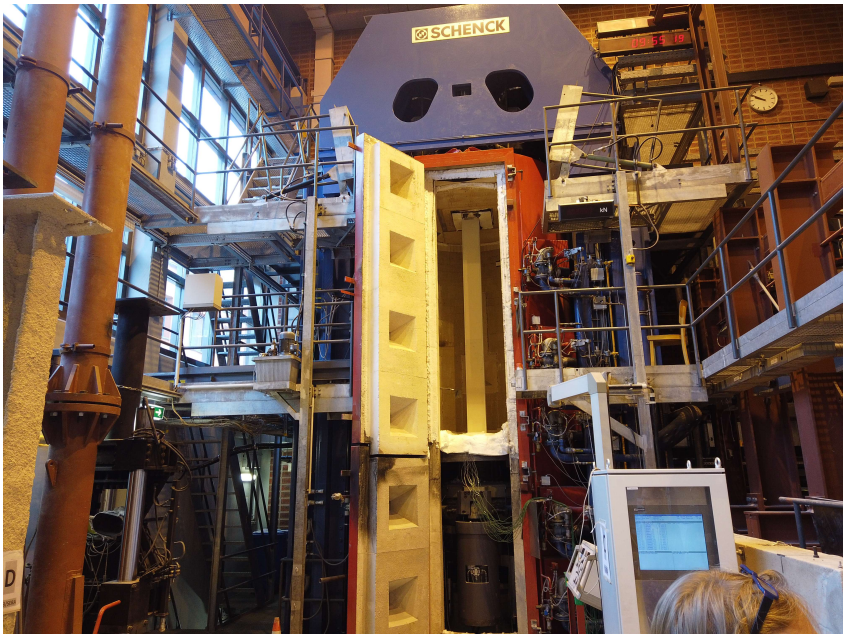

(a)

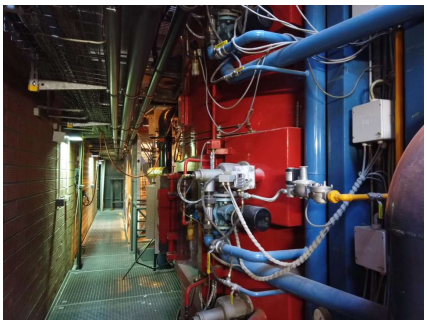

(b)

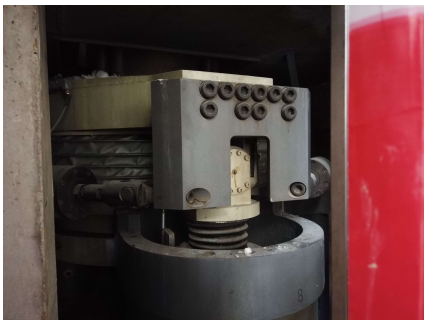

(c)

Figure 6.5: a) Vertical furnace for testing columns; b) furnace's burners; c) Hydraulic system.

Figure 6.5 shows the furnace used for the FFE tests, the furnace's burners and the bottom hydraulic system. Figure 6.6 shows the equipment of the control room.

(a)

(b)

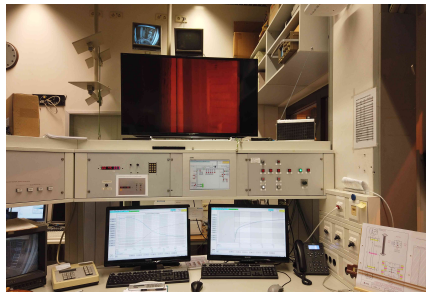

(c)

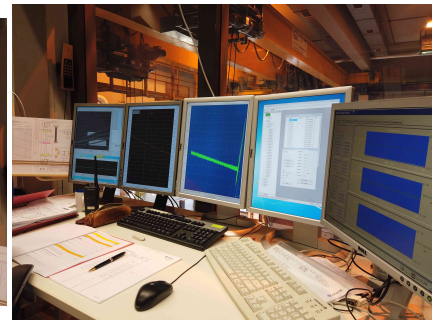

(d)

Figure 6.6: a) equipment to control the hydraulic system; b) equipment to control the furnace; c) equipment to control the temperature sensors, the vent system and the video cameras; d) Master PC (Left) and target PC (Right).

6.2.1 Equivalent stiffness of the numerical substructure during the fire events

The steel frame of Figure 6.7 was partitioned into two substructures: the physical substructure (PS) is represented by the internal column at the ground floor, whereas the remaining part of the frame, which is the numerical substructure (NS), is simulated by the numerical model.

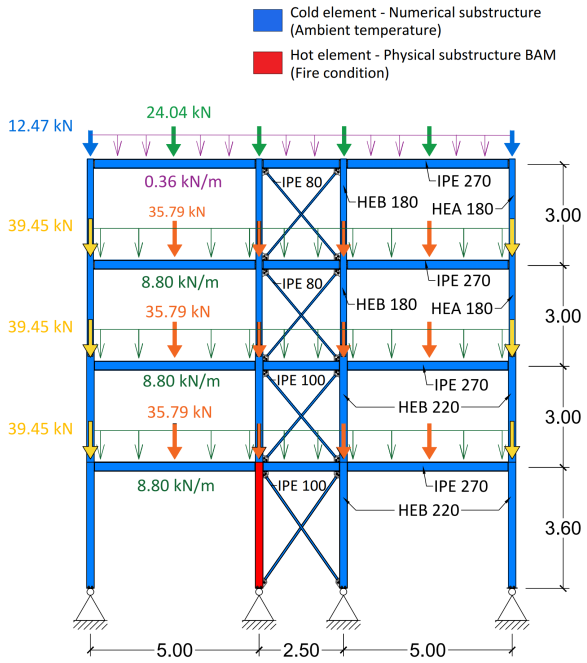

(a)

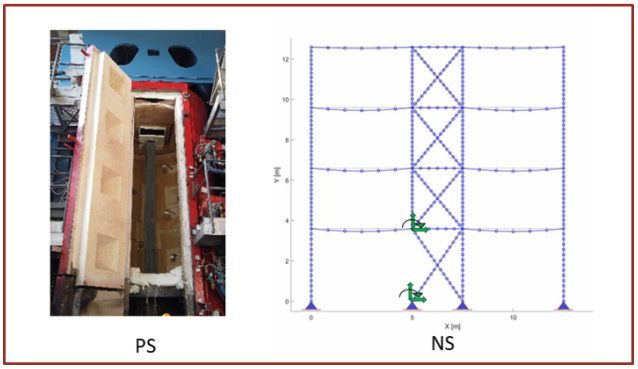

(b)

Figure 6.7: (a) Emulated steel frame; (b) Substructuring scheme adopted for the FFE tests.

The numerical model of Figure 6.7b was used to determine the equivalent stiffness of the surrounding structure, which is used by the target PC to simulated the effect of the upper part of the structure using the substructuring method.

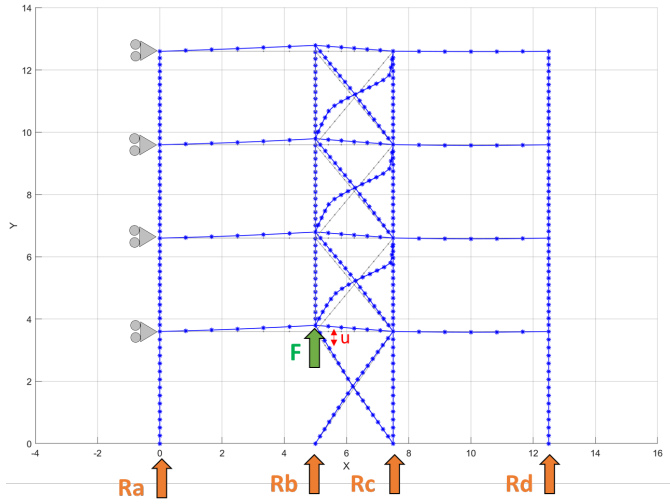

Figure 6.8: Static non-linear analysis to determine the axial stiffness value of the surrounding structure.

The axial stiffness of the upper part of the structure was numerically estimated by a static non-linear analysis. In detail, the full structure was subjected to gravity loads and to the selected accelerogram through non-linear time-history analysis. Then the physical column was removed and the frame was constrained at each floor to reproduce the boundary condition of the actual experimental setup at BAM. Finally, a monotonic displacement-controlled pattern, which continuously increases, was performed, as depicted in Figure 6.8. As shown in Figure 6.9 the equivalent stiffness of the surrounding structure after the seismic event is neither constant nor linear. Due to this reason, it was not possible to exactly reproduce the same axial force condition in the column during the test. However, the value of K was chosen to reach a similar critical temperature.

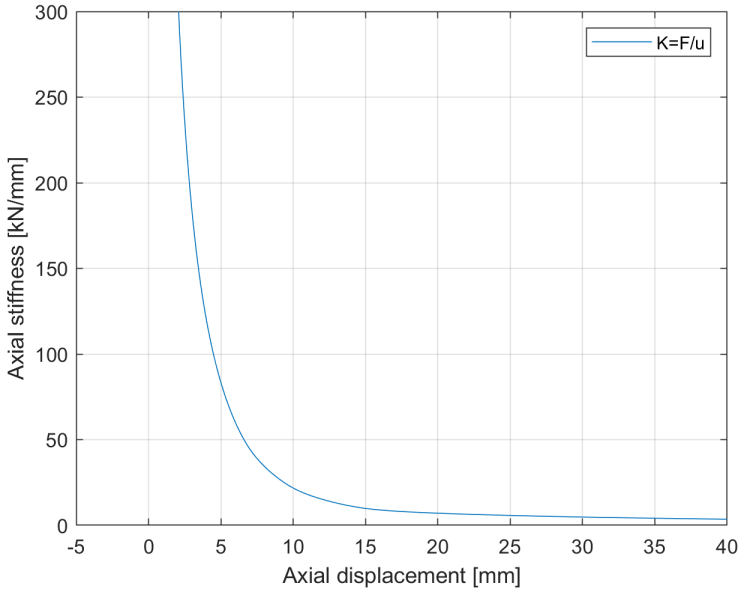

Figure 6.9: Axial stiffness of the surrounding structure vs axial displacement curve.

In this respect, two 3D models of the physical specimen were modeled in OpenSees with two different boundary conditions on top, i.e. pinned (Case A) and fixed conditions (Case B). The column was modeled with 15 non-linear thermomechanical beam elements. It was first subjected to the gravity load, then to horizontal and vertical displacement histories resulting from seismic non-linear dynamic analysis. Afterwards, thermal action was applied with different constant axial stiffness values (K between 5 and 15 kN/mm) representative of the surrounding structure, as boundary conditions. In order to determine the more appropriate equivalent axial stiffness value, Figure 6.12 shows the results in terms of the axial force and vertical displacement compared with the numerical analysis conducted on the whole structure. As it is possible to observe, a good value of the equivalent stiffness of the surrounding structure after the damage caused by the earthquake was equal to 5.3 kN/mm and this value was used in the tests. Moreover, the case with fixed conditions at the top of the column better agreed with the outcomes of the reference solution.

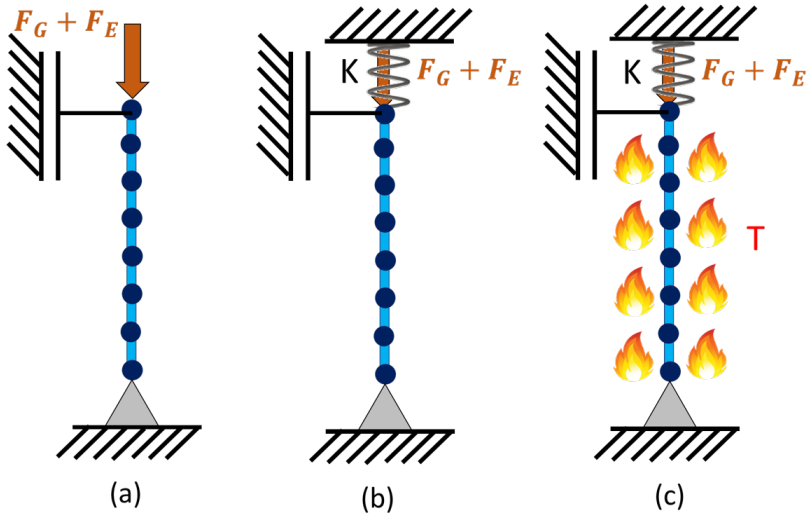

Figure 6.10: Equivalent stiffness - Option A: a) The gravity load and the earthquake load (F=290.77 kN) is applied to the column; b) An axial spring with a constant equivalent stiffness (K) is modelled; c) A time-temperature curves is used.

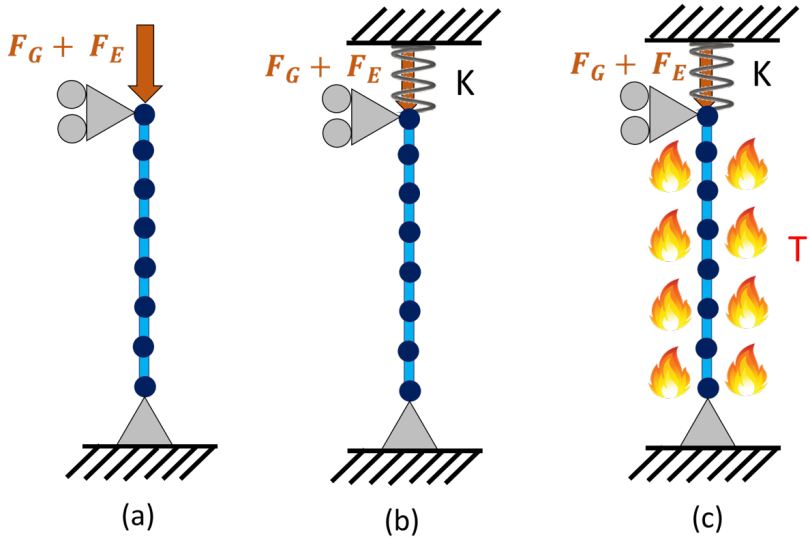

Figure 6.11: Equivalent stiffness - Option A: a) The gravity load and the earthquake load (F=290.77 kN) is applied to the column; b) An axial spring with a constant equivalent stiffness (K) is modelled; c) A time-temperature curves is used.

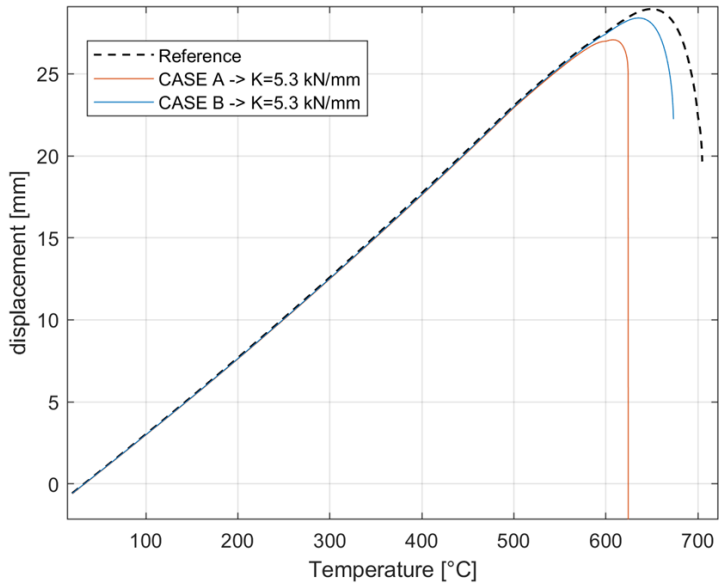

(a)

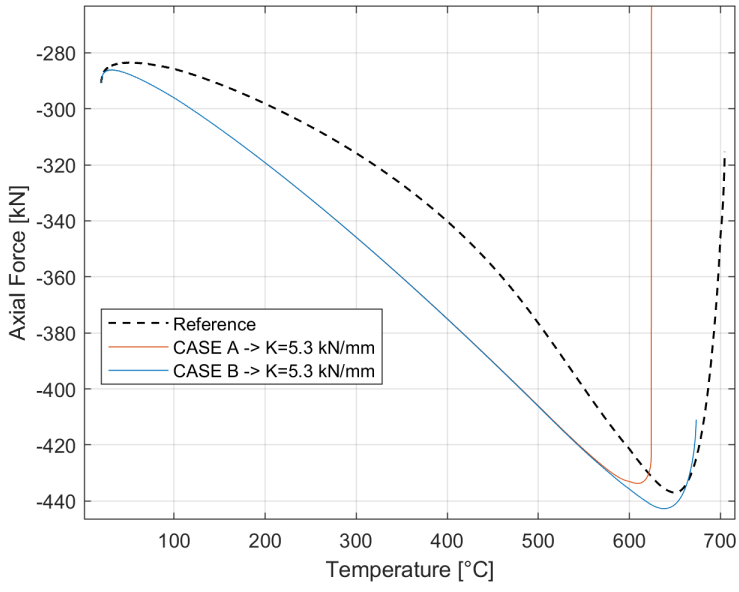

(b)

Figure 6.12: Comparison between the reference numerical solution and the single column with constant axial stiffness: a) axial displacements vs temperature curve; b) axial forces vs temperature curve.

6.3 Procedure

Each test was conducted as follows: The column instrumented with the thermocouples was placed in the vertical position inside the furnace using a special crane. All the instruments were connected to the data acquisition station connected to a remote acquisition pc in the control room. Once safely inside the furnace, the column was fixed only on the bottom with threaded M48 bolts to the bottom hydraulic jacks of the furnace and the gravity load was applied to the column. After the mechanical load procedure, the column was also fixed on top with threaded bolts to the upper hydraulic jacks and the column was subjected to the horizontal and vertical displacement time-histories computed through numerical modeling to simulate the earthquake event. After the earthquake time-history, the rods and bolts on the top of the specimen were removed while the column was kept constant loaded. The bottom and top plates of the column were insulated using ceramic wool. Then, the door of the furnace was closed and the column was heated by the ISO 834 standard heating curve and a constant numerical axial stiffness representative of the surrounding structure was applied as boundary condition at the top of the physical column. During the fire part of the FFE tests, the axial force of the column was measured and displacements were then imposed on the column in order to keep the two substructures in mechanical equilibrium.

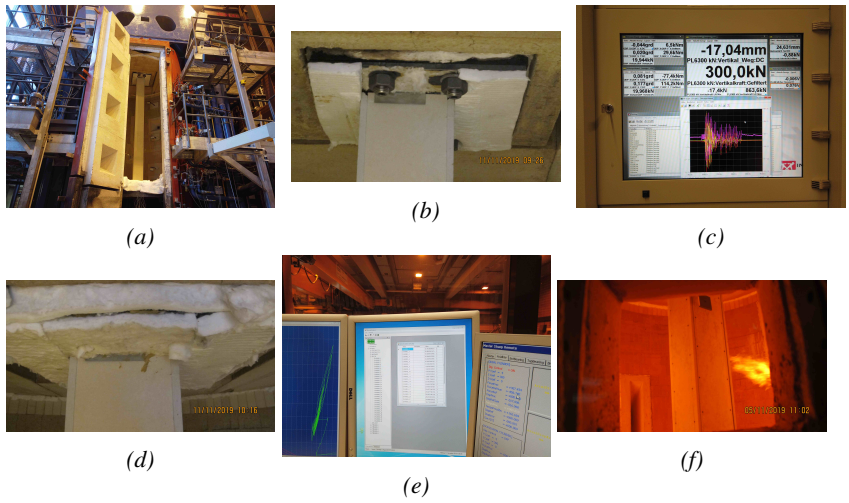

(a) *(b)* *(c)* *(d)* *(e)* *(f)*

Figure 6.13: Test procedure: a) specimen inside e vertical furnace; b) top plate during the earthquake; c) earthquake event; d) top plate during the fire; e) constant numerical axial stiffness; f) fire event.

6.4 Experimental tests and results

Five FFE tests were conducted at BAM:

- Test #0 Column E: without fire protection;
- Test #1 Column A: without fire protection;
- Test #2 Column B: PROMATECT-H fire protection boards - system designed for seismic regions;
- Test #3 Column C: PROMATECT-H fire protection boards (standard system, not designed for seismic regions);
- Test #4 Column D: PROMASPRAY P300 series (CAFCO 300), gypsum-based wet mix spray-applied fire resistive material, designed for applications in seismic regions, in which a mechanical reinforcing mesh was placed in the middle of the applied material.

6.4.1 Test #0 Column E

The specimen used in the test was HEB220 bare steel column steel grade S355. Figure 6.14 shows the geometrical dimensions and cross-section of the specimen used in the test of column E. This column was instrumented with six thermocouples per section (four for the flanges and two for the webs) in 3 sections along the height of the column (sections B, D and F). Other two additional thermocouples were placed on the end plates (sections A and G). The total length of the column was 3.62m, including the end plates, which were 20mm thick. These end plates were square 600 x 600 mm, with 4 holes for bolts M48. The top plate is shifted 30mm to the north in respect of the bottom plate to be centred in respect of the horizontal actuator stroke of $\pm 30mm$. There is no corresponding capability to move the bottom loading environment also 30 mm to the north, i.e. a corresponding horizontal actuator at the bottom does not exist. As a consequence, the axial load as a resulting force of the stresses between the top plate and the loading environment block of the furnace would also be 30 mm out of the centre of the specimen with respect to the weak axis. The test procedure was the same explained in Chapter 6.3.

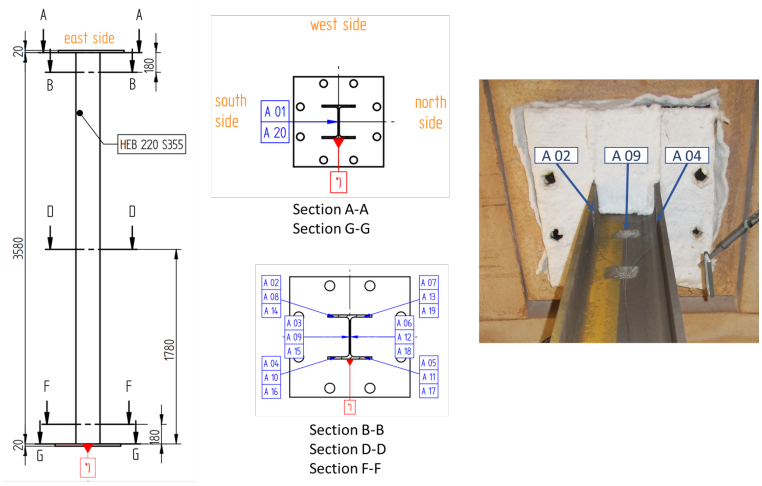

Figure 6.14: Column test E: cross section with position of the thermocouples.

Figure 6.15 shows views of the column of test BAM E before during and after test.

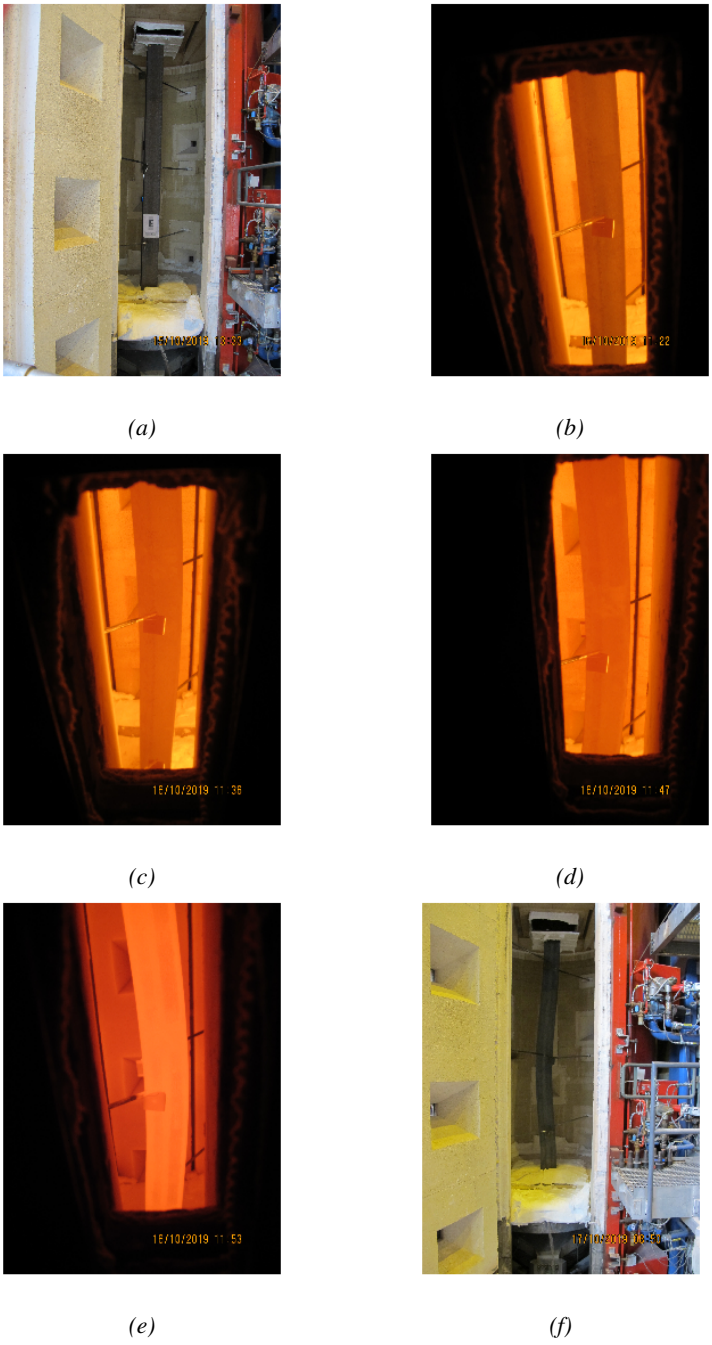

(a) *(b)*

(c) *(d)*

(e) *(f)*

Figure 6.15: Views of column of test E: a) before test; b) time = 30 minutes; c) time = 43 minutes; d) time = 54 minutes; e) time = 60 minutes; d) after test.

In these pictures, it is possible to observe the lateral deflections and

buckling of the column that occurred around the weak axis, as expected, and negligible displacements around the strong axis.

Figure 6.16 presents the evolution of temperatures in the different sections of the column measured using the twenty thermocouples, compared with the ISO834 curve and the mean gas temperature inside the furnace.

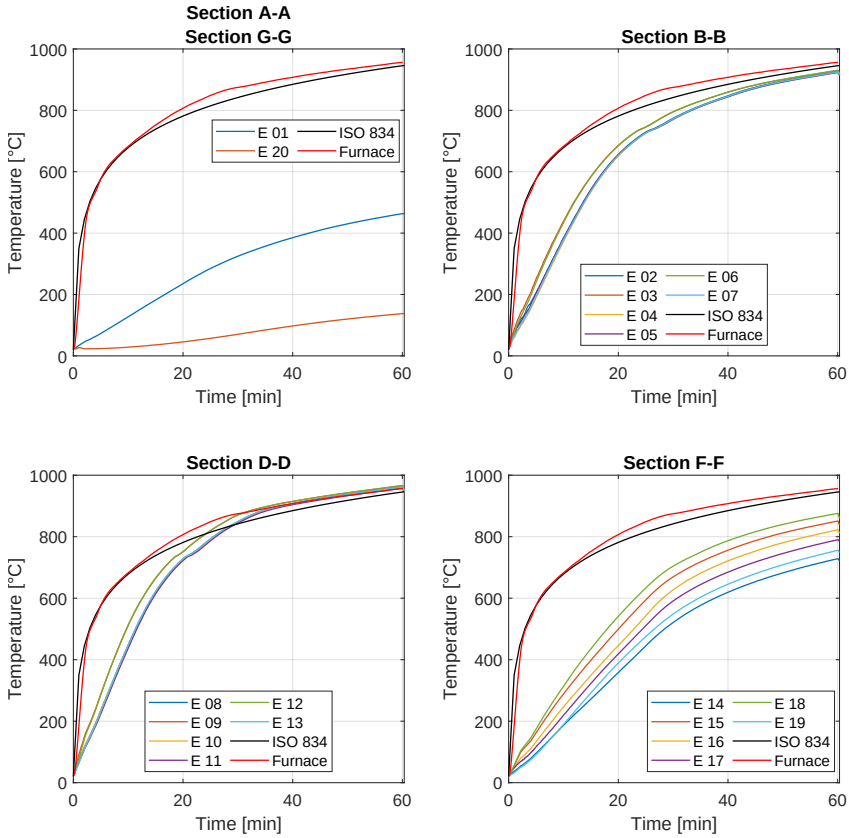

Figure 6.16: Column test E: evolution of the temperatures during the test.

Figures 6.17, 6.18, 6.19, 6.20 and 6.21 show the evolution of axial force, axial displacement, horizontal force and horizontal displacement of the column during the three phases of the test; Phase I: application of the gravity load. Phase II: earthquake. Phase III: fire after the earthquake.

Figure 6.21a presents the comparison of the horizontal force against to the horizontal displacement during the earthquake test. Figure 6.21b presents the comparison of the axial force against the axial displacement during the fire after the earthquake.

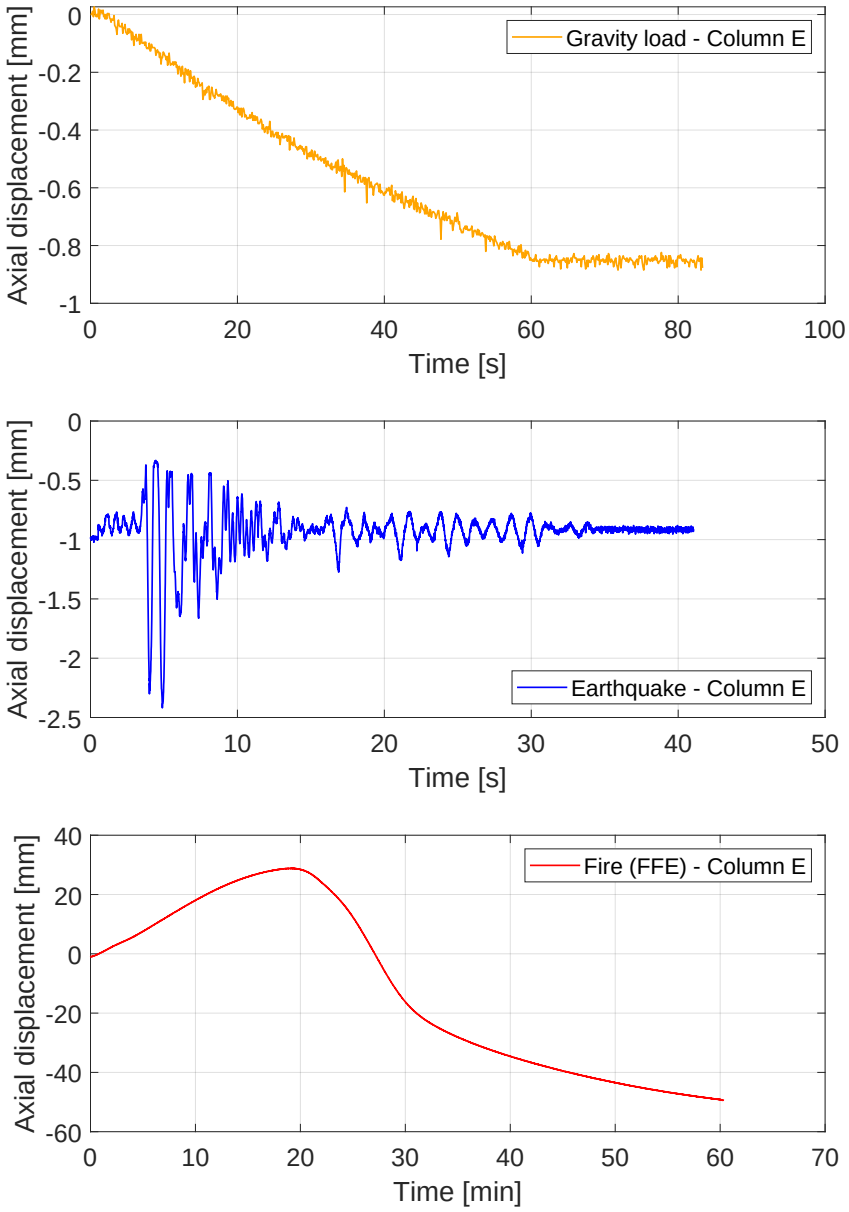

Figure 6.17: Column test E: evolution of the axial displacement.

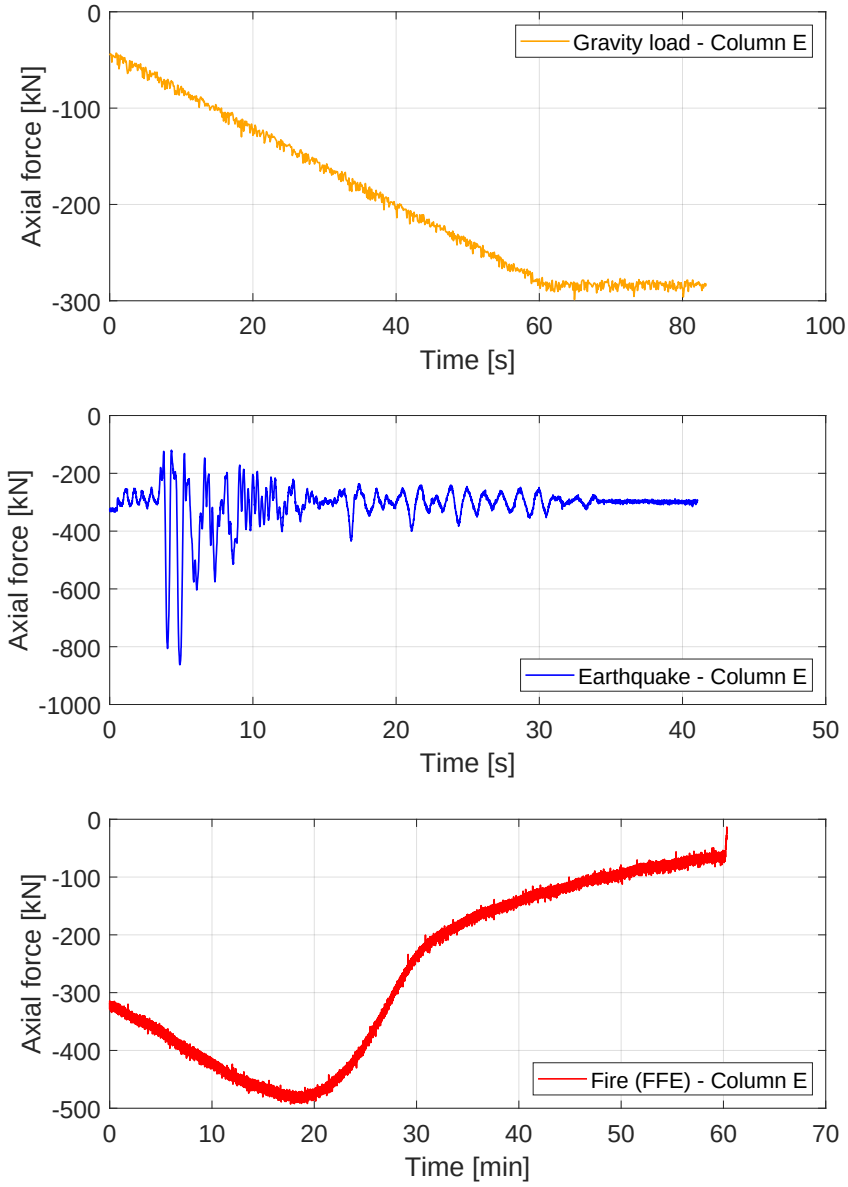

Figure 6.18: Column test E: evolution of the axial force.

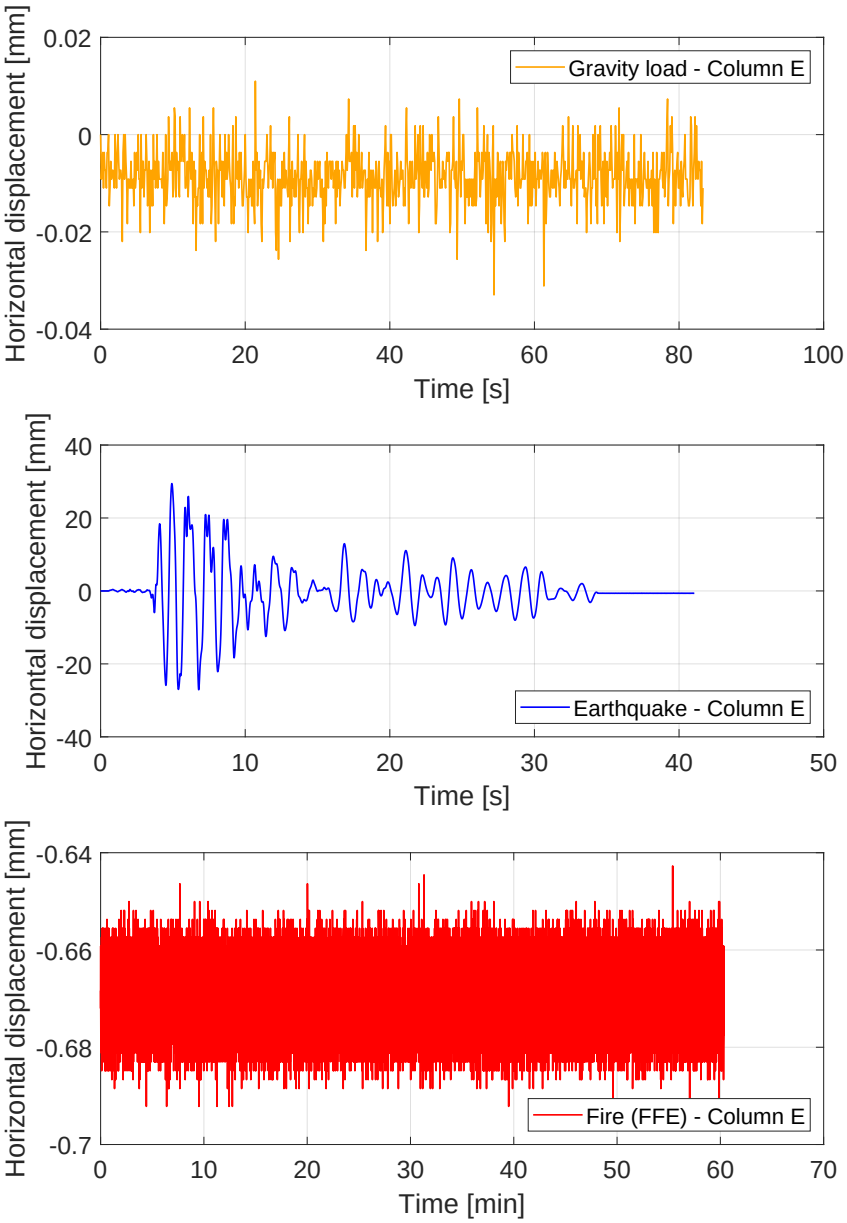

Figure 6.19: Column test E: evolution of the horizontal displacement.

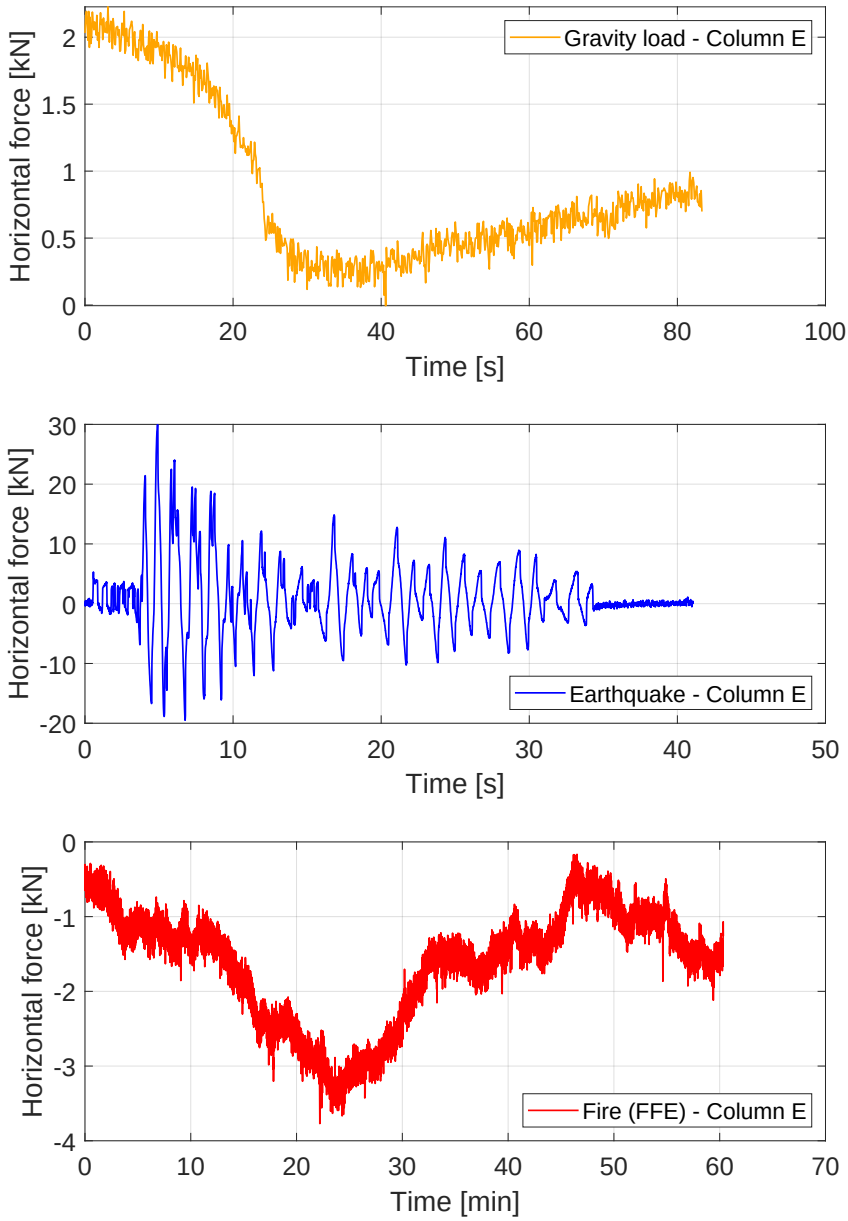

Figure 6.20: Column test E: evolution of the horizontal force.

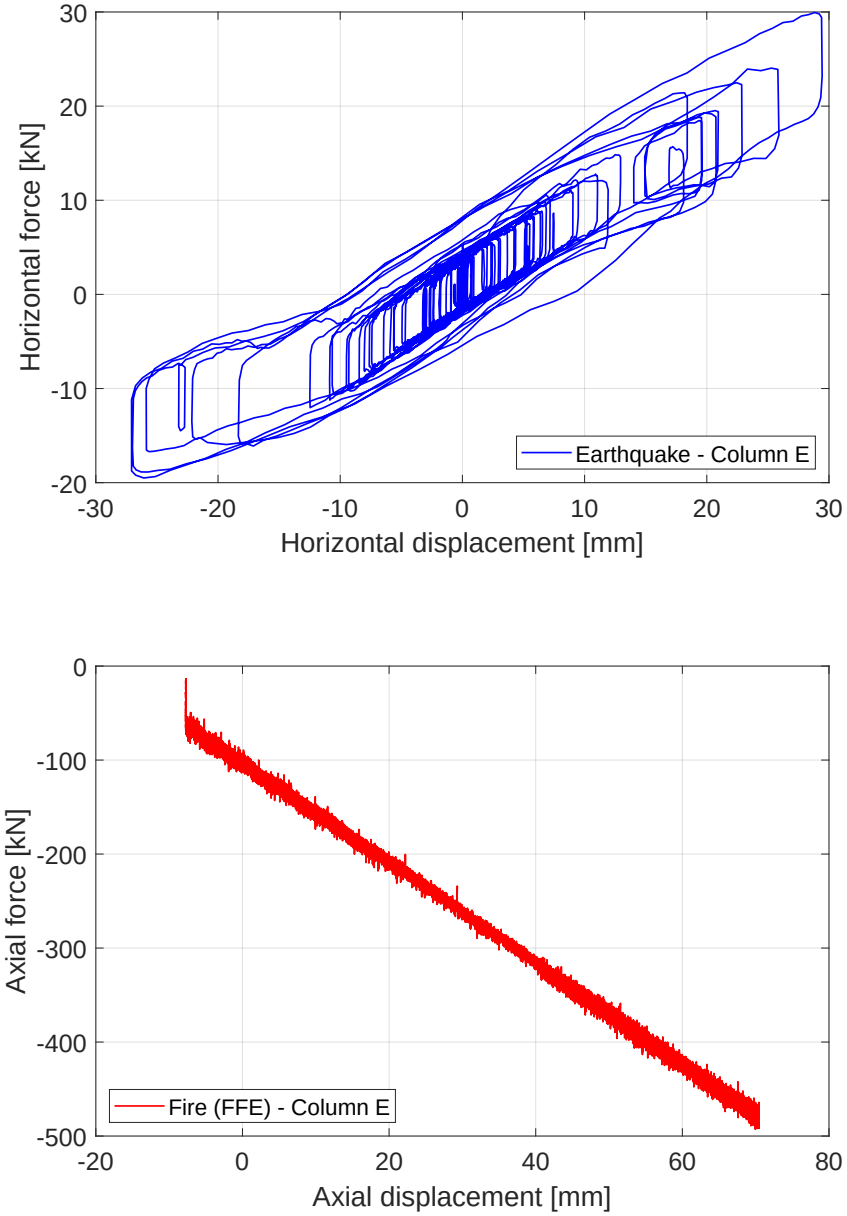

Figure 6.21: Column test E: displacement vs force.

As shown from the pictures and the experimental results, the buckling of the column occurred 18 minutes after the start of the fire.

6.4.2 Test #1 Column A

The specimen used in the test was HEB220 bare steel column steel grade S355. Figure 6.22 shows the geometrical dimensions and cross section of the specimen used in the test of column A. This column was instrumented with six thermocouples per section (four for the flanges and two for the webs) in 3 sections along the height of the column (sections B, D and F). Other two additional thermocouples were placed on the end plates (sections A and G). The total length of the column was 3.62m, including the end plates, which were 20mm thick. These end plates were square 600 x 600 mm, with 4 holes for bolts M48. The top plate is shifted 30mm to the north in respect of the bottom plate to be centred in respect of the horizontal actuator stroke of $\pm 30mm$. There is no corresponding capability to move the bottom loading environment also 30 mm to the north, i.e. a corresponding horizontal actuator at the bottom does not exist. As a consequence, the axial load as a resulting force of the stresses between the top plate and the loading environment block of the furnace would also be 30 mm out of the centre of the specimen with respect to the weak axis. The test procedure was the same explained in Chapter 6.3.

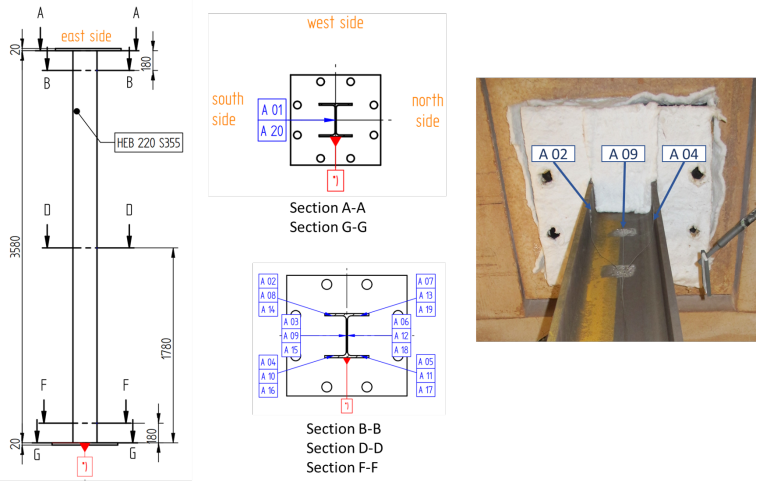

Figure 6.22: Column test A: cross section with position of the thermocouples.

Figure 6.23 shows views of the column of test BAM A before during and after test.

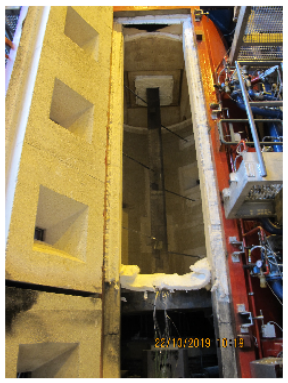

(a)

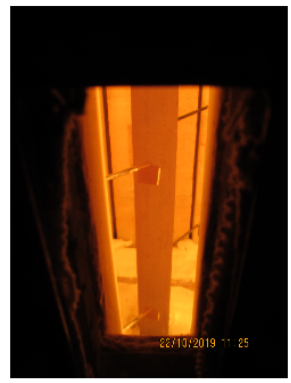

(b)

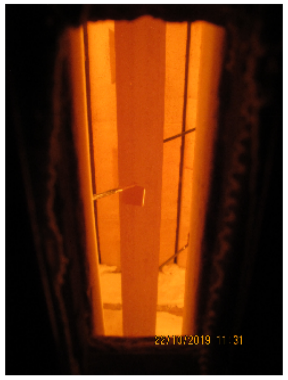

(c)

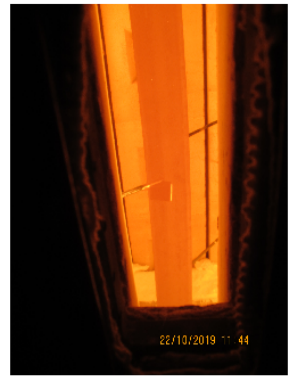

(d)

(e)

(f)

Figure 6.23: Views of column of test E: a) before test; b) time = 35 minutes; c) time = 41 minutes; d) time = 54 minutes; e) time = 60 minutes; d) after test.

In these pictures, it is possible to observe the lateral deflections and

buckling of the column that occurred around the weak axis, as expected, and negligible displacements around the strong axis.

Figure 6.24 presents the evolution of temperatures in the different sections of the column measured using the twenty thermocouples, compared with the ISO834 curve and the mean gas temperature inside the furnace.

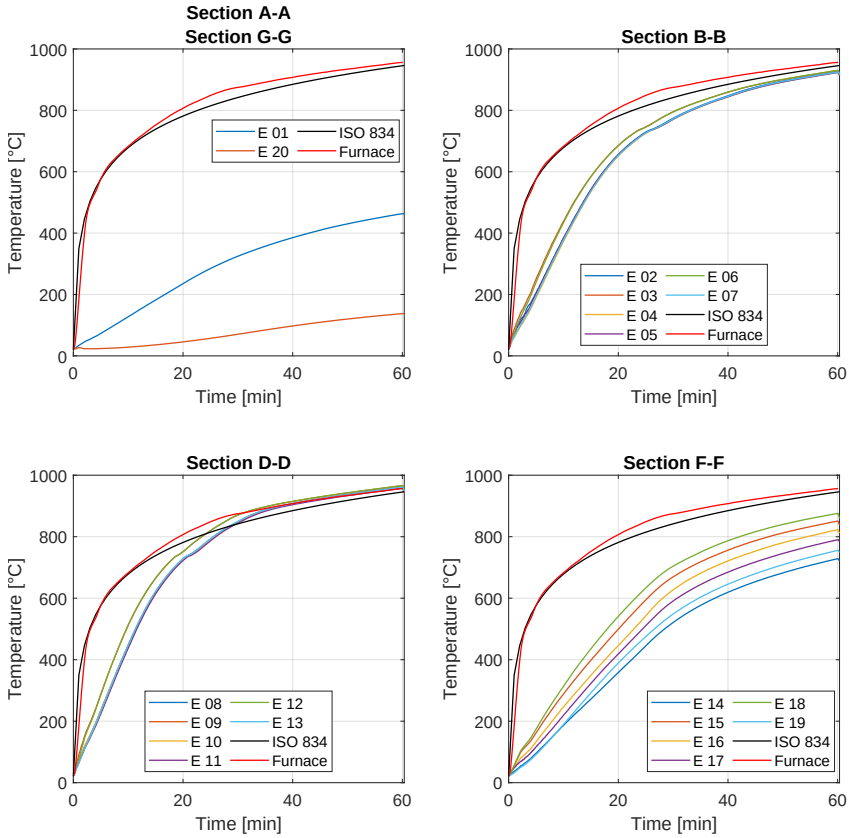

Figure 6.24: Column test A: evolution of the temperatures during the test.

Figures 6.25, 6.26, 6.27, 6.28 and 6.29 show the evolution of axial force, axial displacement, horizontal force and horizontal displacement of the column during the three phases of the test; Phase I: application of the gravity load. Phase II: earthquake. Phase III: fire after the earthquake.

Figure 6.29a presents the comparison of the horizontal force against to the horizontal displacement during the earthquake test. Figure 6.29b presents the comparison of the axial force against the axial displacement during the fire after the earthquake.

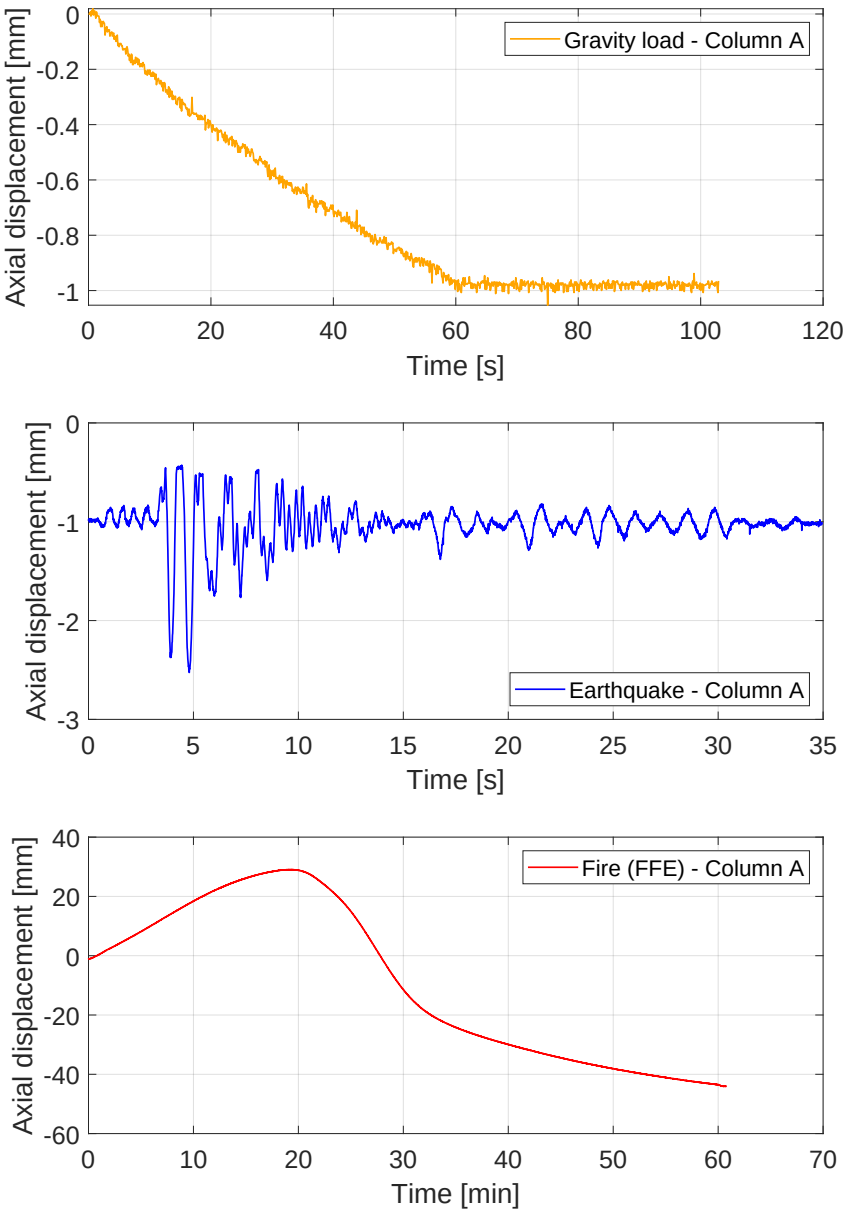

Figure 6.25: Column test A: evolution of the axial displacement.

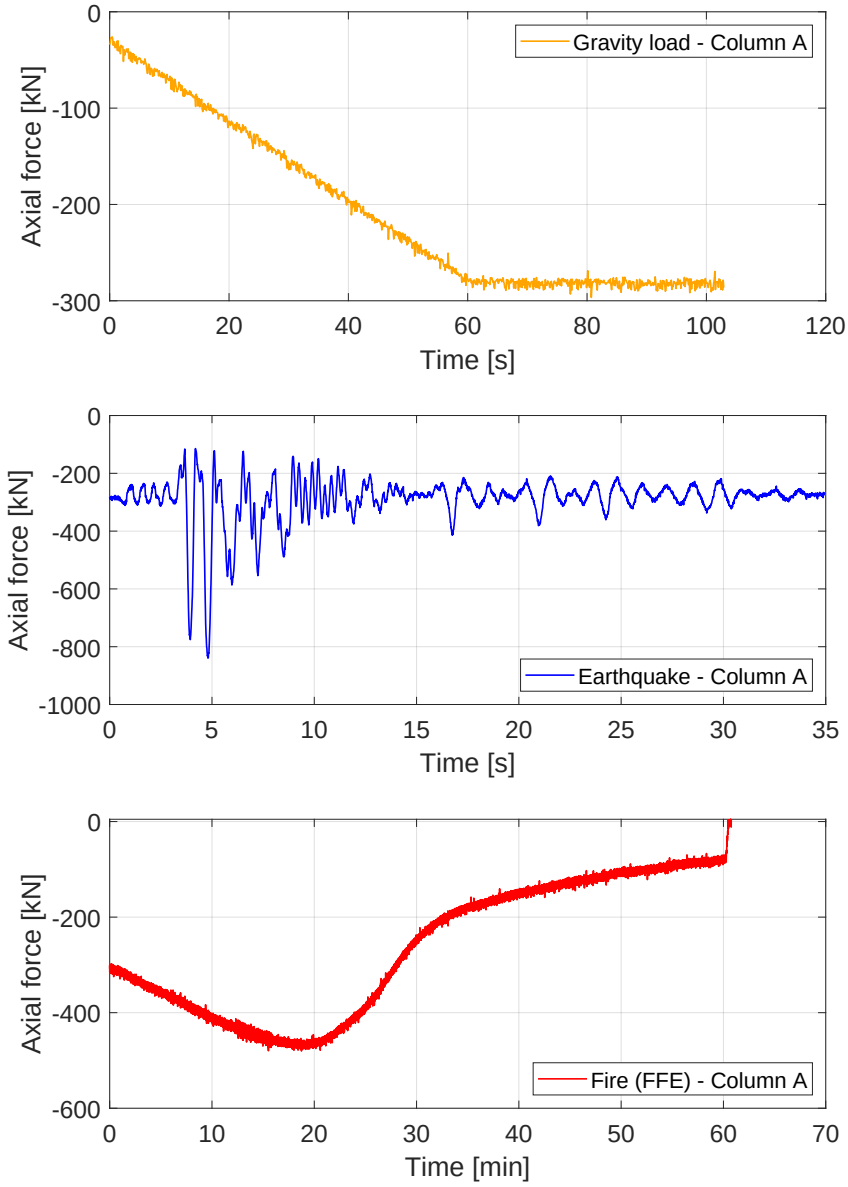

Figure 6.26: Column test A: evolution of the axial force.

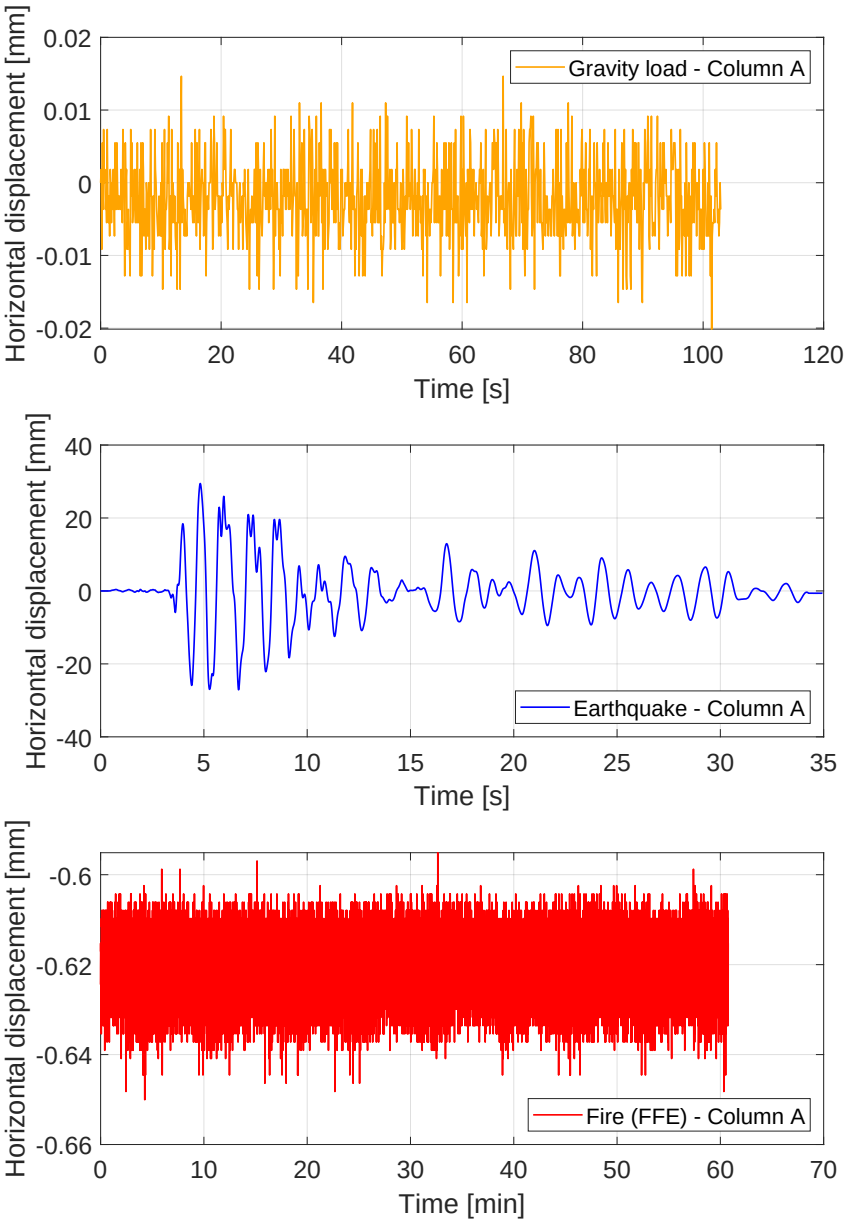

Figure 6.27: Column test A: evolution of the horizontal displacement.

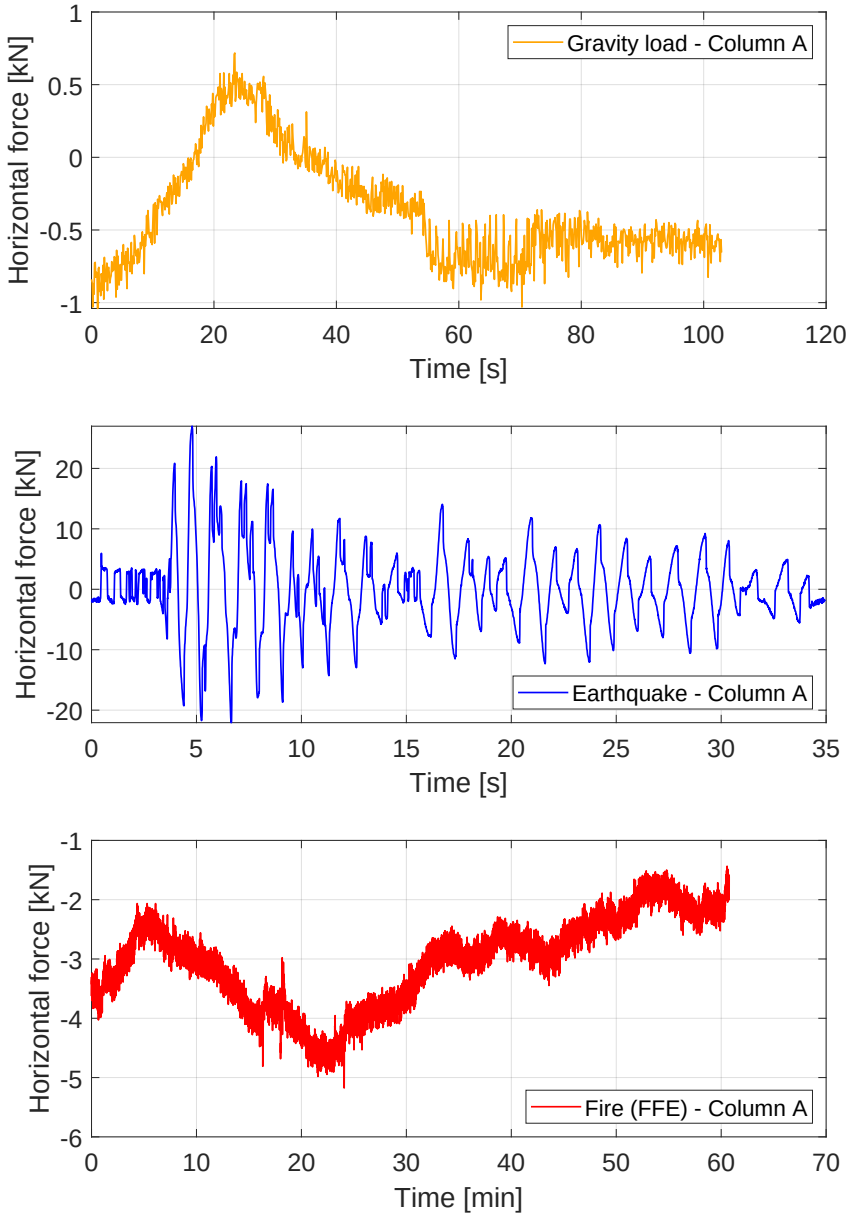

Figure 6.28: Column test A: evolution of the horizontal force.

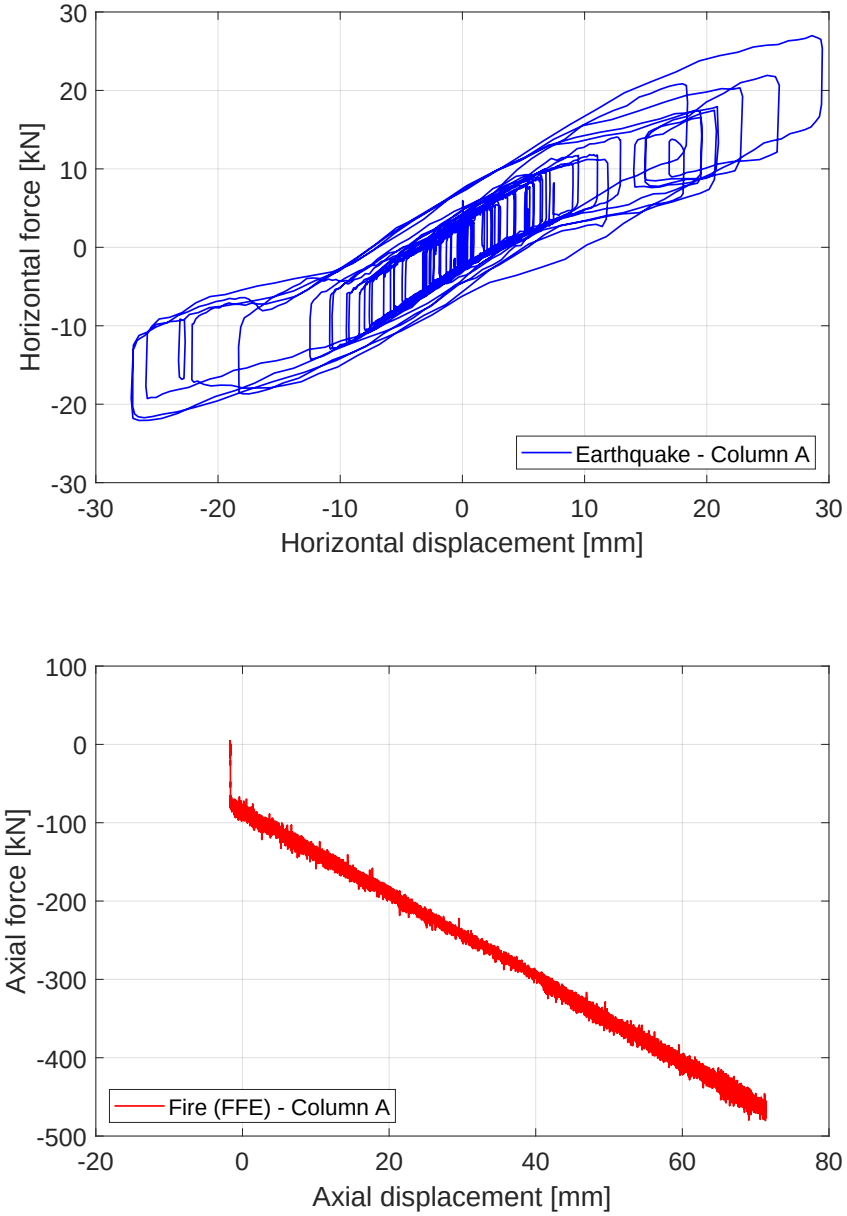

Figure 6.29: Column test A: displacement vs force.

As shown from the pictures and the experimental results, the buckling of the column occurred 19 minutes after the start of the fire.

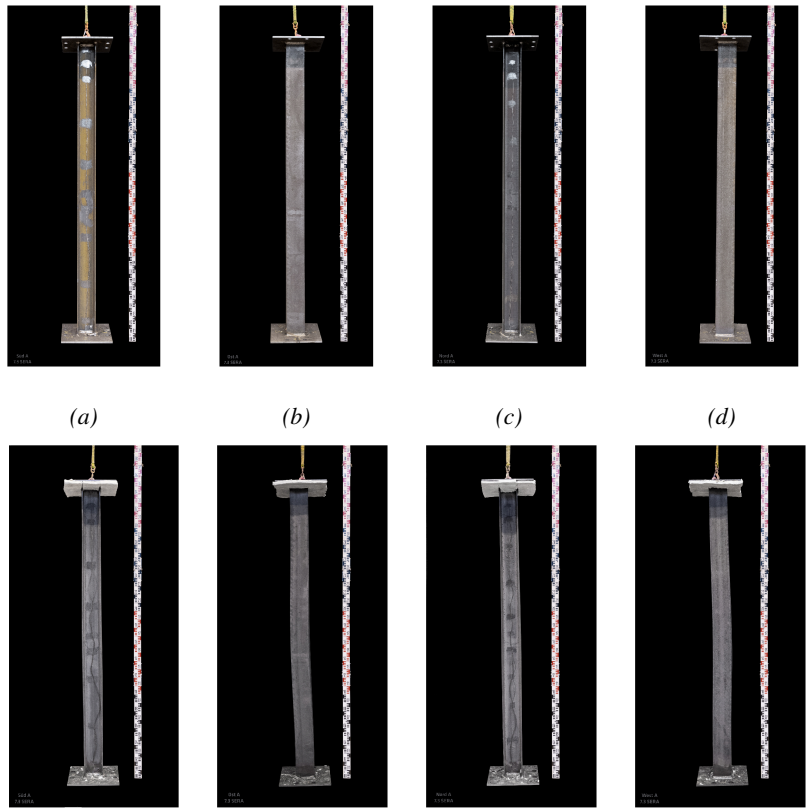

(a) *(b)* *(c)* *(d)*

(e) *(f)* *(g)* *(h)*

Figure 6.30: Comparison before and after the test a) south side (before); b) east side (before); c) north side (before); d) west side (before); e) south side (after); f) east side (after); g) north side (after); h) west side (after).

6.4.3 Test #2 Column B

The specimen used in the test was HEB220 steel column steel grade S355 with fire protection system PROMATECT®-H and reinforced joints designed for seismic region.

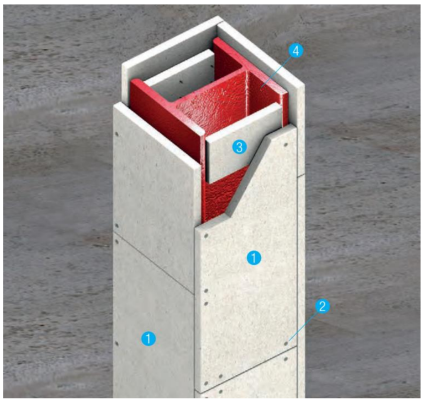

Figure 6.31: Steel column with PROMATECT®-200 and reinforced joints.

PROMATECT®-H is a mineral bound fibre reinforced calcium silicate board, non-combustible (A1) in accordance with EN 13501-1 [3]. Technical data and properties of the fire protection are reported in Table 6.1.

Table 6.1: Technical data and properties of PROMATECT®-H

Technical data and properties	Value
Fire Reaction Class	A1, non-combustible
Alkalinity:	12 pH
Dry Density:	870 kg/m³
Nominal moisture content ambient:	2 %
Thermal Conductivity at 20°C:	0.175 W/m K
Flexural Strength Longitudinal:	7.6 N/mm²
Tensile Strength Longitudinal:	4.8 N/mm²
Compressive strength:	9.3 N/mm²

Figure 6.32 shows the geometrical dimensions and cross section of the specimen used in the test of column B. This column was instrumented with six thermocouples per section (four for the flanges and two for the webs) in 3 sections along the height of the column (sections B, D and F). Other two additional thermocouples were placed on the end plates (sections A and G). The total length of the column was 3.62m, including

the end plates, which were 20mm thick. These end plates were square 600 x 600 mm, with 4 holes for bolts M48. The top plate is shifted 30mm to the north in respect of the bottom plate to be centred in respect of the horizontal actuator stroke of $\pm 30mm$. There is no corresponding capability to move the bottom loading environment also 30 mm to the north, i.e. a corresponding horizontal actuator at the bottom does not exist. Consequently, the axial load as a resulting force of the stresses between the top plate and the loading environment block of the furnace would also be 30 mm out of the centre of the specimen with respect to the weak axis. The test procedure was the same explained in Chapter 6.3.

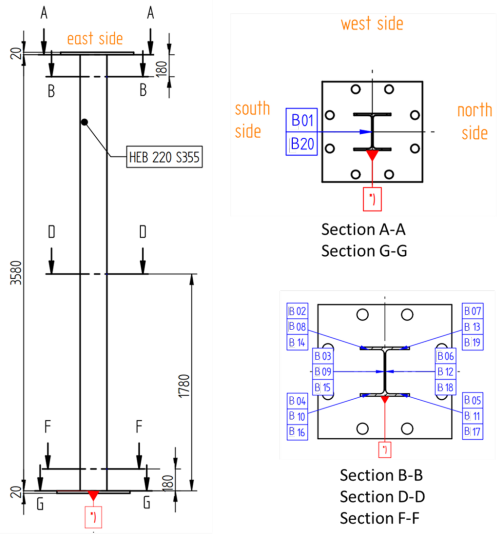

Figure 6.32: Column test B: cross section with position of the thermocouples.

Test column B was interrupted due to a malfunction of a component and then was restarted. The problem happened 38 minutes after the start of the fire, a component of the control unit (Figure 6.33b), that exchange the data between the sensors and the pc with the numerical simulation (target PC), stopped working due to overheating.

In this situation, the control unit was unable to update the memory values of the target PC and therefore, the target PC started to compute wrong target displacements using the outdated values and it sent wrong instructions to the master PC. In detail, the target PC sent the instruction for moving the vertical actuator to increase the axial force. But, without receiving the updated data, this instruction was repeated, as in a loop, until the axial value in the column reached the interlock value and the

master PC cut off the target PC instructions and the column was automatically discharged to prevent damage to the specimen (Figure 6.33a and 6.33c). Before installing the specimen, it is best practice to set upper and lower displacement and force limit detectors (Interlocks) to levels that minimize the chance of accidental damage to the test specimen or the equipment. For BAM tests, one interlock was set: the axial force was limited to 1500 kN in compression to protect the specimen from an excessive compression force.

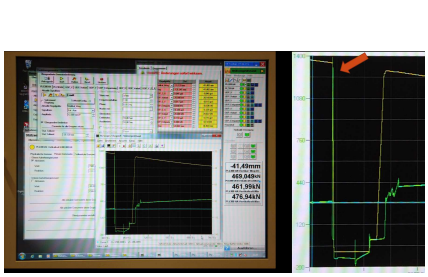

(a)

(b)

(c)

Figure 6.33: Test interruption: a) axial force and axial displacement; b) component subjected to the malfunction (overheat); c) axial force and axial displacement.

In this situation, it was impossible to stop the fire test and start again from the beginning without using a new specimen. Therefore, we decided to try to restore the test. After identifying the issue, the target PC was rebooted, while the displacement value of the vertical actuator was manually restored using the master PC. Then, the system was switched back to the hybrid test configuration using the target PC (Figure 6.34).

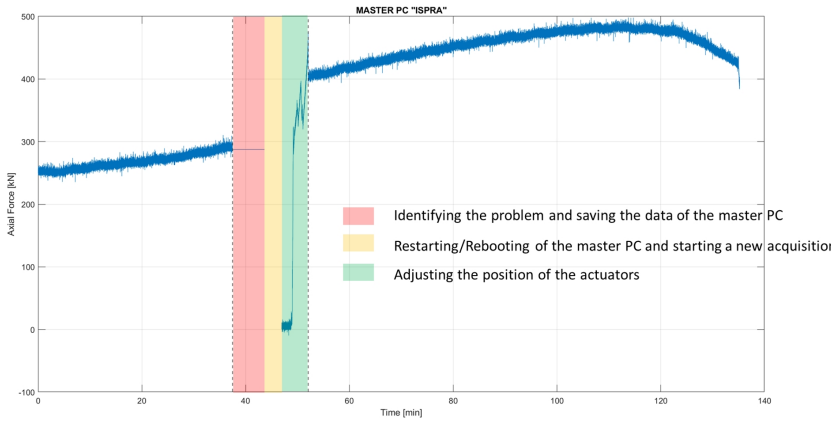

(a)

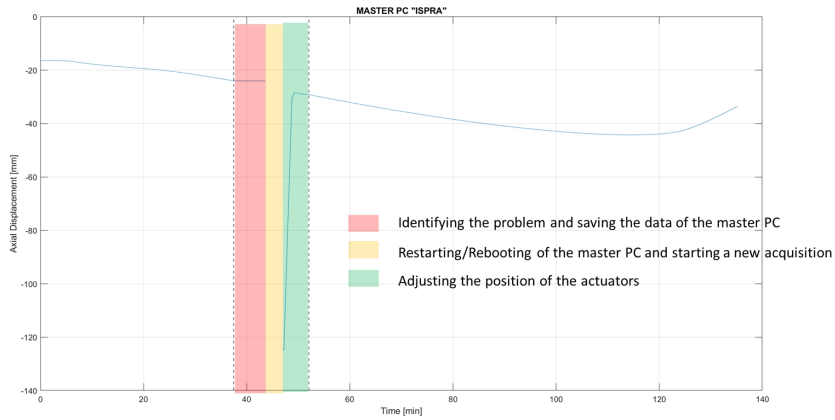

(b)

Figure 6.34: a) axial force; b) axial displacement.

Figure 6.35 shows views of the column of test BAM B before, during and after the test.

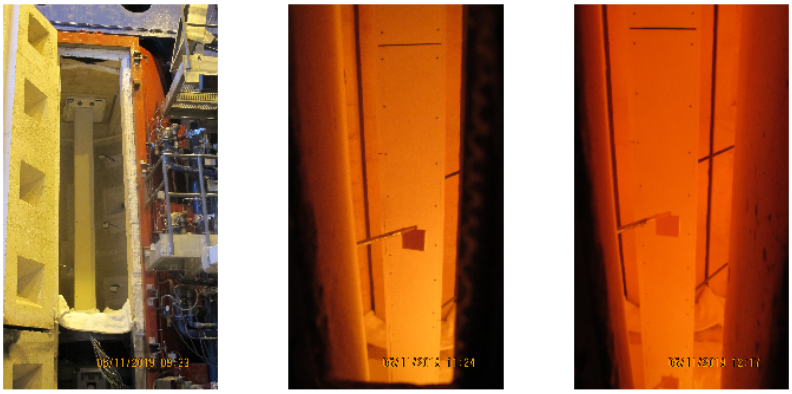

(a) *(b)* *(c)*

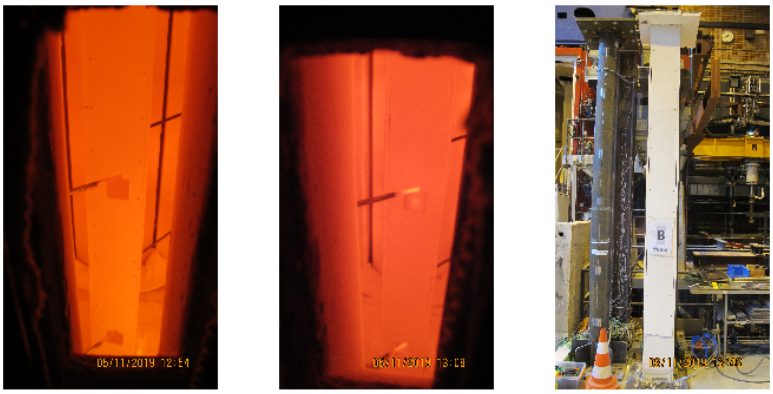

(d) *(e)* *(f)*

Figure 6.35: Views of column of test B: a) before test; b) time = 26 minutes; c) time = 79 minutes; d) time = 116 minutes; e) time = 130 minutes; d) after test.

In these pictures, it is possible to observe the lateral deflections and buckling of the column that occurred around the weak axis, as expected, and negligible displacements around the strong axis.

Figure 6.36 presents the evolution of temperatures in the different sections of the column measured using the twenty thermocouples, compared with the ISO834 curve and the mean gas temperature inside the furnace.

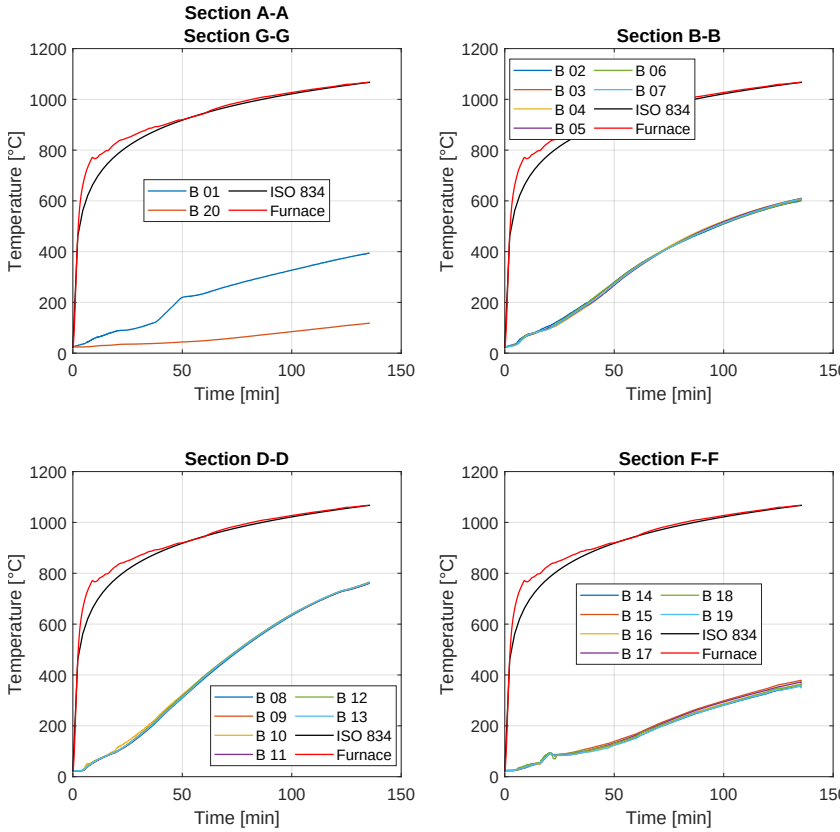

Figure 6.36: Column test B: evolution of the temperatures during the test.

Figures 6.37, 6.38, 6.39, 6.40 and 6.41 show the evolution of axial force, axial displacement, horizontal force and horizontal displacement of the column during the three phases of the test; Phase I: application of the gravity load. Phase II: earthquake. Phase III: fire after the earthquake.

Figure 6.41a presents the comparison of the horizontal force against the horizontal displacement during the earthquake test. Figure 6.41b presents the comparison of the axial force against the axial displacement during the fire after the earthquake.

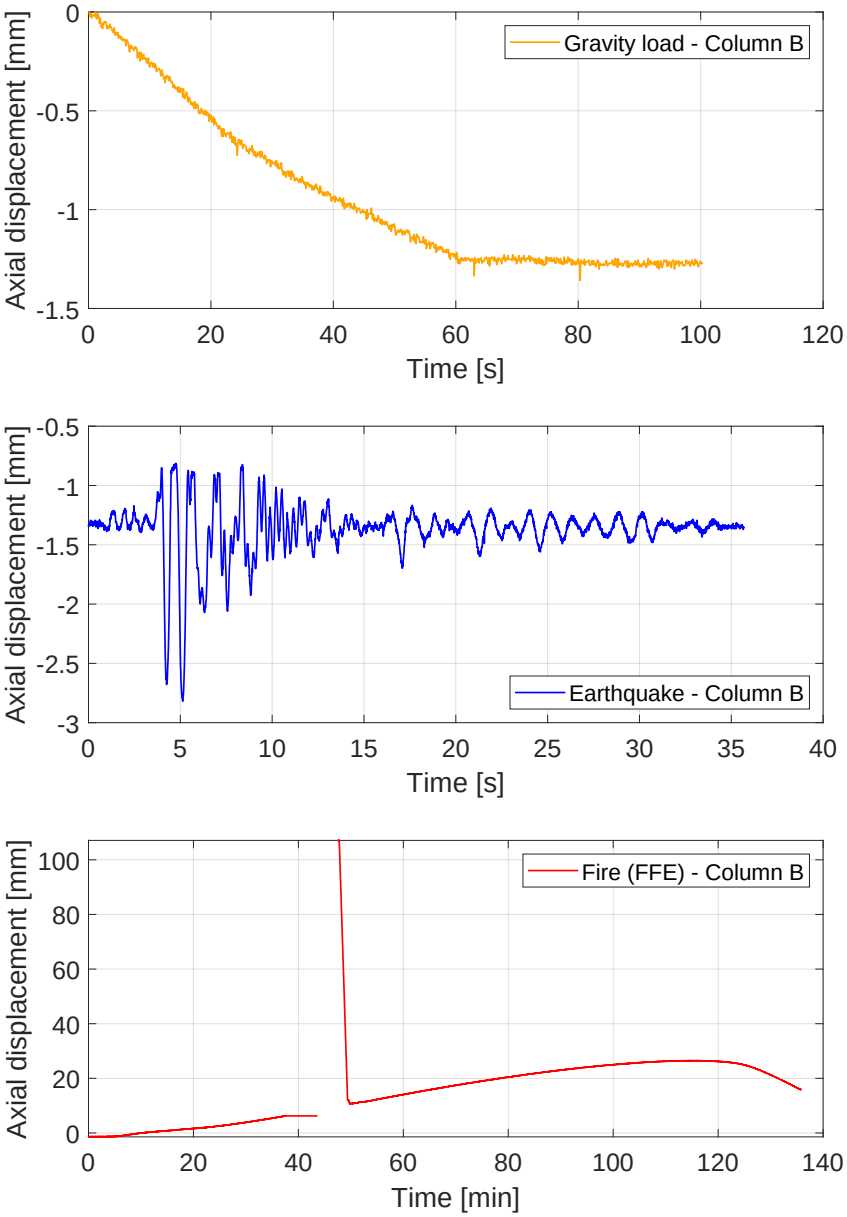

Figure 6.37: Column test B: evolution of the axial displacement.

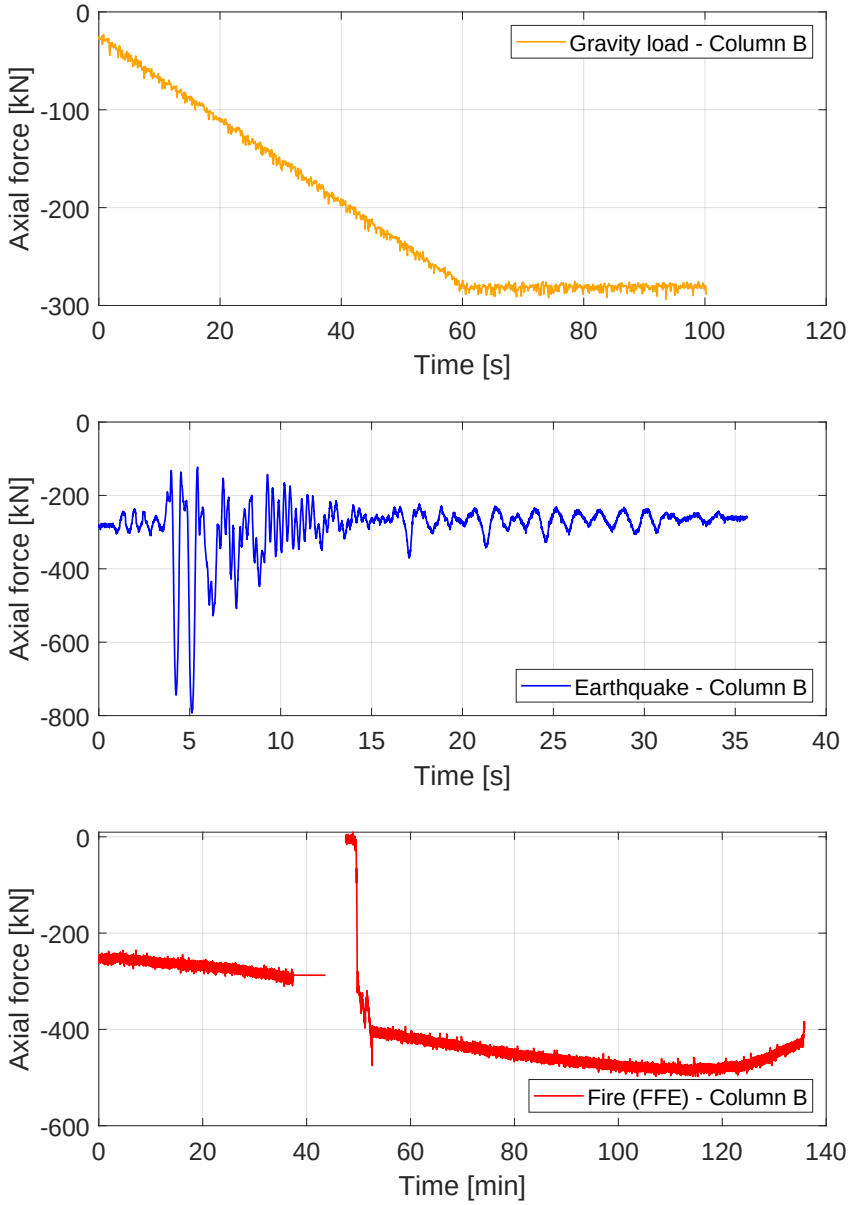

Figure 6.38: Column test B: evolution of the axial force.

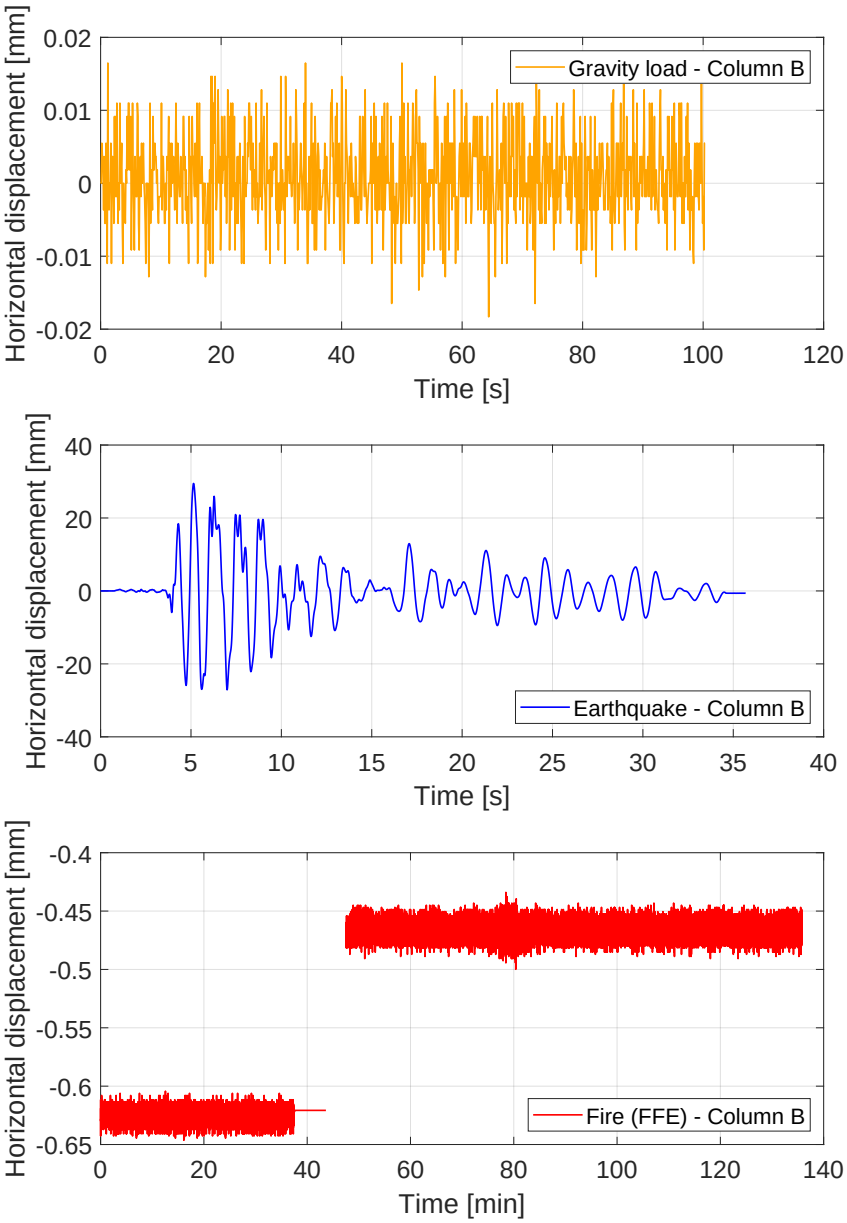

Figure 6.39: Column test B: evolution of the horizontal displacement.

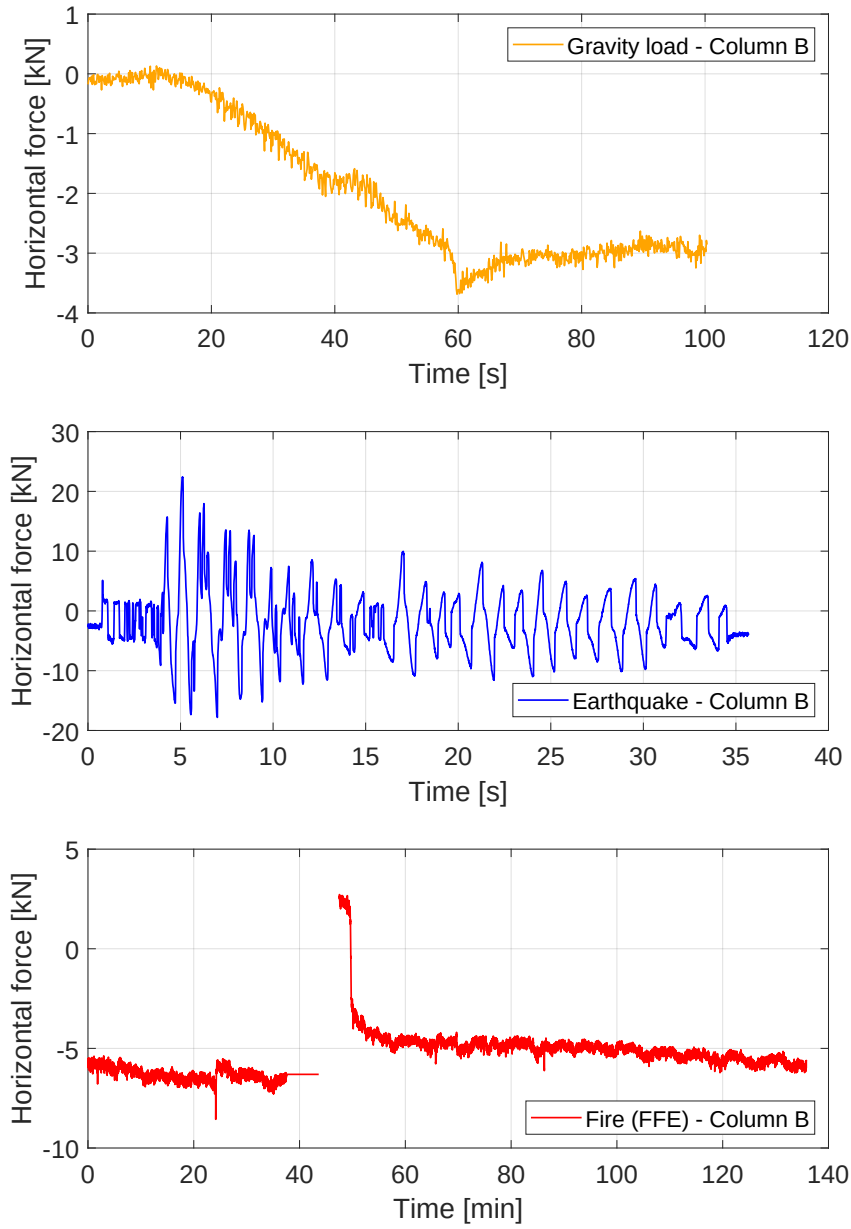

Figure 6.40: Column test B: evolution of the horizontal force.

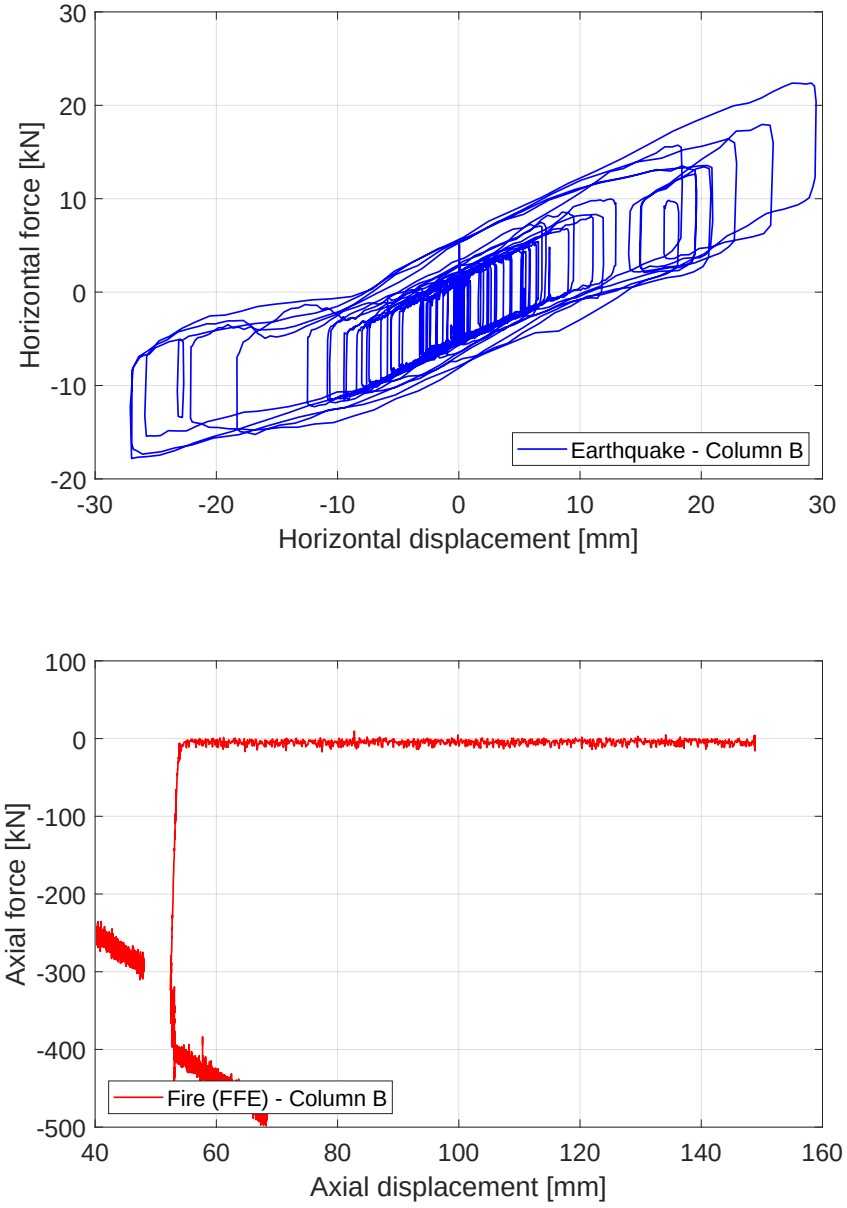

Figure 6.41: Column test B: displacement vs force.

As show from the pictures and the experimental results, the buckling of the column occurred 125 minutes after the start of the fire.

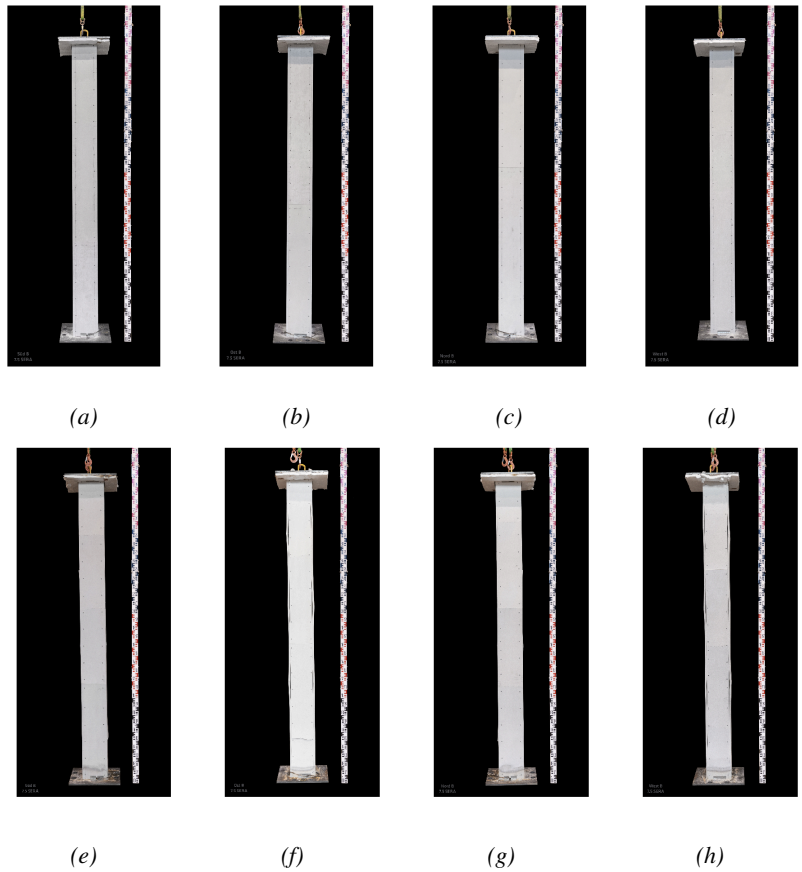

(a) *(b)* *(c)* *(d)*

(e) *(f)* *(g)* *(h)*

Figure 6.42: Comparison before and after the test a) south side (before); b) east side (before); c) north side (before); d) west side (before); e) south side (after); f) east side (after); g) north side (after); h) west side (after).

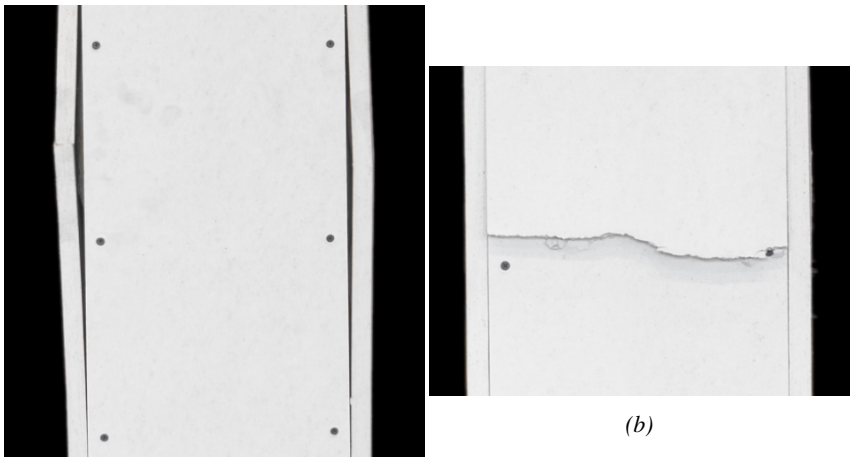

(a) *(b)*

Figure 6.43: Damage on the fire protection elements due to the combination of seismic and fire actions: test #2 column B

6.4.4 Test #4 Column C

The specimen used in the test was HEB220 steel column steel grade S355 with fire protection system PROMATECT®-H and normal joints.

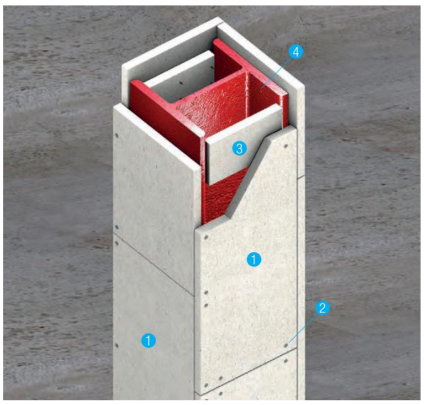

Figure 6.44: Steel column with PROMATECT®-H and normal joints.

PROMATECT®-H is a mineral bound fibre reinforced calcium silicate board, non-combustible (A1) in accordance with EN 13501-1 [3]. Technical data and properties of the fire protection are reported in Table 6.2.

Table 6.2: Technical data and properties of PROMATECT®-H

Technical data and properties	Value
Fire Reaction Class	A1, non-combustible
Alkalinity:	12 pH
Dry Density:	870 kg/m³
Nominal moisture content ambient:	2 %
Thermal Conductivity at 20°C:	0.175 W/m K
Flexural Strength Longitudinal:	7.6 N/mm²
Tensile Strength Longitudinal:	4.8 N/mm²
Compressive strength:	9.3 N/mm²

Figure 6.45 shows the geometrical dimensions and cross section of the specimen used in the test of column C. This column was instrumented with six thermocouples per section (four for the flanges and two for the webs) in 3 sections along the height of the column (sections B, D and F). Other two additional thermocouples were placed on the end plates (sections A and G). The total length of the column was 3.62m, including the end plates, which were 20mm thick. These end plates were square

600 x 600 mm, with 4 holes for bolts M48. The top plate is shifted 30mm to the north in respect of the bottom plate to be centred in respect of the horizontal actuator stroke of $\pm 30mm$. There is no corresponding capability to move the bottom loading environment also 30 mm to the north, i.e. a corresponding horizontal actuator at the bottom does not exist. Consequently, the axial load as a resulting force of the stresses between the top plate and the loading environment block of the furnace would also be 30 mm out of the centre of the specimen with respect to the weak axis. The test procedure was the same explained in Chapter 6.3.

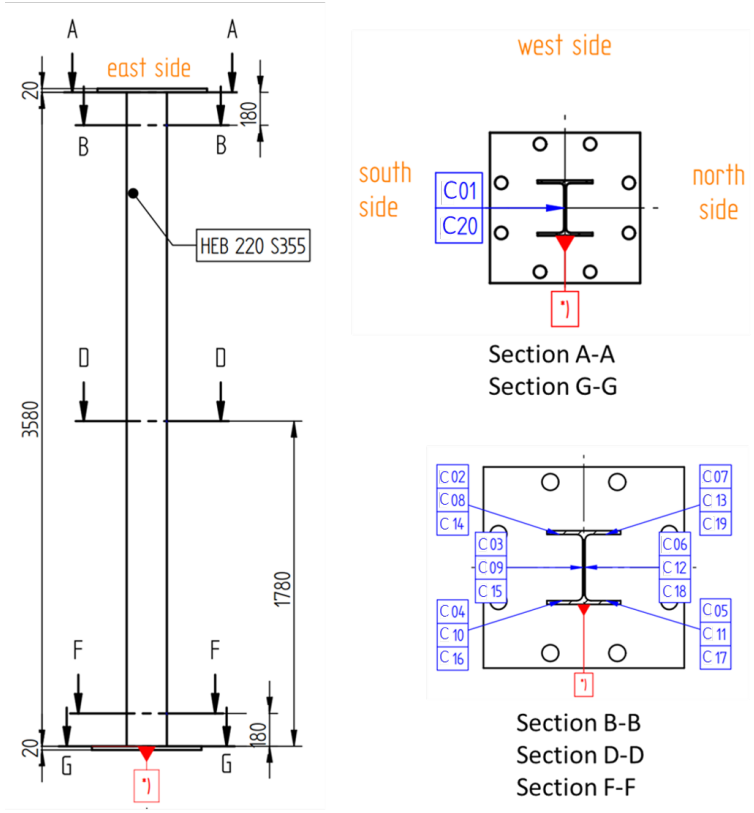

Figure 6.45: Column test C: cross section with position of the thermocouples.

Figure 6.46 shows views of the column of test BAM C before during and after test.

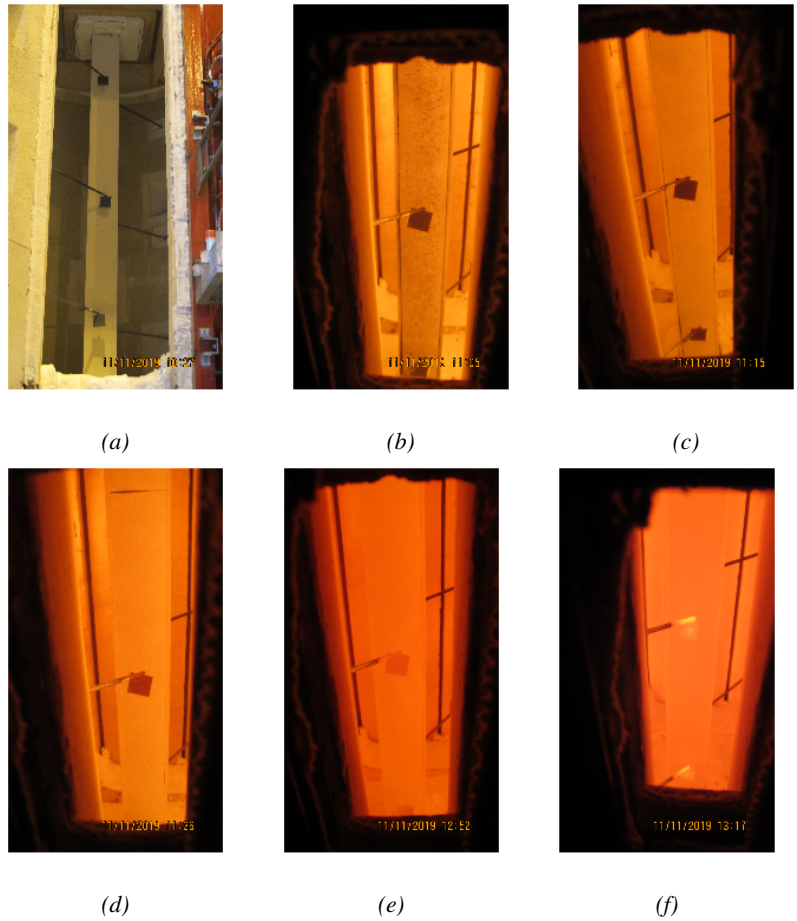

(a) *(b)* *(c)*

(d) *(e)* *(f)*

Figure 6.46: Views of column of test C: a) before test; b) time = 38 minutes; c) time = 48 minutes; d) time = 69 minutes; e) time = 85 minutes; d) time = 110 minutes.

In these pictures, it is possible to observe the lateral deflections and buckling of the column that occurred around the weak axis, as expected, and negligible displacements around the strong axis.

Figure 6.47 presents the evolution of temperatures in the different sections of the column measured using the twenty thermocouples, compared with the ISO834 curve and the mean gas temperature inside the furnace.

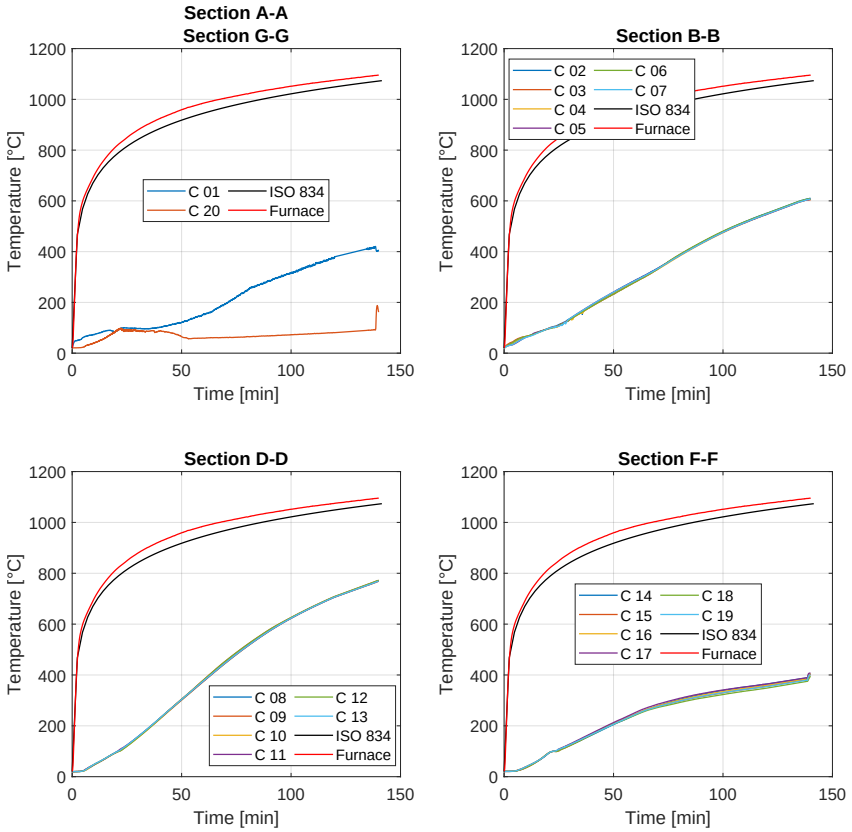

Figure 6.47: Column test C: evolution of the temperatures during the test.

Figures 6.48, 6.49, 6.50, 6.51 and 6.52 show the evolution of axial force, axial displacement, horizontal force and horizontal displacement of the column during the three phases of the test; Phase I: application of the gravity load. Phase II: earthquake. Phase III: fire after the earthquake.

Figure 6.52a presents the comparison of the horizontal force against the horizontal displacement during the earthquake test. Figure 6.52b presents the comparison of the axial force against the axial displacement during the fire after the earthquake.

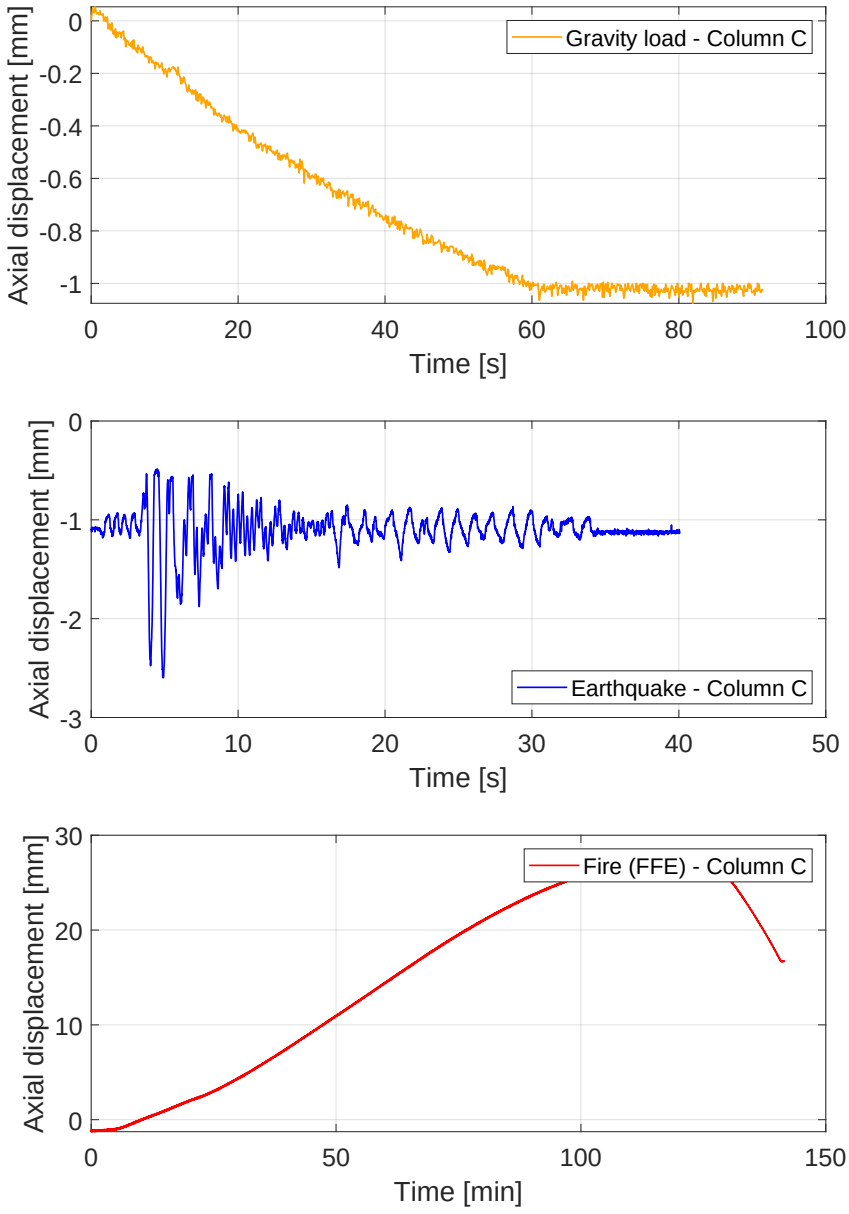

Figure 6.48: Column test C: evolution of the axial displacement.

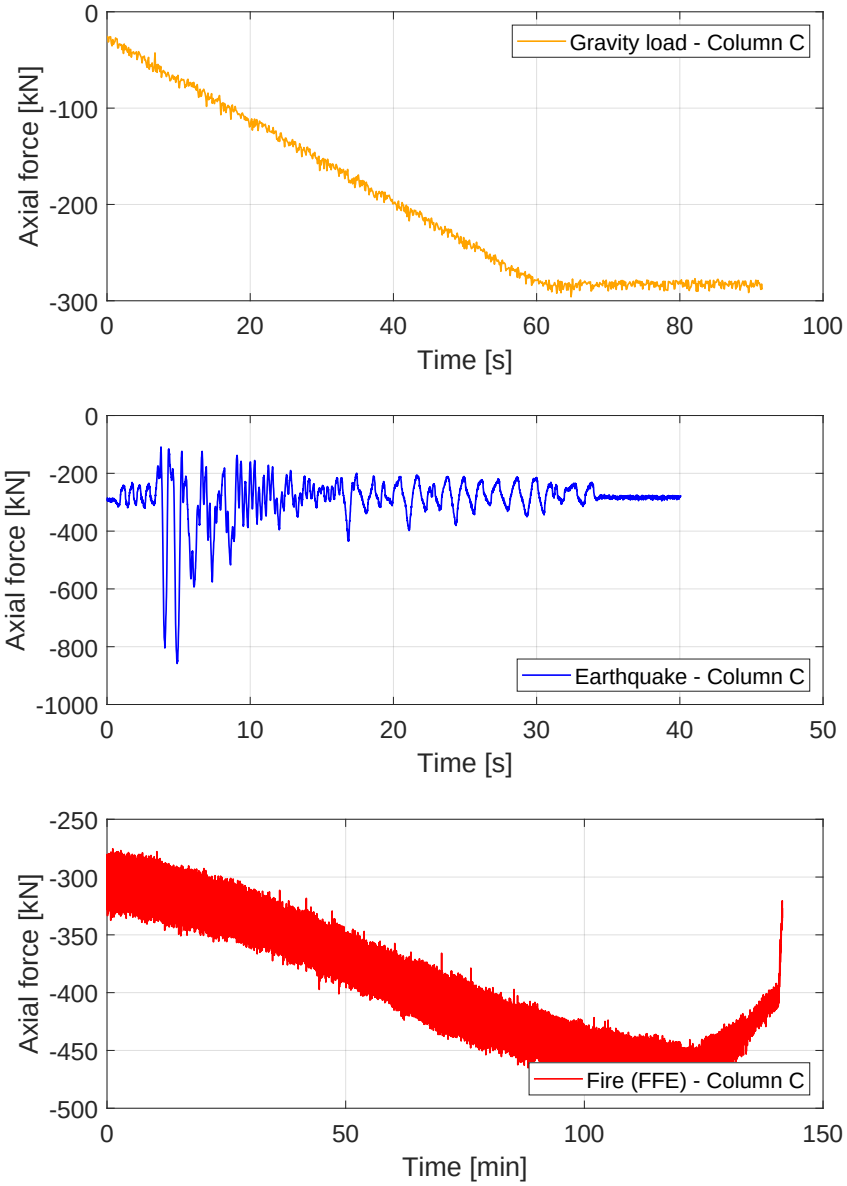

Figure 6.49: Column test C: evolution of the axial force.

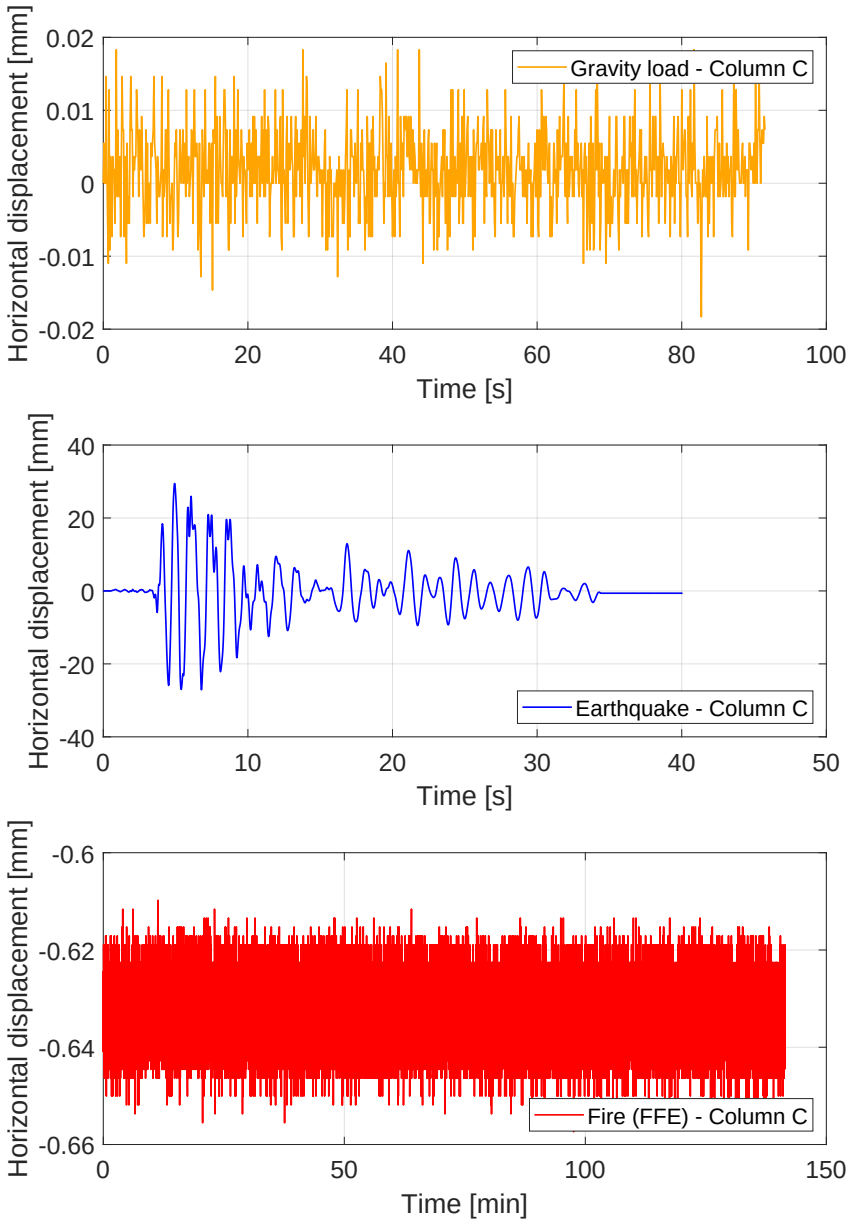

Figure 6.50: Column test C: evolution of the horizontal displacement.

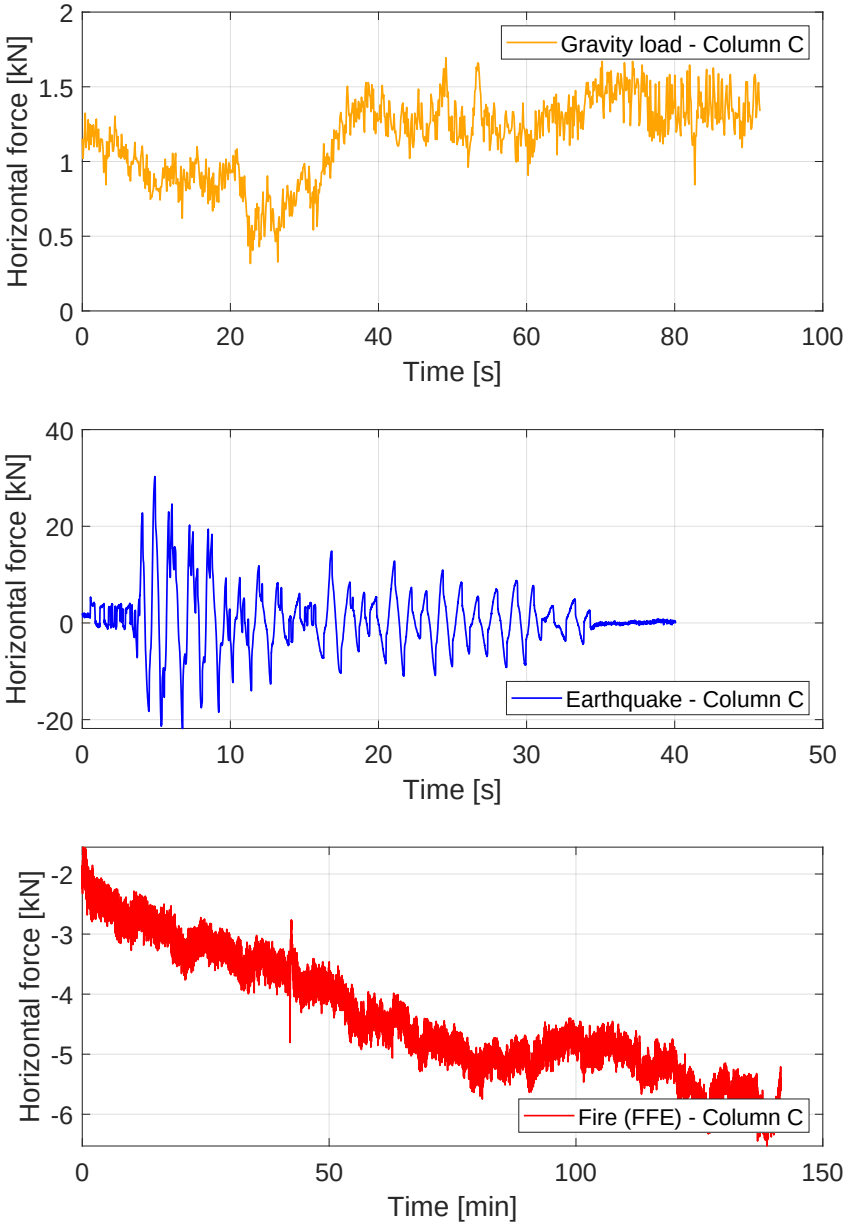

Figure 6.51: Column test C: evolution of the horizontal force.

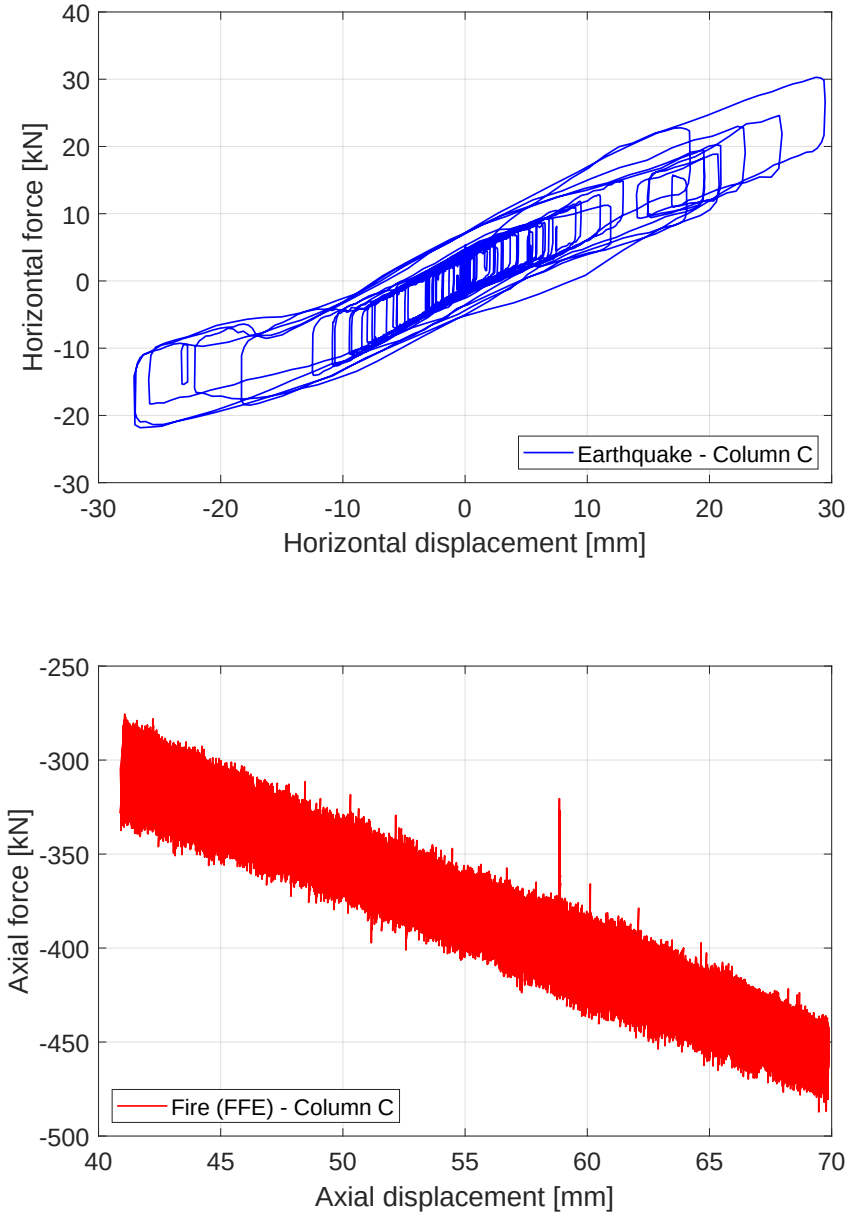

Figure 6.52: Column test C: displacement vs force.

As shown from the pictures and the experimental results, the buckling of the column occurred 125 minutes after the start of the fire.

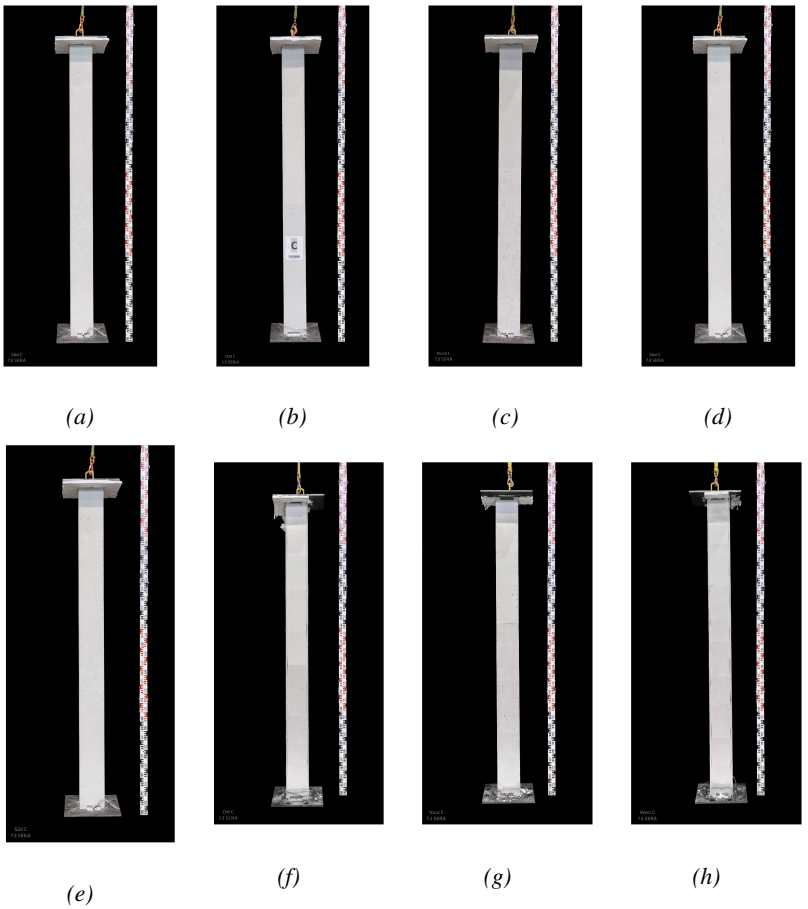

(a) *(b)* *(c)* *(d)*

(e) *(f)* *(g)* *(h)*

Figure 6.53: Comparison before and after the test a) south side (before); b) east side (before); c) north side (before); d) west side (before); e) south side (after); f) east side (after); g) north side (after); h) west side (after).

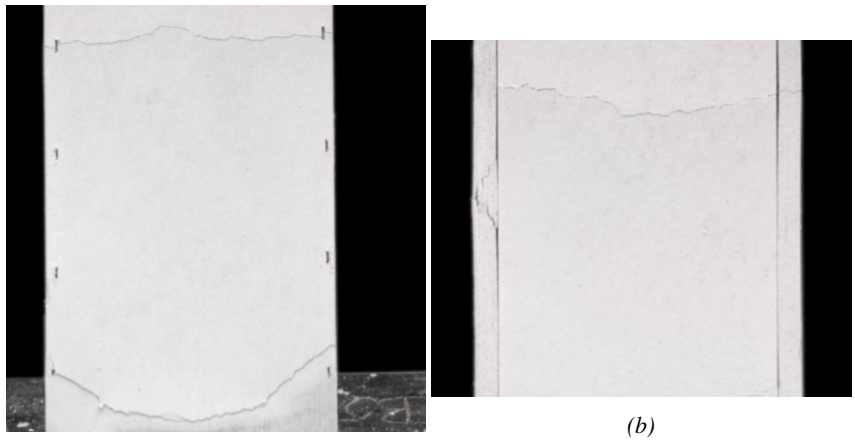

(a) *(b)*

Figure 6.54: Damage on the fire protection elements due to the combination of seismic and fire actions: test #2 column B

6.4.5 Test #5 Column D

The specimen used in the test was HEB220 steel column steel grade S355 with fire protection system PROMASPRAY®-P300 series (CAFCO 300), a gypsum-based wet mix spray-applied fire-resistive material, designed for applications in seismic regions, in which a mechanical reinforcing mesh was placed in the middle of the applied material, as illustrated in Figure 6.55

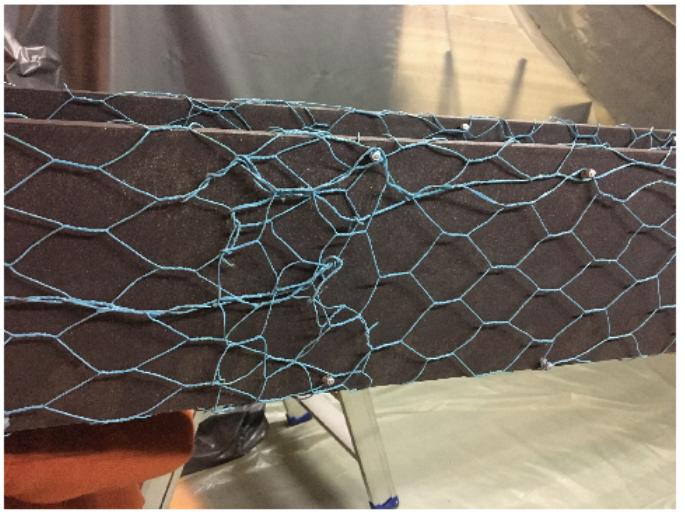

(a)

(b)

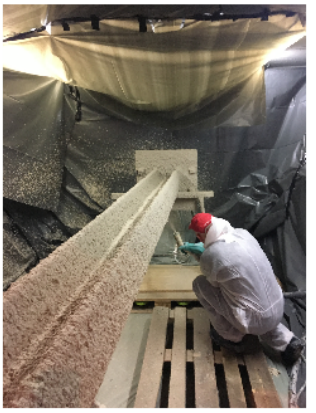

(c)

Figure 6.55: a) and b) layer of mechanical reinforcing mesh; c) PROMOSPRAY®-P300 series (CAFCO 300) application.

Technical data and properties of the fire protection are reported in Table 6.3.

Table 6.3: Technical data and properties of PROMOSPRAY®-P300 series (CAFCO 300)

Technical data and properties	**Value**
Fire Reaction Class	A1, non-combustible
Alkalinity:	8.5 pH
Density:	365 kg/m³
Thermal Conductivity at 20°C:	0.078 W/m K

Figure 6.56 shows the geometrical dimensions and cross section of the specimen used in the test of column D. This column was instrumented with six thermocouples per section (four for the flanges and two for the webs) in 3 sections along the height of the column (sections B, D and F). Other two additional thermocouples were placed on the end plates (sections A and G).

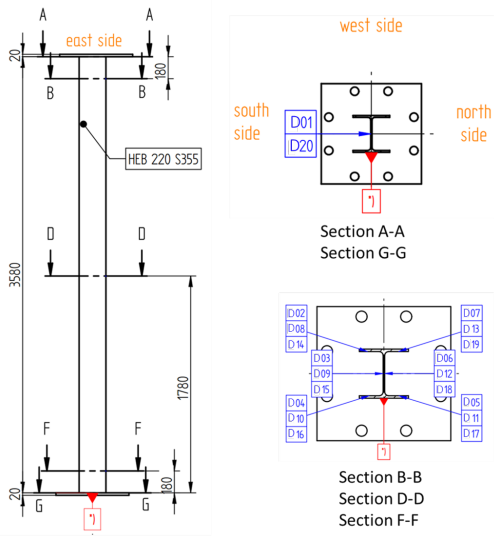

Figure 6.56: Column test D: cross section with position of the thermocouples.

The total length of the column was 3.62m, including the end plates, which were 20mm thick. These end plates were square 600 x 600 mm, with 4 holes for bolts M48. The top plate is shifted 30mm to the north in respect of the bottom plate to be centred in respect of the horizontal actuator stroke of $\pm 30mm$. There is no corresponding capability to move the bottom loading environment also 30 mm to the north, i.e. a corre-

sponding horizontal actuator at the bottom does not exist. Consequently, the axial load as a resulting force of the stresses between the top plate and the loading environment block of the furnace would also be 30 mm out of the centre of the specimen with respect to the weak axis. The test procedure was the same explained in Chapter 6.3.

Figure 6.57 shows views of the column of test BAM D before during and after test.

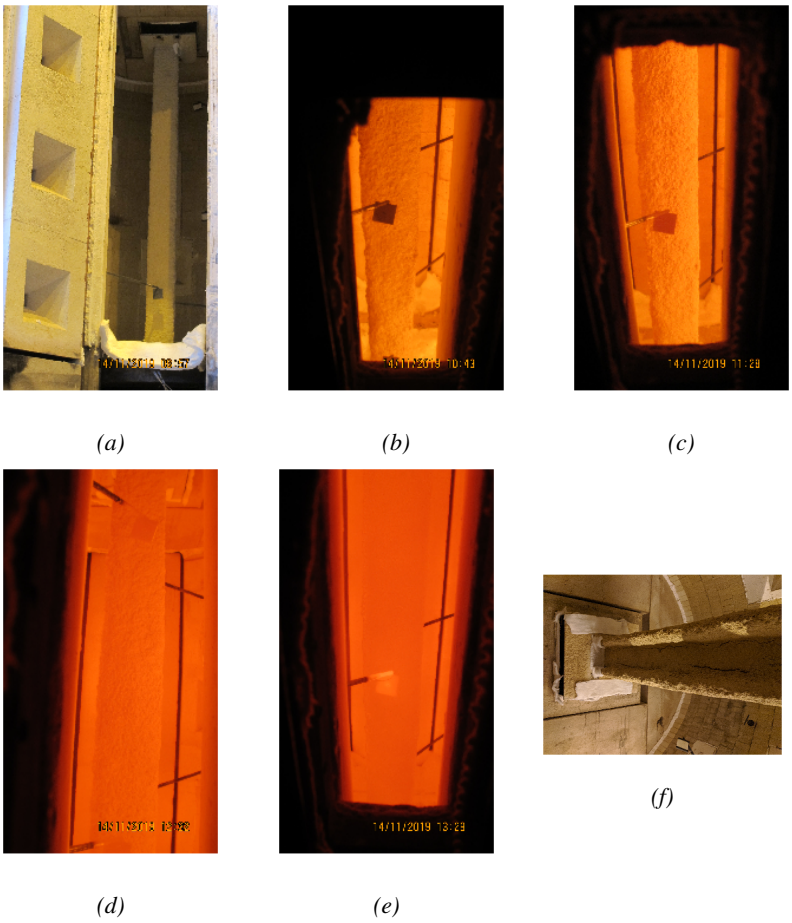

Figure 6.57: Views of column of test D: a) before test; b) time = 5 minutes; c) time = 49 minutes; d) time = 113 minutes; e) time = 170 minutes; d) after test.

In these pictures, it is possible to observe the lateral deflections and buckling of the column that occurred around the weak axis, as expected, and negligible displacements around the strong axis.

Figure 6.58 presents the evolution of temperatures in the different sections of the column measured using the twenty thermocouples, com-

pared with the ISO834 curve and the mean gas temperature inside the furnace.

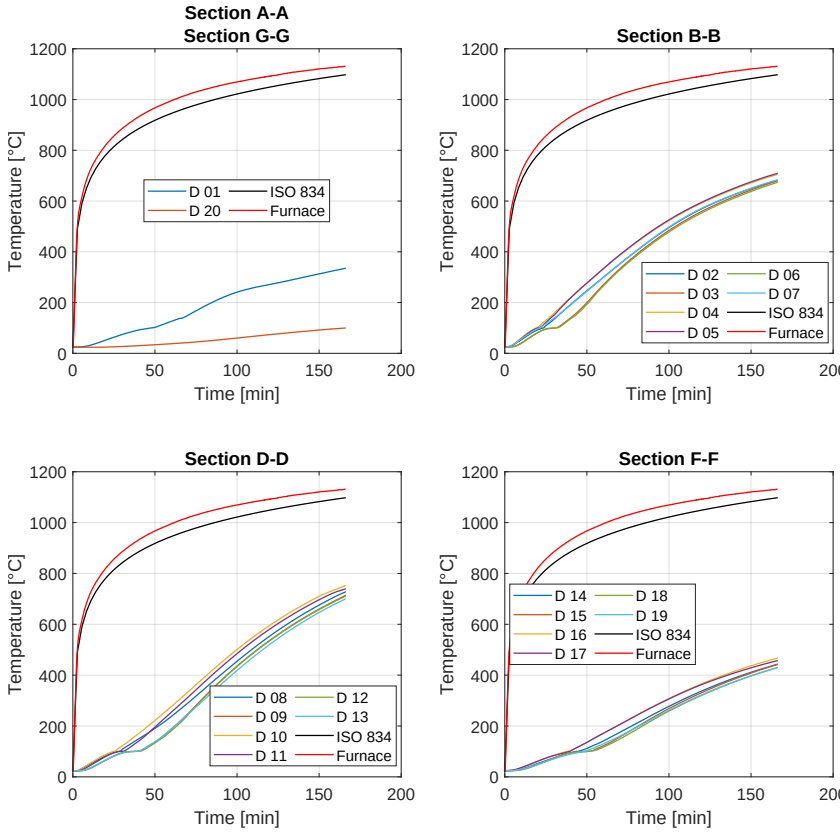

Figure 6.58: Column test D: evolution of the temperatures during the test.

Figures 6.59, 6.60, 6.61, 6.62 and 6.63 show the evolution of axial force, axial displacement, horizontal force and horizontal displacement of the column during the three phases of the test; Phase I: application of the gravity load. Phase II: earthquake. Phase III: fire after the earthquake.

Figure 6.63a presents the comparison of the horizontal force against the horizontal displacement during the earthquake test. Figure 6.63b presents the comparison of the axial force against the axial displacement during the fire after the earthquake.

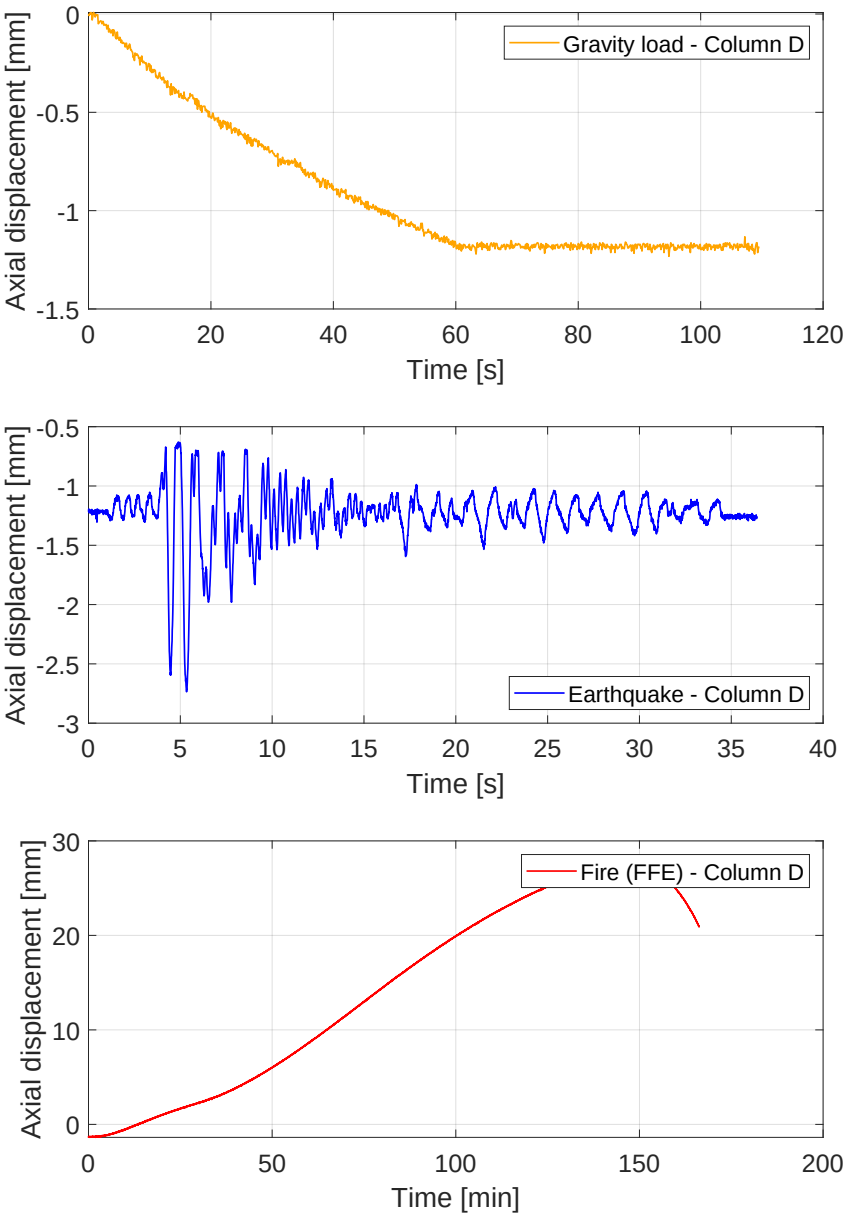

Figure 6.59: Column test D: evolution of the axial displacement.

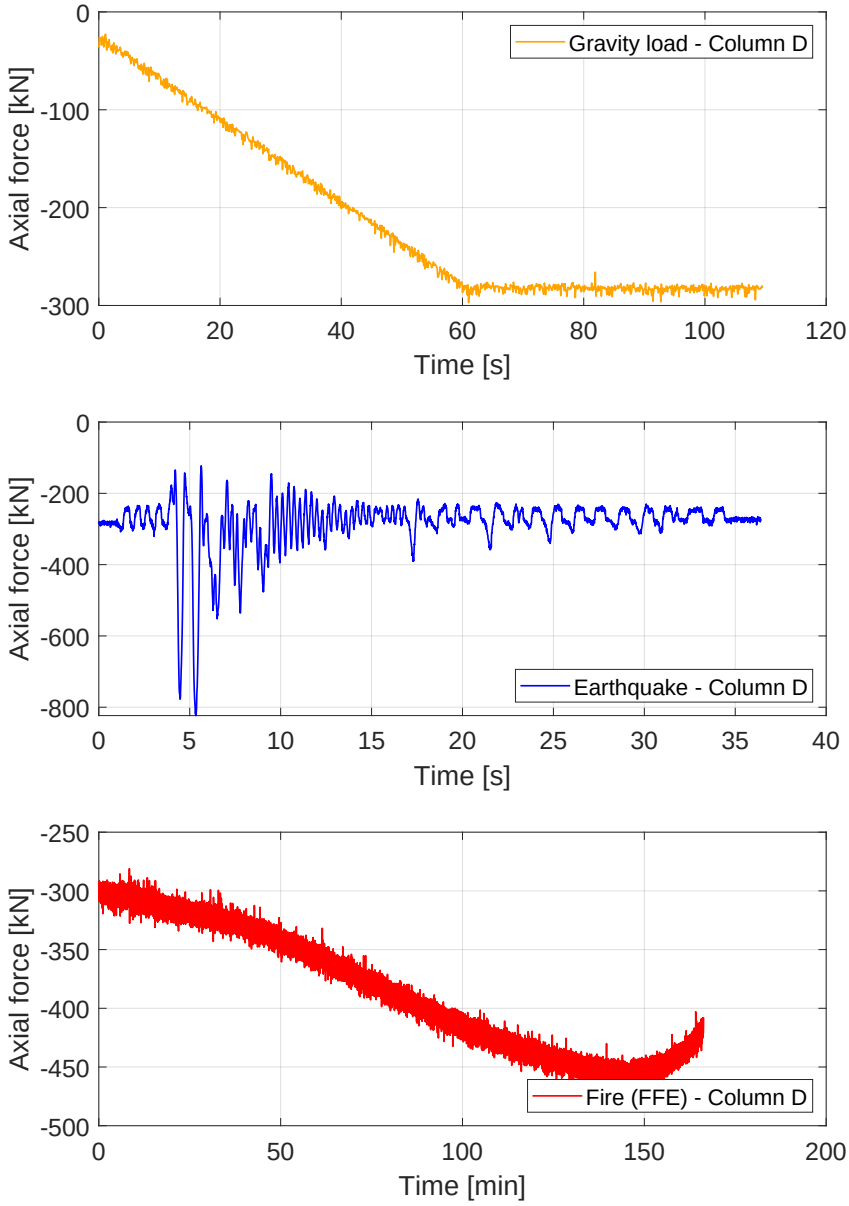

Figure 6.60: Column test D: evolution of the axial force.

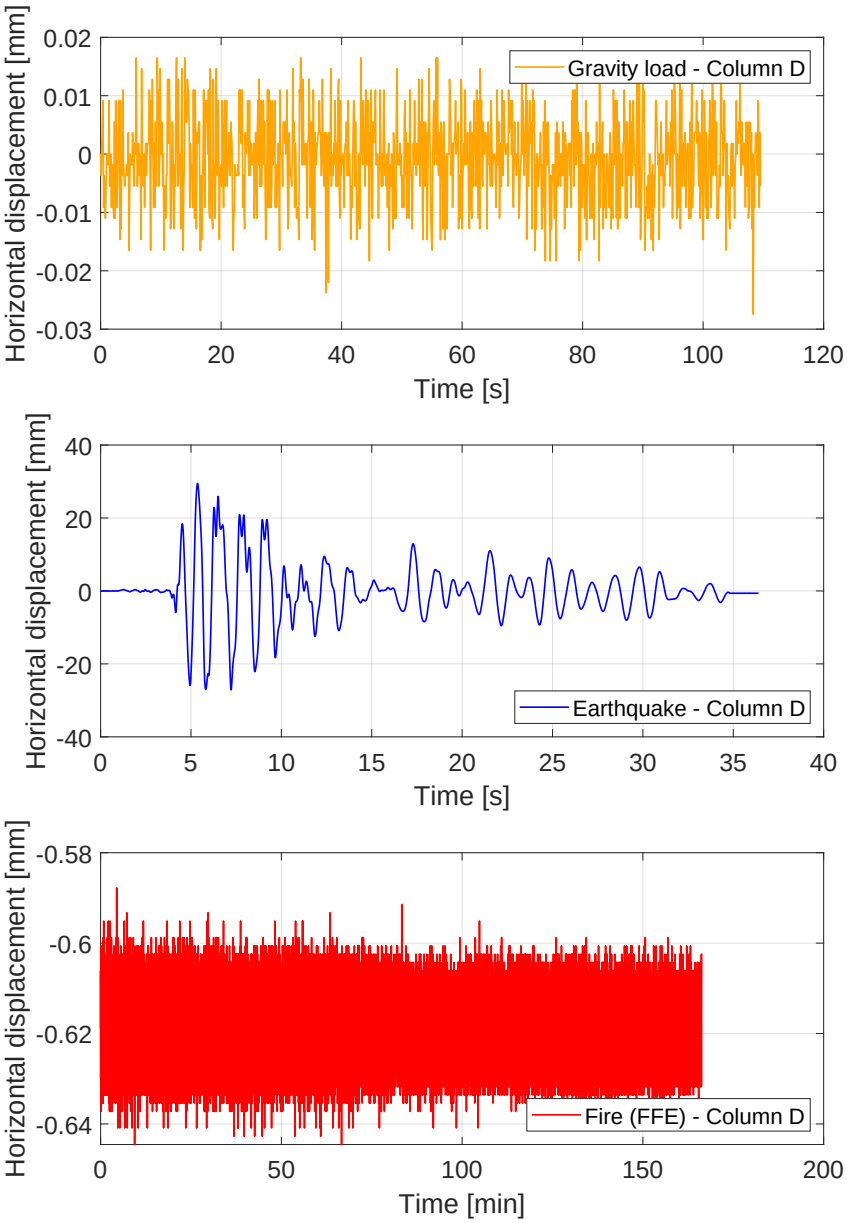

Figure 6.61: Column test D: evolution of the horizontal displacement.

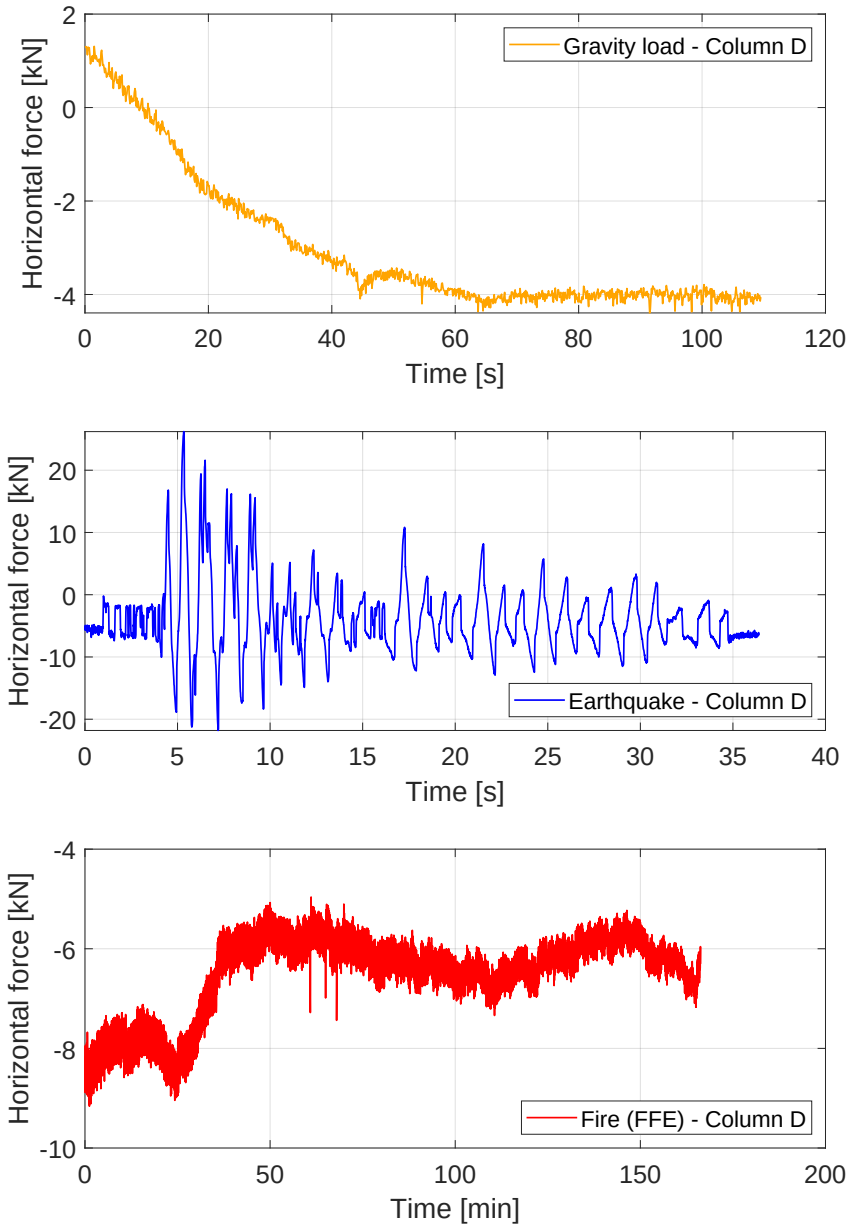

Figure 6.62: Column test D: evolution of the horizontal force.

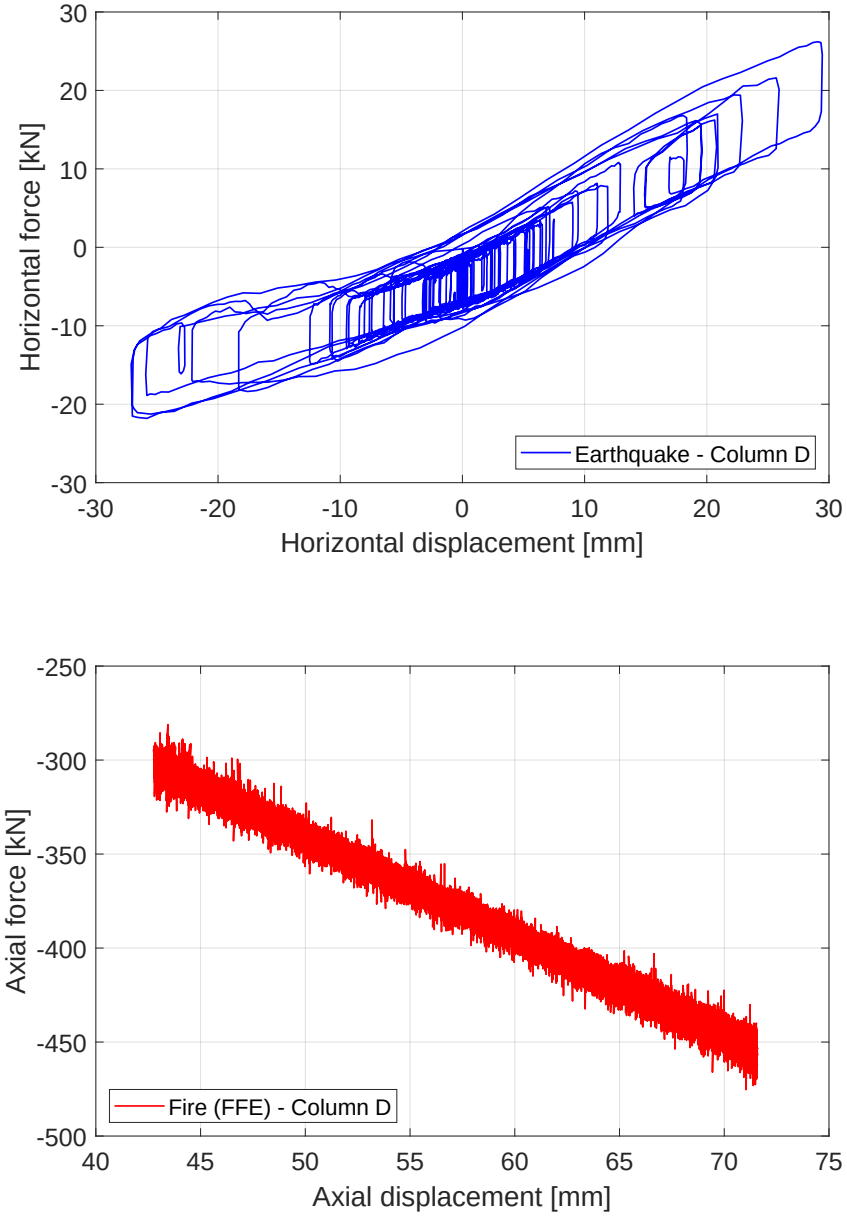

Figure 6.63: Column test D: displacement vs force.

As shown from the pictures and the experimental results, the buckling of the column occurred 140 minutes after the start of the fire.

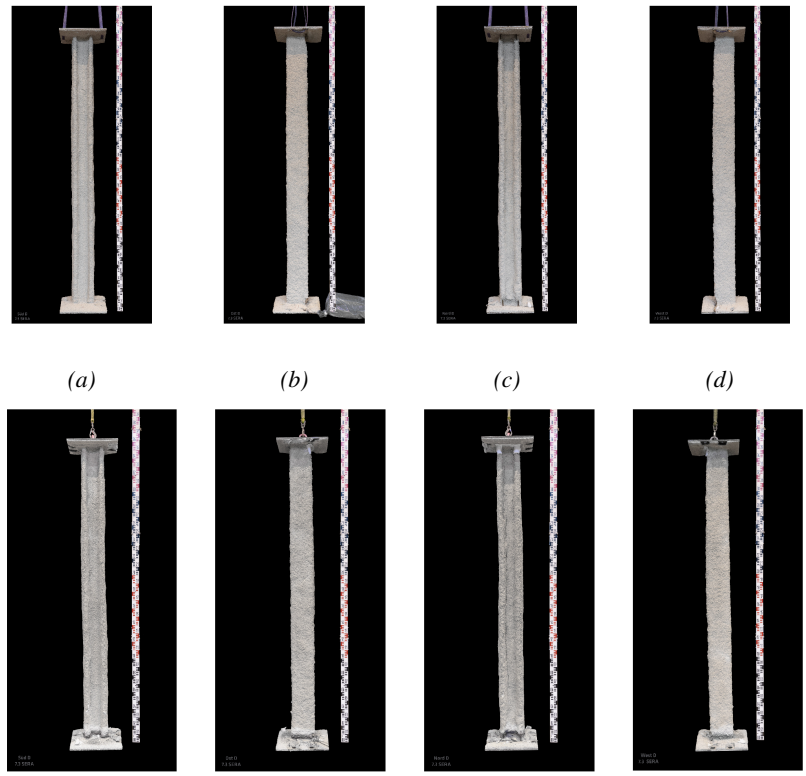

Figure 6.64: Comparison before and after the test a) south side (before); b) east side (before); c) north side (before); d) west side (before); e) south side (after); f) east side (after); g) north side (after); h) west side (after).

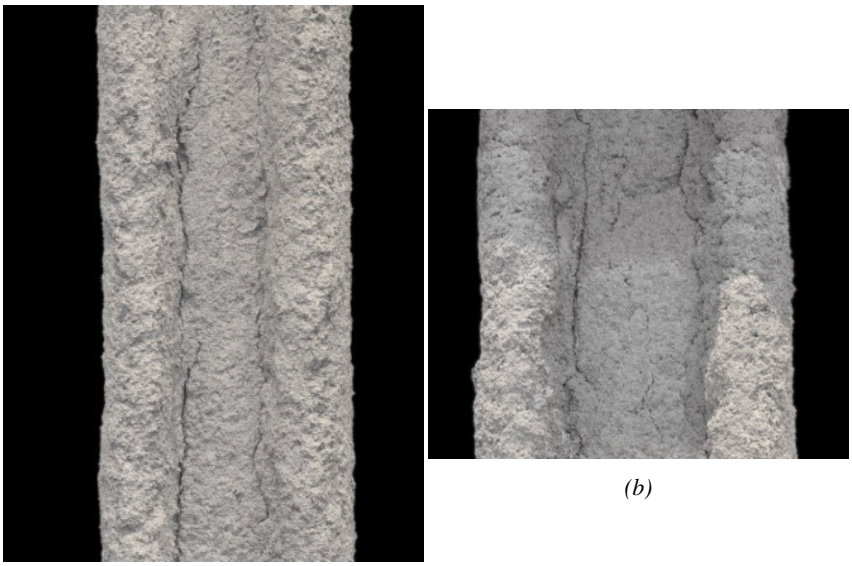

(a) *(b)*

Figure 6.65: Damage on the fire protection elements due to the combination of seismic and fire actions: test #2 column B

6.5 Photogrammetry 3D model

After each tests several photos of the specimen, in addition to the official ones, were taken in order to reconstruct a 3D model of the columns after the tests using the photogrammetry techniques.

The photogrammetry software:

- Determine the relative position and orientation of the camera pose for each photo relative to the imaging subject, as shown in Figure 8.81a.
- Generate a sparse and dense point cloud of 3D points from finding and matching locations in two or more photographs that depict the same feature on the imaging subject, as shown in Figure 8.81b.
- Generate 3D model with texture using point clouds, as shown in Figure 6.67.

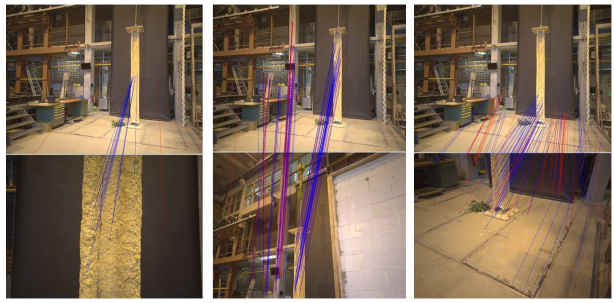

(a)

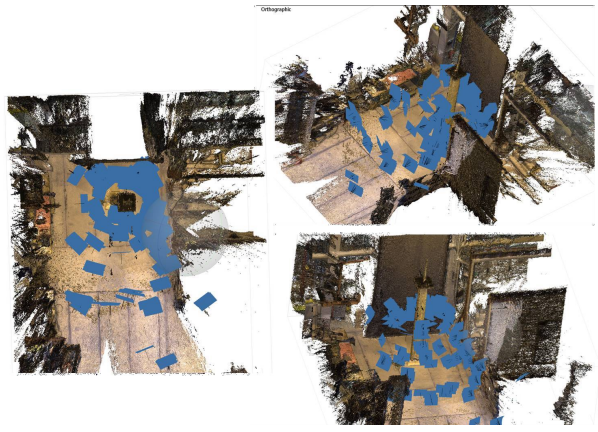

(b)

Figure 6.66: a) example matches between photos; b) Point Clouds.

(a) *(b)*

Figure 6.67: 3D model of the column #D obtained using the photogrammetry methodology: a) wired model; b) Textured model.

Photogrammetry allows to perform visual comparison and also measurements in order to evaluate the evolution of damage before and after each test.

6.6 Main outcomes and discussion

The EQUFIRE project focused on a three-bay, four-storey steel frame with concentric bracing in the central span, subjected to fire following an earthquake, with the aim to study the performance of structural and non-structural components. Five preliminary FFE substructure tests were carried out at the BAM laboratory. Tests for fire after earthquake were carried out on two steel columns without fire protection and three columns with different fire protection solutions: conventional and earthquake-proof boards system and gypsum-based wet mix spray-applied fire-resistive material. In terms of fire protection, no severe damage was observed that would undermine the fire resistance of the columns. More significant damage to the fire protection of the dissipative elements (bracing system) is expected during the FFE test series at the ELSA Reaction Wall. Indeed, testing a complete bracing system, including the dissipative braces, should reproduce the actual earthquake conditions, where the compressed brace is expected to cause more severe damage to the fire protection elements due to buckling under large horizontal displacement.

Acknowledgements

This work has received funding from the European Union's Horizon 2020 research and innovation program under the SERA grant agreement No. 730900 and the related TA project EQUFIRE. Author would acknowledge Manfred Korzen (BAM), Philippe Buchet (EC-JRC) as well as Sven Riemer (BAM) KaiUwe Ziener (BAM), F. Klemmstein (BAM), B. Klaffke (BAM), I.Uzelac (BAM), F Kiesel (BAM), Sascha Hothan (BAM), Marco Antonelli and Peter Schultz (ETEX-PROMAT), for their invaluable contribution to the experimental campaign at BAM.

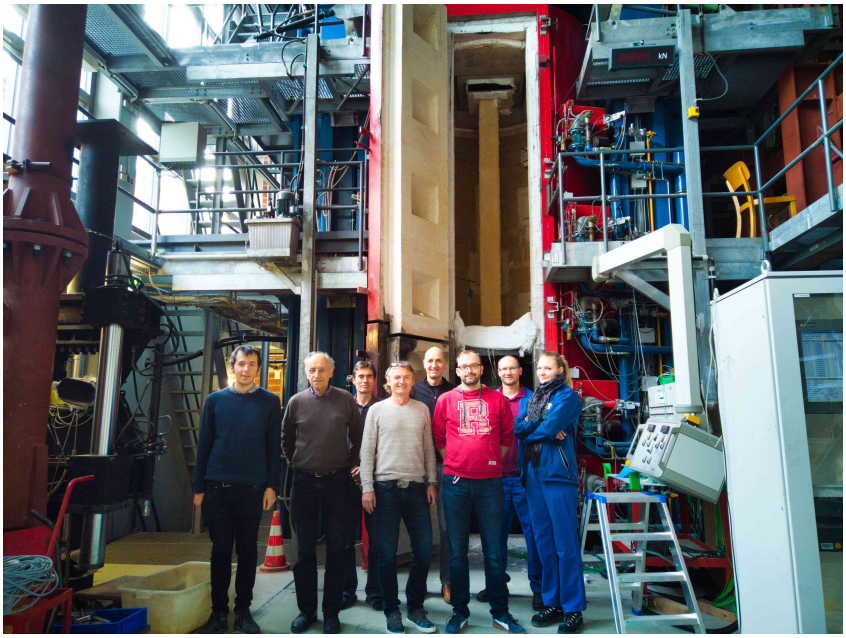

Figure 6.68: EQUFIRE tests at Fire Engineering laboratory (BAM) (From Left: P. Covi, M. Korzen, S. Riemer, K. Ziener, F. Klemmstein, B. Klaffke, I.Uzelac, F Kiesel), November 2019.

Bibliography

[1] Z.-F. Pan, R. Schriever, H. M. Bock, and M. Korzen, "Comparison of the temperature distribution in isolated steel columns tested in two furnaces," *Fire technology*, vol. 33, no. 4, pp. 316–335, 1997.

[2] M. Korzen, G. Magonette, and P. Buchet, "Mechanical Loading of Columns in Fire Tests by Means of the Substructuring Method," *Zeitschrift für Angewandte Mathematik und Mechanik*, vol. 79, pp. 617–S618, 1999.

[3] CEN, "Fire classification of construction products and building elements - Part 1: Classification using data from reaction to fire tests," european standard, European Union, Dec. 2018.

7.0 Numerical-experimental analysis of a braced steel frame subjected to fire following earthquake

This chapter contains the following unpublished paper under preparation:

"Numerical-experimental analysis of abraced steel frame subjected to fire following earth-quake." *Patrick Covi, Nicola Tondini, Manfred Korzen, Georgios Tsionis.*

Abstract

Many historical events have shown that, after an earthquake, fire may be triggered by the seismic-induced rupture of gas piping, failure of electrical systems, etc. The current engineering design methods still ignore many aspects of multi-hazard and in particular, fire following earthquake (FFE) analysis. In this respect, this paper aims to study the behaviour of a braced steel frame subjected to seismic-induced fire. In particular, FFE numerical analyses were conducted on a four-storey three-bay braced steel frame with concentric bracings. The results of the numerical analyses served to design the FFE tests performed on unprotected and protected columns belonging to the bracing system. The fire tests after the seismic event were carried out by considering the effects of the surrounding seismically damaged structure. Results of the FFE tests on unprotected and protected columns are reported along with the numerical model calibration.

7.1 Introduction

Earthquakes are destructive and unpredictable events with catastrophic consequences for both people and built environment. Moreover, secondary triggered effects can strike further an already weakened community, i.e. ground shaking, surface faults, landslides and tsunamis. In this respect, also fires following earthquake (FFE) have historically produced large post-earthquake damage and losses in terms of lives, buildings and economic costs, like the San Francisco earthquake (1906), the Kobe earthquake (1995), the Turkey earthquake (2011), the Tohoku earthquake (2011) and the Christchurch earthquakes (2011). In detail, FFEs are a considerable threat as they can be widespread both at the

building level and at the regional level within the seismic affected area owing to the rupture of gas lines, failure of electrical systems etc. and at the same time failure of the compartmentation measures. Moreover, they are more difficult to tackle by the fire brigades because of their possible large number and extent as well as of possible disruptions within the infrastructural network that hinder their timely intervention and within the water supply system.

In this context, the structural fire performance can worsen significantly because the fire acts on an already damaged structure. Furthermore, passive and active fire protections may have also been damaged by the seismic action and the fire can spread more rapidly if compartmentation measures have failed. Thus, the seismic performance of the non-structural components may directly affect the fire performance of the structural members. As a consequence, the minimization of the non-structural damage is paramount in mitigating the possible drop in structural fire performance. The loss of fire protection is particularly dangerous for steel structures because the high thermal conductivity associated with small profile thicknesses entails quick temperature rise in the profiles with consequent fast loss of strength and stiffness. Most of the literature involve numerical simulations on steel moment-resisting frames [1][2][3][4] and only a few of them are dedicated to buckling-restrained and conventional brace systems [5][6]. Both developed a framework for evaluating the post-earthquake performance of steel structures in a multi-hazard context that incorporates tools capable of probabilistic structural analyses under fire and seismic loads. Experimental studies have been performed on single elements [7], beam-concrete joints made of filled steel tubes [8], and full-scale reinforced concrete frames [9][10]. The literature study reveals that several numerical studies on the post-earthquake fire behaviour of structural components have been carried out without being supported by comprehensive experimental research. Moreover, works on non-structural components are also very limited. On these premises, the European project called EQUFIRE was funded.

7.2 SERA EQUFIRE project

The EQUFIRE project aims to provide experimental data to investigate the post-earthquake fire performance of steel structures. It is part of the Transnational Access activities of the SERA project (www.sera-eu.org) at the ELSA Reaction Wall of the European Commission - Joint Research Centre (JRC). The project focuses on analysing the behaviour of a braced steel structure subjected to FFE through full-scale tests based on

hybrid simulation at the ELSA Reaction Wall and through tests on single elements at the furnace of the Federal Institute for Materials Research and Testing (BAM).

7.3 Case study

7.3.1 Design of the prototype building

A four-storey three-bay steel structure with concentric bracings in the central bay was selected as case study for simulations and experimental tests, as shown in Figure 1. This frame is part of an office building with a square plan (12.5 m x 12.5 m) and the location of the building was assumed to be in the city of Lisbon (Portugal); thus, in an area of medium-high seismicity. The storey height is 3.0 m except for the height of the first floor, which is equal to 3.6 m. The lateral force resisting system consists of concentrically braced frames (CBF). Figure 1 also shows the member sizes and the column that was then heated after the seismic event, i.e. the column represented in red. Due to experimental constraints, only one member was heated at BAM, whereas the whole first floor was built at the JRC.

Two different steel grades were used, namely S275 and S355 (EN 10025-2, 2019). Steel grade S275 was adopted for the dissipative elements, i.e. the bracings, while steel grade S355 was selected for the non-dissipative members, i.e. columns, beams and connections. It is worth pointing out that the yield strength for the bracings was taken as the mean value, i.e. 330 MPa, considering a coefficient of variation equal to 0.12, whereas for the non-dissipative members was taken the experimental value obtained through material testing, i.e. 436 MPa. In detail, IPE sections with the weak axis in the plane of the frame were used for the bracing elements to force in-plane buckling for essentially two reasons: i) to avoid damage in the walls where the bracing is inserted in; ii) to keep a 2D modeling of the frame representative so that to maintain low computational demand for the hybrid tests. In accordance with the Eurocode 8 [11], the frame was designed according to the capacity design criterion by employing a response-spectrum analysis (RSA). In particular, a “High Ductility Class (DCH)” was employed with dissipation in the bracing members. Then, nonlinear time-history analyses with natural accelerograms were employed to investigate the seismic response of the structure. The general assumptions were the following:

- The columns were considered continuous along the height of the structure.

- All connections were assumed as pinned.
- The building was regular in plan and in elevation.
- The building was located in Lisbon characterised by peak ground acceleration equal to 0.186g and type B soil.

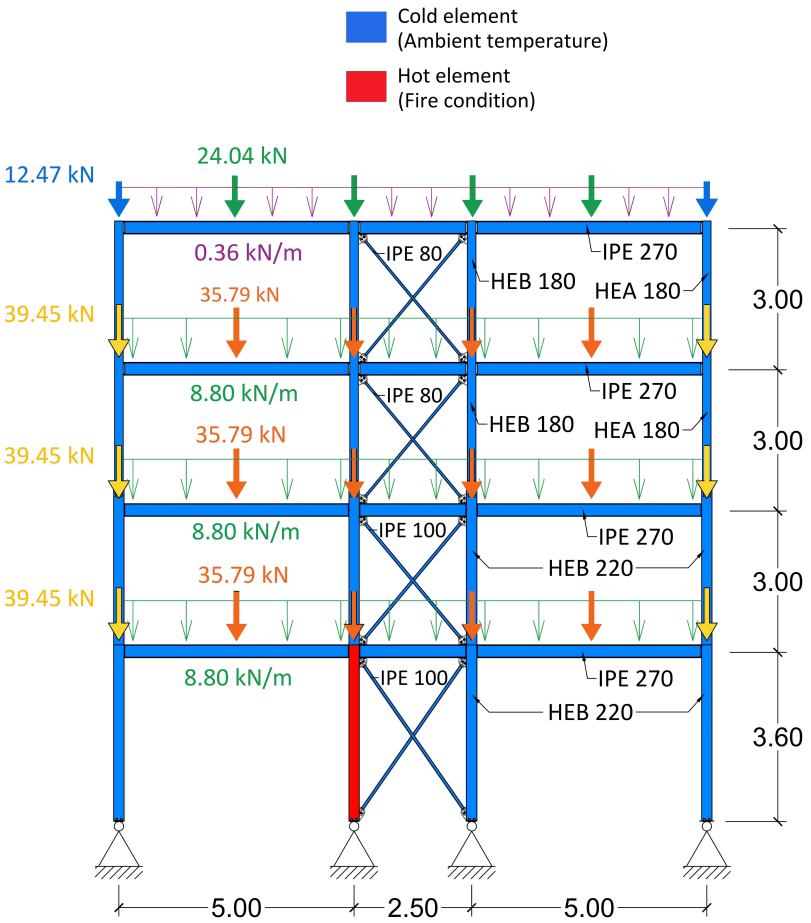

Figure 7.1: Test frame. Dimensions are in meters.

7.3.2 Set of accelerograms

In order to perform nonlinear time-history analyses, it was fundamental to model the seismic hazard through adequate selection and scaling of ground motion records. In this respect, a set of fifteen accelerograms for

the SD limit state was selected considering the type of spectrum, magnitude range, distance range, style-of-faulting, local site conditions, period range, and ground motion components using the INGV/EPOS/ORFEUS European Strong motion Database [12]. As shown in Figure 2, accelerograms were modified to match the target spectrum in the period range of 0.4÷0.9s that includes the fundamental period of the structure, i.e. 0.67 s. The accelerograms were used to perform nonlinear time-history analyses and fire following earthquake (FFE) analyses. A 2D and 3D model of the building was developed in OpenSees [13] software to conduct seismic, fire and FFE numerical analyses of the braced steel frame.

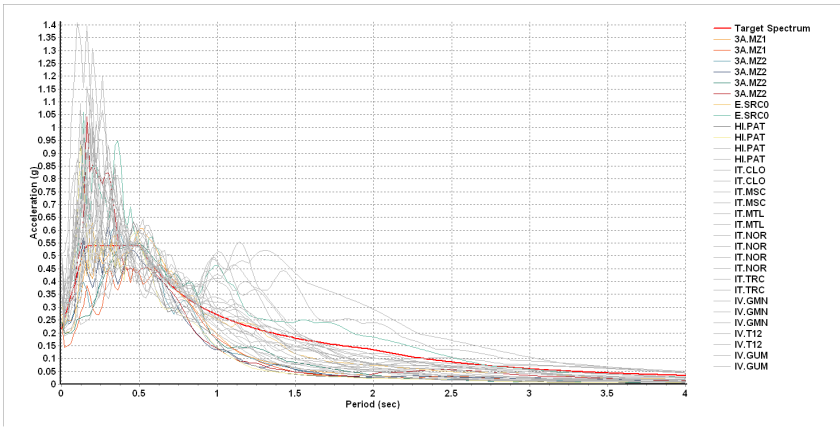

Figure 7.2: Comparison of the response spectra for original and modified vs the target spectrum.

The accelerogram shown in Figure 3 was selected for the experimental hybrid tests and the numerical analyses, based on three main requirements:

- The selected accelerogram had to cause significant damage to the bracings.
- The horizontal displacement of the first floor had to be equal or lower than ± 30 mm to be compatible with the horizontal actuator stroke of the BAM furnace.
- The axial force of the internal columns at the beginning of the second floor had to be below 1000 kN to be compatible with the actuators used to impose the vertical loads on the specimen at the ELSA Reaction Wall.

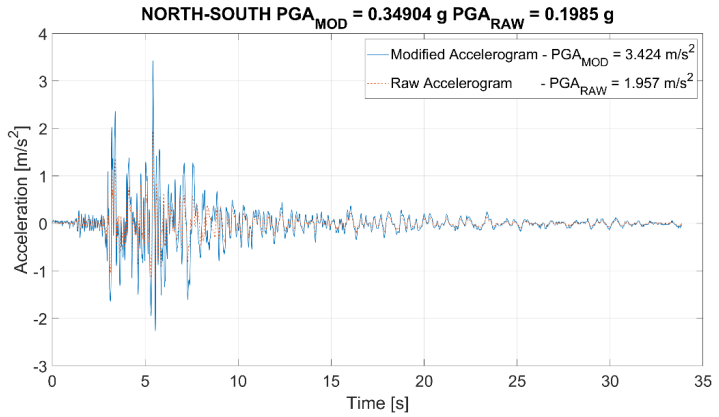

Figure 7.3: Selected accelerogram for simulations and tests.

7.4 Numerical models

Three different finite element models were created:

- Model #2D_OPENSEES: A 2D FEM model of the full frame using OpenSees.
- Model #3D_OPENSEES: A 3D FEM model of the column inside the furnace using Opensees.
- Model #3D_SAFIR: A 3D FEM model of the column inside the furnace using SAFIR.

7.4.1 Model #2D_OPENSEES

A 2D non-linear finite element model in OpenSees was developed to evaluate the FFE response of the full structure, which is expected to experience large plastic deformations in the bracing elements due to the seismic action and in the column due to the fire exposure. The fibre displacement-based beam-column element was used to model the beams, columns and braces. Seven non-linear beam elements based on corotational formulation and the uniaxial Giuffre-Menegotto-Pinto steel material, with isotropic strain hardening (Steel02Material) [14] and geometric nonlinearities was used for the bracing diagonals. Nonlinear beam elements were used for all elements to check that non-dissipative elements remain in the elastic field owing to the seismic action. Geometric imperfections were included to allow for buckling EN 1993-1-1 [15]. Masses were considered lumped on the floors, following the assumption of rigid

diaphragms. The constitutive law provided by EN 1993-1-2 [11] was adopted to model the mechanical properties of steel at elevated temperature when for the column that was heated after the earthquake.
The columns and the braces were oriented according to the weak axis in the plane of the frame in order to force in-plane buckling so that a 2D modelling was representative. This model was also used to determine an axial stiffness representative of the surrounding structure of the column inside the furnace, as explained in more detail in paragraph 7.5.2.

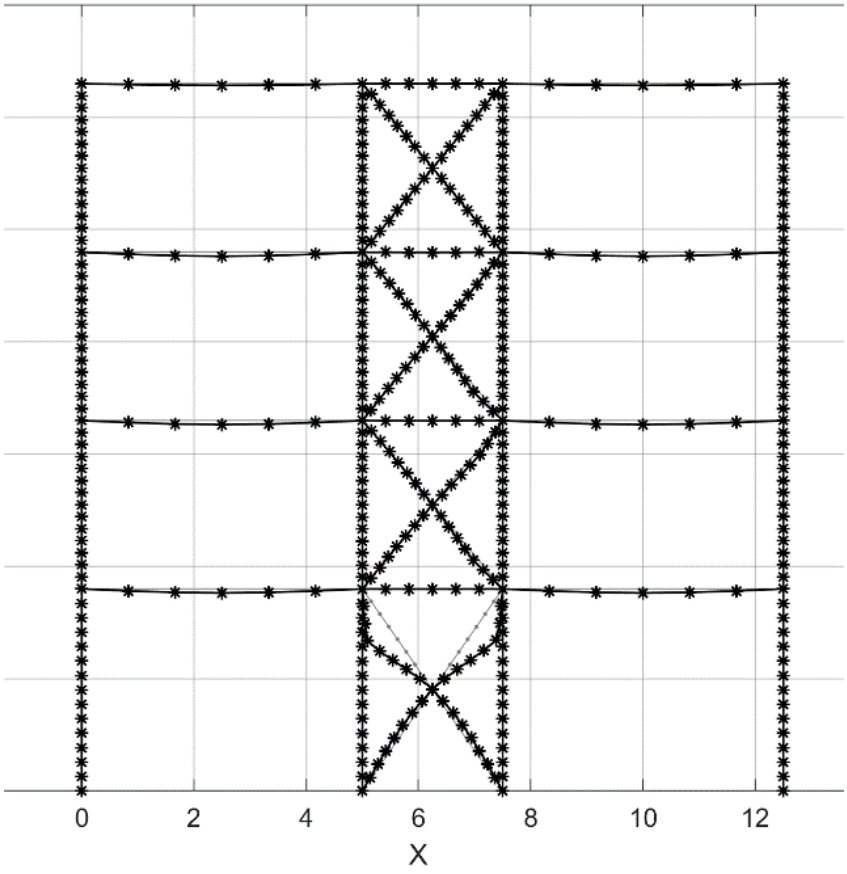

Figure 7.4: 2D non-linear finite element model of the full frame in OpenSees

7.4.2 Model #3D_OPENSEES

A 3D non-linear finite element model was developed to evaluate the FFE response of the unprotected columns inside the furnace. The fibre displacement-based beam-column element was used to model the column. Fifteen non-linear beam elements based on corotational formula-

tion and the constitutive law provided by EN 1993-1-2 [11] was adopted to model the mechanical properties of steel at elevated temperature when for the column that was heated after the earthquake.
It was first subjected to the gravity load, then to horizontal and vertical displacement histories resulting from seismic non-linear dynamic analysis. Afterwards, thermal action was applied with a constant axial stiffness value equals to 5.3 kN/mm representative of the surrounding structure, as boundary conditions according to paragraph 7.5.2.

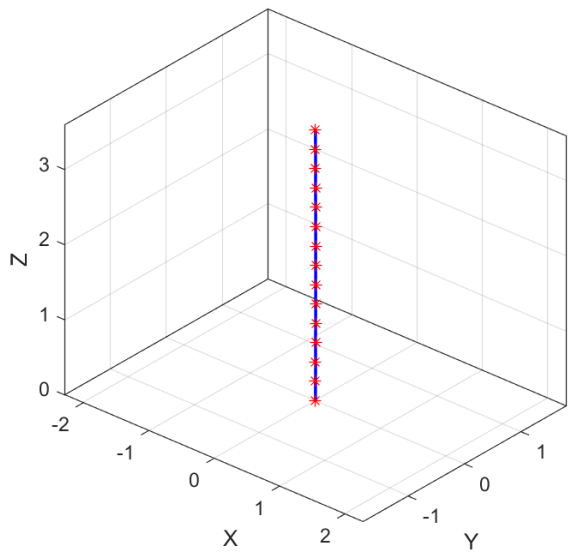

Figure 7.5: 3D non-linear finite element model of the column in OpenSees

7.4.3 Model #3D_SAFIR

Two 3D non-linear finite element models with different types of elements were developed to evaluate the FFE response of the columns inside the furnace. One model was created using beam elements and the other one using shell elements.
In detail, those models were used to simulate both the protected and unprotected columns subjected to only the fire event because SAFIR is not able to perform seismic analyses. Therefore, before starting the fire procedure, the column was first subjected to the same axial load resulting from the column of the #2D_OPENSEES model after the earthquake time history. This choice was possible because the column remains in the elastic field owing to the seismic action. Afterwards, thermal action was

applied with a constant axial stiffness value equals to 5.3 kN/mm representative of the surrounding structure, as boundary conditions according to paragraph 7.5.2.

Beam element

The column was subdivided vertically into 72 elements of 0.05 m length.

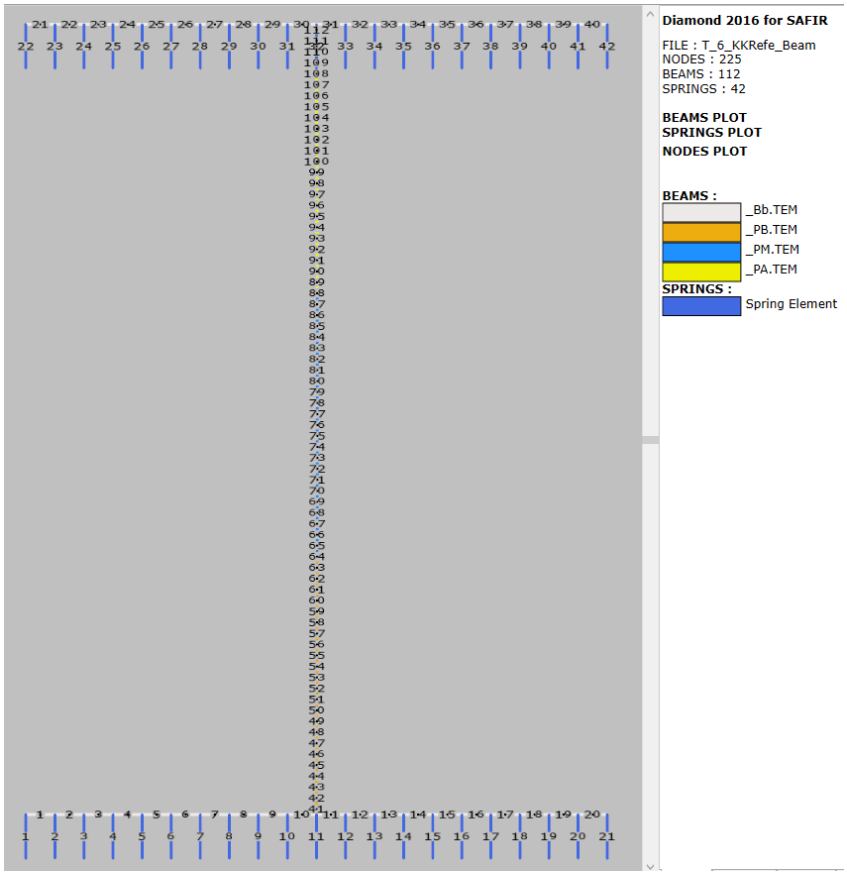

Figure 7.6: Mesh column using beam elements

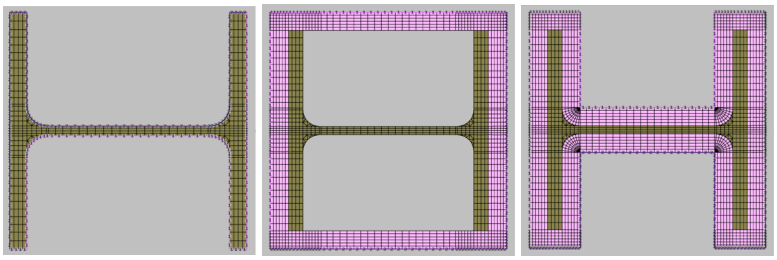

(a) *(b)* *(c)*

Figure 7.7: Sections: a) Columns #A and #E; b) Columns #B and #C; c) Column #D.

Shell element

The column was subdivided vertically into 72 sections of 0.05 m in length to maintain congruence with the subdivision of the Beam elements. The flanges were subdivided into four elements over the width and the core was subdivided into 16 elements over the length.

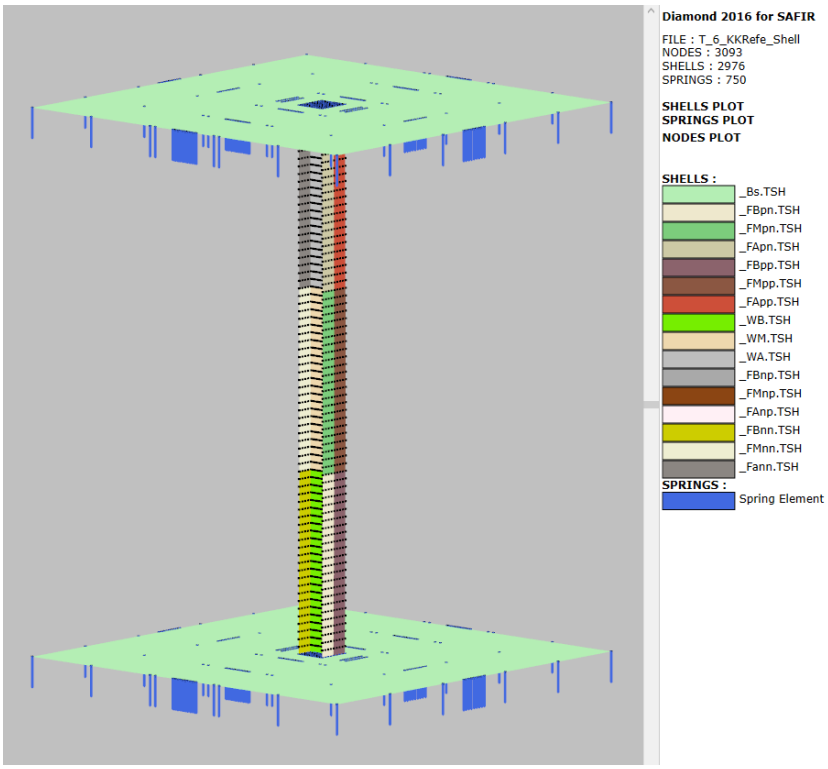

Figure 7.8: Mesh column using beam elements

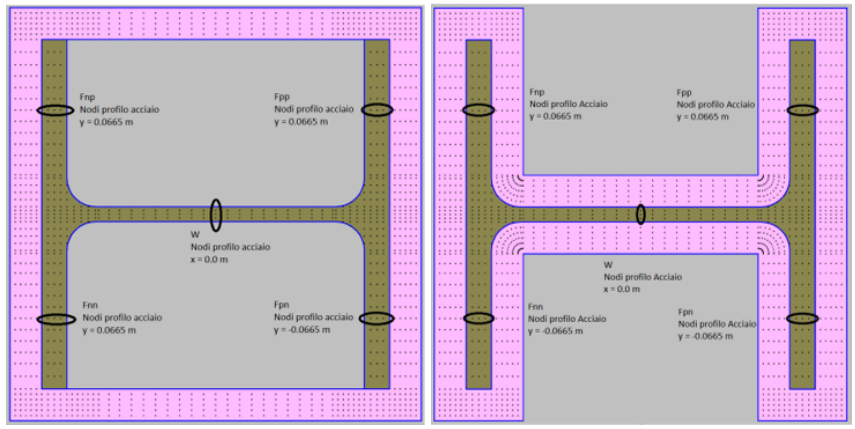

(a) *(b)*

Figure 7.9: Sections: a) Columns #B and #C; b) Column #D.

7.4.4 Fire following earthquake simulation

Figure 7.10 illustrates the results of the numerical simulation of the FFE test on the bare structure (without fire protection) using the model #2D_-OPENSEES for the selected acceleration time-history followed by the ISO 834 [16] heating curve. As is possible to observe, the energy dissipation is concentrated in the braces and, in particular, on the ground floor. The internal columns and all the other elements remained in the elastic field during the seismic event. After the earthquake, the fire was initiated and collapse occurred 24 minutes after the start of the fire. Figure 7.10 also shows the final deformed configuration of the steel frame at the end of the simulation.

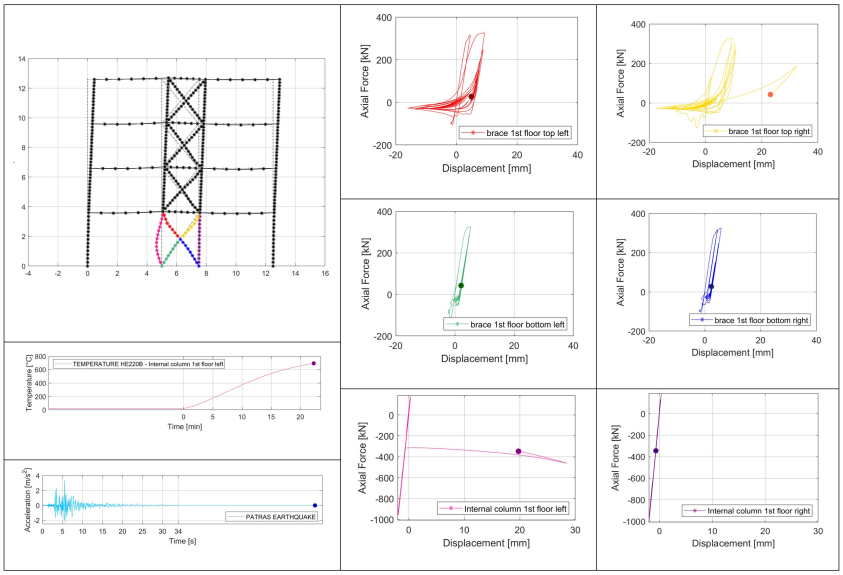

Figure 7.10: Numerical fire following earthquake simulation using OpenSees

7.5 FFE tests at BAM

7.5.1 Experimental setup

The experimental tests at BAM were performed using a substructuring technique as shown in Figure 7.11, in which the physical column was firstly subjected to the horizontal and vertical displacement time-histories computed through numerical modelling (see Section 7.4). Then, the column was heated by the ISO 834 standard heating curve and a constant numerical axial stiffness representative of the surrounding structure was applied as a boundary condition at the top of the physical column. During the fire part of the FFE tests, the axial force of the column was measured and displacements were then imposed on the column to keep the two substructures in mechanical equilibrium. Five FFE tests were conducted at BAM:

- Test #0 Column E: without fire protection system;
- Test #1 Column A: without fire protection system;
- Test #2 Column B: fire protection system, PROMATECT-H, designed for seismic region;
- Test #3 Column C: fire protection system, PROMATECT-H, not designed for seismic region;

- Test #4 Column D: sprayed vermiculite-type fire protection, PROMASPRAY P300 series, designed for applications in seismic region". The mechanical reinforcing mesh retained the sprayed coating. It was located in the middle of the overall coating thickness.

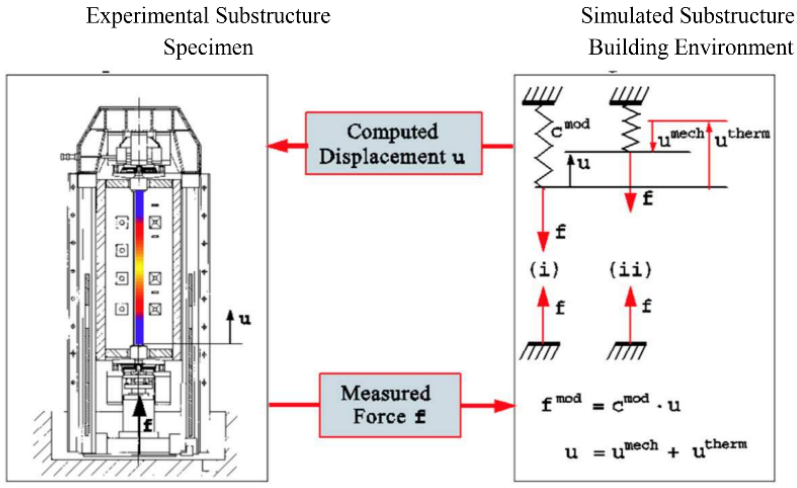

Figure 7.11: Sub-structuring method [17]

7.5.2 Equivalent stiffness of the numerical substructure during the fire events

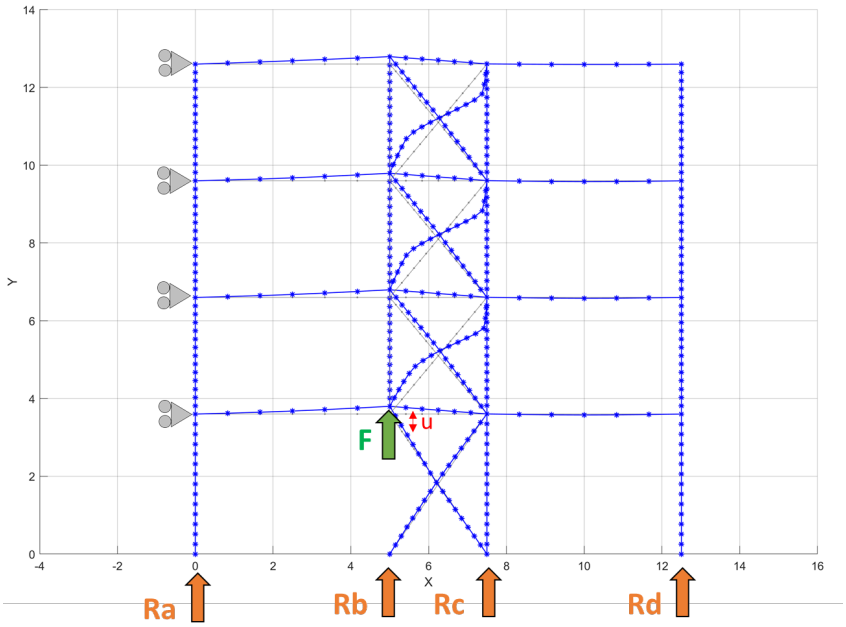

Figure 7.12: Static non-linear analysis to determine the axial stiffness value of the surrounding structure.

The axial stiffness of the upper part of the structure was numerically estimated by a static non-linear analysis. In detail, the full structure was subjected to gravity loads and to the selected accelerogram through non-linear time-history analysis. Then the physical column was removed and the frame was constrained at each floor to reproduce the boundary condition of the actual experimental setup at BAM. Finally, a monotonic displacement-controlled pattern, which continuously increases, was performed, as depicted in Figure 7.12. As shown in Figure 7.13 the equivalent stiffness of the surrounding structure after the seismic event is neither constant nor linear. Due to this reason, it was not possible to exactly reproduce the same axial force condition in the column during the test. However, the value of K was chosen to reach a similar critical temperature.

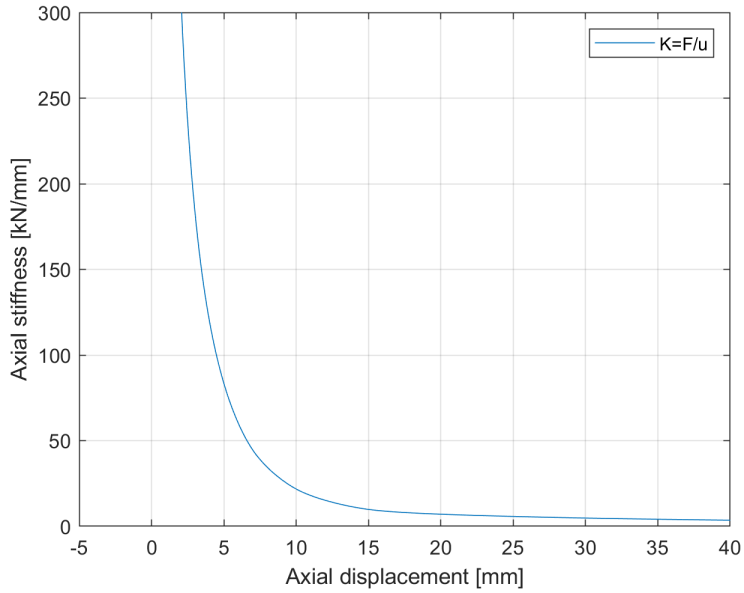

Figure 7.13: Axial stiffness of the surrounding structure vs axial displacement curve.

In this respect, two 3D models of the physical specimen were modelled in OpenSees with two different boundary conditions on top, i.e. pinned (Case A) and fixed conditions (Case B). The column was modelled with 15 non-linear thermomechanical beam elements. It was first subjected to the gravity load, then to horizontal and vertical displacement histories resulting from seismic non-linear dynamic analysis. Afterwards, thermal action was applied with different constant axial stiffness values (K between 5 and 15 kN/mm) representative of the surrounding structure, as boundary conditions. In order to determine the more appropriate equivalent axial stiffness value, Figure 7.14 shows the results in terms of the axial force and vertical displacement compared with the numerical analysis conducted on the whole structure. As it is possible to observe, a good value of the equivalent stiffness of the surrounding structure after the damage caused by the earthquake was equal to 5.3 kN/mm and this value was used in the tests. Moreover, the case with fixed conditions at the top of the column better agreed with the outcomes of the reference solution.

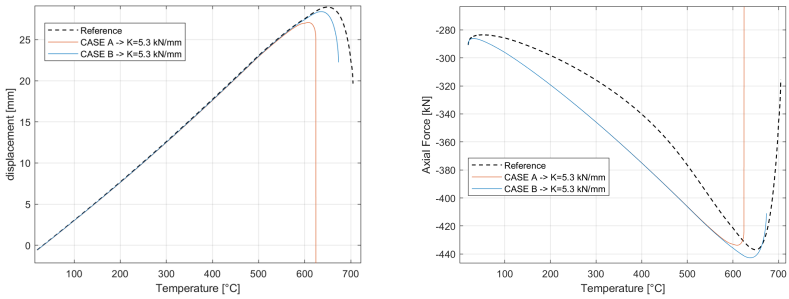

(a) *(b)*

Figure 7.14: Comparison between the reference numerical solution and the single column with constant axial stiffness: a) axial displacements vs temperature curve; b) axial forces vs temperature curve.

The results of the experimental tests at BAM are summarised in the following. The response history of the steel frame computed with 2D model in OpenSees was compared against the results of the experimental tests at BAM. Figure 7.15 shows the horizontal and axial displacement imposed to the specimens and the recorded axial force from the load cell. Overall the agreement is good. However, it is possible to observe that, due to the fairly high axial stiffness of the column, the actuator could not exactly follow the displacement time history, which implied some discrepancies in the applied force. There is a little difference in negative axial displacements, because the vertical actuator of the furnace cannot apply tension forces to the specimen.

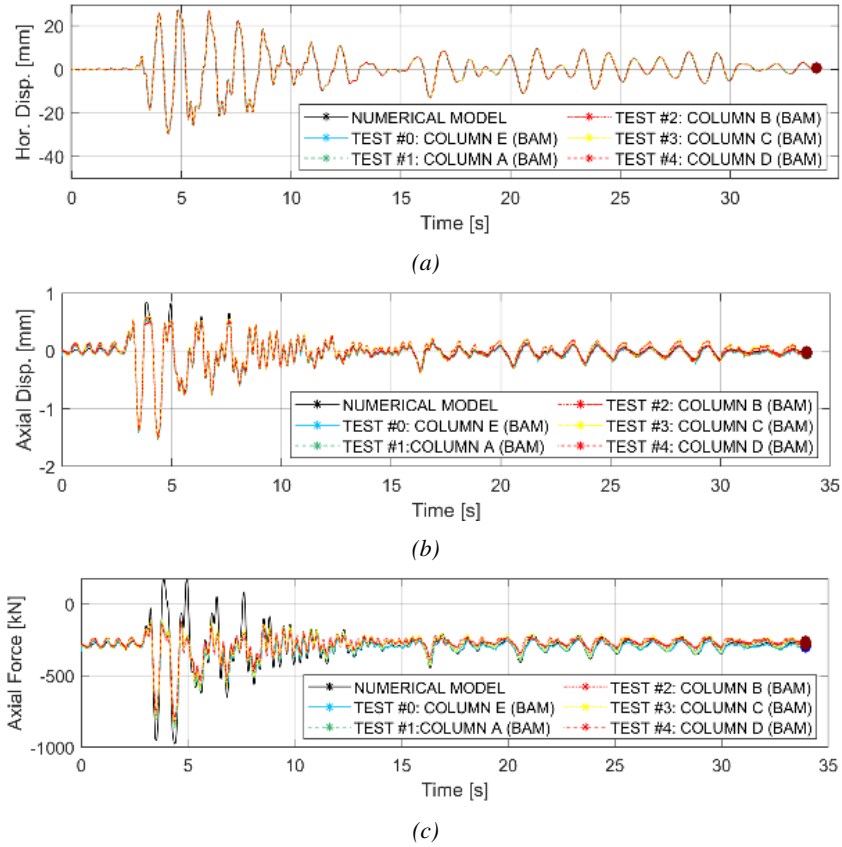

Figure 7.15: Seismic test: Comparison between the numerical solution and the tests: a) axial displacement and b) axial force.

However, at the end of the seismic event, the recorded axial force was consistent with the one obtained through numerical simulation. As expected, in all tests, the columns remained in the elastic range being non-dissipative elements of the bracing system.
Figure 7.16 shows the results of the fire tests after the seismic event for the two unprotected columns, i.e. Test #0 Column E and Test #1 Column A. The mean temperature in the cross section, as well as the experimental axial displacement and the axial force, are reported in Figure 7.16.

Moreover, the comparison with the numerical models before the calibration is also shown in Figure 7.16. The analysis before the calibration was performed by considering pinned boundary conditions and the standard ISO 834 [16] heating curve was employed. Good agreement between the experimental outcomes and the numerical prediction obtained from the model of the whole frame can be observed for the first 23 min, the time at which the numerical model experienced failure.

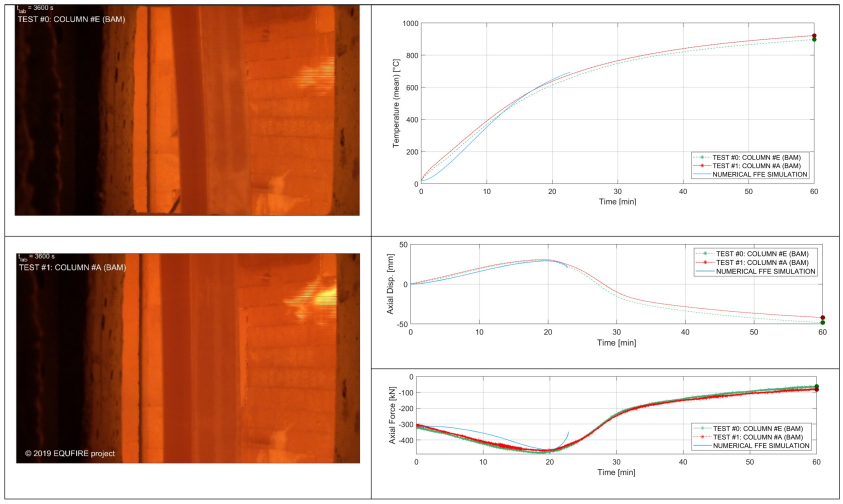

Figure 7.16: Comparison between the results of the numerical model and the FFE tests on the unprotected columns.

The complete comparison of the different numerical models against the experimental unprotected column tests is shown in Figure 7.17. Good agreement between the experimental outcomes and the numerical simulations can be observed in general for the first 17 min. Nonetheless, the experimental tests did not exhibit failure for the first 60 min.

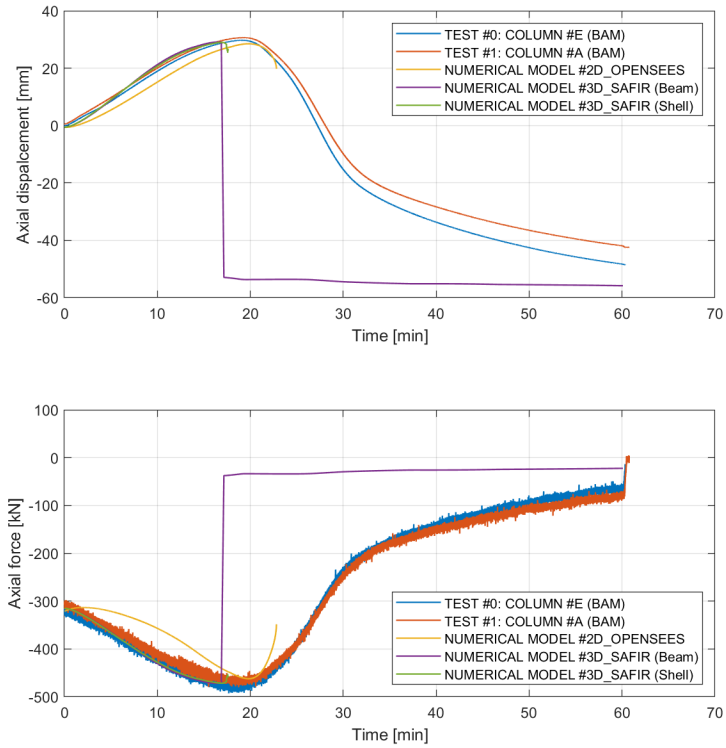

Figure 7.17: COLUMN #B: Comparison between numerical models and the tests on columns with fire protection.

Figure 7.18 presents the comparison of the evolution of the mean temperature, axial displacement and axial force of the FFE tests on the specimens with the three fire protection solutions (standard boards system, seismic-resistant boards system and vermiculite sprayed coating). Test #2 on column B was interrupted due to a malfunction of a component and then was restarted. The specimens with the two different fire protection boards systems (columns B and C) showed similar performance. The gypsum-based wet mix spray-applied fire-resistive material delayed the development of the temperature in column D with respect to columns B and C.

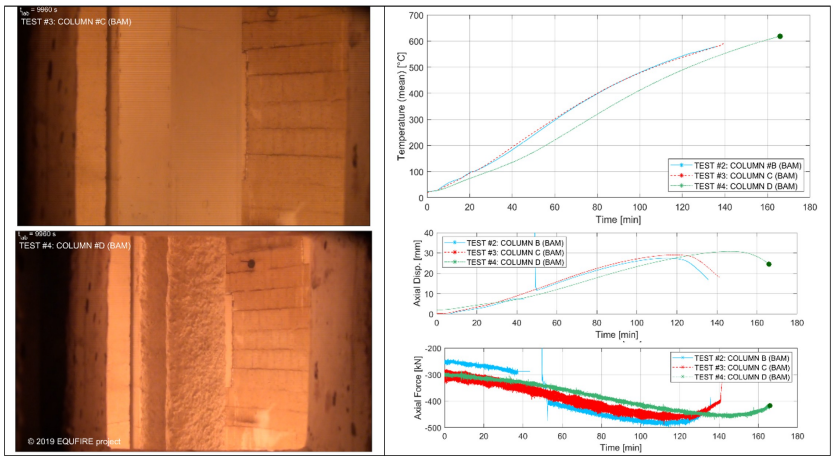

Figure 7.18: Results of the FFE tests on columns with fire protection.

The comparisons between the experimental tests on the columns with fire protection and the numerical models before the calibration are showed in Figure 7.19, Figure 7.20 and Figure 7.21.

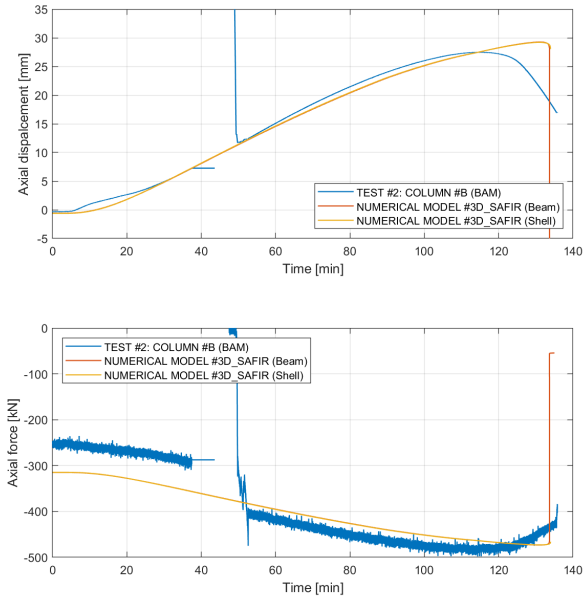

Figure 7.19: COLUMN #B: Comparison between numerical models and the tests on columns with fire protection.

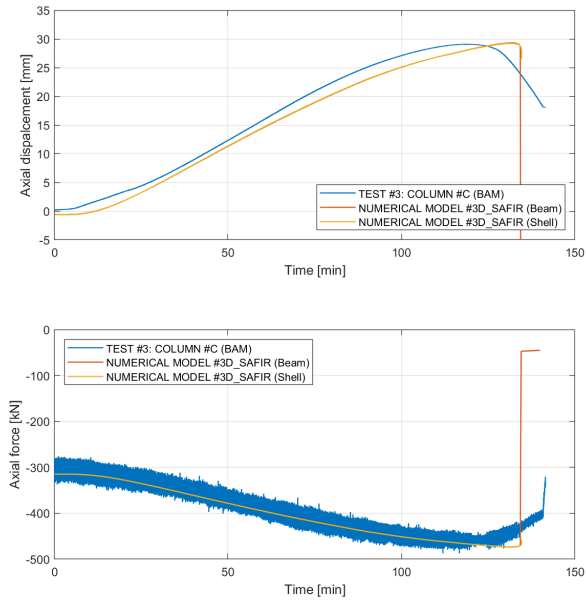

Figure 7.20: COLUMN #C: Comparison between numerical models and the tests on columns with fire protection.

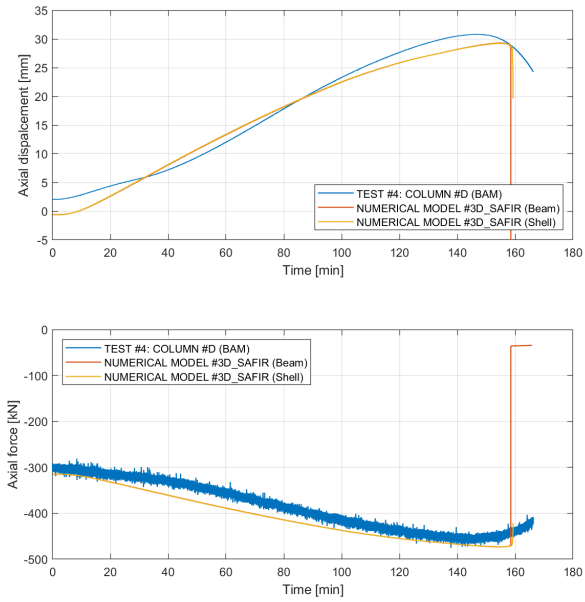

Figure 7.21: COLUMN #D: Comparison between numerical models and the tests on columns with fire protection.

It is also worth pointing out that since the column was designed according to the capacity design, the utilisation factor in the fire situation was relatively low and equal to 0.15. For the fire part, a calibration of the boundary conditions is needed in order to obtain more accurate models.

7.6 Model calibration

The calibration of numerical models consists in three different aspects to be considered:

- A rotational stiffness based on the real type of joint.
- A more representative temperature distribution.
- The real load state after the earthquake event measured in the laboratory.

The first calibration of the column numerical model consisted in modelling the boundary conditions by estimating the actual initial rotational stiffness based on the type of joint, as shown in Figure 7.22.

Figure 7.22: Axial stiffness of the surrounding structure vs axial displacement curve.

In fact, the preliminary numerical analyses were carried out with pinned connections at the bottom end. However, the actual bottom end joint was not a nominal pin but instead, it was made of a steel plate welded at the column and bolted to the base of the furnace. Therefore, even if the bolts were arranged in such a way to minimise the lever arm, some bending forces will always develop. For this reason, in the calibrated model, the column was considered rotationally restrained at both ends using rotational springs that reproduce as close as possible the actual stiffness of the joints. The rotational stiffness K_{rot} of the base connection was numerically estimated by using a 3D finite element model of the joint and the estimated value was equal to 3.1 MNm/rad as shown in Figure 7.23.

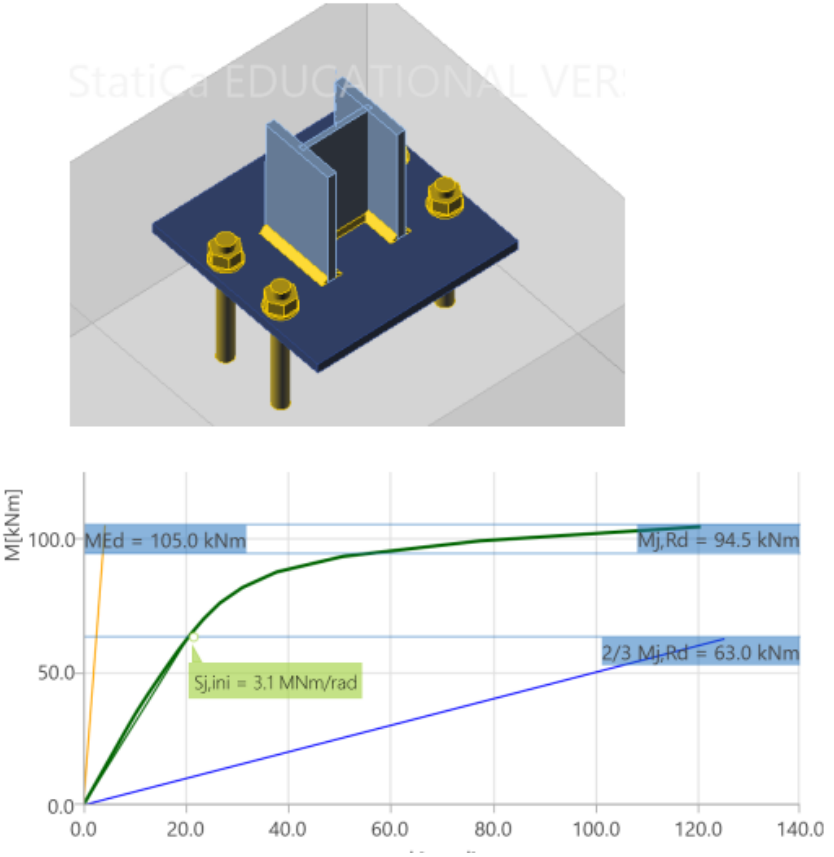

Figure 7.23: 3D finite element model of the joint.

In order to simplify, the same value of rotational stiffness was also given at the top end of the column because the joint was similar.

Moreover, the columns were fitted with thermocouples to measure the temperatures in different points of the cross-section. Three sections along the height of the column were considered, with six thermocouples. Additional 2 sections at the top and bottom plate were considered, with one thermocouple. Twenty thermocouples per column were installed as shown in Figure 7.24a. Therefore, for each specimen, the recorded temperature evolution in the column along its height was applied in order to be more representative of the actual temperature distribution, as illustrated in Figure 7.24b.

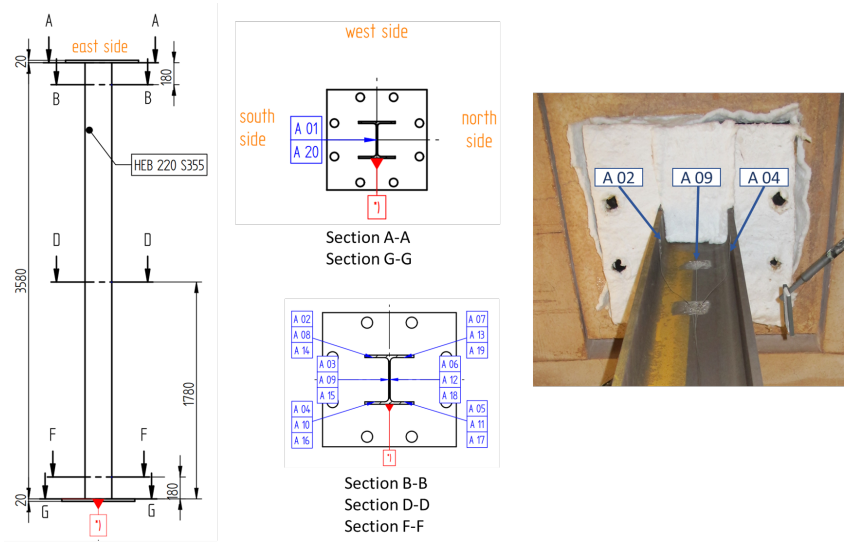

(a)

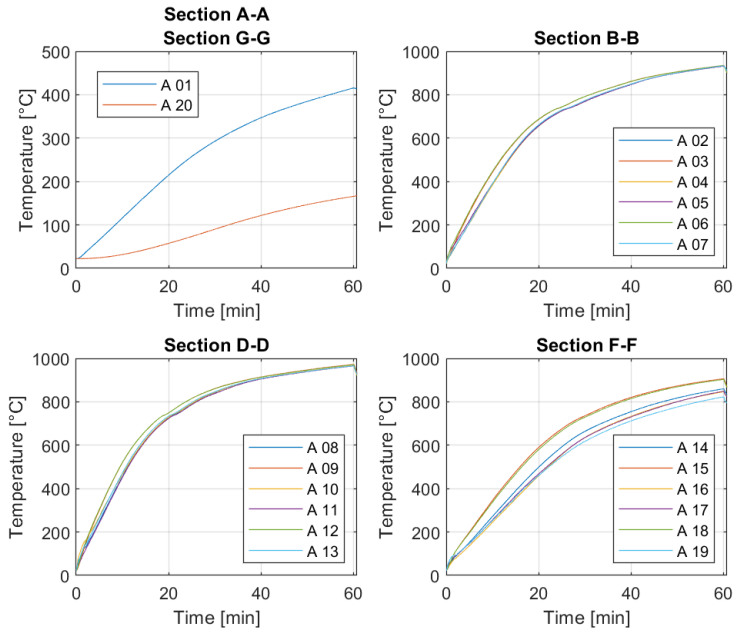

(b)

Figure 7.24: Column test A: a) cross section with position of the thermocouples; b) evolution of the temperatures during the test.

A difference in the axial force can be observed between the value measured immediately after the end of the seismic event and before the start of the fire, as illustrated in Figure 7.25. In a real FFE scenario, this

value remains constant, but in all the laboratory tests did not occur.

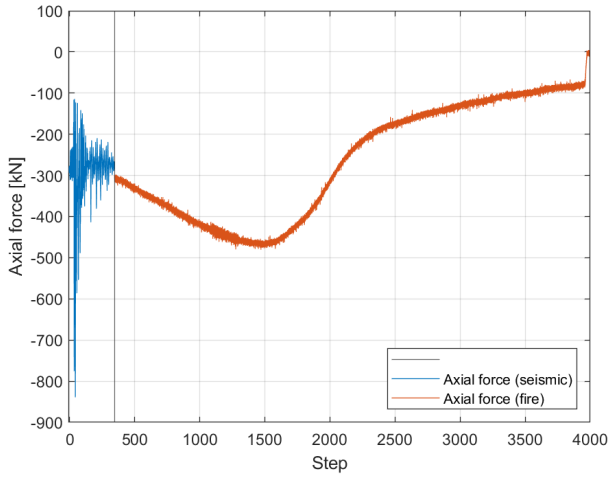

Figure 7.25: Axial force during FFE test of column A

In detail, due to laboratory reasons, the bolts of the top plate were removed before the fire test, keeping the column in position only by contact between the actuator and the end plates. This unscrewing operation is the main reason for the variation in the axial force measured at the column before the fire event.

(a) *(b)*

Figure 7.26: Comparison of the top plate connection: a) during earthquake event (presence of bolts); b) during fire event (absence of bolts).

7.7 Opensees calibrated model

7.7.1 Calibration

The column was modelled with 3D thermomechanical beam elements. Geometric imperfections were included, whereas the residual stresses were neglected. An axial spring was applied at the top of the column. The rotational stiffness Krot = 3.1 MNm/rad of connection was given at the top end and at the base. Moreover, for each specimen, the recorded temperature evolution in the column along its height was applied in order to be more representative of the actual temperature distribution, as illustrated in Figure 7.27.

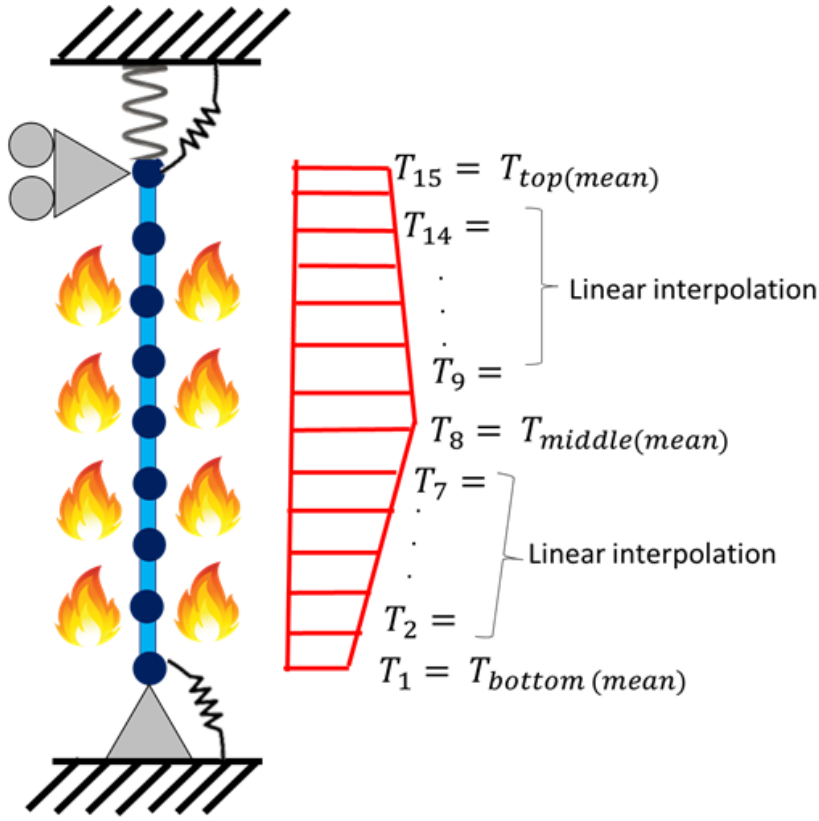

Figure 7.27: Axial stiffness of the surrounding structure vs axial displacement curve.

7.7.2 Results

The results of the model calibration are shown in Figure 7.28, in which it is possible to observe that a better agreement with experimental data, especially for the axial force, was achieved. Nevertheless, the numerical model reached failure after 28 min. This discrepancy may be caused by a temperature gradient within the cross-section, that was not considered in the modelling and by the actual rotational stiffness at the boundary conditions, which might have varied as the fire test progressed. Indeed, since the column ends were protected, as shown in Figure 11, an increase in rotational stiffness offered by the joint relative to the hot column as the steel temperature increased can be expected. Thus, a decrease of effective length could occur and this phenomenon was not taken into account because the rotational stiffness was kept constant during the simulation.

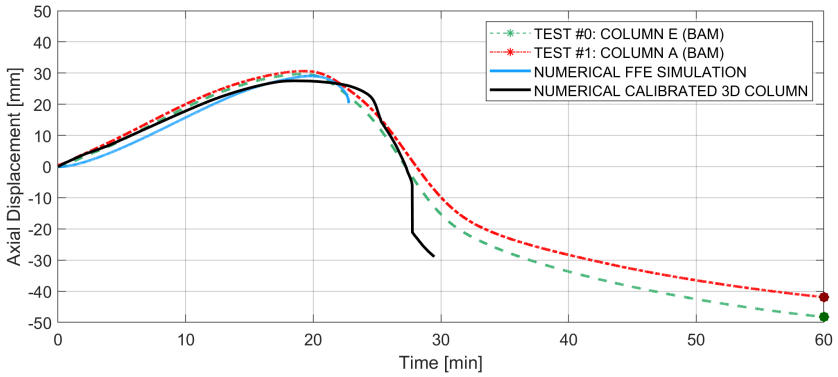

(a)

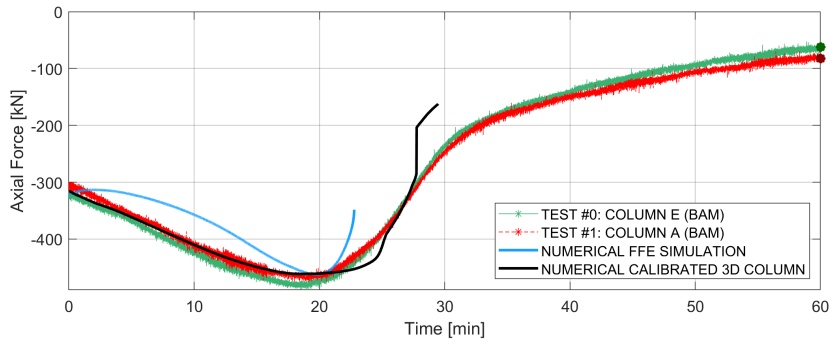

(b)

Figure 7.28: Comparison between the results of the numerical model, the calibrated 3D column and the FFE tests on the unprotected columns.

7.8 Safir calibrated model

7.8.1 Thermal Model (SAFIR)

The thermal model is used in SAFIR to calculate the temperature time-history within structural elements. To do this, the section is discretized into a mesh of finite elements, to which the thermal characteristics of the materials are assigned. In order to apply the temperature time-history, the elements of the column have been divided into an appropriate number of zones equal to the numbers of the thermocouples installed on the column, as showed in Figure 7.29. The temperatures measured by thermocouples are assigned to the outer perimeter of the corresponding zones.

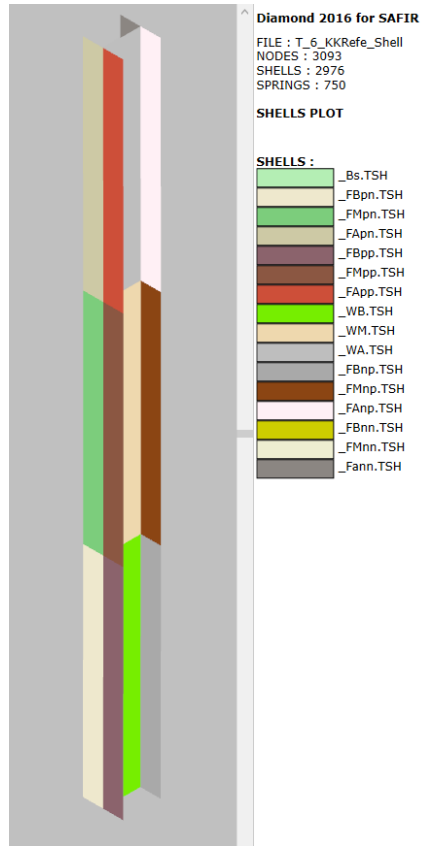

Figure 7.29: ix zones subdivision

7.8.2 Calibration checks

In order to verify the correct behaviour of the springs in Safir, an analysis of the end plates was carried out at ambient temperature.
A compressive force was applied at the top of the column in order to measure the vertical displacement and compare it with the analytical formulae. The structural scheme is schematised by two springs in series with a force applied at the interface between the two springs and the calibration is performed with:

- F Applied axial force equal to 315 kN,
- Ktr Translational stiffness of 5.3 kN/m
- Ec Modulus of elasticity of column: 210 GPa
- Ac Column area 0.009104 m²

The calculation of the deformation by analytical method, therefore returns the value of:

$$vi = Ned/((A_C * E_c)/L_c + k_t r) = \\ = (-315kN)/((0.009104\ m^2 * 210\ GPa)/(3.6\ m) + 5.3e6\ kN/mm) = -0.587\ mm \tag{7.1}$$

Model	Vertical displacement [mm]	Difference
Analytical method	-0.587	
Beam elements	-0.5941	+1.21%
Shell elements	-0.6234	+6.20%

Table 7.1

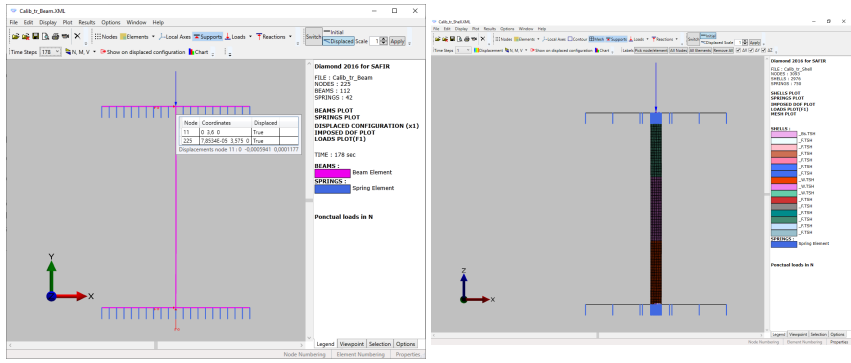

(a) *(b)*

Figure 7.30: Axial spring results: a) beam elements; b) shell elements.

The difference from the analytical results is considered acceptable.

The model of the column was released at the top and a moment was applied to the lower end in order to verify the correctness of the rotations. Structurally it can be schematised as a simple rotational spring. Calibration takes place with:

- M Applied moment of 3.1 kNm
- Krot Rotational stiffness of 3.1 MNm/rad

Calculating the deformation analytically gives the value of:

$$\theta = M/K_T r = 3.1e3/3.1e6 = 0.001 rad \tag{7.2}$$

Model	**Rotational displacement [rad]**	**Difference**
Analytical method	0.001000	
Beam elements	0.001004	+0.40%
Shell elements	0.00096	-4.00%

Table 7.2

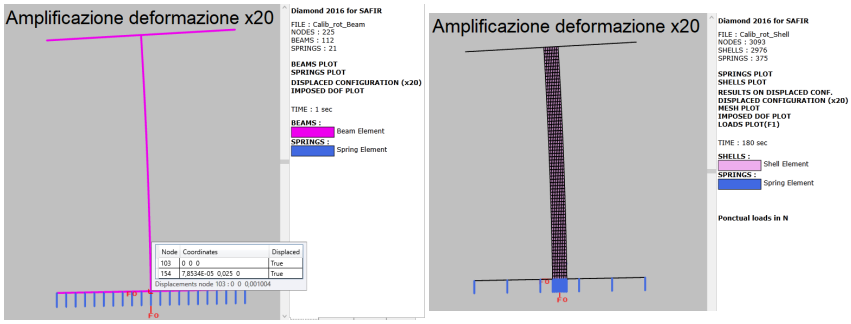

(a) *(b)*

Figure 7.31: Axial spring results: a) beam elements; b) shell elements.

The difference from the analytical results is considered acceptable.

7.8.3 Results

BAM Test #A

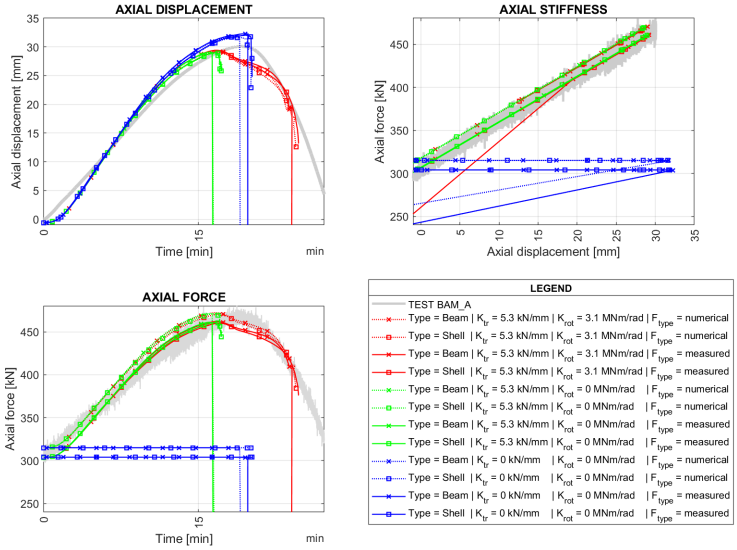

Figure 7.32: Column #A - calibration results.

The comparisons between the experimental data (grey curve) and the processing results in the various configurations are summarised as follows:

- Good agreement between the experimental outcomes and the numerical simulations can be observed;

- Hinge Constraint (blue lines):

  - It approximates well the collapse time (assumed as the time of maximum axial displacement);

  - Deflection at collapse is slightly overestimated, due to the absence of the translational spring;

  - The simulation is not able to replicate the post-critical behaviour;

  - Axial force remains constant because the column is not axially restrained;

- Translational spring (green lines):

  - Underestimates the collapse time (assumed as the time of maximum axial displacement);

  - Deformation at collapse is well approximated;

- Rotational spring and translational spring (red lines):

  - Underestimates time to collapse (assumed as time to maximum axial displacement);

  - Deformation at collapse is well approximated;

BAM Test #E

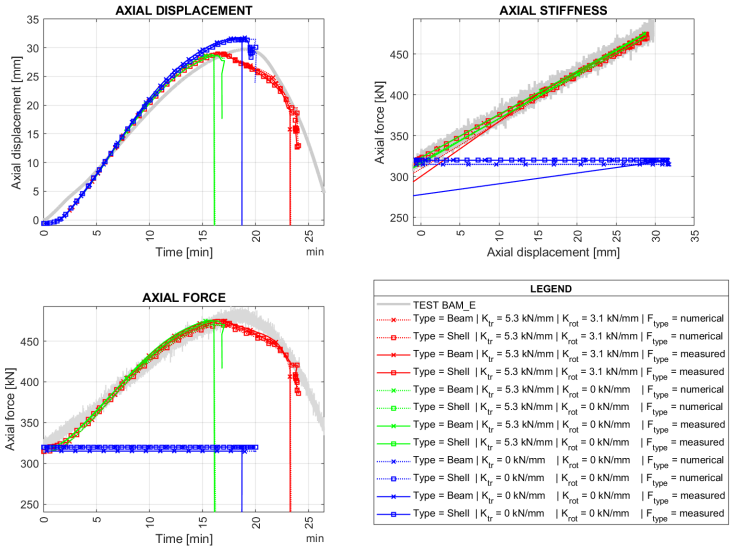

Figure 7.33: Column #E - calibration results.

The comparisons between the experimental data (grey curve) and the processing results in the various configurations are summarised as follows:

- Good agreement between the experimental outcomes and the numerical simulations can be observed;
- Hinge Constraint (blue lines):
  - It approximates well the collapse time (assumed as the time of maximum axial displacement);
  - Deflection at collapse is slightly overestimated, due to the absence of the translational spring;
  - The simulation is not able to replicate the post-critical behaviour;
  - Axial force remains constant because the column is not axially restrained;
- Translational spring (green lines):
  - Underestimates the collapse time (assumed as the time of maximum axial displacement);

- Deformation at collapse is well approximated;

- Rotational spring and translational spring (red lines):
  - Underestimates time to collapse (assumed as time to maximum axial displacement);
  - Deformation at collapse is well approximated;

BAM Test #B

As previously described, test #2 on column B was interrupted due to a malfunction of a component and then was restarted.

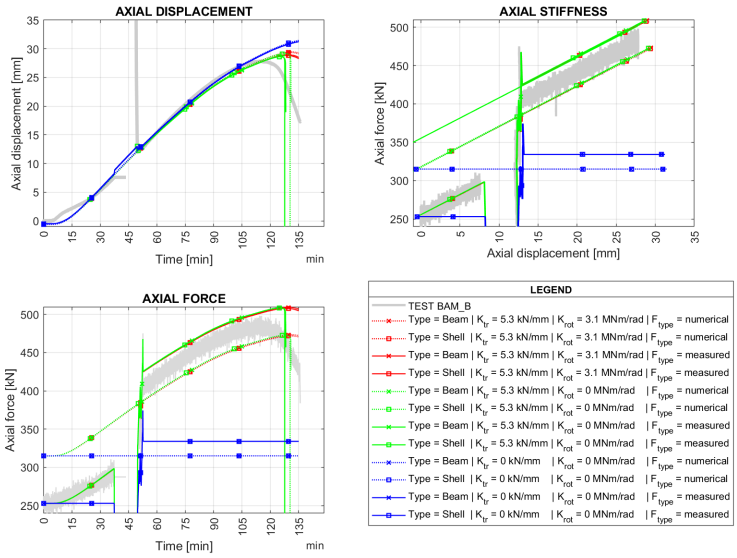

Figure 7.34: Column #B - calibration results.

The comparisons between the experimental data (grey curve) and the processing results in the various configurations are summarised as follows:

- The results come close to the detected behaviour during the test, but completely fail to detect the collapse.

- The increased force applied after resuming the test succeeds in approaching the detected behaviour. However, it fails to detect the collapse of the column for all types of constraints.

- The initial force before the fire test (253 kN) is very different from the expected force (315 kN).

BAM Test #C

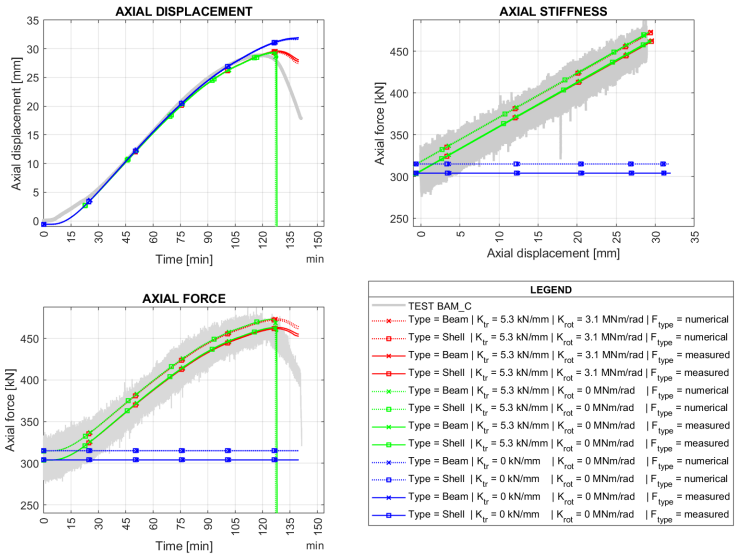

Figure 7.35: Column #C - calibration results.

The comparisons between the experimental data (grey curve) and the processing results in the various configurations are summarised as follows:

- The simulations slightly overestimate the collapse time (assumed to be the time of maximum axial displacement);
- Good agreement between the experimental outcomes and the numerical simulations can be observed in general for the phase before the collapse;
- Hinge Constraint (blue lines):
  - The simulation stops before collapse is reached;
  - Axial force remains constant because the column is not axially restrained;
- Translational spring (green lines):

  - Underestimates the collapse time (assumed as the time of maximum axial displacement);
  - Deformation at collapse is well approximated;

- Rotational spring and translational spring (red lines):
  - Overestimates time to collapse (assumed as time to maximum axial displacement);
  - Simulation stops before post-critical behaviour;

BAM Test #D

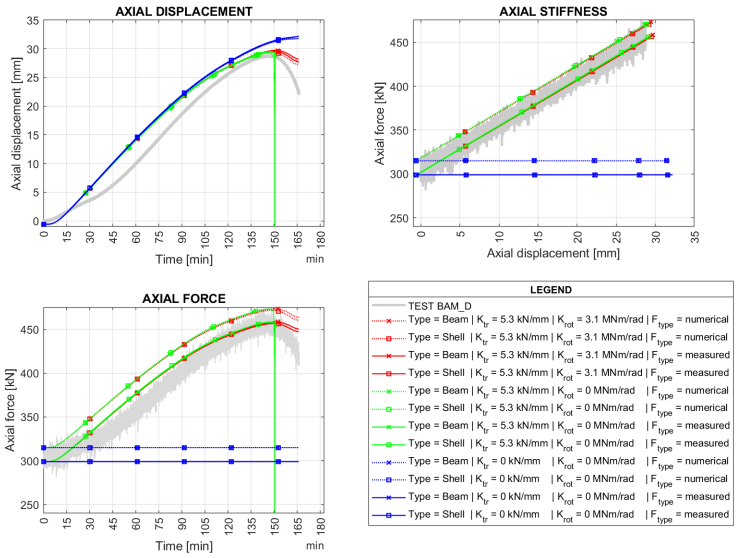

Figure 7.36: Column #D - calibration results.

The comparisons between the experimental data (grey curve) and the processing results in the various configurations are summarised as follows:

- The simulations slightly overestimate the time of collapse (assumed to be the time of maximum axial displacement);
- The simulations show an overall good behaviour but there are some differences in the axial displacement between the 30th and the 90th minute;

7.9 Conclusion

The paper presented part of the results of an experimental and numerical FFE analysis on a braced steel frame and, in particular, on columns belonging to the bracing system. The research activity was performed within the European EQUFIRE project. The numerical model developed in OpenSees was able to perform highly non-linear multi-hazard analyses and it served to design the FFE tests. The numerical model developed in SAFIR was able to perform only the fire analyses. The specimens, as expected, remained in the elastic range after the seismic event at the Significant Damage limit state. During the successive fire tests performed by considering the effects of the surrounding structure through a constant axial stiffness, no failure was detected of exposure to the ISO 834 heating curve. The main reason was the low utilisation factor in the fire situation. Model calibration was performed with beam finite elements that exhibited good agreement but also failure. This latter discrepancy may be caused by a temperature gradient within the cross-section, that was not considered in the modelling and by the actual rotational stiffness at the boundary conditions, which might have varied as the fire test progressed.

Acknowledgements

This work has received funding from the European Union's Horizon 2020 research and innovation program under the SERA grant agreement No. 730900 and the related TA project EQUFIRE. Authors would also acknowledge Philippe Buchet (EC-JRC) as well as Sven Riemer (BAM) KaiUwe Ziener (BAM), Marco Antonelli and Peter Schultz (ETEX-PROMAT) for their invaluable contribution to the experimental campaign.

Bibliography

[1] G. Della Corte, R. Landolfo, and F. Mazzolani, "Post-earthquake fire resistance of moment resisting steel frames," *Fire Safety Journal*, vol. 38, no. 7, pp. 593–612, 2003.

[2] M. Memari, H. Mahmoud, and B. Ellingwood, "Post-earthquake fire performance of moment resisting frames with reduced beam section connections," *Journal of Constructional Steel Research*, vol. 103, pp. 215–229, 2014.

[3] B. Behnam and H. R. Ronagh, "Post-earthquake fire performance-based behavior of unprotected moment resisting 2d steel frames," *KSCE Journal of Civil Engineering*, vol. 19, no. 1, pp. 274–284, 2015.

[4] W. J. Keller and S. Pessiki, "Effect of earthquake-induced damage to spray-applied fire-resistive insulation on the response of steel moment-frame beam-column connections during fire exposure," *Journal of Fire Protection Engineering*, vol. 22, no. 4, pp. 271–299, 2012.

[5] E. Talebi, M. M. Tahir, F. Zahmatkesh, A. B. Kueh, and A. M. Said, "Fire resistance of a damaged building employing buckling restrained braced system," *Advanced Steel Construction*, vol. 14, no. 1, pp. 1–21, 2018.

[6] N. E. Khorasani, M. E. Garlock, and S. E. Quiel, "Modeling steel structures in opensees: Enhancements for fire and multi-hazard probabilistic analyses," *Computers & Structures*, vol. 157, pp. 218–231, 2015.

[7] N. L. Braxtan and S. P. Pessiki, "Postearthquake fire performance of sprayed fire-resistive material on steel moment frames," *Journal of Structural Engineering*, vol. 137, no. 9, pp. 946–953, 2011.

[8] R. Pucinotti, O. Bursi, and J.-F. Demonceau, "Post-earthquake fire and seismic performance of welded steel–concrete composite beam-to-column joints," *Journal of constructional steel research*, vol. 67, no. 9, pp. 1358–1375, 2011.

[9] P. Kamath, U. K. Sharma, V. Kumar, P. Bhargava, A. Usmani, B. Singh, Y. Singh, J. Torero, M. Gillie, and P. Pankaj, "Full-scale fire test on an earthquake-damaged reinforced concrete frame," *Fire Safety Journal*, vol. 73, pp. 1–19, 2015.

[10] B. J. Meacham, "Post-earthquake fire performance of buildings: Summary of a large-scale experiment and conceptual framework for integrated performance-based seismic and fire design," *Fire Technology*, vol. 52, no. 4, pp. 1133–1157, 2016.

[11] CEN, "Eurocode 3: Design of steel structures - Part 1-2: General rules - Structural fire design," european standard, European Union, May 2005.

[12] L. Luzi, R. Puglia, E. Russo, and W. Orfeus, "Engineering strong motion database, version 1.0," *Istituto Nazionale di Geofisica e Vulcanologia, Observatories & Research Facilities for European Seismology. doi*, vol. 10, 2016.

[13] F. McKenna, "Opensees: a framework for earthquake engineering simulation," *Computing in Science & Engineering*, vol. 13, no. 4, pp. 58–66, 2011.

[14] F. C. Filippou, E. P. Popov, and V. V. Bertero, "Effects of bond deterioration on hysteretic behavior of reinforced concrete joints," 1983.

[15] CEN, "Eurocode 3: Design of steel structures - Part 1-1: General rules and rules for buildings," european standard, European Union, May 2005.

[16] ISO834, "Fire-resistance tests -Elements of building construction- Part 1: General requirements," international standard, International Standard ISO 834, 1999.

[17] M. Korzen, G. Magonette, and P. Buchet, "Mechanical Loading of Columns in Fire Tests by Means of the Substructuring Method," *Zeitschrift für Angewandte Mathematik und Mechanik*, vol. 79, pp. 617–S618, 1999.

8.0 Seismic pseudo-dynamic tests at JRC

8.1 Introduction

Five seismic pseudo-dynamic tests were performed at the European Laboratory for Structural Assessment of the Joint Research Centre (JRC), in Ispra (Italy), between November 2020 and May 2021. This chapter presents the experimental set-up of the ELSA laboratory (JRC), the experimental tests and results, and it describes the dynamic substructuring of a finite element (FE) model of the EQUFIRE frame and the development of a time integration procedure that allows for mixing displacement- and force-controlled degrees-of-freedom (DOFs) for hybrid simulation (HS).

8.1.1 ELSA laboratory JRC

The kernel of the European Laboratory for Structural Assessment (ELSA) [1] is the Reaction Wall. It consists of a reinforced concrete vertical wall and a horizontal floor rigidly connected together to test the vulnerability of buildings to earthquakes and other hazards.

ELSA operates a 16 m-tall, 21 m-long reaction wall, with two reaction platforms of total surface 760 m2 that allow testing real-scale specimens on both sides of the wall. The laboratory is equipped with 28 actuators with capacities between 0.2 and 3 MN and strokes between ±0.125 and 1.0 m. The actuators control system is designed in-house to perform tests with the continuous pseudo-dynamic method with substructuring, that permits testing elements of large structures, bidirectional testing of multi-storey buildings, and testing of strain-rate dependent devices.

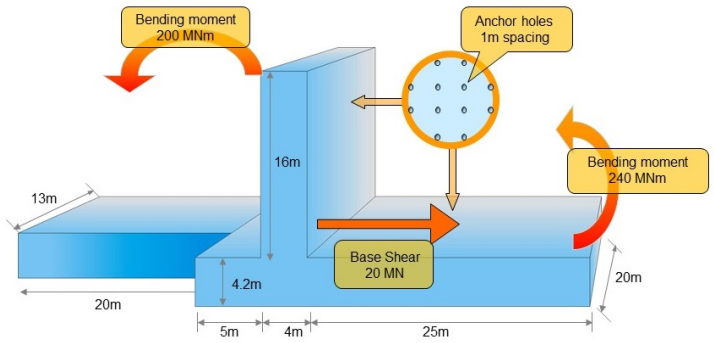

Figure 8.1: Dimensions and capacity of the ELSA Reaction Wall [1]

8.2 Experimental programme and setup at JRC

The experimental mock-up at ELSA Reaction Wall (Figure 8.2) represents the ground floor of the four-storey frame. It is a three-bay steel frame with concentric bracing in the central bay. The span of the outer bays is 5 m, while the interior one has a span of 2.5 m. The inter-storey height is 3.6 m corresponding to the column height at BAM. A secondary frame, parallel to the main one is used to prevent out-of-plane deformation during the test. The earthquake simulator testing program was designed to subject the frame to unidirectional loading only. The two frames are fixed to the strong floor and tare-connected together by steel rods, which do not alter the seismic response of the mock-up.

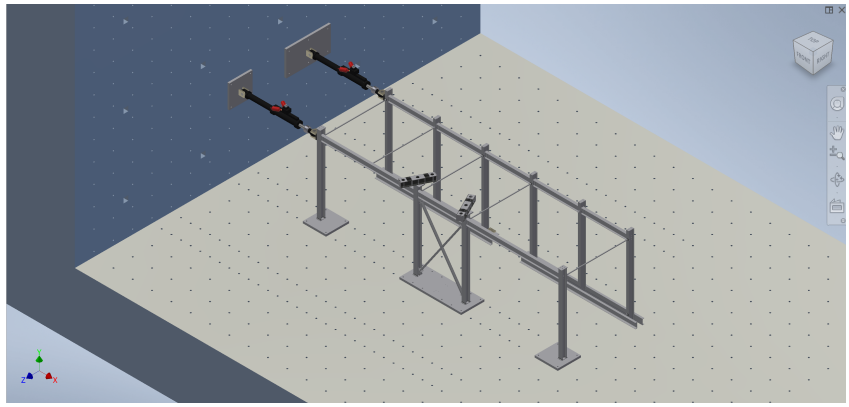

(a)

(b)

(c)

Figure 8.2: a) Render of the experimental setup. b) General view of the specimen and experimental setup at the ELSA Reaction Wall; c) detail of the brace.

The columns and beams of the frame are made of S355 steel, while the braces are made of S275 steel. The profiles used are HEB220 for columns, IPE270 for beams and IPE100 for braces.

Two 600 kN pistons apply the vertical load on each internal column, whereas lateral loads are applied through 500 kN actuators connected to the ELSA Reaction Wall, one for the main frame and another for the secondary frame. Load cells measure the loads applied by the vertical and horizontal actuators. Since the frame is statically indeterminate, the two central columns and the three beams are equipped with strain gauges that measure their internal axial loads. Displacement transducers measure the vertical deformation of the central columns, the axial deformation of the braces, as well as the lateral displacement of the whole frame. Figure 8.3 shows the sensors location. To further reduce any possible interference from the secondary frame and eliminate any relative displacement during testing, the actuator of the safety frame applies the same displacement as

the actuator of the main one. The procedure for the hybrid tests at the ELSA Reaction Wall is described in section 8.4. Five tests are foreseen with the acceleration time history shown in Figure 8.4:

- Test 1, bare frame without fire protection;
- Test 2, frame with PROMATECT-H fire protection boards - system designed for seismic regions;
- Test 3, frame with PROMATECT-H fire protection boards (standard system, not designed for seismic regions);
- Test 4, frame with PROMASPRAY P300 series gypsum-based wet mix spray-applied fire resistive material, designed for applications in seismic regions, in which a mechanical reinforcing mesh was placed in the middle of the applied material and with walls made of autoclaved aerated concrete blocks built in the two longest bays, to verify whether these can provide effective fire compartmentation without altering the seismic response of the frame.

The bracing and the column on which the fire protection has been applied will be replaced at the end of each of the tests.

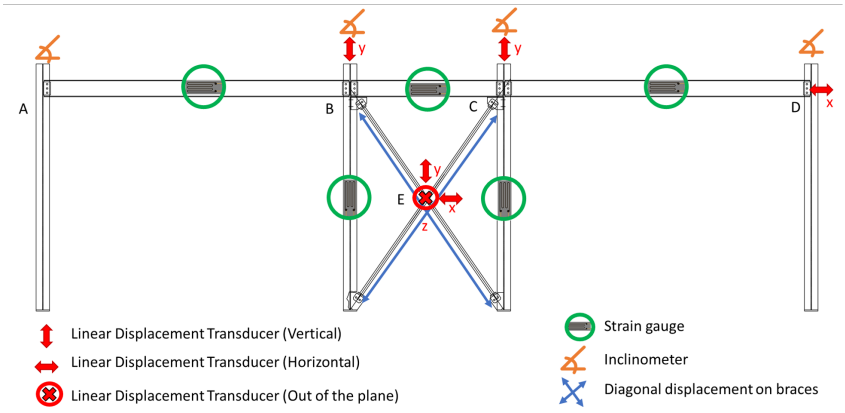

Figure 8.3: Sensors setup.

As explained in chapter 3 Among the fifteen accelerograms, the one shown in Figure 8.4 was selected. However, only the most significant portion of the full accelerogram was used for the experimental hybrid tests in order to reduce the total time of each test.

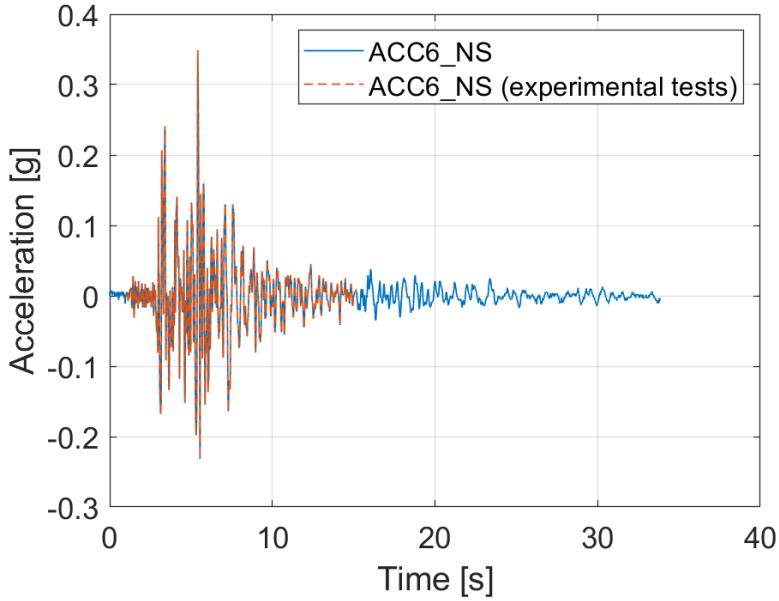

Figure 8.4: Earthquake acceleration time-history (ACC6_NS).

8.3 Dynamic substructuring of the EQUFIRE frame

8.3.1 OpenSees model

It was decided to couple the PS and NS at translational DoFs, whilst continuity of the rotational DoFs was neglected. Figure 8.5 also illustrates the possible subdivision between the NS and PS by highlighting the controlled DoFs with an actuator. It is possible to observe that, since it is challenging to control rotations directly, only translational DoFs are controlled. Nonetheless, if the budget does not allow only the base floor could be physically modelled in the laboratory by accepting a lower degree of accuracy.

Therefore, it was decided to perform a numerical simulation using the OpenSees model of the frame developed in Chapter 3, in which an internal hinge at the base of each column of the second floor was implemented. This choice was made in order to check that the assumption of only control of the translational DoFs is a good representation of the real structure.

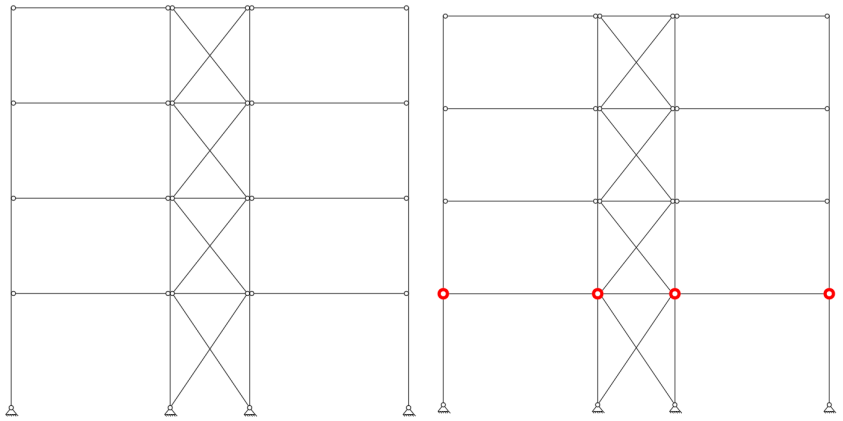

(a) *(b)*

Figure 8.5: Frame EQUFIRE a) Real frame; b) Substructure.

Modal analysis

A modal analysis was performed in order to compare the fundamental period of the different numerical models. The results are very similar, as reported in Tables 8.1 and 8.2.

Table 8.1: Fundamental periods of structures 3D model of the full structure versus the substructuring model.

Mode	**Period 3D Full structure [s]**	**Period Substructure [s]**	**NENERR**	**RMSE [s]**
1st mode	0.674	0.668	-0.915%	0.006
2nd mode	0.225	0.222	-0.935%	0.002

Table 8.2: Fundamental periods of structures 2D model of the frame versus the substructuring model.

Mode	**Period 2D Frame [s]**	**Period Substructure [s]**	**NENERR**	**RMSE [s]**
1st mode	0.667	0.668	-0.003%	1.84e-5
2nd mode	0.223	0.222	-0.007%	1.53e-5

Pushover

The results and the comparison of the non-linear static analyses analysis are shown in Figure 8.6. The comparison shows a good agreement between the 3D model of the entire structure, the 2D model of the frame and the substructure model.

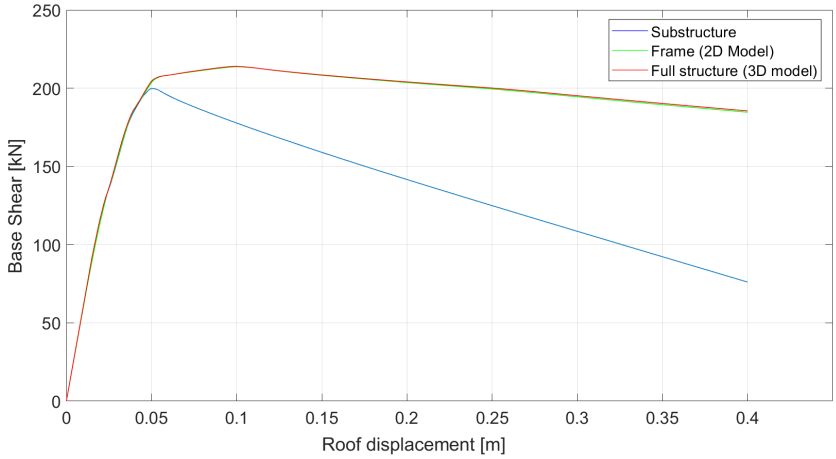

Figure 8.6: Capacity curve (Pushover) comparison.

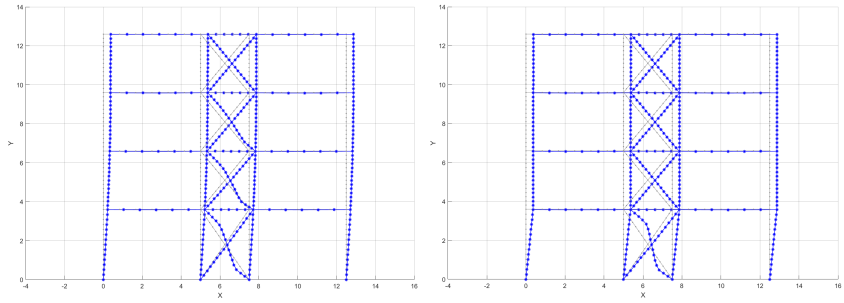

(a) *(b)*

Figure 8.7: Pushover deformation a) Real frame; b) Substructure.

Non-linear dynamic analysis: ACC6_NS

The results and the comparison of the non-linear dynamic analysis analyses using the modified accelerogram ACC6_NS are showed in Figures 8.8, 8.9, 8.10 and 8.11. The comparison shows a good agreement between the 3D model of the full structure, 2D model of the frame and the substructure model.

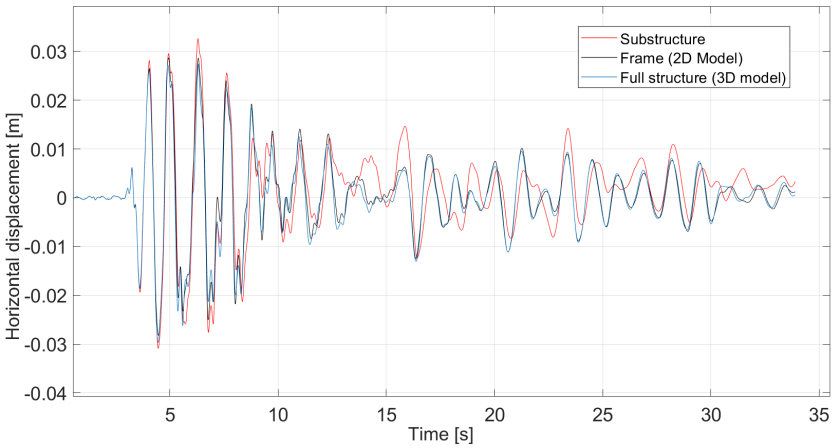

Figure 8.8: Comparison of the horizontal displacements at first floor (ACC6_-NS).

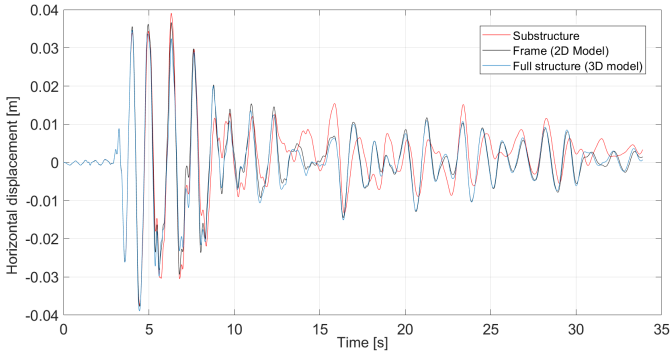

Figure 8.9: Comparison of the horizontal displacements at second floor (ACC6_NS).

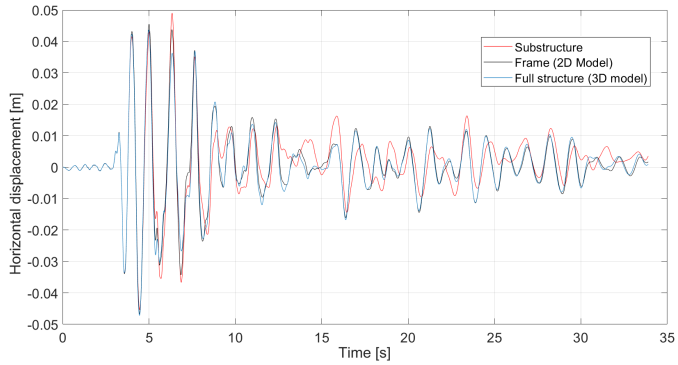

Figure 8.10: Comparison of the horizontal displacements at third floor (ACC6_NS).

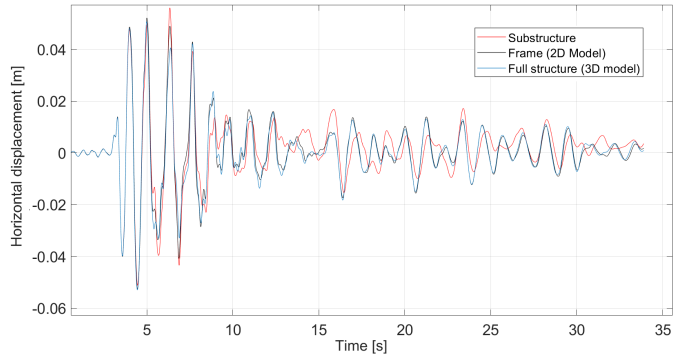

Figure 8.11: Comparison of the horizontal displacements at fourth floor (ACC6_NS).

The substructure model, presented in this section, is a good representative of the full structure and it was chosen as the configuration for the experimental campaign.

8.3.2 MATLAB model

A finite-element (FE) model of the EQUFIRE frame was implemented in MATLAB in line with the specification provided by the design report of Chapter 3. All elements are linear except the first-level bracing, which are characterized by a bilinear elastic behaviour that mimics the axial force cut-off due to buckling. Then, interface boundary conditions between PS and NS were simplified in order to account for the actual coupling conditions adopted during experiments. The following figure compares the first eigenmodes of the reference and the simplified

FE models. In detail, the reference FE model is characterized by the coupling of both rotational and translational DOFs at the interface between PS and NS. On the other hand, the coupling of rotational DOFs is discarded for all interface nodes between PS and NS. Moreover, in the simplified FE model, also vertical DOFs are uncoupled on the external columns.

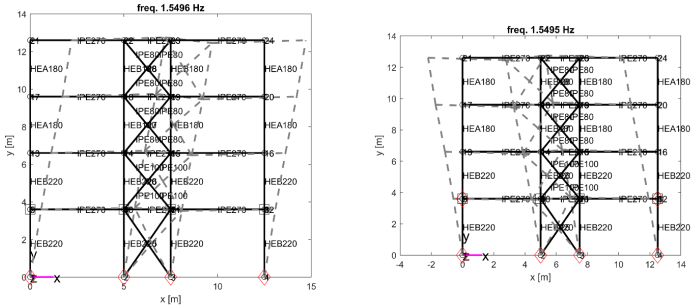

Figure 8.12: – First eigenmode of the: a) reference and the b) simplified FE models of the EQUFIRE frame case study.

As can be appreciated from Figure 8.12, the first eigenmode is almost unaltered both in terms of frequency and deformational shape. Figure 2 compares the time history responses of both models subjected to the selected ground motion excitation.

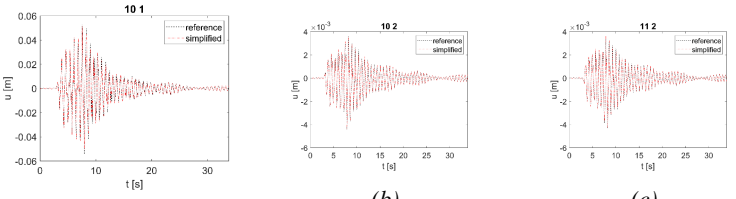

(a) *(b)* *(c)*

Figure 8.13: Displacement response histories of coupled DOFs of both reference and simplified FE models: a) horizontal displacement of the left inner column, b) vertical displacement of the left inner column, c) vertical displacement of the right inner column.

A consistent response between reference and simplified FE models is also observed in the nonlinear bracing on the ground floor.

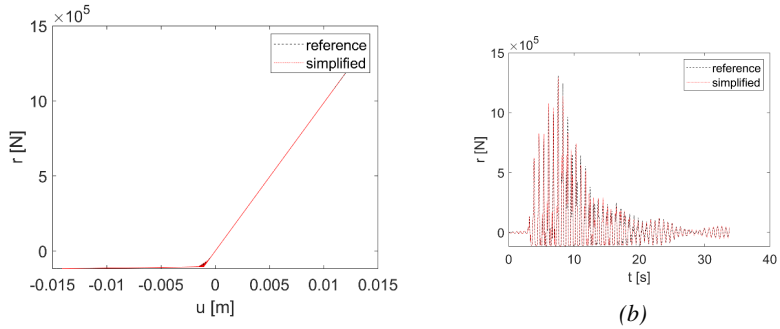

(a) *(b)*

Figure 8.14: Ground-level diagonal bracing #1: a) displacement-force response, b) restoring force history.

Two separate FE models were developed for the PS and NS to be used for the simulation of the experiments. Both are reported in the following picture with coupling DOFs highlighted.

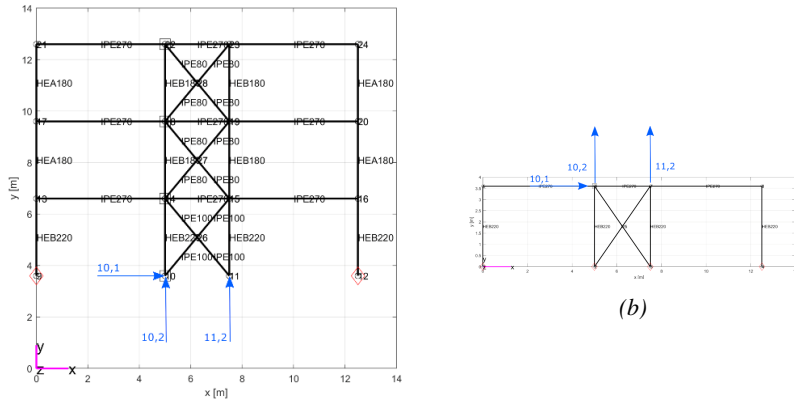

(a) *(b)*

Figure 8.15: FE models of the: a) NS and the b) PS with coupled DOFs highlighted in blue.

As can be observed in Figure 3, only 3-DOFs are coupled between PS and NS. In fact, a master-slave relation is imposed on all horizontal DOFs of the first story to follow DOF (10,1). Since external columns are connected to the inner braced frame by means of truss elements, their vertical base displacement is blocked on the NS.

8.4 Simulation algorithm for the hybrid tests

8.4.1 Time integration scheme for hybrid simulation

In order to enable hybrid simulation with mixed force and displacement controlled DOFs, a specific simulation algorithm was developed [2] [3]. The NS is characterized by a dynamic balance equation that is solved with the Newmark-α method:

$$\begin{aligned} &\mathbf{M}^N \ddot{\mathbf{u}}_{k+1}^N + \left[(1+\alpha)\,\mathbf{C}_{k+1}^N \dot{\mathbf{u}}_{k+1}^N - \alpha \mathbf{C}_k^N \dot{\mathbf{u}}_k^N\right] \\ &\quad + \left[(1+\alpha)\,\mathbf{r}_{k+1}^N\left(\mathbf{u}_{k+1}^N\right) - \alpha \mathbf{r}_k^N\left(\mathbf{u}_k^N\right)\right] \\ &- \left[(1+\alpha)\,\mathbf{f}_{k+1}^N - \alpha \mathbf{f}_k^N\right] - \left[(1+\alpha)\,\mathbf{L}^{N,v^T}\lambda_{k+1}^v - \alpha \mathbf{L}^{N,v^T}\lambda_k^v\right] \\ &\quad - \left[(1+\alpha)\,\mathbf{L}^{N,h^T}\lambda_{k+1}^h - \alpha \mathbf{L}^{N,h^T}\lambda_k^h\right] = \mathbf{0} \end{aligned} \tag{8.1}$$

Since the vertical DOFs of the PS are characterized by high stiffness, force control is used instead of displacement control. The latter is limited to the horizontal DOFs of the PS. Accordingly, the PS is characterized by two static balance equations; one refers to the vertical force-controlled DOFs, whereas the other refers to the horizontal displacement-controlled DOFs. Superscripts h and v are used to distinguish between vertical and horizontal DOFs.

$$\begin{cases} \mathbf{r}_{k+1}^{P,h}\left(\mathbf{u}_{k+1}^{P,h}, \mathbf{r}_{k+1}^{P,v}\right) - \mathbf{L}^{P,h^T}\lambda_{k+1}^h = \mathbf{0} \\ \mathbf{r}_{k+1}^{P,v} - \mathbf{L}^{P,v^T}\lambda_{k+1}^v = \mathbf{0} \end{cases} \tag{8.2}$$

A pair of Lagrange multiplier vectors are introduced to enforce both horizontal and vertical displacement compatibility between PS and NS. The two following equations define the compatibility between NS and PS.

$$\begin{cases} \mathbf{L}^{N,h}\mathbf{u}_{k+1}^N + \mathbf{L}^{P,h}\mathbf{u}_{k+1}^{P,h} = \mathbf{0} \\ \mathbf{L}^{N,v}\mathbf{u}_{k+1}^N + \mathbf{L}^{P,v}\mathbf{u}_{k+1}^{P,v}(\mathbf{u}_{k+1}^{P,h}, \mathbf{r}_{k+1}^{P,v}) = \mathbf{0} \end{cases} \tag{8.3}$$

The solution to the system of equation is computed via operator-splitting, which means with a single Newton iteration and a constant Jacobian. The solution variables read,

$$\ddot{\mathbf{u}}_{k+1}^N, \lambda_{k+1}^v, \lambda_{k+1}^h, \mathbf{u}_{k+1}^{P,h}\mathbf{r}_{k+1}^{P,v} \tag{8.4}$$

As anticipated, vertical DOFs are controlled in force during the hybrid simulation whereas horizontal DOFs are controlled in displacement. The solution is pursued with a predictor-corrector strategy.

$$\begin{array}{c} \mathbf{u}_{k+1}^{N} = \widetilde{\mathbf{u}}_{k+1}^{N} + \Delta\mathbf{u}_{k+1}^{N} \\ \lambda_{k+1}^{v} = \widetilde{\lambda}_{k+1}^{v} + \Delta\lambda_{k+1}^{v} \\ \lambda_{k+1}^{h} = \widetilde{\lambda}_{k+1}^{h} + \Delta\lambda_{k+1}^{h} \\ \mathbf{u}_{k+1}^{P,h} = \widetilde{\mathbf{u}}_{k+1}^{P,h} + \Delta\mathbf{u}_{k+1}^{P,h} \\ \mathbf{r}_{k+1}^{P,v} = \widetilde{\mathbf{r}}_{k+1}^{P,v} + \Delta\mathbf{r}_{k+1}^{P,v} \end{array} \tag{8.5}$$

with,

$$\begin{array}{c} \widetilde{\mathbf{u}}_{k+1}^{N} = \mathbf{u}_{k}^{N} + \dot{\mathbf{u}}_{k}^{N}\Delta t + \ddot{\mathbf{u}}_{k}^{N}\left(\frac{1}{2} - \beta\right)\Delta t^{2} \\ \widetilde{\lambda}_{k+1}^{v} = \lambda_{k}^{v} \\ \widetilde{\lambda}_{k+1}^{h} = \lambda_{k}^{h} \\ \widetilde{\mathbf{u}}_{k+1}^{P,h} = \mathbf{u}_{k}^{P,h} \\ \widetilde{\mathbf{r}}_{k+1}^{P,v} = \mathbf{r}_{k}^{P,v} \end{array} \tag{8.6}$$

In order to compute the Jacobian, quantities that are dual to solution variables must be linearized. With regard to the NS, the linearization of the balance equation with respect to the acceleration reads,

$$\frac{\Delta\mathbf{r}_{k+1}^{N}}{\Delta\ddot{\mathbf{u}}_{k+1}^{N}} = \mathbf{D}^{N} = \mathbf{K}^{N}\beta\Delta t^{2}\left(1+\alpha\right) + \mathbf{C}^{N}\gamma\Delta t\left(1+\alpha\right) + \mathbf{M}^{N} \tag{8.7}$$

However, for the PS, which is partially controlled in displacement (h-DOFs) and partially in force (v-DOFs), the linearization is more complicated. If one looks at the PS tangent stiffness matrix,

$$\begin{bmatrix} \Delta\mathbf{r}_{k+1}^{P,h} \\ \Delta\mathbf{r}_{k+1}^{P,v} \end{bmatrix} = \begin{bmatrix} \mathbf{K}^{P,hh} & \mathbf{K}^{P,hv} \\ \mathbf{K}^{P,vh} & \mathbf{K}^{P,vv} \end{bmatrix} \begin{bmatrix} \Delta\mathbf{u}_{k+1}^{P,h} \\ \Delta\mathbf{u}_{k+1}^{P,v} \end{bmatrix} \tag{8.8}$$

Terms must be rearranged to express the linearization with respect to control variables $\Delta\mathbf{u}_{k+1}^{P,h}$ (horizontal displacement h-DOFs) and $\Delta\mathbf{r}_{k+1}^{P,v}$ (vertical force v-DOFs). By rearranging the second row block we immediately find the expression of the variation of $\Delta\mathbf{u}_{k+1}^{P,v}$,

$$\begin{array}{c} \Delta\mathbf{u}_{k+1}^{P,v} = \mathbf{K}^{P,vv^{-1}}\left[\Delta\mathbf{r}_{k+1}^{P,v} - \mathbf{K}^{P,vh}\Delta\mathbf{u}_{k+1}^{P,h}\right] = \\ = \mathbf{K}^{P,vv^{-1}}\Delta\mathbf{r}_{k+1}^{P,v} - \mathbf{K}^{P,vv^{-1}}\mathbf{K}^{P,vh}\Delta\mathbf{u}_{k+1}^{P,h} \end{array} \tag{8.9}$$

Then, replacing the obtained expression into the first row block equation, we find the expression of the variation of $\Delta\mathbf{r}_{k+1}^{P,h}$,

$$\begin{aligned}\Delta\mathbf{r}_{k+1}^{P,h} &= \mathbf{K}^{P,hh}\Delta\mathbf{u}_{k+1}^{P,h} + \\ &+\mathbf{K}^{P,hv}\mathbf{K}^{P,vv^{-1}}\left[\Delta\mathbf{r}_{k+1}^{P,v} - \mathbf{K}^{P,vh}\Delta\mathbf{u}_{k+1}^{P,h}\right] = \\ &= \left[\mathbf{K}^{P,hh} - \mathbf{K}^{P,hv}\mathbf{K}^{P,vv^{-1}}\mathbf{K}^{P,vh}\right]\Delta\mathbf{u}_{k+1}^{P,h} + \mathbf{K}^{P,hv}\mathbf{K}^{P,vv^{-1}}\Delta\mathbf{r}_{k+1}^{P,v}\end{aligned} \tag{8.10}$$

Accordingly, the Jacobian of the full set of balance and compatibility equations reads,

$$\mathbf{J} = \begin{bmatrix} \mathbf{D}^N & -(1+\alpha)\mathbf{L}^{N,h^T} & -(1+\alpha)\mathbf{L}^{N,v^T} & \mathbf{0} & \mathbf{0} \\ \mathbf{0} & -\mathbf{L}^{P,h^T} & \mathbf{0} & \mathbf{K}^{P,hh} - \mathbf{K}^{P,hv}\mathbf{K}^{P,vv^{-1}}\mathbf{K}^{P,vh} & \mathbf{K}^{P,hv}\mathbf{K}^{P,vv^{-1}} \\ \mathbf{0} & \mathbf{0} & -\mathbf{L}^{P,v^T} & \mathbf{0} & \mathbf{I} \\ \mathbf{L}^{N,h}\beta\Delta t^2 & \mathbf{0} & \mathbf{0} & \mathbf{L}^{P,h} & \mathbf{0} \\ \mathbf{L}^{N,v}\beta\Delta t^2 & \mathbf{0} & \mathbf{0} & -\mathbf{L}^{P,v}\mathbf{K}^{P,vv^{-1}}\mathbf{K}^{P,vh} & \mathbf{L}^{P,v}\mathbf{K}^{P,vv^{-1}} \end{bmatrix} \tag{8.11}$$

The procedure was verified considering the virtual hybrid earthquake simulation presented in the next section.

8.4.2 Virtual hybrid earthquake simulation

In order to demonstrate the effectiveness of the framework before using it during the experimental tests, a virtual hybrid earthquake simulation (RT-HES) was conceived using the same test substructures. Results of the virtual real-time hybrid test were then verified against the monolithic solution developed in the finite element software OpenSees [4].

Figure 8.16a shows the member sizes and the magnitude of the gravity loads acting simultaneously with the earthquake event. The IPE 100 and IPE 80 profiles composing the bracing system were oriented according to the weak axis in the plane of the frame in order to force in-plane buckling so that a 2D modeling was representative. As shown in Figure 8.16b, it was decided to couple the PS and NS at translational DoFs, whilst continuity of the rotational DoFs was neglected. Figure 8.16b also illustrates the possible subdivision between the NS and PS by highlighting the controlled DoFs with an actuator. It is possible to observe that, since it is challenging to control rotations directly, only translational DoFs are controlled.

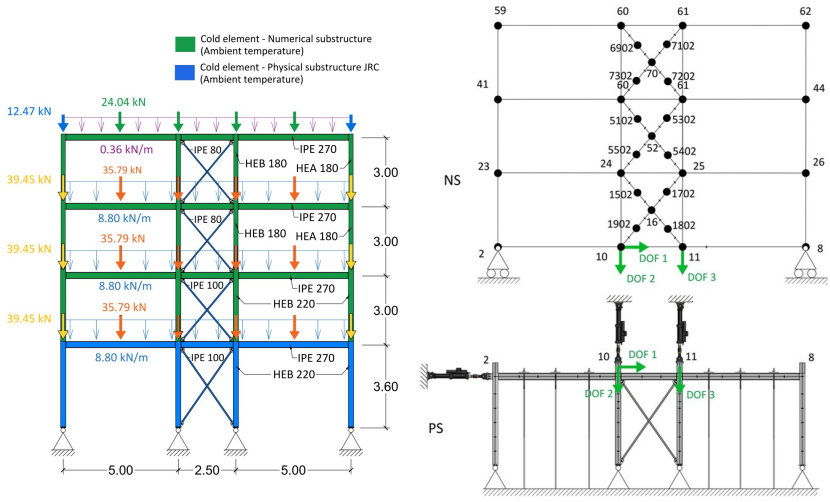

Figure 8.16: a) Emulated steel frame (dimensions in m); b) substructuring scheme adopted for HES.

Nonetheless, if the budget does not allow only the base floor could be physically modeled in the laboratory by accepting a lower degree of accuracy. Each column and beam element were discretized using one element, while each brace element was discretized using eight elements. The choice to use only one element for beams and columns was made because those elements are designed to remain in the elastic range during the earthquake event. The partitioned simulation was then verified against nonlinear dynamic FE analysis of the whole frame performed in OpenSees [4], which employs fiber-based nonlinear Bernoulli beam elements.

As anticipated, the RT-HES of the steel braced frame is numerically simulated. The proposed algorithm of Chapter 8.4 is implemented into a MATLAB FE environment developed in house. Such a simulation environment comes with a nonlinear beam element, which accounts for geometric nonlinearity and nonlinear material behaviour based on Giuffrè-Menegotto-Pinto formulation. The beam element is based on large deformation theory (corotational formulation) under the assumption of small strains [5]. The analysis provides a complete load-deformation history for two-dimensional steel frames.

The results of the virtual RT-HSS campaign are summarized herein. It is possible to observe a very good degree of accuracy between the partitioned and the monolithic solution.

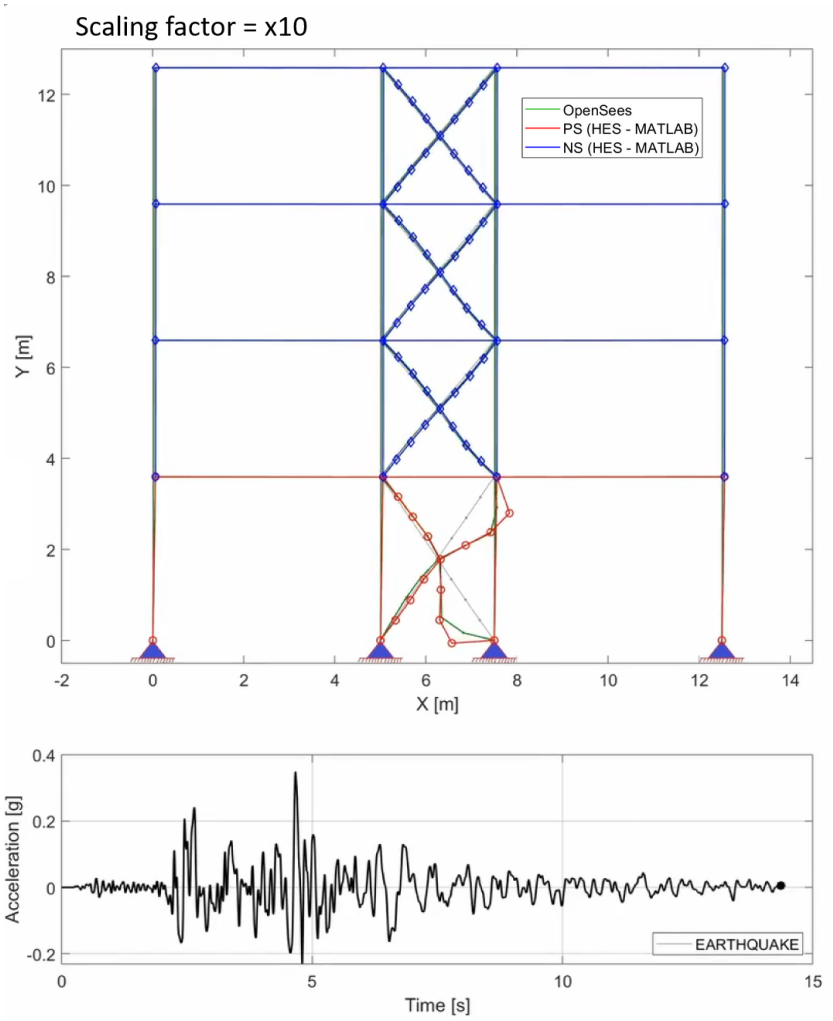

Figure 8.17: Deformed shape at the end of the simulation and acceleration time-history.

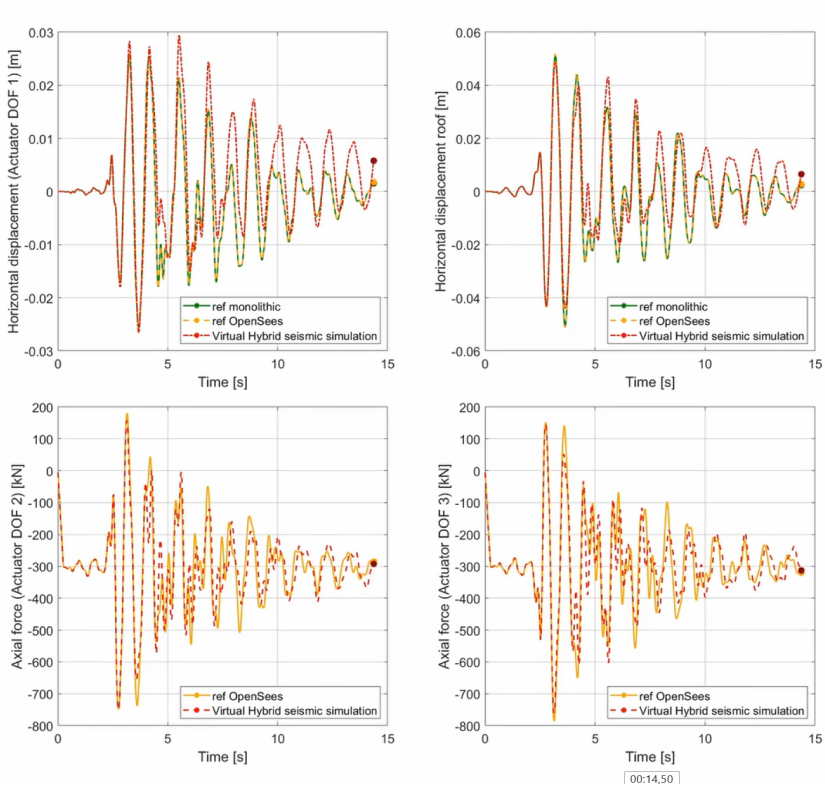

Figure 8.18: Virtual Hybrid Earthquake simulation results.

8.5 Experimental tests

The proposed procedure was also implemented in the JRC simulation environment in order to perform the experiential tests. In this section, plots with the evolution of forces and displacements of the hybrid tests carried out at the JRC laboratory are presented. A great deal of data was obtained from the tests carried out. However, only some of these results will be presented in this thesis.

8.5.1 Frame #A

The physical substructure (PS) used in the tests was the bare frame without fire protection as explained in Chapter 8.2. The substructured model and in-house algorithm presented in Chapter 8.4 was used for this test.

(a) *(b)*

Figure 8.19: a) General view of the specimen and experimental setup at the ELSA Reaction Wall; b) detail of the brace.

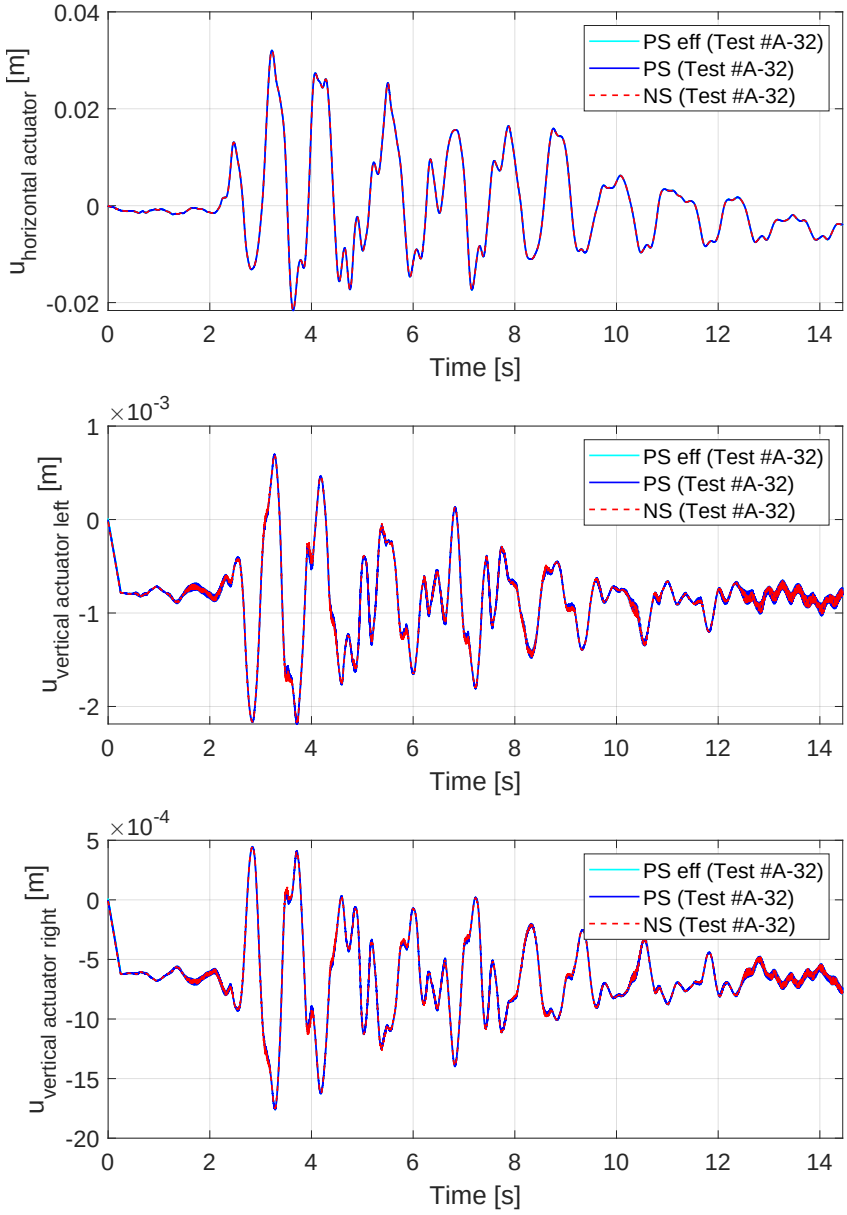

Figure 8.20: Test #A-32: evolution of the displacements of the three coupled DOFs between NS and PS.

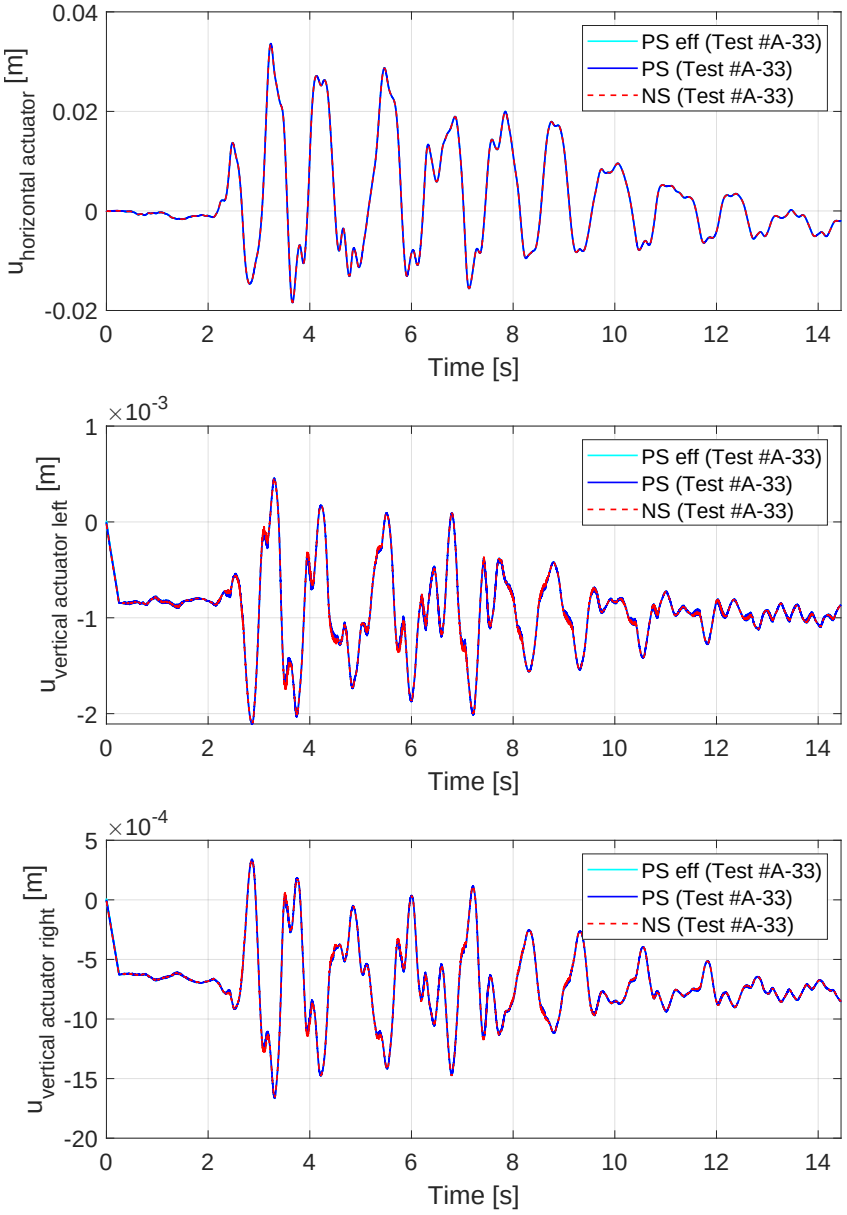

Figure 8.21: Test #A-33: evolution of the displacements of the three coupled DOFs between NS and PS.

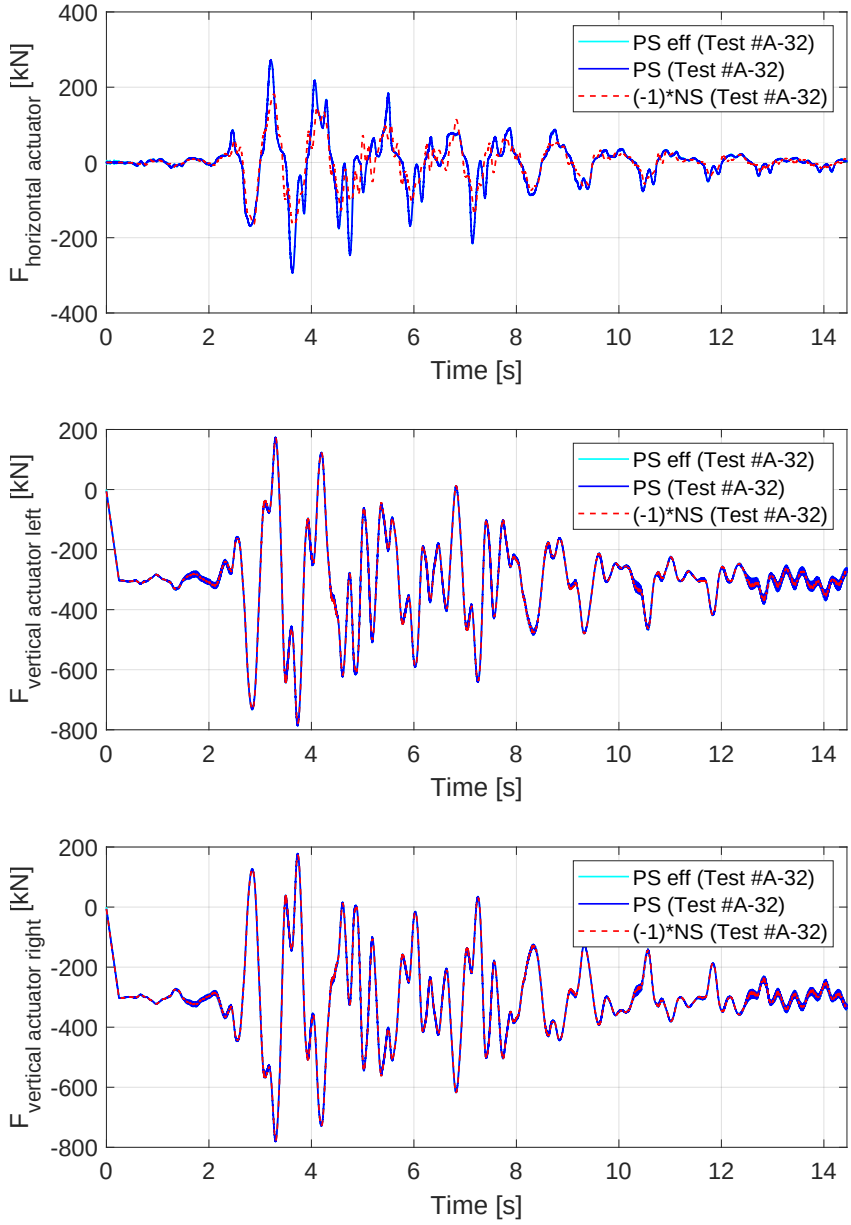

Figure 8.22: Test #A-32: evolution of the forces of the three coupled DOFs between NS and PS.

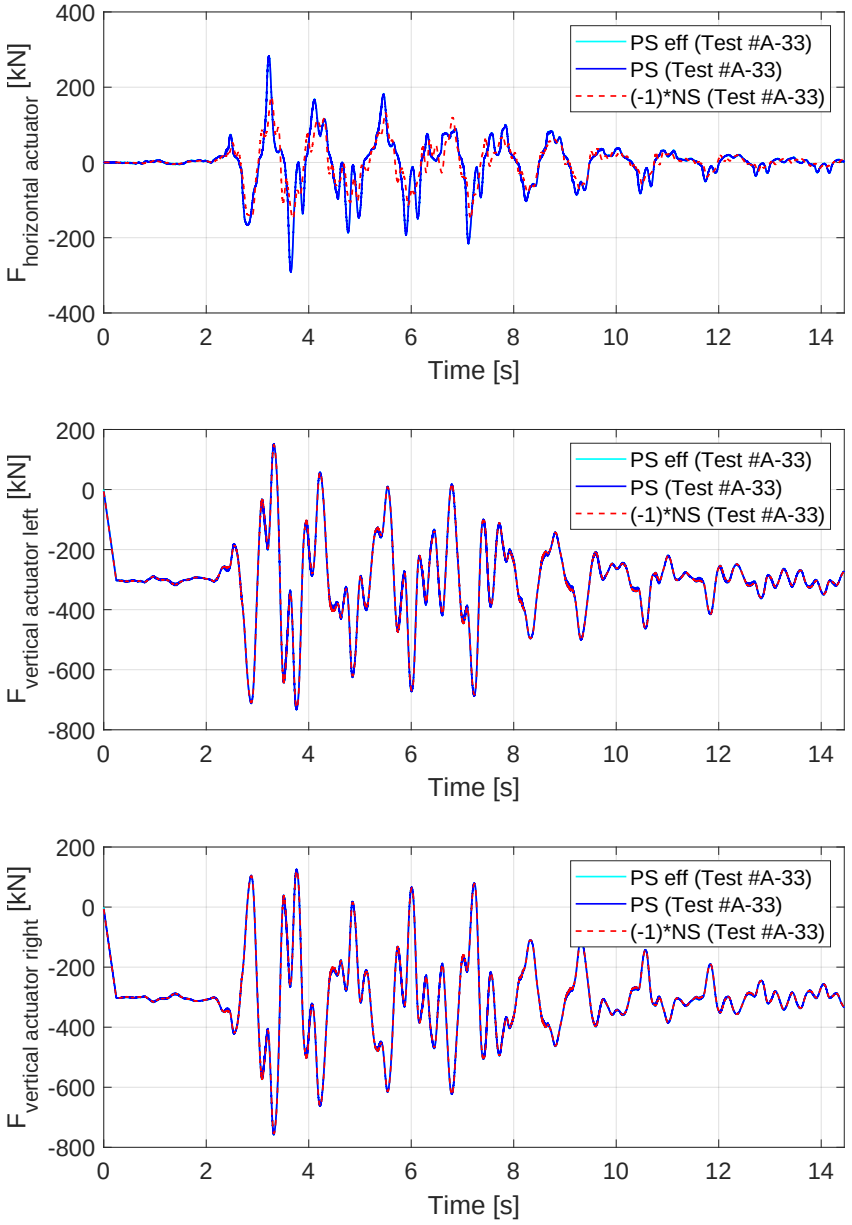

Figure 8.23: Test #A-33: evolution of the forces of the three coupled DOFs between NS and PS.

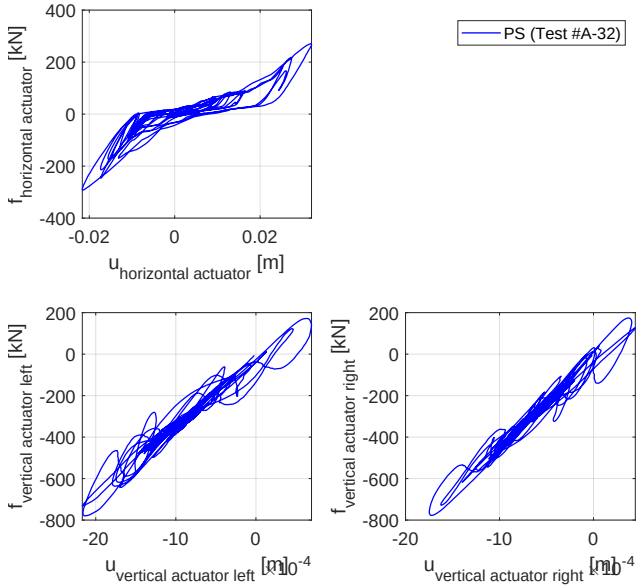

Figure 8.24: Test #A-32: evolution of the stiffness of the three coupled DOFs between NS and PS.

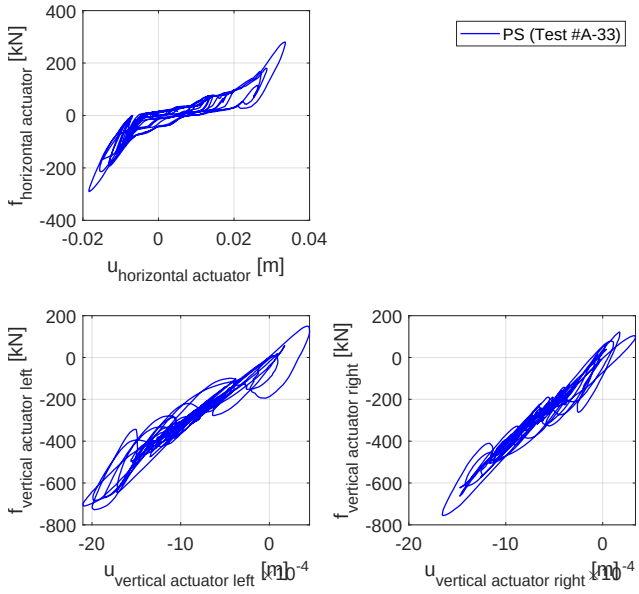

Figure 8.25: Test #A-33: evolution of the stiffness of the three coupled DOFs between NS and PS.

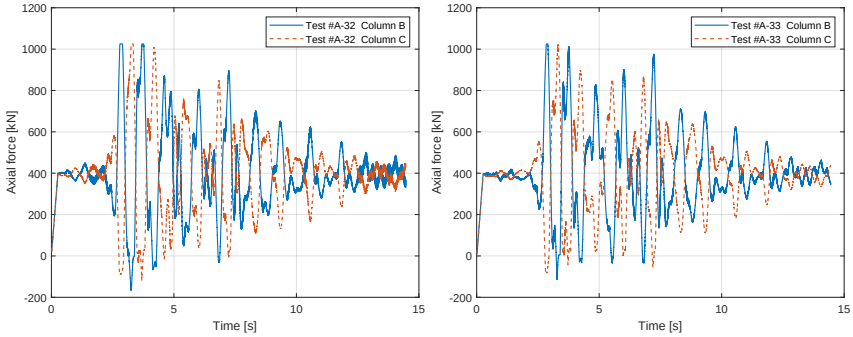

(a) *(b)*

Figure 8.26: Axial force of the internal columns: a) test #A-32; b) test #A-33.

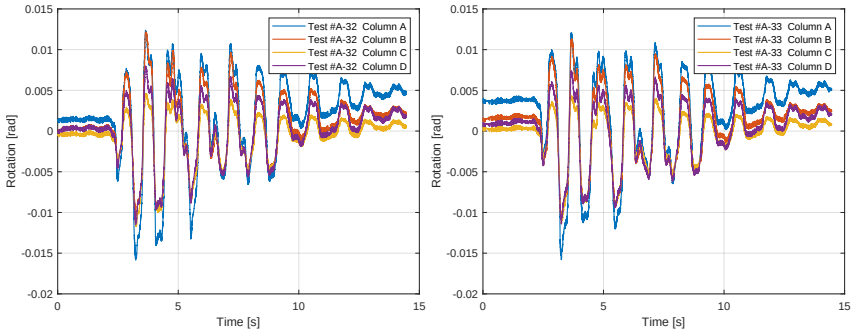

(a) *(b)*

Figure 8.27: Columns' rotation: a) test #A-32; b) test #A-33.

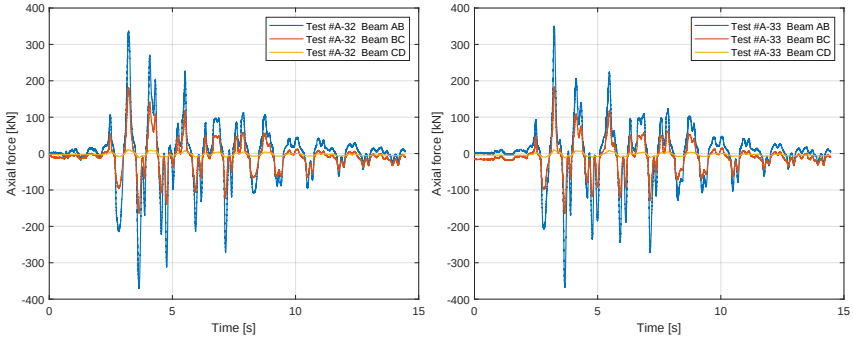

(a) *(b)*

Figure 8.28: Beams' axial force: a) test #A-32; b) test #A-33.

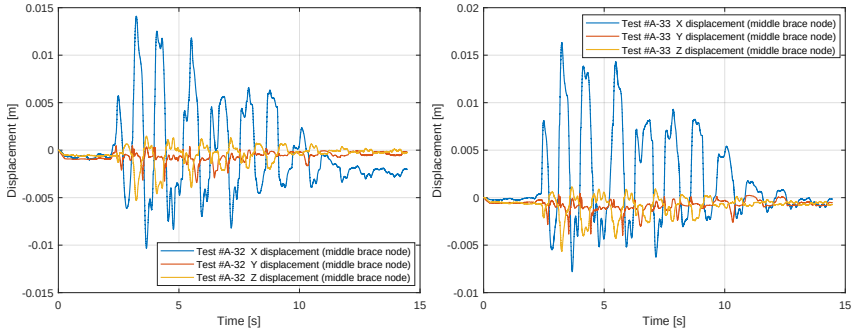

(a) *(b)*

Figure 8.29: Displacement of the center node of the braces: a) test #A-32; b) test #A-33.

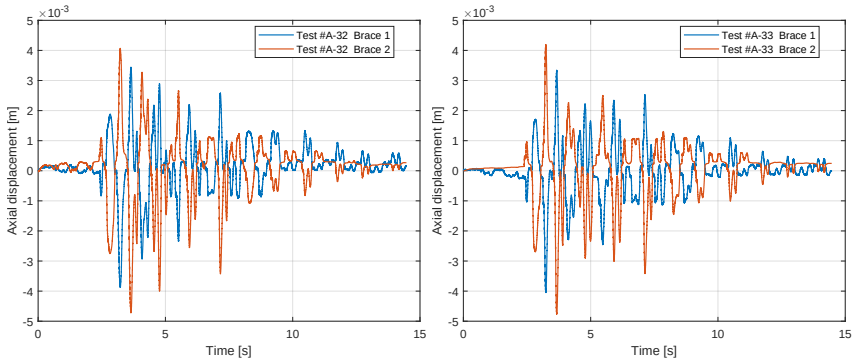

(a) *(b)*

Figure 8.30: Axial displacement of the braces: a) test #A-32; b) test #A-33.

8.5.2 Frame #B

The physical substructure (PS) used in the tests was the frame with PROMATECT-H fire protection boards system and normal joints as shown in Figure 8.31 and explained in Chapter 8.2.

(a) *(b)*

Figure 8.31: a) General view of the specimen and experimental setup at the ELSA Reaction Wall; b) detail of the brace.

PROMATECT®-H is a mineral bound fibre reinforced calcium silicate board, non-combustible (A1) in accordance with EN 13501-1 [6]. Technical data and properties of the fire protection are reported in Table 8.3.

Table 8.3: Technical data and properties of PROMATECT®-H

Technical data and properties	Value
Fire Reaction Class	A1, non-combustible
Alkalinity:	9 pH
Dry Density:	750 kg/m³
Nominal moisture content ambient:	2 %
Thermal Conductivity at 20°C:	0.189 W/m K
Flexural Strength Longitudinal:	3 N/mm²
Tensile Strength Longitudinal:	1.2 N/mm²
Compressive strength:	6.6 N/mm²

The test procedure and instruments were the same explained in Chapter 8.2. Seven tests were performed, in detail:

- One preliminary test to check the setup and the algorithm (Test #B-01).
- Two preliminary cyclic tests $\pm 5mm$ for stiffness identification of the frame. (Test #B-02 and Test #B-03)

- One hybrid test with $ACC_{test} = 0.2 \cdot ACC_{EQUFIRE}$ (Test #B-04).
- One hybrid test with $ACC_{test} = 0.3 \cdot ACC_{EQUFIRE}$ (Test #B-05).
- Two official hybrid tests with $ACC_{test} = 1.0 \cdot ACC_{EQUFIRE}$ (Test #B-06 and Test #B-07).

The substructured model and in-house algorithm presented in Chapter 8.4 was used for hybrid tests.

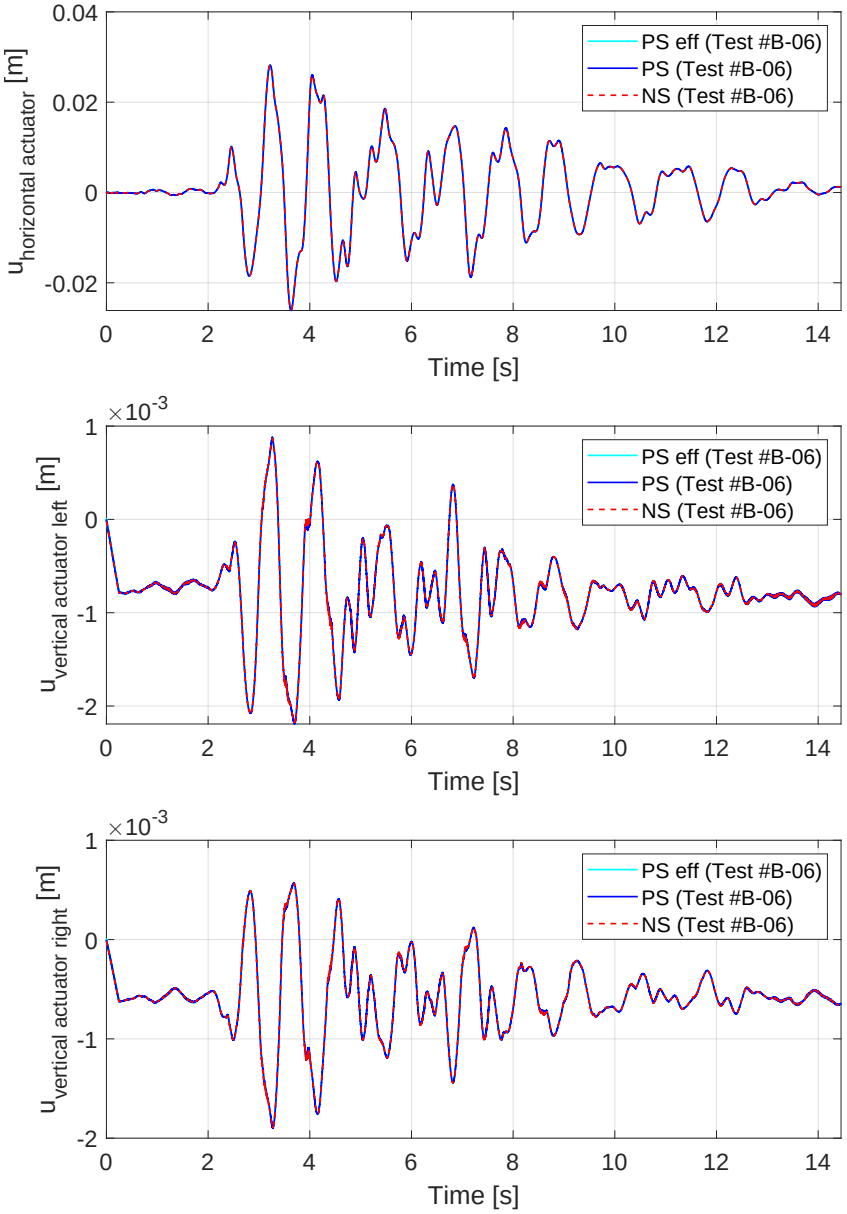

Figure 8.32: Test #B-06: evolution of the displacements of the three coupled DOFs between NS and PS.

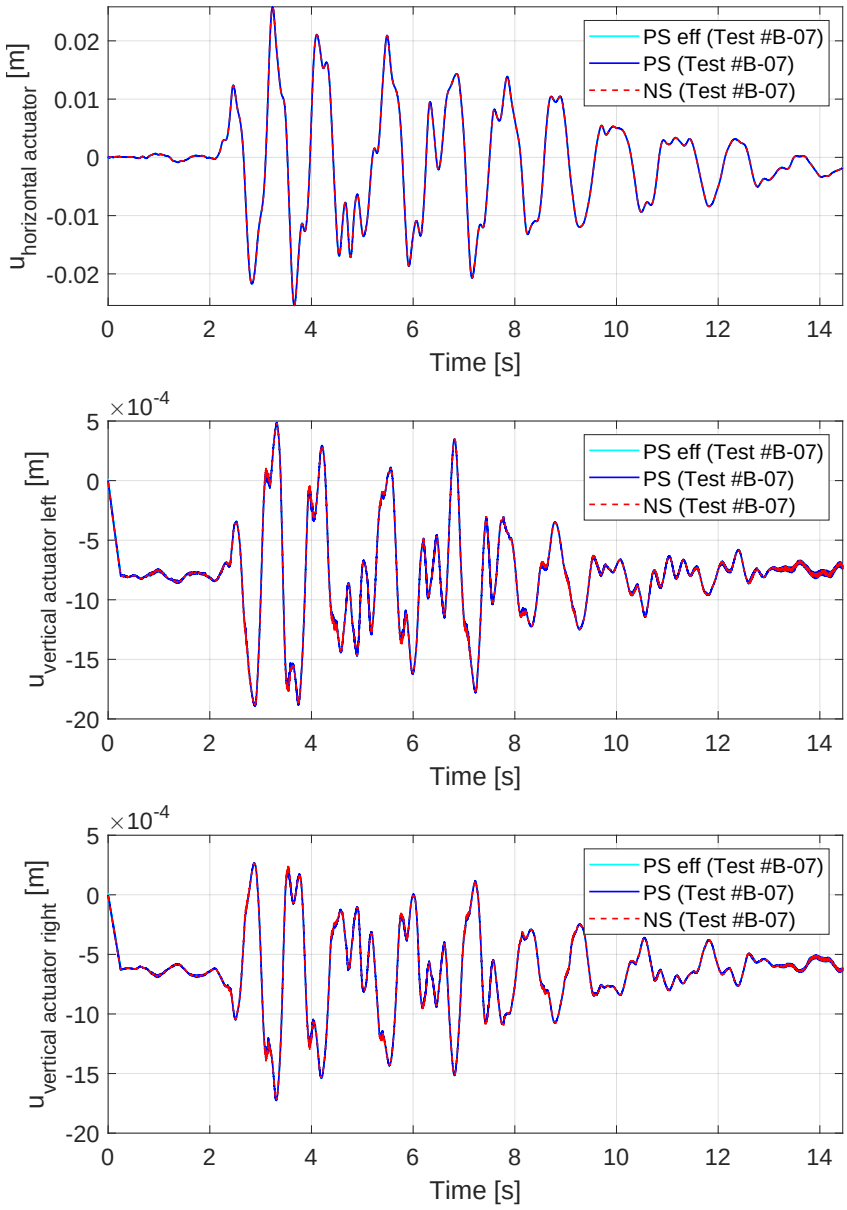

Figure 8.33: Test #B-07: evolution of the displacements of the three coupled DOFs between NS and PS.

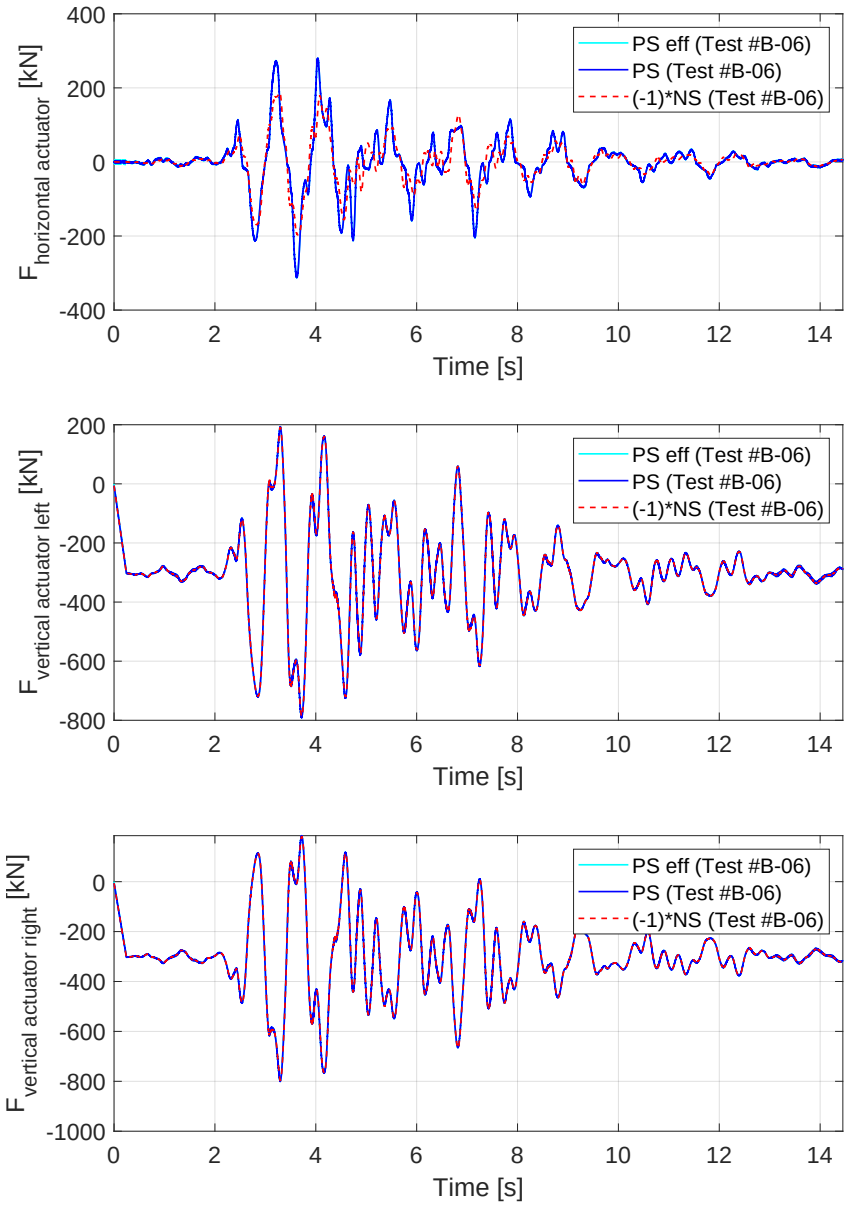

Figure 8.34: Test #B-06: evolution of the forces of the three coupled DOFs between NS and PS.

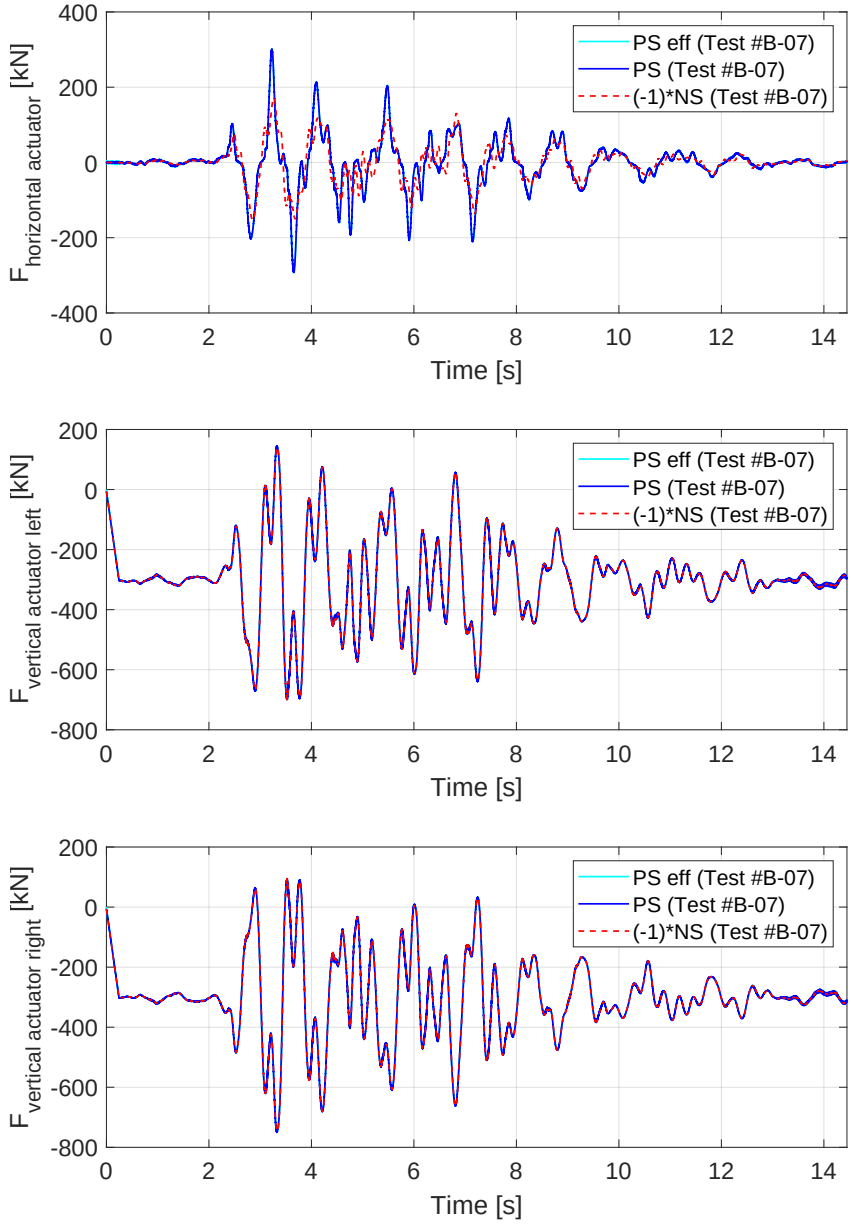

Figure 8.35: Test #B-07: evolution of the forces of the three coupled DOFs between NS and PS.

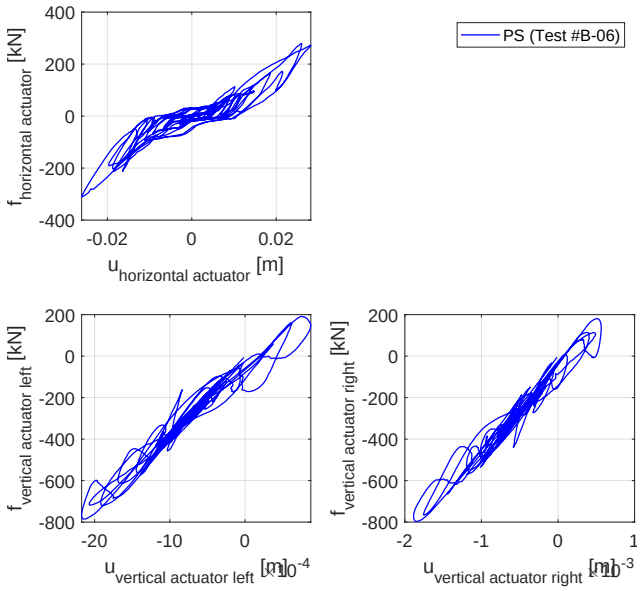

Figure 8.36: Test #B-06: evolution of the stiffness of the three coupled DOFs between NS and PS.

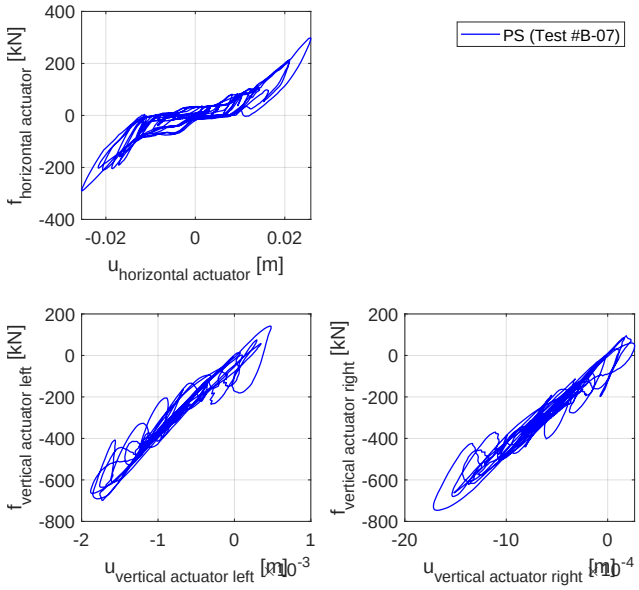

Figure 8.37: Test #B-07: evolution of the stiffness of the three coupled DOFs between NS and PS.

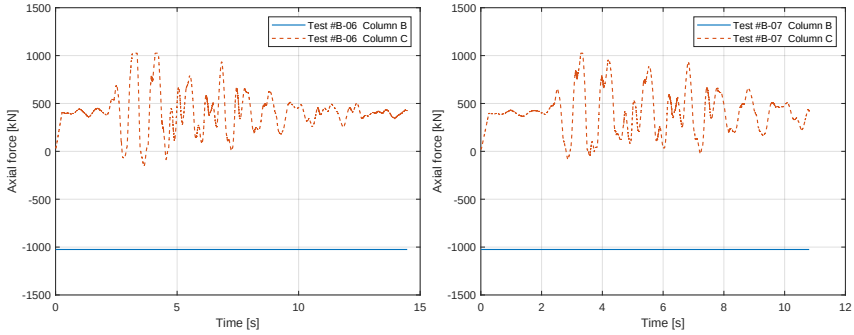

(a) *(b)*

Figure 8.38: Axial force of the internal columns: a) test #B-06; b) test #B-07.

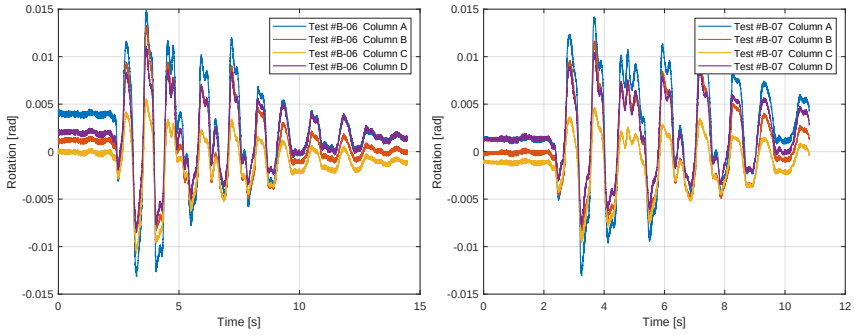

(a) *(b)*

Figure 8.39: Columns' rotation: a) test #B-06; b) test #B-07.

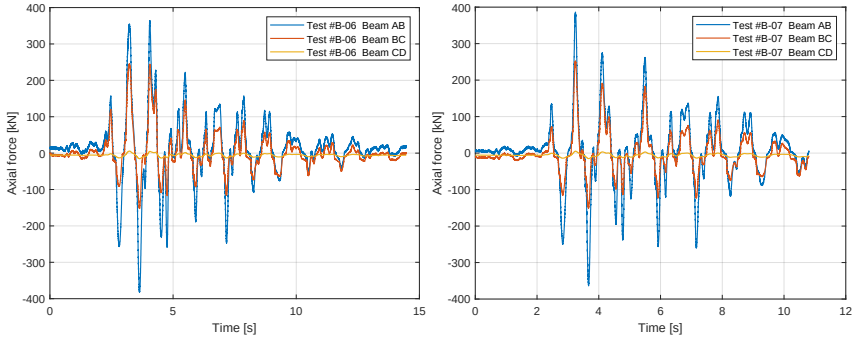

(a) *(b)*

Figure 8.40: Beams' axial force: a) test #B-06; b) test #B-07.

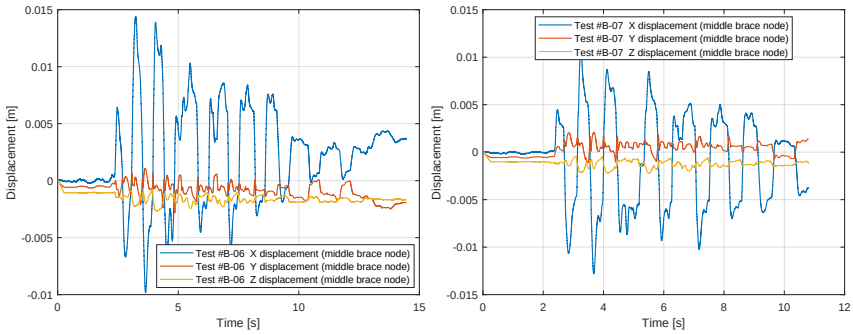

(a) *(b)*

Figure 8.41: Displacement of the center node of the braces: a) test #B-06; b) test #B-07.

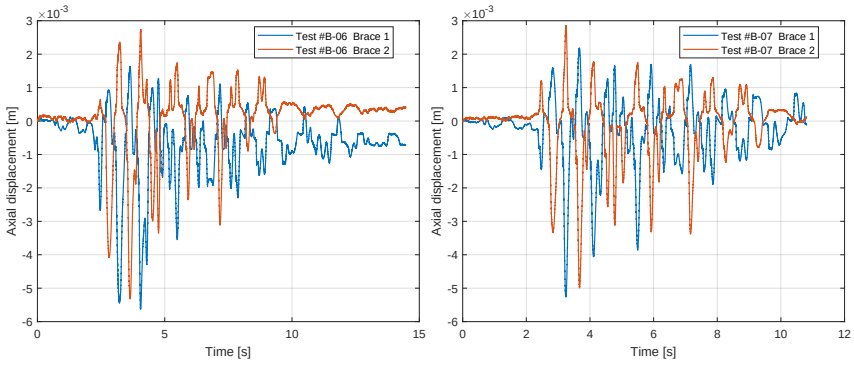

(a) *(b)*

Figure 8.42: Axial displacement of the braces: a) test #B-06; b) test #B-07.

After the two seismic tests, there was some minor damage to the casing of the braces and the column, as shown in Figure 8.43.

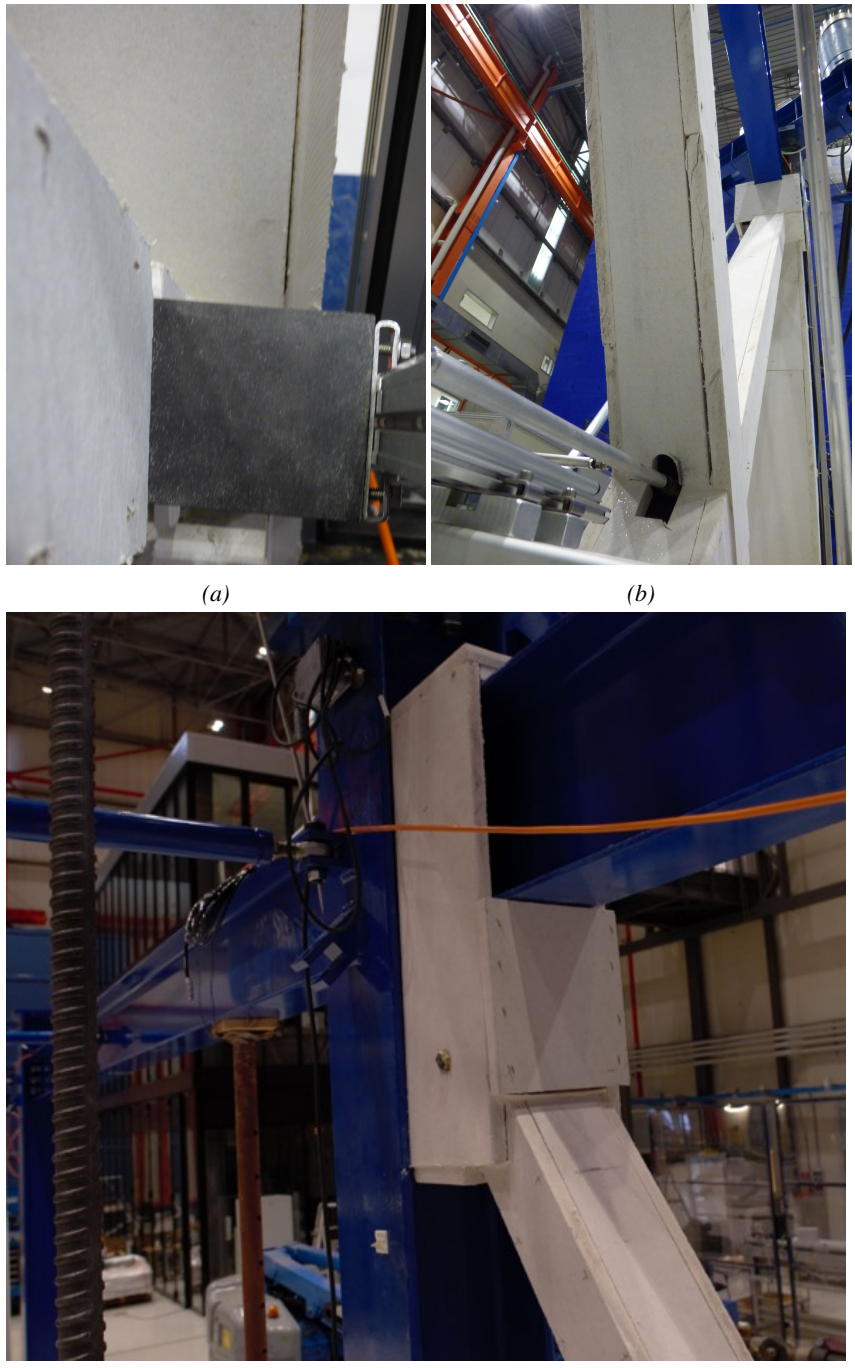

(a) *(b)*

(c)

Figure 8.43: Damages after two seismic tests at 1.0g: a) damage of the casing of the column; b) detachment of the boards at the bracing crossing; c) damage of the casing of the bottom connection.

8.5.3 Frame #C

The physical substructure (PS) used in the tests was the frame with PROMATECT-H fire protection boards system designed for seismic regions as shown in Figure 8.44 and explained in Chapter 8.2.

(a) *(b)*

Figure 8.44: a) General view of the specimen and experimental setup at the ELSA Reaction Wall; b) detail of the brace.

PROMATECT®-H is a mineral bound fibre reinforced calcium silicate board, non-combustible (A1) in accordance with EN 13501-1 [6]. Technical data and properties of the fire protection are reported in Table 8.4.

Table 8.4: Technical data and properties of PROMATECT®-H

Technical data and properties	Value
Fire Reaction Class	A1, non-combustible
Alkalinity:	9 pH
Dry Density:	750 kg/m³
Nominal moisture content ambient:	2 %
Thermal Conductivity at 20°C:	0.189 W/m K
Flexural Strength Longitudinal:	3 N/mm²
Tensile Strength Longitudinal:	1.2 N/mm²
Compressive strength:	6.6 N/mm²

The test procedure and instruments were the same explained in Chapter 8.2. Six tests were performed, in detail:

- One preliminary test to check the setup and the algorithm (Test #C-01).
- One preliminary cyclic tests $\pm 5mm$ for stiffness identification of the frame. (Test #C-02)

- One hybrid test with $ACC_{test} = 0.2 \cdot ACC_{EQUFIRE}$ (Test #C-03).
- Two official hybrid tests with $ACC_{test} = 1.0 \cdot ACC_{EQUFIRE}$ (Test #C-04 and Test #C-05).
- One cyclic test $\pm 30mm.$ (Test #C-06)

The substructured model and in-house algorithm presented in Chapter 8.4 was used for hybrid tests.

Figure 8.45 and Figure 8.46 present the evolution of the displacements as function of time of Test Test #C-04 and Test #C-05. The test #C-05 stopped unexpectedly when the computer running the simulation went in sleep mode, but hopefully, it happened during the small oscillations at the end of the accelerogram.

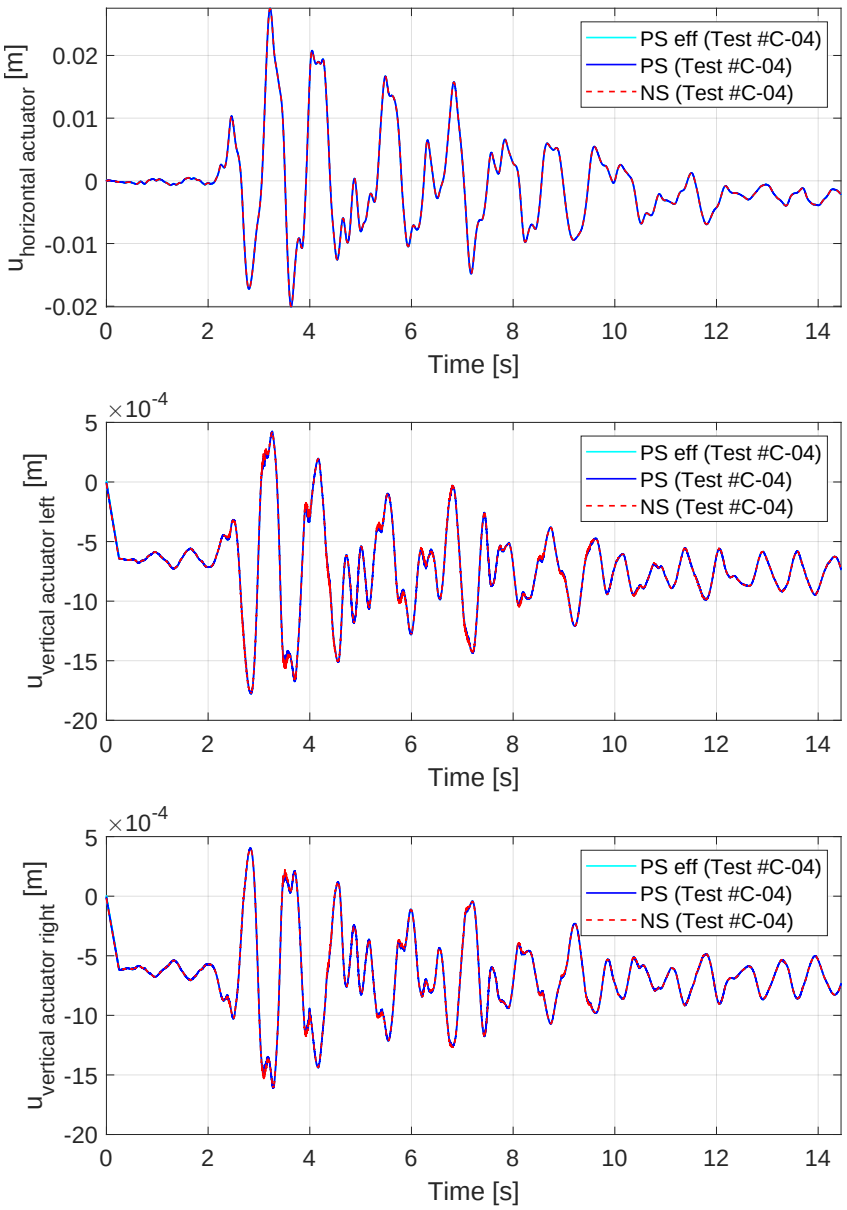

Figure 8.45: Test #C-04: evolution of the displacements of the three coupled DOFs between NS and PS.

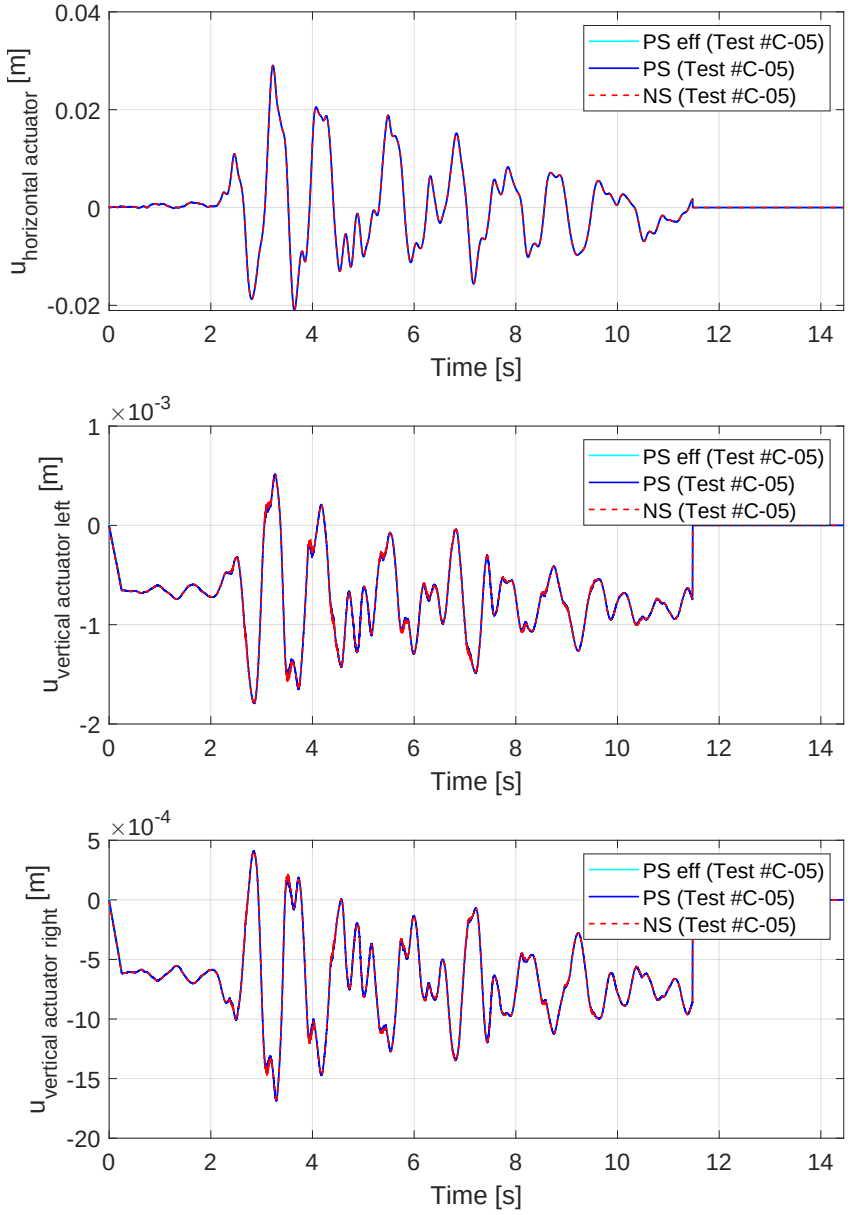

Figure 8.46: Test #C-05: evolution of the displacements of the three coupled DOFs between NS and PS.

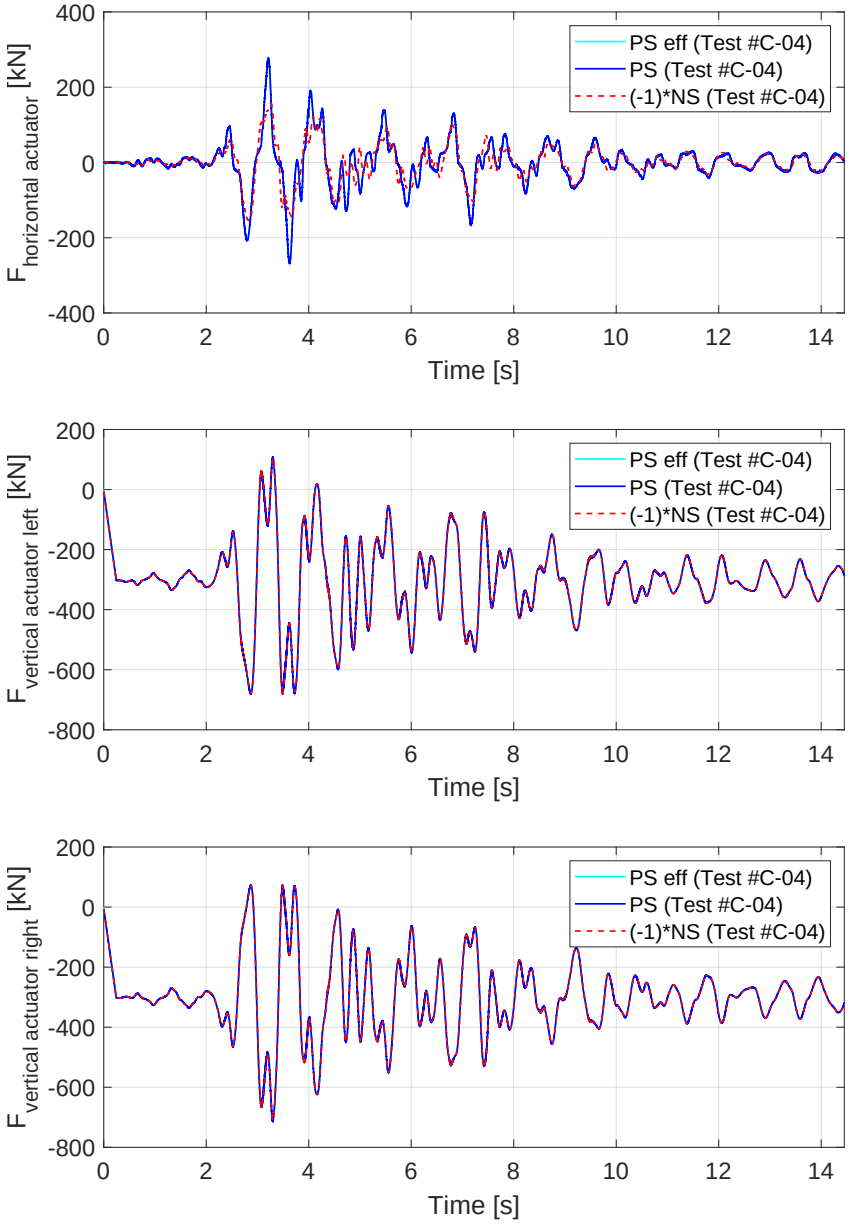

Figure 8.47: Test #C-04: evolution of the forces of the three coupled DOFs between NS and PS.

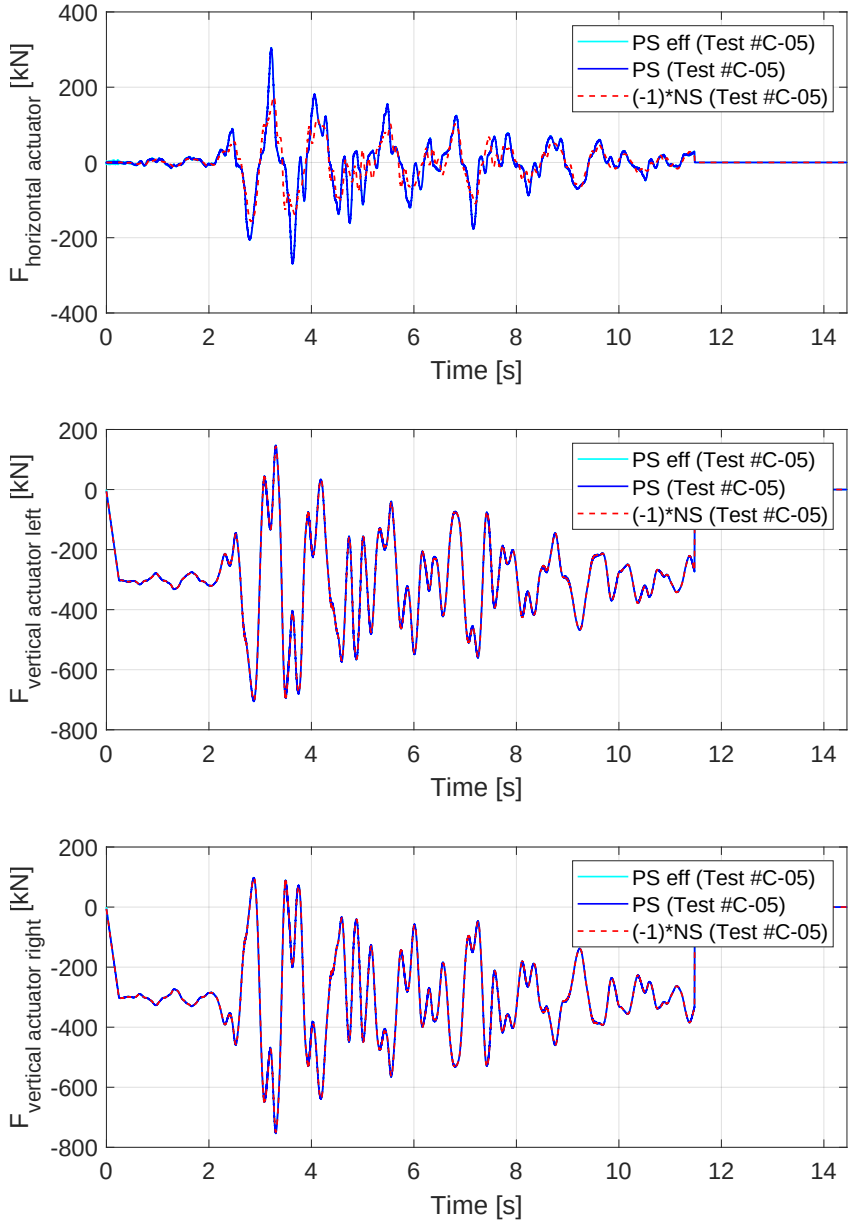

Figure 8.48: Test #C-05: evolution of the forces of the three coupled DOFs between NS and PS.

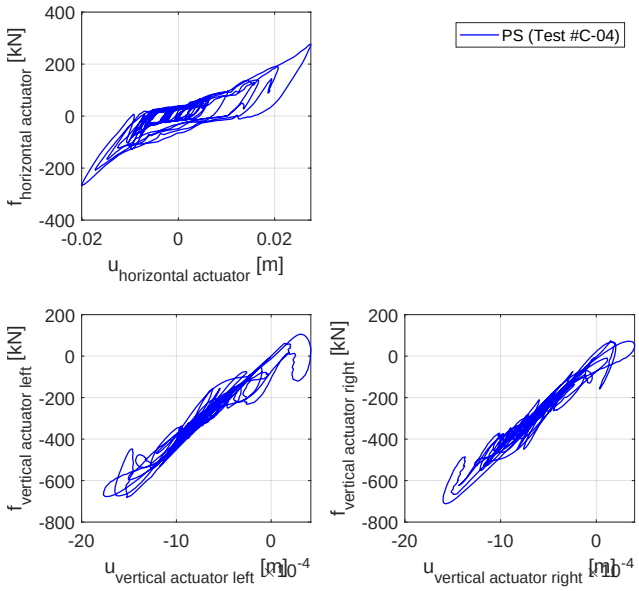

Figure 8.49: Test #C-04: evolution of the stiffness of the three coupled DOFs between NS and PS.

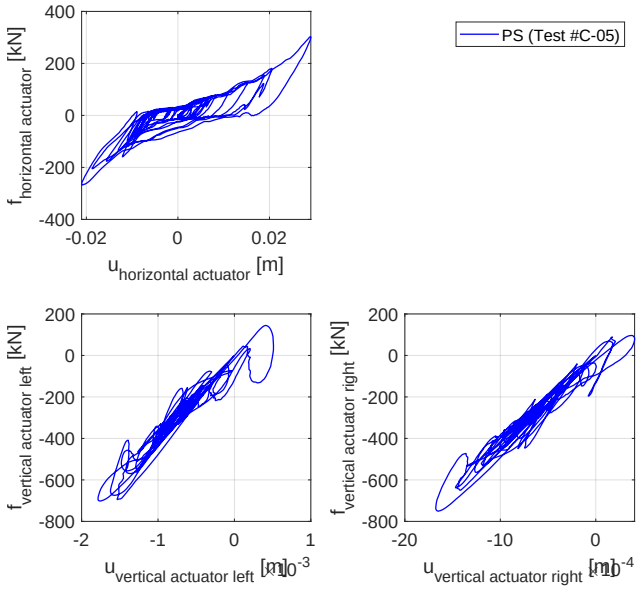

Figure 8.50: Test #C-05: evolution of the stiffness of the three coupled DOFs between NS and PS.

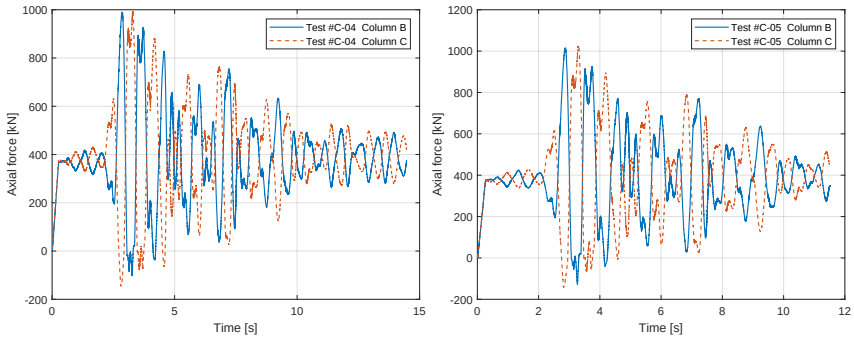

(a) *(b)*

Figure 8.51: Axial force of the internal columns: a) test #C-04; b) test #C-05.

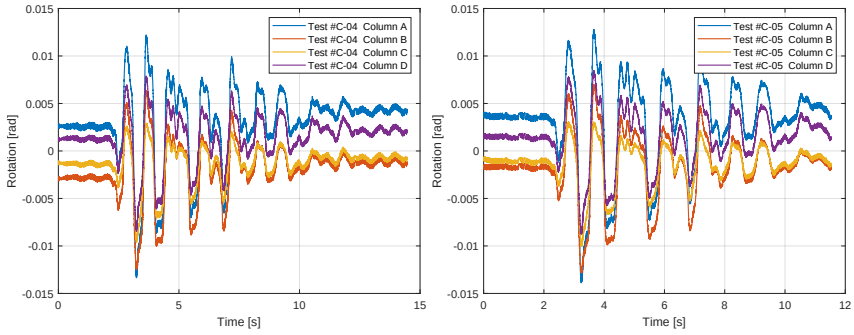

(a) *(b)*

Figure 8.52: Columns' rotation: a) test #C-04; b) test #C-05.

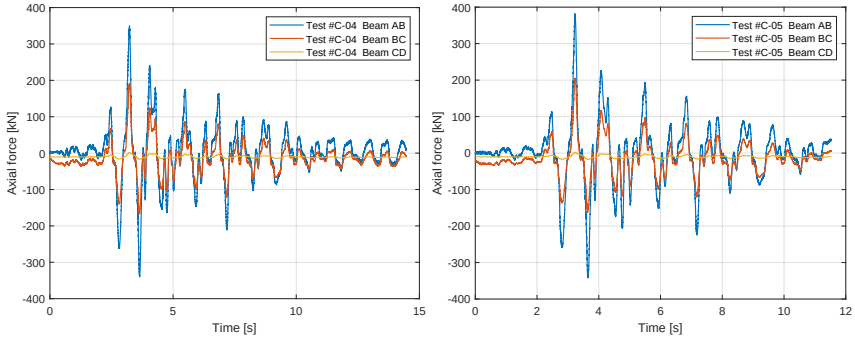

(a) *(b)*

Figure 8.53: Beams' axial force: a) test #C-04; b) test #C-05.

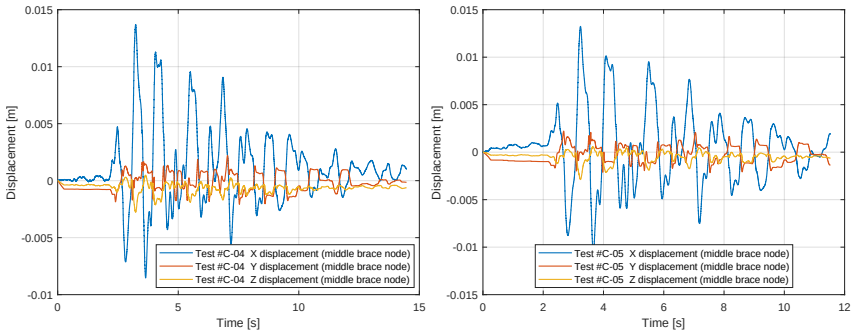

(a) *(b)*

Figure 8.54: Displacement of the center node of the braces: a) test #C-04; b) test #C-05.

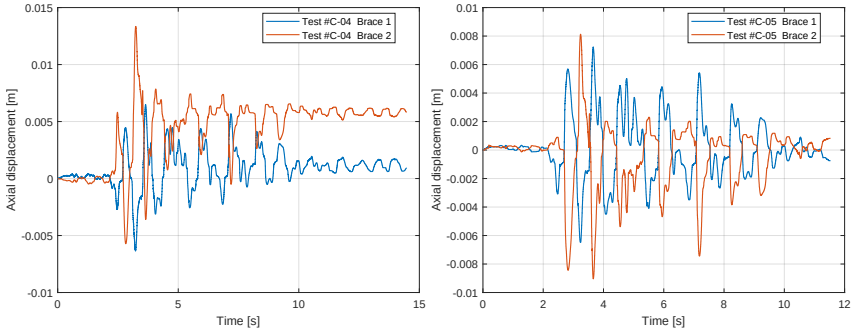

(a) *(b)*

Figure 8.55: Axial displacement of the braces: a) test #C-04; b) test #C-05.

After the two seismic tests a cyclic test was conducted (horizontal displacement $\pm 30mm$).

After the two seismic tests there was some minor damage of the casing of the connection, as shown in Figure 8.56. More damage occurred after the cyclic test, as shown in Figure 8.57.

Figure 8.56: Damages after two seismic tests at 1.0g

(a)

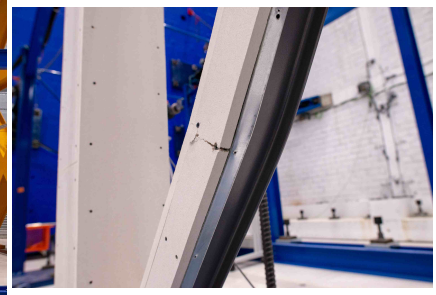

(b)

Figure 8.57: Damages after the cyclic test tests.

8.5.4 Frame #D

The physical substructure (PS) used in the test was the frame with fire protection system PROMASPRAY®-P300 series (CAFCO 300) and two fire barrier walls, as shown in Figure 8.58 and explained in Chapter 8.2.

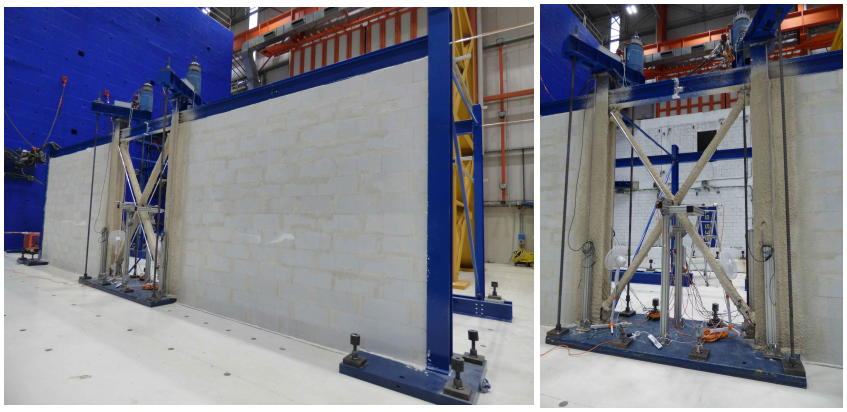

(a) *(b)*

Figure 8.58: a) General view of the specimen and experimental setup at the ELSA Reaction Wall; b) detail of the brace.

The PROMASPRAY®-P300 series (CAFCO 300) is a gypsum-based wet mix spray-applied fire-resistive material, designed for applications in seismic regions, in which a mechanical reinforcing mesh was placed in the middle of the applied material.

Table 8.5: Technical data and properties of PROMOSPRAY®- P300 series (CAFCO 300)

Technical data and properties	**Value**
Fire Reaction Class	A1, non-combustible
Alkalinity:	8.5 pH
Density:	365 kg/m³
Thermal Conductivity at 20°C:	0.078 W/m K

In this test, two different solutions for the walls were used (one solution on the right side and one on the left side). In this respect, both of the walls were made with the same block type; the only difference was to use a masonry reinforcement solution (Murfor) in one of the two walls. Murfor is a prefabricated bed joint reinforcement consisting of two parallel wires welded together with a continuous truss wire. This significantly increases the strength of the masonry (cracks control) and

so it is possible to see the different behaviour of the walls under the seismic force. An elastic protection joint was used between the wall and the frame.

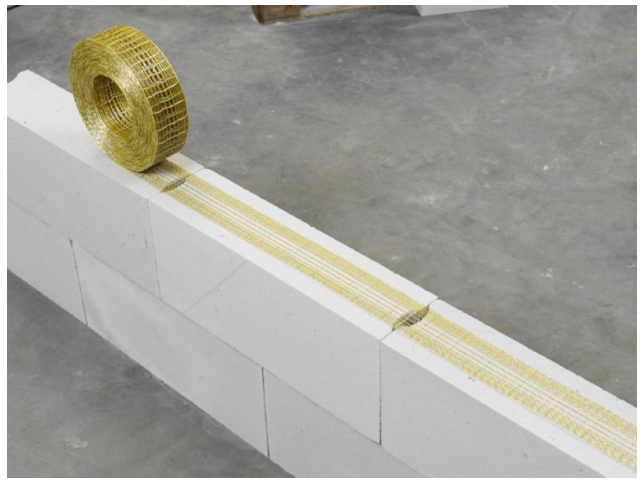

Figure 8.59: Xella®Murfor system.

(a) *(b)*

Figure 8.60: Construction of the Xella®fire barrier walls.

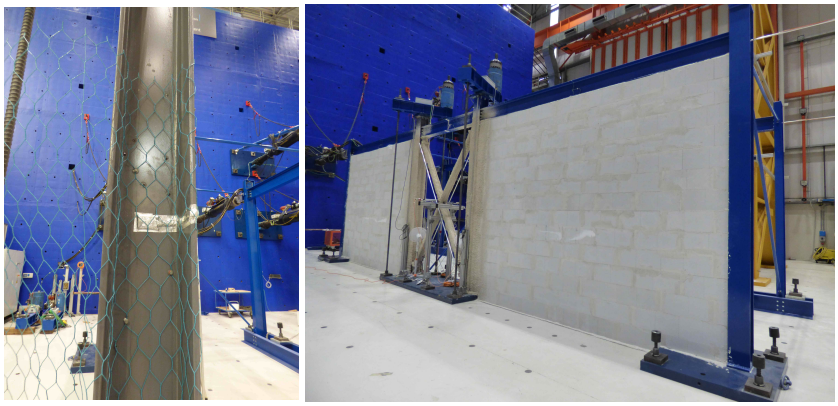

(a) *(b)*

Figure 8.61: Fire protection system PROMASPRAY®-P300 series (CAFCO 300)

Figure 8.62 and Figure 8.63 present the evolution of the displacements as function of time of Test Test #D-03 and Test #D-04.

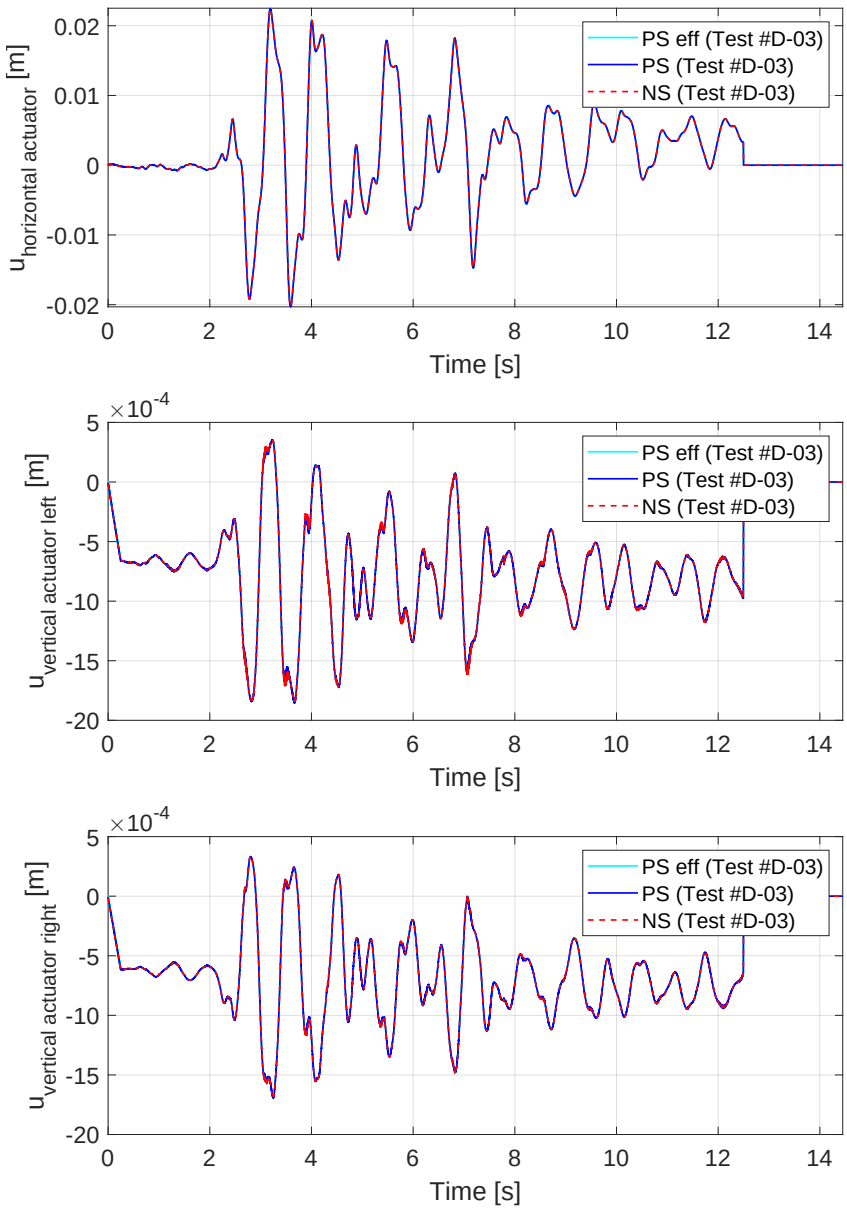

Figure 8.62: Test #D-03: evolution of the displacements of the three coupled DOFs between NS and PS.

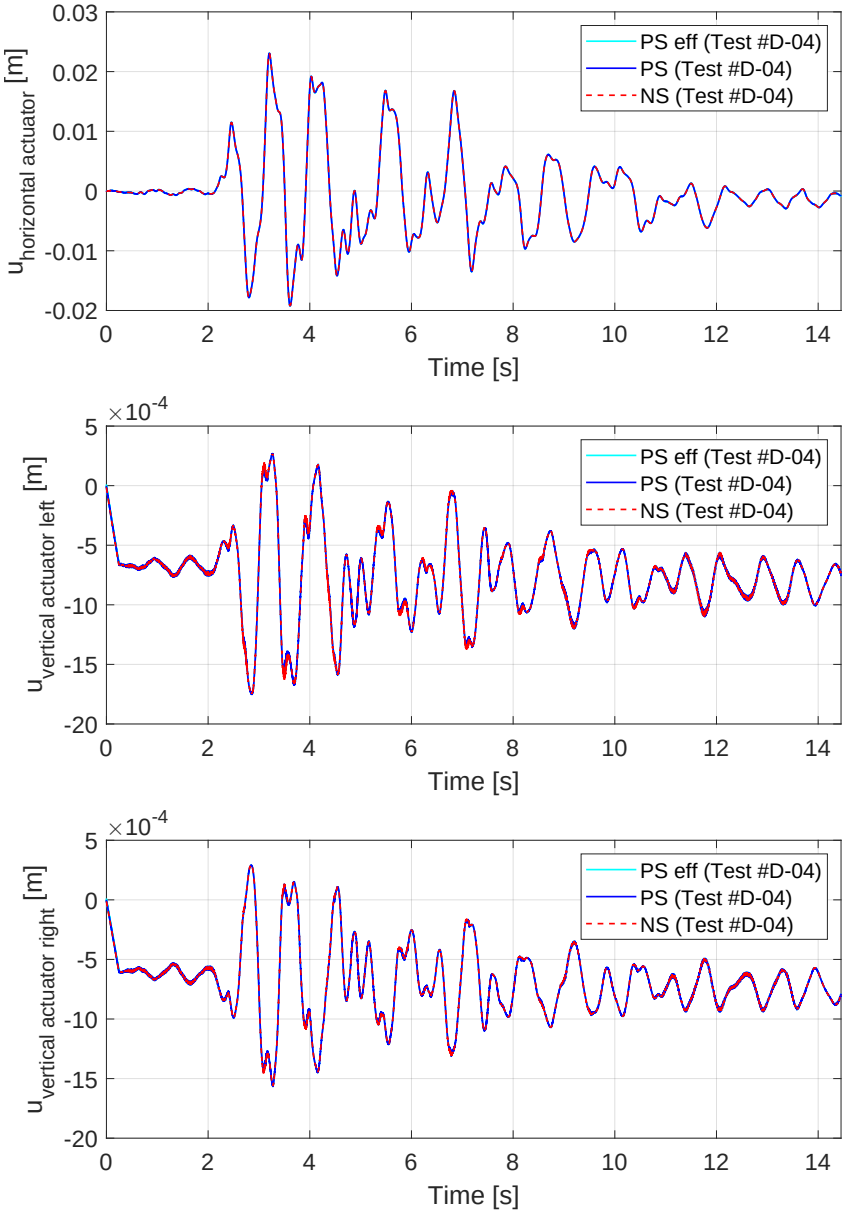

Figure 8.63: Test #D-04: evolution of the displacements of the three coupled DOFs between NS and PS.

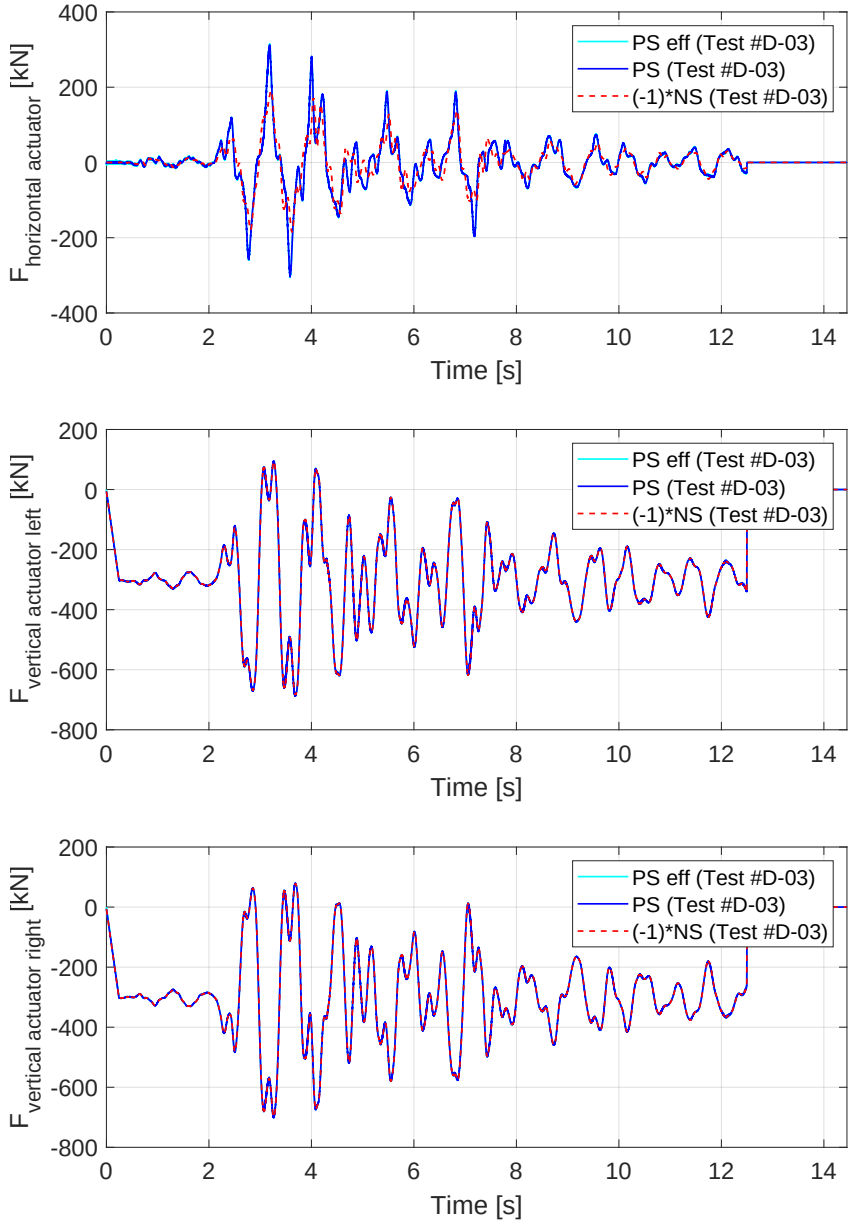

Figure 8.64: Test #D-03: evolution of the forces of the three coupled DOFs between NS and PS.

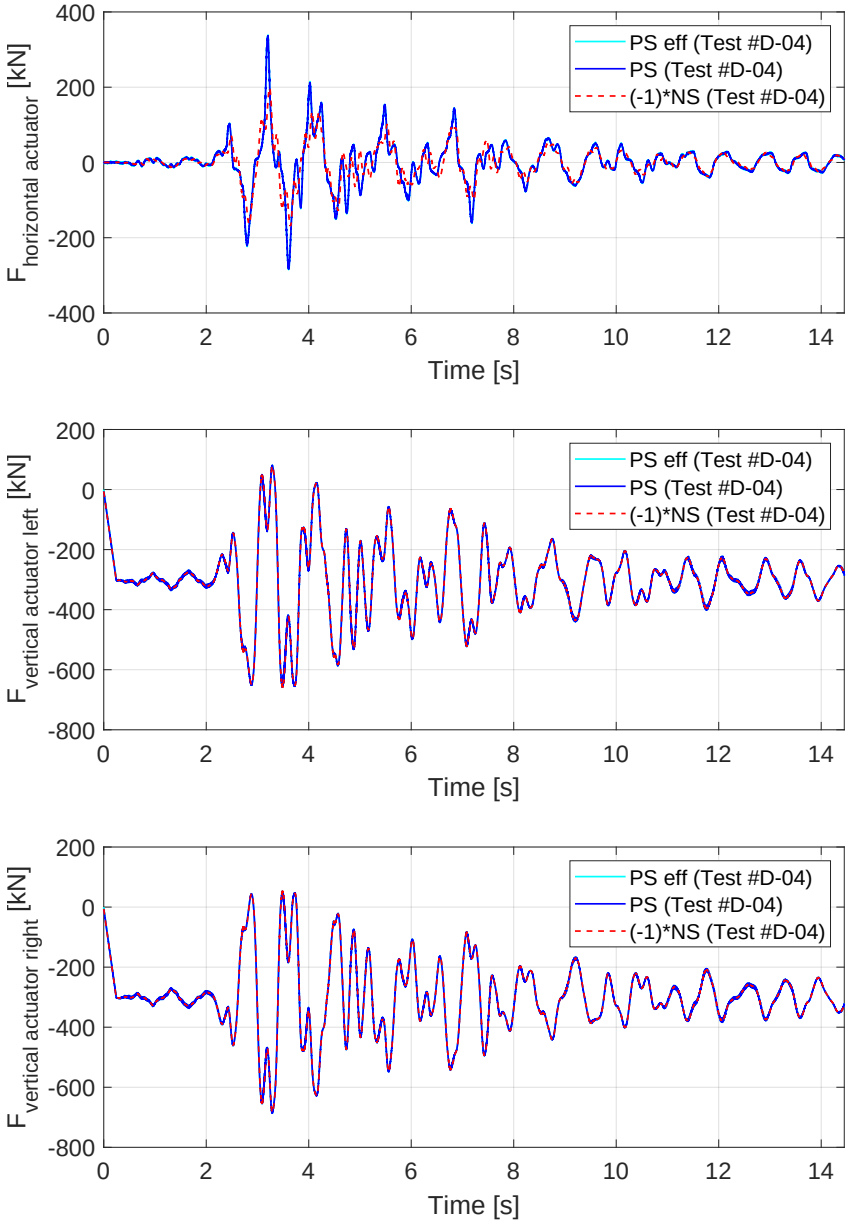

Figure 8.65: Test #D-04: evolution of the forces of the three coupled DOFs between NS and PS.

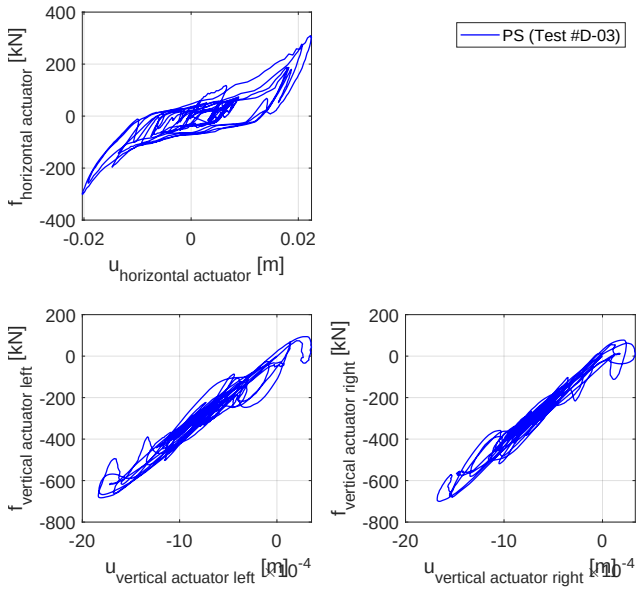

Figure 8.66: Test #D-03: evolution of the stiffness of the three coupled DOFs between NS and PS.

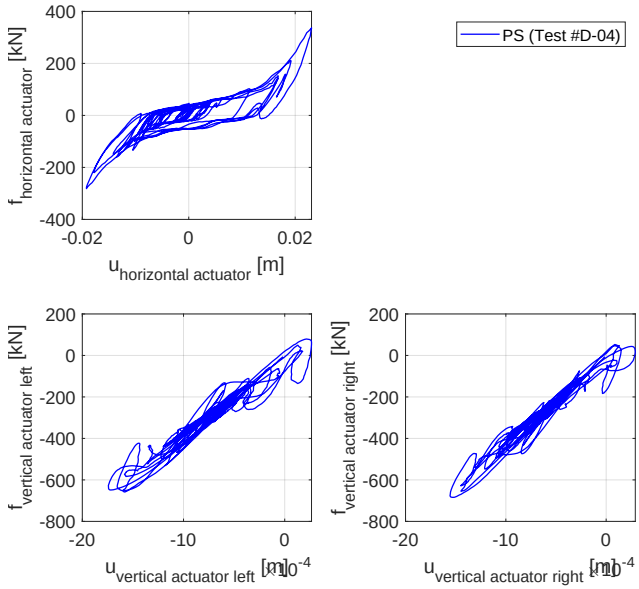

Figure 8.67: Test #D-04: evolution of the stiffness of the three coupled DOFs between NS and PS.

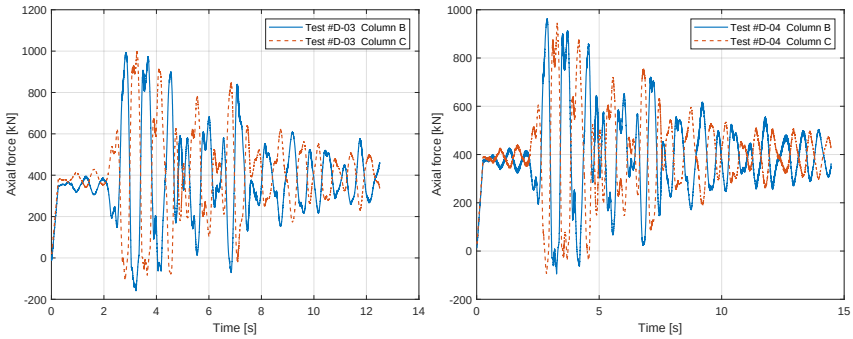

(a) *(b)*

Figure 8.68: Axial force of the internal columns: a) test #D-03; b) test #D-04.

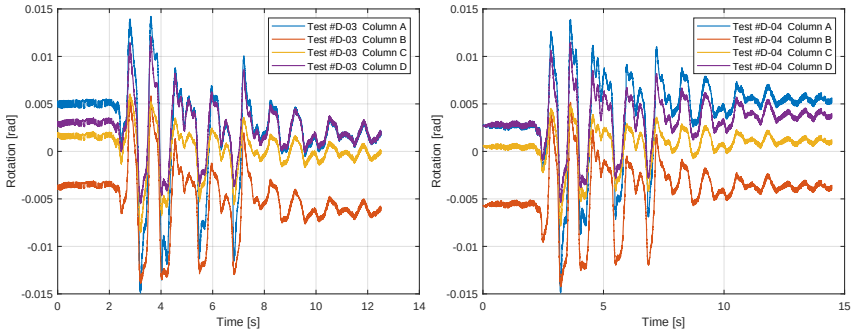

(a) *(b)*

Figure 8.69: Columns' rotation: a) test #D-03; b) test #D-04.

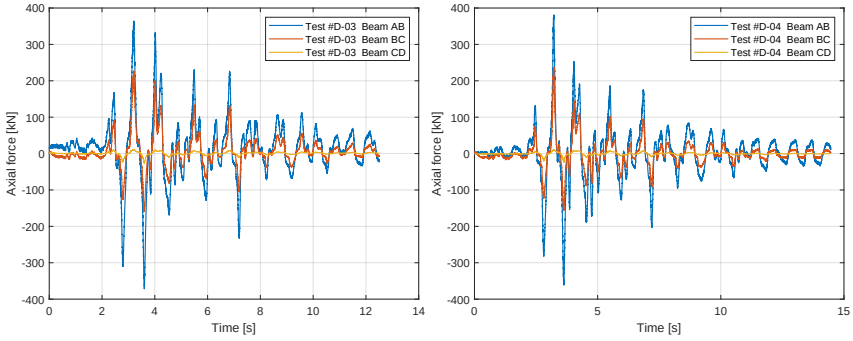

(a) *(b)*

Figure 8.70: Beams' axial force: a) test #D-03; b) test #D-04.

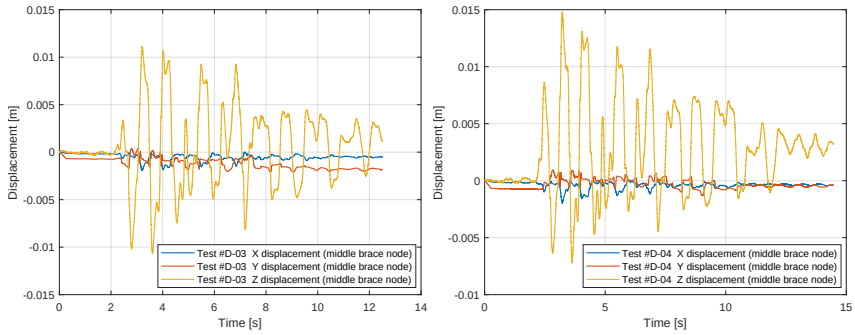

(a) *(b)*

Figure 8.71: Displacement of the center node of the braces: a) test #D-04; b) test #D-05.

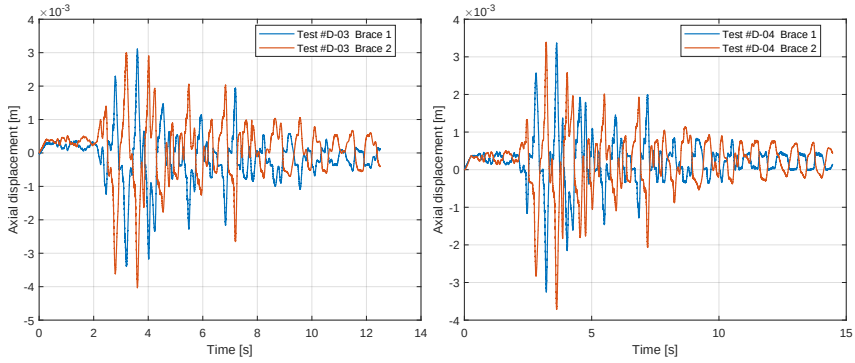

(a) *(b)*

Figure 8.72: Axial displacement of the braces: a) test #D-03; b) test #D-04.

A cyclic test was conducted after the two seismic tests (horizontal displacement $\pm 35mm$).

After the two seismic tests, there was some minor damage to the protection between the columns and the walls, as shown in Figure 8.73. More damage occurred after the cyclic test, as shown in Figure 8.74.

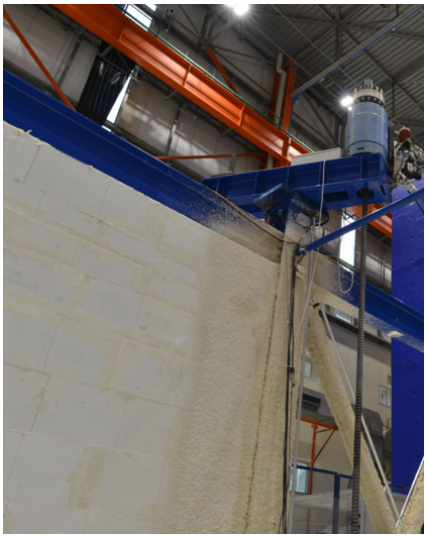

(a)

(b)

(c)

Figure 8.73: Damages after two seismic tests at 1.0g.

(a) *(b)*

(c)

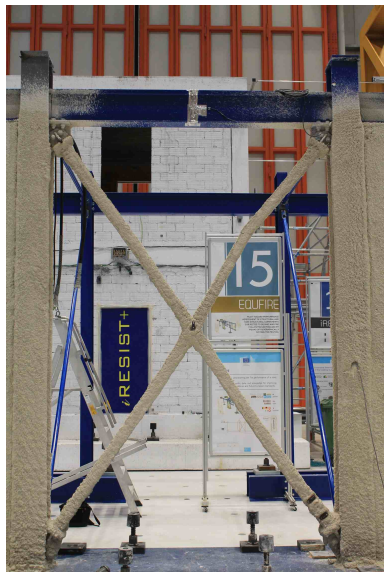

(d)

Figure 8.74: Damages after the cyclic test tests.

8.6 Comparison Virtual HES simulation versus experimental tests

This section presents the comparison between the virtual HES simulation (Chapter 8.4.2), the experimental tests (Chapter 8.5) and the numerical simulation performed using OpenSees.

8.6.1 Frame #A

The comparison regarding the experimental test of Frame #A in terms of displacements and forces of the 3-DOFs PS are reported in Figure 8.75 and Figure 8.76.

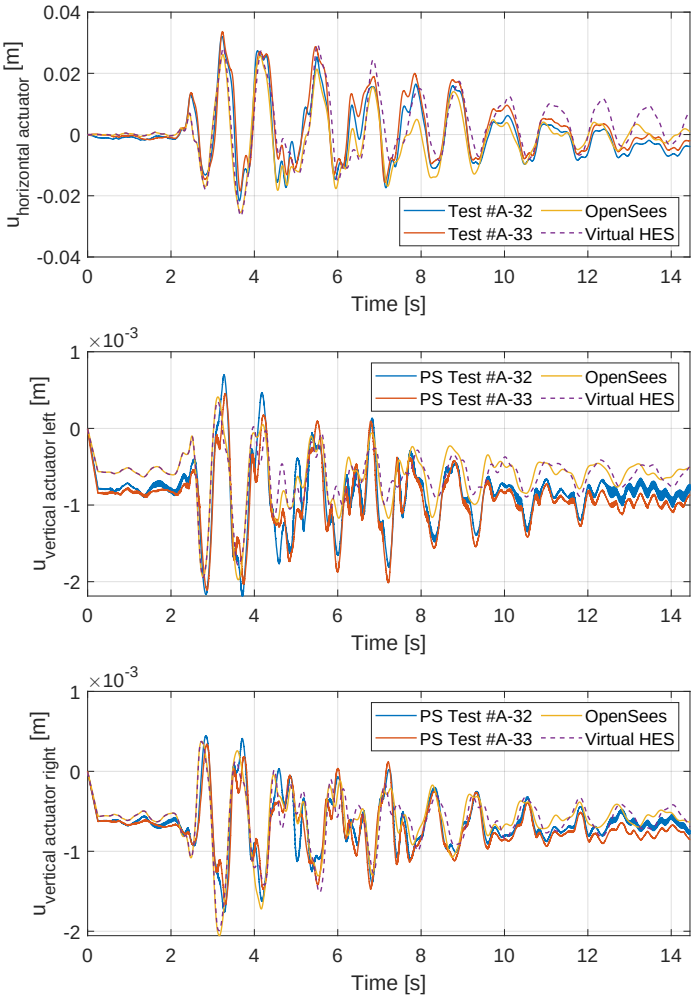

Figure 8.75: comparison of the displacements (Test #A-32 and #A-33)

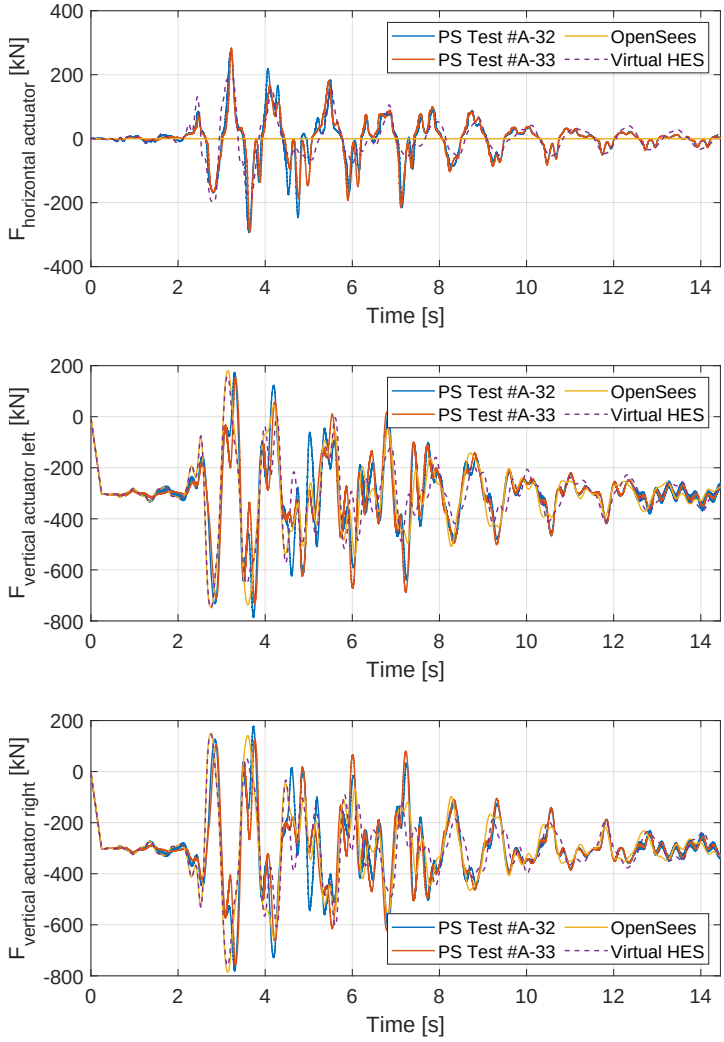

Figure 8.76: comparison of the forces (Test #A-32 and #A-33)

8.6.2 Frame #B

The comparison regarding the experimental test of Frame #B in terms of displacements and forces of the 3-DOFs PS are reported in Figure 8.77 and Figure 8.78.

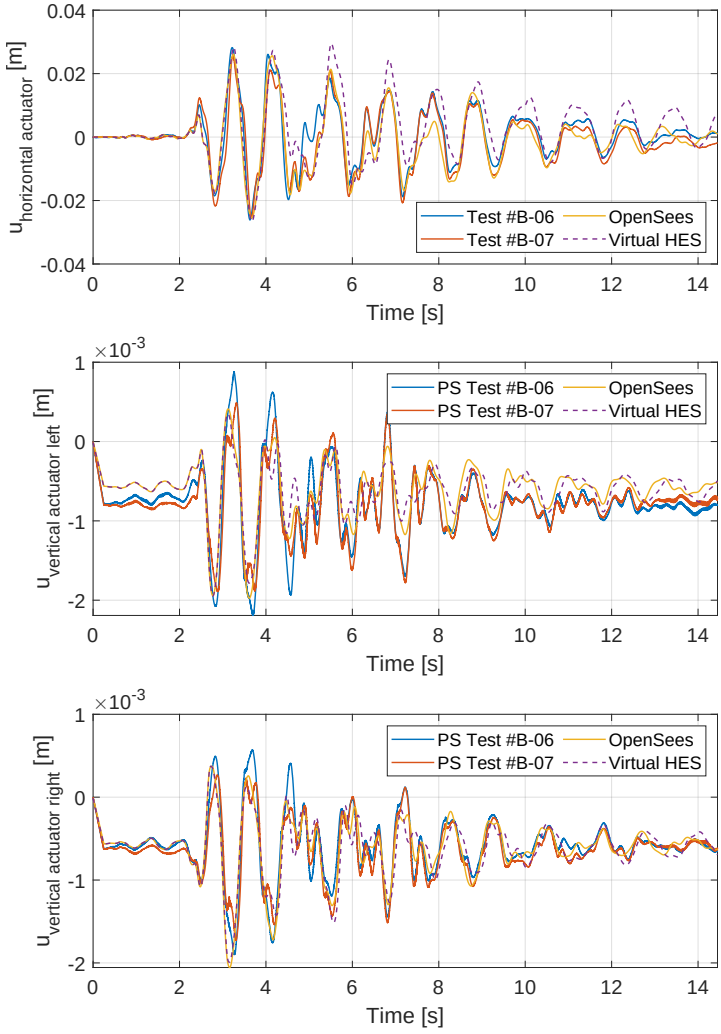

Figure 8.77: comparison of the displacements (Test #B-06 and #B-07)

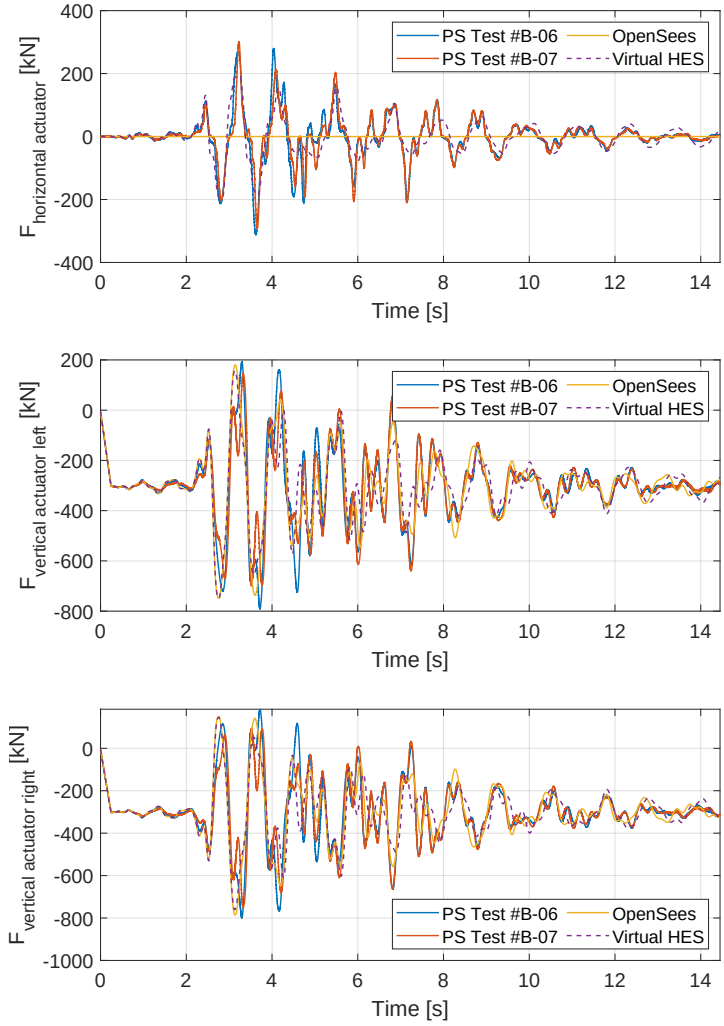

Figure 8.78: comparison of the forces (Test #B-06 and #A-07)

8.6.3 Frame #C

The comparison regarding the experimental test of Frame #C in terms of displacements and forces of the 3-DOFs PS are reported in Figure 8.79 and Figure 8.80.

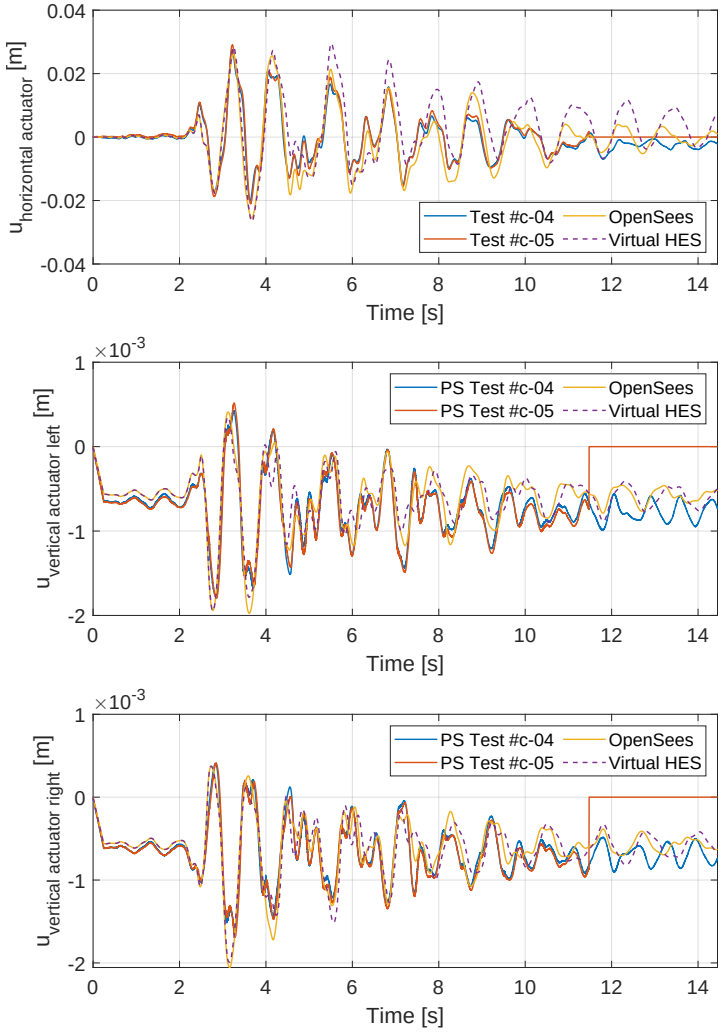

Figure 8.79: comparison of the displacements (Test #C-04 and #C-05)

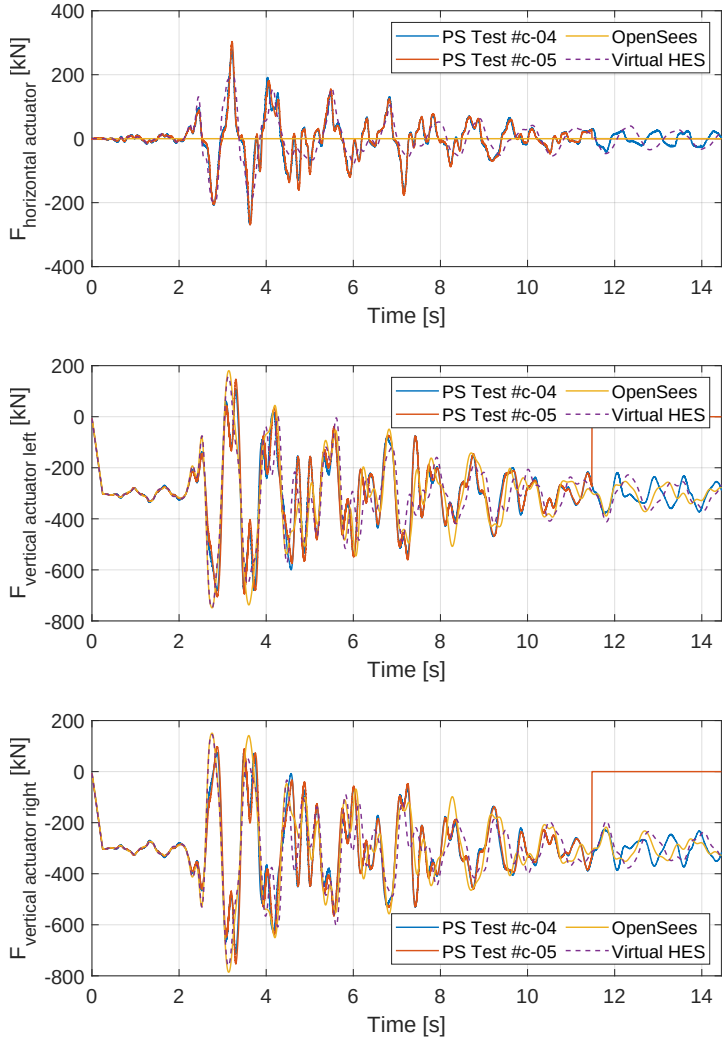

Figure 8.80: comparison of the forces (Test #C-04 and #C-05)

8.7 Photogrammetry 3D models

After each test, several photos of the specimen were taken in addition to the official ones. The same Photogrammetry procedure, done with the experimental tests at BAM, was used in order to obtain a 3D model of the bracing system.

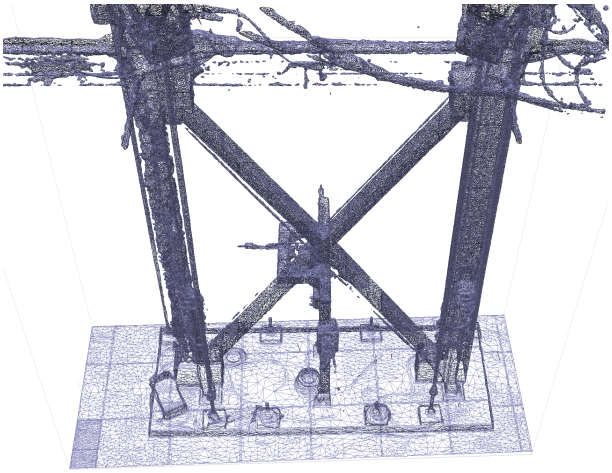

(a)

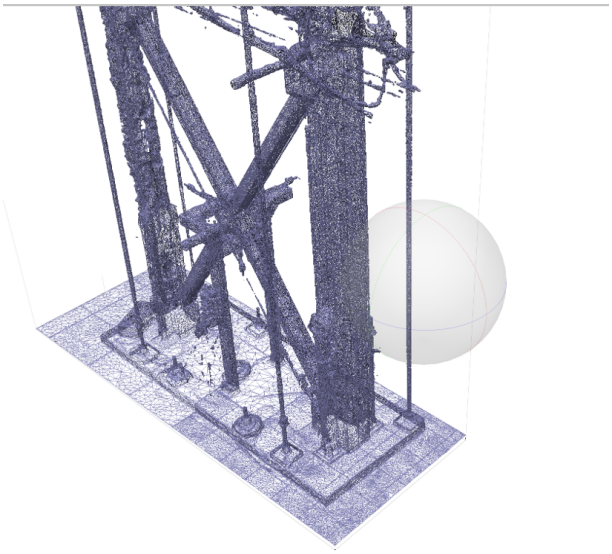

(b)

Figure 8.81: 3D model of the Frame #B obtained using the photogrammetry methodology: a) wired model b) Textured model

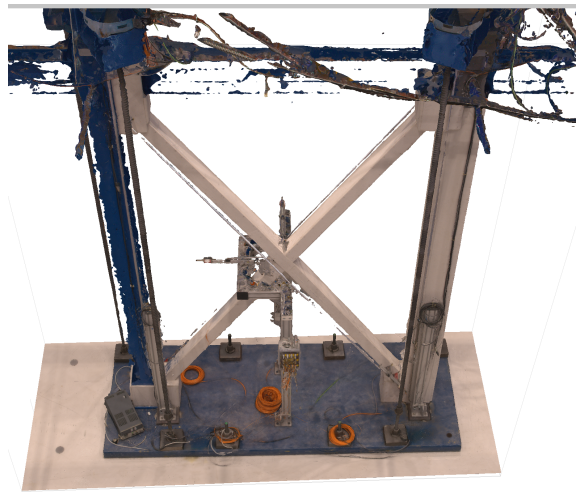

(a)

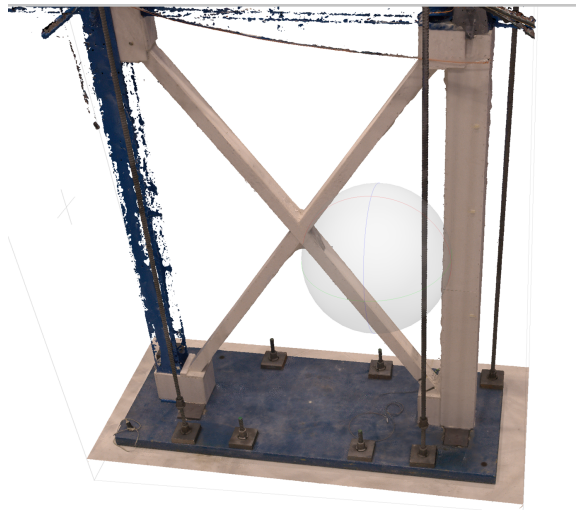

(b)

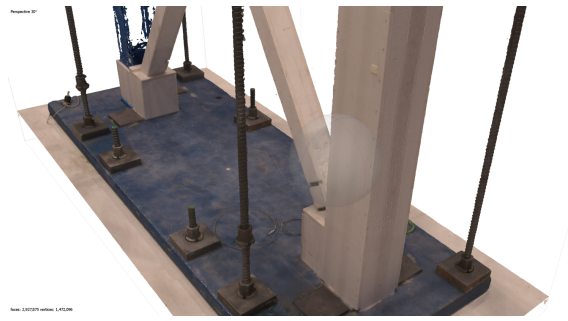

(c)

Figure 8.82: 3D textured model of the Frame #B obtained using the photogrammetry methodology.

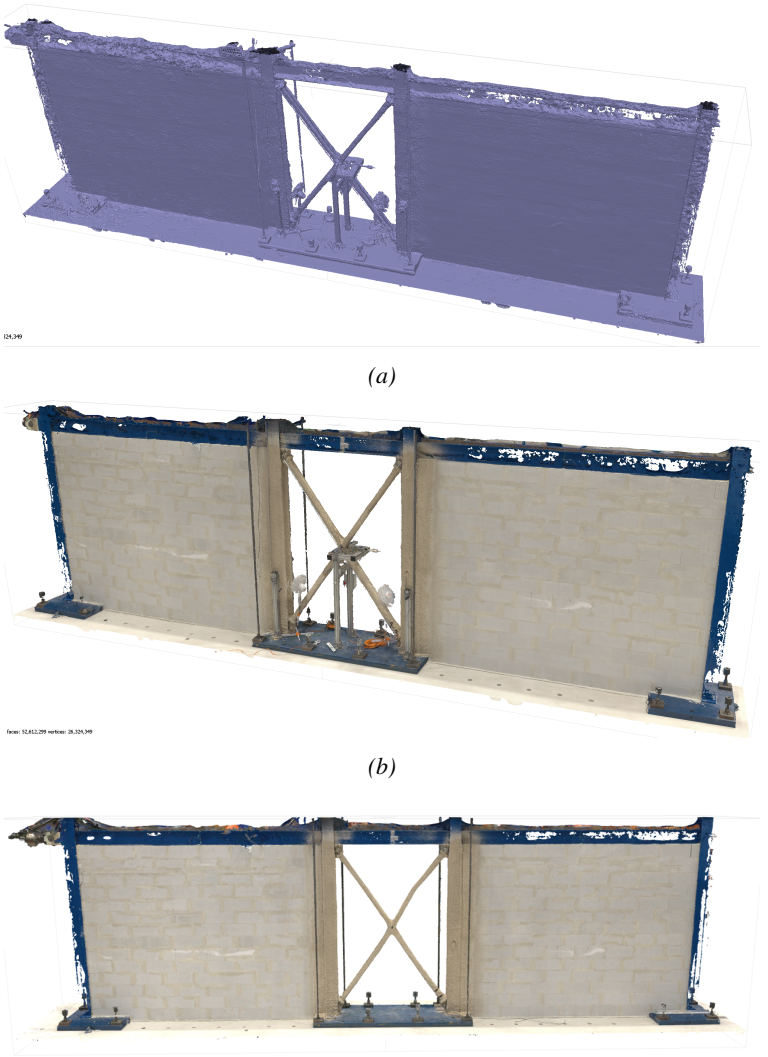

(a)

(b)

(c)

Figure 8.83: 3D model of the Frame #D obtained using the photogrammetry methodology: a) wired model; b) Textured model before the tests; c) Textured model after the final tests.

(a)

(b)

Figure 8.84: Comparison: a) 3D model of the Frame #D obtained using the photogrammetry methodology; b) Real pictures.

As illustrated in Figures 8.81 and 8.83, the photogrammetry's algorithm has some difficulty reconstructing the uniform blue column and beam. This happened for essentially a combination of three reasons:

- uniform colour/texture.
- similar colour on the background.
- Some pictures are not automatically taken into account due to the

failure of the algorithm in the estimation of the relative position (In that case, a manual procedure can be used to detect some tie points to help avoid this problem).

Photogrammetry allows performing visual comparisons and measurements to evaluate the evolution of damage before and after each test.

8.8 Main outcomes and discussion

The chapter presented the main results of an experimental and numerical FFE analysis on a braced steel frame. The research activity was performed within the European EQUFIRE project. Several Hybrid seismic tests were carried out on one steel frame without fire protection and three frames with different fire protection solutions: conventional and earthquake-proof boards system and gypsum-based wet mix spray-applied fire-resistive material. In terms of fire protection, no severe damage was observed that would undermine the fire resistance of the columns or braces.

The results presented in this chapter showed the effectiveness of the dynamic Substructuring and time Integration Procedure for the Hybrid Simulation of the Seismic Response of the EQUFIRE frame both in the experimental tests and in the virtual Hybrid earthquake simulation. Reduced-order models of both NS and PS of the EQUFIRE frame were derived starting from a nonlinear FE model developed according to the Chapter 3. The substructured model is characterized by a 6-DOFs NS and a 3-DOFs PS. With regard to the PS, one horizontal and two vertical DOFs couple NS and PS. The horizontal DOF is controlled in displacement, whereas vertical DOFs, which are stiff, are controlled in force. A time integration procedure was developed to allows for mixed force-displacement control of PS DOFs.

Acknowledgements

This work has received funding from the European Union's Horizon 2020 research and innovation program under the SERA grant agreement No. 730900 and the related TA project EQUFIRE. Author would acknowledge Giuseppe Abbiati (Aarhus university), Georgios Tsionis (JRC), Pierre Pegon (JRC), Marco Lamperti Tornaghi (JRC), Francisco Javier Molina (JRC), Artur Pinto (JRC), Martin Poljansek (JRC), Patrick Petit (JRC), Marco Antonelli (Etex group - Promat), Francesca Tambornini (Etex group - Promat), Alessandro Miliani (Xella Italia) and Bar-

bara Gilardi (Xella Italia) for their invaluable contribution to the experimental campaign at JRC.

Figure 8.85: EQUFIRE tests at European Laboratory for Structural Assessment (ELSA) of the Joint Research Centre (JRC) (From Left: P. Covi, N. Tondini, A. Pinto, P. Pegon, G. Tsionis), May 2021.

Bibliography

[1] EU, "Elsa website (https://ec.europa.eu/jrc/en/research-facility/elsa)," 2017.

[2] M. L. Tornaghi, G. Tsionis, P. Pegon, J. Molina, M. Peroni, M. Korzen, S. Riemer, K. Ziener, N. Tondini, P. Covi, G. Abbiati, and Antonelli, "EQUFIRE: Multi-hazard performance assessment of structural and non-structural components subjected to seismic action and fire following earthquake using hybrid simulation," sera proceedings, SERA, 2020.

[3] G. Abbiati and P. Pegon, "Dynamic Substructuring and Time Integration Procedure for the Hybrid Simulation of the Seismic Response of the EQUFIRE frame," equfire internal report, SERA, 2020.

[4] F. McKenna, "Opensees: a framework for earthquake engineering simulation," *Computing in Science & Engineering*, vol. 13, no. 4, pp. 58–66, 2011.

[5] J.-M. Battini, *Co-rotational beam elements in instability problems*. PhD thesis, KTH, 2002.

[6] CEN, "Fire classification of construction products and building elements - Part 1: Classification using data from reaction to fire tests," european standard, European Union, Dec. 2018.

9.0 Calibration of the finite element numerical model with experimental data of the JRC tests.

9.1 Introduction

Several tests were carried out on a steel frame building with concentric braces by seismic pseudo-dynamic tests of a real-scale one-storey frame at the ELSA Reaction Wall. Results of the tests on the unprotected frame are reported along with the numerical advanced 3D model calibration of the frame. Concentrically braced frames (CBF) are commonly used as the seismic resisting system in buildings. During large seismic events, they may experience buckling of the braces. Typical modeling approaches for bracing frame connections use either fully restrained or fully pinned models. However, gusset plate connection is neither pinned nor fixed and its flexibility must be modeled explicitly to capture the nonlinear response.

9.2 Advanced 3D frame model

9.2.1 SCBF connections

The connection between the bracing diagonal elements and the rest of the frame has been designed specifically for the EQUFIRE case. The test involves a hybrid test with a two-dimensional model used as the numerical substructure to simulate the effect of the remaining part of the structure in the laboratory. The choice of a 2D model was made because the solution calculated at each step of the test need to be obtained within the shortest possible time. This requires that the out-of-plane buckling effects of the braces are negligible, which is why the IPE profiles are oriented with the weak axis lying in the plane to limit out-of-plane buckling. The bracing is connected to the connection plate through a special element with only two bolts, as illustrated in Figure 9.1.

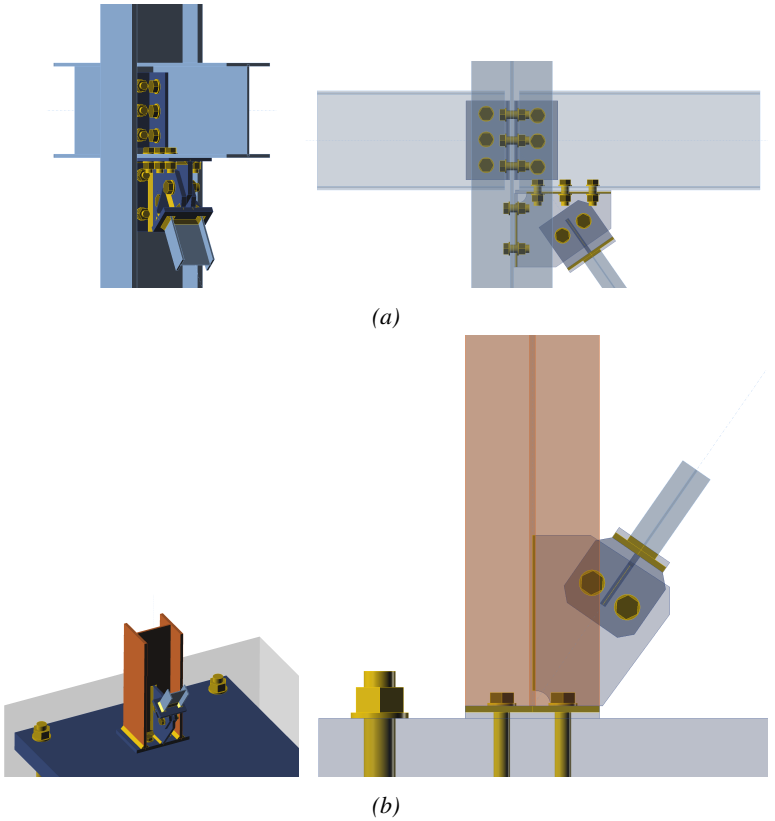

Figure 9.1: 3D render of the EQUFIRE connection

Typical modeling approaches for bracing frame connections use either fully restrained or fully pinned models. However, several test results and studies (i.e. [1][2]) show that the gusset plate connection is neither pinned nor fixed and its flexibility must be modeled explicitly to capture the nonlinear response.

Hsiao et al. ([1][2]) provide recommendations for appropriate modeling assumptions that include rigid links in the connection region to model the enhanced stiffness in the region. The primary response is simulated using a nonlinear, zero-length rotational spring, which has a spring stiffness based upon the gusset plate material and geometry and is located at the ends of the brace. This modeling approach simulates the out-of-plane rotational behaviour of the gusset plate connections and provided correct boundary conditions for the brace members. Rigid end zones were used for the remainder of the connections beyond the brace.

Also Vesna Terzic [3] provides recommendations for appropriate modeling for bracing frame connections in OpenSees. The peculiarity of this

study is in the comparison of the seismic response of the frame with three different modellings of the connections:

- Force-based fiber elements [4] (Figure 9.2a);
- Rotational hinge [1] (Figure 9.2b);
- Pin connection.

In all these models, the connection zone is assumed to be rigid concerning the rest of the structural elements (as highlighted in Figure 9.2). At the same time, the stiffness of the plate is simulated in different ways depending on the chosen option. The first one adopts a finite fibre element, with a dependent extension of the connection geometry, whose response depends on flexural stiffness both inside and outside the plane. On the other hand, the second solution employs a zero-length element with a uniaxial nonlinear material, modelling the out-of-plane rotational spring. The plate's out-of-plane flexural stiffness is thus implemented in the model, while perfect continuity is recreated in-plane. Finally, the perfect hinge modelling is essentially a similar case to the previous one, from which it differs by removing the out-of-plane flexural stiffness. The study showed that, unlike the perfect-hinge schematic, the first two models generate similar and more accurate responses.

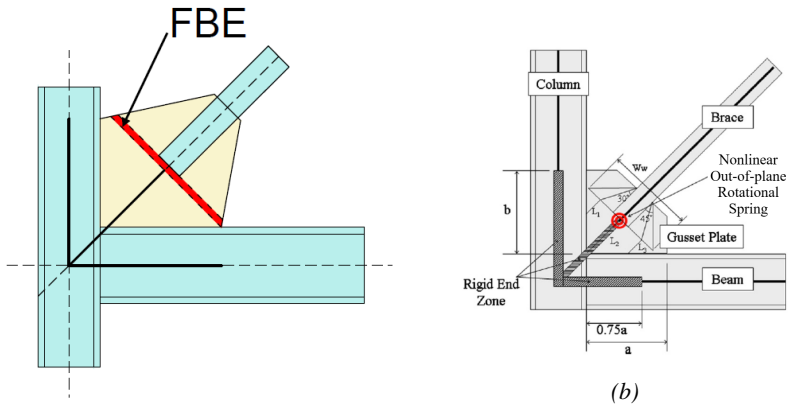

Figure 9.2: a) Force-based fiber elements (Uriz and Mahin, 2008 [4]); b) Rotational hinge (Hsiao et al., 2012 [1])

A first comparison between the connection of the frame studied by V. Terzic [3] (Figure 9.2) and that of the EQUFIRE case study (Figure

9.1) reveals a substantial difference in the typology used. The first solution provides an extensive welded connection between a tubular element and the plate, while the latter provides a practically punctual connection through only two bolts. For this reason, the use of modelling similar to the one adopted by Uriz and Mahin [4] was considered untrue for the case under examination, simply because of the impossibility of finding a geometric correspondence with the force-based element in reality. On the other hand, modelling with a rotational spring is more reliable for this case.

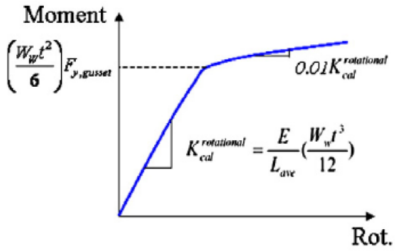

Figure 9.3: Nonlinear rotational spring model.

The nonlinear rotational spring is defined through a moment-rotation model based on the Giuffré-Menegotto-Pinto formulation shown in Figure 9.3, whose stiffness and strength parameters are defined by treating the plate as an equivalent cantilever beam subject to a moment applied to the free end. The geometry of such an equivalent cantilever beam is defined by the modified Thornton method employed by Hsiao. Thornton investigated the compressive capacity of the gusset plates, and proposed a method to estimate the buckling strength based on the Whitmore width and the effective length of the gusset. The Whitmore section defines the equivalent cantilever beam: this is a rectangular section with one side equal to the thickness of the plate and the other obtained using a 45 projection angle along the whole extension of the connection between brace and plate, whether welded or bolted. Therefore, the Whitmore width is identified as W_W, as shown in Figure 9.2b. The length of the equivalent cantilever beam is equal to the arithmetic mean of the three lengths shown in Figure 9.2b: the length L_2 is measured from the centre of the Whitmore width up to the interface with the beam or column element, while the lengths L_1 and L_3 are measured starting from the extremes of the width obtained with 30 distribution. Referring to the symbology adopted in Figure 9.3 we have:

- The initial rotation stiffness is calculated as follows:

$$K_{cal}^{rotational} = \frac{E \cdot J}{L_{ave}} \tag{9.1}$$

where:

E is the elastic modulus;

t is the thickness of the plate;

$J = \frac{W_W \cdot t^3}{12}$ is the area moment of inertia in the weak-plane of the Whitmore 's section (out-plane buckling);

$L_{ave} = \frac{L_1 + L_2 + L_3}{3}$ is the average Thornton's length;

- The elastic bending moment resistance of the Whitmore's section equals:

$$M_{y,gusset} = W_{el} \cdot F_{y,gusset} \tag{9.2}$$

dove:

$W_{el} = \frac{W_W \cdot t^2}{6}$ is the elastic section modulus of the Whitmore's section;

$F_{y,gusset}$ is the yield strength.

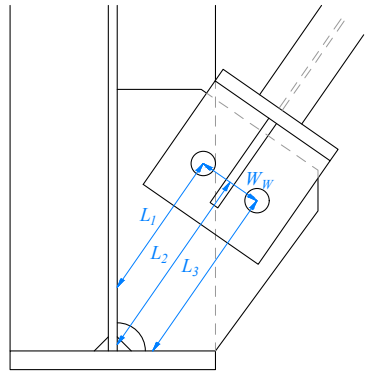

Figure 9.4: Bracing connection at base (Whitmore's section).

Regarding the EQUFIRE case study connections, the Whitmore width was considered equal to the distance between the bolts, while the lengths

L_1, L_2 and L_3 were measured from the centre and ends of this width. As an example, the base plate connection is showed in Figure 9.4. In detail, it has been considered as a particular case of the Thornton model in which the diffusion starts and ends at the only row of bolts present. This choice was adopted due to a comparison between the response of the frame modelled with Whitmore width equal to the bolt spacing and that of the same frame in which, however, W_W is associated with the maximum width of the plate. The comparison shows substantial equality between the two models. Similarly, modelling as an out-of-plane hinge generates entirely comparable results. It can, therefore, be seen that, in the present case study, it is the elastic finite elements that simulate the rigid zone of the connection that makes the difference rather than the plate model itself.

9.2.2 Finite element model

As presented in Figure 9.5 and Figure 9.6, an advanced nonlinear finite element model in OpenSees was developed to evaluate the response of the structure. The fibre displacement-based beam-column element was used to model the beams, columns and braces. Seven nonlinear beam elements based on corotational formulation and the uniaxial SteelFFEThermal material, with isotropic strain hardening and geometric nonlinearities, was used for the elements. Nonlinear beam elements were also used for all elements to check that non-dissipative elements remain in the elastic field owing to the seismic action. Geometric imperfections were included to allow for buckling EN 1993-1-1 [5]. Masses were considered lumped on the floors, following the assumption of rigid diaphragms.

The uniaxial SteelFFEThermal constitutive steel model is a custom material class used for nonlinear fire following earthquake analyses. A detailed explanation of the class material can be found in Chapter 10.2.1 and herein is summarized: The SteelFFEThermal material has the same primary expression as the Giuffrè-Menegotto-Pinto uniaxial steel stress-strain model at ambient temperature. When the temperature of an element starts increasing, the material class switches the constitutive law from the Giuffrè-Menegotto-Pinto model to the constitutive law provided by EN 1993-1-2 [6] for steel at elevated temperature.

Three rigid zones can be identified (blue lines in Figure 9.5a): The first extends from the work point of the connection to the physical end of the brace. The second extends from the work point to the physical end of the gusset plate along the length of the column. The third extends from the work point along the length of the beam. These zones are modelled using elastic beam elements with higher stiffness and area of the section.

(a) *(b)*

Figure 9.5: a) advanced 3D frame modelled in OpenSees: nonlinear elements in red, elastic elements in blue; b) Fiber Section.

(a) *(b)*

Figure 9.6: geometric imperfections (scaled): a) 3D view, b) XZ plan.

9.3 Numerical finite element models comparison

A modal analysis was performed in OpenSees and the proper periods reported in Table 9.1 have been obtained. The results were also compared with the values obtained from other Opensees models where the bracing connections were modelled as simple internal hinges: the complete three-dimensional structure modelled with SAP2000, the same 3D modelled with Opensees and the 2D frame. As it turned out, the higher stiffness of the current model means that lower period values are recorded. The results are very similar, as reported in Tables 9.1.

Table 9.1

Model	Mode	Mass ratio	Period [s]	Frequency [Hz]	Circular Frequency [rad/s]
3d Frame	1st	84.4%	0.627	1.595	10.021
with connections	2nd	13.8%	0.207	4.831	30.357
Full structure	1st	83.9%	0.659	1.518	9.534
SAP 2000	2nd	14.3%	0.218	4.587	28.822
2D Frame	1st	83.7%	0.668	1.498	9.409
Opensees	2nd	13.0%	0.217	4.613	28.982
3D full structure	1st	85.5%	0.674	1.484	9.324
Opensees	2nd	12.3%	0.223	4.488	28.201

The fundamental periods of the structure taken into account for the comparison are the first two modes of vibration shown in Figure 9.7. They have been selected according to the European standard concerning main modes with significant participating mass for the global response: all modes with a modal participating mass higher than 5% of the total mass and a number of modes such that the sum of the participating modal masses is higher than 90% of the total mass of the structure have to be considered.

(a) *(b)*

Figure 9.7: Modal shapes: a) 1st mode; b) 2nd mode.

Figure 9.8 presents the pushover comparison results between the advanced 3D frame model with a detailed reproduction of the connections and the previous ones, i.e. complete three-dimensional structure and flat frame both with internal perfect hinge constraints. A similarity can be noted in the first section, although clearly, the stiffness conferred by the new modelling of the connections translates into a greater slope of the elastic section and a more significant shear at the base. The substantial difference can be seen instead on the plastic branch of the curve: unlike the previous ones, the presence of the rigid sections in the connections of the new model means that for large deformations, a further displace-

ment requires a greater input of force, a sort of hardening effect due to the condition of extreme deformation of the frame.

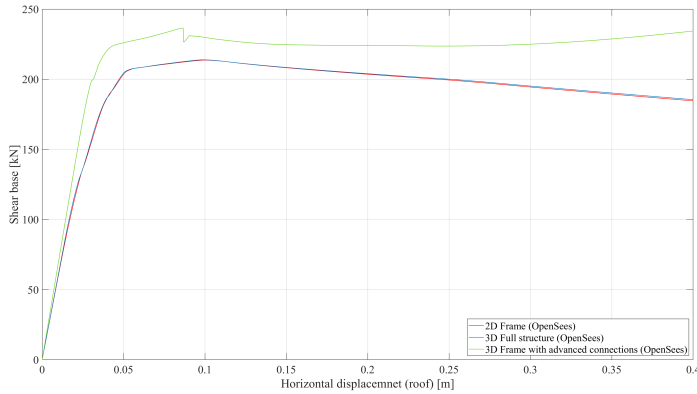

Figure 9.8: Pushover comparison

Figures 9.9 and 9.10 present the nonlinear dynamic comparison results between the advanced 3D frame model and the 3D full structure model with internal perfect hinge constraints. A more rigid stiffness response between the advanced and the internal hinges FE models is observed in the nonlinear bracing on the ground floor and in the horizontal displacement of each floor.

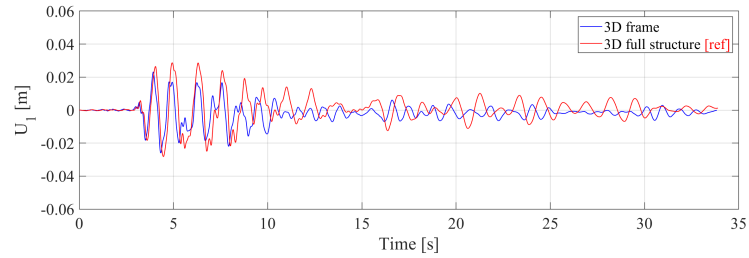

(a)

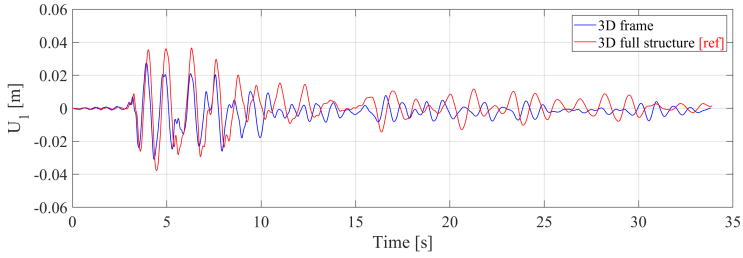

(b)

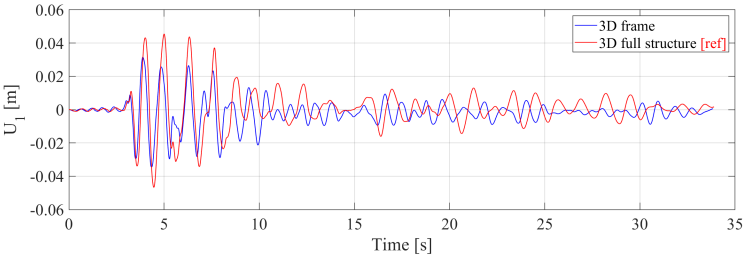

(c)

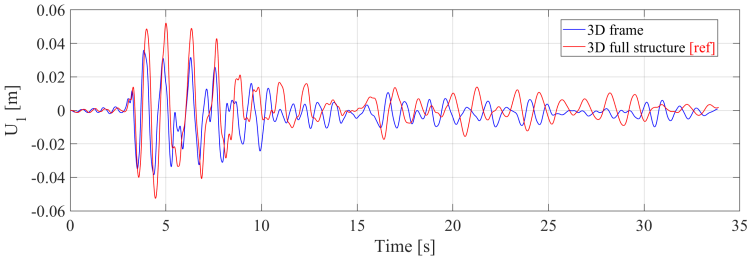

(d)

Figure 9.9: Horizontal displacement (ACC6_NS): a) 1st floor; b) 2nd floor; c) 3rd floor; d) 4thh floor.

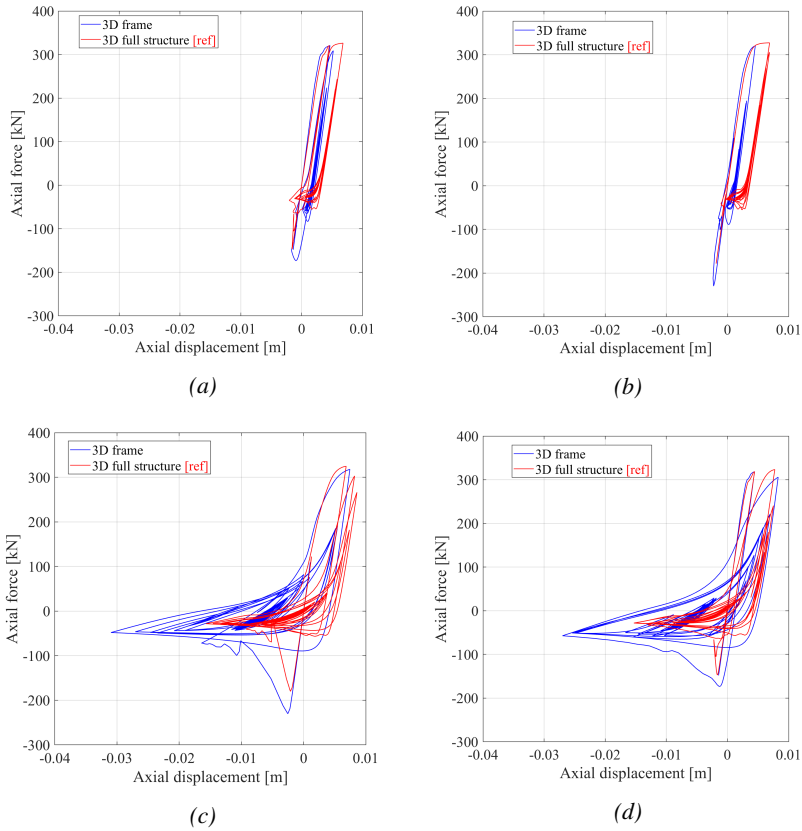

Figure 9.10: Disipation braces at 1st floor: a) top-left; b) top-right; c) bottom-left; d) bottom-right

9.4 3D advanced frame model calibration

The calibration of numerical model consists in five different aspects to be considered:

- Numerical finite element model with gusset plate connections (already done in the previous sections).
- Damping parameters (Rayleigh).
- Real gravity loads.
- Effective yield strength of steel grades.
- Bolt hole clearance (gap).

The following sensitivity analyses have been conducted for each calibration parameter. The parameters were modified one by one, leaving the other parameters fixed using the model explained in Chapter 9.2.

9.4.1 Damping parameters (Rayleigh)

Rayleigh damping is built as a linear combination of the structural mass and stiffness matrices M and K defined as:

$$\mathbf{C} = \alpha_m \cdot \mathbf{M} + \beta_K \cdot \mathbf{K} \tag{9.3}$$

where:

- α_m is the mass proportional Rayleigh damping coefficient.
- $\mathbf{M}$ is the system structural mass matrix.
- β_K is the stiffness proportional Rayleigh damping coefficient.
- $\mathbf{K}$ is the system structural stiffness matrix.

In addition to classical Rayleigh damping, OpenSees offers a separated Rayleigh damping model in which $\mathbf{C}$ is defined as:

$$\begin{aligned}\mathbf{C} = \alpha_m \cdot \mathbf{M} + \beta_{Kcurrent} \cdot \mathbf{K_{current}} + \beta_{Kinit} \cdot \mathbf{K_{init}} \\ + \beta_{Kcomm} \cdot \mathbf{K_{comm}}\end{aligned} \tag{9.4}$$

where:

- $\beta_{Kcurrent}$ factor applied to elements current stiffness matrix $\mathbf{K_{current}}$.
- β_{Kini} factor applied to elements initial stiffness matrix $\mathbf{K_{ini}}$.
- β_{Kcomm} factor applied to elements committed stiffness matrix $\mathbf{K_{comm}}$.

In the finite-element (FE) model of the EQUFIRE frame implemented in MATLAB the Rayleigh damping is defined as:

$$\mathbf{C} = \alpha_m \cdot \mathbf{M} + \beta_{Kinit} \cdot \mathbf{K_{init}} \tag{9.5}$$

This choice was made to save computational time during the experimental tests.

Figure 9.11 compares the horizontal actuator displacement obtained during the first experimental test using the Equation 9.5 and the horizontal displacement of the equivalent node of the numerical simulation obtained using OpenSees. In detail, two numerical simulations were performed, one using $\beta_{Kcurrent}$ applied to the current stiffness matrix ($\mathbf{K_{current}}$) and the other one using β_{Kini} applied to the initial stiffness matrix ($\mathbf{K_{ini}}$) as explained in Equation 9.4.

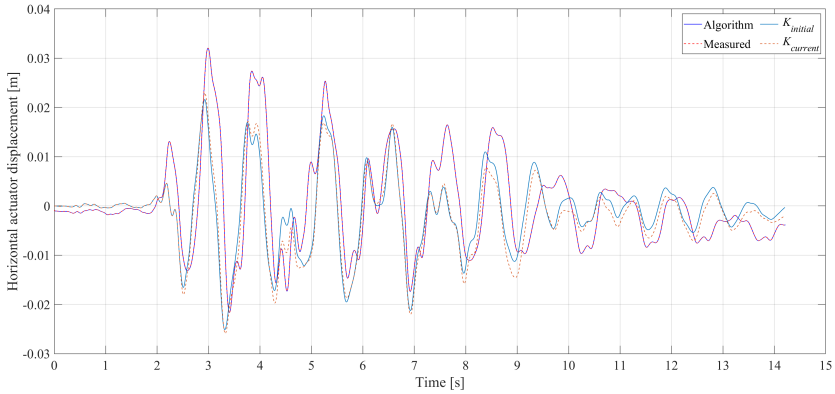

Figure 9.11: Horizontal displacement comparison of the first floor.

The two numerical results are very close. For consistency with the test algorithm used in the laboratory (Equation 9.5) the β_{Kini} applied to the initial stiffness matrix ($\mathbf{K_{ini}}$) was chosen.

9.4.2 Loads

In a real scenario, both the primary and secondary beams support dead and live loads, as illustrated in Figure 9.12a. Depending on the design of the structure the most of the loads are supported by the secondary beams first, and then the support reactions are transferred to the primary beam as concentrated loads. The primary beams are supported off the columns. Therefore the support reactions of primary beams are transferred to the columns as concentrated loads.

The experimental mock-up at ELSA Reaction Wall represents the ground floor of the four-storey frame, and the rest of the frame was numerically simulated. Only two actuators apply the vertical load on each internal column for the physical substructure. Therefore, an equivalent nodal load scheme was calculated to simulate the real gravity loads effect by loading only at column and beam endpoints, as shown in Figure 9.12b.

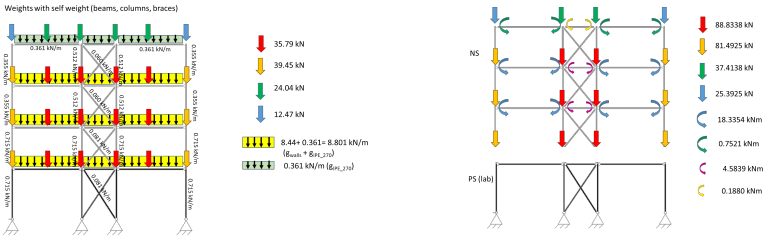

(a) *(b)*

Figure 9.12: Loads a) real gravity load configuration b) equivalent experimental gravity load configuration

This choice was made to reduce the complexity of the experimental setup without using additional actuators or the realization of a portion of the building's slab. It is worth mentioning that beams are not the dissipative elements of a bracing frame during the seismic event.

Figure 9.13 shows the comparison between the experimental results and the two numerical simulations, one with the real gravity load configuration and the other one with the experimental load configuration. No noticeable difference was found between the two load configurations in the numerical results. Therefore, for the advanced numerical model, the real gravity load configuration was chosen to capture the beams' effective forces and deformations.

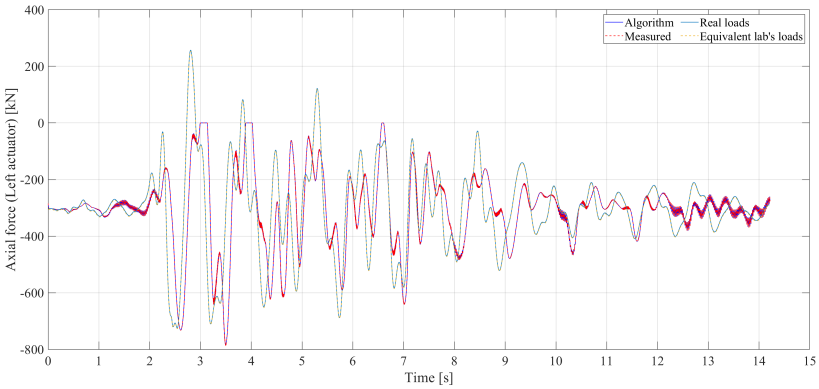

Figure 9.13: Horizontal displacement comparison of the first floor.

9.4.3 Effective yield strength of steel grades

Given the uncertainty of the actual yield strength of the steel grades, the expected values given in the design could be used. However, a sensitivity analysis on the yield strength (Fy) value of the S275 steel grade used

for the braces was performed. Sensitivity analysis is used to identify the impact of an input variable on the outcomes under alternative assumptions. The input variables are varied over a range, and their effect on the outcome is observed. If the output varies noticeably when changing the input variable from minimum to maximum over a selected range, then the output can be defined as sensitive otherwise, it can be defined as insensitive or robust. In detail, the Fy of the braces is varied over a range of yield strength from 275 MPa, corresponding to the nominal yield strength, to 425 MPa, which is a very high and unrealistic value expected for an S275 steel grade. Instead, the yield strength value of the S355 steel grade used for the beams and columns was not considered for the sensitivity analysis because those elements are designed to remain in the elastic range during the earthquake event.

Figure 4.7 shows the outcomes of the sensitivity analysis compared to the horizontal displacement of the experimental test. Slight differences can be observed from the outcomes, but it is impossible to establish the real yield strength of S275 steel grade compared with the experimental data. Since the value of 330 MPa, is the expected yield strength defined in the design and used up in all the other numerical simulations, it was decided to maintain this assumption. Moreover, it is notable to mention that tensile tests are planned to obtain the real Fy values (The real Fy results are not available at the time of writing this thesis).

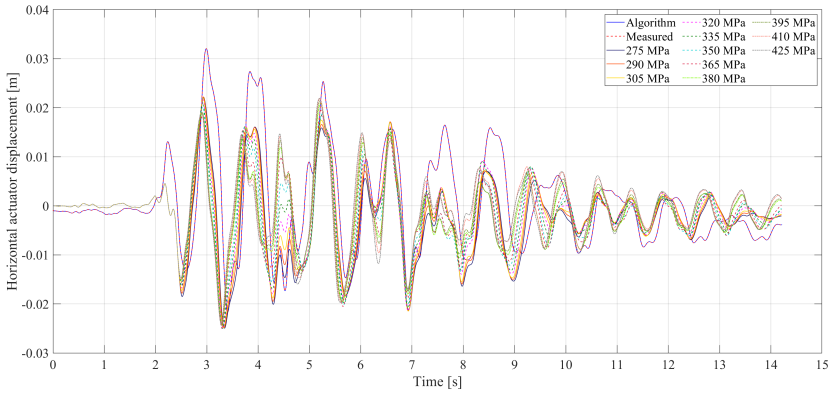

Figure 9.14: Outcomes of the S275 steel grade sensitivity analysis compared to the horizontal displacement of the experimental test.

9.4.4 Bolt hole clearance

In this section, the effect of bolt clearance in bolted steel connections is taken into account, because this aspect can influence the overall dis-

placement behaviour of the structure, especially in steel structures with lots of bolted connections. In order to assemble a steel connection, the plates and steel members must have a larger hole size compared to the body diameter of the bolt to ensure the bolt's installation. The standard regarding the bolt clearance can be found in the EN 1090-2 and for standard holes are briefly summarized herein:

- +1 mm for M12
- +2 mm for M16 up M24
- +3mm for M27 and bigger

A zerolength element was added in the axial directions of beams and braces near the connections in order to model the gap caused by the bolt hole clearance, as shown in Figure 9.15 (Option B). The zerolength element contains three uniaxial materials connected in parallel:

- Two elastic perfectly-plastic gap uniaxial material object, one in the positive direction and another in the negative opposite direction to simulate the gap.
- an axial spring characterized by a very low stiffness value in order to prevent convergence problems caused by snap movements.

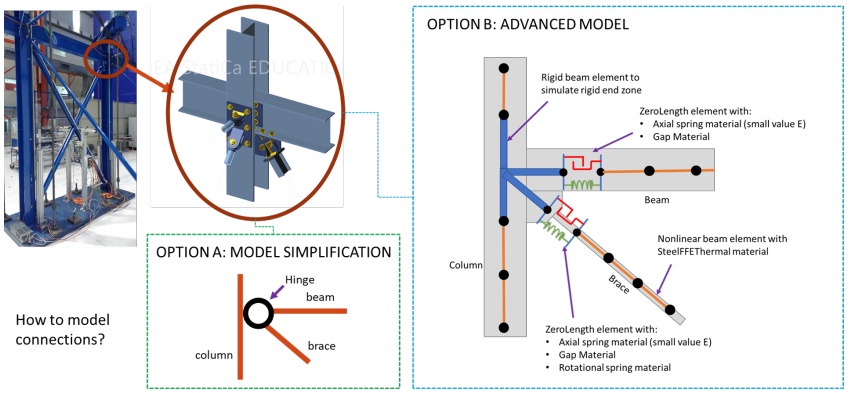

Figure 9.15: Connection model

Based on the normative prescription that requires a maximum clearance of 2 mm for bolts with a diameter of 24 mm, used in the present case, the following clearance values have been established:

- the hole-bolt clearance of the beams has been activated only in the left connection in order to avoid the convergence problems that would otherwise occur by activating them on both ends (numerical noise caused by an unrealistic oscillation of the beam between the two connections with gaps); for this reason, the clearance values have been concentrated only in the left end and therefore with values equal to 0.0 mm in compression and 4.0 mm in tension;
- In the connections of the braces at the base of the columns, 0.0 mm in compression and 2.0 mm in tension for the left brace, while for the right brace 2.0 mm in compression and 0.0 mm in tension;
- In the upper connections of the braces, on the other hand, a slightly higher gap value has been taken into account in order to take into account not only the clearance in the connection between brace and plate, but also that between plate and column; for this purpose, it has been established 3.0 mm in compression and 0.0 mm in tension for the left upwind and 0.0 mm in compression and 3.0 mm in tension for the right upwind.

The comparison in terms of the horizontal displacement (Figure 9.16) demonstrates that the numerical model with the bolt hole clearance has similar behaviour to the experimental frame.

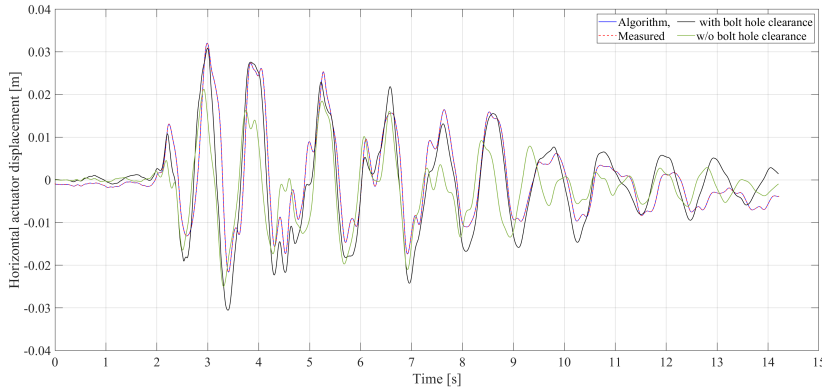

Figure 9.16: Horizontal displacement comparison of the first floor.

9.5 Comparison between the advanced FE model and the experimental results

This section illustrates the comparison between the experimental test A#32 and the advanced finite element model before and after the cali-

bration. The results of the model calibration are shown in Figures 9.17, 9.18, 9.19, 9.20 9.21 and 9.22. It is possible to observe a better agreement of the calibrated model with experimental data.

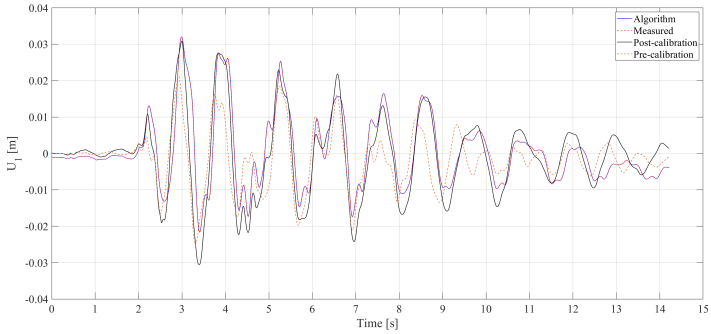

(a)

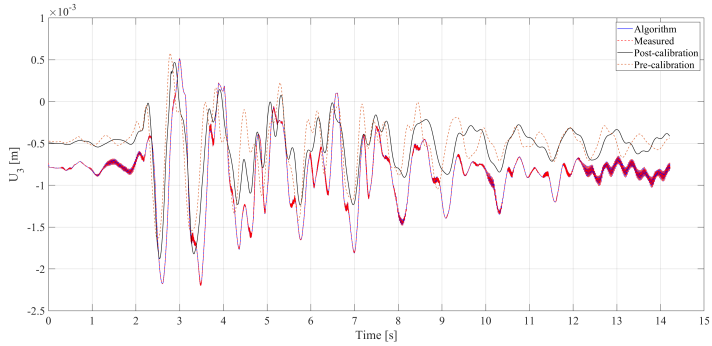

(b)

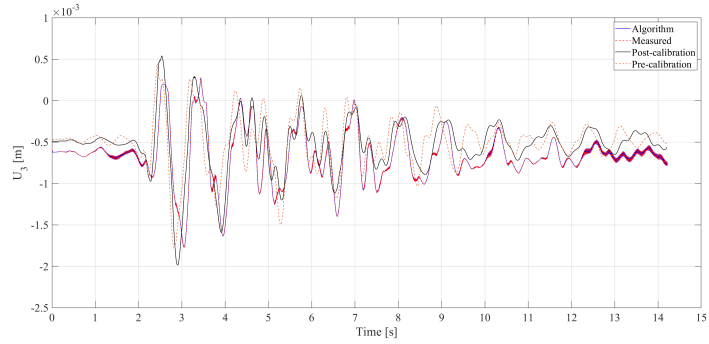

(c)

Figure 9.17: Comparison of the displacements: a) DOF 1 (Horizontal actuator); b) DOF 2 (Vertical left actuator); b) DOF 3 (Vertical right actuator).

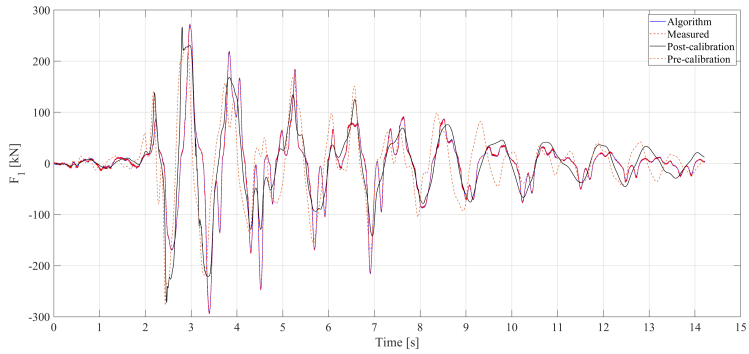

(a)

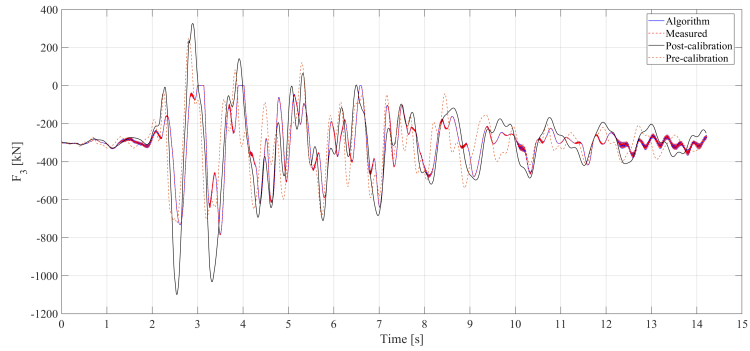

(b)

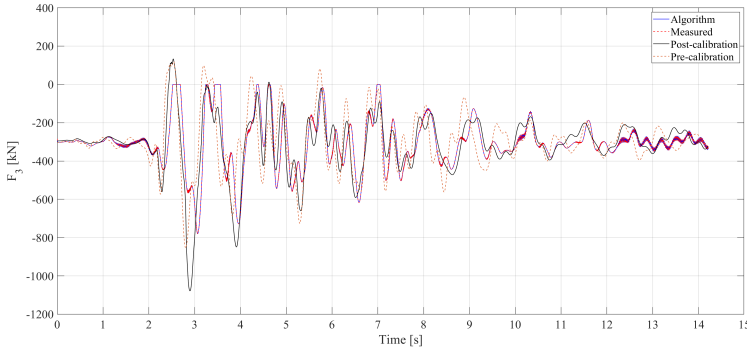

(c)

Figure 9.18: Comparison of the forces: a) DOF 1 (Horizontal actuator); b) DOF 2 (Vertical left actuator); b) DOF 3 (Vertical right actuator).

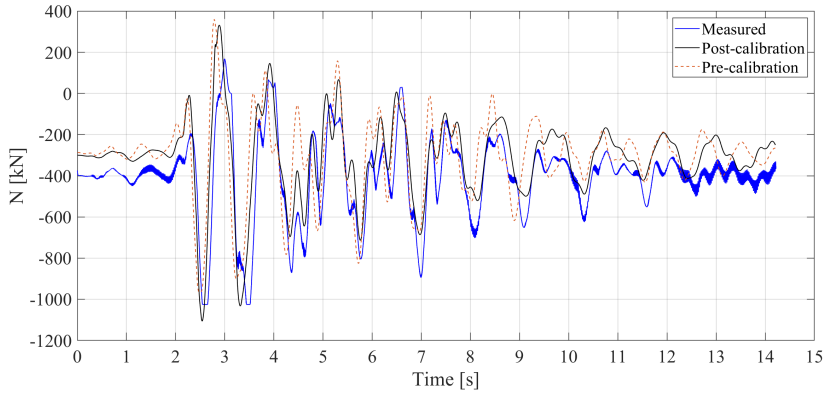

(a)

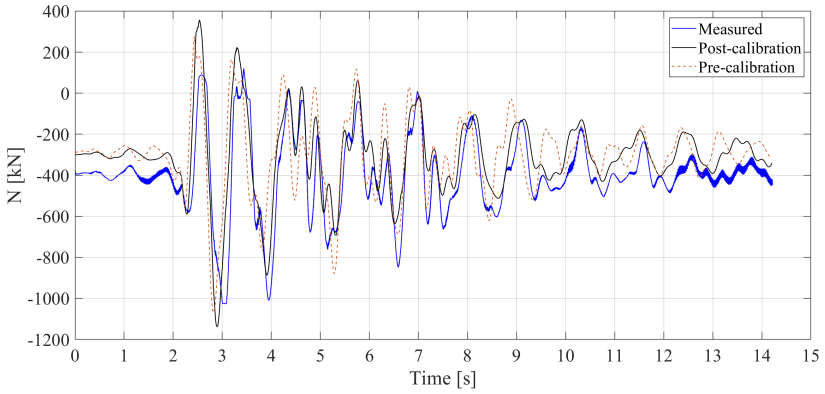

(b)

Figure 9.19: Comparison of the force inside the columns: a) Internal left column (column B); b) Internal right column (column C).

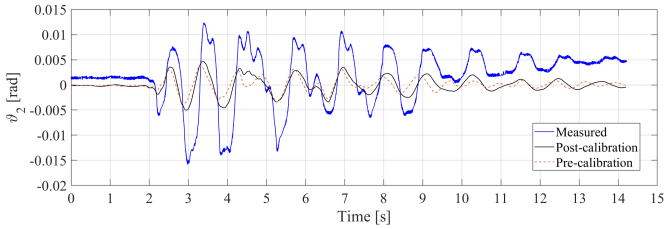

(a)

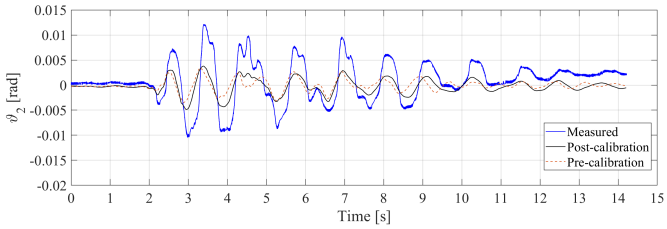

(b)

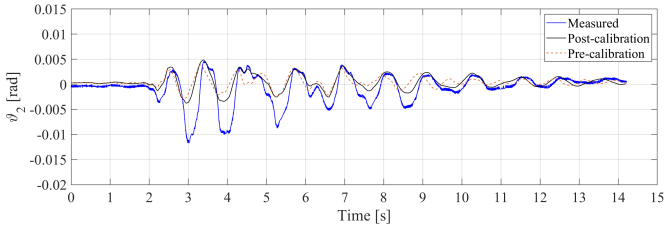

(c)

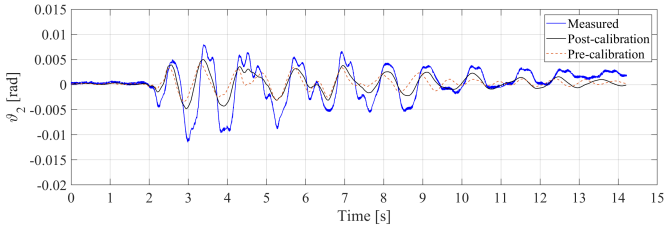

(d)

Figure 9.20: Comparison of the rotation of the columns: a) external left column (column A); b) internal left column (column B); c) internal right column (column C); d) external right column (Column D).

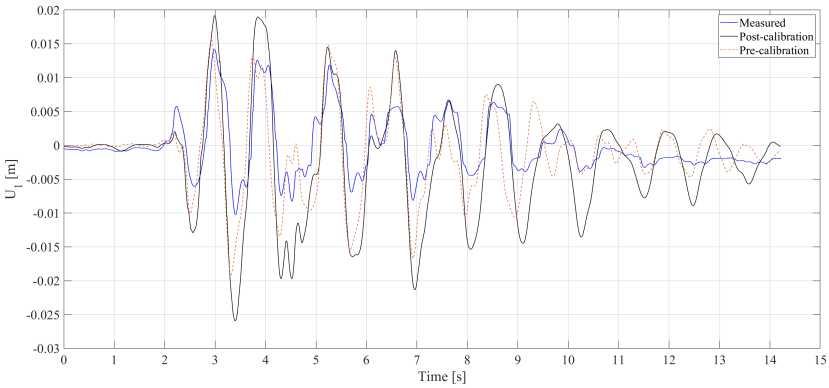

(a)

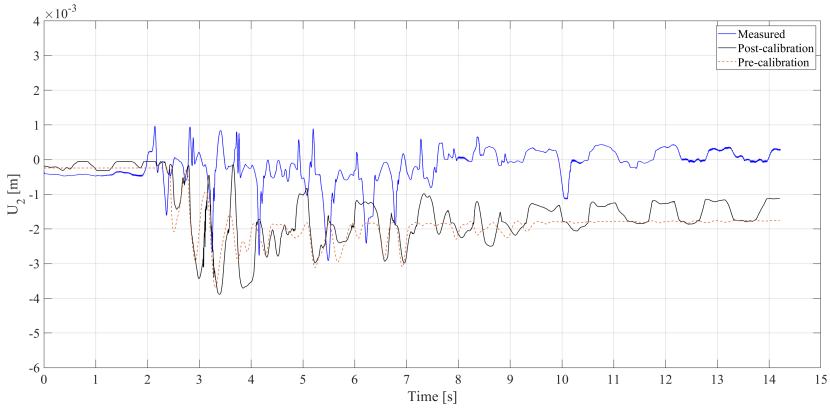

(b)

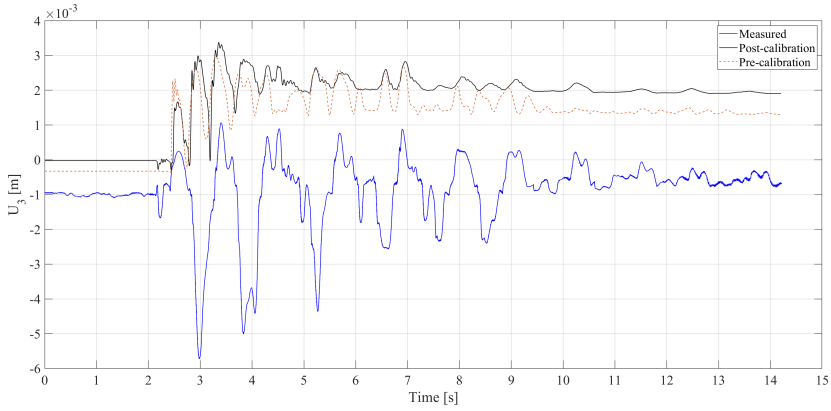

(c)

Figure 9.21: Comparison of the displacements of the middle point of the bracing system: a) horizontal in-plane displacement; b) horizontal out of plane displacement; c) vertical displacement).

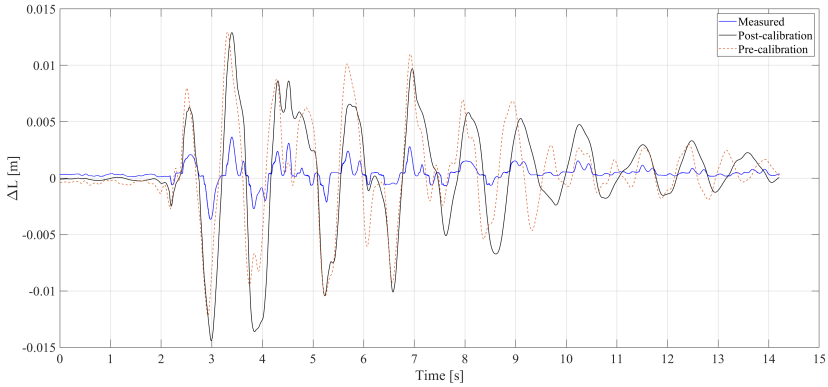

(a)

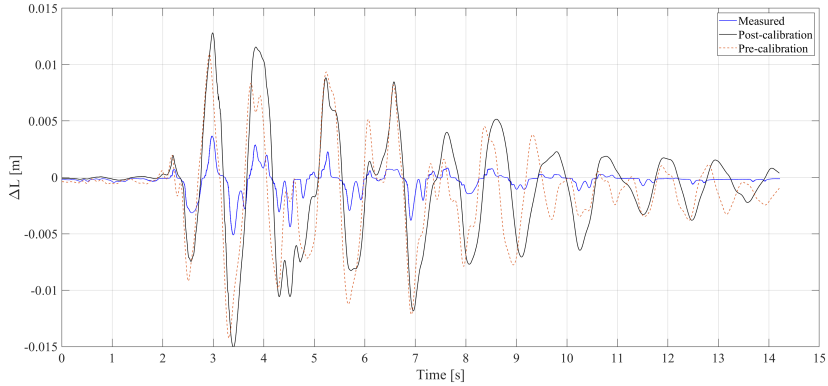

(b)

se

Figure 9.22: Comparison of the axial displacement of the braces: a) brace 1; b) brace 2.

9.6 FFE comparison

This section illustrates the results of the numerical simulation of the FFE test on the bare structure (without fire protection) for the selected acceleration time-history of the EQUFIRE tests followed by a fire scenario shown in Figure 9.23b. The first two floors were subjected to fire. The fire ignition is located at ground floor and for the vertical spread rate, the flashover time is set. The OZone software [7] [8] was used to generate the gas temperature for each compartment reported in Figure 9.23a and the SAFIR software [9] was used to perform the thermal analyses of the sections subjected to the fire in order to obtain the temperature time-history input for OpenSees.

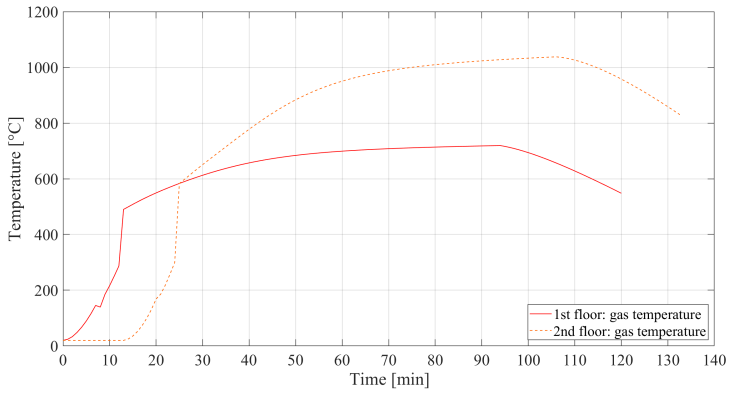

(a)

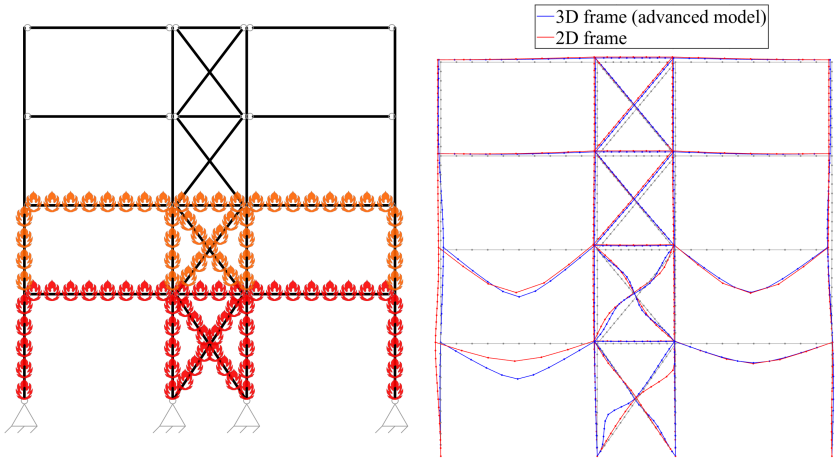

(b) *(c)*

Figure 9.23: a) gas temperature of ground floor and first floor; b) fire scenario after the ACC6_NS earthquake; c) deformed shape of the frame at the end of the simulation.

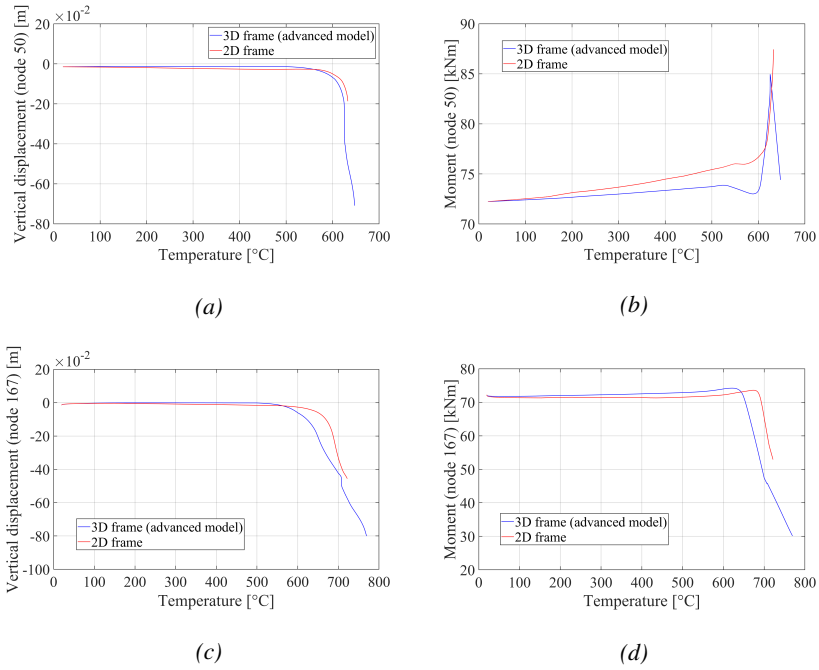

Figure 9.24: Results of the FFE numerical analysis.

Figures 9.23 and 9.24 illustrate the results of the numerical simulation of the FFE test using the calibrated finite element model compared to the 2D model of the frame. Figure 9.23c also shows the final deformed configuration of the steel frame at the end of the simulation. The comparison demonstrates good agreement. There is a little difference in vertical displacements and moments, because it was not possible to assign a thermal load to the rigid zones of Figure 9.5 modelled with elastic elements.

Other several FFE analyses were performed using the accelerogram set presented in Chapter 3 and using different fire scenarios.

9.7 Main outcomes and discussion

The chapter presented part of the results of an experimental and numerical FFE analysis on a braced steel frame. Model calibration was performed with beam finite elements that exhibited good agreement with the experimental results. Based on the accuracy of the advanced numerical models, they are considered adequate to be used in the nonlinear dynamic analyses as representative of the frame and building design in Chapter 3.

Bibliography

[1] P.-C. Hsiao, D. E. Lehman, and C. W. Roeder, "A model to simulate special concentrically braced frames beyond brace fracture," *Earthquake engineering & structural dynamics*, vol. 42, no. 2, pp. 183–200, 2013.

[2] P. Hsiao, D. Lehman, and C. Roeder, "Evaluation of collapse potential and the response modification coefficient of scbfs," in *Structures Congress 2013: Bridging Your Passion with Your Profession*, pp. 2675–2692, 2013.

[3] Vesna Terzic, "Modeling scb frames using beam-column elements."

[4] P. Uriz, F. C. Filippou, and S. A. Mahin, "Model for cyclic inelastic buckling of steel braces," *Journal of structural engineering*, vol. 134, no. 4, pp. 619–628, 2008.

[5] CEN, "Eurocode 3: Design of steel structures - Part 1-1: General rules and rules for buildings," european standard, European Union, May 2005.

[6] CEN, "Eurocode 3: Design of steel structures - Part 1-2: General rules - Structural fire design," european standard, European Union, May 2005.

[7] J.-F. Cadorin and J.-M. Franssen, "A tool to design steel elements submitted to compartment fires—ozone v2. part 1: pre-and post-flashover compartment fire model," *Fire Safety Journal*, vol. 38, no. 5, pp. 395–427, 2003.

[8] J.-F. Cadorin, D. Pintea, J.-C. Dotreppe, and J.-M. Franssen, "A tool to design steel elements submitted to compartment fires—ozone v2. part 2: Methodology and application," *Fire safety journal*, vol. 38, no. 5, pp. 429–451, 2003.

[9] J.-M. Franssen and T. Gernay, "Modeling structures in fire with SAFIR®: Theoretical background and capabilities," *Journal of Structural Fire Engineering*, vol. 8, no. 3, pp. 300–323, 2017.

10.0 Fire following earthquake framework for multi-hazard probabilistic analyses

10.1 Introduction

The work presented in this chapter is a step towards developing a framework for structures subjected to fire following earthquake. A modified version of the OpenSees software was developed to perform probabilistic analysis of structures subjected to FFE. This chapter includes the necessary modifications of the software to create the FFE framework. This framework is used to evaluate the performance of an 8-story steel bracing office building under fire following earthquake events.

10.2 OpenSees Software

The Open System for Earthquake Engineering Simulation (OpenSees) [1] is a finite element program and object-oriented software framework that was developed at the University of California, Berkeley, mainly for simulating the dynamic response of structural and geotechnical systems. OpenSees was originally developed as the computational platform for research in performance-based earthquake engineering at the Pacific Earthquake Engineering Research Center. It is now widely used as a finite element application to study the response of structures across all natural hazards, including Fire, Wind, Earthquake, and Wave action due to Tsunami or Storm Surge.

The OpenSees development for modelling structures in fire was first started at the University of Edinburgh in 2009 by Professor Asif Usmani and his research team. Many students and researchers worked on this long-term project with their own contributions, enabling OpenSees to perform analyses for a structure subjected to fire.

Elhami-Khorasani [2] presents modifications to the current source code that enable post-earthquake fire analysis for steel structures, and the enhancement to adapt reliability analysis in the thermal module of Steel01Thermal class. However, the code modifications can also be extended to other classes such as Steel02Thermal.

Currently, there are two different branches and development teams that are developing OpenSees:

- The Official branch of OpenSees sponsored by the Pacific Earthquake Engineering Research Center.
- A forked version of OpenSees, called "OpenSees for Fire" and it is maintained by Liming Jiang and Professor Asif Usmani.

This chapter refers to version 3.2.0 of the official branch and the source code is available from the OpenSees Github repository.

OpenSees supplies a wide assortment of materials that are useful to define the cross-section of the elements. Each material is represented in the software by its stress-strain relationship, that describes its behaviour for different situation (cyclic, linear, seismic, fire). For the fire, actually, three are three steel materials that are compatible with the thermal loads:

- Steel01Thermal: based on Steel01, with temperature-dependent properties defined (Strucutral steel, EN1993-1-2:2005)
- Steel02Thermal: based on Steel02, with temperature-dependent properties defined (Structural steel, EN1993-1-2:2005)
- SteelECThermal is developed for modelling steel material at elevated temperature, and providing different types of steel material definition according to EN1992-1-2:2004, EN1993-1-2:2005.

In order to perform FFE analyses, a material class, that is able to perform both fire and seismic analyses, is needed. In version 3.2.0 the Steel01Thermal class is the only thermomechanical material class that is capable of handling correctly cyclic seismic load, fire load and accommodate a strain reversal. Strain reversal is required to capture the response of the elements during the cooling phase. However, for the FFE framework, it is important to have also a robust and general material law also for the seismic analyses. At ambient temperature, the Steel01Thermal material is characterized by a bilinear kinematic hardening model and it is not based on the more complete Giuffre-Menegotto-Pinto model. Furthermore, a probabilistic model for the temperature-dependent strength of steel is needed in the material. Due to those reasons, a new uniaxial material class was developed based on Giuffre-Menegotto-Pinto and Steel01Thermal.

10.2.1 New Material: SteelFFEThermal

The architecture of OpenSees allows new materials, elements and other classes to be added to the software. The framework is developed by keeping element and material implementations separate and a new material

class can be implemented and used with an existing element formulation without modifying the element classes.

The new material class is presented in Figure 10.1 consists of three modules: the coordinator module, the earthquake/cyclic module and the fire module. The basic idea of this new material class is to combine and improve two existing material concepts for two different fields: Steel02 for seismic and cyclic behaviour and steel01Thermal for the fire part.

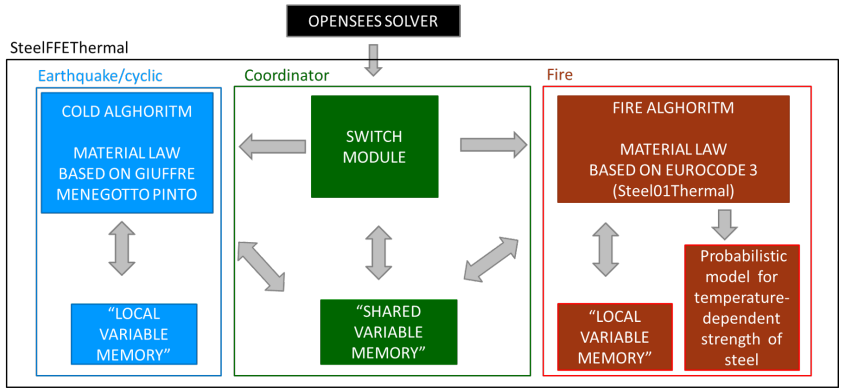

Figure 10.1: SteelFFEThermal basic idea

Earthquake/cyclic module

The earthquake/cyclic module is based on the Giuffrè-Menegotto-Pinto model already present in Opensees (Steel02). The Giuffrè-Menegotto-Pinto model is a uniaxial constitutive stress-strain law used for steel members and steel reinforcement bars in concrete members. The material model was initially developed by Giuffrè-Pinto [3] and is subsequently enriched by Menegotto and Pinto [3]. The hysteretic curve is expressed by:

$$\sigma^* = b\epsilon^* + \frac{(1-b)\epsilon}{(1+|\epsilon^*|^R)^{1/R}} \tag{10.1}$$

with

$$\epsilon^* = \frac{\epsilon - \epsilon_r}{\epsilon_0 - \epsilon_r} \tag{10.2}$$

$$\sigma^* = \frac{\sigma - \sigma_r}{\sigma_0 - \sigma_r} \tag{10.3}$$

$$R = R_0 - \frac{a_1 \xi}{a_2 + \xi} \tag{10.4}$$

where:

- b is the strain-hardening ratio defined by the ratio between the intended slope at the target point and the unloading stiffness at the origin.
- (ϵ_0, σ_0) correspond to the strain and stress at the intersection point of the two asymptote straight lines as shown in Figure 10.2.
- (ϵ_r, σ_r) correspond to the strain and stress of the unloading point.
- R is a coefficient that influences the shape of the unloading and reloading curves in order to represent Bauschinger's effect.
- R0 is the value of parameter R during the first loading and should be experimentally determined along with constants a1 and a2.
- ξ is the strain difference between the tangents intersection point and the target point normalized with respect to the yield strain.

After each reversal, the point sets (ϵ_0, σ_0) and (ϵ_r, σ_r) are updated.

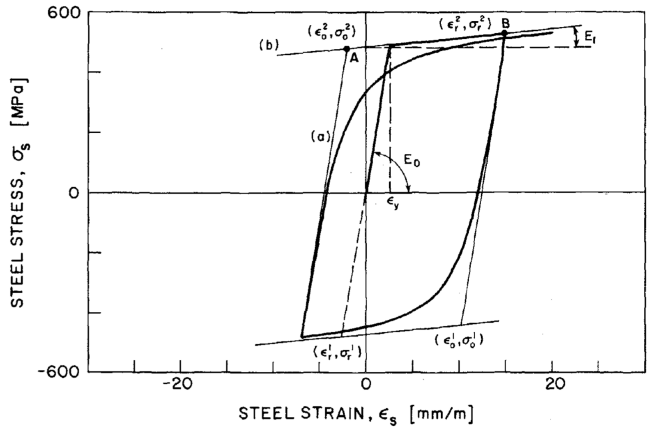

Figure 10.2: Giuffrè-Menegotto-Pinto Steel model [4].

In the early 1980s, Filippou et al. [4] included the possibility that the model considered isotropic strain hardening by shifting the position of the yield asymptote before computing the new asymptote intersection point following a strain reversal.

$$\frac{\sigma_{st}}{\sigma_0} = a_3(\frac{\epsilon_{max}}{\epsilon_0} - a_4) \tag{10.5}$$

where:

- ϵ_{max} is the absolute maximum strain at the instant of strain reversal.
- a3 and a4 are experimentally determined parameters.

Fire module

For the fire module, the steel01Thermal described by Elhami-Khorasani [2] was modified in order to increase the computational speed and include the probabilistic model for temperature-dependent strength of steel developed by Elhami-Khorasani [5]. The procedure for the integration of the constitutive law for two consecutive time steps with increasing temperatures is described in Figure 10.3 and herein summarize: The material model includes the nonlinearity of stress-strain at elevated temperatures, based EN 1993-1-2 [6], to account for strain reversals. When a thermal increment $\Delta T = T_{(i+1)} - T_{(i)}$ is introduced from a converged solution at temperature $T(i)$ point A, the plastic strain $e_{pl(i)}$ is calculated by "unloading" from point A with slope $E(i)$ to the intercept with strain axis. The plastic strain $e_{pl(i)}$ is assumed as a reference point in order to process a new loading at temperature $T_{(i+1)}$ and a new stress-strain curve considering the reduced yield strength, proportional limit, and modulus of elasticity is constructed. During the reloading phase the new elastic module $E_{(i+1)}$, based on $T_{(t+1)}$, is used. For a detailed description of the procedure, the reader is addressed to the paper of Elhami-Khorasani and co-workers [2].

In order to increase the computational speed, several optimizations in the code regarding the syntax and variables were done, but without changing the methodology. A speed comparison using two case studies can be found in Section 10.5.1.

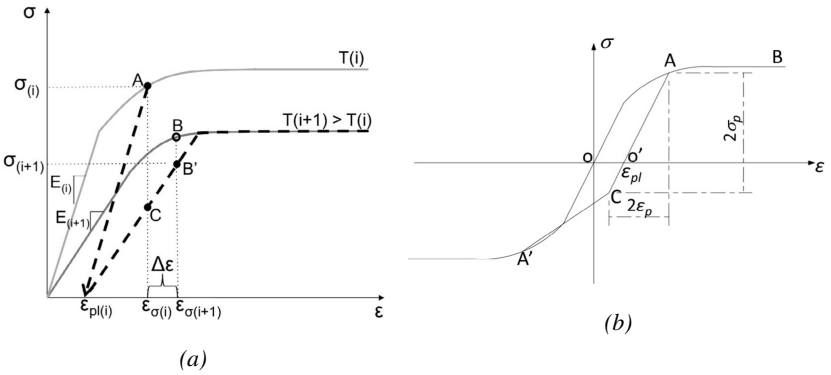

Figure 10.3: Uniaxial constitutive law at high temperature (Elhami-Khorasani 2015)[2]: a) unloading/reloading procedure. b) plastic strain and strain reversals.

A probabilistic model for temperature-dependent strength of steel was included in the SteelFFEThermal class. In detail for steel, the logistic model presented by Elhami-Khorasani et al. [5] and by Ramla Qureshi [7] is taken as is, with a focus on the logistic distribution using the EC3 steel model as a deterministic base and applied to the $k_{y,2\%,T}$ dataset, as shown in Figure 10.4. This function, expressed in Equation 10.6, is instrumental toward investigating probabilistic material strength degradation models. The parameters have been calculated using a Bayesian updating rule, and the modeling error that approximates variance in residuals is inculcated as 0.43ϵ, where ϵ is the standard normal distribution.

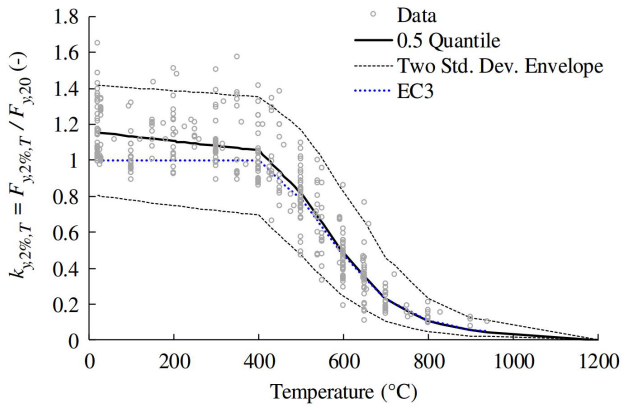

Figure 10.4: Strength retention factors versus temperature based on a continuous logistic fit for steel $k_{y,2\%,T}$ [5][7].

$$k_{y,2\%,T} = \frac{1.7 \cdot \exp\left[logit(\hat{k}^*_{y,2\%,T}) + 0.412 - 0.81 \cdot 10^{-3} \cdot T + 0.58 \cdot 10^{-6} \cdot T^1.9 + 0.43 \cdot \epsilon\right]}{\exp\left[logit(\hat{k}^*_{y,2\%,T}) + 0.412 - 0.81 \cdot 10^{-3} \cdot T + 0.58 \cdot 10^{-6} \cdot T^1.9 + 0.43 \cdot \epsilon\right]} \tag{10.6}$$

where:

$$logit(\hat{k}^*_{y,2\%,T}) = \ln \frac{\hat{k}^*_{y,2\%,T}}{1 - \hat{k}^*_{y,2\%,T}} \tag{10.7}$$

$$\hat{k}^*_{y,2\%,T} = \frac{\hat{k}_{y,2\%,T} + 10^{-6}}{1.7} \tag{10.8}$$

and $\hat{k}_{y,2\%,T}$ = temperature-specific retention factor as prescribed by the EC3.

Coordinator module

At each step, the coordinator module checks the temperature of the fiber. If the temperature is equal to or below $20°C$ the coordinator activates the Earthquake/cyclic module, otherwise it switches to the fire module without losing the actual plastic deformations.

10.3 FFE framework: basic idea

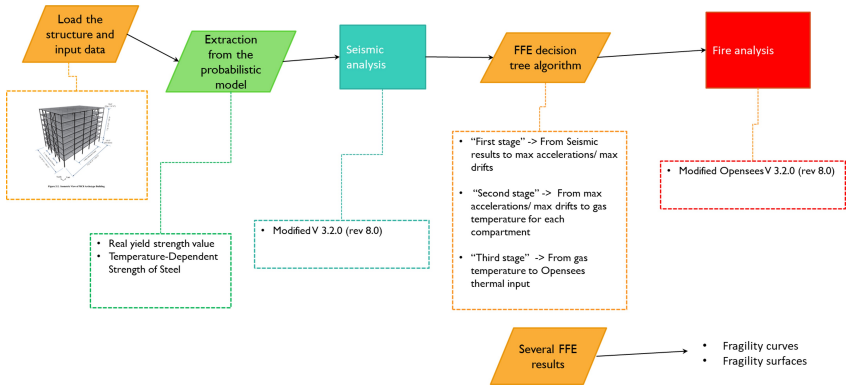

Figure 10.5: FFE framework basic idea.

The basic concept of the FFE framework is illustrated in Figure 10.5. First of all is required to create a standard Tcl script input file for Opensees,

which defines the problem geometry, loading, formulation of the case study. Before launching the script with a modified version of the OpenSees software, it is also required to define the probabilistic parameters used for the extraction of the strength retention factors of the logistic function of Equation (10.6 and yield strength value at ambient temperature. Research conducted by Holický and Sýkora [8] recommends variability at an ambient temperature with a lognormal distribution, with the mean value equal to the characteristic value plus two standard deviations and the value of the coefficient of variation as 0.07. This choice was made because deviations in strength of steel profiles can be caused due to different material composition, the size of crystalline grains, and whether the steel was rolled. After the probabilistic parameters were extracted, the gravity and seismic analyses are performed. Then OpenSees enters in a "standby mode" state and a background MATLAB process executes the FFE decision tree algorithm to automatically generate the fire scenario based on the earthquake results. A detailed explanation of this algorithm could be found in the next section. Finally, the resumed OpenSees process performs the fire analysis using the data generated by the FFE decision tree algorithm.

This Framework could be used to perform several FFE analyses with different probabilistic data and earthquake sets and scale values in order to obtain enough data to construct fragility curves and fragility surfaces.

10.4 FFE decision tree algorithm

Post-earthquake ignition sources identified from past earthquakes are reviewed by Botting(1998). Also Scawthorn (1992) discusses ignition sources and predicts post-earthquake ignition rates for typical high rise buildings for different earthquake intensities. In brief, the principal ignition sources are overturning of electrical appliances, short-circuiting of electrical equipment, gas leakage from damaged equipment and pipework and leakage of flammable fluids. Another major concern is the high potential for ignition as electricity and gas supplies are restored some time after the earthquake. Leaking gas and damaged electrical appliances were identified as initiating a greater than average incidence of fires in the days following the Kobe and Northridge earthquakes.

10.4.1 "First stage"

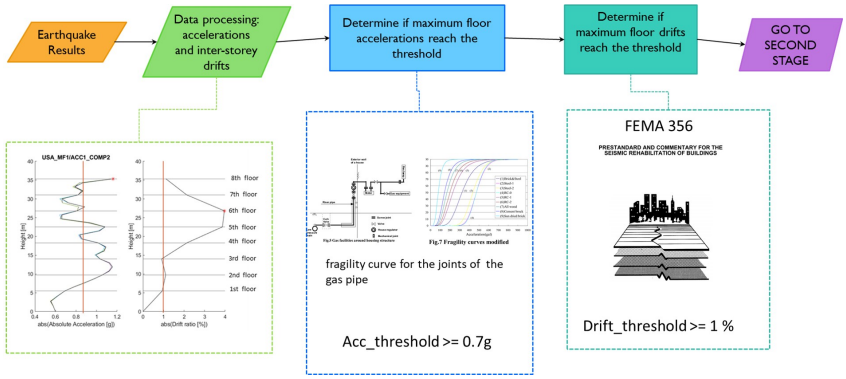

Figure 10.6: First stage scheme.

After the earthquake analysis, OpenSees enters in a "standby mode" state until the FFE decision tree algorithm generates the data for the fire. Figure 10.6 illustrates the schematic procedure of the first stage. As the first step, the FFE decision tree reads the acceleration data and the inter-story drift data in order to identify the maximum values for each floor and compartment.

The principal assumptions that determine the possibility to have a fire after the earthquake are as follows:

- Assumption A: The acceleration of almost one floor must be greater than or equal to $0.7g$.
- Assumption B: The Inter-story drift ratio of almost one floor must be greater than or equal to 1.0%.

The assumption "A" refers to the possibility to have some damage to the gas network in or near the building, like leakage from a screw joint or mechanical joints that are the weakest point of the gas network. Ueno et al. l [9] presents a set of fragility curves for 9 building categories to estimate fragilities of low-pressure gas facilities from experience due to 1995 Kobe Earthquake. The fragility curves are defined as the correlation between the acceleration and the probability to come at a certain damage state:

- Major: Occurrence of leakage or rupture
- Moderate: Fear to fall into the major damage/Possibly to maintain in the damage free state by improving the present situations.

- Minor or None: Immediately possible to continue or restart the operation.

The acceleration threshold of $0.7g$ was defined using the fragility curve of the mean of steel-1 and steel-2 categories. As shown in Figure 10.7, a complete major damage is expected when the acceleration reaches a value of $0.7g$.

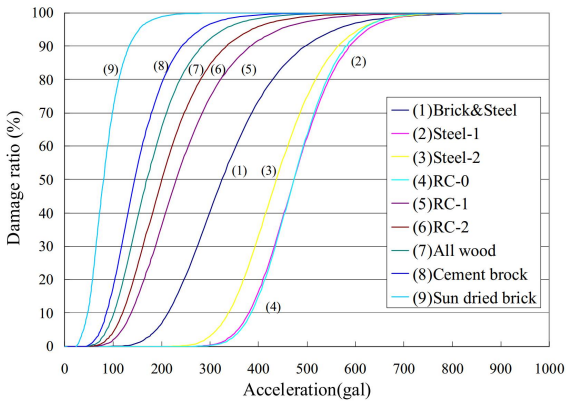

Figure 10.7: Gas pipe fragility curve [9].

The assumption "B" refers to the possibility to have some damage to the electrical services that can be expressed as a function of the deflections of the building. An inter-story drift ratio value equal to 1.0% was chosen because it is a value between the Life-safety limit state (0.5 %) and the Collapse limit state (2.0%) of steel braced frame defined in the FEMA P-356 [10].

10.4.2 "Second stage"

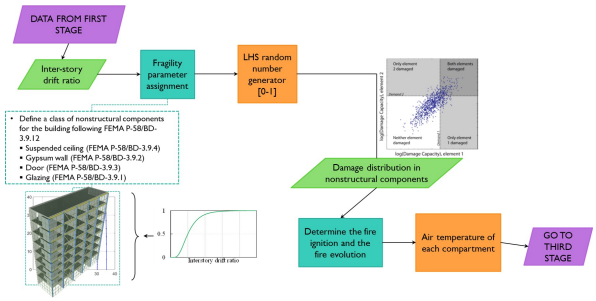

Figure 10.8: Second stage scheme.

The evolution of fire inside a compartment is required as an input to the fire spread model and the following parameters are taken into account:

- Size of the compartment.
- Curtain wall type (drift sensitive damage).
- Glazing damage (drift sensitive).
- Doors are open or not.
- Sprinklers are not installed or are not operational due to the earthquake.

Sprinkler systems are subject to damage from inertia loads on the suspended pipework, movement across seismic joints, and impact with suspended ceilings. Sprinkler systems have proved to be vulnerable in many past earthquakes. Principal damage scenarios are lack of restraint to the system pipework and damage to heads due to impact with ceilings [11] [12].

Walls, partitions and external glazing are vulnerable to damage in a moderate earthquake due to the loads applied as the building deflects. Fire separations may suffer significant cracking and lose their fire integrity.

Damage to non-structural partitions is a function of the racking loads imposed by the deflections of the building. Damage is, therefore, more likely in flexible framed buildings, unless the partitions are separated from the structure to allow differential movement, and may occur in moderate earthquakes situations [12] [13]. Smoke transmission can be expected once the lining material cracks and fire spread becomes possible when the linings separate from the framing. In detail, If a specific damage state is reached, there is enough damage in the partition wall that would affect the fire spread rate. The FEMA P-58/BD-3.9.2 defines three damage states: Minor damage (DS1), in which the partition walls can be repaired by patching, re-taping, sanding; Severe cracking (DS2), crushing or out of plane buckling of gypsum wallboards; Severe damage (DS3) to partition including gypsum and steel framing. Only the damage state DS3 has an effect on the horizontal fire spread ratio. In the framework, the horizontal fire spread is set 30 minutes for the normal undamaged conditions and it is reduced to 15 minutes if the probability of damage state DS3 exceeds a defined value depending on the case study.

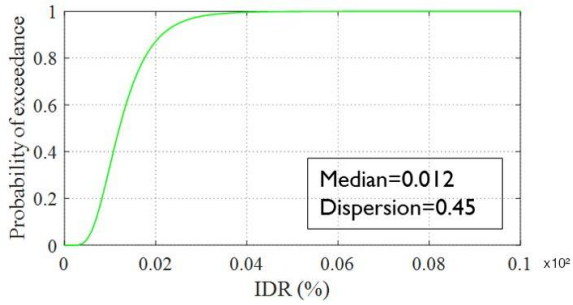

Figure 10.9: Partition fragility curve (Walls BD-3.9.2 - table 13 for DS3, Full connections) [14].

The loss of exterior glazing will change the ventilation factors for a fire compartment and may allow the development of larger fires than anticipated in the design. The damage of the glazing is a function of the deflections of the building and can be expressed using a fragility curve based on the glazing type. Glazing is assumed to be a monolithic, non-laminated, annealed glazing with a thickness of 6.35 mm (1/4 in), clearance of 10.92 mm (0.43 in), an aspect ratio of 6:5, and dry sealant. The glazing fragility curve is illustrated in Figure 10.10.

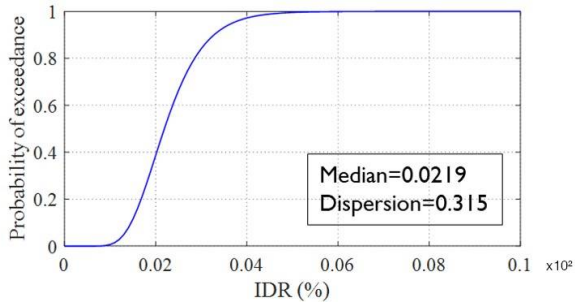

Figure 10.10: Glazing fragility curve (FEMA P-58/BD-3.9.1) [15]

It is possible to have accidental ignition in more than one location, due to damage to gas or electrical services or appliances. For this reason, the framework could select more than one ignition after the earthquake. Anyhow all the compartments selected as ignition points must satisfy the assumptions A and B of the first stage.

For the vertical spread rate, the flashover time is set. All those values can be changed according to the proprieties of the case study and those parameters and fragility curves are used to determine the presence and the evolution of the fire in each compartment.

The OZone software [16] [17] is used to generate multiples fire scenarios for each different compartment proprieties and damage states of walls, glazing and doors. During the FFE decision tree process, the data generated by the first stage is used to assign the fire scenarios to the compartments of the case study subjected to fire based on the different combinations of the assumptions described in this section.

10.4.3 "Third stage"

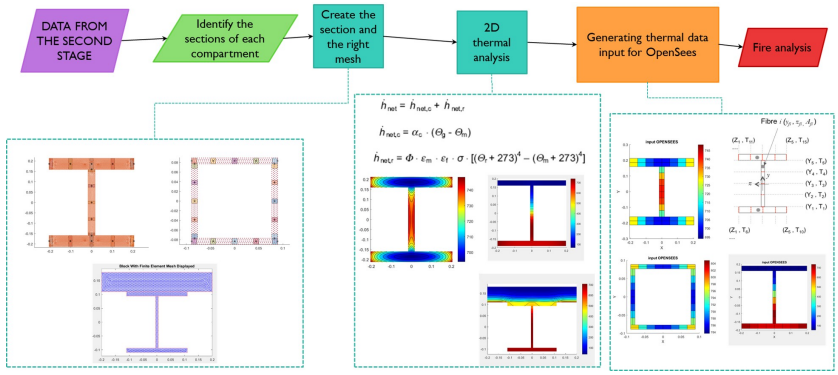

Figure 10.11: Third stage scheme.

Actually, it is not possible to perform the thermal analyses automatically inside OpenSees 3.2.0 (Berkeley Official branch) or using other appropriate external software (i.e. SAFIR), due to the lack of an official Application Programming Interface (API), which is a software intermediary that allows two applications to talk to each other. Due to this reason, a MATLAB script was developed to perform thermal analyses based on the Partial Differential Equation Toolbox, which provides functions for solving structural mechanics, heat transfer, and general partial differential equations (PDEs) using finite element analysis.

Figure 10.8 illustrates the schematic procedure of the second stage. The framework creates a two-dimensional thermal finite element analysis for each compartment and automatically assigns the boundary conditions. The thermal analysis is conducted for each heated member of the selected compartment (columns, beams and braces) using cross-sections that are discretized with an appropriate mesh size. The thermal modeling of the beam section includes the effective shape and width of the concrete slab. The applied fire curve is the curve generated in the second stage.

In detail, the MATLAB script creates a "thermalModel" object that

contains information about a heat transfer problem: the geometry, material properties, internal heat sources, temperature on the boundaries, heat fluxes through the boundaries, mesh, and initial conditions. Thermal actions are given by the net heat flux $\dot{h}_{net,d}$ to the surface of the member. On the fire exposed surfaces the net heat flux is determined by considering heat transfer by convection and radiation as:

$$\dot{h}_{net,d} = \dot{h}_{net,c} + \dot{h}_{net,r} \tag{10.9}$$

where $\dot{h}_{net,c}$ is the net convective heat flux component and $\dot{h}_{net,r}$ is the net radiative heat flux component. The following equation gives the net convective heat flux component:

$$\dot{h}_{net,c} = \alpha_c \cdot (\theta_g - \theta_m) \tag{10.10}$$

where:

- α_c is the coefficient of heat transfer by convection.
- θ_g is the gas temperature in the vicinity of the fire exposed member.
- θ_m is the surface temperature of the member.

For simplicity, EN1991-1-2 (2002) provides an approximation of the net heat flux [W/m2] due to radiation as follows:

$$\dot{h}_{net,r} = \theta \cdot \epsilon_m \cdot \epsilon_r \cdot \sigma \cdot [(\theta_r + 273)^4 - (\theta_m + 273)^4] \tag{10.11}$$

where:

- Θ is the configuration factor.
- ϵ_m is the surface emissivity of the member.
- ϵ_f is the emissivity of the fire.
- σ is the Stephan Boltzmann constant ($5.67x10^{-8} W/m^2K^4$).
- θ_r is the effective radiation temperature of the fire environment.
- θ_m is the surface temperature of the member.

The configuration factor Θ takes into account varying radiative heat flux levels on the fire exposed surface of the members depending on the position and shallow effects. Annexe G (informative) of EN1991-1-2 gives the method for calculating the value of Θ, which will be discussed in the next section. Conservatively, Θ can be taken as 1.0.

The specific heat of steel is determined from the following:

- for $20°C \leq \theta_a \leq 600°C$:

$$c_a = 425 + 7.73 \cdot 10^{-1}\theta_a - 1.69 \cdot 10^{-3}\theta_a^2 + 2.22 \cdot 10^{-6}\theta_a^3 \tag{10.12}$$

- for $600°C \leq \theta_a \leq 735°C$:

$$c_a = 666 + \frac{13002}{738 - \theta_a} \tag{10.13}$$

- for $735°C \leq \theta_a \leq 900°C$:

$$c_a = 545 + \frac{17820}{\theta_a - 731} \tag{10.14}$$

- for $900°C \leq \theta_a \leq 1200°C$:

$$c_a = 650 \tag{10.15}$$

A uniform room temperature equal to $20°$ is assigned to the section as an initial condition.

10.4.4 OpenSees: bug fix and other improvements

In order to achieve the development of the FFE Framework, other minor improvements and bugs fixed in the OpenSees source code (v3.2.0) were made. Those changes are summarized as follows:

- Bug fix: FiberSectionGJThermal was restored instead of FiberSection3dThermal to prevent the convergence problems due to the torsion missing parameters.

- Bug fix: "print -JSON" command will not produce a correct data objects results consisting of attribute-value pairs and array data types. Several changes were made to fix errors and adding information about loads, constraints and equaldofs.

- Bug fix: Steel02Thermal will not save the temperature data on the output file recorder. This problem was fixed.

- Improvement: add new warning message and data output when the strain in a fiber of steel material exceeds 0.15.

The modified source code of OpenSees was compiled in Windows and CentOS (Linux) environments.

10.5 Validation

10.5.1 SteelFFEThermal

Earthquake/cyclic simulation (cold module)

The case study is a simply supported beam with reverse cyclic loading applied at the right end node. The geometry, applied load, cross section and material properties at ambient temperature are reported in Figure 10.12a. Fifteen non-linear beam elements based on the fibre displacement-based beam-column element and the corotational formulation was adopted. Geometric imperfections were included to allow for buckling EN 1993-1-1 [18]. The structure was also studied, under the same assumptions, using the Steel02 and SteelFFEThermal material. In this way, it was possible to compare the official Giuffrè-Menegotto-Pinto (GMP) material and the cold module of the SteelFFEThermal based on the same formulation.

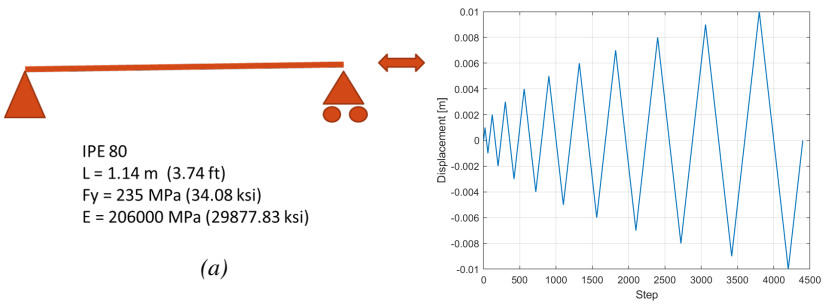

(a)

(b)

Figure 10.12: Case study: a) geometry and data; b) reverse Cyclic Loading applied at the right end node.

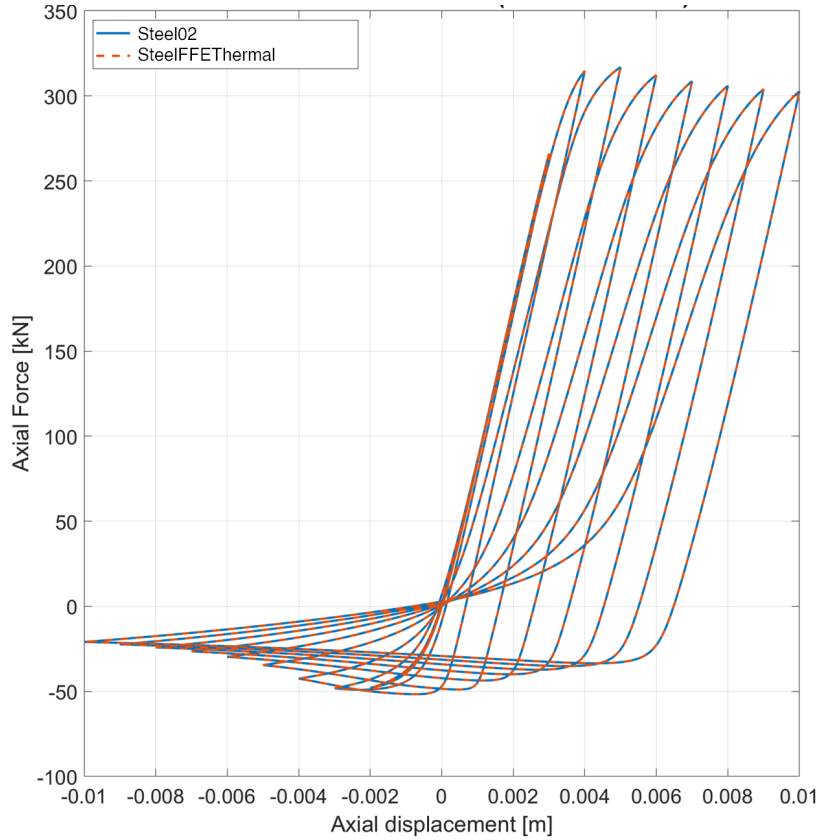

Figure 10.13: Axial load versus axial displacement response.

Figure 10.13 illustrates the Axial force versus axial displacement response comparison between Steel02 and SteelFFEThermal. As expected, due to the same material formulation, both the material classes showed the same results.

Fire simulation (Fire module)

The case study is a simply supported beam with a concentrated load at midspan. The geometry, applied load, cross section and material properties at ambient temperature are reported in Figure 10.14a. Fifteen non-linear beam elements based on the fibre displacement-based beam-column element and the corotational formulation was adopted. It was first subjected to the gravity load, then thermal action was applied. As illustrated in Figure 10.14b, the thermal action on the beams is represented by a piecewise-defined function defined by three parts: the ISO 834 standard heating curve for the first 16 minutes, a constant temper-

ature value equal to $725°C$ for 2 minutes and linear cooling phase for 31 minutes. The cross-section temperature distribution is assumed to be uniform in the beam.

The structure was also studied, under the same assumptions, using the Steel01Thermal and SteelFFEThermal material. In this way, it was possible to compare the steel material at elevated temperature and the fire module of the SteelFFEThermal based on the same formulation.

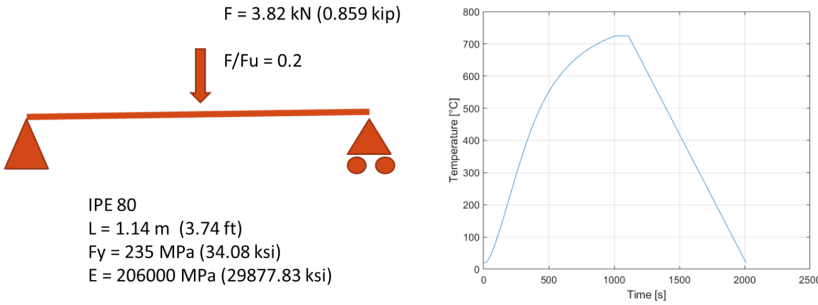

(a) *(b)*

Figure 10.14: Case study: a) geometry and data; b) evolution in time of the temperature in the cross section.

Figure 10.15a illustrates the comparison the vertical displacement at the mid-span of the beam. The analysis showed a good agreement of the SteelFFEThermal and a better computational time speed compared to Steel01thermal, as shown in Figure 10.15b.

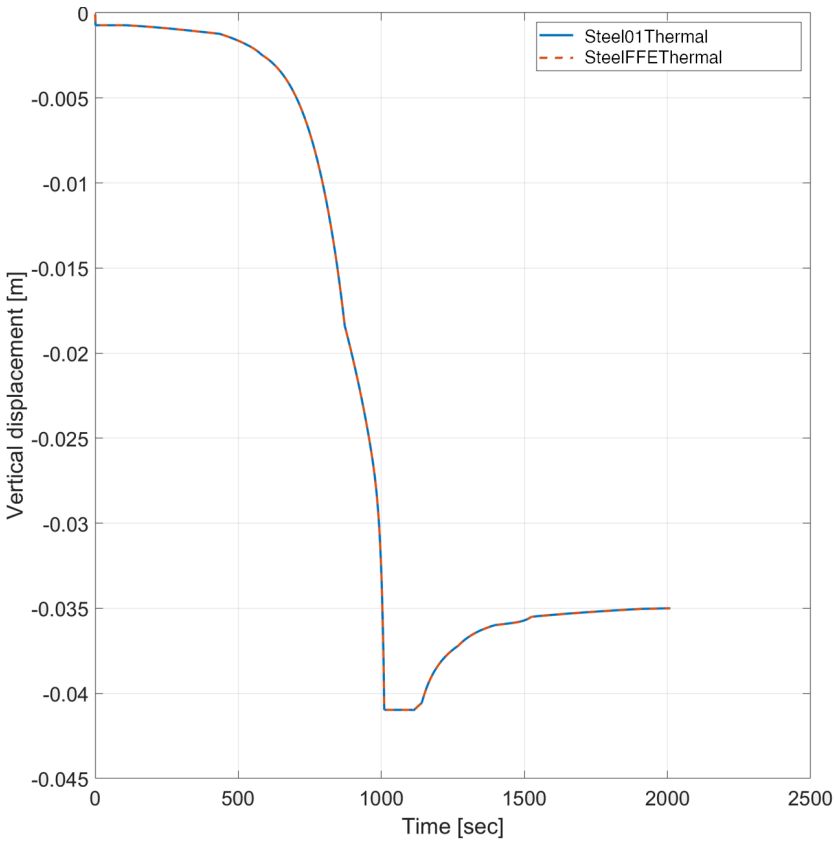

(a)

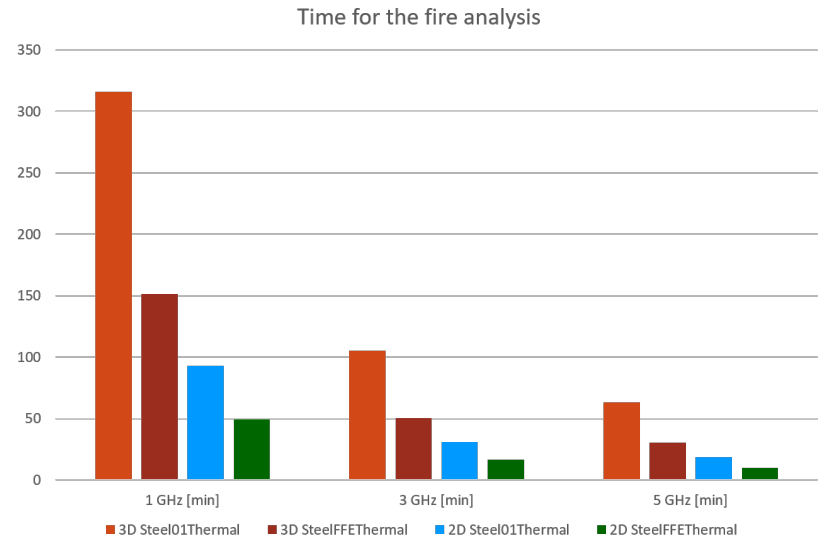

(b)

Figure 10.15: a) Vertical displacement at the mid-span; b) Computational time comparison.

FFE simulation (cold and Fire module)

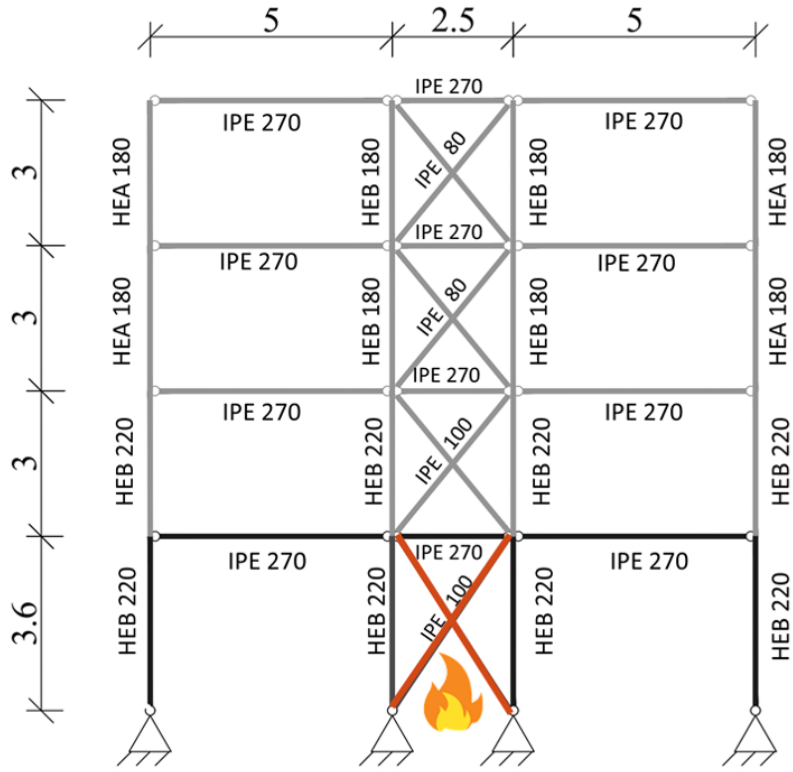

Figure 10.16: Test frame. Dimensions are in meters.

The EQUFIRE case study, already presented in Chapter 3, was used to check the SteelFFEThermal class in a FFE scenario. The frame was first subjected to the gravity load, then to horizontal and vertical displacement histories resulting from seismic non-linear dynamic analysis. Afterwards, thermal action was applied. Non-linear beam elements were used for all elements to check that non-dissipative elements remain in the elastic field owing to the seismic action. Geometric imperfections were included to allow for buckling EN 1993-1-1 [18]. Masses were considered lumped on the floors, following the assumption of rigid diaphragms. For the braces the following input values was used: $R0 = 20$, $cR1 = 0.925$, $cR2 = 0.15$. Figure 10.17 illustrates the results of the numerical simulation of the FFE test on the bare structure (without fire protection) for the selected acceleration time-history followed a thermal load that is represented by a piecewise-defined function defined by two

parts: the ISO 834 standard heating curve for the first 22 minutes, and linear cooling phase for 15 minutes. The thermal load was applied only at the bracing system at ground floor, in order to check the new material class behaviour on an element subjected to plastic damage during the earthquake event. As is possible to observe, the energy dissipation is concentrated in the braces and in particular at the ground floor 10.18.

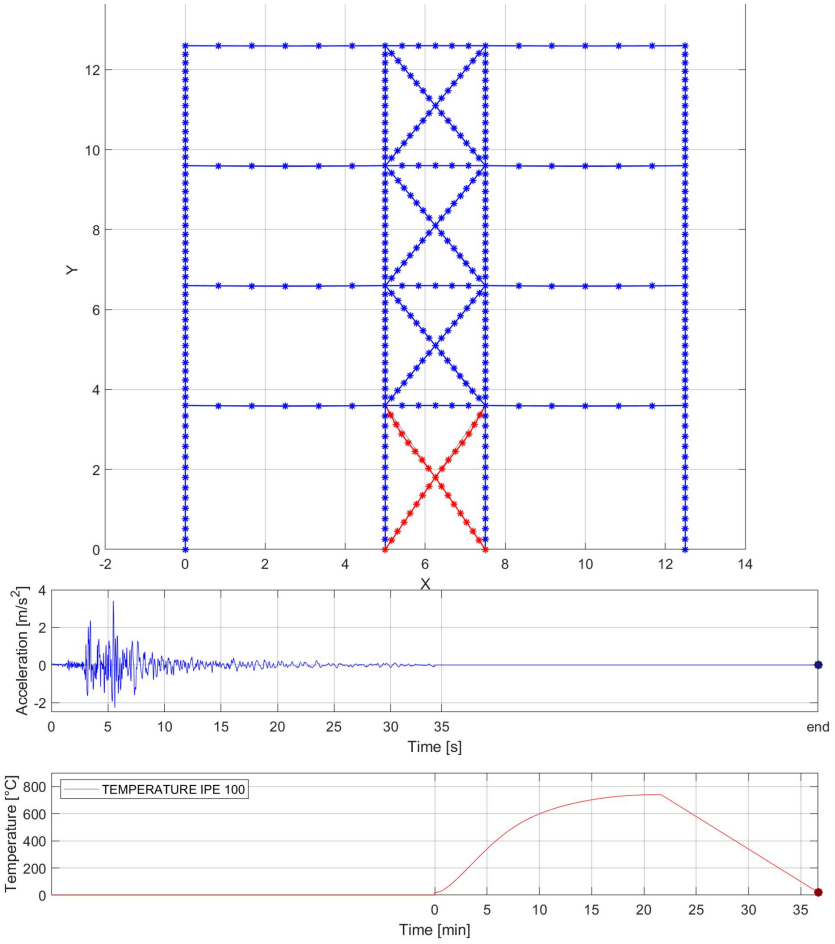

Figure 10.17: Deformed shape of the numerical model at the end of the FFE simulation, earthquake acceleration time-history and thermal load of the braces

Figure 10.18, 10.19 and 10.20 illustrate the results in terms of axial force, axial displacements of braces and columns of the ground floor.

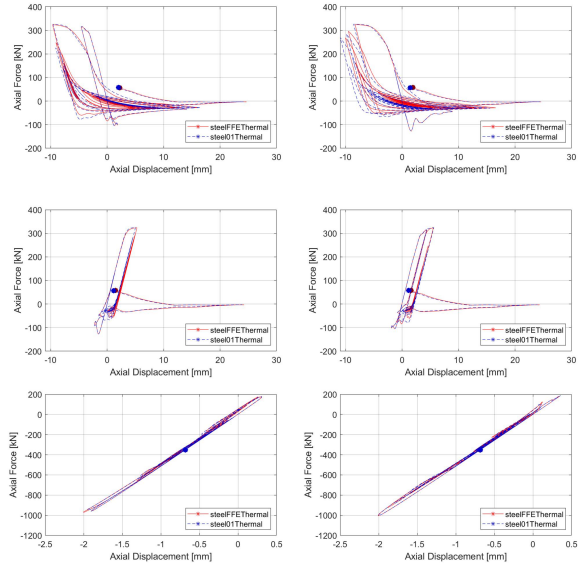

Figure 10.18: Axial force versus axial displacement response: a) brace top right; b) brace top left; c) brace bottom left; d) brace bottom right; e) internal column left; f) internal column right.

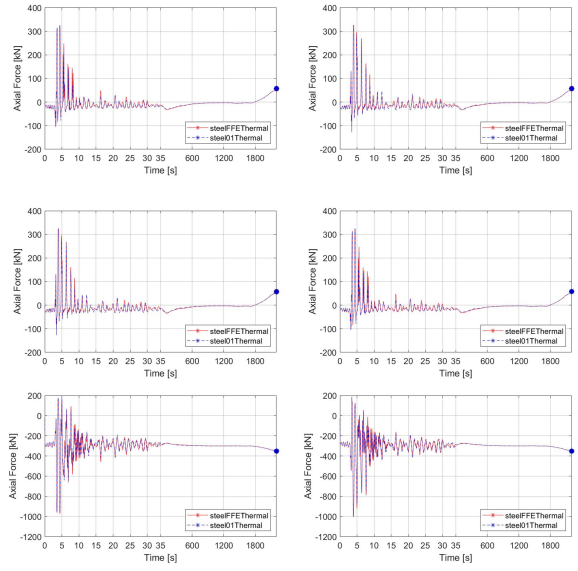

Figure 10.19: Axial force: a) brace top right; b) brace top left; c) brace bottom left; d) brace bottom right; e) internal column left; f) internal column right.

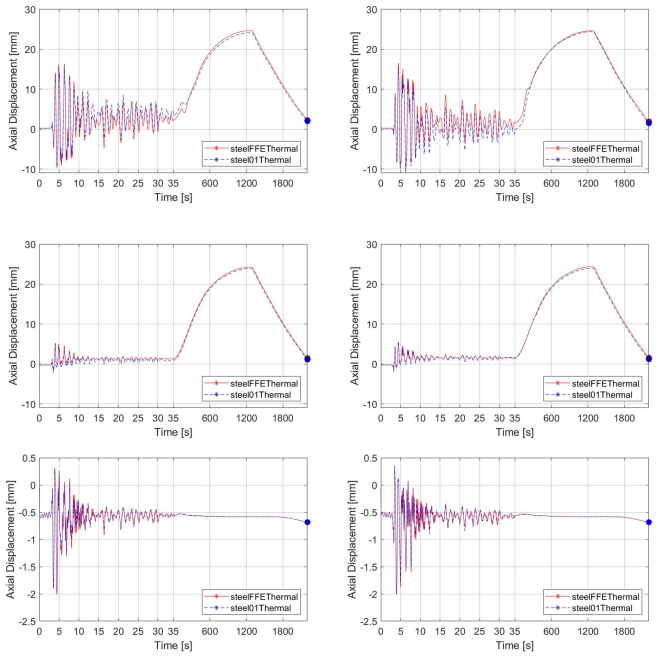

Figure 10.20: Axial displacement: a) brace top right; b) brace top left; c) brace bottom left; d) brace bottom right; e) internal column left; f) internal column right.

The analysis showed a good agreement between the Steel01Thermal and the SteelFFEthermal class. However, there is a difference in the axial displacements and forces, especially during the earthquake, because the steel01Thermal material class is not based on the Giuffrè-Menegotto-Pinto formulation as the cold module of the SteelFFEthermal class. In fact, at ambient temperature, the steel01thermal can be classified as a uniaxial bilinear steel material object with kinematic hardening and optional isotropic hardening, as illustrated in Figure 10.21.

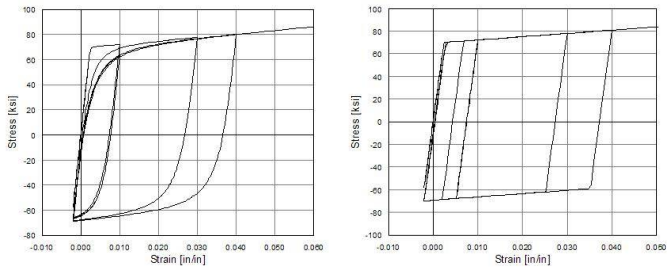

(a) *(b)*

Figure 10.21: Hysteretic Behavior of Model w/o Isotropic Hardening at ambient temperature: a) Giuffrè-Menegotto-Pinto Material (Steel02, SteelFFEThermal cold module); b) uniaxial bilinear steel material (Steel01, Steel01Thermal)

Therefore, it is not possible to properly compare the two classes and expecting the same results. However, the FFE simulation was repeated with some changes in material input parameter of the SteelFFEThermal class: $R0 = 50$, $cR1 = 0.0$, $cR2 = 1.0$. This choice was made in order to approximate the Giuffrè-Menegotto-Pinto formulation to a uniaxial bilinear steel material at ambient temperature as the Steel01Thermal. The comparison demonstrates the same results obtained from the Steel01Thermal material and the SteelFFEThermal class ($R0 = 50$, $cR1 = 0.0$, $cR2 = 1.0$) and it confirms the validity of the new uniaxial material class.

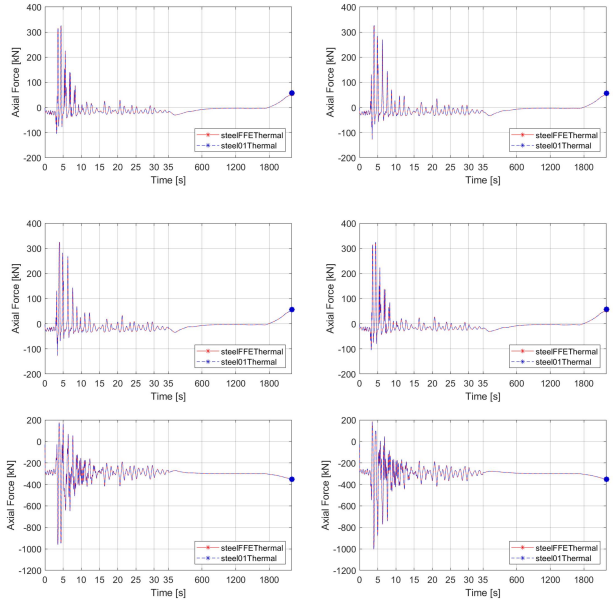

Figure 10.22: Axial force: a) brace top right; b) brace top left; c) brace bottom left; d) brace bottom right; e) internal column left; f) internal column right.

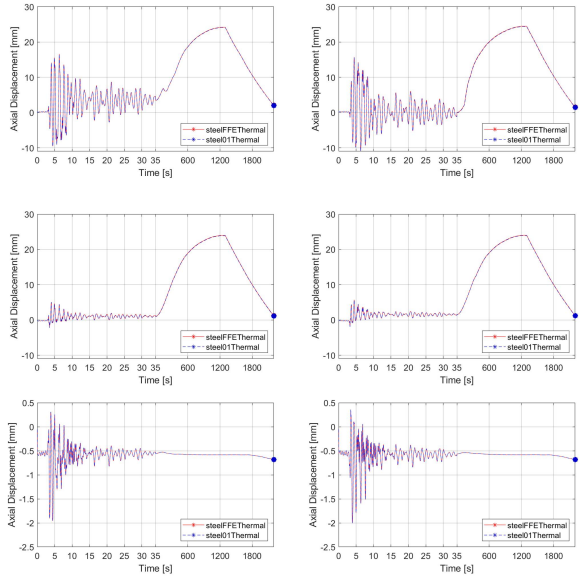

Figure 10.23: Axial displacement: a) brace top right; b) brace top left; c) brace bottom left; d) brace bottom right; e) internal column left; f) internal column right.

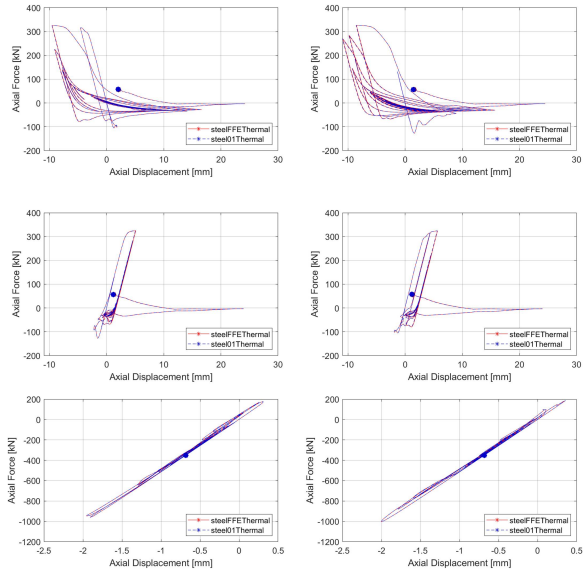

Figure 10.24: Axial force versus axial displacement response: a) brace top right; b) brace top left; c) brace bottom left; d) brace bottom right; e) internal column left; f) internal column right.

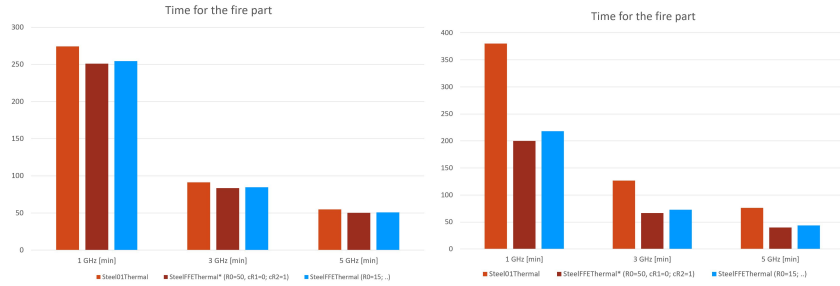

(a) *(b)*

Figure 10.25: Computational time comparison: a) earthquake simulation; b) fire following earthquake.

10.5.2 Thermal section (Third stage)

Two bare steel section models (W14x283 and HSS7x7x1/2) were created using a 2D heat transfer module developed in section 10.4.3 to simulate the distribution of temperature across the depth of sections. The sections which are the same as considered in the case study reported in Section 10.6. As explained in Section 10.4.3, the thermal conductivity and specific heat of steel were defined according to the Eurocode equations. The

ISO 834 fire was applied on all four faces of the sections and a mesh size of 0.002 m was chosen.

Thermal action can be defined in OpenSees on temperature data points to set up multiple temperature zones, which are up to 15 zones for 3D beam-column element, as shown in Figure 10.26a. Due to this reason, the Matlab script extracts the temperature data from those nodes and generates the input data for OpenSees.

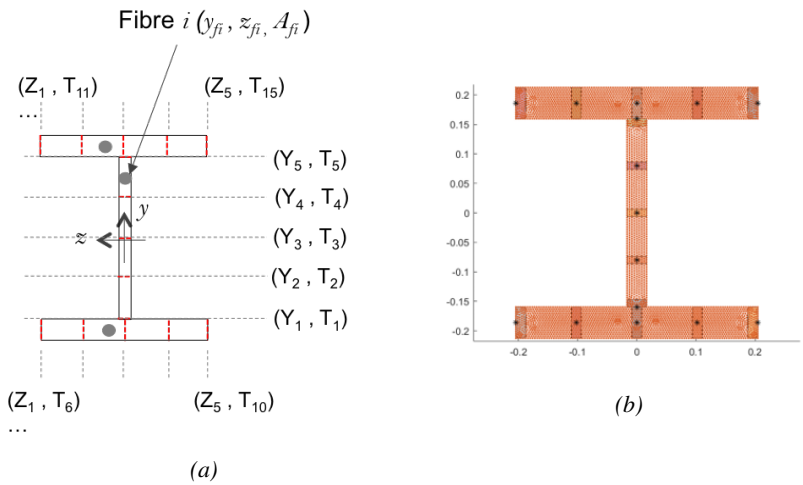

Figure 10.26: a) 15 temperature zones defined using Beam3dThermalAction (OpenSees); b) extraction of 15 temperature zones (MATLAB);

Figure 10.27 illustrates the temperature distribution in the W14x283 section at 33 minutes of heat exposure. In detail 10.27a shows the results of the 2D thermal analysis and 10.27b the equivalent input generated for OpenSees.

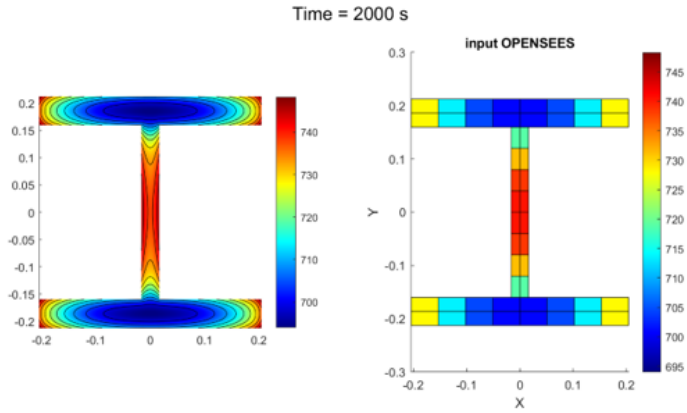

Figure 10.27: Temperature distribution in the W14x283 section at 33 minutes of heat exposure: a) MATLAB thermal model; b) Equivalent OpenSees.

Figure 10.28 and Figure 10.30 present the temperature distribution within the cross section being studied in the points on the steel profile. Almost identical results confirm the validity of the simulation model.

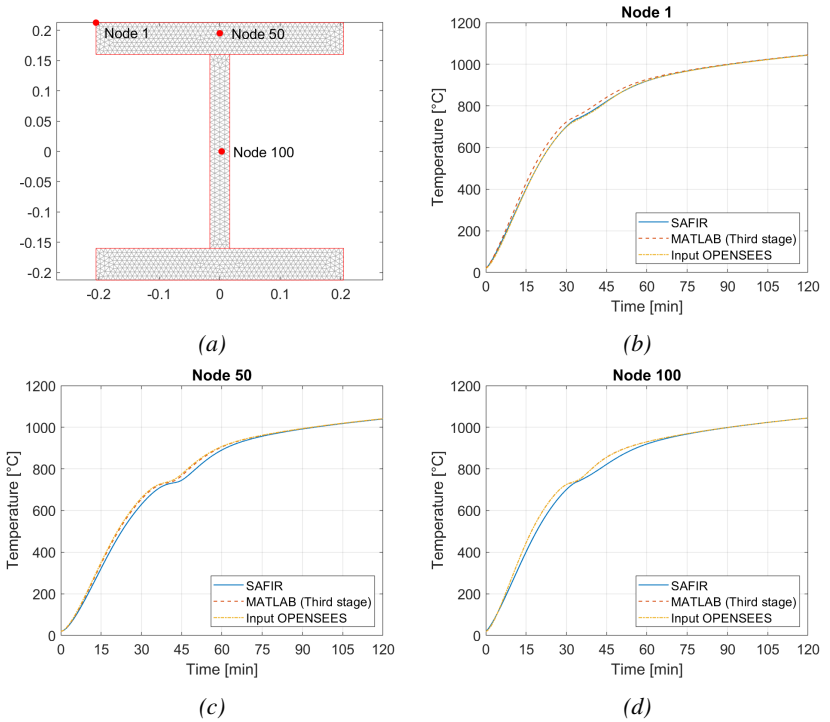

Figure 10.28: Temperature distribution of the W14x283 cross section in the points on the steel profile.

Figure 10.29 illustrates the temperature distribution in the HSS7x7x1/2 section at 33 minutes of heat exposure. In detail 10.29a shows the results of the 2D thermal analysis and 10.29b the equivalent input generated for OpenSees.

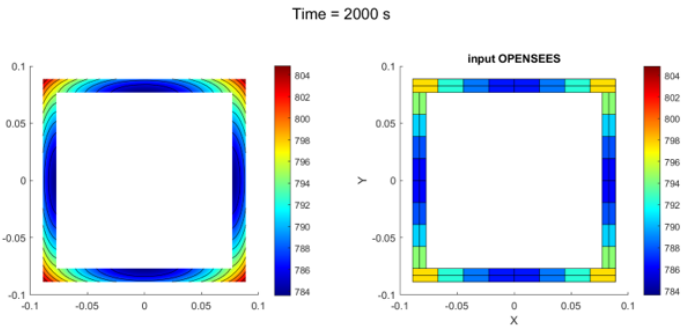

Figure 10.29: Temperature distribution in the HSS7x7x1/2 section at 33 minutes of heat exposure: a) MATLAB thermal model; b) Equivalent OpenSees.

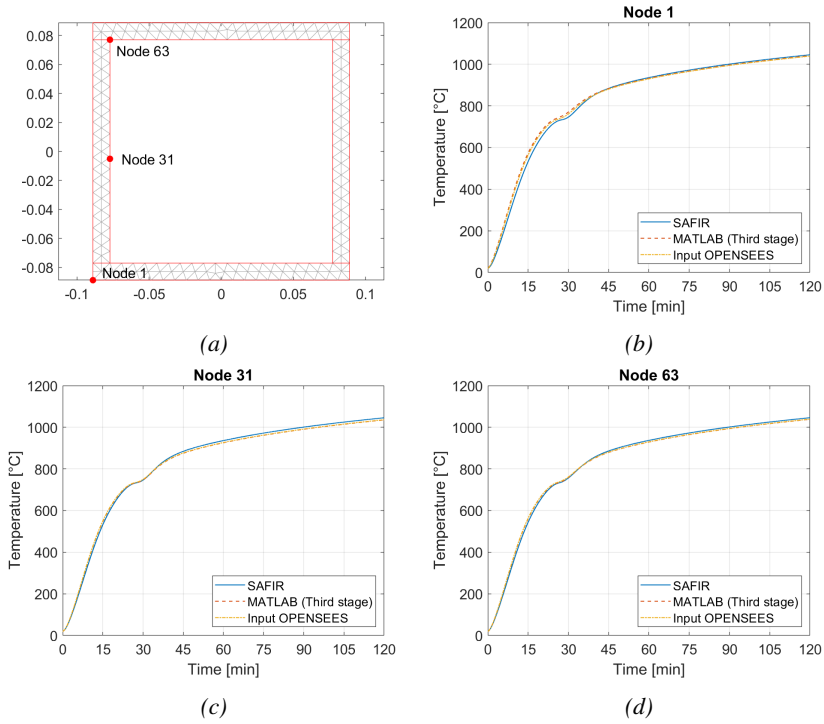

Figure 10.30: Temperature distribution of the HSS7x7x1/2 cross section in the points on the steel profile.

10.6 Multi-hazard Fire Following analysis

The methodology is applied to an eight-storey three-bay steel frame with concentric bracings in two central bays. This frame is part of an office building presented and designed in NIST Technical Note 1863-2 [19]. The plan dimensions for all floors and roofs are 46.33 m (152 feet), with five 9.14 meter (30-foot) bays, in the E-W direction and 31.01 m (102 feet), with five 6.10 m (20-foot) bays, in the N-S direction. The storey height is 4.28 m (14 feet) with the exception of the first floor, which is 5.49 m (18 feet) high. The building is designed for a high seismicity area, such as somewhere along the west coast of the United States.

Figure 10.31 also shows the member sizes and the location of the test frame. Figure 10.32 shows the gravity loads acting simultaneously with the seismic load and the fire load.

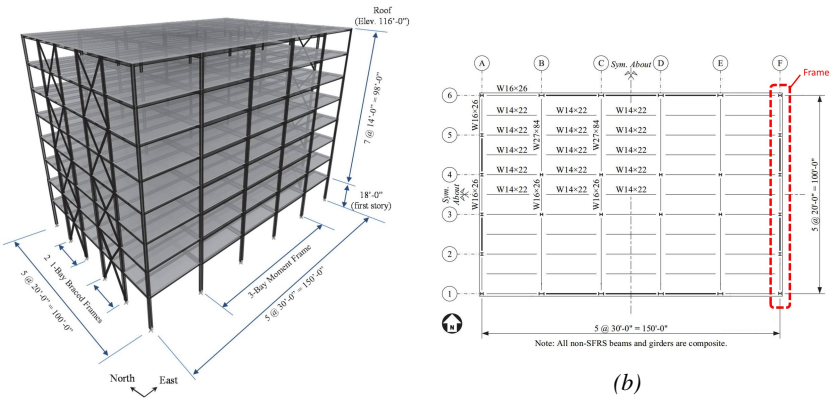

Figure 10.31: Building [19]: a) Isometric view b) plan view.

The following material types and corresponding nominal properties were assumed in design and in the numerical simulation:

- Wide-Flange Sections: A992 Grade 50, Fy = 344.74 MPa (50 ksi), Ry = 1.1
- HSS Sections: A500 Grade B, Fy = 317.16 MPa (46 ksi), Ry = 1.4
- Connections: A572 Grade 50, Fy = 344.74 MPa (50 ksi), Ry = 1.1
- E = 199947.96 MPa (29000 ksi), G = 77221.28 MPa (11200 ksi), $\nu = 0.3$

The design loads on the building are considered based on ASCE recommendations. The floor and roof dead load consist of the weight of the steel members, metal deck, and concrete slab weight. A total dead load (comprising of the self-weight of floor slab and superimposed load) of 2.92 kN/m2 (61 psf) and a live load of 2.39 kN/m2 (50 psf) is used. For the roof level, the total dead and live load values are taken as 2.68 kN/m2 (56 psf) and 1.44 kN/m2 (30 psf), respectively. A 3.65 kN/m (250 plf) superimposed dead load is also applied to the horizontal perimeter framing to account for facade (curtain wall) weight. Seismic loads are according to the Equivalent Lateral Force (ELF) and Response Spectrum Analysis (RSA) procedure in ASCE7.

The following parameters summarize the seismic hazard used for the design:

- Building Risk Category: II

- Site Soil Conditions: Site Class D, Stiff Soil – ASCE 7 Table 20.3-1
- Spectral Response Acceleration Parameters: shown in Table 10.1.
- SDC: D—taken as Dmax as used in FEMA P695

Table 10.1: Spectral Response Acceleration Parameters.

SDC	S_s **[g]**	S_1 **[g]**	F_a	F_v	$S_{MS} = F_a S_s$ **[g]**	$S_{M1} = F_v S_1$ **[g]**	$S_{DS} = 2/3 S_{MS}$ **[g]**	$S_{DS} = 2/3 S_{M1}$ **[g]**	$3.5 \cdot T_S$ **[sec]**
D_{max}	1.5	0.6	1.0	1.5	1.5	0.9	1.0	0.6	2.1

For the numerical analyses, the structural response of the N-S perimeter frame is investigated.

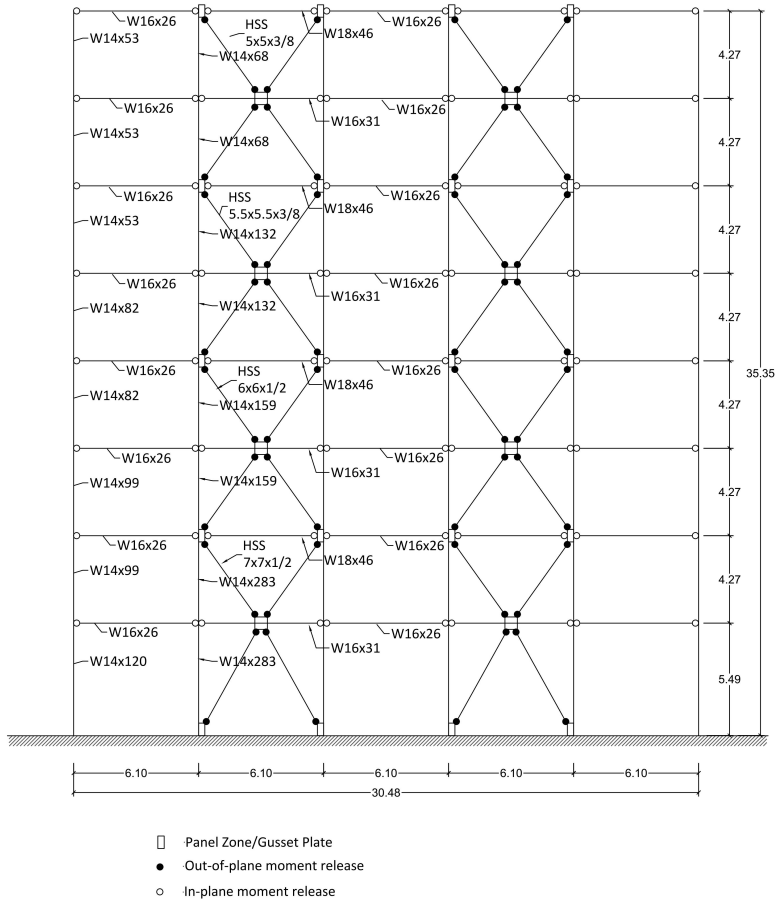

Figure 10.32: Configuration of the frame (Dimensions are in meters).

10.6.1 Ground Motions

The far-field record set (22 records, each with two horizontal components) from FEMA P695[14] is selected as the input motion database; 14 of the 44 horizontal component records are selected as the ground motion set for each FFE analysis. The accelerograms were modified to match the target spectrum in the period range of $0.2 \cdot T_1$ and $1.5 \cdot T_1$ that includes the fundamental period of the structure T_1.

Table 10.2 summarizes the 14 strong motion records used for the FFE analyses for the N-S direction.

Table 10.2: Accelerograms.

ID	Event name	Station	Year	MW	PGA
1	Northridge	Beverly Hills - Mulhol	1994	6.7	0.52
2	Northridge	Canyon Country-WLC	1994	6.7	0.48
3	Duzce, Turkey	Bolu	1999	7.1	0.82
5	Imperial Valley	Delta	1979	6.5	0.35
6	Imperial Valley	El Centro Array #11	1979	6.5	0.38
8	Kobe, Japan	Shin-Osaka	1995	6.9	0.24
9	Kocaeli, Turkey	Duzce	1999	7.5	0.36
10	Kocaeli, Turkey	Arcelik	1999	7.5	0.22
11	Landers	Yermo Fire Station	1992	7.3	0.24
14	Loma Prieta	Gilroy Array #3	1989	6.9	0.56
16	Superstition Hills	El Centro Imp. Co.	1987	6.5	0.36
17	Superstition Hills	Poe Road (temp)	1987	6.5	0.45
18	Cape Mendocino	Rio Dell Overpass	1992	7	0.55
19	Chi-Chi, Taiwan	CHY101	1999	7.6	0.44

Figure 10.33 illustrates the set of acceleration response spectra, original and scaled, and the scaled average spectrum.

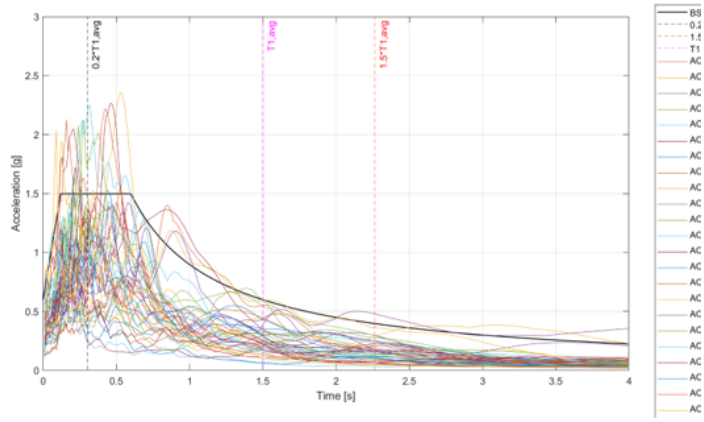

(a)

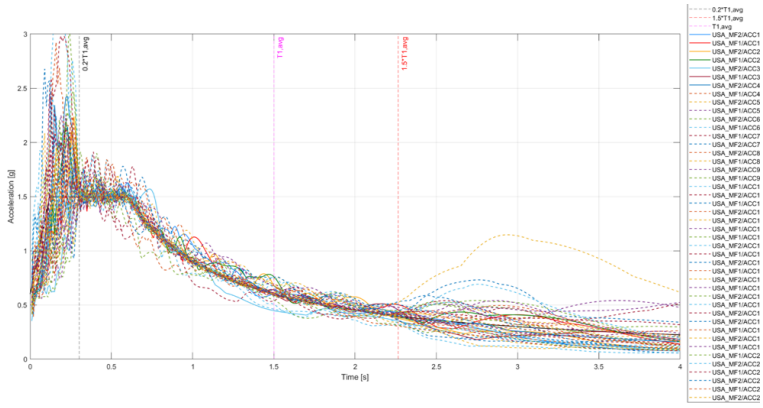

(b)

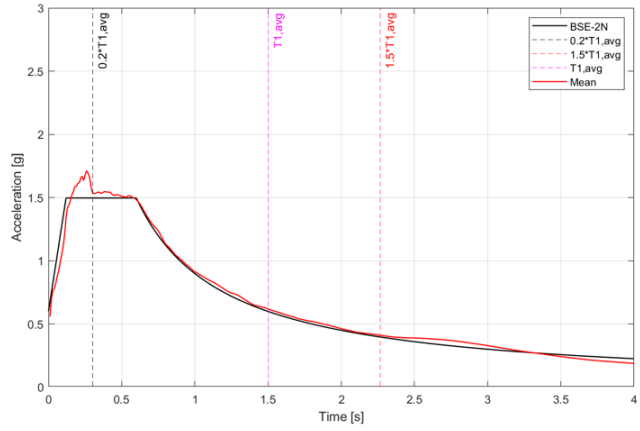

(c)

Figure 10.33: Acceleration Response Spectra: a) Original; b) Scaled; c) Scaled Average Spectrum.

10.6.2 FE model

The frame is modeled with nonlinear displacement-based beam-column elements using the SteelFFEThermal uniaxial material developed in section 10.2.1. Each column was discretized with four elements, while each beam and brace element were discretized using eight elements to get adequate precision in the calculation of displacements, stresses and strains in sections of each member. Fiber sections are selected to define the cross section of the beams, columns and braces.

A leaning column is linked to the frame using horizontal equaldof to simulate the stiffness of the other columns behind the frame. The leaning column is modeled with elastic beam-column elements with a large cross section area and moment of inertia that is equal to the sum of the geometrical proprieties of the other columns.

Some modifications of the 3D frame model are required when the analysis switches from earthquake to fire. In detail, the leaning column is connected to the frame by equalDOF to ensure the axially rigid contribution given by the outsider columns. Therefore, after the seismic analysis is completed, the horizontal diaphragms and the leaning column were removed.

The heat transfer analysis is automatically performed to obtain steel temperatures for each element in the compartment subjected to fire using the FFE decision tree explained in section 10.4. Figure 10.34 shows the boundary conditions for the heat transfer analyses of the columns, braces and beams.

A solution Algorithm of type Newton is used for the nonlinear problem.

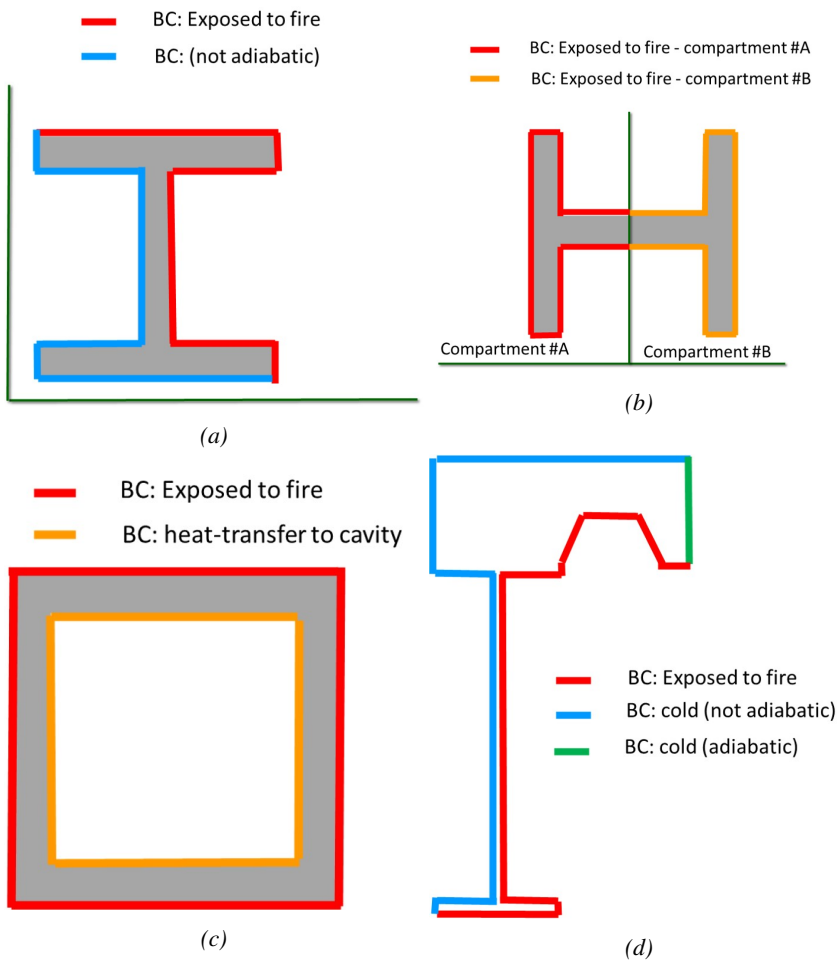

Figure 10.34: Boundary conditions for thermal analysis: a) external column; b) column between two compartments (internal column); c) brace; d) beam.

10.6.3 Results

The modal analysis is carried out and the periods calculated by the NIST report are listed as following: $T_1 = 1.50s$, $T_2 = 0.49s$, $T_3 = 0.28s$; while the ones obtained in OpenSees are $T_1 = 1.498s$, $T_2 = 0.477s$, $T_3 = 0.254s$. The results are very similar.

Among the fourteen accelerograms, the one shown in Figure 10.35, know as the Northridge earthquake was reported in this section as an example for the FFE test. The earthquake occurred at 4:31 am, Monday, January 17, 1994. As reported in Chapter 10.6.1, the accelerogram was modified to match the target spectrum in the period range of $0.2 \cdot T_1$ and

$1.5 \cdot T_1$ that includes the fundamental period of the structure T_1.

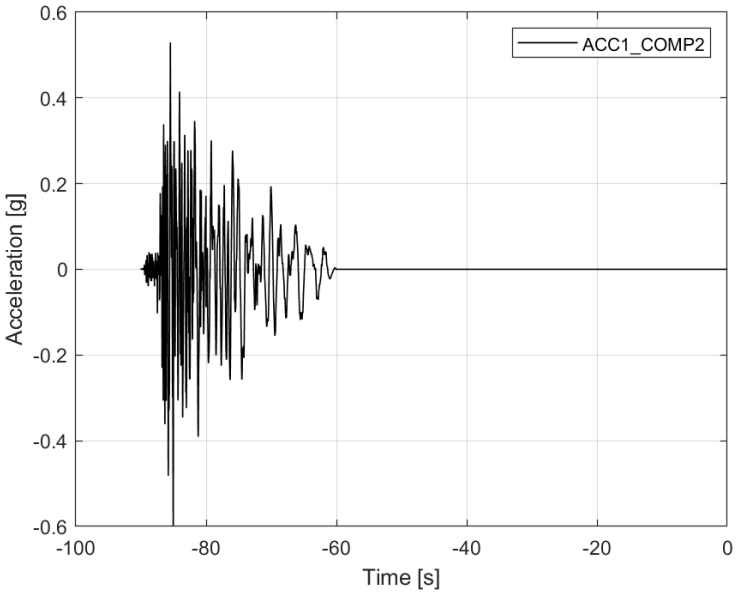

Figure 10.35: Earthquake acceleration time-history.

Figures 10.36, 10.37 and 10.38 illustrate the results of the numerical simulation of the seismic test on the bare structure for the selected acceleration time-history. In detail, the horizontal displacements of each floor are shown in Figure 10.36. Figures 10.37 and 10.38 illustrate energy dissipation of the bracing system.

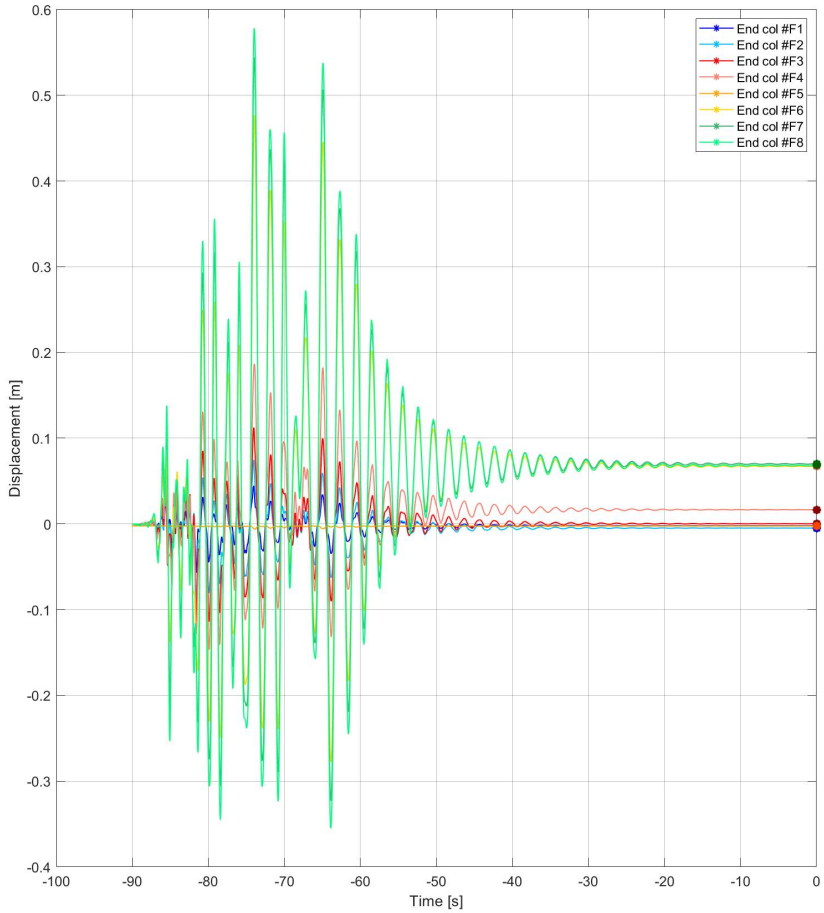

Figure 10.36: Horizontal displacements of each floor.

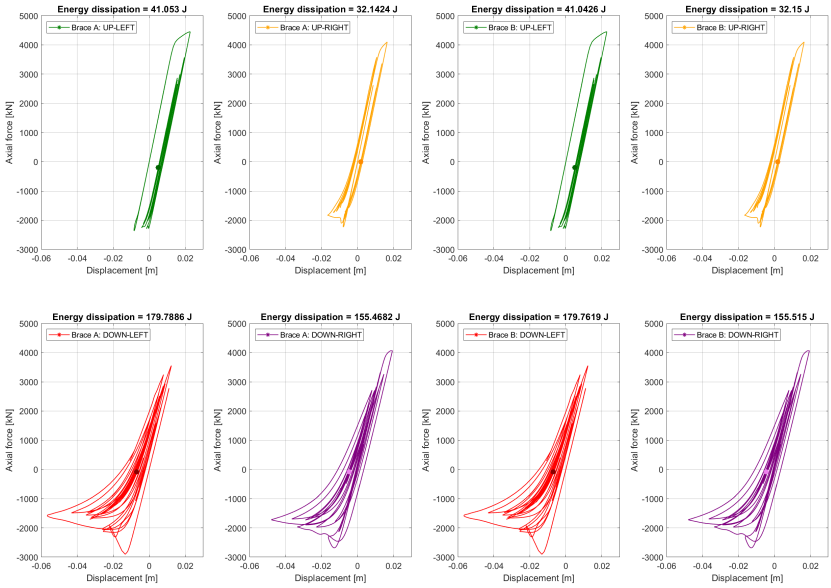

(a)

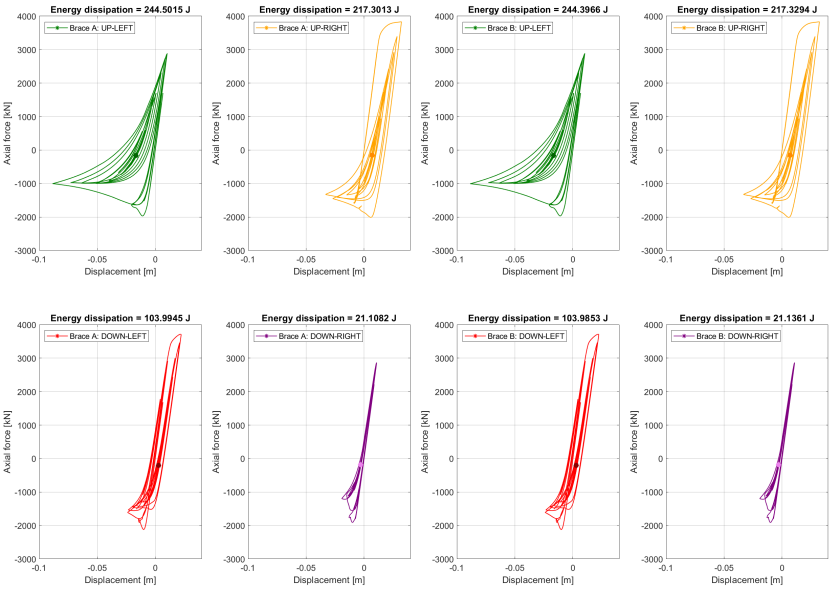

(b)

Figure 10.37: Energy dissipations of the braces: a) 8th and 7th floors; b) 6th and 5th floors.

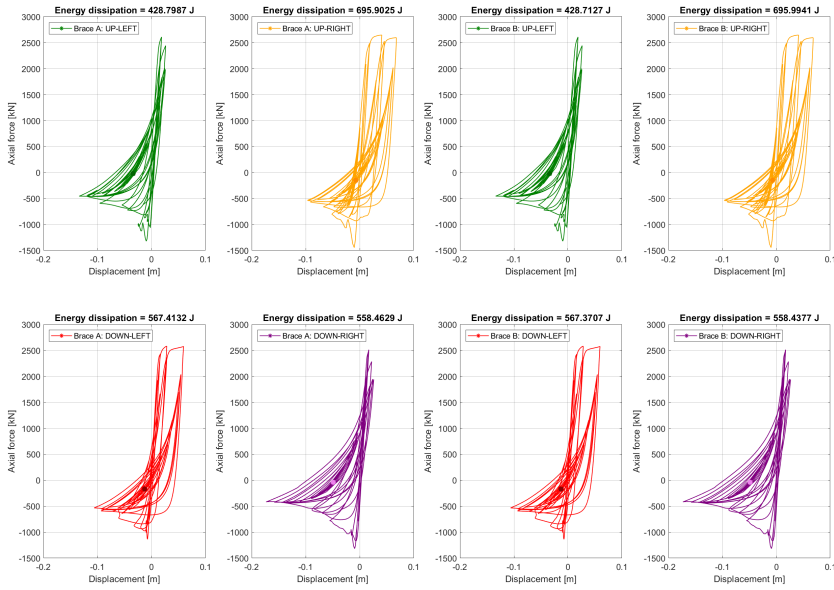

(a)

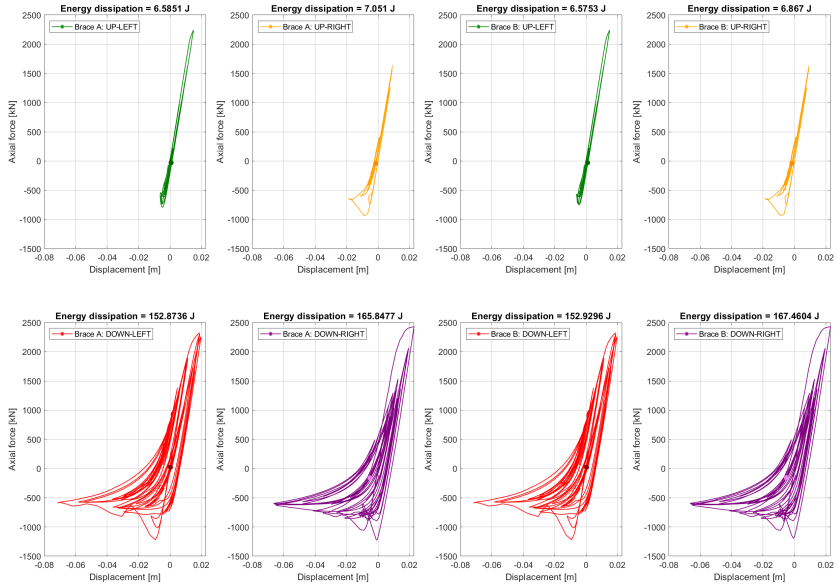

(b)

Figure 10.38: Energy dissipations of the braces: a) 4th and 3rd floors; b) 2nd and 1st floors.

Figure 10.39 presents the first stage results of the FFE decision tree algorithm. The acceleration of each floor exceeds the 0.7g threshold; instead, only the 4th, 5th, 6th, 7th and 8th floors exceed the 1% threshold in terms of inter-story drift ratio (IDR). Therefore the floors from 4th to 8th are candidates for ignition of a FFE.

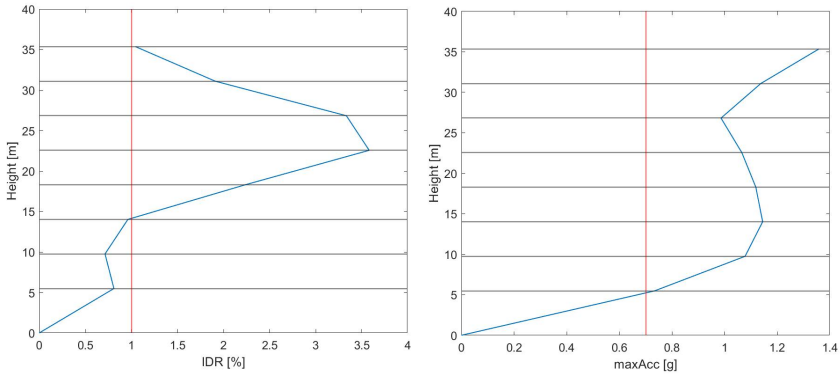

(a) *(b)*

Figure 10.39: First stage results of FFE decision tree algorithm: a) interstory drift ratio (IDR); b) maximum acceleration.

Figures 10.40, 10.41 and 10.42 present the second stage results of the FFE decision tree algorithm.

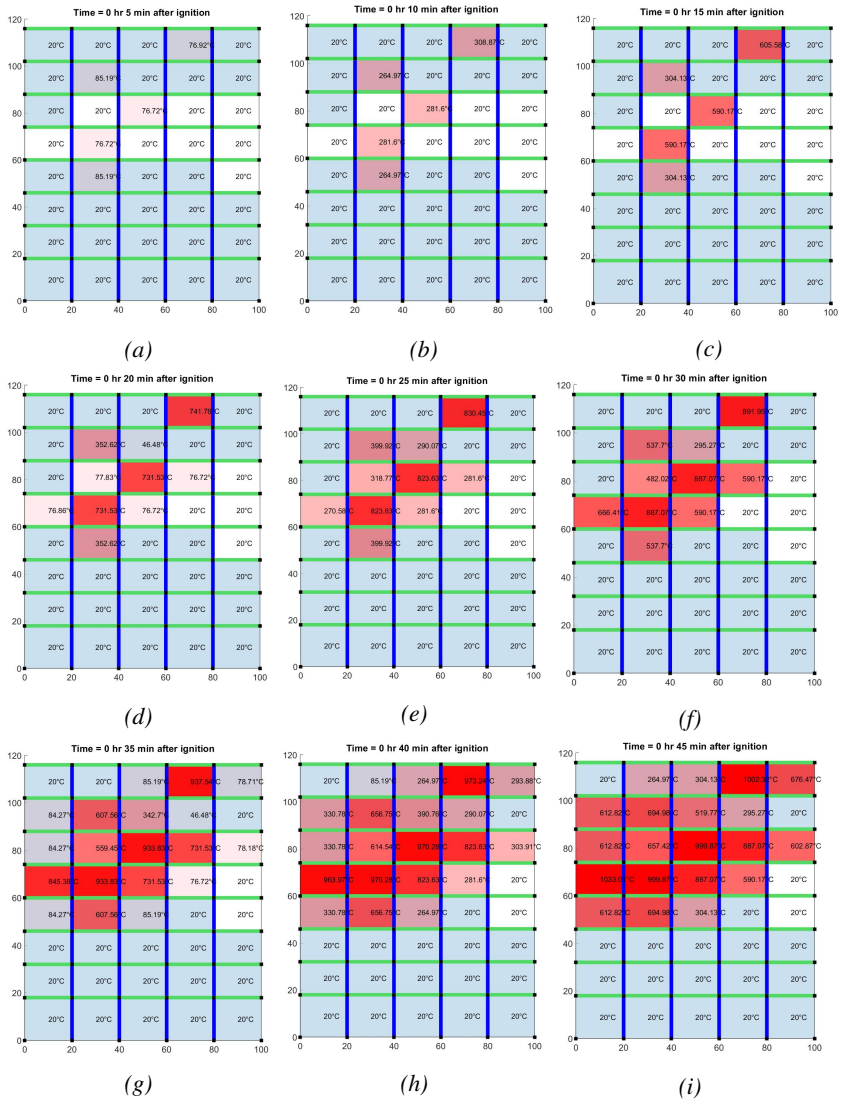

Figure 10.40: Evolution of the temperature in each compartments: a) 5 min; b) 10 min; c) 15 min; d) 20 min; e) 25 min; f) 30 min; g) 35 min; h) 40 min; i) 45 min after the ignition.

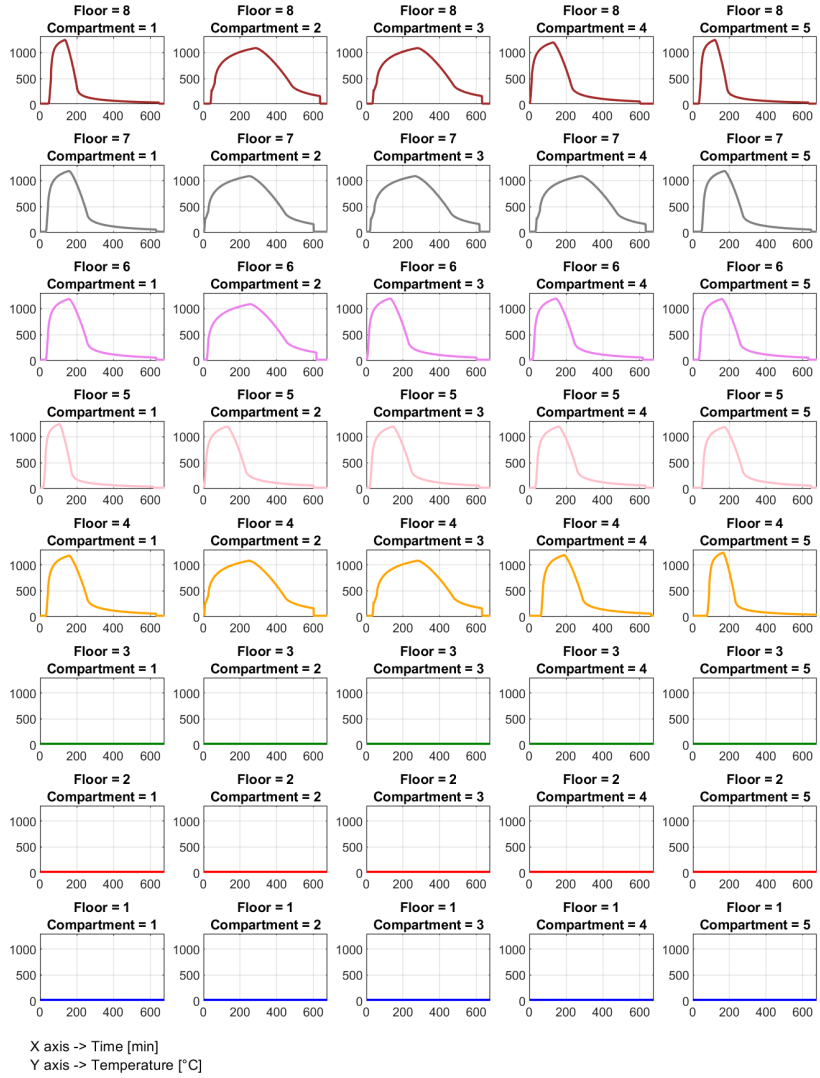

Figure 10.41: Evolution of the temperature inside the compartments.

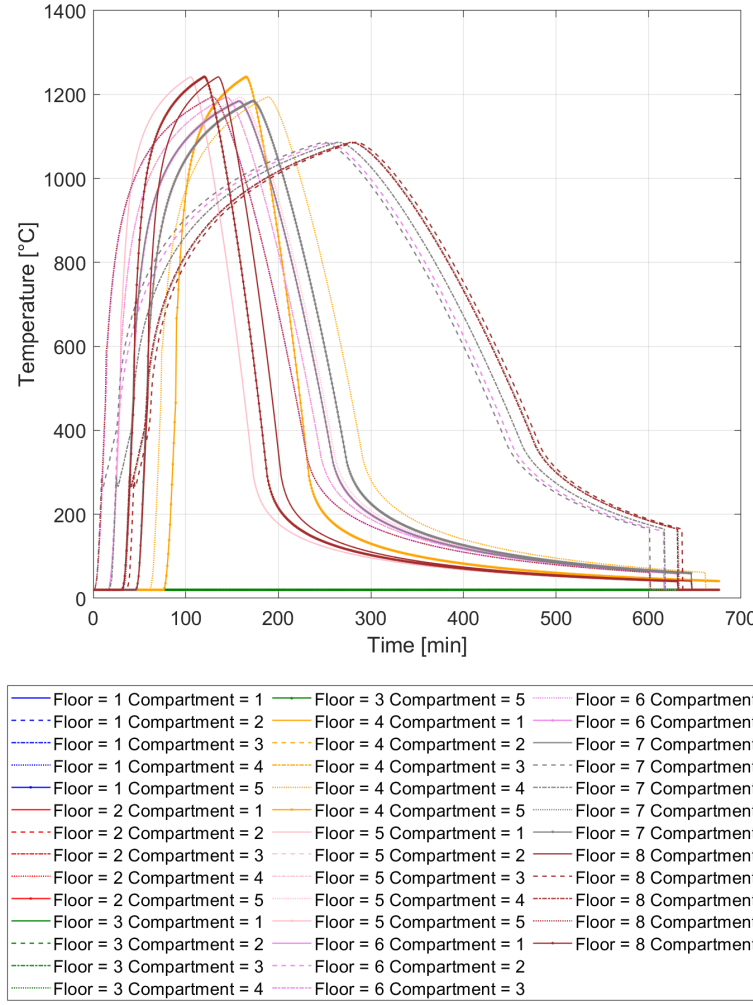

Figure 10.42: Evolution of the temperature inside the compartments.

Figure 10.43 illustrates the deflection of the beams and the horizontal displacement of the columns during the FFE.

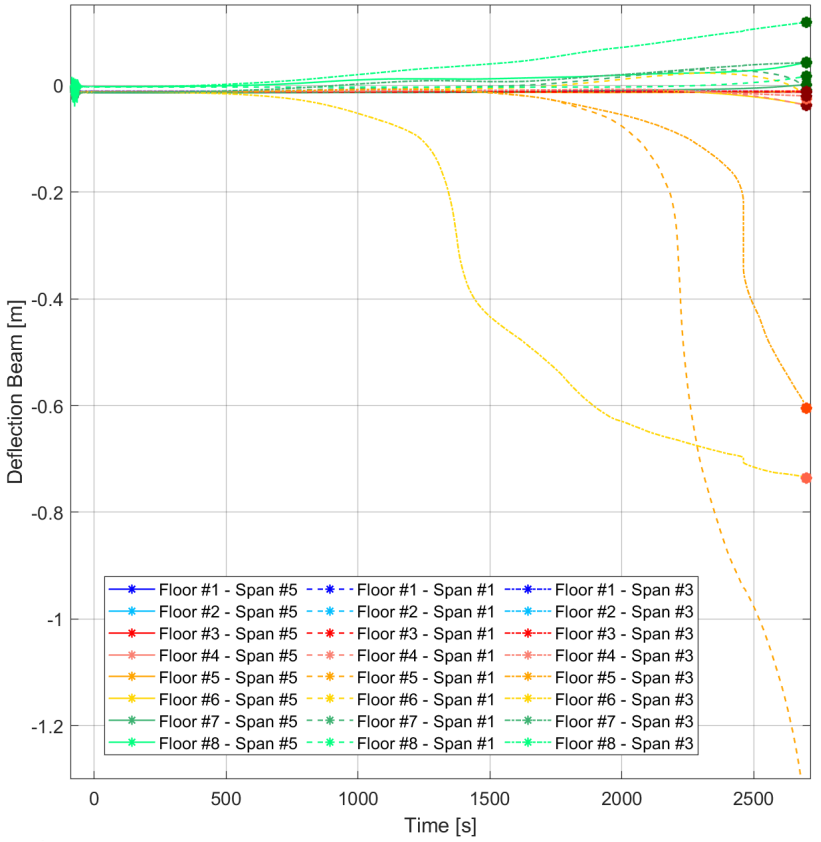

(a)

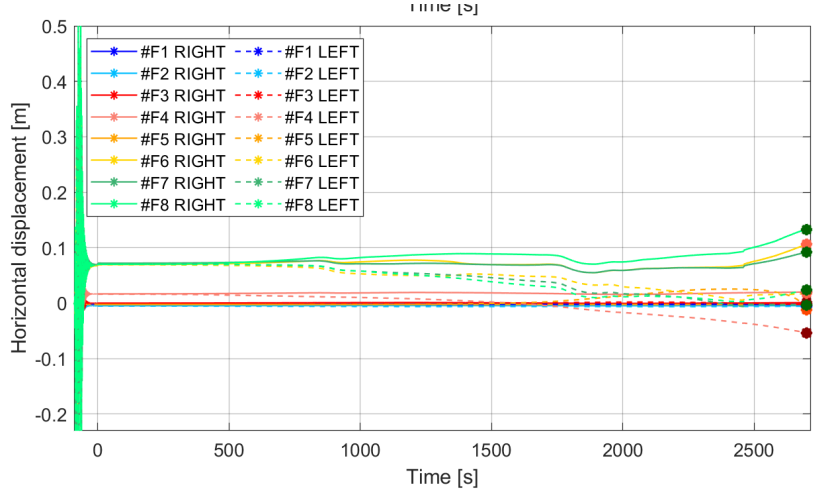

(b)

Figure 10.43: a) Beam deflection; b) Horizontal displacement of end columns at each floor.

Figure 10.44 also shows the final deformed configuration of the steel frame at the end of the FFE simulation.

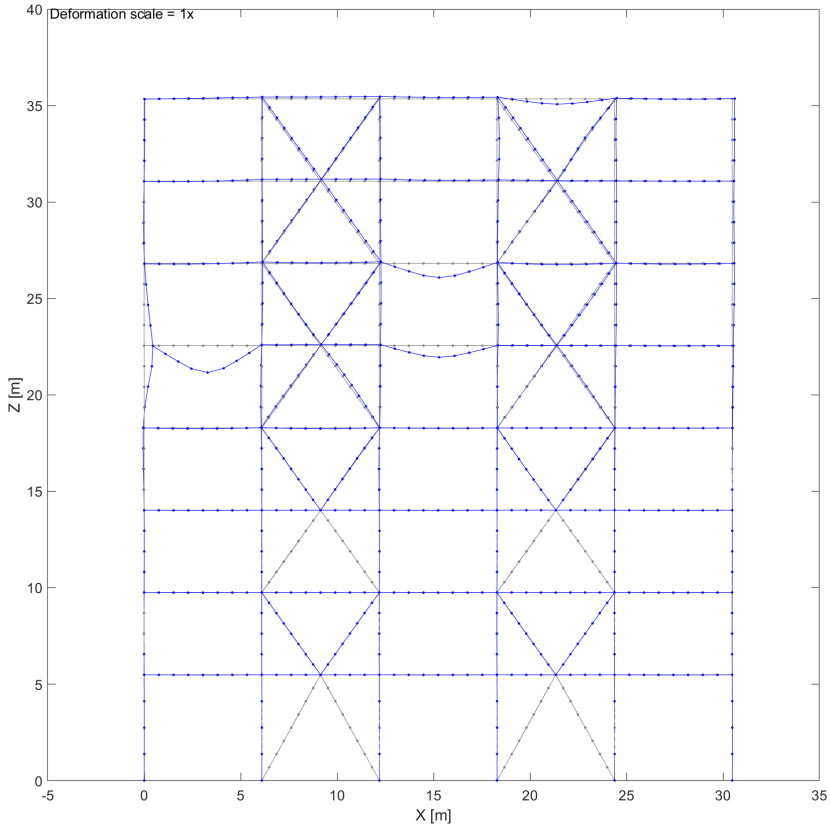

Figure 10.44: Deformed shape of the numerical model at the end of the FFE simulation.

10.7 Main outcomes and discussion

This chapter provides an improvement tool for probabilistic Fire Following Earthquake analysis using the available software OpenSees. The improvements regard the creation of a new uniaxial material for FFE analyses and a FFE decision tree algorithm. The SteelFFEThermal material class contains two materials, one based on the Giuffrè-Menegotto-pinto for the earthquake event and the other one a modified version of the Steel01Thermal in order to increase the computational speed and include the probabilistic model for temperature-dependent strength of steel for the fire part. A coordination module is also included in the material

to automatically choose the more appropriate module based on the temperature and without losing the plastic deformations. It is possible to observe an excellent degree of accuracy between the validation case studies using SteelFFEThermal and the reference solutions. The computational speed during the fire simulation is twice as fast as Steel01Thermal. The thermal analysis module is compared to a reference FE model of the same thermal section implemented in SAFIR. The results agree reasonably well with the reference solution. Based on the validations and the results of an eight-storey three-bay steel frame with concentric bracings in two central bays, the FFE framework presented in this chapter could be used for advanced probabilistic Fire Following Earthquake analyses in order to obtain fragility curves and fragility surfaces.

Bibliography

[1] F. McKenna, "Opensees: a framework for earthquake engineering simulation," *Computing in Science & Engineering*, vol. 13, no. 4, pp. 58–66, 2011.

[2] N. E. Khorasani, M. E. Garlock, and S. E. Quiel, "Modeling steel structures in opensees: Enhancements for fire and multi-hazard probabilistic analyses," *Computers & Structures*, vol. 157, pp. 218–231, 2015.

[3] M. Menegotto, "Method of analysis for cyclically loaded rc plane frames including changes in geometry and non-elastic behavior of elements under combined normal force and bending," in *Proc. of IABSE symposium on resistance and ultimate deformability of structures acted on by well defined repeated loads*, pp. 15–22, 1973.

[4] F. C. Filippou, E. P. Popov, and V. V. Bertero, "Effects of bond deterioration on hysteretic behavior of reinforced concrete joints," 1983.

[5] N. E. Khorasani, P. Gardoni, and M. Garlock, "Probabilistic fire analysis: material models and evaluation of steel structural members," *Journal of Structural Engineering*, vol. 141, no. 12, p. 04015050, 2015.

[6] CEN, "Eurocode 3: Design of steel structures - Part 1-2: General rules - Structural fire design," european standard, European Union, May 2005.

[7] R. Qureshi, S. Ni, N. Elhami Khorasani, R. Van Coile, D. Hopkin, and T. Gernay, "Probabilistic models for temperature-dependent strength of steel and concrete," *Journal of Structural Engineering*, vol. 146, no. 6, p. 04020102, 2020.

[8] M. Holickỳ and M. Sỳkora, "Stochastic models in analysis of structural reliability," in *Proceedings of the international symposium on stochastic models in reliability engineering, life sciences and operation management, Beer Sheva, Israel*, 2010.

[9] J. Ueno, S. Takada, Y. Ogawa, M. Matsumoto, S. Fujita, N. Hassani, and F. S. Ardakani, "Research and development on fragility of components for the gas distribution system in greater tehran, iran," *Conferene Proceedings, in Proc. 13th WCEE, Vancouver, BC Canada, Paper*, no. 193, 2004.

[10] B. FEMA, "Prestandard and commentary for the seismic rehabilitation of buildings," 2000.

[11] W. Gates and G. McGavin, "Lessons learned from the 1994 northridge earthquake on the vulnerability of nonstructural systems," in *Proceedings of the Seminar on Seismic Design, Retrofit, and Performance of Nonstructural Components, ATC*, vol. 29, pp. 93–106, 1998.

[12] J. TAYLOR, "Post earthquake fire in tall buildings and the new zealand building code," 2003.

[13] D. Brunsdon and W. Clark, *Modern multi-storey buildings and moderate earthquakes*. Business Continuance Planning Limited, 2000.

[14] C. Kircher, G. Deierlein, J. Hooper, H. Krawinkler, S. Mahin, B. Shing, and J. Wallace, "Evaluation of the fema p-695 methodology for quantification of building seismic performance factors," 2010.

[15] A. Memari, W. O'Brien, P. Kremer, and R. Behr, "Architectural glass seismic behavior fragility curve development," *Report No. FEMA P-58/BD-3.9*, vol. 2, 2011.

[16] J.-F. Cadorin and J.-M. Franssen, "A tool to design steel elements submitted to compartment fires—ozone v2. part 1: pre-and post-flashover compartment fire model," *Fire Safety Journal*, vol. 38, no. 5, pp. 395–427, 2003.

[17] J.-F. Cadorin, D. Pintea, J.-C. Dotreppe, and J.-M. Franssen, "A tool to design steel elements submitted to compartment fires—ozone v2. part 2: Methodology and application," *Fire safety journal*, vol. 38, no. 5, pp. 429–451, 2003.

[18] CEN, "Eurocode 3: Design of steel structures - Part 1-1: General rules and rules for buildings," european standard, European Union, May 2005.

[19] J. L. Harris and M. S. Speicher, "Assessment of first generation performance-based seismic design methods for new steel buildings volume 2: Special concentrically braced frames.(national institute of standards and technology, gaithersburg, md)," *NIST Technical Note*, vol. 2, pp. 1863–2, 1868.

11.0 Conclusions and future developments

11.1 Summary and Conclusions

Fires following earthquake can be ignited due to, for instance, failure of gas lines and of power lines. They can be a serious problem, especially if the water lines that feed the fire hydrants are broken too and the infrastructural network has undergone significant disruptions.

Large-scale tests of an entire structure are generally prohibitively expensive, both in terms of finances and time. Therefore it is convenient to adopt a Hybrid testing methodology that combines physical testing and computer modelling, offering a more efficient and affordable way to examine how large civil structures respond. Therefore, a MATLAB™ framework for partitioned analyses and the Real-Time Hybrid Fire Simulation (RT-HFS) algorithm is presented. In detail, a RT-HFS algorithm for thermomechanical coupled analysis for hybrid dynamic simulations is presented in Chapter 4 and Chapter 5. The effectiveness of the proposed method is demonstrated using two purely numerical virtual experimental simulations of the proposed RT-HFS method.

The first virtual experimental, presented in Chapter 4, regards the response of a realistic steel moment-resisting frame subject to fire at the ground and first floor. The second virtual experimental, presented in Chapter 5, regards the case study selected in the EQUFIRE project. In detail, a four-story three-bay steel frame with concentric bracing in the central bay was selected.

The obtained responses of the two case studies are validated against reference nonlinear static response analyses of the same frames and fires performed using the SAFIR FE software. The time-history responses of the frames obtained via real-time simulations showed good agreement between the monolithic and the partitioned solutions. The validation carried out in a fully numerical framework shows promising outcomes for future experimental implementations.

The EQUFIRE project focused on a three-bay, four-storey steel frame with concentric bracing in the central span, designed in Chapter 3 and subjected to fire following an earthquake, with the aim to study the performance of structural and non-structural components. Five preliminary FFE substructure tests were carried out at the BAM laboratory. Tests for fire after earthquake were carried out on two steel columns without fire protection and three columns with different fire protection so-

lutions: conventional and earthquake-proof boards system and gypsum-based wet mix spray-applied fire-resistive material. In terms of fire protection, no serious damage was observed that would undermine the fire resistance of the columns.

Chapter 7 presented part of the results of an experimental and numerical FFE analysis on a braced steel frame and in particular on columns belonging to the bracing system. The numerical model developed in OpenSees was able to perform highly non-linear multi-hazard analyses and it served to design the FFE tests. The numerical model developed in SAFIR was able to perform only the fire analyses. Model calibration was performed with beam finite elements that exhibited good agreement but also failure. The actual rotational stiffness may cause this latter discrepancy at the boundary conditions, which might have varied as the fire test progressed.

Chapter 8 presented the main results of an experimental and numerical FFE analysis on a braced steel frame. Several Hybrid seismic tests were carried out on one steel frame without fire protection and three frames with different fire protection solutions: conventional and earthquake-proof boards system and gypsum-based wet mix spray-applied fire-resistive material. In terms of fire protection, no serious damage was observed that would undermine the fire resistance of the columns or braces. The results presented in this chapter showed the effectiveness of the dynamic Substructuring and Time Integration Procedure for the Hybrid Simulation of the Seismic Response of the EQUFIRE frame both in the experimental tests and in the virtual Hybrid earthquake simulation. Hybrid fire and seismic simulation emerged as a viable solution for performing component level experiments that account for the interaction between the tested specimen and a realistic yet virtual subassembly instantiated in a finite-element software.

Chapter 9 presented part of the results of an experimental and numerical FFE analysis on a braced steel frame. The advanced numerical model developed in OpenSees was able to perform highly non-linear multi-hazard analyses and it served to design the FFE tests. Model calibration was performed with finite beam elements that exhibited good agreement.

Chapter 10 presented a framework for structures subjected to fire following earthquake based on a modified version of the OpenSees software and several scripts developed in MATLAB in order to perform probabilistic analysis of structures subjected to FFE. A new material class was created. The SteelFFEThermal material has the same basic expression as the Giuffrè-Menegotto-Pinto uniaxial Steel Stress-Strain model. When the temperature of an element starts increasing, the ma-

terial class switches the constitutive law from the Giuffrè-Menegotto-Pinto model to the constitutive law provided by EN 1993-1-2 for steel at elevated temperature. The fire scenario is automatically chosen based on the earthquake analysis results using a FFE decision tree algorithm. As an example, this framework is used to evaluate the performance of an 8-story steel bracing office building under fire following earthquake events. Based on the validations and the example results, the FFE framework developed could be used for advanced probabilistic Fire Following Earthquake analyses to obtain fragility curves and fragility surfaces.

11.2 Future developments

The work presented in can be extended by widening the capabilities of Hybrid testing presented in Chapter 4, 5 and 8.5. In detail, the RT-HFS and the HFE could be merged and modified in order to perform a full real FFE using geographically distributed hybrid testing. The concept of geographically distributed testing is that individual substructures do not need to be within the same facility and do not need to be in the same laboratory but can be linked by data transfer methods with minimal latency between the laboratories, like RTC (Real-Time Communications).

Fires following earthquake (FFE) have historically produced enormous post-earthquake damage and losses in terms of lives, buildings and economic costs, like the San Francisco earthquake (1906), the Kobe earthquake (1995), the Turkey earthquake (2011), the Tohoku earthquake (2011) and the Christchurch earthquakes (2011). The structural fire performance can worsen significantly because the fire acts on a structure damaged by the seismic event. On these premises, the purpose of this work is the investigation of the experimental and numerical response of structural and non-structural components of steel structures subjected to fire following earthquake (FFE) to increase the knowledge and provide a robust framework for hybrid fire testing and hybrid fire following earthquake testing. A partitioned algorithm to test a real case study with substructuring techniques was developed. The framework is developed in MATLAB and it is also based on the implementation of nonlinear finite elements to model the effects of earthquake forces and post-earthquake effects such as fire and thermal loads on structures. These elements should be able to capture geometrical and mechanical non-linearities to deal with large displacements. Two numerical validation procedures of the partitioned algorithm simulating two virtual hybrid fire testing and one virtual hybrid seismic testing were carried out. Two sets of experimental tests in two different laboratories were performed to provide valuable data for the calibration and comparison of numerical finite element case studies reproducing the conditions used in the tests. Another goal of this thesis is to develop a fire following earthquake numerical framework based on a modified version of the OpenSees software and several scripts developed in MATLAB to perform probabilistic analyses of structures subjected to FFE. A new material class, namely SteelFFEThermal, was implemented to simulate the steel behaviour subjected to FFE events.

Patrick Covi